THE PHYSICAL REVIEW

VOLUME 95 NUMBER 4

AUGUST 15, 1954

OF THE

AMERICAN PHYSICAL SOCIETY

THE
PHYSICAL REVIEW

A journal of experimental and theoretical physics established by E. L. Nichols in 1893

SECOND SERIES, VOL. 95, NO. 4 AUGUST 15, 1954

On the Theory of Liquid He^3-He^4 Mixtures*

LOUIS GOLDSTEIN
University of California, Los Alamos, Scientific Laboratory, Los Alamos, New Mexico
(Received November 9, 1953)

An asymptotic theory of liquid He^3-He^4 mixtures is presented, in which the component fluids are described, approximately, in terms of ideal symmetric and antisymmetric fluids. The theory yields results in at least semiqualitative agreement with the data if the antisymmetric fluid is taken to be of negligible degeneracy. The computed isothermal mixing energies and entropies are good approximations to the preliminary data on these quantities obtained in this Laboratory. The present model exhibits complete miscibility at all temperatures together with a vanishing total and mixing entropies, in all possible mixtures, at the approach of the absolute zero. It is shown that the mixtures undergo third-order phase changes along their transition line, where their constant-volume and constant-pressure heat capacities have sharp peaks, with lambda-point type discontinuities of their temperature derivatives. On mixing the ideal symmetric fluid with an ideal antisymmetric or classical fluid the original first-order phase change of the former, as a result of its momentum space condensation, has thus been modified.

The theory requires that, below the phase transition line of the mixtures, the momentum space condensed and uncondensed atom groupings be such that the latter group should include all the He^3 atoms. As a result, the observed modifications in the velocities of propagation of second sound waves from their values in pure liquid He II are automatically accounted for. The theory also accounts, in this way, for the large observed changes in the second sound wave field tensions in mixtures from their values in pure liquid He^4. It also explains the decrease observed in this Laboratory of the He^4 film-flow rates in mixtures as compared with the rates in liquid He^4, if this rate is taken to be proportional to the fraction of condensed atoms.

The paper ends with a brief discussion of the transition surface of mixtures in the pressure-temperature-He^3 mole fraction affine space. Here the likelihood of a further depression of mixture phase transformation temperatures by application of external pressure is pointed out. Finally, the apparent analogies between the perturbations of the phase transformation of liquid He^4 by external pressure and by mixing it with liquid He^3 are briefly reviewed.

INTRODUCTION

THE experimental investigations of the mutual perturbations of liquid He^3 and He^4, while still in a somewhat preliminary stage, appear to be of great interest in supplying, eventually, important information for a better understanding of the properties of these liquids. In view of the rather fragmentary status of the theory of these liquids, it seems justified to consider the behavior of mixtures of their respective asymptotic models, ideal or almost ideal Bose-Einstein (B.E.) and Fermi-Dirac (F.D.) fluids. These fluid models should describe completely the properties of these liquids under conditions wherein the ordinary interatomic interactions could be compensated for or actually switched off by some mechanism. Clearly, such mixtures of ideal or almost ideal quantum fluids cannot be expected to represent correctly the actual liquid He^3-He^4 mixtures, since the overall properties of the component liquids themselves cannot be accounted for, in a satisfactory way, by these asymptotic ideal fluids. It is to be noted, though, in this connection that neither in liquid He^4 nor in liquid He^3 can one presently rule out the explicit asymptotic intervention of symmetric and antisymmetric statistics, over most of the temperature range, in determining some of their macroscopic properties. On the contrary, the condensation in momentum space of the ideal B.E. fluid, together with its perturbation by mixing it with an essentially ideal classical or F.D. fluid, provides so far the most elementary semiquantitative description of the remarkable transitions exhibited by the pure liquid He^4 or its mixtures with liquid He^3. The pure liquid and its mixtures are herein in equilibrium with their respective vapor phases. To be sure, the details of the formalism of ideal or slightly modified B.E. fluids cannot be accepted in attempting to describe the overall behavior of liquid He^4. In the case of liquid He^3, where the data are rather scarce, no simple fact has as yet emerged to indicate any degree of degeneration

* Some of the results obtained in this paper have been given in an abstract of the Rochester, New York, meeting of the American Physical Society [Phys. Rev. **92**, 850 (1953)].

resulting from antisymmetric statistics, at least at temperatures larger than about 1.0°K.[1]

We have studied the properties of liquid He^3-He^4 mixtures, with the essentially asymptotic validity of the ideal quantum fluid models kept in mind. Beside the necessary limitations of any asymptotic theory we have discarded here the problems connected with the mixing processes. We will thus limit ourselves to the study of equilibrium conditions, i.e., reversible processes. More exactly, in those processes which occur in an irreversible way, only states associated with statistical equilibrium will be considered. It may be noted in this connection that if the superfluid He^4 atoms were to flow alone in a very narrow channel, the so-called "semipermeable channel," the mixing of liquid He^3 and He^4 may approach the limiting reversible process.[2]

The possibilities for experimental investigations of the equilibrium properties of mixtures of the two symmetric isotopes, He^4 and He^6, the latter considered to be also a liquid over a wide temperature range overlapping the liquid region of He^4, appear to be remote with practicable He^6 concentrations. The major part of this paper will thus be devoted to a study of mixtures of an ideal symmetric and an ideal antisymmetric fluid. A mean constant potential energy per atom, smeared over the whole volume of the fluid, does not change the formalism of the separated fluids. On mixing, additional assumptions would, however, be necessary in the choice of such a mean potential energy, and this did not seem to be warranted in the present asymptotic theory. Hence, no explicit use will be made of such binding potential energies. The theory also has limitations in its validity over the lower end of the temperature range of the mixtures, i.e., at temperatures low in comparison with their transition temperatures, where a solid type of ordering process could occur as in pure liquid He^4, i.e., through the occurrence of a Debye type of heat capacity.

In connection with the theory of ideal symmetric and antisymmetric fluid mixtures, we will study briefly their elementary reversible hydrodynamic properties such as the velocity of propagation of the temperature or second sound waves and the stresses exerted by the second sound radiation field on a Rayleigh disk. Some of the semi-empirical features of the He^4 component will hereby be used. Similarly the transition surface of these mixtures will be discussed briefly in the space of the variables such as pressure, He^3 mole fraction and transition temperature. The object of this discussion will be mainly to compare the effect of He^3 admixture to that of applying external pressure on pure liquid He^4 in lowering the normal transition temperature of He^4.

[1] The lack of degeneracy of liquid He^3 in the range 1.2–2.8°K has been experimentally demonstrated by Fairbank, Ard, Dehmelt, Gordy, and Williams, Phys. Rev. **92**, 208 (1953), by observing the T^{-1} variation of the molar paramagnetic susceptibility, due to the He^3 nuclei.

[2] H. London, Proceedings of the Low Temperature Physics Conference (Oxford, 1951), p. 157.

I. THE MOMENTUM SPACE CONDENSATION OF MIXTURES OF IDEAL SYMMETRIC AND ANTISYMMETRIC FLUIDS

Let us assume that N_s ideal symmetric (s) point atoms occupying volume V_s with an average volume per atom v_s, and N_a ideal antisymmetric (a) point atoms in a volume V_a with an average volume per atom v_a, are mixed and occupy after mixing, a volume[3]

$$\begin{aligned}\bar{V}&=V_a+V_s+\delta\bar{V}\\&=N_a v_a+N_s v_s+(N_a+N_s)\delta\bar{v},\end{aligned}\tag{1.1}$$

$\delta\bar{V}$ denoting a possible change in volume on mixing as a result of the actual interatomic interactions between the two types of atoms. In the absence of the latter, $\delta\bar{V}$ vanishes identically. Moreover, one has to have

$$\lim_{N_a \text{ or } N_s\to 0}\delta\bar{V}\to 0.$$

It is of interest to consider some slight interaction which under certain conditions could be taken to be so small as to have no first-order effect on the properties of the system under discussion. Let then $g_{s\lambda}, \bar{n}_{s\lambda}, g_{a\mu}, \bar{n}_{a\mu}(\lambda, \mu=1, 2, \cdots)$ denote the degeneracies and occupation numbers of the states λ, μ of the s and a atoms in volume $\bar{V}$. The probability of the preceding distribution is then, in a first approximation,

$$\bar{P}(g_{s\lambda},\bar{n}_{s\lambda};g_{a\mu},\bar{n}_{a\mu})=\bar{P}_s(g_{s\lambda},\bar{n}_{s\lambda})\bar{P}_a(g_{a\mu},\bar{n}_{a\mu}),\tag{1.2}$$

$\bar{P}_s$ and $\bar{P}_a$ being associated with the symmetric and antisymmetric fluid atoms, respectively. The condition of maximum probability is then given by the extremum condition,

$$\begin{aligned}\delta\log\bar{P}&=\delta\log\bar{P}_s+\delta\log\bar{P}_a\\&=\sum\frac{\partial\log\bar{P}_s}{\partial\bar{n}_s}d\bar{n}_{s\lambda}+\sum\frac{\partial\log\bar{P}_a}{\partial\bar{n}_a}d\bar{n}_{a\mu}=0,\end{aligned}\tag{1.3}$$

with the subsidiary conditions,

$$\begin{aligned}&\delta N_s=\textstyle\sum\delta\bar{n}_{s\lambda}=0,\quad \delta N_a=\sum_\mu\delta\bar{n}_{a\mu}=0,\\&\delta\bar{E}=\textstyle\sum_\lambda\bar{\epsilon}_\lambda\delta\bar{n}_{s\lambda}+\sum_\mu\bar{\epsilon}_\mu\delta\bar{n}_{a\mu}=0,\end{aligned}\tag{1.4}$$

$\bar{E}$ being the total energy of the system in the above state and the $\bar{\epsilon}_\nu$'s the free particle energy levels in volume $\bar{V}$. With the undetermined multipliers $\bar{\alpha}_s$ and $\bar{\alpha}_a$ of δN_s and δN_a, and the multiplier β of $\delta\bar{E}$, one obtains at once the extremum condition,

$$\begin{aligned}&\sum_\lambda\left(\frac{\partial\log\bar{P}_s}{\partial\bar{n}_{s\lambda}}-\bar{\alpha}_s-\beta\bar{\epsilon}_\lambda\right)\delta\bar{n}_{s\lambda}\\&\qquad+\sum_\mu\left(\frac{\delta\log\bar{P}_a}{\partial\bar{n}_{a\mu}}-\bar{\alpha}_a-\beta\bar{\epsilon}_\mu\right)\delta\bar{n}_{a\mu}=0.\end{aligned}\tag{1.5}$$

[3] All symbols with a bar such as $\bar{V}$, $\bar{p}$, etc., will be reserved to denote properties of the mixtures, unless stated otherwise.

In the limit of vanishingly small interactions between the s and a atoms, themselves, the $\delta\bar{n}_{s\lambda}$'s and $\delta\bar{n}_{a\mu}$'s are independent. One obtains then, with

$$\bar{P}_s=\prod_\lambda \frac{(\bar{n}_{s\lambda}+g_{s\lambda}-1)!}{\bar{n}_{s\lambda}!(g_{s\lambda}-1)!}\Big/\frac{(N_s+\bar{G}_s-1)!}{N_s!(\bar{G}_s-1)!},$$

and

$$\bar{P}_a=\prod_\mu \frac{g_{a\mu}!}{\bar{n}_{a\mu}!(g_{a\mu}-\bar{n}_{a\mu})!}\Big/\frac{\bar{G}_a!}{N_a!(\bar{G}_a-N_a)!},$$

$$N_s=\textstyle\sum_\lambda \bar{n}_{s\lambda},\quad \bar{G}_s=\sum_\lambda g_{s\lambda},\quad N_a=\sum_\mu \bar{n}_{a\mu};\quad \bar{G}_a=\sum g_{a\mu},$$

the distribution laws of the mixture, as

$$\begin{aligned}\bar{n}_{s\lambda}/g_{s\lambda}&=[\exp(\bar{\alpha}_s+\beta\bar{\epsilon}_\lambda)-1]^{-1},\\ \bar{n}_{a\mu}/g_{a\mu}&=[\exp(\bar{\alpha}_a+\beta\bar{\epsilon}_\mu)+1]^{-1}.\end{aligned}\tag{1.6}$$

The determination of the parameter β proceeds as in the case of the separated fluids, i.e., this parameter has the value $1/kT$, k being Boltzmann's constant. The values of the characteristic parameters $\bar{\alpha}_s$ and $\bar{\alpha}_a$ are, in turn, determined by the total number of atoms N_s and N_a. With the asymptotic free particle energy level spectrum in volume $\bar{V}$, one obtains

$$\begin{aligned}1&=(\bar{V}/N_s)g_s(2\pi m_s kT/h^2)^{\frac{3}{2}}F_s(\bar{\alpha}_s),\quad 0\leqslant\bar{\alpha}_s\leqslant\infty,\\ 1&=(\bar{V}/N_a)g_a(2\pi m_a kT/h^2)^{\frac{3}{2}}F_a(\bar{\alpha}_a),\qquad -\infty\leqslant\bar{\alpha}_a\leqslant\infty.\end{aligned}\tag{1.7}$$

Here g_s and g_a refer to the spin degeneracies alone, m_s and m_a are the masses of the symmetric and antisymmetric atoms, and

$$\begin{aligned}F_s(x)&=\sum_1^\infty n^{-\frac{3}{2}}\exp(-nx);\quad F_s(0)=\zeta(3/2)=2.612,\\ F_a(x)&=\sum_1^\infty(-)^{n-1}n^{-\frac{3}{2}}\exp(-nx);\\ &\qquad F_a(0)=(1-2^{-\frac{3}{2}})F_s(0).\end{aligned}\tag{1.8}$$

As a result of the volume condition (1.1), the two ideal fluids of the mixture cease to be independent.

A repetition of the reasoning on the momentum space condensation of the pure ideal symmetric fluid in our case of mixtures shows, using the first of Eqs. (1.7), that the symmetric component starts condensing in momentum space at a temperature

$$\begin{aligned}\bar{T}_s(x)&=(h^2/2\pi m_s k)[N_s/g_sF_s(0)\bar{V}]^{\frac{2}{3}}\\ &=\left(\frac{h^2}{2\pi m_s k}\right)\left(\frac{1}{F_s(0)g_s\bar{v}_s}\right)^{\frac{2}{3}}\\ &\quad\times\left\{(1-x)\Big/\left[1+x\left(\frac{\bar{v}_a}{\bar{v}_s}-1\right)+\frac{\delta\bar{v}}{\bar{v}_s}\right]\right\}^{\frac{2}{3}}\\ &=T_s(0)\left\{(1-x)\Big/\left[1+x\left(\frac{\bar{v}_a}{\bar{v}_s}-1\right)+\frac{\delta\bar{v}}{\bar{v}_s}\right]\right\}^{\frac{2}{3}},\end{aligned}\tag{1.9}$$

where $T_s(0)$ is the pure symmetric fluid condensation temperature at the volume per atom v_s, while x is the mole fraction of the antisymmetric component, *viz.*,

$$x=N_a/(N_a+N_s).\tag{1.10}$$

If the small interaction between the a and s atoms is completely neglected by assuming that $\delta\bar{v}\to 0$, then (1.9) reduces to the form given previously by Heer and Daunt.[4] Physically the decrease of the mixture condensation temperature is associated with the decrease in the strength of the attractive statistical forces, which exist between the atoms of ideal symmetric fluids, as a result of the decrease of their concentration from n_s or (N_s/V_s) to $\bar{n}_s$ or $(N_s/\bar{V})$. On the present model, the condensation temperatures form the locus

$$\bar{T}_s(x)[\bar{v}_s(x)]^{\frac{2}{3}}=\bar{T}_s(x)/[\bar{n}_s(x)]^{\frac{2}{3}}=\text{const},\tag{1.11}$$

in the temperature-volume diagram of these mixtures.

One of the arguments tending to justify the application of the present asymptotic model to an approximate description of liquid He^3-He^4 mixtures lies in the possibility that the λ transitions in pure liquid He^4 or those of the mixtures are connected with the momentum space condensation of the He^4 atoms. With this in mind, it seems necessary to discuss the volume condition (1.1) in the light of recent accurate measurements[5] of λ temperatures of mixtures at small He^3-mole fraction values, i.e., at $x\ll 1$.

As mentioned above, apropos of (1.1), the mean volume increase $\delta\bar{v}$ is such that $\lim_{x\to 0}\delta\bar{v}\to 0$. Hence, from (1.9),

$$\begin{aligned}\lim_{x\to 0}\frac{d}{dx}&[\bar{T}_s(x)/T_s(0)]\\ &=-\frac{2}{3}\left[\left(\frac{\bar{v}_a}{\bar{v}_s}\right)+\frac{1}{\bar{v}_s}\left(\frac{d\delta\bar{v}}{dx}\right)_{x=0}\right]_{T_s(0)}\end{aligned}\tag{1.12}$$

which shows that the negative slope of the transition line in the (T,x) plane, in the limit of vanishing x, is rather large,[5] since $d\delta\bar{v}/dx>0$ because of the experimentally observed[6] positive isothermal mixing energy of these mixtures and because[7] of $\bar{v}_a/\bar{v}_s\sim 1.4$. It is only by introducing a volume contraction on mixing that it would be possible to obtain slopes comparable to the ones observed.[5] Such an assumption would be difficult if not impossible to reconcile with the positive mixing energies.

It is thus seen that while the momentum space condensation of the symmetric atoms supplies a good qualitative picture for the observed depression of the λ temperatures of liquid He^3-He^4 mixtures, the details

[4] C. V. Heer and J. G. Daunt, Phys. Rev. **81**, 447 (1951); J. G. Daunt, Phil. Mag. Supplement **1**, 209 (1952).

[5] J. C. King and H. A. Fairbank, Phys. Rev. **91**, 489 (1953).

[6] Sommers, Keller, and Dash, Phys. Rev. **91**, 489 (1953) and Phys. Rev. **92**, 1345 (1953); H. S. Sommers, Phys. Rev. **88**, 113 (1952).

[7] Grilly, Hammel, and Sydoriak, Phys. Rev. **75**, 1103 (1949).

of the process are not described quantitatively by the theory.

We shall, henceforth, neglect the volume change $\delta\bar{v}$ and write for the condensation temperatures of mixtures

$$\frac{\bar{T}_s(x)}{T_s(0)}=\left\{(1-x)\Big/\left[1+x\left(\frac{v_a}{v_s}-1\right)\right]\right\}^{\frac{2}{3}}. \quad (1.13)$$

Actually (v_a/v_s) is somewhat temperature dependent so that, strictly speaking, the preceding equation is only an approximation even if the volume change on mixing is neglected. One can, however, escape this difficulty by simply considering the $x[\bar{T}_s/T_s(0)]$ function rather than its inverse (1.13). One has thus, at any temperature $T\leqslant T_s(0)$, a unique critical mole fraction x_c of the antisymmetric atoms, or

$$x_c=(1-\tau^{\frac{3}{2}})\Big/\left[1+\tau^{\frac{3}{2}}\left(\frac{v_a(\tau)}{v_s(\tau)}-1\right)\right], \qquad \tau=T/T_s(0). \quad (1.14)$$

Hence,

$$(dx_c/d\tau)_{\tau=1}=-\tfrac{3}{2}(v_s/v_a)_{\tau=1}; \quad (dx_c/d\tau)_{\tau=0}=0,$$

the first of which differs considerably from the observed slope[5] in the vicinity of $\tau=1$, as mentioned above.

In the (x,τ) plane, the physically accessible region of the mixtures is thus the strip $(0\leqslant x\leqslant 1, 0\leqslant\tau\leqslant\infty)$, which is divided into the superfluid and normal regions by the $x_c(\tau)$ transition line. The transitions leading from any point (x,τ) of one of the regions to a point (x',τ') of the other region are assigned to definite paths in this plane. The paths associated with $x=$ const, $v=$ const, or $x=$ const, $p=$ const, i.e., the constant mole fraction-constant volume or constant mole fraction-constant pressure paths are of particular interest in helping to define the nature of the transformations occurring in crossing the transition line.

The over-all properties of the antisymmetric component of the mixture are governed by the temperature ratios $T/\bar{T}_a(x)$, $k\bar{T}_a(x)$ being the degeneration energy of this component at the absolute zero. With the volume condition

$$\bar{V}=N_s v_s+N_a v_a, \quad (1.15)$$

the degeneration temperature of the a component is

$$[\bar{T}_a(x)/T_a(1)]^{\frac{2}{3}}=[\tau_a(x)]^{\frac{2}{3}}=\frac{xv_a(\bar{T}_a)}{v_s(\bar{T}_a)}\Big/\left[1+x\left(\frac{v_a(\bar{T}_a)}{v_s(\bar{T}_a)}-1\right)\right], \quad (1.16)$$

$$T_a(1)=(\hbar^2/2m_a k)[\Gamma(5/2)/g_a v_a]^{\frac{2}{3}}.$$

Or, the degeneration line of the a component is, in the $[x,\tau_a=T/T_a(1)]$ plane,

$$x_c(\tau_a)=\tau_a^{\frac{3}{2}}\Big/\left[\frac{v_a(T)}{v_s(T)}-\tau_a^{\frac{3}{2}}\left(\frac{v_a}{v_s}-1\right)\right]. \quad (1.17)$$

In the (x,T) plane, the preceding line is only of academic interest insofar as the properties of the antisymmetric component change in an entirely continuous way when the degeneration line is crossed. This line has a trend opposite to that of the transition of the symmetric component, since the degeneration temperature vanishes in the limit $x\to 0$, and reaches the pure antisymmetric fluid degeneration temperature in the limit $x\to 1$. It will, however, be seen below that in order to obtain results qualitatively comparable with the rather scarce data on some of the properties of liquid He^3-He^4 mixtures, the degeneration of the a component will have to be taken small or negligible at temperatures $T\gtrsim 1.0°K$.

II. STATISTICAL THERMODYNAMICS OF THE MIXTURE

II. 1. Mixing Energies

Since both components of the mixture possess characteristic degeneration temperatures, the system is expected to behave in different ways in different temperature regions. First of all, the mixtures can be divided into two groups according as $\bar{T}_s(x)\geqslant\bar{T}_a(x)$ or $\bar{T}_s(x)\leqslant\bar{T}_a(x)$. In the first group, the transition of the symmetric component occurs at a temperature higher than the degeneration temperature of the a component. This behavior is expected in mixtures rich in the symmetric fluid component and this group may be called the S group. In mixtures rich in the antisymmetric fluid component, A group, the opposite behavior would prevail. The different temperature regions of the S and A mixtures, with their respective symbols, are

$$T<\bar{T}_a,(--); \quad \bar{T}_a\leqslant T\leqslant\bar{T}_s,(-+); \quad T\geqslant\bar{T}_s,(++); \quad (S),$$

$$T\leqslant\bar{T}_s(--); \quad \bar{T}_s\leqslant T\leqslant\bar{T}_a(+-); \quad T\geqslant T_a(++); \quad (A),$$

the first sign in these notations being associated with the s component.

Using the formalism of the ideal fluids, the total energy of the S mixtures, in volume $\bar{V}$ at temperature T is

$$\bar{E}_{++}(\bar{V},T)_S=\bar{E}_{s+}(\bar{V},T)+\bar{E}_{a+}(\bar{V},T)=\tfrac{3}{2}kT[N_s G_s(\bar{\alpha}_s)/F_s(\bar{\alpha}_s)+N_a G_a(\bar{\alpha}_a)/F_a(\bar{\alpha}_a)], \quad (2.1)$$

$$G_s(x)=\sum_1^\infty n^{-5/2}\exp(-nx);$$

$$G_s(0)=\zeta(5/2)=1.341;$$

$$G_a(x)=\sum_1^\infty(-)^{n-1}n^{-5/2}\exp(-nx), \quad (2.2)$$

$$G_a(0)=(1-2^{-\frac{3}{2}})G_s(0)=0.8669,$$

the parameters $\bar{\alpha}_s$ and $\bar{\alpha}_a$ being given by (1.7). In the lower temperature range $(-+)$,

$$\bar{E}_{-+}(\bar{V},T)_S=\bar{E}_{s-}(\bar{V},T)+\bar{E}_{a+}(\bar{V},T)$$
$$=\tfrac{3}{2}kT\left\{N_s\left[\frac{T}{\bar{T}_s(x)}\right]^{\frac{1}{2}}\left[\frac{G_s(0)}{F_s(0)}\right]+N_a\left[\frac{G_a(\bar{\alpha}_a)}{F_a(\bar{\alpha}_a)}\right]\right\}, \quad (2.3)$$

and in the $(--)$ region, one has

$$\bar{E}_{--}(\bar{V},T)_S=\bar{E}_{s-}(\bar{V},T)+\bar{E}_{a-}(\bar{V},T), \quad (2.4)$$

where $\bar{E}_{a-}(\bar{V},T)$ has an expression similar to that of $\bar{E}_{a+}(\bar{V},T)$, with the appropriate extension of the G_a/F_a ratio into the temperature range $T\lesssim\bar{T}_a$. Similar expressions hold in A mixtures.

The isothermal energy of mixing is, by definition, in the $(++)$ region,

$$\Delta\bar{E}_{++}=\bar{E}_{++}(\bar{V},T)-[E_{s+}(V_s,T)+E_{a+}(V_a,T)]$$
$$=[\bar{E}_{s+}(\bar{V},T)-E_{s+}(V_s,T)]+[\bar{E}_{a+}(\bar{V},T)-E_{a+}(V_a,T)]$$
$$=\Delta\bar{E}_{s+}+\Delta\bar{E}_{a+}, \quad (2.5)$$

V_s and V_a denoting the volumes of the component fluids before mixing. Explicitly, the component isothermal mixing energies,[8] are

$$\Delta\bar{E}_{s+}=\tfrac{3}{2}N_skT\{[G_s(\bar{\alpha}_s)/F_s(\bar{\alpha}_s)]-[G_s(\alpha_s)/F_s(\alpha_s)]\},$$
$$\Delta\bar{E}_{a+}=\tfrac{3}{2}N_akT\{[G_a(\bar{\alpha}_a)/F_a(\bar{\alpha}_a)]-[G_a(\alpha_a)/F_a(\alpha_a)]\}. \quad (2.6)$$

Here, the "pure fluid" parameters α_s and α_a are determined by

$$1=(V_s/N_s)g_s(2\pi m_skT/h^2)^{\frac{3}{2}}F_s(\alpha_s)=[T/T_s(0)]^{\frac{3}{2}}F_s(\alpha_s)/F_s(0),$$
$$1=(V_a/N_a)g_a(2\pi m_akT/h^2)^{\frac{3}{2}}F_a(\alpha_a)=[T/T_a(1)]^{\frac{3}{2}}\Gamma(5/2)F_a(\alpha_a). \quad (2.7)$$

Both F and G, for both fluids, are monotonically decreasing functions of their arguments. Since $\bar{V}>V_s$ and $\bar{V}>V_a$, Eqs. (1.7) and (2.7) show, that under isothermal conditions,

$$\bar{\alpha}_s(T)\gtrless\alpha_s(T), \quad \bar{\alpha}_a(T)\gtrless\alpha_a(T), \quad (2.8)$$

i.e., the statistical parameters always increase on mixing or that the component fluids become less degenerate on mixing. However, one shows easily that

$$d/d\alpha_s(G_s/F_s)>0, \quad d/d\alpha_a(G_a/F_a)<0. \quad (2.9)$$

[8] These component mixing energies should not be confused with the partial ones, which are defined by $(\partial\Delta\bar{E}/\partial N_s)_{N_a}$ and $(\partial\Delta\bar{E}/\partial N_a)_{N_s}$, respectively.

Hence, Eqs. (1.9) state the rather general result, valid actually for all conditions of degeneracy or at all temperatures, that the isothermal component mixing energy of ideal symmetric fluids is positive, that of antisymmetric fluids is negative.

It is worthwhile to consider briefly the physical meaning of the preceding simple results. Let us take first the case of symmetric fluids. We may write their total energy, above the condensation temperature T_0, in the form

$$E_{s+}(V_s,T)=\tfrac{3}{2}N_skTG_s(\alpha_s)/F_s(\alpha_s)$$
$$=\tfrac{3}{2}N_skT+\tfrac{3}{2}N_skT\left(\frac{G_s(\alpha_s)}{F_s(\alpha_s)}-1\right)$$
$$=E_{sk}(T)+E_{sp}(V_s,T), \quad T\gtrsim T, \quad (2.10)$$

where E_{sk} is the mean classical kinetic energy of translational origin, and

$$E_{sp+}(V_s,T)\lesssim 0, \quad \alpha_s\gtrsim 0, \quad (2.11)$$

is an apparent mean attractive potential energy resulting from the peculiar statistical attraction of the symmetric atoms in phase space. The condensation process is caused by this attraction and occurs at a temperature T_0 at which the potential energy per atom is

$$\left(\frac{E_{sp}}{N_s}\right)_{T_0}=\tfrac{3}{2}kT_0\left(\frac{G_s(0)}{F_s(0)}-1\right)$$
$$=-0.73kT_0. \quad (2.12)$$

The numerical value of the so-defined potential energy is thus, at the start of the transition, practically the same as that of the total energy $\frac{3}{2}kT_0\zeta(5/2)/\zeta(3/2)$ or $0.77kT_0$, or about one-half of the ideal classical translational energy. On isothermal mixing, $\alpha_s\to\bar{\alpha}_s$, and with $\bar{\alpha}_s>\alpha_s$, the negative potential energy increases since any one symmetric fluid atom has now less symmetric atom neighbors as before mixing. The total energy of the symmetric fluid component in the mixture is now larger than it was before mixing, and, hence, its component isothermal energy of mixing is positive.

Below the condensation temperature T_0, with $\alpha_s\sim N_s^{-1}\cong 0$, one has

$$E_{s-}(V_s,T)=\tfrac{3}{2}N_skT(T/T_0)^{\frac{3}{2}}G_s(0)/F_s(0)$$
$$=\tfrac{3}{2}N_skT+\tfrac{3}{2}N_skT\times\{(T/T_0)^{\frac{3}{2}}[G_s(0)/F_s(0)]-1\} \quad (2.13)$$

or,

$$E_{sp-}(T)=\tfrac{3}{2}N_skT\{(T/T_0)^{\frac{3}{2}}[G_s(0)/F_s(0)]-1\}\gtrsim E_{sp}(T_0), \quad (2.14)$$

showing that the statistical attraction decreases in this temperature range or the apparent statistical potential energy increases and tends to vanish at the approach of the absolute zero as the total energy itself.

In antisymmetric fluids, we have in analogy with (2.10),

$$E_{a+}(V_a,T)=\tfrac{3}{2}N_akT+\tfrac{3}{2}N_akT \times\{-1+[G_a(\alpha_a)/F_a(\alpha_a)]\}. \quad (2.15)$$

The apparent potential energy of repulsion of statistical origin is thus,

$$E_{ap+}(V_a,T)=\tfrac{3}{2}N_akT[-1+(G_a/F_a)]\geqslant 0 \quad (2.16)$$

and, also, with $G_a/F_a\geqslant 1$,

$$E_{ap-}(V_a,T)\geqslant 0. \quad (2.17)$$

These relations lead at once to the elementary physical interpretation of the result obtained above on the negative component isothermal mixing energy of antisymmetric fluids.

As mentioned earlier, the antisymmetric component will be taken to be of negligible degeneracy. Hence, to this approximation, the isothermal mixing energy reduces to $\Delta\bar{E}_s$, the component mixing energy of the symmetric fluid. By expressing the mixing energy per atom of the mixture, one finds [x denoting the a-component mole fraction, Eq. (1.10)]:

$$[T\geqslant T_s(0)]:\quad \Delta\bar{E}_s(x,T)/(N_s+N_a) =\Delta\bar{e}_s(x,T) =\tfrac{3}{2}(1-x)kT\left[\frac{G_s(\bar{\alpha}_s)}{F_s(\bar{\alpha}_s)}-\frac{G_s(\alpha_s)}{F_s(\alpha_s)}\right], \quad (2.18a)$$

$$[\bar{T}_s(x)\leqslant T\leqslant T_s(0)]:\quad \Delta\bar{e}_s(x,T) =\tfrac{3}{2}(1-x)kT\left[\frac{G_s(\bar{\alpha}_s)}{F_s(\bar{\alpha}_s)}-\left(\frac{T}{T_0}\right)^{\frac{1}{2}}\frac{G_s(0)}{F_s(0)}\right], \quad (2.18b)$$

$$[T\leqslant \bar{T}_s(x)]:\quad \Delta\bar{e}_s(x,T) =\tfrac{3}{2}(1-x)kT^{3/2}\frac{G_s(0)}{F_s(0)}\{[\bar{T}_s(x)]^{-\frac{1}{2}}-[T_s(0)]^{-\frac{1}{2}}\}. \quad (2.18c)$$

At a constant temperature, the isothermal mixing energies vanish at both ends of the x scale, and have at least one maximum at some intermediate x value. This simple behavior is, however, valid without restriction in the high temperature region, $T\geqslant T_s(0)$. At lower temperatures the variation of $\Delta\bar{e}(x,T)$ with the mole fraction x is more complicated. This can be seen indirectly on the temperature variation of the mixing energy, keeping the mole fraction x constant. This energy has indeed a three-branched representation, given by (2.18). These branches join, however, smoothly at $\bar{T}_s(x)$ and $T_s(0)$, i.e., they are continuous together with their first derivatives. They have simple contacts at these points or common tangents.

A comparison of the computed mixing energies with a measured heat or enthalpy of mixing[6] will be postponed for a subsequent section.

II. 2. Entropies of Mixing

With the entropies of the component fluids,

$$\bar{S}_\mu/k=N_\mu\bar{\alpha}_\mu+(5/3)\bar{E}_\mu/kT, \quad (\mu=s,a) \quad (2.19)$$

in the mixture, and those of the separated fluids,

$$S_\mu/k=N_\mu\alpha_\mu+(5/3)E_\mu/kT, \quad (2.20)$$

one obtains the following mixing entropy, at temperature T, per atom of the mixture,

$$\Delta\bar{S}(x,T)/(N_s+N_a)k=\Delta\bar{s}/k =(1-x)(\bar{\alpha}_s-\alpha_s)+x(\bar{\alpha}_a-\alpha_a) +(5/3)\Delta\bar{e}(x,T)/kT. \quad (2.21)$$

The parameters α having rather complicated expressions, since they are obtained by inverting Eqs. (1.7) and (2.7), it is of interest to discuss the simple limiting expressions of $\Delta\bar{s}/k$, namely its high- and low-temperature limit. With (1.7) and (2.7), one obtains

$$\lim_{T\gg T_s(x)}(-\bar{\alpha}_s)=\ln\left[F_s(0)\left(\frac{\bar{T}_s(x)}{T}\right)^{\frac{1}{2}}\right],$$

$$\lim_{T\gg T_s(0)}(-\alpha_s)=\ln\left[F_s(0)\left(\frac{T_s(0)}{T}\right)^{\frac{1}{2}}\right],$$

$$\lim_{T\gg T_a(x)}(-\bar{\alpha}_a)=\ln\left[\left(\frac{\bar{T}_a(x)}{T}\right)^{\frac{1}{2}}\left(\frac{1}{\Gamma(5/2)}\right)\right],$$

$$\lim_{T\gg T_a(1)}(-\alpha_a)=\ln\left[\left(\frac{T_a(1)}{T}\right)^{\frac{1}{2}}\left(\frac{1}{\Gamma(5/2)}\right)\right].$$

Substituting into (2.21), using Eqs. (1.13) and (1.16) for the transition temperatures $\bar{T}_s(x)$ and $\bar{T}_a(x)$, neglecting the entropy term originating in the mixing energy, which vanishes at high temperatures, one finds

$$\lim_{T\ \text{large}}\frac{\Delta\bar{s}(x,T)}{k}=(1-x)\ln\left(\frac{T_s(0)}{\bar{T}_s(x)}\right)^{\frac{1}{2}} +x\ln\left(\frac{T_a(1)}{\bar{T}_a(x)}\right)^{\frac{1}{2}}$$

$$=-[(1-x)\ln(1-x)+x\ln x] +\ln\frac{1+x[(v_a/v_s)-1]}{(v_a/v_s)^x}. \quad (2.22)$$

The preceding entropy expression reduces to its classical ideal solution limit, the negative bracket on the right-hand side, if the argument of the logarithm reduces to unity, i.e., if the volume condition

$$xv_a+(1-x)v_s=v_a{}^xv_s{}^{(1-x)} \quad (2.23)$$

is satisfied. This condition is the same as the one used in the theory of classical ideal solutions. This, of course, had to be expected since in the limit of high tempera-

tures the ideal quantum fluids become classical asymptotically.

In the limit of very low temperatures, the simple linear superposition of the component entropies (2.19), leads, with $T \ll \bar{T}_s(x)$ and $T \ll \bar{T}_a(x)$, to the vanishing of both the total entropy of the mixture and the entropy of mixing (2.21). However, it does not seem justified to interpret this effect as "unmixing"[4] as $T \to 0$. On the contrary, with known amounts of ideal symmetric and antisymmetric fluids occupying a given volume, this vanishing of the mixing entropy and the total entropy, at all values of the mixing parameter or mole fraction x, may be looked upon as an interesting confirmation of the Nernst law in mixtures. While the present discussion, at very low temperatures, of the ideal quantum fluid mixtures is, to a large extent, of academic interest only, it is noteworthy that these mixtures do realize, in all proportions x, a zero-entropy state at the approach of the absolute zero. No additional assumptions concerning this last point is needed here, in contrast with the case of solid binary mixtures or solutions. In the latter systems it is necessary to assume that the two lowest states have a finite energy separation to insure the vanishing of the entropy in the limit $T \to 0$, while they take on the classical mixing entropy value in the limit of high temperatures.[9] In the latter case, it is also tacitly assumed that $v_1 = v_2 = \bar{v}$, which reduces (2.23) to an identity.

The above result in the present asymptotic theory of mixtures, in the limit of $T \to 0$, is based on the still unproved proposition of complete miscibility of the two ideal quantum fluids at all temperatures. Clearly, for the justification of the present model, from the point of view of the existence of the mixtures of ideal quantum fluids, the miscibility proposition is of importance. The proof of this proposition is somewhat long and it will only be outlined in a later section, after the discussion of the Gibbs potentials of these mixtures.

One may state, at any rate, that He^3-He^4 mixtures provide a unique series of systems whose very low temperature investigations, in both liquid and solid phases, should be of great importance in further extending the experimental verification of the Nernst law in mixtures.

Let us consider finally a mixing process whereby

$$S_s(T_i)+S_a(T_i)=\bar{S}_s(T_f)+\bar{S}_a(T_f), \qquad (2.24)$$

or the total entropy before mixing is the same as the total entropy after mixing; T_i and T_f denote here the initial and final temperatures, respectively. No general explicit solution of (2.24) is, however, available giving T_f as a function of T_i and other variables, such as the mole fraction x and the volumes, for instance. A discussion of the adiabatic invariants of the present model, reserved for a subsequent section, will allow, however, to give directly the function $T_f(T_i,x)$.

Qualitatively speaking, the isothermal mixing energies being positive or the isothermal mixing process being accompanied by energy absorption, the adiabatic mixing process cannot but produce a fall in the temperature in the final state from its value in the initial unmixed state, i.e., $T_f < T_i$. Indeed, the total entropy being kept constant, the entropy arising from the increased disorder on mixing has to be compensated for by a decrease of entropy of thermal disorder, i.e., the temperature has to fall. In other words, the configurational mixing energy has to be provided for, under adiabatic mixing conditions, by the only energy source available, namely, the thermal energy of the initial system of separated fluids. Hence, the temperature has to decrease on mixing. The use of the mixing entropy of He^3-He^4 mixtures for cooling purposes was first pointed out by London.[2] The idealized adiabatic mixing process suggested by him will be considered later.

II. 3. Free Energies of the Mixture

The Helmholtz free-energy or thermodynamic potential at constant volume is the sum of the component fluid free energies,

$$\bar{F}(x,T)=\bar{F}_s(x,T)+\bar{F}_a(x,T), \qquad (2.25)$$

with the free energies per atom

$$\begin{aligned} \bar{F}_s/N_s &= \bar{\varphi}_s = -kT\bar{\alpha}_s - \tfrac{2}{3}\bar{E}_s/N_s; \\ \bar{\varphi}_a &= \bar{F}_a/N_a = -kT\bar{\alpha}_a - \tfrac{2}{3}\bar{E}_a/N_a. \end{aligned} \qquad (2.26)$$

Now,

$$(\partial\bar{F}/\partial\bar{V})_T = -N_\lambda kT(\partial\bar{\alpha}_\lambda/\partial\bar{V})_T - \tfrac{2}{3}(\partial\bar{E}_\lambda/\partial\bar{V})_T, \ (\lambda = s, a)$$

which, with (2.1) yields first[10]

$$\begin{aligned} &\tfrac{2}{3}(\partial\bar{E}/\partial\bar{V})_T \\ &\quad = N_\lambda kT[(G_\lambda' F_\lambda - F_\lambda' G_\lambda)/F_\lambda^2](\partial\bar{\alpha}_\lambda/\partial\bar{V})_T \\ &\quad = N_\lambda kT[-1+E_\lambda G_\lambda/F_\lambda^2](\partial\bar{\alpha}_\lambda/\partial\bar{V})_T, \end{aligned} \qquad (2.26a)$$

where,

$$G_\lambda' = dG_\lambda/dz = -F_\lambda(z); \quad E_\lambda(z) = -dF_\lambda/dz.$$

$$\begin{aligned} E_s(z) &= \sum_1^\infty n^{-\frac{1}{2}} \exp(-nz); \\ E_a(z) &= \sum_1^\infty (-)^{n-1} n^{-\frac{1}{2}} \exp(-nz), \end{aligned} \qquad (2.26b)$$

and, with the Eqs. (1.8) defining $\bar{\alpha}_\lambda$, we obtain

$$(\partial\bar{\alpha}_\lambda/\partial\bar{V})_T = F_\lambda/\bar{V}E_\lambda,$$

leading to the equation of state

$$\begin{aligned} \bar{p} &= -(\partial\bar{F}/\partial\bar{V})_{s,T} \\ &= \tfrac{2}{3}(\bar{E}_s+\bar{E}_a)/\bar{V} = \bar{p}_s + \bar{p}_a. \end{aligned} \qquad (2.27)$$

[9] O. Stern, Ann. Physik **49**, 823 (1916); see also P. S. Epstein, *Textbook of Thermodynamics* (John Wiley and Sons, Inc., New York, 1937), pp. 245–251.

[10] The mixture free energies $\bar{F}$ and $\bar{G}$, the Gibbs free energy discussed below, should not be confused with the functions $F(z)$, $G(z)$ which are defined by (1.8) and (2.2).

The virial theorem is thus valid here both in the mixture and in its components. One has then,

$$\bar{p}(x,T,\bar{V})=\left(\frac{kT}{\bar{V}}\right)\left[N_s\left(\frac{G_s(\bar{\alpha}_s)}{F_s(\bar{\alpha}_s)}\right)+N_a\left(\frac{G_a(\bar{\alpha}_a)}{F_a(\bar{\alpha}_a)}\right)\right],\quad T\geqslant\bar{T}_s(x),$$
$$\bar{p}(x,T,\bar{V})=\left(\frac{kT}{\bar{V}}\right)\left[N_s\left(\frac{G_s(0)}{F_s(0)}\right)\left(\frac{T}{\bar{T}_s(x)}\right)^{\frac{3}{2}}+N_a\left(\frac{G_a(\bar{\alpha}_a)}{F_a(\bar{\alpha}_a)}\right)\right],\quad T\leqslant\bar{T}_s(x),\tag{2.28}$$

where, as mentioned already, the a component has only a small if not vanishing degeneracy, at temperatures $T\geqslant 1.0°\mathrm{K}$. Equations (2.28) describe the isothermal curves of the mixture in the pressure-volume plane, the mole fraction x of the a component being an additional parameter. It will be seen that these isothermals do not coincide with the isobars of the system in any region of the $(\bar{p},\bar{V})$ plane. While the partial pressure $\bar{p}_s$ is independent of the volume, below some volume $\bar{V}$ associated with $\bar{T}_s(x)$, the partial pressure $\bar{p}_a$ always depends on the volume. This contrasts with the behavior of the pure symmetric fluid component, which undergoing a first-order phase change at $T\leqslant T_s(0)$, exhibits in this low-temperature range coincident isothermal isobars. The first-order phase change of the symmetric fluid has thus been modified in the mixture. While the latter undergoes some phase change, as shown above, because of the momentum space condensation of its s component, the order of the phase change of the mixture as a whole has been lifted. Its precise nature will be studied in a later section.

The Gibbs function or thermodynamic potential at constant pressure of the mixture is found to be

$$\begin{aligned}&\bar{G}_+/kT=-N_s\bar{\alpha}_s-N_a\bar{\alpha}_a,\quad T\geqslant\bar{T}_s(x),\text{ or }x\geqslant x_c(T),\\&\bar{G}_-/kT=-N_a\bar{\alpha}_a,\qquad\quad T\leqslant\bar{T}_s(x),\text{ or }x\leqslant x_c(T).\end{aligned}\tag{2.29}$$

The parameters $\bar{\alpha}_j(j=s,a)$, are the negative Gibbs potentials per atom, in units of kT, as in the theory of the pure separated ideal quantum fluids. We have,

$$\bar{\alpha}_j=-\bar{G}_j/N_jkT=-\bar{\mu}_j/kT,\qquad j=s,a,$$

$\bar{\mu}_j$ being the constant pressure chemical potential of the component j. Using Eqs. (1.7) and (2.2), one obtains with the pressure (2.28), at $T=\text{const}$,

$$d(\bar{p}/kT)=(1/\bar{V})(N_sd\bar{\alpha}_s+N_ad\bar{\alpha}_a),$$

taking into account the relations (2.26a). And if this vanishes because $\bar{p}=\text{const}$, also, then

$$N_sd\bar{\alpha}_s+N_ad\bar{\alpha}_a=0,\tag{2.30}$$

which is the general form of the so-called Gibbs-Duhem relations.[11] Hence, in a constant pressure, constant temperature transformation, (2.29) and (2.30) lead to

$$d(\bar{G}/kT)=-\bar{\alpha}_sdN_s-\bar{\alpha}_adN_a.\tag{2.31}$$

Dividing (2.30) by the change in mole fraction dx associated with the transformation, one obtains, using the mole fractions in (2.30),

$$(1-x)(d\bar{\alpha}_s/dx)+xd\bar{\alpha}_a/dx=0,\tag{2.30a}$$

of which use will be made in the course of the proof of complete miscibility of the two ideal quantum fluids. It is to be noted that below $\bar{T}_s(x)$, or at some temperature $T\leqslant T_s(0)$, such that $x\leqslant x_c(T)$, $\bar{\alpha}_s$ vanishes and the mixture's Gibbs potential reduces to that of its antisymmetric component fluid, as indicated in (2.29).

The Gibbs free energy of mixing is,

$$\begin{aligned}\Delta\bar{G}/kT&=(\bar{G}-G)/kT\\&=-N_s(\bar{\alpha}_s-\alpha_s)-N_a(\bar{\alpha}_a-\alpha_a).\end{aligned}\tag{2.32}$$

Expressing this per atom of the mixture, one obtains, in an isothermal-isobar process,

$$\begin{aligned}\Delta\bar{H}/(N_s+N_a)kT&=(\Delta\bar{G}+T\Delta\bar{S})/(N_s+N_a)kT\\&=\Delta\bar{h}/kT\\&=(5/3)\Delta\bar{e}/kT,\end{aligned}\tag{2.33}$$

where (2.21), the mixing entropy expression, has been used.

In a preliminary experiment Sommers, Keller, and Dash[6] found that the isothermal mixing energy, at 1.02°K, whereby a 8.6 percent liquid He^3-He^4 mixture has been obtained, was 0.17 cal/mole of mixture. Using (2.18c), the present model gives for this case a mixing energy of 0.1 cal/mole of mixture. In addition, these workers find that the mixing entropy under these conditions is about 0.52 cal/mole degree. The mixing entropy formula (2.21) yields 0.47 cal/mole degree. Here, the He^3-component was taken to be nondegenerate. It is thus seen that the order of magnitude of the mixing energy is reproduced by the present model. The fair agreement of the entropies was to be expected on account of it being quite close to the classical ideal mixing entropy. Clearly, a more detailed analysis of the usefulness of the present asymptotic theory as far as mixing energy and entropy values are concerned has to be postponed until more data become available on these mixtures.

II. 4. The Miscibility Problem

We should like to prove here that ideal symmetric and antisymmetric fluids are miscible in all proportions at all temperatures. A detailed proof of the complete miscibility would be rather long, so that only a brief outline of the proof will be given here.

[11] J. W. Gibbs, *Collected Works* (Longmans, Green and Company, New York, 1931), Vol. 1, p. 88; P. Duhem, Compt. rend. 102, 1449 (1886).

Our problem is equivalent to a discussion of the stability of these mixtures through the variations of their Gibbs potential as a function of the composition determined by the mole fraction x of the a component, for instance.[12] The temperature will thereby be kept constant. The proof obtained at one temperature will then be seen to be valid at all temperatures.

We have seen, Eq. (2.29), that the Gibbs potential per atom of the mixture, in units of kT, is

$$\bar{G}/(N_s+N_a)kT=\bar{g}(x,T)/kT = -(1-x)\bar{\alpha}_s-x\bar{\alpha}_a. \quad (2.34)$$

The potential $\bar{g}(x,T)$ vanishes at both ends of the interval $0\leqslant x\leqslant 1$; it has thus at least one extremum. The x slope of the $\bar{g}(x,T)$ function is

$$(d/dx)(\bar{g}/kT)=\bar{\alpha}_s-\bar{\alpha}_a -[(1-x)(d\bar{\alpha}_s/dx)+x(d\bar{\alpha}_a/dx)]. \quad (2.35)$$

But, the bracket, on the right-hand side vanishes by the Gibbs-Duhem relation (2.30a), and the slope reduces to

$$(d/dx)(\bar{g}/kT)=\bar{\alpha}_s-\bar{\alpha}_a. \quad (2.35a)$$

In the limit of $x\to\epsilon$, $\epsilon\ll 1$, $\bar{\alpha}_a$ is positive and large and tends toward $+\infty$, while $\bar{\alpha}_s\to\alpha_s$ which is some finite number. Hence

$$\lim_{x\to\epsilon(\epsilon\ll 1)}(d/dx)(\bar{g}/kT)=-\infty.$$

In the other limit,

$$\lim_{x\to(1-\epsilon)}(d/dx)(\bar{g}/kT)=+\infty,$$

since here $\bar{\alpha}_s\sim\alpha_s\to\infty$. The slope (2.35a) has thus to vanish at least once in the interval $0\leqslant x\leqslant 1$. Now $\bar{\alpha}_s(x)$ is monotonic and increases from $\alpha_s\gtrless 0$, at very small x values, toward $+\infty$ at $x\sim 1$. Simultaneously, $\bar{\alpha}_a$ decreases monotonically from $+\infty$, at $x\sim 0$, to some positive finite value or, at low temperatures, to very large negative values, since at low temperatures the degeneracy of the a component will have to be taken into account. This proves that $\bar{g}(x,T)/kT$ has only a single extremum, the curves $\bar{\alpha}_s(x)$ and $\bar{\alpha}_a(x)$ intersecting only once in the interval $0\leqslant x\leqslant 1$. Furthermore, using (2.30a) again,

$$(d^2/dx^2)(\bar{g}/kT)=(d\bar{\alpha}_s/dx)-(d\bar{\alpha}_a/dx) =x^{-1}(d\bar{\alpha}_s/dx)>0, \quad (2.36)$$

which is always positive. This proves that $\bar{g}/kT$ has a single minimum in the interval $0\leqslant x\leqslant 1$ and that it turns its concavity toward decreasing $\bar{g}$ values. Hence, a chord connecting any two points of the $(\bar{g}/kT)$ curve always lies above the arc. Let x_A and x_B, $x_A<x_B$, the abscissas of two points, $(\bar{g}_A/kT)$ and $(\bar{g}_B/kT)$ the corresponding Gibbs potentials of these two mixtures, and consider now the modifications of our system when it follows the chord passing through these two points. According to thermodynamics the appearance of such a straight line segment in the Gibbs potential or any other thermodynamic variables, is associated with a phase separation. In our case, a system of composition $(x_A+\epsilon)$, $\epsilon>0$, is a two-phase system with phase (x_A) in the proportion $(x_B-\epsilon)/(x_B-x_A)$ and phase x_B in the proportion $\epsilon/(x_B-x_A)$. As the representative point moves from x_A toward x_B, the phase of composition x_A is being exhausted and the phase x_B enriched. However, along this chord this two-phase system has always a higher Gibbs potential than the monophase systems described by the curve $(\bar{g}/kT)$. The two-phase system is thus thermodynamically unstable and the mixture can only undergo those transformations whereby its potential follows the continuous curve of $(\bar{g}/kT)$. This proves that the two fluids are miscible in all proportions.

It is easy to see that the preceding proof remains valid at all temperatures.

While experimentally no phase separation has as yet been obtained in liquid He^3-He^4 mixtures, its existence has been discussed by Sommers[6] on the basis of his measurements of solution vapor pressures.

II. 5. Some Additional Properties of the Mixtures

We have seen above, Eq. (2.27), that the virial theorem is valid in the present theory of ideal quantum fluid mixtures. In an adiabatic transformation of such a system, by definition, no transitions are induced between the various energy levels, i.e., the occupation numbers (1.6) are adiabatic invariants; the virial theorem is used further below.

$$\bar{n}_{s\lambda}(T)=\text{const},\quad \bar{n}_{a\mu}(T)=\text{const},\quad (\text{all }\lambda,\mu;\ d\bar{S}=0). \quad (2.37)$$

Let us consider the occupation numbers in the lowest levels, where

$$\bar{\epsilon}_{s0}=\bar{\epsilon}_{a0}\cong 0,$$

or

$$\bar{n}_{s0}(T)=\bar{g}_{s0}\{[\exp\bar{\alpha}_s(T)]-1\}^{-1};$$
$$\bar{n}_{a0}(T)=\bar{g}_{a0}\{[\exp\bar{\alpha}_a(T)]+1\}^{-1}.$$

The level degeneracies $\bar{g}_{s\lambda}$, $\bar{g}_{a\mu}$ (all λ, μ) are fundamental or elementary adiabatic invariants as first shown by Ehrenfest.[13] Hence the parameters

$$\bar{\alpha}_s(T)=\text{const},\quad \bar{\alpha}_a(T)=\text{const},\quad (d\bar{S}=0), \quad (2.38)$$

are adiabatic invariants together with all continuous functions of these parameters. The functions $F_s(\bar{\alpha}_s)$, $F_a(\bar{\alpha}_a)$, $G_s(\bar{\alpha}_s)$, $G_a(\bar{\alpha}_a)$, etc., are thus adiabatic invariants. Equations (1.7) then lead at once to the adiabatic invariants

$$T^{\frac{3}{2}}\bar{v}_s=\text{const},\quad T^{\frac{3}{2}}\bar{v}_a=\text{const},$$
$$T\bar{v}_s^{\frac{3}{2}}=\text{const},\quad T\bar{v}_a^{\frac{3}{2}}=\text{const},\quad T(\bar{v}_s^{\frac{3}{2}}+\bar{v}_a^{\frac{3}{2}})=\text{const}. \quad (2.39)$$

[12] A simple method of discussion of this problem has been given by H. A. Lorentz; see his *Lectures on Theoretical Physics* (Macmillan and Company Ltd., London, 1927), Vol. I, pp. 69–73.

[13] P. Ehrenfest, Physik. Z. 15, 660 (1914).

But in these transformations the numbers $\bar{n}_{s\lambda}$ and $\bar{n}_{a\mu}$ being invariants, so are the numbers N_s and N_a. Hence, with (1.7), one also has the following adiabatic invariant

$$T\bar{V}^{\frac{2}{3}}=\text{const}, \quad (d\bar{S}=0). \tag{2.40}$$

The free particle energy levels in volume $\bar{V}$ are

$$\bar{\epsilon}_{j\nu}=(h^2/m_j\bar{V}^{\frac{2}{3}})f(\nu), \quad (j=s, a),$$

where $f(\nu)$ is some function of translational quantum numbers, ν standing for all three of them. These quantum numbers as well as the function $f(\nu)$ are trivial adiabatic invariants. From the invariance of the $\bar{n}_{j\nu}$'s and the parameters $\bar{\alpha}_j$, the adiabatic invariance of $\bar{\epsilon}_{j\nu}/T$ results at once. This again yields the invariant (2.40).

With the component fluid energies being

$$\bar{E}_j(T,\bar{V})=\sum_\lambda \bar{n}_{j\lambda}\bar{\epsilon}_{j\lambda}, \quad (j=s, a)$$

one obtains the following invariants,

$$\bar{E}_j\bar{V}^{\frac{2}{3}}=\text{const}, \quad (j=s, a);$$

$$(\bar{E}_s+\bar{E}_a)\bar{V}^{\frac{2}{3}}=\text{const}; \quad (d\bar{S}=0). \tag{2.41}$$

The virial theorem with the preceding adiabatic invariant yields the new invariants,

$$\bar{p}\bar{V}^{5/3}=\text{const}; \quad \bar{p}T^{5/2}=\text{const};$$

$$\bar{p}\bar{V}/T=\text{const} \quad (d\bar{S}=0). \tag{2.42}$$

These definitions of the different adiabatic invariants are valid at all temperatures or at all degrees of statistical degeneracy of these ideal fluids.[14]

We have seen briefly above that the process of mixing adiabatically liquid He^3 with liquid He^4 may be approximately realized by using the superflow of liquid He^4. Let thus, initially, the two separated fluids be at a common temperature T_i, and composed of N_s and N_a atoms, respectively, with the atomic volumes $v_s(T_i)$ and $v_a(T_i)$. Then, in the adiabatic mixing, using Eqs. (2.39) which are, of course, valid also in the unmixed case, one has

$$T_i(v_s^{\frac{2}{3}}+v_a^{\frac{2}{3}})=T_f(\bar{v}_s^{\frac{2}{3}}+\bar{v}_a^{\frac{2}{3}}). \tag{2.43}$$

With the volume condition (1.15), this becomes

$$T_i(v_s^{\frac{2}{3}}+v_a^{\frac{2}{3}})=T_f\left\{\left[v_s+\left(\frac{x}{1-x}\right)v_a\right]^{\frac{2}{3}}+\left[v_a+\left(\frac{1-x}{x}\right)v_s\right]^{\frac{2}{3}}\right\}. \tag{2.43a}$$

If N_s and N_a are so chosen that

$$N_a/(N_a+N_s)=x\ll 1,$$

then

$$T_i(v_s^{\frac{2}{3}}+v_a^{\frac{2}{3}})\cong T_f(v_s/x)^{\frac{2}{3}},$$

and, neglecting the apparently small changes of v_s and v_a[5] at low temperatures,

$$T_f\sim T_i x^{\frac{2}{3}}[1+(v_a/v_s)^{\frac{2}{3}}], \tag{2.43b}$$

which final temperature may be quite small. This is essentially the adiabatic cooling process suggested by London.[2] It should, however, be kept in mind, that Eq. (2.43b) assumes the full use of all the N_s and N_a atoms in the mixing process. Equation (2.43b) represents merely the lower limit of the final temperature which could be achieved by the process in question. It should be noted here that the cooling on mixing of the two liquid He isotopes under good thermal insulation has been first demonstrated experimentally by Sommers, Keller, and Dash[6] in this Laboratory.

II. 6. The Nature of the Phase Transformations of the Mixture. Heat Capacities

The heat capacity at constant volume of the system is, using Eqs. (2.1) and (2.3),

$$\bar{C}_v(x,T)=d\bar{E}/dT$$

$$T\leqslant \bar{T}_s(x) \quad =\frac{15}{4}N_sk\left(\frac{G_s(0)}{F_s(0)}\right)\left(\frac{T}{\bar{T}_s(x)}\right)^{\frac{3}{2}}+\tfrac{3}{2}N_ak\left[\left(\frac{G_a}{F_a}\right)+T\left(\frac{d}{dT}\right)\left(\frac{G_a}{F_a}\right)\right]. \tag{2.44}$$

With calculations similar to those given above, Eqs. (2.26a, b), and with

$$d\bar{\alpha}_j/dT=-\tfrac{3}{2}F_j/TF_j', \quad (j=s, a)$$

resulting from (1.7), one obtains for the heat capacities per mixture atom, in units of k,

$$c_{v-}(x,T)=\frac{\bar{C}_{v-}}{(N_s+N_a)k}=\frac{15}{4}(1-x)\left(\frac{G_s(0)}{F_s(0)}\right)\times\left(\frac{T}{\bar{T}_s(x)}\right)^{\frac{3}{2}}+x\left[\frac{15}{4}\left(\frac{G_a}{F_a}\right)-\frac{9}{4}\left(\frac{F_a}{E_a}\right)\right], \tag{2.45}$$

$$T\leqslant \bar{T}_s(x)$$

$$c_{v+}(x,T)=\frac{\bar{C}_{v+}}{(N_s+N_a)k}=(1-x)\left[\frac{15}{4}\left(\frac{G_s}{F_s}\right)-\frac{9}{4}\left(\frac{F_s}{E_s}\right)\right]+x\left[\frac{15}{4}\left(\frac{G_a}{F_a}\right)-\frac{9}{4}\left(\frac{F_a}{E_a}\right)\right].$$

$$T\geqslant T_s(x)$$

A glance at these heat capacities shows that they are continuous at $\bar{T}_s(x)$, in crossing the transition line.

[14] Several of the preceding invariants have been given for the separated ideal fluids by G. E. Uhlenbeck and E. A. Uehling, Phys. Rev. **39**, 1014 (1932); their proof of the invariance of $(T\bar{V}^{\frac{2}{3}})$ involves, however, an additional thermodynamic relation.

Their temperature derivatives $(d\bar{c}_v/dT)$ are discontinuous at $\bar{T}_s(x)$ having a λ point type discontinuity. One finds here, as in the case of pure symmetric fluids,[15] $D_s(z)$ being $(-dE_s/dz)$,

$$\begin{aligned}\Delta[d\bar{c}_v(x,\bar{T})/dT]_{T_s(x)} &= (d\bar{c}_{v+}/dT)_{T_s(x)}-(d\bar{c}_{v-}/dT)_{T_s(x)}\\ &= -\frac{27}{8}\left[\frac{(1-x)}{\bar{T}_s(x)}\right]\lim_{\alpha_s\to 0}\left[\frac{[F_s(\bar{\alpha}_s)]^2}{[E_s(\bar{\alpha}_s)]^3}D_s(\bar{\alpha}_s)\right]\\ &= -(27/16\pi)[F_s(0)]^2(1-x)/\bar{T}_s(x)\\ &= \Delta[d\bar{c}_v(0)/dT]_{T_s(0)}(1-x)[T_s(0)/\bar{T}_s(x)], \quad (2.46)\end{aligned}$$

$\Delta[d\bar{c}_v(0)/dT]_{T_s(0)}$ being the discontinuity associated with the pure s fluid at the condensation line.[15] The discontinuity (2.46) is, of course, all due to the symmetric fluid component of the mixture; the a-component heat capacity is continuous with all its temperature derivatives at the crossing of the transition line $x_c(T)$. The x dependence of the preceding discontinuity (2.46) is included into the factor

$$\begin{aligned}\gamma(x) &= (1-x)T_s(0)/\bar{T}_s(x)\\ &= (1-x)^{\frac{1}{3}}\left[1+x\left(\frac{v_a[\bar{T}_s(x)]}{v_s[\bar{T}_s(x)]}-1\right)\right]^{\frac{1}{3}}, \quad (2.47)\end{aligned}$$

where the ratio (1.13) of $[\bar{T}_s(x)/T_s(0)]$ has been used. It is seen that the discontinuity reduces to that of the pure symmetric fluid at $T_s(0)$ in the limit $x\to 0$, while it vanishes, as it should, at $x=1$.

The apparent similarity of the behavior of the constant volume heat capacity in mixtures and in the pure symmetric fluid is, however, quite superficial because the mixtures also have a well-defined constant pressure heat capacity in contrast with the pure symmetric fluid. The constant pressure heat capacity of the latter becomes infinite at the transition line as in a system undergoing a first-order phase change.[15]

We have to evaluate now the constant pressure heat capacity of the present mixture model. The simplest procedure appears to be through the use of the thermodynamic relation

$$\bar{C}_p(x,T)/\bar{C}_v(x,T) = (\partial\bar{p}/\partial\bar{V})_S/(\partial\bar{p}/\partial\bar{V})_T.$$

With the first of the adiabatic invariants (2.42) and the pressure equations (2.28), one obtains, omitting all calculations,

$$\begin{aligned}\bar{C}_{p+}(x,T)/(N_s+N_a)k &= \bar{c}_{p+}(x,T)\\ &= \frac{5}{3}\bar{c}_{v+}(x,T)\frac{(1-x)[G_s(\bar{\alpha}_s)/F_s(\bar{\alpha}_s)]+x[G_a(\bar{\alpha}_a)/F_a(\bar{\alpha}_a)]}{(1-x)[F_s(\bar{\alpha}_s)/E_s(\bar{\alpha}_s)]+x[F_a(\bar{\alpha}_a)/E_a(\bar{\alpha}_a)]} \quad (2.48a)\end{aligned}$$

above the transition line of the mixture. It is seen that in the limit of high temperatures, $T\gg\bar{T}_s(x)$ and $T\gg\bar{T}_a(x)$, where the ratios (G/F) and (F/E) reduce essentially to unity, the classical heat capacity ratio of 5/3 is obtained.

Below the transition line, one finds

$$\bar{c}_{p-}(x,T) = \frac{5}{3}\bar{c}_{v-}\left[(1-x)\left(\frac{G_s(0)}{F_s(0)}\right)\times\left(\frac{T}{\bar{T}_s(x)}\right)^{\frac{1}{3}}+\frac{xG_a}{F_a}\right]\left[x\left(\frac{F_a}{E_a}\right)\right]^{-1}. \quad (2.48b)$$

It is seen that $\bar{c}_p(x,T)$ is continuous along the transition line $x_c(T)$. Its temperature derivative is, however, discontinuous exhibiting a λ-point type of discontinuity. A somewhat lengthy calculation, which need not be given here, yields the following discontinuity:

$$\Delta\left(\frac{d\bar{c}_p}{dT}\right) = \frac{25}{9}\Delta\left(\frac{d\bar{c}_v}{dT}\right)\left[\left(\frac{(1-x)}{x}\right)\left(\frac{E_a}{F_a}\right)\times\left(\frac{G_s(0)}{F_s(0)}\right)+\left(\frac{G_aE_a}{F_a^2}\right)\right]^2. \quad (2.49)$$

If the degeneracy of the a component is neglected, this becomes

$$\Delta\left(\frac{d\bar{c}_p}{dT}\right) = \frac{25}{9}\Delta\left(\frac{d\bar{c}_v}{dT}\right)\left[1+\left(\frac{(1-x)}{x}\right)\left(\frac{G_s(0)}{F_s(0)}\right)\right]^2, \quad (2.50)$$

which shows that $\bar{c}_p$ has always a considerably sharper peak than $\bar{c}_v$, along the transition line. It is also seen that as $x\to 0$, the preceding discontinuity tends toward $(-\infty)$ as in the pure symmetric fluid, while it disappears in the limit $x\to 1$, because of the vanishing there of $\Delta[d\bar{c}_v(1)/dT]$.

The preceding results prove that the phase change undergone by the present mixture model is of third order. The first-order phase change exhibited by the pure ideal symmetric fluid[15] has thus been lifted by mixing it with the ideal antisymmetric or ideal Boltzmann fluid. The depression of the transition temperature was seen above to be a consequence of the decrease in the strength of the attractive statistical forces in phase space. One may also say that the mixing process is equivalent to the introduction of statistical forces of repulsion balancing partially the attractive statistical forces existing in the pure symmetric fluid. We have just proved, by evaluating the heat capacities of the mixture together with their temperature derivatives, that such an apparent intervention of repulsive statistical forces lifts the order of the phase change. It is of interest that this result is qualitatively similar to the effect of introducing a class of space-dependent repulsive forces into the formalism of ideal symmetric fluids which we have proved some time ago.[15] These repulsive space-

[15] L. Goldstein, J. Chem. Phys. **14**, 276 (1946).

dependent forces were found to lift the order of the phase change of the ideal symmetric fluid from the first to the third order.

Beside the transformations occurring at constant mole fraction x of the mixture, one may consider those in which the composition changes, the process being isothermal and at constant volume. One finds that the total energy $\tilde{E}(x,\tilde{V},T)$ is continuous together with the derivative $(d\tilde{E}/dx)_{v,T}$ along the transition line $x_c(T)$. However, its second derivative, $(d^2E/dx^2)_{v,T}$ has a λ-point type of behavior in crossing this line. One finds, omitting the calculations, with $0<x_c<1$,

$$\Delta\left(\frac{d^2\tilde{E}}{dx^2}\Big/(N_s+N_a)\right)=\Delta\left(\frac{d^2\tilde{e}}{dx^2}\right)$$
$$=-\frac{3}{2}\left(\frac{k\tilde{T}_s(x)}{(1-x_c)}\right)\left\{\left(\frac{v_a}{v_s}\right)\Big/\left[1+x\left(\frac{v_a}{v_s}-1\right)\right]\right\}^2\lim_{\alpha_s\to 0}\left(\frac{F_s^2D_s}{E_s^3}\right)$$
$$=-\frac{3}{4\pi}\left(\frac{k\tilde{T}_s(x_c)}{(1-x_c)}\right)F_s^2\left\{\left(\frac{v_a}{v_s}\right)\Big/\left[1+x\left(\frac{v_a}{v_s}-1\right)\right]\right\}^2, \quad (2.51)$$

a result similar to the λ-point discontinuities of the temperature derivatives of the constant volume and constant pressure heat capacities. The third-order character of the phase change exhibited by the present asymptotic model may thus be defined as being associated with the λ-point type of discontinuities of the second derivatives $(d^2\tilde{E}/dT^2)_{v,x}$, $(d^2\tilde{E}/dT^2)_{p,x}$, $(d^2\tilde{E}/dx^2)_{v,T}$, etc.

It is worth noting here that an experimental verification of the nature of the phase change in actual mixtures of liquid He^3-He^4 is lacking at the present time. The existence of phenomena involving the superfluid atoms below the transition temperatures of mixtures cannot be taken as either proving or disproving the preservation in mixtures of the apparently second-order phase change attributed currently to pure liquid He^4.

It will be seen on Eqs. (2.46) and (2.51) that by eliminating between them $\lim_{\alpha_s\to 0}[F_s^2(\bar{\alpha}_s)D_s(\bar{\alpha}_s)/E_s^3(\bar{\alpha}_s)]$ one obtains the relation connecting the discontinuities $\Delta(d^2\tilde{e}/dT^2)_{v,x}$ and $\Delta(d^2\tilde{e}/dx^2)_{T,v}$. While replacing into (2.50) $\Delta(d^2\tilde{e}/dT^2)_{v,x}$ by its expression in terms of $\Delta(d^2\tilde{e}/dx^2)_{T,v}$, one obtains an additional relation connecting the discontinuity of the temperature derivative of the constant pressure heat capacity with the discontinuity of the composition derivative $\Delta(d^2\tilde{e}/dx^2)_{T,v}$, along the transition line of the model.

The set of points of the discontinuities $\Delta(d\tilde{c}_v/dT)$ and $\Delta(d\tilde{c}_p/dT)$ are such that their two end points do not belong to the set since as $x\to 1$, these discontinuities vanish strictly in the pure a component, where the third-order phase transformation loses its meaning. At the other limit, $x\to 0$, the discontinuities define the first order phase change of the pure s component.

III. SOME HYDRODYNAMIC PROPERTIES OF THE MIXTURE

Neglecting all dissipative effects, the velocity of propagation of normal compressional waves or first sound is still given by the classical formula

$$[\tilde{s}_1(T,x)]^2=[\partial\tilde{p}(x,T)/\partial\tilde{\rho}]_S$$
$$=(5/3)\tilde{p}/\tilde{\rho}, \quad \tilde{\rho}=[(N_sm_s+N_am_a)/\tilde{V}], \quad (3.1)$$

where use has been made of the first of the adiabatic invariants (2.42). It is known, however, that the ideal symmetric fluid model predicts too small a sound velocity, at liquid He^4 densities, by overestimating the adiabatic compressibility of liquid He^4. Here, the neglect of the interatomic forces leads to the qualitatively incorrect prediction of vanishing sound velocity at very low temperatures where the model loses completely its asymptotic validity. In mixtures of ideal symmetric and antisymmetric fluids, the sound velocity cannot vanish even at very low temperatures because of the finite compressibility of its a component. Using the pressures (2.28), one finds with (3.1),

$$[\tilde{s}_1(T,x)]^2=[\tilde{s}_{1s}(T,x)]^2\left[1+\left(\frac{x}{1-x}\right)\left(\frac{G_a}{F_a}\right)\Big/\left(\frac{G_s}{F_s}\right)\right]\left[1+\left(\frac{xm_a}{(1-x)m_s}\right)\right]^{-1}, \quad (3.2)$$
$$T\geq\tilde{T}_s(x)$$

where $\tilde{s}_{1s}(T,x)$ is the s-component sound velocity

$$[\tilde{s}_{1s}(T,x)]^2=\frac{5}{3}\left(\frac{kT}{m_s}\right)\frac{G_s(\bar{\alpha}_s)}{F_s(\bar{\alpha}_s)}. \quad (3.2a)$$

Since $G_s(\bar{\alpha}_s)/F_s(\bar{\alpha}_s)\geq G_s(\alpha_s)/F_s(\alpha_s)$, and since the ratio of the brackets on the right-hand side of (3.2) is always larger than unity, the sound velocity in the present asymptotic model of the mixtures is always larger than in the separated symmetric fluid at the same temperature. Below the transition line, one obtains

$$[\tilde{s}_1(T,x)]^2=[\tilde{s}_{1s}(T,x)]^2\left[1+\left(\frac{x}{1-x}\right)\left(\frac{G_a}{F_a}\right)\Big/\left(\frac{G_s(0)}{F_s(0)}\right)\left(\frac{T}{\tilde{T}_s(x)}\right)^{\frac{1}{2}}\right]\times\left[1+\left(\frac{xm_a}{(1-x)m_s}\right)\right]^{-1}, \quad (3.3)$$
$$T\leq\tilde{T}_s(x) \qquad T\leq\tilde{T}_s(x)$$
$$[\tilde{s}_{1s}(T,x)]^2=\frac{5}{3}\left(\frac{kT}{m_s}\right)\left(\frac{G_s(0)}{F_s(0)}\right)\left(\frac{T}{\tilde{T}_s(x)}\right)^{\frac{1}{2}}.$$

In the limit of very low temperatures, one obtains, after an elementary calculation,

$$\lim_{T\to 0}[s_1(T,x)]^2=\lim_{T\to 0}(5/3)\frac{\bar{p}_a}{\bar{\rho}}$$
$$=[s_{1a}(T=0,x=1)]^2\left[1+\left(\frac{(1-x)m_s}{xm_a}\right)\right]^{-1}$$
$$\cdot\left(\frac{xv_a}{v_s}\Big/\left[1+x\left(\frac{v_a}{v_s}-1\right)\right]\right)^{\frac{1}{3}}, \quad (3.4)$$

where

$$[s_{1a}(T=0,x=1)]^2=\tfrac{2}{3}kT_a/m_a \quad (3.4a)$$

is the sound velocity at the absolute zero in the completely degenerate pure antisymmetric fluid.

To the approximation of the present asymptotic model, below the transition line the number of uncondensed and condensed atoms is given, respectively, by

$$\bar{N}_\nu(T,x)=\bar{N}_{ns}(T,x)+N_a$$
$$=N_s[T/\bar{T}_s(x)]^{\frac{3}{2}}+N_a; \quad (3.5)$$
$$\bar{N}_\sigma(T,x)=N_s\{1-[T/\bar{T}_s(x)]^{\frac{3}{2}}\}.$$

The density ratio $\tilde{\rho}_\nu(T,x)/\tilde{\rho}(T,x)$ which is almost directly measured in momentum of inertia experiments[16] is thus, in the present model,

$$\frac{\tilde{\rho}_\nu}{\tilde{\rho}}=\left(\frac{T}{\bar{T}_s(x)}\right)^{\frac{3}{2}}\left[1+\left(\frac{x}{1-x}\right)\left(\frac{m_a}{m_s}\right)\Big/\left(\frac{T}{\bar{T}_s(x)}\right)^{\frac{3}{2}}\right]$$
$$\times\left[1+\left(\frac{x}{1-x}\right)\left(\frac{m_a}{m_s}\right)\right]^{-1}, \quad (3.6)$$

since $\bar{T}_s(x)\leqslant T_s(0)$, and in view of the ratio of the two square brackets on the right-hand side of (3.6) being necessarily larger than unity, it is seen that the preceding ratio is always larger in the mixture than it is in the pure symmetric fluid, at the same temperature.

The above subdivision (3.5) of the atoms of the mixture into the superfluid (σ) and normal (ν) atoms, leads inevitably to the following second sound velocity relation, with an asymptotically homogeneous normal fraction,

$$[s_2(T,x)]^2=(\tilde{\rho}_\sigma/\tilde{\rho}_\nu)(kT/\bar{M})(\bar{S}/k)^2/(\bar{C}_v/k) \quad (3.7)$$

generalizing the Tisza relation[17] obtained in the pure symmetric fluid. We have here

$$\tilde{\rho}_\sigma=N_sm_s/\bar{V}, \quad \tilde{\rho}_\nu=\{N_sm_s[T/\bar{T}_s(x)]^{\frac{3}{2}}+N_am_a\}/\bar{V},$$
$$\bar{M}=N_sm_s+N_am_a, \quad (3.8)$$

while $\bar{S}/k$ and $\bar{C}_v/k$ are given by the sum of the component entropies (2.19) and constant volume heat capacities (2.45), respectively. Below the transition line, where temperature or second sound waves can be propagated, we have

$$\bar{S}_-/k=(\bar{S}_{s-}/k)+(\bar{S}_a/k)$$
$$=(\bar{S}_s/k)(1+\bar{S}_a/\bar{S}_s)$$
$$=(\bar{S}_{s-}/k)\left\{1+\left[\left(\frac{x}{1-x}\right)\left(\bar{a}_a+\frac{5}{2}\frac{G_a}{F_a}\right)\Big/\left(\frac{G_s(0)}{F_s(0)}\right)\left(\frac{T}{\bar{T}_s(x)}\right)^{\frac{3}{2}}\right]\right\}, \quad (3.9)$$

where, (2.19) and (2.3) have been used. One obtains similarly with the first of Eqs. (2.45),

$$\frac{\bar{C}_{v-}}{k}=\left(\frac{\bar{C}_{vs-}}{k}\right)\left(1+\frac{\bar{C}_{va}}{\bar{C}_{vs-}}\right)$$
$$=\left(\frac{\bar{C}_{vs-}}{k}\right)\left\{1+\left[\left(\frac{x}{1-x}\right)\left(\frac{G_a}{F_a}\right)\left(1-\frac{3}{5}\frac{F_a^2}{G_aE_a}\right)\Big/\left(\frac{G_s(0)}{F_s(0)}\right)\left(\frac{T}{\bar{T}_s(x)}\right)^{\frac{3}{2}}\right]\right\}. \quad (3.10)$$

With (3.8), (3.9), and (3.10) one may write down at once the explicit expression of the velocity of second sound waves given by (3.7). Since the formula so obtained is quite unwieldy, it will not be given here. Its discussion, in the case of small x values and moderate temperatures, with the degeneracy of the a component neglected shows that

$$s_2(x,T)\gtrsim s_2(0,T), \quad T<\bar{T}_s(x), \quad (3.11)$$
$$x \text{ small},$$

or that the second sound velocity in the mixture is larger than in the pure symmetric fluid at the same temperature. This is caused essentially by the large entropy contribution of the a component, which is here, per atom,

$$\bar{s}_a/k=5/2+\ln[(\bar{V}/N_a)g_s(2\pi m_akT/h^2)^{\frac{3}{2}}]$$
$$=0.432+\ln(1+0.4x)+\ln(T^{\frac{3}{2}}/x), \quad (3.12)$$

where the volume condition (1.15) has been used and where we took

$$v_a/v_s\simeq 1.4 \quad (T\leqslant 2.186^\circ\text{K}),$$

together with (1.16) and $T_a(1)\sim 4.8^\circ$K. In this x and T range, $\bar{c}_{va}\simeq\frac{3}{2}$.

In the limit of very low temperatures, where $T\ll\bar{T}_s(x)$, and $[T/\bar{T}_s(x)]^{\frac{3}{2}}$ is very small, and where by assumption, the a component is also well below its degeneration temperature $\bar{T}_a(x)$,

$$\bar{S}/k\simeq\bar{S}_a/k;\ \bar{C}_v/k\simeq\bar{C}_{va}/k=\bar{S}_a/k=N_a(\pi^2/2)[T/\bar{T}_a(x)],$$

one finds, since

$$\tilde{\rho}_\sigma/\tilde{\rho}_\nu\simeq N_sm_s/N_am_a;$$

[16] E. Andronikashvili, J. Exptl. Theoret. Phys. (U.S.S.R.) **16**, 780 (1946).

[17] L. Tisza, J. phys. radium [8], **1**, 165, 340 (1940); Phys. Rev. **72**, 838 (1947).

by using (3.7) we obtain

$$\lim_{T\ll T_s(x)\ \ T\ll T_a(x)} [\delta_2(x,T)]^2=\left(\frac{\pi^2}{2}\right)\left(\frac{k\bar{T}_a(x)}{m_a}\right)\left(\frac{T}{\bar{T}_a(x)}\right)^2 \times\left[1+\left(\frac{x}{1-x}\right)\left(\frac{\gamma_{1a}}{m_s}\right)\right]^{-1}.$$

But, with (3.4a),

$$k\bar{T}_a(x)/m_a\simeq\tfrac{3}{5}[\delta_{1a}(x,\,T\sim 0)]^2,$$

$\delta_{1a}(x, T\sim 0)$ being the normal sound velocity in an isolated ideal antisymmetric fluid at very low temperatures. Hence,

$$\lim_{T\text{ very low}} \delta_2(x)\simeq 3^{\frac{1}{2}}\pi\delta_{1a}(x,\,T\sim 0)\left(\frac{T}{\bar{T}_a(x)}\right) \times\left[1+\left(\frac{x}{1-x}\right)\left(\frac{m_a}{m_s}\right)\right]^{-\frac{1}{2}}, \quad (3.13)$$

or, in this limit, the second sound velocity tends to vanish linearly with the temperature.

If $T\ll\bar{T}_s(x)$, so that $\bar{\rho}_a/\bar{\rho}_s\sim(N_s m_s/N_a m_a)$, but the degeneracy of the a component is neglected, and moreover x and T are such that,

$$\delta_a/k\sim 1, \quad \mathcal{C}_{va}\sim\tfrac{3}{2},$$

one obtains

$$\delta_2(x,T)\simeq\left(\frac{kT}{m_a}\right)^{\frac{1}{2}}\left\{\frac{2}{3}\Big/\left[1+\left(\frac{x}{1-x}\right)\left(\frac{m_a}{m_s}\right)\right]\right\}^{\frac{1}{2}}, \quad (3.14)$$

or a $T^{\frac{1}{2}}$ variation of the second sound velocity which is now, to within a constant factor, the normal sound velocity in an ideal fluid of atoms of mass m_a.

It seems of interest to follow through the consequences of superfluid-normal fluid division (3.5) of the present model of mixtures by evaluating the second sound wave field pressure exerted on a solid immersed in the fluid. According to Pellam[18] the torque exerted by the second sound wave field on a flat circular disk of radius a, which rotates around an axis coinciding with one of its diameters, the axis being perpendicular to the direction of propagation of the waves, the plane being at a 45° angle to this direction, is, in the mixture,

$$\frac{\bar{\tau}(x,T)}{\langle\dot{H}^2\rangle_{\text{Av}}}=\frac{4}{3}a^3\bar{\rho}\left(\frac{\bar{\rho}_v}{\bar{\rho}_s}\right)\Big/\left(\frac{\bar{S}T}{\bar{V}}\right)^2, \quad (3.15)$$

where $\dot{H}$ is the instantaneous heat current density associated with the second sound waves. The preceding torque originates, in a way similar to what happens in the normal sound wave field, in the tensions developed by the complicated flow pattern in the fluid caused by the presence of the solid obstacle. If the densities (3.8) together with the total mixture entropy (2.19) are introduced into (3.15) one obtains the explicit expression of the second sound torque in the present model. This torque expression is again quite long and need not be written down. One observes, however, at once that as a result of the large value of the total entropy of the mixture, at moderate x values and not too low temperatures, the torque in the mixture is necessarily smaller than in the pure symmetric fluid at the same temperature, disk dimensions, and heat current densities.

In order to test the validity of the simple superposition law expressed by Eqs. (3.5) on the inclusion of the a-component atoms into the normal fluid fraction of the mixture, it seems necessary to introduce into the formalism the semiempirical formulas which describe fairly well the normal-superfluid division of liquid He II. This means that throughout the second sound velocity and torque formulas, the $(T/\bar{T}_s(x))^4$ ratios will be replaced by $(T/\bar{T}_s(x))^{5.5}$, while the entropy of the He^4 component will be taken to be, throughout,

$$\frac{\bar{S}_s(T,x)}{k}=\left(\frac{\bar{S}_s[\bar{T}_s(x)]}{k}\right)\left(\frac{T}{\bar{T}_s(x)}\right)^{5.5}, \quad (3.16)$$

and the heat capacity at constant volume,

$$\bar{C}_{vs}(T,x)/k=5.5[\bar{S}_s(T,x)/k]. \quad (3.17)$$

The He^3-component entropy per atom will be taken to be given by (3.12), while, at the relatively low x-value mixtures, we use

$$\bar{T}_s(x)\simeq(2.186)(1-x)^{\frac{1}{2}}, \quad (3.18)$$

which is equivalent practically to the empirical transition temperatures.[5]

The results of the calculations of the second sound velocities of propagation together with the observed values[19] are to be found in Table I. In Table II we give

TABLE I. Observed[a] and calculated second sound wave velocities $\delta_2(x,T)$, in mixtures of various He^3-mole fractions (x), at different temperatures T.

T °K	(x =0.003) Obs. m/sec	Calc. m/sec	(x =0.008) Obs. m/sec	Calc. m/sec	(x =0.043) Obs. m/sec	Calc. m/sec
0.9	32.5	64.4	···	96.1	35.6	113.9
1.0	29.5	47.0	···	72.7	36.1	106.1
1.1	26.0	36.2	···	53.8	35.1	90.7
1.2	23.6	29.8	···	42.3	33.6	74.2
1.3	22.5	26.2	25.7	34.7	32.0	60.3
1.4	21.9	24.1	24.4	30.0	30.4	49.6
1.5	21.6	22.7	23.5	26.8	28.5	41.3
1.6	21.4	21.7	22.9	24.5	26.8	34.8
1.7	···	20.6	21.9	22.6	24.5	29.8
1.8	···	19.4	21.1	20.8	22.1	25.3
1.9	···	17.7	19.9	18.6	19.6	20.9
2.0	···	15.2	···	15.6	16.0	15.6
2.1	···	10.9	···	10.7	7.0	6.9

[a] See reference 19.

[18] J. R. Pellam and W. H. Hanson, Phys. Rev. **85**, 216 (1952); J. R. Pellam and P. M. Morse, Phys. Rev. **78**, 474 (1950).

[19] E. Lynton and H. A. Fairbank, Phys. Rev. **80**, 1043 (1950); J. C. King and H. A. Fairbank, Phys. Rev. **90**, 989 (1953).

the torques in a single mixture, together with the ratios of the mixture and pure liquid He II torques at the same temperature.[20] It will be seen that at temperatures higher than about 1.4°K, the calculated second sound velocity values are in fair agreement with the observed ones. One probable reason for the increasing discrepancies below this temperature may be associated with the fact that the empirical power laws (3.16) and (3.17) become increasingly worse at these temperatures. As far as the torques are concerned, beside a semi-qualitative observation[21] on its very large reduction, at low temperatures, in an approximately 4 percent liquid He^3-He^4 mixture, measurements are not yet available.

At very low temperatures, where the second sound velocities tend to vanish with decreasing temperature,[22] and where the symmetric fluid component is in the T^3 or phonon excitation region, the agreement between the calculated and observed second sound velocity values is only qualitative. Here the present theory predicts, in agreement with the observations a second sound velocity increasing with decreasing x values and increasing temperatures. However, the calculated velocities differ considerably from the observed ones. This is, however, not too surprising, in view of the rather questionable validity of the present asymptotic model at these low temperatures.

Results similar to those expressed by Eqs. (3.13) and (3.14) have been also obtained by Pomeranchuk[23] in an investigation of second sound propagation in mixtures where a direct interaction between the He^3 and He^4 atoms is postulated. The decrease of the second sound wave field torque in mixtures has been predicted previously by Koide and Usui.[24]

As a rule, an inspection of the relations describing certain phenomena in liquid He II will suggest, on the basis of the superposition law (3.5), whether these same phenomena are inhibited or not in mixtures of liquid He^3-He^4, below their transition temperature. For instance, the intensity of the thermomechanical effect represented by[25]

$$\text{grad}p=(S/V)\,\text{grad}T \tag{3.19}$$

will be seen to be increased in mixtures over that observed in liquid He II for the same value of grad$T$ and at the same temperature, because of the increased value of the entropy in mixtures. *Vice versa*, the mechanocaloric effect, which is the inverse effect of the preceding one should be reduced. Similarly, if the film flow rate is taken to be proportional to (ρ_s/ρ), or the superfluid fraction of the system, this ratio being smaller in mixtures than in liquid He II, the film flow rate should become smaller in mixtures than in liquid He II, the temperatures being the same. This appears to be in agreement with the observations[26] of Hammel and Schuch.

TABLE II. Calculated second sound wave field torques $\tau(x,T)$ and torque ratios $\tau(x,T)/\tau(0,T)$ exerted on a flat circular disk of unit radius whose plane is at a 45° angle with the direction of propagation of the second sound waves, when the mean heat current density is 1 joule/cm² sec, at $x=0.043$ and various temperatures T.

T °K	$\tau(x,T)$ cgs units	$\tau(x,T)/\tau(0,T)$
0.9	5.91	0.0053
1.0	4.85	0.0108
1.1	4.21	0.0219
1.2	3.80	0.0425
1.3	3.50	0.0770
1.4	3.25	0.128
1.5	3.02	0.199
1.6	2.81	0.288
1.7	2.67	0.392
1.8	2.64	0.510
1.9	2.85	0.655
2.0	3.77	0.896
2.1	14.3	2.52
2.123	∞	∞

It should finally be noted that the so-called heat-flush effect[27] which is similar to a thermomechanical type effect within a liquid He^3-He^4 mixture, whereby the He^3 atoms are collected in the cold region of the liquid constitutes rather convincing evidence for the dragging of the He^3 atoms by the normal He^4 atoms. Clearly, this qualitative effect does not prove the superposition law (3.5) which demands that all the He^3 atoms be included into the normal portion of the mixture.

IV. THE TRANSITION SURFACE OF LIQUID He^3-He^4 MIXTURES. CONCLUDING REMARKS

In the space of the coordinates (T,p,x), the relation

$$\bar{T}_\lambda=\bar{T}_\lambda(p,x),$$

defines the transition surface of the mixtures. This surface cuts the $(p,\bar{T}_\lambda)$ plane or the $x=0$ plane along the liquid He^4 lambda line. Let the pressure axis be vertical and the T axis such that a positive rotation around the p axis would bring it into coincidence with the mole-fraction x axis. In this coordinate system, the transition surface is limited downward by a curve whose projection on the (T,x) plane is the transition line $\bar{T}_\lambda(x)$, Eqs. (1.13) or (1.14). The transition surface and the coordinate planes (p,x) and (T,x) intersect at the point $(p=0, T=0, x=1)$.

It is an experimentally established fact that

$$\partial T_\lambda(0)/\partial p<0,$$

or that the λ temperature of liquid He^4 decreases when external pressure is applied to the liquid. Since one also

[20] The entropy and heat capacity data used here are those given by Kramers, Vasscher, and Gorter, Physica **18**, 329 (1952).
[21] B. Weinstock and J. R. Pellam, Phys. Rev. **89**, 521 (1953).
[22] See the second work quoted in reference 19.
[23] I. Pomeranchuk, J. Exptl. Theoret. Phys. (U.S.S.R.) **19**, 42 (1949); see also P. J. Price, Phys. Rev. **89**, 1209 (1953).
[24] S. Koide and T. Usui, Progr. Theoret. Phys. (Japan) **6**, 506 (1951).
[25] H. London, Proc. Roy. Soc. (London) **A171**, 484 (1939).
[26] E. F. Hammel and A. F. Schuch, Phys. Rev. **87**, 154 (1952).
[27] Lane, Fairbank, Aldrich, and Nier, Phys. Rev. **73**, 256 (1948).

has

$$\partial \bar{T}_s(x)/\partial x<0,$$

it appears reasonable to expect that over all the physically accessible portion of this surface, one should have

$$[\partial \bar{T}_s(x)/\partial p]_{x=0}<0,$$

or that the transition temperature of mixtures be also depressed by applying external pressure.

We had previously pointed out[28] that the ideal symmetric fluid approximation of liquid He^4 cannot account for the observed pressure effect of its transition temperature. The ideal-fluid model yields $\partial T_0/\partial p>0$ in contrast with the data. It was then suggested[28] that the observed slope of the λ line is associated with the intervention of the interatomic forces.

At any rate, the two types of perturbations, namely, mixing liquid He^4 with liquid He^3 and applying pressure to liquid He^4, depress the transition temperature. Whatever the actual details of the transition may turn out to be, it appears reasonable to say, at the present time, that it belongs to a class of order-disorder type of transformations. The ordering process would hereby be determined, approximately, by a negative ordering mean potential energy per atom, say $-V_0$. The latter will be assumed to be a constant in these qualitative discussions. It is then expected that for thermal energies or temperatures such that

$$T\lesssim T_0=V_0/k,$$

the ordering process should progress, with complete order established at the approach of the absolute zero. The details of the laws of this progressing transformation at $T<T_0$ are precisely the quantitative expressions of the resistance with which the disorderly thermal motions tend to counteract the ordering phenomenon originating in the existence of the mean potential type of energy $(-V_0)$. It is then not unreasonable to conceive of the possibility of modifying the value of this ordering potential energy and with it the transition temperature. That this is indeed the case as far as the momentum space ordering of the ideal symmetric fluid component is concerned, as a result of the admixture of the ideal He^3-component, has been proved rigorously in the present paper. The pressure effect on the transition might be looked upon as bringing into play the repulsive interatomic forces which appear to increase $-V_0$, or to decrease the transition temperature. While it is hard to suppress the feeling that the modification of the ordering potential energy and the accompanying decrease of the transition temperature by application of external pressure appear to describe qualitatively the observations, an acceptable proof of this interpretation will have to await the development of the theory where the interatomic forces are fully taken into account. It should be noted that in these qualitative considerations the approximation of a type of superposition of an ordering energy and the interatomic potential energy has been tacitly assumed.

A final remark may be justified here concerning the problem of invariance of the order of the phase change after perturbation. The external pressure effect on pure liquid He^4 does not seem to modify the nature of the transition occurring at the nonperturbed original λ point. The asymptotic ideal quantum fluid mixture model studied above was shown to undergo such a change in the order of its phase transformation. Experimentally, it has as yet not been established whether the transition of liquid He^3—He^4 mixtures is actually a lambda transformation or not. Experimental investigations of this problem in mixtures would be of great interest for a better understanding of the properties of liquid helium through its perturbed phase transformations.

[28] L. Goldstein, J. Chem. Phys. **9**, 472 (1941).

Energy Distribution Function of Electrons in Pure Helium*

FRITZ H. REDER,† AND SANBORN C. BROWN
Department of Physics and Research Laboratory of Electronics, Massachusetts Institute of Technology, Cambridge, Massachusetts

(Received May 14, 1954)

A solution for the Boltzmann transport equation is presented, which allows us to predict high-frequency gas discharge breakdown fields in gases with constant collision frequency of the electron. Theoretical values are in good agreement with the experimental data. This is used to justify the use of our distribution function for determining the average electron energy and the various power losses of an electron in a discharge as a function of E/p.

THE validity of calculating microwave gas discharge breakdown using the electron energy distribution as derived from the Boltzmann transport equation has been amply demonstrated.[1] From the details of such distribution functions we can calculate useful gas discharge parameters. In the following paper the energy distribution function for electrons in pure helium is derived, checked against breakdown measurements, and then used to determine the average energy of the electrons, and the various power losses in a discharge, all as a function of E/p. Previous determinations of the high-frequency gas discharge breakdown in helium was carried out for this gas containing an admixture of mercury to eliminate the excitation levels of helium from the breakdown condition.[2] The present calculation for pure helium requires the use of the excitation function.

Breakdown occurs in a microwave gas discharge in the pressure range here considered, at that electric field where the particle number increased by ionization equals that lost by diffusion. The value of this field, E, may be calculated as a function of the gas pressure, p, the characteristic diffusion length $\Lambda=L/\pi$ (where L is the height of the resonant cavity), and the applied radian frequency ω. To eliminate the frequency dependence, an effective field E_e is introduced such that $E_e=(E\nu_c)(\nu_c^2+\omega^2)^{-\frac{1}{2}}$. Here ν_c is the elastic collision frequency of electrons, considered to be a constant with energy, and equal for helium to $2.55\times10^9 p$. E_e can be thought of as that equivalent dc field which supplies an electron with the same power as the ac field E.

ENERGY DISTRIBUTION FUNCTION

The electron energy distribution function is determined by setting up the electron continuity equation and accounting for the production and loss of electrons in phase space. When both excitations and ionizations are present we must include a term in the Boltzmann transport equation to account for the energy loss due to all inelastic collisions. The total inelastic collision frequency for electrons in helium has been measured by Maier-Leibnitz[3] and an analytic approximation to the experimental data, shown in Fig. 1, is taken to be

$$(\nu_x+\nu_i)/\nu_c=h_0u-h_1-h_2/u, \tag{1}$$

where $h_0=0.0175$ volt^{-1}, $h_1=0.665$, and $h_2=-6.6$ volts. Figure 1 also shows the analytic approximation of the experimental ionization function

$$\nu_i/\nu_c=h_i(u-u_i), \tag{2}$$

with $h_i=5.48\times10^{-3}$ volt^{-1}; u_i is the ionization potential equal to 24.48 volts. The excitation potential u_x is taken as 19.9 volts to allow a simple step approximation for the initial part of the excitation function. It is assumed that the electrons suffering inelastic collisions lose all their energy.

The Boltzmann transport equation is usually developed in terms of the electron velocity. However, for a constant collision frequency it is convenient to introduce a dimensionless independent variable w in the final differential equation for the symmetric component $f(v)$:

$$u=u_Bw;\quad u_B=u_c(M/3m);\quad u_c=(e/m)(E_e/\nu_c)^2,$$

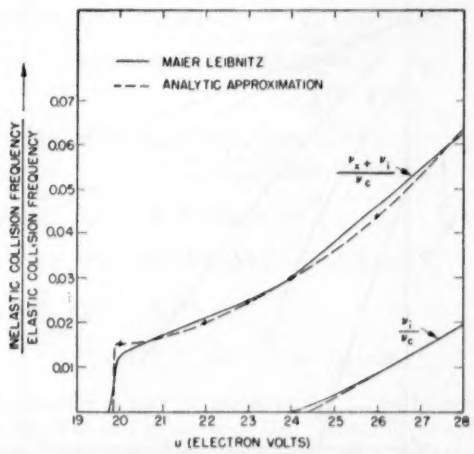

FIG. 1. Inelastic collision frequencies of electrons in helium as a function of electron energy.

* This work was supported in part by the Signal Corps, Air Materiel Command, and the U. S. Office of Naval Research.

† Now at the Signal Corps Engineering Laboratories, Watson, New Jersey.

[1] A. D. MacDonald and S. C. Brown, Phys. Rev. **76**, 1634 (1949).

[2] A. D. MacDonald and S. C. Brown, Phys. Rev. **75**, 411 (1949).

[3] H. Maier-Liebnitz, Z. Physik **95**, 499 (1935).

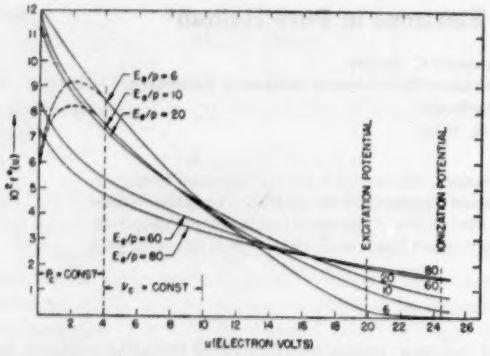

FIG. 2. Energy distribution function of electrons in helium.

where u_e is the average energy gain of an electron from the field between two successive collisions, and M is the mass of the gas atom.

The differential equation for $f(w)$ is then

$$f''+f'[1+(3/2w)]+f[(A/w)-(u_E/\Delta E_e)^2]=0, \qquad A=\tfrac{3}{2}-(M/2m)(\nu_x+\nu_i)/\nu_e. \tag{3}$$

This equation is of second order and has a pole at first order at the origin, $w=0$, and an essential singularity at infinity, $w=\infty$. Since Eq. (1) is not valid for $u<u_x$, we have to divide the energy scale at $w=w_x$ and to discuss the integration of Eq. (3) in the two regions separately.

In the elastic collision range, below w_x, Eq. (3) takes the form:

$$f_e''+f_e'[1+(3/2w)]+f_e[(3/2w)-(u_E/\Delta E_e)^2]=0. \tag{4}$$

MacDonald and Brown[2] have worked out this case and find the solution in terms of confluent hypergeometric functions to be

$$f_e(w)=\{[M_1(w)+C_e w^{-\frac{1}{2}}M_2(w)]\times\exp[-(g+1)w/2]\}C_{eN}, \tag{5}$$

where

$$M_1(w)=M(\alpha:\tfrac{3}{2}:gw); \quad M_2(w)=M(\alpha-\tfrac{1}{2};\tfrac{1}{2};gw),$$
$$\alpha=\tfrac{3}{4}(g+1)/g; \quad g^2=1+4(u_E/\Delta E_e)^2,$$

and C_e and C_{eN} are integration constants.

In the range of inelastic collisions between the electrons and the gas molecules, when the electron energy lies above u_x, Eq. (3) may be written as

$$f_i''+f_i'[1+(3/2w)]-f_iG(w)=0, \tag{6}$$
$$G(w)=\tfrac{1}{2}(g^2-1)^{\frac{1}{2}}+h_0u_e(M^2/6m^2)-[\tfrac{3}{2}+Mh_1/2m](1/w)-(3h_2/2u_e)(1/w)^2.$$

There exists only one asymptotic solution for Eq. (6) which fulfills the boundary condition that the distribution function vanishes at infinity, namely:

$$f_i(w)=C_{eN}C_i w^{(K-1)}[\exp(-a_1w)]\times[1+\sum_{n=1}^{\infty}(\prod_{r=1}^{n}p^{(r)}/n!(a_0w)^n],$$
$$a_0=[g^2+6h_0(u_E^2/u_e)]^{\frac{1}{2}}; \quad a_1=\tfrac{1}{2}(a_0+1); \tag{7}$$
$$K=(M/2m)h_1/a_0, \quad p^{(r)}=\tfrac{1}{16}-3h_2/2u_e-[K+\tfrac{1}{2}-r]^2;$$
$$\prod_{r=1}^{n}=p^{(1)}p^{(2)}\cdots p^n.$$

The integration constants C_e and C_i can now be calculated by joining f_e and f_i in value and slope at $w=w_x$. As a result of these processes we find:

$$C_e=-w_x^{\frac{1}{2}}(M_{1x}/M_{2x})(T_1/T_0),$$
$$C_i=(1/2T_0M_{2x}w_x^{K+\frac{1}{2}})\exp[(a_0+g)w_x/2],$$
$$T_0=\textstyle\sum_x'+\sum_x[(K-\frac{1}{4})/w_x-(a_0-g)/2-gM_{2x}'/M_{2x}],$$
$$T_i=T_0+\textstyle\sum_x[g(M_{2x}'/M_{2x}-M_{1x}'/M_{1x})-1/2w_x], \tag{8}$$
$$\textstyle\sum_x=\sum_{r=0}^{\infty}P_r; \quad P_0=1; \quad P_r=P_{r-1}(p^{(r)}/ra_0w_x),$$
$$\textstyle\sum_x'=-(1/w_x)\sum_{r=0}^{\infty}rP_r; \quad M_{1x}=M_1(w_x); \quad M_{2x}=M_2(w_x),$$
$$gM_1'=\partial M_1(w)/\partial w; \quad gM_2'=\partial M_2(w)/\partial w.$$

Finally, the distribution function has to be transformed from velocity space to the more convenient energy space, and it has to be normalized. The transformation follows from $f^*(u)du=4\pi v^2f(w)dv$, where this function is the fraction of electrons within the energy limits $u\pm\frac{1}{2}du$. The normalization yields C_{eN} from $C_{eN}=\int_0^\infty(f^*(u)/C_{eN})du=1$. Here $f^*(u)/C_{eN}$ means that we transform Eqs. (5) and (7) first to the form $f^*(u)$ and then set $C_{eN}=1$. The integral is best evaluated graphically.

Figures 2 and 3 show the distribution function $f^*(u)$ for a few typical values of (E_e/p), Fig. 2 in the energy

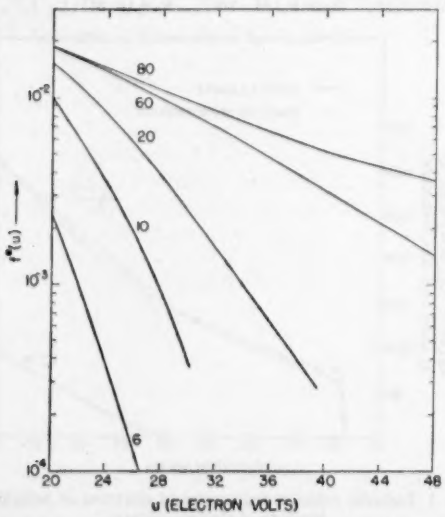

FIG. 3. Energy distribution function of electrons in helium in the inelastic collision range.

range 0–24 volts and Fig. 3 in the range from 20 to 48 volts. The shape of the solid curves for u less than 4 ev. is only an approximation to the real behavior for several reasons: in this range, ν_c is not constant but decreases as $u^{\frac{1}{2}}$, and we have neglected the fact that those electrons which suffer inelastic collisions with gas atoms at high energies will fall back to energies close to, but not at, the origin. Our simplified treatment is justified as long as we use the distribution function only for the averaging of functions which vanish at $u=0$, determining such quantities as the diffusion coefficient or the electron energy. The distribution function can be calculated for the case of ν_c not constant, below 4 ev, though it makes no difference in the value of the breakdown potential as long as E_e/p does not become smaller than 5 volts/cm mm Hg.

The usefulness of the concept of an effective field E_e is well illustrated in Fig. 4 by a comparison of dc distribution functions calculated by Smit[4] and by Dunlop and Emeleus[5] with our distribution function for the same values of E/p. The correction for ν_c proportional to $u^{\frac{1}{2}}$ has been used in these plots.

THE BREAKDOWN EQUATION

Experimental methods are lacking for directly checking on energy distribution function. However, if calculated distribution functions correctly predict the details of a microwave breakdown, considerable confidence can be gained in the validity of the theoretical formulation. The distribution function derived in this present work was checked in this way.

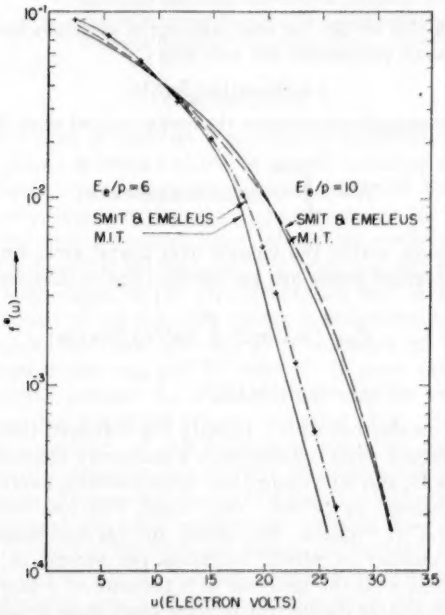

FIG. 4. Comparison of our energy distribution function of electrons in helium with that given by Smit (see reference 4) and by Dunlop and Emeleus (see reference 5).

[4] I. A. Smit, Physica **3**, 543 (1936).
[5] S. H. Dunlop and K. G. Emeleus, Brit. J. Appl. Phys. **12**, 163 (1951).

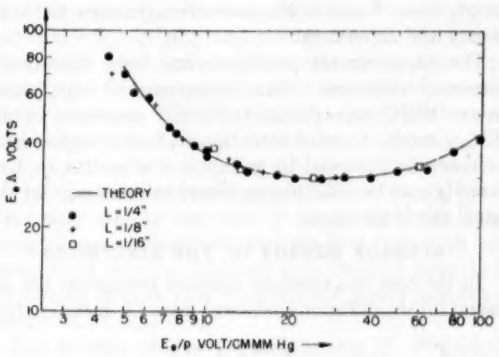

FIG. 5. High-frequency gas discharge breakdown in pure helium.

The breakdown condition can be written, $D=\Lambda^2\langle\nu_i\rangle$, where both the diffusion coefficient and the ionization frequency terms depend on the distribution function. They are calculated from

$$D=\int_0^\infty (2e/3m\nu_c)uf^*(u)du,$$

$$\langle\nu_i\rangle=h_i\int_{u_i}^\infty \nu_c(u-u_i)f^*(u)du.$$

In the elastic range, the diffusion integral can be represented by confluent hypergeometric functions. In the inelastic range, we approximate the functions by Taylor series around w_i and w_x.

Inserting D and $\langle\nu_i\rangle$ in the breakdown equation yields a transcendental equation for $E_e\Lambda$ and E_e/p which may be evaluated in the form:

$$\frac{(M/m)(h_i/u_i)(C_i/C_e)(u_E/a_1)^2 w_i^{k+\frac{1}{2}}\sum_i \exp(-a_1w_i)}{1+(2w_x^{\frac{1}{2}}/C_eC_{eN})(f_{ex}+\partial f_{ex}/\partial w)\times(1-\psi)=1,}$$

$$\psi=(2m/M)(u_i/h_i)[a_1/(\Lambda E_e)^2](u_x/u_i)^{k+\frac{1}{2}}\times(\textstyle\sum_D/\sum_i)\exp[a_1(w_i-w_x)],$$

$$\sum_i=\sum_{n,r=0}^{\infty} B_n^{(r)};\quad B_n^{(0)}=(u_x/u_i)^nP_n; \tag{10}$$

$$B_n^{(r)}=B_n^{(r-1)}[(r+1)/r][(k+\tfrac{3}{4}-n-r)/(a_1w_i)],$$

$$\sum_D=\sum_{n,r=0}^{\infty} A_n^{(r)};\quad A_n^{(0)}=P_n;$$

$$A_n^{(r)}=A_n^{(r-1)}[(k+7/4-n-r)/(a_1w_x)].$$

The quantity ψ may be neglected for $E_e/p<10$ v/cm mm Hg. The first equation of (10) represents the ratio of the net number of electrons produced in the region $u>u_x$ due to the ionization and diffusion, to the number of electrons lost in the elastic collision range $u<u_x$ due to diffusion. This ratio must be equal to unity in a

steady state. Figure 5 illustrates the agreement between theory and experiment.

The experimental procedure has been adequately discussed elsewhere.[6] Our measurements were taken in an *OFHC* copper resonant cavity operating in the TM_{010} mode. Careful attention to insure high purity helium was observed by pumping the system to 10^{-8} mm Hg and by substituting liquid helium traps for the usual liquid air traps.

AVERAGE ENERGY OF THE ELECTRONS

In the case of a constant collision frequency, the integral for the diffusion coefficient gives the mean energy:

$$\langle u\rangle=\int_0^\infty uf^*(u)du=\phi\left(\frac{u_E}{a_1}\right)^2\left(\frac{u_i}{u_x}\right)^{k+\frac{1}{2}}\times\frac{(\Lambda E_e)^2C_{eN}\sum_i}{M_{2x}T_0}\exp\left[-a_1(w_i-w_x)+\frac{g-1}{2}w_x\right],$$

$$\phi=(M/2m)(2e/m)^{\frac{1}{2}}(\pi h_i/u_i^{\frac{1}{2}}).$$

The results of this calculation are shown in Fig. 6, extending to higher E_e/p the values given by Townsend and Bailey[7] and Smit.[4] Because the temperature motion of the gas atoms has been neglected, $\langle u\rangle$ approaches zero as E/p approaches zero.

DISTRIBUTION OF POWER LOSSES

The power input per electron is $P=\nu_e u_e$, which follows directly from the definition of u_e. This power is dissipated in several ways. Part of it goes into heat in the gas by recoil of atoms struck by the electrons. Part is carried as kinetic energy of the electrons to the walls of the container; this is called the diffusion loss. The rest goes into inelastic collisions and divides into radiation loss and ionization loss. This partition as a function of E_e/p is of interest and can be calculated from the distribution function.

The solution of the diffusion equation for the boundary conditions of parallel plates yields $n=n_0\cos(z/\Lambda)$, where n is the electron density at z and n_0 that at the central plane. Inserting this in the flow equation gives

$$\Gamma_z=-D\partial n/\partial z;\quad D=(2e/m)(u/3\nu_e).$$

From this we get the total number of electrons lost to the walls per second per unit area:

$$z=(4e/m)(n_0/3\nu_e\Lambda)u.$$

Since each electron carries the energy u, and since there are

$$N=2\int_0^{L/2}n_0\cos(z/\Lambda)dz=2\Lambda n_0$$

electrons within the volume over a unit area, we get the average power loss per electron due to diffusion:

$$P_D=(2e/3m\Lambda^2)\int_0^\infty(u^2/\nu_e)f^*(u)du;$$

$$P_D/P=2\langle n^2\rangle/3(\Lambda E_e)^2.$$

If an electron with a velocity v is scattered through an angle α when colliding with a stationary molecule of mass M, and if its energy loss to the recoiling molecules is assumed to be only very small, this loss will be $(2m/M)(1-\cos\alpha)u$. We define by $vp\sigma(v,\alpha)\sin\alpha d\alpha d\psi$ the number of elastic collisions per second of one electron with the molecule at a pressure of p mm Hg which scatter the electron into the space angle $\sin\alpha d\alpha d\psi$. The power loss per electron is then

$$(2m/M)u\left[vp\int_{\alpha=0}^{\pi}\int_{\psi=0}^{2\pi}(1-\cos\alpha)\sigma(v,\alpha)\sin\alpha d\alpha d\psi\right]=(2m/M)u\nu_e.$$

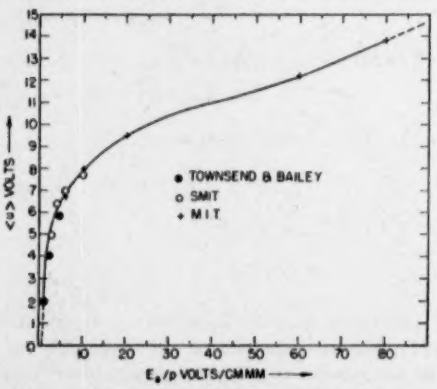

FIG. 6. Average energy of electrons in helium.

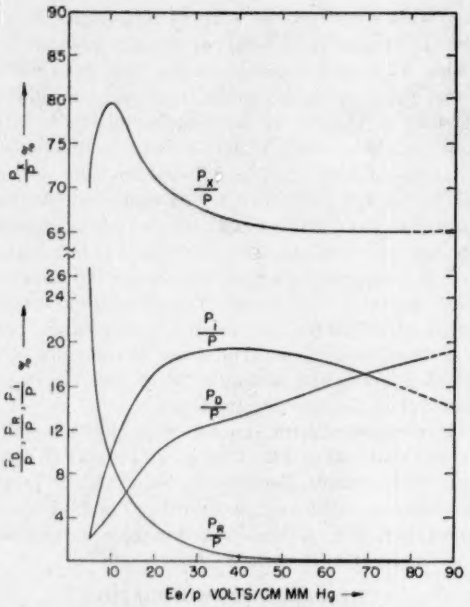

FIG. 7. Various power losses of an electron in a microwave gas discharge in helium in percent of input power.

[6] S. C. Brown and D. J. Rose, J. Appl. Phys. **23**, 711 (1952).
[7] J. S. Townsend and V. A. Bailey, Phil. Mag. **42**, 873 (1921).

The average power loss due to recoil is therefore

$$P_R=(2m/M)\nu_c\langle u\rangle; \quad P_R/P=(2m/M)\langle u\rangle/u_c.$$

The ionization power loss per electron is found from u_i and $\langle\nu_i\rangle$:

$$P_i=u_i\langle\nu_i\rangle; \quad \frac{P_i}{P}=\frac{u_i}{u_c}\frac{\langle\nu_i\rangle}{\nu_c}=\frac{h_iu_i}{u_c}\int_{u_i}^{\infty}(u-u_i)f^*(u)du.$$

The radiation power loss per electron may be determined from the energy balance

$$P_x=P-P_D-P_R-P_i,$$

$$P_x/P=1-2\langle u^2\rangle/3(\Delta E_e)^2-2m\langle u\rangle/Mu_c-u_i\langle\nu_i\rangle/u_c\nu_c.$$

The relative power losses as referred to the power gain, $P=u_c\nu_c$, from the electric field are plotted as functions of E_e/p in Fig. 7. It can be seen from this plot that the recoil loss becomes predominant at $E_e/p<5$ but that it is negligibly small for $E_e/p>30$. The ionization power loss shows a flat maximum in the range $30<E_e/p<50$, where the breakdown potential reaches its flat minimum. The diffusion loss is steadily increasing with increasing E_e/p, or decreasing p, as might be expected. Finally it is shown that the radiation loss is by far the predominant loss mechanism for $E_e/p>5$. This may also be expected if we consider the large energy losses u_x involved, and the fact that there are many more exciting collisions than ionizing ones. It is interesting to note that the radiation power loss has a maximum at $E_e/p=10$.

The authors wish to thank Professor W. P. Allis of Massachusetts Institute of Technology for many valuable discussions, and Professor A. Smekal of the University of Graz for his interest.

PHYSICAL REVIEW VOLUME 95, NUMBER 4 AUGUST 15, 1954

Build-Up Measurements on Cobalt-60 Gamma Radiation in Iron and Lead

C. GARRETT AND G. N. WHYTE
Division of Applied Physics, National Research Council, Ottawa, Canada
(Received April 13, 1954)

The transmission of gamma radiation from a "point isotropic" source of cobalt-60 through iron and lead has been measured out to a thickness of approximately 15 mean-free-paths. The dose build-up factors derived from the observed transmissions agree satisfactorily with the calculations based on the work of the National Bureau of Standards group and carried out by the Nuclear Development Associates.

INTRODUCTION

IF a mass of material of appreciable lateral extent is placed between a source of gamma radiation and a detector, the gamma-ray intensity observed by the detector is greater than that to be expected on the basis of the total or "narrow-beam" absorption coefficient of the radiation in the material. The extra intensity is due to interactions of the primary gamma rays in which only part of the quantum energy is transferred to the medium and part survives as a quantum of lower energy which may still be detected. In some cases of practical interest the total intensity may be several times that due to the primary radiation alone.

The problem of this buildup of secondary gamma radiation in matter has recently been the subject of a number of theoretical studies.[1] Of the actual calculations performed, the most complete are probably those based on the work of the National Bureau of Standards group and carried out by Nuclear Development Associates; preliminary results of this work (hereafter referred to as the NDA-NBS calculations) have been reported by Fano[2] and by Goldstein *et al.*[3]

The calculations for materials of low atomic number —where photoelectric absorption plays a relatively minor role—have been checked experimentally with cobalt-60 gamma rays by a variety of measurements of energy spectra and buildup factors in water;[4–7] the agreement in this region is excellent. But at higher atomic numbers the agreement is less certain. The transmission measurements of Beach *et al.*,[8] using plane parallel geometry, suggest a discrepancy with the theory beyond about 4 mean free paths. In lead the build-up factors measured by Elliot *et al.*,[9] using photographic films as detectors, are fairly consistent with the theoretical ones out to about 10 mean free paths, but they suffer from uncertainty in the response of the film at low energies. On the other hand, Dixon[10] has

[1] Summarized by U. Fano, J. Research Natl. Bur. Standards **51**, 95 (1953).
[2] U. Fano, Nucleonics **11**, Nos. 8, 9 (1953), and **11**, No. 9, 55 (1953).
[3] Goldstein, Wilkins, and Spencer, Phys. Rev. **89**, 1150 (1953); Goldstein, Wilkins, and Preiser, "Interim Report on the NDA-NBS Calculations of Gamma Ray Penetration," NDA Memo 15C-20 (Nuclear Development Associates, White Plains, New York, 1953).
[4] Gladys R. White, Phys. Rev. **80**, 154 (1950).
[5] Evans Hayward, Phys. Rev. **86**, 493 (1952).
[6] M. A. Van Dilla and G. J. Hine, Nucleonics **10**, No. 7, 54 (1952).
[7] M. M. Weiss and W. Bernstein, Phys. Rev. **92**, 1264 (1953).
[8] Beach, Theus, and Faust, Phys. Rev. **92**, 355 (1953).
[9] Elliot, Farrar, Myers, and Ravilious, Phys. Rev. **85**, 1085 (1952).
[10] W. R. Dixon, Phys. Rev. **85**, 498 (1952).

made measurements in lead on the collimated beam from a large cobalt-60 teletherapy unit, using an ionization chamber with a bakelite wall. This gave readings directly in terms of dose rates, allowing a comparison with the calculations of dose buildup, but an exact comparison was hampered by two other factors: (a) the geometry, which did not correspond exactly to either point isotropic or plane monodirectional source conditions, and (b) the presence in the primary beam of a large and uncertain amount of scattered radiation originating both in the source and in the walls of the collimator. It was therefore felt that an experiment was needed in a material of high atomic number under conditions that could be readily interpreted.

In the present experiment the gamma-ray dose rate in the absorbing medium was measured as a function of distance from a cobalt-60 source imbedded in the medium. Measurements were made in both iron and lead.

EXPERIMENTAL ARRANGEMENT

The apparatus consisted of a cobalt-60 source and a condenser ionization chamber, both imbedded in a mass of the absorbing material.

Because of the large range of attenuations to be investigated, it was necessary to use sources of three different strengths. For small attenuations a 10-mC cobalt cylinder 6 mm in diameter and 6 mm long was used; at larger distances this was replaced by a stronger source consisting of a 500-mC cobalt pellet 6 mm in diameter by 7 mm long in the center of an aluminum cylinder, 1.9 cm in diameter by 4.5 cm long; and for the largest attenuations the source was an aluminum irradiation can containing 300 curies of radioactive cobalt pellets in a cylindrical shell 4.0 cm long, 1.8 cm in outside diameter, and 0.3 cm thick.

The ionization chambers were Baldwin-Farmer types BD-2 and BD-11. These are small condenser chambers made of an "air-equivalent" Bakelite-graphite material. The BD-2 has an air volume roughly in the form of a hemispherical shell 0.4 cm in diameter. Its wall thickness was increased to greater than 0.4 gm/cm^2 by the addition of a Lucite cap, in order to ensure secondary-electron equilibrium. The BD-11 has an air volume 3.6 cm long by 1.3 cm in diameter with a 2-mm wall to which was added a 4-mm thick Lucite cap.

For the measurements in iron the source was placed in a cylindrical hole in an iron block, the sides and back of which were shielded with further iron blocks to a thickness of 20 cm. The iron between the source and the detector was in the form of plates 45 cm square by 1.28 cm thick, which could be inserted or removed in order to vary the distance of the detector from the source. The ionization chamber itself was imbedded in a slot in one of the plates, and more plates were added to provide 5 cm of iron behind the chamber. Thus, in effect, the chamber could be placed at a variable distance from the source in a solid mass of iron.

The arrangement for measurements in lead was the same as that for iron except that the lead plates were 30 cm square.

RESULTS

The ionization rate was measured for iron thicknesses from 0 to 260 g/cm^2 and for lead thicknesses from 0 to 290 g/cm^2. At the smallest thicknesses the 10-mC source and the small ionization chamber were used, and the transmission curve was extended in sections by changing to larger sources and the larger chamber. The sections of the curve measured with the different sources and chambers were normalized in the regions where they overlapped.

In order to eliminate the inverse-square-law variation of the primary intensity with distance, the readings were multiplied by the square of the distance from the center of the source to the center of the chamber, i.e., all readings were corrected to a distance of one meter.

The rate for zero absorber thickness was obtained by measuring the ionization rate in the small chamber when it and the 10-mC source were suspended 10 cm apart on thin strips of paper well away from any scattering material, and correcting to 1 meter. The experimental transmissions were then obtained by taking the ratios of the ionization rates measured in the medium to the rate measured with the bare source, all rates being normalized to correspond to the 10-mC source and the small chamber.[11]

Before comparing these results with theory it is necessary to consider the question of degraded radiation from the source. The theoretical calculations refer to a point source of mono-energetic radiation. But in any actual source some fraction of the emitted gamma rays will undergo Compton interactions in the source material itself and will emerge with reduced energy. When there is no absorbing material between the source and the detector this degraded radiation will produce a contribution to the ionization rate proportional to its intensity. But when a large thickness of absorber intervenes, the degraded radiation, being more strongly absorbed than the primary beam, will be reduced to a negligible fraction of that beam and will produce no effect in the detector; the observed intensity will be the same as if there were no degraded radiation coming from the source. Thus, in calculating the transmissions at large attenuations for comparison with theory, one should consider only the intensity of primary radiation from the source, and the observed transmissions should be increased by an amount corresponding to the fraction of the source radiation which has been degraded in energy.

An estimate of the amount of degraded radiation emerging from the 10-mC source in addition to the undegraded primary radiation, based on the dimensions of the source and the cross section for Compton scatter-

[11] These experimental transmissions will be tabulated in National Research Council Report No. 3257.

ing, yielded a value of about 8 percent. The observed transmissions were therefore multiplied by a factor of 1.08 in order to eliminate the effect of this radiation. At small attenuations this procedure becomes questionable, since a significant fraction of the degraded radiation may get through to the detector. In the case of lead most of it should be removed in the first few primary mean free paths, so that little error will be introduced by multiplying by 1.08 throughout; in the case of iron the first few values will be somewhat high.

In order to find the build-up factors associated with the measured transmissions it is necessary to divide the experimental transmissions by the corresponding transmissions for the primary radiation. These latter were worked out on the basis of theoretical absorption coefficients calculated by White:[12] for iron, $\mu(1.17)=0.0549$ cm^2/g, $\mu(1.33)=0.0516$ cm^2/g, and for lead, $\mu(1.17)=0.0585$ cm^2/g, $\mu(1.33)=0.0537$ cm^2/g. (The values for lead include a downward correction of 10 percent in the photoelectric coefficient of Hulme *et al.*[13] made on the basis of an analysis of the data of Colgate[14] on narrow-beam absorption.) The build-up factors obtained in this way are shown by the circles in Figs. 1 and 2.

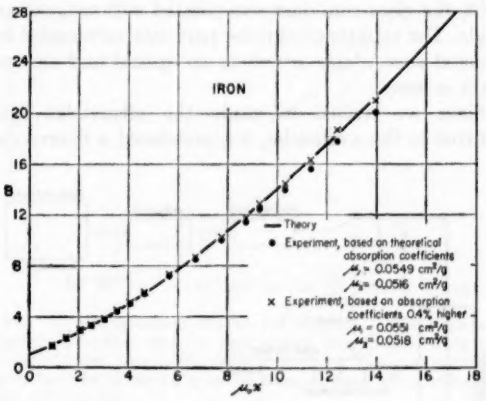

FIG. 1. Build-up factors in iron.

The solid line on each graph shows the theoretical build-up factor as a function of absorber thickness, obtained by interpolation from the tables of Fano.[2] The absorber thickness $\mu_0 x$ is expressed in primary mean free paths, μ_0 being the initial narrow-beam absorption coefficient of the primary radiation.

[12] Gladys R. White (private communication).
[13] H. R. Hulme, Proc. Roy. Soc. (London) **A133**, 381 (1931); Hulme, McDougall, Buckingham, and Fowler, Proc. Roy. Soc. (London) **A149**, 131 (1935).
[14] S. A. Colgate, Phys. Rev. **87**, 592 (1952).

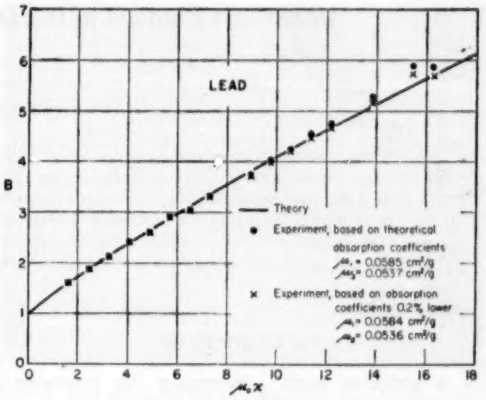

FIG. 2. Build-up factors in lead.

DISCUSSION

The agreement between experiment and theory is quite good, although there is some divergence at large thicknesses. Since the ionization measurements were made to an accuracy of about 1 percent, and since the values obtained for the measured transmissions near the ends of the curves depend on three normalizations of different portions of the curve, the last few points may be in error by 2 or 3 percent. In addition, the values obtained for the "experimental" build-up factors are very sensitive to the absorption coefficient used in calculating the primary transmissions; thus an increase of 0.4 percent in the coefficients for iron would lead to the values indicated by the crosses in Fig. 1, while a decrease of 0.2 percent in the case of lead would result in the crosses in Fig. 2. That is, a change of less than half a percent in the absorption coefficients in each case would eliminate any discrepancy between theory and experiment. In fact, however, some of the disagreement is likely due to experimental error, so that the values of the shifts in absorption coefficients given above are not significant.

Even neglecting the possibility that the theoretical absorption coefficients used above may be somewhat in error, the discrepancy between theory and experiment is within the limits of accuracy claimed for the calculations (about 5 percent at 15 mean free paths). These results therefore extend confirmation of the NDA-NBS build-up calculations in the region of 1 Mev to intermediate and high atomic numbers.

ACKNOWLEDGMENT

We are grateful to Dr. U. Fano, Dr. L. V. Spencer, Dr. Evans Hayward, and Dr. Gladys White, all of the National Bureau of Standards, for several helpful discussions.

Ultraviolet Photons in the Decay of Metastable Argon Atoms

L. COLLI
Laboratori CISE, Milan, Italy
(Received December 29, 1953)

Some measurements of the lifetime of uv photons emitted by the excited states of argon are reported, when the excitation is obtained by the impact of the electrons in a Townsend avalanche. The measurements were made by converting the ultraviolet into visible light by means of a fluorescent screen and by observing the visible light with a photomultiplier. The results are that the energy of the uv photons is about 10 ev and that the law of emission in time is represented by the formula $\exp -t/\tau_A - \exp -t/\tau_M$, where $\tau_A = 3.4\times10^{-6}$ sec and $\tau_M = 1/9p^2$ sec (p = gas pressure in mm Hg).

INTRODUCTION

IN a previous work[1] concerning the processes of discharge in cylindrical counters containing argon of high purity, we have pointed out the production of photons, probably ultraviolet, in Townsend avalanches on the wire. These photons have been found to be responsible, through a photocathodic process, for the starting and the maintenance of the corona current. The aim of the present work is to investigate directly the existence of these photons and to study their origin.

EXPERIMENTAL APPARATUS

The apparatus consists of a counter contained in a glass cylinder which is mounted on a glass vacuum system. The glass envelope also contains a furnace, consisting of an iron tube containing turnings of a Ca-Mg alloy, which can be heated to 500°C and is used to purify the argon.[1] The whole device can be evacuated to 10^{-6} mm Hg. Argon of high purity is used in the measurements, and the purity is checked by measuring the drift velocity of electrons in an electric field to be better than 99.9 percent purity. The argon is further purified by circulation in the furnace.

The experimental conditions have been found to be always reproducible.

The counter, shown in Fig. 1, is made of 6 nickel wires placed in a circle 18 mm in diameter, and a central tungsten wire of 0.1-mm diameter. The length of the counter is 100 mm. A gun containing polonium is put at one end of the counter for the purpose of shooting α particles in a direction parallel to the wire and at a distance of 2 mm from it.

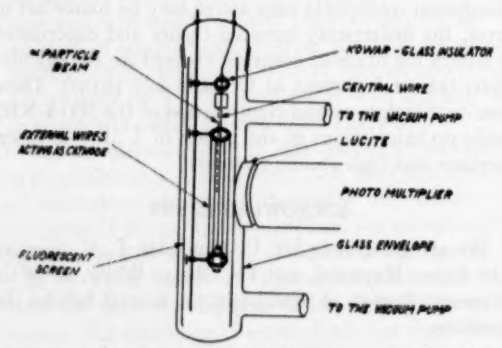

FIG. 1. Counter-photomultiplier ensemble used to analyze the light emitted in the Townsend avalanche.

The photons emitted in the avalanche were observed with a photomultiplier which was placed facing the glass container of the counter. In order to obtain more light, the glass container was painted with magnesium oxide. The counter-phototube part was surrounded by a metal case which served as an optical and electrostatic screen.

Since we wished to study the ultraviolet light emitted in the avalanche, we introduced a fluorescent screen consisting of a glass tube of a diameter a little larger than the counter, covered internally by a thin layer of the vacuum grease Apiezon L. As is well known, this grease converts the ultraviolet light into visible light which in turn is measured by the phototube. This glass tube may be made to cover the counter.

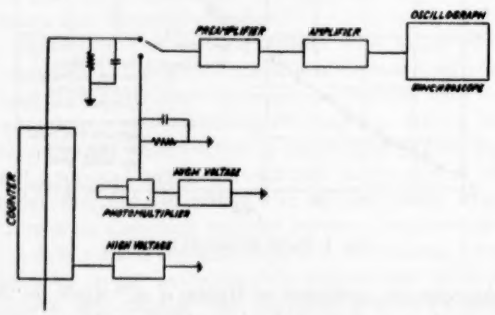

FIG. 2. Electronic equipment. The rise time of the system is 3×10^{-7} sec. When required, a similar system is employed with a rise time of 10^{-7} sec.

The photomultiplier is of the type EMI 6262. The electronic arrangement is shown in Fig. 2. The output pulse of the collector of the phototube or of the counter anode is sent to a Model 100 amplifier and then to a Dumont synchroscope. The rise time of the electronic system is 3×10^{-7} sec and the time constant is of the order 1×10^{-7} sec.

[1] L. Colli and U. Facchini, Phys. Rev. 88, 987 (1952).

EXPERIMENTAL MEASUREMENT

Observations are made as follows: a gradually increased voltage is applied to the counter and simultaneously observations are made of the electron pulse given by the counter for each α particle and of the corresponding light pulse measured by the photomultiplier.

The results are of particular interest in the proportional multiplication range; here every α particle gives rise to a Townsend avalanche on the wire. It is possible to measure the amplitude of the electron pulses on the wire *versus* the voltage applied, obtaining thus the usual multiplication curve. The same kind of measurement can be done on the light pulses measured by the photomultiplier, obtaining a multiplication curve for the light pulse amplitude (Fig. 3).

We have studied the pulses whose electron multiplication coefficient N had rather low values of 10 to 50. At

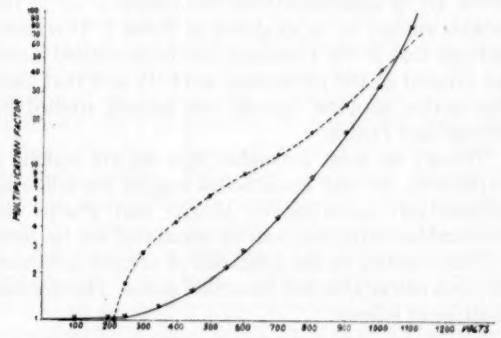

FIG. 3. Multiplication curves for electron pulses from the counter (solid-line) and for light pulses (dotted-line) from the photomultiplier, due to the same α particles. The multiplication factor for light pulses are given on an arbitrary scale. Argon pressure: 400 mm Hg.

these rather low values the contribution to the pulses due to secondary processes (the so-called γ processes) are negligible in comparison to the avalanche. Under these conditions the electron pulses observed with the synchroscope have a duration of 5×10^{-7} sec for pressures ranging from 70 to 700 mm Hg. This indicates that all the processes of the avalanche and of the collection of the electrons do not exceed this duration.

The light pulses, observed by the phototube under the same conditions of applied voltage and pressure, have the following characteristics: if the amplitude of the pulse, when the counter is surrounded by the glass tube painted internally by Apiezon L, is given the value 1, the amplitude of the pulse obtained when the counter is surrounded by an unpainted glass tube will be $\sim$0.03; this shows that most of the light emitted in the avalanche is ultraviolet and is absorbed by the glass. Further measurements with absorbers of fused and crystalline quartz and of thin lithium fluoride

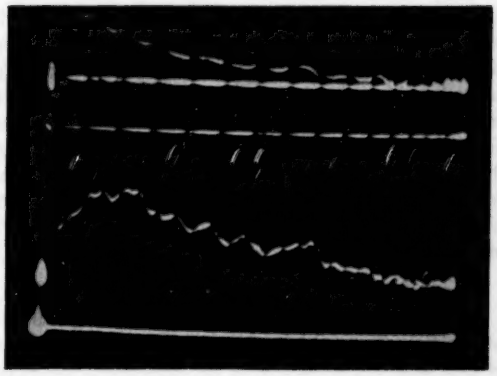

FIG. 4. Two shapes of light pulses. The photograph above is taken at 700 mm Hg pressure, the one below at 140 mm Hg; markers at 1×10^{-6} sec.

allowed an estimate of the wavelength of this light as 1250A$\pm$150.

SHAPE OF THE LIGHT PULSES

The following part of the work concerns the shape of the light pulses and particularly their duration. It is therefore necessary to know the behavior of Apiezon L grease in its characteristic as a "phosphor," particularly as regards the lifetime of fluorescent light. For this reason, a source of ultraviolet light was used in the form of an electric discharge in air lasting 5×10^{-8} sec.[2] From the observation of the ultraviolet light pulse corresponding to the discharge converted by the Apiezon L, we have established that the lifetime of the fluorescent light emitted by the grease is less than 5×10^{-7} sec.

Let us now consider the shape of the light pulses emitted by the argon counter. Two types of these pulses, given by single α particles, are illustrated in Fig. 4. The first type was photographed at a pressure of 700 mm Hg and shows a rapid rise in the order of 0.5×10^{-6} sec and a descent with a decay time of the order of 3.5×10^{-6} sec. The second type was taken at a pressure of 140 mm Hg and shows a rise in the order of 4×10^{-6} sec and a descent of an approximate decay time of 6×10^{-6} sec. In both cases the duration of the emission of light is much longer than the duration of the electric pulse in the avalanche.

The shape of these light pulses is well represented by a formula of the type

$$y=C[\exp(-t/\tau_A)-\exp(-t/\tau_M)],$$

where C is a normalization constant, and τ_A, τ_M two constants to be chosen to fit the results. From our measurements, τ_M is equal to 3.4×10^{-6} sec and does not vary with the pressure. For τ_A we obtain a value which depends on the pressure according to the law

[2] Beams, Kuhlthan, Lapsley, McQueen, Snoddy, and Whitehead, J. Opt. Soc. Am. 37, 868 (1947).

$\tau_A = 1/9p^2$, where p is expressed in mm Hg and τ_A in sec (Table I). These values are independent of the multiplication factor of the counter, if it is within the limits in which the secondary processes are negligible, and are independent of the geometrical arrangement used for the collection of the uv light. To this purpose, the diameter of the glass tube which carries the fluorescent screen was varied. For the two diameters used (30 and 70 mm) there was no difference in the shape of the pulses.

TABLE I. Values for τ_A and τ_M.

Pressure, mm Hg	τ_A = lifetime (in μsec) of metastable atoms calculated with the low $\tau_A = 1/9p^2$	Measured τ_A (μsec)	τ_M = measured lifetime of molecule (μsec)
650	0.26	...	3.3±0.5
590	0.32	...	3.2±0.5
340	0.96	1.0 ±0.2	3.5±0.5
235	2.0	2.0 ±0.4	3.5±0.5
180	3.4	3.5 ±0.5	3.3±0.5
140	5.7	5.65±1	3.3±0.5
70	22.5	20.0 ±2	3.3±0.5

DISCUSSION

The results reported show that the emission of the ultraviolet photons takes place at a certain interval of time after the formation of the avalanche. The shape of the pulses at all the observed pressures can be explained only if we assume the existence of two consecutive processes.

Let us suppose that A is the state representing the excited atoms formed in the avalanche and B an intermediate state which we shall not discuss now. In accordance with the results obtained, we must have a transition from A to B and another from B resulting in photon emission, where, for instance, the transition A to B takes place during a time τ_A and the emission of photons $B \rightarrow h\nu$ during a time τ_M.

We will now try to give a theoretical interpretation of these experiments. For this purpose we have to consider the scheme of excitation levels of the argon atom.[3] From the fact that the photons emitted are mostly ultraviolet, it is possible to exclude transitions from one excited level to another as these transitions give rise only to visible photons. We can therefore restrict ourselves to considering the first four levels.

Among the four lower excited levels, the $^3P_1$ and $^1P_1$ are radiant resonance levels, the $^3P_2$ and $^3P_0$ are metastable levels. The $^3P_1$ and $^1P_1$ levels will decay to the ground state giving out resonance photons. The resonance photons, as is known, will undergo a diffusion process through which they are captured and re-emitted many times by the nonexcited atoms in the gas. Holstein[4] developed a theory of this process according to which the duration of this imprisonment process should be of the order of 10^{-5} to 10^{-4} sec and must depend on the diameter of the encasement. In a pressure range corresponding to the one studied, the complete temporal behavior of the resonance photons diffusion should be roughly independent of the pressure. From our results it would seem that the photons observed by us, or at least, most of them are not emitted by means of a process of this kind.

We shall therefore consider the metastable level $^3P_2$. This metastable level has very long lifetime of its own; the processes causing its destruction are due to collisions with nonexcited atoms of the gas. The destruction time of the $^3P_2$ metastable level in argon has been recently investigated by Molnar and Phelps,[5] at pressures from 1 to 10 mm Hg. From these measurements the metastable lifetime by destruction was found to be of the order of a few milliseconds, following the law $\tau = 1/9p_2$. These destruction times of the metastable levels are in agreement with the values of τ_A in the process studied by us as shown in Table I. This could indicate that in the Townsend avalanche excited atoms are created at the metastable level $^3P_2$ and that their destruction happens through the process studied by Molnar and Phelps.

Though we must remember that we are making a hypothesis, we may nevertheless suggest the following explanation: according to Molnar and Phelps the metastable destruction can be accounted for by some collision leading to the formation of excited molecules, between metastable and unexcited atoms. The reaction must be as follows:

$$A^* + A + A = A_2^* + A.$$

The three-body collision, required for the conservation of the momentum, accounts for the law $\tau_A \div 1/p^2$. It is possible to assume that the excited molecules of argon so formed decay by dissociation and release a photon of an energy that should be of about 10 ev. This photon, not being a resonance photon, cannot be absorbed any more by the argon and could be the one observed. The lifetime of 3.4×10^{-6} sec, independent of pressure, may be attributed to the excited molecule.

A theoretical study of the molecular state of the type we are considering has been made only in the case of helium. The theoretical calculation in the case of argon has not been made.

ACKNOWLEDGMENTS

Thanks are due Professor G. Bolla and Professor L. Loeb and G. Weissler for interesting discussions, and Dr. U. Facchini for advice and help throughout the measurements.

[3] W. de Groot and F. M. Penning, *Handbuch der Physik* (J. Springer, Verlag, Berlin, 1933), Vol. 23, p. 1.

[4] T. Holstein, Phys. Rev. **72**, 1212 (1947); **83**, 1159 (1951).

[5] A. V. Phelps and J. P. Molnar, Phys. Rev. **89**, 1202 (1953).

Lambda Transition of Liquid Helium*

D. TER HAAR
Department of Natural Philosophy, St. Salvator's College, St. Andrews, Scotland
(Received May 13, 1954)

An approximate partition function for a system of interacting Bose-Einstein particles is derived, which is nearly the same as the one derived by Feynman, by neglecting the noncommutability of the potential and kinetic energy operators.

Reasons are given for believing that the approximations introduced in deriving the partition function rather than those introduced in the further development of the partition function are responsible for the difference between the observed and the predicted order of the transition.

1. INTRODUCTION

THE strange behavior of liquid helium,[1] especially its lambda transition and its properties below the lambda point, has been the subject of many theoretical investigations, partly of a phenomenological nature, and partly of a more fundamental nature. Recently, Feynman[2] has approached the problem anew starting from first principles. In F-II and F-III Feynman is mainly concerned with the properties of helium near the absolute zero, or at any rate in the He II region, and we do not wish to discuss that aspect of his theory. In F-I, however, Feynman discusses the partition function of a system of interacting Bose-Einstein particles. Using the space-time approach[3] which he had previously developed for quantum-mechanical problems, Feynman writes down the exact partition function in this case. The further discussion then consists of two steps. The first step is the writing down of an approximate partition function, essentially by considering in detail which trajectories will give the more important contributions to the partition function. The result is given by Eq. (F-I.5). The second step consists of expressing the Helmholtz free energy as a power series in the activity. As Feynman uses petit ensembles, this is done by the method of steepest descents. The coefficients in the power series are then evaluated approximately and it appears that the resultant power series has a singularity corresponding to a third-order transition, using Ehrenfest's classification.[4] In F-I it is suggested that the difference between the predicted order of the transition and the observed second order transition is due to the approximations introduced in the last stage.

In the present paper we wish to show, firstly, how a method developed by Kramers[5] can be used to evaluate the partition function. In Sec. 2 it is shown that to a first approximation this method leads to a partition function which is very similar to the approximate partition function of F-I. The second point we want to discuss is whether the approximate partition function can lead to a transition of the right order. In Sec. 3 we shall give reasons for believing that in going over from the exact to the approximate partition function one has already changed the order of the transition.

2. THE APPROXIMATE PARTITION FUNCTION

We shall use the method of the grand canonical ensembles. We must then evaluate the so-called grand potential q (ESM, p. 137) which is the logarithm of the grand partition function Z and given by the equation (ESM, p. 182)

$$e^q = Z = \text{Trace} \exp(\boldsymbol{n}\nu - \beta \boldsymbol{H}) = \sum_{n=0}^{\infty} e^{n\nu} \text{Trace} \exp(-\beta \boldsymbol{H}_n), \quad (1)$$

where $\boldsymbol{n}$ is the number operator and $\boldsymbol{H}_n$ the Hamiltonian operator of a system of n particles. The quantity ν is the partial thermal potential (or partial chemical potential) divided by kT (k: Boltzmann's constant; T: absolute temperature), while $\beta = 1/kT$.[6]

One can show (see ESM, pp. 182 to 184) that the right-hand side of (1) can be written as follows:

$$e^q = \sum_{n=0}^{\infty} [e^{n\nu}/n!] \int d^n x \times [\exp(-\beta \boldsymbol{H}_n) \sum_P \prod_i \delta(\mathbf{x}_i - \mathbf{x}_{Pi})]_{\mathbf{x}_i' = \mathbf{x}_i}, \quad (2)$$

where $d^n x$ is a short hand notation for the $3n$-dimensional elementary volume $dx_1 dy_1 \cdots dy_n dz_n$, where $\delta(\mathbf{x})$ is the three dimensional delta function, the $\boldsymbol{H}_n$ operate on the $\mathbf{x}_i$ only, where Pi stands for a permutation of the i, where the summation over P is over all possible

* The contents of this paper were given as an invited talk to the American Physical Society at Washington, D. C., on April 30th, 1954.

[1] For a comprehensive account see W. H. Keesom, *Helium* (Elsevier Publishing Company, Amsterdam, 1942).

[2] R. P. Feynman, Phys. Rev. **91**, 1291, 1301 (1953); **94**, 262 (1954); hereafter referred to as F-I, F-II, and F-III. See also, G. V. Chester, Phys. Rev. **93**, 1412 (1954); **94**, 246 (1954); hereafter referred to as C-I and C-II.

[3] R. P. Feynman, Revs. Modern Phys. **20**, 367 (1948).

[4] P. Ehrenfest, Proc. Roy. Acad. Sci. (Amsterdam) **36**, 153 (1933).

[5] H. A. Kramers (unpublished). For an account see D. ter Haar, *Elements of Statistical Mechanics* (Rinehart and Company, Inc., New York, 1954), p. 184 ff. (to be referred to as ESM).

[6] In ESM we use μ instead of β.

$n!$ permutations, and where the product is over $i=1$ to n.[7]

Up to this point we have not introduced any approximations. We write now

$$\exp(-\beta H_n)=\exp(-\beta U_n)\cdot\exp(-\beta T_n), \quad (3)$$

where U_n is the potential and T_n the kinetic energy operator of the system,

$$U_n=\sum_{i<j} V_{ij}, \quad T_n=-(\hbar^2/2m)\sum_i \nabla_i^2, \quad (4)$$

where $V_{ij}=V(r_{ij})$ is the potential energy between atoms i and j for which we assume a central force type of potential energy, depending on the distance apart r_{ij} only, where $\hbar$ is Dirac's constant, where m is the mass of one atom, and where ∇_i^2 is the Laplacian corresponding to the ith atom.

If we use approximation (3) we get, upon using for the delta functions their Fourier integrals (compare ESM, p. 185[8]),

$$e^q=\sum_n (e^r/v_0)^n \int d^n x \sum_P \exp(-\beta\sum_{i<j} V_{ij}) \times\exp[-(m/2\hbar^2\beta)\sum_i (\mathbf{x}_i-\mathbf{x}_{Pij})^2], \quad (5)$$

where

$$v_0=(2\pi\beta\hbar^2/m)^{\frac{1}{2}}. \quad (6)$$

Comparing (5) with (F-I.5) we see the following differences. (i) In (5) we have the atomic mass m instead of an effective mass m'. (ii) Instead of an undetermined weight function ρ we have the function $\exp(-\beta\sum V_{ij})$ which has practically the same properties as Feynman's ρ as can easily be ascertained.

Our expression (5) is the same as expression (3) in C-I. This is not surprising as the inclusion of commutators would involve a power series in $\hbar$.[9]

It would be interesting to evaluate the neglected terms. This is in general not a very easy process, but might be possible, if we approximate $V(r)$ by the function

$$V(r)=A,\ 0\leqslant r\leqslant a; \quad V(r)=-B,\ a<r<b; \quad V(r)=0,\ b\leqslant r, \quad (7)$$

or even

$$V(r)=A,\ 0\leqslant r\leqslant a; \quad V(r)=0,\ a<r. \quad (8)$$

The first potential is one with a hard core followed by an attractive potential well, and the second one, in the limit of $A\to\infty$, is that of hard spheres. From experimental data (see, e.g., ESM, p. 202) it follows that $a\cong 2.6$A, $b\cong 4$A, while $B\cong 10^{-15}$ erg.

In the case of $V(r)$ being given by (7) or (8) the correction terms, which arise through the commutator of T with U will all contain delta functions of the form $\delta(r_{ij}-a)$ and $\delta(r_{ij}-b)$, and their derivatives. One might hope to use a power series expansion in terms of βB. This was done by Chester in C-II with striking success as long as only the first two terms of the expansion were taken along. In view of the fact that near the lambda point βB is of the order of magnitude 3, we do not feel that such an expansion will be very useful for our particular purpose. We hope, however, at a later date to return to the question of the neglected terms.

3. THE TRANSITION

It is well known[10] how one can obtain from (1) a power series in the activity (e^r) for the grand potential. If we write

$$q=\sum_s b_s e^{sr}, \quad (9)$$

the asymptotic behavior of the b_s will determine the nature and position of the phase transition, if it exists. Essentially, the coefficients b_n are obtained by integrating certain expressions over a so-called cluster of atoms. Two atoms are said to belong to different clusters, if one cannot get from the one to the other over a chain of atoms such that two neighboring atoms in the chain are never further apart than the range of the interatomic forces or than $v_0^{1/3}$, whichever is the larger.

Feynman's approximations in the second stage of his theory consist in taking into account instead of all interactions between the atoms in the cluster, only those interactions which occur along the sides of a polygon. That is, instead of considering interactions between each atom and the $n-1$ other atoms in the cluster, he only considers interactions between each atom and its two neighbors in the polygon.

We do not think, however, that this will lead to serious mistakes, and in particular, contrary to the opinions expressed in F-I and C-I, we do not feel that the order of the transition has been influenced by these approximations. There are two reasons for this. First of all, from C-II we see that taking correction terms of the kind which we might expect in the present case into account can alter the order of the transition. Secondly, we note that both (5) and the equation of state as derived by Feynman's approximation method from (5) are exact for the case of a perfect Bose-Einstein gas. In this case therefore the neglect of all interactions other than those along the polygons did not alter the order of the transition.

It might be argued that the interatomic forces would (or could) alter this result. However, we are dealing

[7] If we would have been dealing with a system of Fermi-Dirac particles, the terms in the summation over all permutations would be multiplied with a factor δ_P which is $+1$ for even and -1 for odd permutations. One can easily introduce this factor δ_P in all subsequent equations and thus obtain the partition function for a system of interacting Fermi-Dirac particles.

[8] There are a few misprints on p. 185 of ESM in the section giving the derivation of Eq. (ESM 8.421); the minus signs in the expression $\exp[-\mu(\hbar^2/2m)\nabla^2]$ should not be there.

[9] One has to be slightly careful, as in the limit $\hbar\to 0$ the only term in the summation over all permutations which will be left is the one with the identical permutation; one can therefore not say that (5) is the classical limit of the partition function.

[10] See, e.g., ESM, Chapter VIII and IX.

with a quantum-mechanical system and the range of the quantum-mechanical diffraction effects—which is essentially $v_0^{1/3}$—is as important as the range of the interatomic forces, as at temperatures of the order of the lambda point $v_0^{1/3}$ is about 3.4A. This means that even though we are dealing with a perfect gas, nevertheless there is an interaction sphere around each atom, and its radius is actually larger than that of the classical helium atom. Any influence from the neglected configurations should thus, in our opinion, show up also in the case of the perfect Bose-Einstein gas.

There is another disturbing fact concerning the partition function (F-I.5) or (5). These expressions should be valid for the gas phase of helium, as the approximation (3) should be least inaccurate at high temperatures and low densities. That means that on lowering the temperature the partition function should reveal the gas-liquid transition before the lambda transition, but this does not happen in the case of (F-I.5) or (5) (compare also the remarks at the end of C-II). This becomes understandable, if we remind ourselves that essentially the attractive forces are neglected in deriving (F-I.5) or (5) (compare the discussion in F-I).

This paper was written while the author was at Purdue University, and I would like to express my thanks to Dr. K. Lark-Horovitz for the hospitality shown to me in his department. In conclusion, I would like to express my gratitude to Dr. R. P. Feynman for pointing out to me some serious mistakes in the first draft of this paper and for making it plausible to me that my original belief that (5) would be exact in the case of hard spheres may not be correct.

PHYSICAL REVIEW VOLUME 95, NUMBER 4 AUGUST 15, 1954

Microwave Determination of the Probability of Collision of Electrons in Helium*

LAWRENCE GOULD† AND SANBORN C. BROWN
Department of Physics and Research Laboratory of Electronics, Massachusetts Institute of Technology, Cambridge, Massachusetts

(Received May 10, 1954)

A previously reported microwave method for determining the collision probability for momentum transfer of slow electrons has been modified so that a variation in average electron energy from 0.012 ev to 3 ev may be obtained. Measurements of the ratio of the real part to the imaginary part of the electron conductivity are performed in the afterglow of a pulsed helium discharge in a microwave resonant cavity. The average electron energy is varied by applying a microwave electric field in the afterglow and, under appropriate assumptions, the average electron energy is determined theoretically from this field. Measurements are also obtained by varying the gas temperature from 77°K to 700°K. The value of the collision probability for momentum transfer in helium is 18.3±2 percent cm³/cm³ per mm Hg from 0 to 0.75 electron volts and increases slowly to a peak value of 19.2±2 percent at 2.2 ev.

IN a recent paper by Phelps, Fundingsland, and Brown,[1] a microwave method was described for determining the probability of collision for momentum transfer by measuring the conductivity of a decaying plasma after the electrons reach thermal equilibrium with the gas. The method has been modified so that a variation in average electron energy from 0.012 to 3 electron volts was obtained. The electron conductivity in the afterglow was studied as a function of experimental parameters and the effects of electron energy, impurities in the gas, ambipolar diffusion, nonuniform electric heating fields, and energy gradients were investigated. The experimental conditions were such that the electron energy distribution function was known. This enabled an expression for the probability of collision for momentum transfer as a function of electron energy to be determined from the experimental data.

* This work was supported in part by the Signal Corps, the Air Materiel Command, and the U. S. Office of Naval Research.
† Now at Microwave Associates, Boston, Massachusetts.
[1] Phelps, Fundingsland, and Brown, Phys. Rev. **84**, 559 (1951).

ELECTRON CONDUCTIVITY RATIO IN THE AFTERGLOW

Margenau[2] has given a general theory for the behavior of electrons in a gas under the action of a high-frequency field when only elastic collisions need be considered. From his results the complex electron conductivity σ_c may be written as:

$$\sigma_c=\sigma_r+j\sigma_i=-\frac{4\pi}{3}\frac{ne^2}{m\omega}\int_0^\infty\frac{[(\nu_m/\omega)-j]}{1+(\nu_m/\omega)^2}v^3\frac{df_0}{dv}dv. \quad (1)$$

Here n is the electron density, e and m are the electronic charge and mass, ω is the radian frequency of the applied field, f_0 is the first term in the spherical harmonic expansion of the normalized electron velocity distribution function for electrons of velocity v. The collision frequency for momentum transfer ν_m is related to the probability of collision for momentum transfer, P_m, by $\nu_m=P_m p_0 v$, where p_0 is the pressure normalized to zero degrees centigrade.

[2] H. Margenau, Phys. Rev. **69**, 508 (1946).

In a microwave cavity, the quantity which is measured is the electron conductivity averaged with respect to the measuring electric field E_m over the volume of the plasma and is given by the relation

$$\langle\sigma_e\rangle=\langle\sigma_r\rangle+j\langle\sigma_i\rangle=\int_V \sigma_e E_m^2 dV \Big/ \int_V E_m^2 dV. \quad (2)$$

Since ν_m is generally a complicated function of velocity, Eq. (1) is difficult to manipulate mathematically. The assumption that $\nu_m^2 \ll \omega^2$ over the velocity range covered by the distribution function f_0 is physically true and simplifies the mathematics. The ratio of the real part of the conductivity to the imaginary part divided by the pressure, designated by ρ, is obtained by Eqs. (1) and (2) yielding

$$\rho=\frac{1}{p_0}\frac{\langle\sigma_r\rangle}{\langle\sigma_i\rangle}=\frac{\int_V n\left[\int_0^\infty (P_m/\omega)v^4(df_0/dv)dv\right]E_m^2 dV}{\int_V n\left[\int_0^\infty v^3(df_0/dv)dv\right]E_m^2 dV} \quad (3)$$

for the case $\nu_m^2 \ll \omega^2$. When the energy distribution function is independent of position in the cavity, the quantity ρ is independent of averaging with respect to the electron density and measuring field. Measurements of ρ as a function of energy give information about the velocity dependence of P_m or f_0. For the more complicated case where f_0 is a function of position in the cavity, the spatial variation of the electron density and the measuring field must be known before any information about P_m or f_0 may be obtained. Equation (3) and the associated conductivity measurements are used in this experiment to obtain the velocity dependence of P_m over as wide a range of velocity as is possible with the present microwave technique. The experimental conditions must be arranged so that the electron energy distribution function is known.

ELECTRON ENERGY DISTRIBUTION FUNCTION

In the afterglow of a pulsed discharge the electrons, whose average energy is high during the discharge, lose their energy through elastic collisions with the gas atoms. Eventually the electrons reach energy equilibrium with the gas atoms and have a Maxwellian distribution with an electron temperature T_e the same as the gas temperature T_g. The electron temperature T_e is defined in terms of the average electron energy by $\langle u\rangle=\frac{3}{2}kT_e$. Above one mm Hg pressure in helium, energy equilibrium is established between electrons and gas atoms within one millisecond after the discharge has ceased. By either heating or cooling the cavity, the electron temperature may be varied over a range of 77°K to 700°K and the distribution function will be Maxwellian. Application of an electric field in a plasma can also increase the average electron energy. In this case, the energy distribution function, and hence the average energy, will depend upon a balance between the energy gained from the field and the energy lost due to recoil with the gas and the energy transported to the walls by diffusion, conduction, and convection. Energy losses due to inelastic collisions, attachment, and recombination may be neglected. Margenau[2] has shown the steady state distribution function for electrons in an atomic gas, in the absence of inelastic collisions and diffusion losses, to be Maxwellian under the assumption that $\nu_m^2 \ll \omega^2$. The equivalent electron temperature is given by

$$T_e=T_g+Me^2E_h^2/(6\omega^2km^2), \quad (4)$$

where E_h is the applied heating field. However, in a microwave cavity the heating field is a function of position and deviations from Eq. (4) resulting from energy gradients may become important.

The expression for the average energy when the energy is a function of position can be shown to be given by

$$T_e=T_g+a_0E_h^2+b_0\nabla\cdot(n\nabla T_e)/np_0^2, \quad (5)$$

where

$$a_0=Me^2/(6\omega^2km^2) \quad \text{and} \quad b_0=M/(6mP_m^2).$$

It is seen that the first two terms, which represent thermal energy and energy gained from the field, are identical with those in Eq. (4). The term containing $\nabla\cdot(n\nabla T_e)$ represents the first-order change in average energy resulting from conduction and convection of energy from regions of high energy to regions of low energy. Equation (5) is derived under the assumption that P_m is constant, which is a good approximation in helium at low energies.

In order to interpret Eq. (3), one must know not only the energy distribution function, but also the electron density distribution. The spatial distribution of the temperature given by Eq. (4) will be used as a first approximation to determine the electron density distribution when the average energy is a function of position. It will be assumed that the dominant electron loss mechanism is ambipolar diffusion.

ELECTRON DENSITY DISTRIBUTION

The correct density distribution can be obtained by solving the ambipolar diffusion equations taking into account the spatial variation of electron energy. The equations[3] governing the diffusion of electrons in a space charge field E_s are

$$\Gamma_-=-\nabla(D_-n_-)-\mu_-\mathbf{E}_sn_-, \quad (6)$$

$$\Gamma_+=-\nabla(D_+n_+)+\mu_+\mathbf{E}_sn_+, \quad (7)$$

$$\partial n_\pm/\partial t=\nabla\cdot\Gamma_\pm, \quad (8)$$

where Γ_- and Γ_+ are the electron and positive ion particle currents, n_- and n_+ are the electron and positive ion densities, D_+ and μ_+ are the positive ion diffusion

[3] W. Schottky, Physik. Z. **25**, 342 (1924).

coefficient and mobility, D_- and μ_- are the electron diffusion coefficient and mobility defined by

$$D_-n_-=\int_0^\infty (v^3/3\nu_m)f_0 4\pi v^2 dv, \tag{9}$$

$$\mu_-n_-=\int_0^\infty (e/3m\nu_m)(\partial f_0/\partial v)4\pi v^3 dv. \tag{10}$$

For the Maxwellian distribution function whose temperature is given by Eq. (4) D_- and μ_- are functions of position. In solving Eqs. (6), (7), and (8) the usual assumptions of ambipolar diffusion are made, i.e., $\Gamma_+\approx\Gamma_-=\Gamma$ and $n_+\approx n_-=n$. Eliminating E_s from Eqs. (6) and (7) one finds

$$\Gamma=[-\mu_+\nabla(D_-n)-\mu_-\nabla(D_+n)]/(\mu_++\mu_-). \tag{11}$$

Since $\mu_+\ll\mu_-$ and D_+ and μ_+ are essentially independent of position, Eq. (11) becomes

$$\Gamma=-D_+[\nabla n+\mu_+\nabla(D_-n)/D_+\mu_-]. \tag{12}$$

In order to evaluate Eqs. (9) and (10), the velocity variation of ν_m must be known. The simplest assumption is that $\nu_m=cp_0v^h$, although any power series in v may be manipulated equally well in the following treatment. The ratio of $\nabla(D_-n)\mu_-$ in Eq. (12) is obtained from Eqs. (9) and (10) by using the above assumption for ν_m:

$$\nabla(D_-n)/\mu_-=(k/e)\nabla(T_e^{(1-h/2)}n)/T_e^{-h/2}. \tag{13}$$

Combining Eqs. (8), (12), and (13) and using the relation $D_+/\mu_+=kT_g/e$, one obtains

$$\partial n/\partial t=-D_+\nabla\cdot[\nabla n+\nabla(T_e^{(1-h/2)}n)/T_gT_e^{-h/2}]. \tag{14}$$

It is assumed that the variation of density with time has the form

$$n=n_0\exp(-\gamma t), \tag{15}$$

and, hence, Eq. (14) becomes

$$(1+T_e/T_g)\nabla^2 n+(2-h/2)\nabla n\cdot\nabla(T_e/T_g)+n[(1-h/2)\nabla^2(T_e/T_g)+\gamma/D_+]=0. \tag{16}$$

The problem consists of solving Eq. (16) for its characteristic functions corresponding to the proper boundary condition, proper spatial variation of T_e, and a given value of h. In general, the characteristic function corresponding to the lowest characteristic value is the important physical solution. Equation (16) is solved for two different cavities. One is a rectangular parallelepiped in which the plasma fills the entire cavity; the other is also a cavity of the same shape but with the plasma contained in a cubical bottle concentric with the cavity. The applied electric field has a spatial configuration corresponding to the fundamental mode of the cavity and is a function of only two coordinates. The boundary conditions for the cavity are that the electron density vanish along the walls of dimension A, B, and C and for the bottle

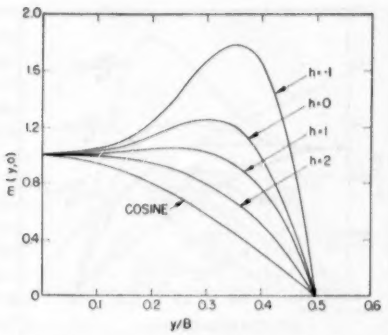

FIG. 1. Electron density as a function of position for various values of h and $T_{e0}/T_g=4$.

that the density vanish along the walls of dimension d. The dimensions of this particular cavity are $A=7.16$ cm, $B=7.88$ cm, and $C=6.48$ cm. The dimensions of the cavity containing the bottle are $A=6.90$ cm, $B=7.51$ cm, $C=6.28$ cm, and the dimension of the bottle is $d=2.82$ cm.

Since the heating field is a function of two directions, y and z, the electron density may be written as $n=n_0m(y,z)\cos(\pi x/A)$. Equation (16) may be separated into a two-dimensional second-order differential The equation is transformed to a difference equation which is solved numerically by relaxation techniques. The results for the cavity in which the plasma fills the entire volume are best depicted by plotting $m(y,z)$ as a function of y/B for $z=0$ and are shown in Fig. 1. The curves give $m(y,0)$ for various values of h for T_{e0}, the electron temperature at the center of the cavity, equal to $4T_g$. The curves are compared with a cosine distribution which is the solution of Eq. (16) when the temperature distribution is independent of position. For larger ratios of T_{e0}/T_g, the deviation from a cosine distribution increases.

The shape of the curves in Fig. 1 for the various values of h is readily explainable. The off-center maximum is caused by the lower temperature near the walls, the electron pressure decreasing monotonously toward the walls. This effect is enhanced for $h<2$ as then the diffusion coefficient increases with temperature. resulting in a flatter electron pressure distribution near the center with steep gradients near the walls. In Fig. 2 curves of $m(y,0)$ as a function of y/B are shown by the solid curves when $h=1$, i.e., P_m constant, for a range of T_{e0}/T_g from 4 to 11. The curves illustrate the increase in the density distribution peaks near the walls as the electron temperature T_{e0} increases. From the results shown, it is obvious that in any calculations involving the density averaged over the volume of the plasma it is necessary to use the proper density distribution.

A similar calculation was performed for the cavity containing a cubical bottle of dimension d. The results are shown by the dotted curves in Fig. 2 for $h=1$ and

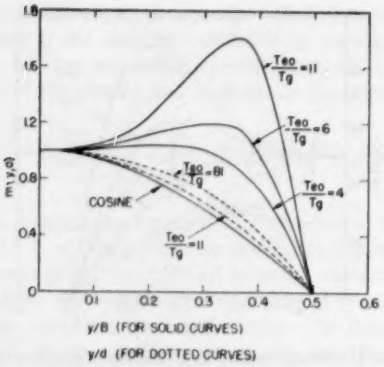

FIG. 2. Electron density as a function of position for various values of T_{e0}/T_g and $h=1$.

$T_{e0}/T_g=11$ and 81. Since the nonuniformity of the heating field is small over the volume of the bottle, the deviation of the curves from a cosine is negligible. Hence, over this region of electron temperature, a cosine distribution is sufficiently accurate for representing the density distribution provided that ambipolar diffusion is the dominant loss mechanism.

ELECTRON CONDUCTIVITY RATIO FOR CONSTANT COLLISION PROBABILITY

When the energy distribution function is Maxwellian, the conductivity ratio given by Eq. (3) becomes

$$\rho=\rho_0\int_V n(T_e/T_g)^{\frac{1}{2}}E_m^2dV\Big/\int_V nE_m^2dV, \qquad (17)$$

where $\rho_0=1.505(P_m/\omega)(2kT_g/m)^{\frac{1}{2}}$ for the case when the collision probability is constant. This is approximately valid for helium. The solution of Eq. (17) is considered when a heating field is present. The electron density distribution is predicted by the theory of ambipolar diffusion in a nonuniform field and the electron temperature is given by Eq. (5). Thus the effects of a nonuniform heating field and the associated energy gradients on the electron density and temperature distributions are included to a first-order approximation. For the cavity in which the plasma fills the entire volume, the solution of Eq. (17) for T_{e0}/T_g greater than 10 is given approximately by

$$\rho=\rho_0 f(T_{e0}/T_g)(1+3/p_0^2). \qquad (18)$$

The function $f(T_{e0}/T_g)$ is obtained from a numerical integration of Eq. (17). Below $T_{e0}/T_g=10$, the correction factor $3/p_0^2$, decreases becoming zero at $T_{e0}/T_g=1$. We can see from Eq. (18) that at pressures below 10 mm Hg, the influence of energy gradients becomes important and the value of ρ increases.

A similar calculation is performed for the bottle enclosed in a cavity, yielding the following expression valid for T_{e0}/T_g greater than 10:

$$\rho=\rho_0 0.93[(T_{e0}/T_g)-1]^{\frac{1}{2}}[1+0.03/p_0^2]. \qquad (19)$$

At a pressure of 1 mm Hg or below, the perturbation term becomes important. It should be remembered that the condition of $\nu_m^2\ll\omega^2$ is imposed throughout the discussion. In order to insure that $\nu_m^2\leq 0.04\omega^2$, at a frequency of 3000 megacycles one must have

$$p_0\leq 350/T_e^{\frac{1}{2}}. \qquad (20)$$

Therefore, 2000°K is approximately the maximum temperature that can be maintained in the cavity alone before gradients have an important influence and still satisfy the condition of Eq. (20). In the bottle 25 000°K is approximately the maximum temperature. From the above discussion, it follows that the conductivity measurements above thermal energies should be made in a bottle so that a wide range of electron energy can be obtained without introducing complicated correction factors into the theory. For this case, when ambipolar diffusion is the dominant loss mechanism, the density distribution is well approximated by a cosine distribution and the electron temperature is determined by Eq. (4).

EXPERIMENTAL PROCEDURE

The technique used for measuring the electron conductivity ratio ρ is described in a paper by Gould and Brown.[4] The presence of a plasma introduces a change in the conductance and susceptance of the cavity. This change can be determined by measuring the ratio of the microwave power transmitted through the cavity to the power incident as a function of signal frequency in the vicinity of cavity resonance. The microwave cavity used in the experiment is a rectangular parallelepiped and is designed to resonate in its three fundamental modes at wavelengths of 9.5, 10.0, and 10.5 cm. The 9.5-cm mode is used to produce a pulsed discharge in helium of variable pulse length. The 10.0-cm mode is used to increase the average electron energy in the afterglow, and the 10.5-cm mode is used to measure the characteristics of the plasma. The apparatus and procedure associated with each mode will be discussed separately and will be referred to as the breakdown mode, heating mode, and measuring mode. The general block diagram of the experimental microwave equipment is shown in Fig. 3. $\frac{1}{8}$-in. coaxial transmission line is used throughout.

In the breakdown mode, a tunable pulsed magnetron (QK61), supplying 100-watts peak power, is used to produce a pulsed discharge in the cavity. This magnetron is pulsed for a duration varying between 0.1 to 5 milliseconds and at a repetition rate varying from 20 to 120 cps. A well regulated pulsed voltage supply, used to modulate the magnetron output, is necessary in order to stabilize the discharge so that accurate measurements in the afterglow can be performed.

In the measuring mode, a continuous-wave tunable magnetron (QK59) is used for measuring the conduc-

[4] L. Gould and S. C. Brown, J. Appl. Phys. **24**, 1053 (1953).

tivity ratio during the afterglow. The microwave power, incident on the cavity, is adjusted by the proper attenuation to a few microwatts so that the value of the measuring electric field is less than 0.1 volt/cm. The perturbation of the plasma characteristics from a field of this value is negligible. The ratio of the transmitted power to the incident power is measured by the power measuring section which uses transient receivers.[5] These receivers are operative for a period of 20 to 100 microseconds and can be delayed in time with respect to the breakdown pulse so that any time in the afterglow can be measured. At a particular time in the afterglow, the signal frequency is adjusted to the resonant frequency of the cavity and plasma, and the apparent ratio of the incident to transmitted power is adjusted to unity by varying the gain of the receivers. A plot of the change in this ratio as a function of the square of the signal frequency change from resonance is linear. The frequency change is measured directly by the frequency measuring section. Similar measurements are obtained with no plasma in the cavity. The difference in the slopes of the linear plots with and without a plasma present (plasma conductance) divided by the difference in the resonant frequency for both cases (plasma susceptance) yields the ratio of the real to the imaginary part of the conductivity, σ_r/σ_i. The accuracy of the conductivity measurements by this null technique is ± 2 percent.

In the heating mode, a continuous wave tunable magnetron (QK60) is used for producing the electric field in the cavity which increases the average electron energy. Measurements of the unloaded Q, obtained from standing wave ratio measurements as a function of signal frequency, and the power incident on the cavity, determine the electric field in the cavity within an accuracy of ± 3 percent. In the afterglow of a discharge the electric field, for a constant incident power, will be a function of the electron density. The electric field will have a maximum value at that time in the afterglow when the signal frequency corresponds to the resonant frequency of the cavity and plasma.

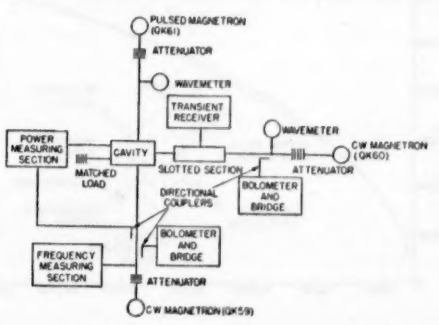

FIG. 3. General block diagram of experimental equipment.

[5] Rose, Kerr, Biondi, Everhart, and Brown, Technical Report No. 140, Research Laboratory of Electronics, Massachusetts Institute of Technology (unpublished).

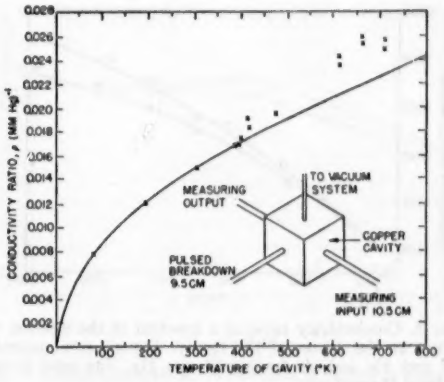

FIG. 4. Conductivity ratio as a function of cavity temperature. The x's are the experimental points and the solid line the theoretical curve for $P_m = 18.3$.

The electric field should remain constant for a sufficiently long time so that the electrons can reach equilibrium with the electric field. If the unloaded Q of the cavity is low, the change in Q due to the presence of plasma will be small, thus minimizing the variation of the electric field with electron density. An output loop connected to a matched load is adjusted so that it only couples out power from the heating mode. By changing the coupling between the cavity and the matched load, an additional loss is reflected back into the cavity and the unloaded Q for this mode, measured at the input terminals of the cavity, decreases. A decrease in Q_u from 5000 to 200 is easily obtained by this method. For the applied fields used in this experiment, the time necessary for equilibrium is of the order of tenths of milliseconds. Unloaded Q's of the order of several hundred allow the electric field to remain constant for the order of a millisecond thus insuring equilibrium with the field. It is during this interval of time that the electron conductivity ratio is measured.

For the vacuum system, a standard forepump and a three stage oil diffusion pump are used in conjunction with metal valves[6] wherever necessary. The helium pressure is measured by a McCleod gauge calibrated to an accuracy of ± 1 percent over a range of 0.10 to 20 mm Hg. The method for introducing the helium is as follows: A "fritted" glass filter, one end of which has a break-off seal, is connected to the main vacuum system by a metal valve. The glass filter may be placed in a liquid helium Dewar flask. A liter Pyrex bottle, connected to the cavity side of the system by another valve, serves as a reservoir for the helium. After the system is baked, a vacuum of about 10^{-7} mm Hg is obtained when the system is isolated from the pumps. At this point liquid helium is poured into the Dewar flask. When the "fritted" glass filter is completely immersed in the liquid helium, the break-off seal is broken and helium is evaporated into the system.

[6] S. C. Brown and J. E. Coyle, Rev. Sci. Instr. **23**, 570 (1952).

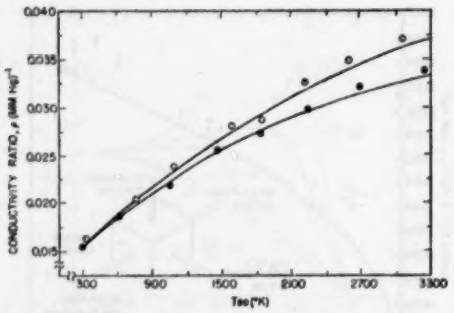

FIG. 5. Conductivity ratio as a function of the electron temperature at the center of the cavity. Experimental points for $p_0=5$ mm Hg and x's for $p_0=10$ mm Hg. The solid lines are calculated theoretically.

If impurities are present, experimentally measured values of ρ are not independent of pressure or time as indicated by Eq. (3). Constancy of ρ as a function of these variables was taken as a measure of gas purity, and the helium produced from liquid helium as just described met these conditions.

RESULTS

Measurements of ρ as a function of gas temperature and pressure were obtained in a copper cavity. Provisions were made for cooling the cavity to dry ice (195°K) and liquid air (77°K) temperatures and for heating the cavity from room temperature to 400°C. The results are shown in Fig. 4. Included in the figure is a sketch of the cavity showing the relative positions of the coupling lines for the measuring mode and the pulsed breakdown mode. The crosses represent the experimental points and the solid line represents the theoretical curve for ρ when P_m is constant and equal to 18.3 cm²/cm³ per mm Hg. According to Eq. (17), for the case of P_m constant, ρ is given by

$$\rho=1.505(P_m/\omega)(2kT_e/m)^{\frac{1}{2}}. \tag{21}$$

It is seen that the experimental points agree with the above equation over the range of 77°K to 400°K. Above 400°K, the values of ρ obtained are higher than the theoretical curve. It is believed that impurities liberated from the walls of the cavity at the higher temperatures produced the higher values of ρ. At a given temperature, the high values of ρ could be lowered by outgassing the cavity for several days at a temperature of 430°C.

Measurements of ρ as a function of the heating electric field were obtained in the copper cavity. The electric field was measured according to the usual microwave techniques.[5] Transient operation was used to measure the Q of the heating mode simultaneously with the electron conductivity measurements. The results are shown in Fig. 5. The experimental data are represented by the crosses and points. The dotted curves are theoretical results for ρ corresponding to Eq. (18) in which the effects of energy gradients are included and P_m is 18.3 cm²/cm³ per mm Hg and constant. It is seen that the predicted increase in ρ due to the importance of energy gradients is evident from the data at 5 mm Hg. At $T_{e0}=3300$°K the difference between the theoretical curves for $p_0=5$ mm and 10 mm Hg is 12 percent. The experimental data show that the density distribution predicted from the theory of ambipolar diffusion in nonuniform fields is the proper one. In general, interpretation of measurements in the cavity would be rather difficult for gases in which P_m is not known, since a knowledge of P_m is necessary to calculate the proper density distribution for the evaluation of ρ.

Measurements of ρ as a function of the heating electric field were also obtained for the case of the bottle enclosed in the cavity. The averaged experimental results for ρ as a function of the electron temperature are shown in Fig. 6. The scatter in data is ± 2 percent. The relation between the electron temperature and the electric field is given by Eq. (4) which, for helium, is $T_{e0}=(T_g+72.5E_{0h}^2)$, where the field is in volts/cm. Included in Fig. 6 is a sketch of the cavity and bottle showing the relative positions of the coupling lines for the measuring, heating, and breakdown modes.

The relation between ρ and P_m depends upon the spatial distribution of the electron density and the electric field. The electric field configuration is assumed to be that of the fundamental mode. The electron density distribution is assumed to be cosinusoidal. If a power series in velocity is assumed for P_m, the collision probability, is of the form

$$P_m=b_1+b_2v+b_3v^2. \tag{22}$$

Equation (3) becomes

$$\rho=\sum_{s=1}^{3}A_sI_s, \tag{23}$$

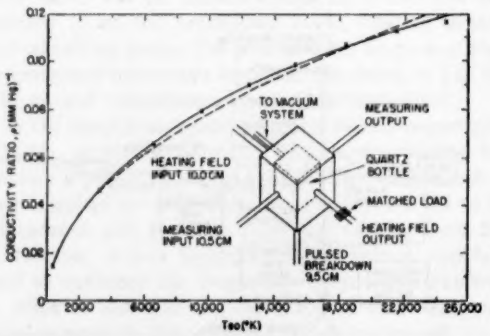

FIG. 6. Conductivity ratio as a function of the electron temperature at the center of the quartz bottle. The solid line represents the experimental curve, the dotted line the theoretical curve, $P_m=18.3$, and the x's are calculated from the power series approximation.

where

$$A_s=(2kT_g/m)^{s/2}b_s[(3+s)/2]!\omega(3/2)!,$$

$$I_s=\left[\int_V n(T_e/T_g)^{s/2}E_m^2dV\right]\Big/\int_V nE_m^2dV$$

$$=1.065\int_0^{\pi/2}\int_0^{\pi/2}(1+a\cos^2 0.393u\cos^2 0.449w)^{s/2}$$

$$\times\cos w\cos u\cos^3 0.393dwdu,$$

and $a=0.241E_{0h}^2$ when $T_g=300°$K.

The expression I_s can be calculated analytically when s is an even number and must be calculated numerically when s is an odd number. I_s is only a function of the electric field, E_{0h}. When P_m is equal to 18.3 and constant (s equal to one) the plot of ρ as a function of T_{e0} is shown in Fig. 6 as the dotted curve. The experimental and the theoretical curves agree up to a temperature of 4000°K. At low electron energies, both the thermal and the heating field measurements yield the same value for P_m. This indicates that the higher values of ρ obtained in the thermal measurements above 400°K are not the true values but are probably due to impurities. For a more accurate determination of the velocity dependence of P_m, the experimental curve for ρ can be expressed in terms of a series in I_s. The coefficients A_s are determined from the experimental curve in Fig. 6. The values of b_s can be obtained from the values of A_s, according to Eq. (23), giving the following expression for P_m:

$$(P_m=18.1+2.91\times10^{-8}v-2.1\times10^{-16}v^2), \qquad (24)$$

where v is in cm per second.

A plot of the momentum transfer collision probability as a function of electron velocity in square root of volts is shown as a solid curve, in Fig. 7. This plot is compared with the total collision probability data of Normand[7] using the dc method. Below a velocity of 1.5 volts[1], Normand's data have an oscillatory behavior. Since the microwave method cannot distinguish such a behavior, the curve shown in Fig. 7 is an average of Normand's data. In addition, the momentum transfer collision probability for the dc method is derived by using Normand's data and the angular distribution data of Ramsauer and Kollath.[8] It is seen that there is good agreement between the microwave and the dc method.

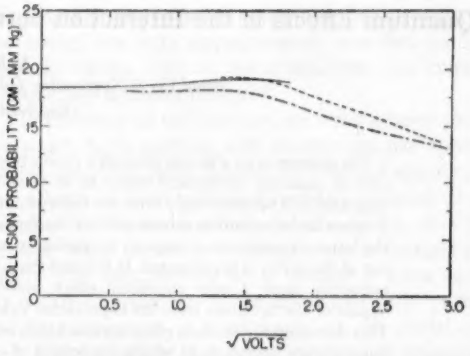

FIG. 7. Collision probability of electrons in helium as a function of electron velocity. Solid line is the momentum transfer collision probability as determined by the microwave method. Short-dash line represents the collision as measured by Normand. Long-and-short-dash line gives the momentum transfer collision probability calculated from the measurements of Normand, and Ramsauer and Kollath.

The authors wish to acknowledge the technical assistance of Mr. J. J. McCarthy.

[7] C. E. Normand, Phys. Rev. **35**, 1217 (1930).
[8] C. Ramsauer and R. Kollath, Ann. Physik **12**, 529 (1932).

Quantum Effects in the Interaction between Electrons and High-Frequency Fields. I

I. R. SENITZKY
Signal Corps Engineering Laboratories, Fort Monmouth, New Jersey
(Received February 5, 1954)

The passage of an electron through a cavity resonator is considered for the purpose of studying the appearance of quantum mechanical effects in an essentially classical experiment as the frequency of the electromagnetic field becomes high. Both the electron and the field must be represented, initially, by wave packets—in space and momentum coordinates for the former, and in electric field and vector potential coordinates for the latter—in order to correspond to classically meaningful systems. The velocity of the electron at the output of the cavity is investigated. It is found that the expectation value of velocity has a quantum-mechanical correction term. A more significant effect, however, is the nonvanishing of the expectation value of the square of the deviation from the expectation value (mean square deviation from the mean) of the velocity. This deviation is a random phenomenon which will produce noise in an electron beam. An expression for the mean square deviation, in which the results of electron and field quantization are separately apparent, is derived, and its significance is discussed. An order-of-magnitude calculation is made for the ratio of minimum possible mean square deviation of velocity to velocity increment due to the field, and the frequency for which this ratio becomes unity is calculated for a particular set of conditions to be of the order of 3×10^{12}/sec.

THE trend, in recent years, toward the generation of higher and higher frequencies by means of microwave generators, has brought about the following questions: How high must the frequency be in order that quantum mechanical effects become apparent, and what will these effects be? Several authors[1–4] have discussed these questions, but, as has been pointed out elsewhere,[5] in a largely unsatisfactory manner. The purpose of the present paper is to analyze a problem the solution of which will help answer the broad questions just raised. Additional pertinent problems will be treated subsequently.

An essential aspect of many microwave generators and amplifiers is the passage of an electron beam through an oscillating cavity, resulting in a velocity modulation of the beam. The beam is then examined as it passes an analyzer, perhaps another cavity. The effect on the analyzer depends on the velocity of the electron after it has passed through the first cavity. We, therefore, consider the problem of an electron passing through an oscillating cavity, and investigate its velocity.

Due to the fact that in a quantum mechanical description of a system all dynamical variables cannot be specified exactly, there is a large variety of physically different ways in which to describe a system in quantum mechanics, the proper choice depending on the preparation of the system. Thus, a moving particle may be described by a plane wave or by one of a variety of wave packets. Similarly, the state of the radiation oscillators in the cavity can be described by means of one of many types of wave functions of the vector potential or electric field coordinates. A problem analogous to the one of selecting the proper wave function to describe a simple system does not ordinarily exist in classical mechanics, where it is assumed that all dynamical variables may be specified exactly, so that no guidance can be found in the classical treatment.

The only type of state which has any meaning in classical mechanics is one for which there is a wave packet of reasonably small width for every dynamical variable, since the preparation of the system in a classical experiment is such that, in principle, it must be possible to measure all dynamical variables. States which accurately describe systems in classical experiments must, consequently, be such wave packets. If, therefore, we are looking for quantum effects in an essentially classical experiment, we must represent the system by wave packets, both for the electron and the field. It becomes apparent that the quantum effects will be due to the necessarily finite widths of the wave packets.

Since our interest lies in those situations in which quantum mechanical effects first begin to appear, and are therefore small, we will retain only first order terms describing these effects. Also, we will regard the interaction between the electron and the field as a small perturbation. The analysis will be nonrelativistic.

Let the electric and magnetic fields of the cavity be given, respectively, by

$$\mathbf{E}=-4\pi c\mathbf{P}, \quad \mathbf{H}=\nabla\times\mathbf{A}. \tag{1}$$

Then, in the usual way,[6] we expand

$$\mathbf{A}=\sum_j q_j\mathbf{u}_j(\mathbf{r}), \quad \mathbf{P}=\sum_j p_j\mathbf{u}_j(\mathbf{r}), \tag{2}$$

where the subscript j refers to the jth normal mode of the cavity, $\mathbf{u}_j(\mathbf{r})$ is a normalized function describing the spatial dependence of the field,[7] and q and p are the

[1] L. P. Smith, Phys. Rev. **69**, 195 (1946).
[2] D. Gabor, Phil. Mag. **41**, 1180 (1950).
[3] C. Shulman, Phys. Rev. **82**, 116 (1951).
[4] J. C. Ward, Phys. Rev. **80**, 119 (1950).
[5] I. R. Senitzky, Phys. Rev. **91**, 1309 (1953); in particular, reference 7.

[6] See, for instance, L. I. Schiff, *Quantum Mechanics* (McGraw-Hill Book Company, Inc., New York, 1949), Sec. 50.
[7] The function, $\mathbf{u}_j(\mathbf{r})$, is a solution of the equation, $\nabla^2\mathbf{u}+(\omega/c)^2\mathbf{u}=0$, subject to the conditions $\mathbf{n}\times\mathbf{u}=0$ on the boundary of the cavity, $\int|\mathbf{u}|^2d^3\mathbf{r}=1$, and $\mathrm{div}\mathbf{u}=0$. The origin of the coordinate system lies outside of the cavity and is farther from it than the initial width of the electron wave packet.

coordinate and momentum operators of the radiation oscillators, satisfying the commutation relationship $[q_j,p_j]=i\hbar$, all other pairs commuting. We are looking for an initial state of the field for which both the field strength and energy are approximately specified. If the field is left undisturbed, we want these quantities to continue to be specified with the same degree of approximation. If, in addition, we require that the product of the uncertainties in q and in p be a minimum, then the main features of the state of the field are essentially determined,[8] and we proceed to describe it.

In the p representation of the Schrödinger picture, we specify the initial state of the field for the jth mode by the wave function

$$\varphi_j(p_j,0)=\left(\frac{4c^2}{\hbar\omega_j}\right)^{\frac{1}{4}}\exp\left[-\frac{4\pi c^2}{\hbar\omega_j}\left(\tfrac{1}{2}p_j{}^2-\frac{i\delta_{js}E_0}{4\pi c}p_j\right)\right], \quad (3)$$

where E_0 is a nonvanishing constant, and the sth mode is the oscillating one. If the field is not subjected to any external influence, the absolute value of the wave packet described by Eq. (3) remains unchanged for the non-oscillating modes, and oscillates sinusodially about the origin without change in shape with frequency $\omega_s/2\pi$ and amplitude $E_0/4\pi c$ for the oscillating mode; that is, it can be shown[9] that

$$|\varphi_j(p_j,t)|^2=\left(\frac{4c^2}{\hbar\omega_j}\right)^{\frac{1}{2}}\times\exp\left[-\frac{4\pi c^2}{\hbar\omega_j}\left(p_j+\frac{\delta_{js}E_0}{4\pi c}\sin\omega_j t\right)^2\right]. \quad (4)$$

Since $|\varphi_j(p_j,t)|^2$ is the probability of finding a given p at time t, we see that the most probable electric field is just the classical one, $\delta_{js}E_0\mathbf{u}_j(\mathbf{r})\sin\omega_j t$, and the uncertainty in magnitude of the field is determined by the Gaussian distribution of Eq. (4). In the Heisenberg representation, the state of the oscillating mode of the undisturbed field is described by the vector of which the nth component is given by

$$A_n{}^{(s)}=\xi^{\frac{1}{2}n}e^{-\frac{1}{2}\xi}(n!)^{-\frac{1}{2}},$$

where $\xi=E_0{}^2(8\pi\hbar\omega_s)^{-1}$. For the non-oscillating modes, we have $A_n{}^{(j)}=\delta_{n0}$, $j\neq s$. The probability of finding in the cavity an energy $n\hbar\omega_s$, not counting the zero point energy, is given by $|A_n{}^{(s)}|^2$. This is a Poisson distribution, with maximum and mean at $n=\xi=E_0{}^2/8\pi\hbar\omega_s$. We see, thus, that the instantaneous field strength and the energy are both approximately specified by their classical values. This is the closest one can come to a classically meaningful field.[10]

For the state of the electron, we want a wave packet for which both position and momentum are approximately specified. Here, however, we cannot require that the degree of approximation remain constant if the electron is left undisturbed, for the width of a free electron wave packet in coordinate space changes with time. The best we can do is assume a wave packet for which the product of the uncertainties in position and in momentum is a minimum at the initial time $t=0$ and for which both uncertainties are reasonably small. We take the initial state of the electron to be described by the wave packet[11]

$$\varphi(\mathbf{r},0)=b^{-\frac{1}{2}}\pi^{-\frac{1}{4}}\exp(-r^2/2b^2+ik_0x), \quad (5)$$

where b and k_0 are constants related to the width of the wave packet and its velocity, respectively. If the electron is left undisturbed, the probability of finding it at the point $\mathbf{r}$ at time t is given by[12]

$$|\varphi(\mathbf{r},t)|^2=b^{-3}\pi^{-\frac{3}{2}}\left[1+\left(\frac{\hbar t}{mb^2}\right)^2\right]^{-\frac{1}{2}}\times\exp\left[\frac{-(\mathbf{r}-\mathbf{v}_0t)^2}{b^2+(\hbar t/mb)^2}\right], \quad (5a)$$

where $\mathbf{v}_0$ is the vector $(\hbar k_0/m,0,0)$; and the probability of finding the electron with a momentum $\mathbf{p}$ is independent of the time and is given by

$$|\varphi(\mathbf{p})|^2=b^3\hbar^{-3}\pi^{-\frac{3}{2}}\exp[-(b/\hbar)^2(\mathbf{p}-m\mathbf{v}_0)^2]. \quad (6)$$

We note that both of these probabilities are Gaussian distributions, each with a maximum at the respective classical value.

The initial state for the entire system will now be described by the wave function

$$\varphi(\mathbf{r},p_j,0)=\varphi(\mathbf{r},0)\prod_j\varphi_j(p_j,0).$$

[8] The only arbitrariness left is that which corresponds to the choice of initial phase in the classical field; if we consider the Schrödinger picture of a free field which meets the above requirements, then the state of the field at any instant of time can serve as the initial state. A particular choice of initial time does not reduce the generality of our problem, however, since the entrance time of the electron wave packet is yet to be specified.

[9] Equation (4) and the subsequent expressions for $A_n{}^{(s)}$ may be derived by methods similar to those used in the analysis of the harmonic oscillator, such as those found in reference 6, Sec. 14, for example.

[10] In classical mechanics, the width of the wave packets is initially—and continues to be—zero. The closest approach, therefore, of a quantum mechanical situation to the classical one is that in which the wave packets referring to all the dynamical variables have the least possible width. This will occur when the product of the uncertainties in q and p is a minimum, which is the condition used. Moreover, such a situation will give the least possible correction to the classical result, and from this point of view, too, it may be considered closest to the classical situation. It is thus of particular interest in indicating the fundamental quantum mechanical limitations to the classical phenomena.

[11] We have used a spherically symmetrical wave packet for simplicity. The analysis can easily be generalized to the case where the initial wave packet is specified by

$$(b_1b_2b_3)^{-\frac{1}{2}}\pi^{-\frac{3}{4}}\exp(-x^2/2b_1{}^2-y^2/2b_2{}^2-z^2/2b_3{}^2+ik_0x).$$

Note that the wave packet is initially outside of the cavity.

[12] A. Sommerfeld, *Wellenmechanik* (Frederick Ungar Publishing Company, New York, 1947), p. 166.

By starting with the Hamiltonian,

$$H=\tfrac{1}{2}m^{-1}[\mathbf{p}+(e/c)\textstyle\sum_j q_j\mathbf{u}_j]^2 +\textstyle\sum_j[2\pi c^2p_j^2+(\omega_j^2/8\pi c^2)q_j^2], \quad (7)$$

and assuming that the electron velocity is sufficiently small so that we can neglect the effect of the magnetic field on the electron as compared to that of the electric field, the equations of motion in operator form in the Heisenberg picture become

$$d^2\mathbf{r}(t)/dt^2=4\pi c(e/m)\textstyle\sum_j p_j(t)\mathbf{u}_j(t), \quad (8)$$

where, by $\mathbf{u}(t)$ we mean $\mathbf{u}(\mathbf{r}(t))$. These, of course, are formally similar to the classical equations of motion, in view of Eqs. (1) and (2). From Eq. (8) we obtain for the velocity at time t,

$$\mathbf{v}(t)=\mathbf{v}(0)+4\pi c\frac{e}{m}\int_0^t dt_1\sum_j p_j(t_1)\mathbf{u}_j(t_1). \quad (9)$$

We can now use Eq. (9) to calculate the expectation value of the velocity at time t. We can also use the same equation to calculate the expectation value of the square of the deviation from the expectation value (mean square deviation) of the velocity at time t. In a purely classical consideration, this deviation would, of course, vanish. The reason that it does not vanish in a quantum mechanical calculation is that the wave packets cannot have infinitesimal width in both coordinate and momentum spaces. This deviation, when interpreted statistically, is a random phenomenon analogous to a noise current, and we see that it is a purely quantum mechanical effect. We now proceed to calculate both the expectation value and the mean square deviation of the x component of velocity.

The Hamiltonian of Eq. (7) is a constant, so that $p_j(t)$ and $\mathbf{u}_j(t)$ can be obtained from the initial operators by the relationships

$$p_j[t]=\exp[(i/\hbar)Ht]p_j(0)\exp[-(1/\hbar)Ht], \quad (10)$$

$$\mathbf{u}_j(t)=\exp[(i/\hbar)Ht]\mathbf{u}_j[\mathbf{r}(0)]\exp[-(i/\hbar)Ht]. \quad (11)$$

Since we are going to substitute from Eqs. (10) and (11) into the perturbation term in Eq. (9), we can approximate by neglecting the interaction term in the exponents of Eqs. (10) and (11). The right sides of these equations can then be evaluated without much difficulty. Equation (10) becomes that for a freely oscillating field, and $p_j(t)$ can be obtained directly from the equations of motion for a free field to be

$$p_j(t)=p_j(0)\cos\omega_j t-(\omega_j/4\pi c^2)q_j(0)\sin\omega_j t. \quad (12)$$

The right side of Eq. (11) may be evaluated by expressing $\mathbf{u}_j(\mathbf{r})$ in terms of its Fourier transform $\mathbf{U}_j(\mathbf{k})$:

$$\mathbf{u}_j(\mathbf{r})=\int d^3\mathbf{k}\mathbf{U}_j(\mathbf{k})\exp(i\mathbf{k}\cdot\mathbf{r}).$$

The exponential operators can be taken under the integral sign to operate on $\exp(i\mathbf{k}\cdot\mathbf{r})$. Using the relationship,

$$e^Ae^B=e^Be^Ae^{[A,B]}e^{-\frac{1}{2}([A,[A,B]]+[B,[A,B]])}\cdots,$$

where the dots indicate exponentials of higher commutators, we obtain

$$\mathbf{u}_j(t)=\int d^3\mathbf{k}\mathbf{U}(\mathbf{k})\exp\left(\frac{it\hbar k^2}{2m}+i\mathbf{k}\cdot\mathbf{r}\right)\exp\left(\frac{it\hbar\mathbf{k}\cdot\mathbf{p}}{m}\right). \quad (13)$$

We can now find the expectation value of the velocity $\langle\mathbf{v}\rangle$. Bringing the expectation value operation under the time integral in Eq. (9), we have

$$\langle\mathbf{v}(t)\rangle=\langle\mathbf{v}(0)\rangle+4\pi c\frac{e}{m}\int_0^t dt_1\sum_j\langle p_j(t_1)\mathbf{u}_j(t_1)\rangle. \quad (14)$$

Since we have neglected the interaction term in the Hamiltonian occurring in Eqs. (10) and (11), we can write

$$\langle p_j(t)\mathbf{u}_j(t)\rangle=\langle p_j(t)\rangle\langle\mathbf{u}_j(t)\rangle. \quad (15)$$

The expectation value of $p_j(t)$ on the right side of Eq. (15) is that for a free field. It can be obtained immediately in the p representation of the Schrödinger picture by making use of Eq. (4). We obtain

$$\langle p_j(t)\rangle=-\delta_{js}(E_0/4\pi c)\sin\omega_j t. \quad (16)$$

This, as was to be expected, is just the classical time-dependence of the field for the oscillating mode.[13] The expectation value for the non-oscillating modes vanishes, of course.

The expectation value of $\mathbf{u}_j(t)$ can be evaluated in the $\mathbf{r}$ representation.[14] Using Eqs. (13) and (5), we have

$$\langle\mathbf{u}_j(t)\rangle=b^{-3}\pi^{-\frac{1}{2}}\int d^3\mathbf{r}\int d^3\mathbf{k} \times\exp\left(\frac{-r^2}{2b^2}-ik_0x\right)\mathbf{U}(\mathbf{k})\exp\left(\frac{it\hbar k^2}{2m}+i\mathbf{k}\cdot\mathbf{r}\right) \times\exp\frac{it\hbar\mathbf{k}\cdot\mathbf{p}}{m}\exp\left(\frac{-r^2}{2b^2}+ik_0x\right). \quad (17)$$

If we express the function $\exp(-r^2/2b^2)$, on which $\exp(it\hbar\mathbf{k}\cdot\mathbf{p}/m)$ operates, by means of its Fourier transform,

$$\exp(-r^2/2b^2)=b^3(2\pi)^{-\frac{3}{2}}\int d^3\mathbf{k}_1 \times\exp(-k_1^2b^2/2)\exp(i\mathbf{k}_1\cdot\mathbf{r}), \quad (18)$$

[13] The expectation value of the field at a well-defined point, for which we have $\langle\mathbf{u}(\mathbf{r})\rangle=\mathbf{u}(\mathbf{r})$, is just the classical field $E_0\mathbf{u}(\mathbf{r})\sin\omega t$.

[14] The calculation is in the Heisenberg picture. Although it is, perhaps, simpler to calculate $\langle u(t)\rangle$ in the Schrödinger picture, later calculations involving u will require use of the Heisenberg picture, so that for uniformity we use it in the present case, too.

the result of the $\mathbf{p}$ operation may be written down immediately, since $\exp(it\mathbf{k}\cdot\mathbf{p}/m)$ now operates on eigenvalues of $\mathbf{p}$. Integrating then with respect to $\mathbf{r}$ and $\mathbf{k}_1$, we obtain

$$\langle\mathbf{u}_j(t)\rangle=\int d^3\mathbf{k}\mathbf{U}_j(\mathbf{k})\exp(i\mathbf{k}\cdot\mathbf{v}_0t)\exp[-k^2\delta^2(t)], \quad (19)$$

where

$$\delta^2(t)=(b/2)^2+(ht/2mb)^2.$$

It is to be noted that if the second exponential factor under the integral sign were missing, $\langle\mathbf{u}_j(t)\rangle$ would be equal to $\mathbf{u}_j(\mathbf{v}_0t)$, the classical value. It is this factor which accounts for the quantum mechanical effect. It is interesting to note that $2\delta(t)$ is just the half-width at time t of the free electron probability density, as can be seen from Eq. (5a). The first term in $\delta^2(t)$ is due to the original width of the wave packet, and the second term is due to the spreading of the wave packet. The effect of this exponential on the integral is small if $\mathbf{U}_j(\mathbf{k})$ becomes small for those value of k^2 for which the absolute value of the exponent is no longer small compared to unity. We assume that the absolute value of $k^2\delta^2(t)$ is small compared to unity for the range of k^2 from which significant contributions to the integral arise. Then

$$\begin{aligned}\langle\mathbf{u}_j(t)\rangle&\cong\int d^3\mathbf{k}\mathbf{U}_j(\mathbf{k})[1-k^2\delta^2(t)]\exp(i\mathbf{k}\cdot\mathbf{r})\,|_{r=\mathbf{v}_0t}\\&=\int d^3\mathbf{k}\mathbf{U}_j(\mathbf{k})[1+\delta^2(t)\nabla^2]\exp(i\mathbf{k}\cdot\mathbf{r})\,|_{r=\mathbf{v}_0t}\\&=[1+\delta^2(t)\nabla^2]\mathbf{u}_j(\mathbf{r})\,|_{r=\mathbf{v}_0t}\\&=[1-\delta^2(t)(\omega^2/c^2)]\mathbf{u}_j(\mathbf{v}_0t), \quad (20)\end{aligned}$$

where, in the last step, we have made use of the properties of $\mathbf{u}(\mathbf{r})$ described in footnote 7.

For $\mathbf{v}(0)$, we have

$$\langle\mathbf{v}(0)\rangle=(1/m)\langle\mathbf{p}(0)\rangle+(e/mc)\langle\mathbf{A}(0)\rangle.$$

Since the electron wave packet is initially outside the cavity, $\langle\mathbf{A}(0)\rangle$ vanishes, and $\langle\mathbf{p}(0)\rangle$ is seen immediately from Eq. (6) to be $m\mathbf{v}_0$. From Eqs. (14), (15), (16), and (20) we therefore obtain

$$\begin{aligned}\langle\mathbf{v}(t)\rangle=\mathbf{v}_0&+E_0\frac{e}{m}\int_0^t dt_1\mathbf{u}_s(\mathbf{v}_0t_1)\sin\omega t_1\\&-E_0\frac{e}{m}\frac{\omega^2}{c^2}\int_0^t dt_1\delta^2(t_1)\mathbf{u}_s(\mathbf{v}_0t_1)\sin\omega t_1. \quad (21)\end{aligned}$$

The first two terms on the right side of Eq. (21) are the classical expression for the velocity of an electron, with initial velocity $\mathbf{v}_0$, traversing a cavity with electric field $E_0\mathbf{u}_s(\mathbf{r})\sin\omega t$. The last term gives a first order quantum mechanical correction. We could study this effect in detail. However, the dispersion in velocity, as measured by the mean square deviation in velocity, is a much more significant effect. As far as the production of velocity modulation of an electron beam is concerned, the former effect merely changes the signal amplitude slightly, while the latter effect produces noise.

We therefore consider the expectation value of the square of the deviation from $\langle\mathbf{v}(t)\rangle$. Writing

$$v_x(t)=v_x(0)+\Delta v_x, \quad (22)$$

where, from Eq. (9),

$$\Delta v_x=4\pi c\frac{e}{m}\int_0^t\sum_j u_{jx}(t)p_j(t),$$

we have

$$\begin{aligned}\langle[v_x(t)-\langle v_x(t)\rangle]^2\rangle&=[\langle v_x^2(0)\rangle-\langle v_x(0)\rangle^2]\\&+[\langle(\Delta v_x)^2\rangle-\langle\Delta v_x\rangle^2]\\&+[\langle v_x(0)\Delta v_x+\Delta v_xv_x(0)\rangle-2\langle v_x(0)\rangle\langle\Delta v_x\rangle], \quad (23)\end{aligned}$$

since $v_x(0)$ and Δv_x do not commute. The first square bracket on the right side of Eq. (23) can be evaluated easily. From Eq. (6), we obtain

$$\langle v_x^2(0)\rangle-\langle v_x(0)\rangle^2=\hbar^2/2m^2b^2. \quad (24)$$

We proceed now to evaluate the second square bracket. For simplicity of notation, the x subscript will be dropped from the u's henceforth, with the understanding that u stands for the x component of $\mathbf{u}$, and likewise for the $\mathbf{U}$'s. We have, using the expression for Δv_x from Eq. (22),

$$\begin{aligned}\langle(\Delta v_x)^2\rangle=16\pi^2c^2\frac{e^2}{m^2}&\int_0^t dt_1\int_0^t dt_2\\&\times\sum_i\sum_j\langle u_i(t_1)u_j(t_2)p_i(t_1)p_j(t_2)\rangle.\end{aligned}$$

Neglecting the interaction term in the Hamiltonian of Eq. (11), just as in the case of Eq. (15), the integrand becomes

$$\sum_i\sum_j\langle u_i(t_1)u_j(t_2)\rangle\langle p_i(t_1)p_j(t_2)\rangle.$$

If $i\neq j$,

$$\langle p_i(t_1)p_j(t_2)\rangle=\langle p_i(t_1)\rangle\langle p_j(t_2)\rangle=0,$$

since either the ith or the jth mode, or both, are in their lowest energy states (non-oscillating). We thus have

$$\begin{aligned}\langle(\Delta v_x)^2\rangle=16\pi^2c^2\frac{e^2}{m^2}&\int_0^t dt_1\int_0^t dt_2\\&\times\sum_j\langle u_j(t_1)u_j(t_2)\rangle\langle p_j(t_1)p_j(t_2)\rangle. \quad (25)\end{aligned}$$

We evaluate the factors $\langle u_j(t_1)u_j(t_2)\rangle$ and $\langle p_j(t_1)p_j(t_2)\rangle$ separately. From Eqs. (3) and (12), we have [omitting the argument in $p(0)$ and $q(0)$ for simplicity of nota-

tion]:

$$\langle p_j(t_1)p_j(t_2)\rangle$$
$$=\left(\frac{\beta}{\pi}\right)^{\frac{1}{2}}\int_{-\infty}^{\infty}dp_j\exp\left[-\beta\left(\frac{p_j^2}{2}+\frac{i\delta_{js}E_0p_j}{4\pi c}\right)\right]$$
$$\times\{p_j^2\cos\omega_j t_1\cos\omega_j t_2-\beta^{-1}\hbar^{-1}[q_jp_j\sin\omega_j t_1\cos\omega_j t_2$$
$$+p_jq_j\cos\omega_j t_1\sin\omega_j t_2]+\beta^{-2}\hbar^{-2}q_j^2\sin\omega_j t_1\sin\omega_j t_2\}$$
$$\times\exp\left[-\beta\left(\frac{p_j^2}{2}-\frac{i\delta_{js}E_0p_j}{4\pi c}\right)\right],$$

where $\beta=4\pi c^2/\hbar\omega_j$. Making use of the fact that in the p representation q is represented by $ih\partial/\partial p$, we obtain

$$\langle p_j(t_1)p_j(t_2)\rangle=\delta_{js}(4\pi c)^{-2}E_0^2\sin\omega_j t_1\sin\omega_j t_2$$
$$+(8\pi c^2)^{-1}\hbar\omega_j\exp[i\omega_j(t_2-t_1)]. \quad (26)$$

We note that the first term on the right, which is equal to $\langle p_j(t_1)\rangle\langle p_j(t_2)\rangle$, is the classical value, and the second term is of purely quantum mechanical origin. We also note that although the first term vanishes for non-oscillating modes (as it should, being classical), the second term does not.

In order to evaluate $\langle u_j(t_1)u_j(t_2)\rangle$, we use Eqs. (13) and (5), obtaining

$$\langle u_j(t_1)u_j(t_2)\rangle$$
$$=b^{-3}\pi^{-\frac{3}{2}}\int d^3\mathbf{r}\int d^3\mathbf{k}_1\int d^3\mathbf{k}_2U_j(\mathbf{k}_1)U_j(\mathbf{k}_2)$$
$$\times\exp\left(\frac{-r^2}{2b^2}-ik_0x\right)\exp\left(\frac{it_1k_1^2h}{2m}+i\mathbf{k}_1\cdot\mathbf{r}\right)$$
$$\times\exp\left(\frac{it_1\mathbf{k}_1\cdot\mathbf{p}}{m}\right)\exp\left(\frac{it_2k_2^2h}{2m}+i\mathbf{k}_2\cdot\mathbf{r}\right)$$
$$\times\exp\left(\frac{it_2\mathbf{k}_2\cdot\mathbf{p}}{m}\right)\exp\left(\frac{-r^2}{2b^2}+ik_0x\right).$$

As in the case of evaluation involved in Eq. (17), we replace $\exp(-r^2/2b^2)$ on the right of the $\mathbf{p}$ operator by its Fourier integral representation given by Eq. (19), with the variable of integration changed to $\mathbf{k}_3$, say. The $\mathbf{p}$ operation can then be carried through. An integration now with respect to $\mathbf{r}$ and $\mathbf{k}_3$, successively, yields

$$\langle u_j(t_1)u_j(t_2)\rangle$$
$$=\int d^3\mathbf{k}_1\int d^3\mathbf{k}_2U_j(\mathbf{k}_1)\exp(i\mathbf{k}_1\cdot\mathbf{v}_0t_1)U_j(\mathbf{k}_2)$$
$$\times\exp(i\mathbf{k}_2\cdot\mathbf{v}_0t_2)\exp[-k_1^2\delta^2(t_1)]\exp[-k_2^2\delta^2(t_2)]$$
$$\times\exp\{-2\mathbf{k}_1\cdot\mathbf{k}_2\delta^2[(t_1t_2)^{\frac{1}{2}}]\}$$
$$\times\exp[i(h/2m)\mathbf{k}_1\cdot\mathbf{k}_2(t_1-t_2)]. \quad (26a)$$

It is interesting to note that if we omit the last four factors of the integrand, the integral represents the classical value, namely $u_j(\mathbf{v}_0t_1)u_j(\mathbf{v}_0t_2)$. If we omit the last two factors only, we obtain $\langle u_j(t_1)\rangle\langle u_j(t_2)\rangle$. The last two factors of the integrand produce an interference effect between $u_j(t_1)$ and $u_j(t_2)$. The last four factors in the integrand all produce quantum mechanical effects to the extent that they are different from unity in the ranges of $\mathbf{k}_1$ and $\mathbf{k}_2$ which contribute significantly to the integral. As in the case of Eq. (19) for $\langle u_j(t)\rangle$, we assume that these effects are small; that is, that the exponents are small compared to unity in the significant ranges of $\mathbf{k}_1$ and $\mathbf{k}_2$. Applying the same reasoning as used in Eq. (20), we obtain[15]

$$\langle u_j(t_1)u_j(t_2)\rangle\cong\left(1+\left\{\frac{ih(t_2-t_1)}{2m}\right.\right.$$
$$\left.\left.+2\left[\left(\frac{b}{2}\right)^2+\left(\frac{\hbar}{2mb}\right)^2t_1t_2\right]\right\}\nabla_1\cdot\nabla_2\right)$$
$$\times\langle u_j(\mathbf{r}_1)\rangle\langle u_j(\mathbf{r}_2)\rangle\,|_{\mathbf{r}_1=\mathbf{v}_0t_1,\mathbf{r}_2=\mathbf{v}_0t_2},$$

where the subscript on ∇ indicates the coordinate on which it operates. Using Eq. (20) and keeping lowest order terms only, we have

$$\langle u_j(t_1)u_j(t_2)\rangle\cong\left[1+\left(\frac{b}{2}\right)^2(\nabla_1+\nabla_2)^2\right.$$
$$\left.+\left(\frac{\hbar}{2mb}\right)^2(t_1\nabla_1+t_2\nabla_2)^2+\frac{ih(t_2-t_1)}{2m}\nabla_1\cdot\nabla_2\right]$$
$$\times u_j(\mathbf{r}_1)u_j(\mathbf{r}_2)\,|_{\mathbf{r}_1=\mathbf{v}_0t_1,\mathbf{r}_2=\mathbf{v}_0t_2}.$$

We can now evaluate $\langle(\Delta v_x)^2\rangle-\langle\Delta v_x\rangle^2$. From Eqs. (25), (22), and (16), we have

$$\langle(\Delta v_x)^2\rangle-\langle\Delta v_x\rangle^2$$
$$\cong16\pi^2c^2\frac{e^2}{m^2}\int_0^t dt_1\int_0^t dt_2[\sum_j\langle u_j(t_1)u_j(t_2)\rangle$$
$$\times\langle p_j(t_1)p_j(t_2)\rangle-\langle u_s(t_1)\rangle\langle u_s(t_2)\rangle$$
$$\times\langle p_s(t_1)\rangle\langle p_s(t_2)\rangle]. \quad (27)$$

[15] In the previous expansion of the exponential functions [Eq. (20)], we retained terms up to the first power of the exponent, and have considered each term of the exponent to be of the same order; that is $(kht/2mb)^2$ and $(kb/2)^2$ are of the same order of smallness compared to unity for the significant range of $\mathbf{k}$. In the present case the two terms in the exponent of the real exponential function (the next to the last factor in the integrand of Eq. 26a) which is being expanded are obviously of the same order as the above two terms. The imaginary exponent (of the last factor) must be examined separately, however. We have

$$k_1k_2h(t_2-t_1)/2m\sim k^2ht/2m\sim(kht/2mb)(kb/2).$$

Since we have considered $(kb/2)\sim(kht/2mb)$, we see that the absolute value of the imaginary exponent is of the same order as the other exponents.

If we set $\langle p_j(t_1)\rangle\langle p_j(t_2)\rangle \equiv C_j$, $(\hbar\omega_j/8\pi c^2)\exp[i\omega_j(t_2-t_1)] \equiv Q_j$, then, from Eq. (26),

$$\langle p_j(t_1)p_j(t_2)\rangle = C_j + Q_j.$$

C_j is the classical term and Q_j is the quantum mechanical correction. Substituting into Eq. (32), and bearing in mind that $C_j=0$ for $j\neq s$, we obtain

$$\langle(\Delta v_x)^2\rangle - \langle\Delta v_x\rangle^2$$
$$= 16\pi^2c^2\frac{e^2}{m^2}\int_0^t dt_1\int_0^t dt_2\{C_s[\langle u_s(t_1)u_s(t_2)\rangle - \langle u_s(t_1)\rangle\langle u_s(t_2)\rangle] + \sum_j Q_j\langle u_j(t_1)u_j(t_2)\rangle\}.$$

We retain only first-order quantum mechanical correction terms, so that in the summation term under the integral sign we replace $\langle u_j(t_1)u_j(t_2)\rangle$ by $u_j(\mathbf{v}_0t_1)u_j(\mathbf{v}_0t_2)$. We thus obtain

$$\langle(\Delta v_x)^2\rangle - \langle\Delta v_x\rangle^2$$
$$= 16\pi^2c^2\frac{e^2}{m^2}\int_0^t dt_1\int_0^t dt_2\left\{\frac{E_0^2}{8\pi^2c^2}\sin\omega_st_1\sin\omega_st_2 \times\left[t_1t_2\left(\frac{\hbar}{2mb}\right)^2+\left(\frac{b}{2}\right)^2+\frac{i\hbar(t_2-t_1)}{4m}\right] \times\nabla_1\cdot\nabla_2u_s(\mathbf{r}_1)u_s(\mathbf{r}_2)\big|_{\mathbf{r}_1=\mathbf{v}_0t_1,\mathbf{r}_2=\mathbf{v}_0t_2} + \sum_j\frac{\hbar\omega_j}{8\pi c^2}\exp[i\omega_j(t_2-t_1)]u_j(t_1)u_j(t_2)\right\}.$$

The imaginary term drops out in the integration, and we have, after simplification,

$$\langle(\Delta v_x)^2\rangle - \langle\Delta v_x\rangle^2$$
$$= \frac{2\pi e^2}{m^2v_0^2}\sum_j\hbar\omega_j\left|\int_{x_1}^{x_2}dx u_j(x,0,0)\exp[i(\omega_j/v_0)x]\right|^2 + 2E_0^2\frac{e^2}{m^2}\left\{\left[\frac{b}{2v_0}\int_{x_1}^{x_2}dx\left(\sin\frac{\omega_s}{v_0}x\right)\nabla u_s(\mathbf{r})\right]^2 + \left[\frac{\hbar}{2mbv_0^2}\int_{x_1}^{x_2}dx\left(x\sin\frac{\omega_s}{v_0}x\right)\nabla u_s(\mathbf{r})\right]^2\right\}_{y=z=0}, \quad (28)$$

where x_1 and x_2 mark the limits of the part of the x axis lying inside the cavity ($u=0$ outside these limits). We now evaluate the last bracket on the right side of Eq. (23). By means of reasoning similar to that used previously, we obtain[16]

$$\langle v_s(0)\Delta v_s\rangle = 4\pi ic\frac{e\hbar}{m^2}\int_0^t dt_1\langle p_s(t_1)\rangle\left\langle\left(\frac{\partial}{\partial x}\right)u_s(t_1)\right\rangle = -4\pi c\frac{e\hbar}{m^2}\int_0^t dt_1\langle p_s(t_1)\rangle\int d^3\mathbf{k}U(\mathbf{k}) \times\exp[ik_xv_0t_1-k^2\delta^2(t_1)]\left(k_0+\frac{ihk_xt_1}{2mb^2}+\tfrac{1}{2}k_x\right).$$

Similarly,

$$\langle\Delta v_xv_x(0)\rangle = 4\pi ic\frac{e\hbar}{m^2}\int_0^t dt_1\langle p_s(t_1)\rangle\left\langle u_s(t_1)\frac{\partial}{\partial x}\right\rangle = -4\pi c\frac{e\hbar}{m^2}\int_0^t dt_1\langle p_s(t_1)\rangle\int d^3\mathbf{k}U(\mathbf{k})\exp(ik_xv_0t_1) \times\exp[-k^2\delta^2(t_1)]\left(k_0+\frac{ihk_xt_1}{2mb^2}-\tfrac{1}{2}k_x\right).$$

Making use of Eqs. (21) and (16), and retaining only the lowest order term, we obtain

$$\langle\Delta v_xv_x(0)\rangle + \langle v_x(0)\Delta v_x\rangle - 2\langle v_x(0)\rangle\langle\Delta v_x\rangle = \frac{-E_0e\hbar^2}{m^3b^2v_0^2}\int_{x_1}^{x_2}dx\left(x\sin\frac{\omega_s}{v_0}x\right)\frac{\partial}{\partial x}u_s(x,0,0). \quad (29)$$

Substituting Eqs. (24), (28), and (29) into Eq. (23), we finally get

$$\langle v_x^2(t)\rangle - \langle v_x(t)\rangle^2 = \frac{\hbar^2}{2m^2b^2}\left\{1-\frac{2E_0e}{mv_0^2}\int_{x_1}^{x_2}dx\left(x\sin\frac{\omega_s}{v_0}x\right)\frac{\partial}{\partial x}u_s(x,0,0) + \frac{E_0^2e^2}{m^2v_0^4}\left[\int_{x_1}^{x_2}dx\left(x\sin\frac{\omega_s}{v_0}x\right)\nabla u_s(\mathbf{r})\right]_{y=z=0}^2\right\} + \frac{E_0^2e^2b^2}{2m^2v_0^2}\left[\int_{x_1}^{x_2}dx\left(\sin\frac{\omega_s}{v_0}x\right)\nabla u_s(\mathbf{r})\right]_{y=z=0}^2 + \frac{2\pi e^2}{m^2v_0^2}\sum_j\hbar\omega_j\left|\int_{x_1}^{x_2}dx u_j(x,0,0) \times\exp[i(\omega_j/v_0)x]\right|^2. \quad (30)$$

We can see that the first and second terms on the right side of this equation are due to the quantization of the electron, and the third term, the derivation of which has been reported previously,[17] is due to the quantization of the field. The first term may be attributed to both the initial uncertainty in velocity and the spreading of the wave packet subsequent to the time $t=0$; the second term is due to the initial width of the wave packet (or the initial uncertainty in position). The third term contains the effect not only of the oscillating mode but of all the non-oscillating modes. The reason

[16] The $\partial/\partial x$ in the expression $\langle(\partial/\partial x)u_s(t)\rangle$ operates on everything in front of it, not merely on $u_s(t)$.

[17] I. R. Senitzky, Phys. Rev. **90**, 386 (1953).

is that even for the lowest energy modes there is a finite probability of finding a nonzero field. However, the physical meaning of the third term is obscured by the fact that in the absence of a cavity the electron interacts with all the lowest energy modes in free space, and nevertheless the motion of the electron is considered uniform. What we are interested in is the difference between the electron motion in the presence of the cavity and the motion in free space. For the very high frequency modes the apertures of the cavity become large compared to the wavelength; the field (as represented by the function $\mathbf{u}(\mathbf{r})$) leaks out, and does not differ much from the free space field. Therefore our summation should cut off at a certain frequency. Below that frequency, the effect of field quantization in Eq. (30) is small compared to $\hbar^2/2m^2b^2$, and will be neglected, unless there is a resonance effect for a particular mode, that is, unless $u_j(x,0,0)$ has the same periodicity as $\exp[i(\omega_j/v_0)x]$, and the contribution of a particular integral in the summation becomes large. Since there is no resonance effect in free space, this is certainly a real effect due to the cavity and should be taken into consideration.

If we separate the $\partial/\partial x$ terms in the gradients from the other terms in Eq. (30), we can perform an integration by parts on these terms. If, in addition, we assume that the cavity is of such structure that the derivatives of $u(\mathbf{r})$ with respect to y and z vanish at $y=z=0$,[18] we obtain

$$\langle v_x^2(t)\rangle-\langle v_x(t)\rangle^2=\frac{\hbar^2}{2m^2b^2}\left(1-\frac{E_0eu_0}{mv_0\omega_s}A\right)^2+\frac{E_0^2e^2b^2u_0^2}{2m^2v_0^2}B^2+2\pi\hbar\frac{e^2}{m^2}\sum_j\frac{u_0^2}{\omega_j^2}|D_j|^2, \quad (31)$$

where A, B, and D are dimensionless quantities defined by

$$A=\int_{\theta_{s1}}^{\theta_{s2}}d\theta f_s(\theta)[\sin\theta+\theta\cos\theta],$$

$$B=\int_{\theta_{s1}}^{\theta_{s2}}d\theta f_s(\theta)\cos\theta, \quad D_j=\int_{\theta_{j1}}^{\theta_{j2}}d\theta f_j(\theta)e^{i\theta}.$$

We have used the following notation: $\theta_j=\omega_j t$, $u_j(v_0t,0,0)=u_0f_j(\theta_j)$, where $u_0=V^{-\frac{1}{2}}$ and V is the volume of the cavity. The function $f_j(\theta)$ is of the order of unity, since $\mathbf{u}_j(\mathbf{r})$ is normalized over the volume of the cavity.

It is obvious that the mean square deviation in velocity of the electron at the output of the cavity depends on a detailed consideration of the spatial dependence of the field, strength of the field, velocity of the electron, and width of the initial wave packet. In order to obtain an idea of the order of magnitude of the mean square deviation, without going into the many details of a particular experiment, we will introduce some simplifications and assumptions. We consider a case in which there is no resonance interaction between the electron and field. We therefore neglect the quantized field term and assume that A and B are of the order of unity. We also assume that the derivatives of u with respect to y and z vanish, so that we can use Eq. (31). Because of the assumption, made at the beginning of our analysis, that the interaction between electron and field produces a small perturbation, we have $E_0eu_0/mv_0\omega\ll1$.[19] Thus, we obtain (the symbol $\sim$ indicates order of magnitude)

$$\langle v_x^2(t)\rangle-\langle v_x(t)\rangle^2\sim\hbar^2/2m^2b^2+\tfrac{1}{2}E_0^2e^2u_0^2b^2/m^2v_0^2.$$

This, of course, is a function of the initial electron wave-packet half-width b. We can minimize this quantity with respect to b. The result is

$$[\langle v_x^2(t)\rangle-\langle v_x(t)\rangle^2]_{\min}\sim\hbar E_0eu_0m^{-2}v_0^{-1}.$$

The ratio of this expression to the square of the expectation value of velocity increment which the electron undergoes in passing through the cavity is significant, since this ratio is essentially a comparison of noise to signal. From Eq. (21) we have

$$\langle\Delta v_x\rangle\cong E_0\frac{e}{m}\int_0^t dt_1u_s(\mathbf{v}_0t)\sin\omega t=\frac{E_0eu_0}{m\omega_s}\int_{\theta_{s1}}^{\theta_{s2}}d\theta f_s(\theta)\sin\theta\sim E_0eu_0/m\omega_s.$$

We obtain, therefore,

$$\eta\equiv\frac{[\langle v_x^2(t)\rangle-\langle v_x(t)\rangle^2]_{\min}}{\langle\Delta v_x\rangle^2}\sim\frac{\hbar\omega_s^2}{E_0u_0ev_0}.$$

We see that this ratio increases with increase in frequency and decreases with increase in field strength. Rewriting it as $\hbar\omega_s/E_0u_0e(v/\omega_s)$, one notes that it is of the same order of magnitude as the ratio of the energy of a photon to the energy which the electron may receive from the field in a half-cycle. We can also write

$$\eta^2\sim137\pi^2\frac{V}{\lambda^3}\left(\frac{c}{v_0}\right)^2\frac{\hbar\omega_s}{E_0^2/8\pi}. \quad (32)$$

The last factor in this expression is the ratio of the energy of a photon to the most probable energy in the cavity.

It is interesting to consider a numerical example, and find the conditions for which η becomes unity. We assume that the volume of the cavity is of the order of λ^3, and that the initial velocity of the electron is one-tenth that of light. We can then see from Eq. (32) that η becomes unity when the most probable number of photons in the cavity is of the order of 10^5. If, in addition, we make an assumption about the Q of the cavity[20]

[18] This assumption corresponds to the usual experimental arrangement, in which the path of the electron lies where the field is strongest.

[19] This ratio is of the order of the ratio of velocity increment which the electron may obtain in the cavity to the initial velocity.

[20] The unloaded Q of a cavity is defined as $\omega W/\bar{P}$ where W is the energy stored in the cavity, and $\bar{P}$ is the average power loss in the walls. Now (energy stored) $\propto$ (volume) $\propto\lambda^3$. Also, (power loss) $\propto$ (wall area)$\times$(skin depth)$^{-1}\propto\lambda^2\times\lambda^{-\frac{1}{2}}$. Thus $Q\propto\lambda^{\frac{1}{2}}$. We assume

and consider a specific amount of power being fed into the cavity, we can calculate the frequency for which η becomes unity. If we take $Q \sim 10^5 \lambda^{\frac{1}{2}}$, where λ is given in centimeters, and consider the case in which 10^{-4} watts is fed into the cavity, then η becomes unity for $\lambda \sim 10^{-2}$ cm. The electron wave packet half-width b which minimizes the mean square deviation in velocity for this wavelength and the above assumptions is of the order of 10^{-4} cm. Thus, the minimum mean square deviation of the velocity becomes comparable to the modulation in velocity, for the particular conditions assumed, when the wavelength is of the order of a tenth of a millimeter.

the same frequency dependence for the loaded Q, which is the one pertinent to the present discussion.

The author is indebted to Professor Julian Schwinger for enlightening discussions related to the foregoing subject matter and for his reading of the manuscript.

PHYSICAL REVIEW VOLUME 95, NUMBER 4 AUGUST 15, 1954

Penetration of 6-Mev Gamma Rays in Water

P. A. Roys, K. Shure, and J. J. Taylor
Westinghouse Electric Corporation, Pittsburgh, Pennsylvania

(Received March 1, 1954; revised manuscript received May 10, 1954)

The penetration of 6-Mev gamma rays has been studied out to 190 cm in water. The dose rate has been measured with an anthracene scintillation detector as a function of the distance from the N^{16} source. The results agree closely out to 160 cm with the distribution calculated according to the theory of gamma-ray penetration as developed by Spencer and Fano.

A MEASUREMENT has been made of the broad beam penetration of high-energy (~6 Mev) gamma rays from N^{16} in water. Very little experimental data have been heretofore available on broad beam penetration with simple geometries and none at all in this energy region. The results are also of interest as a check on the theoretical method of calculation of gamma-ray penetration as developed by Spencer and Fano.[1]

The N^{16} source is obtained by circulating demineralized water through the high-flux region of the Materials Testing Reactor and then piping it into a flat cylindrical disk, 30 cm in diameter, which serves as the source. The disk is made of a tightly wound coil of $\frac{1}{4}$-in. i.d. Saran tubing. It is located in a large body of water with a minimum of 4 ft of water in all directions from the coil. A detector is positioned so that it can be moved along the axis of the cylindrical disk. Variations in source intensity due to changes in water flow or reactor flux are compensated for by means of a monitor.

The detector and monitor are anthracene scintillation counters. The anthracene cylinders are $1\frac{1}{2}$ in. in diameter and 1 in. high and are optically attached to RCA 5819 photomultiplier tubes. The output current of the photomultiplier is read on a low drift ac electrometer. This current is a measure of the dose rate.

The following important reactions are expected to occur upon neutron irradiation in the reactor: $O^{16}(n,p)N^{16}$, $O^{17}(n,p)N^{17}$, and $O^{18}(n,\gamma)O^{19}$. The N^{16} production should be predominant. In order to verify this and to check on the existence of any spurious activity from impurities, decay curves have been

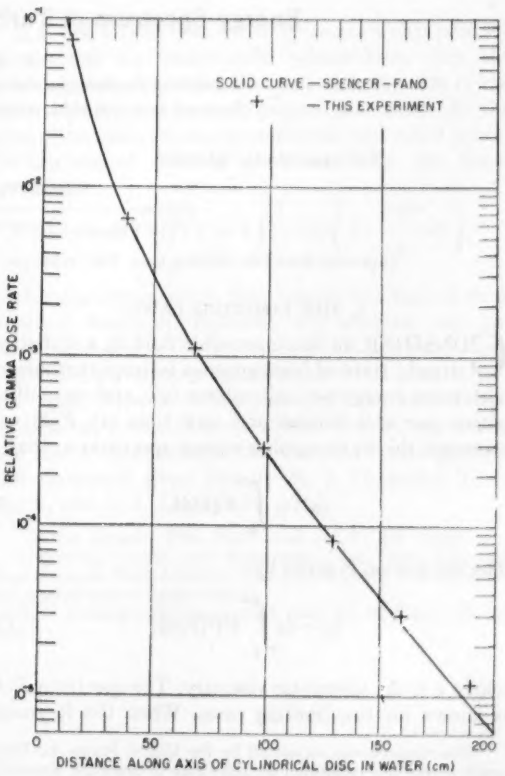

FIG. 1. Relative gamma dose rate as a function of distance from source.

[1] L. V. Spencer and U. Fano, J. Research Natl. Bur. Standards 46, 446 (1951); Phys. Rev. 81, 464 (1951).

taken with the detecting crystal located 22.9 cm in water from the source coil.

The analysis shows a component with a 29-sec half-life (3 percent) and a component with a half-life of 7–8 sec (97 percent) at this distance in water. The half-life of O^{19} is 29 sec and that of N^{16} is 7.35 sec.[2] N^{17} does not emit any gamma radiation while O^{19} emits a gamma ray of 1.6 Mev. The energies of the N^{16} gamma rays have been previously measured and are given as 6.13 Mev and 7.10 Mev in the ratio of 12.5:1.[2] Thus, the source is essentially 6.13 Mev in energy with small components of 7.10 Mev and 1.6 Mev.

The experimental results are shown in Fig. 1. The detector reading corrected for background and compensated for changes in monitor reading is shown as a function of the distance along the cylindrical axis of the source coil. The solid curve is that calculated by the Spencer-Fano method utilizing the calculations provided by the joint NBS-NDA computational program.[3] The calculations take into account the slightly non-uniform source distribution caused by the decay of N^{16} as the water flows through the coil. All three energy components have also been included, but in the region plotted the calculations differ by a maximum of 4 percent (and by less than 1 percent up to 100 cm) from the distribution obtained by assuming a monochromatic source of 6.13 Mev.

The theoretical curve is normalized to the experimental data at the point 11.4 cm from the coil. The experimental points agree very closely with the theoretical curve out to 160 cm. The trend toward disagreement beyond 160 cm is not considered to be conclusive because of a low signal-to-background ratio at these distances. From these results, it is felt that the Spencer-Fano theory is valid in the region investigated.

We are greatly indebted to Dr. George Mechlin and Dr. Warren Witzig for their invaluable assistance in the design and installation of the irradiation loop.

[2] *Nuclear Data*, National Bureau of Standards Circular 499 (U. S. Government Printing Office, Washington, D. C., 1950).

[3] Goldstein, Wilkins, and Spencer, Phys. Rev. **89**, 1150 (1953); NDA Memo 15C-20, 1953 (unpublished).

PHYSICAL REVIEW VOLUME 95, NUMBER 4 AUGUST 15, 1954

Energy Spectrum of Turbulence for the Entire Range*

R. W. DAVIES
American Institute of Aerological Research, Pasadena, California
(Received March 8, 1954; revised manuscript received May 10, 1954)

The wave-number spectrum,

$$F(k)=\frac{(14\nu\langle u^2\rangle)^{2/3}Ck^4\exp\{-14\nu k^2\langle u^2\rangle/\langle\epsilon\rangle\}}{[14\nu\langle u^2\rangle+\frac{3}{4}k^{10/3}C^{3/2}(1-\exp\{-21\nu k^2\langle u^2\rangle/\langle\epsilon\rangle\})]^{2/3}},$$

is derived from two limiting laws. The technique is very similar to that employed in blackbody radiation.

1. THE LIMITING LAWS

CONSIDER an incompressible fluid in a statistical steady state of homogeneous isotropic turbulence with mean energy per unit volume $\langle u^2\rangle$, and mean dissipation per unit volume and unit time $\langle\epsilon\rangle$. $F(k)$ will represent the wave-number energy spectrum so that

$$\langle u^2\rangle=\int_0^\infty F(k)dk. \tag{1}$$

The dissipation is given by

$$\langle\epsilon\rangle=2\nu\int_0^\infty k^2F(k)dk, \tag{2}$$

where ν is the kinematic viscosity. The spectrum $F(k)$ is known for two limiting cases. When the Reynolds number is large (and $\langle\epsilon\rangle$ large),

$$F(k)\sim(\langle\epsilon\rangle)^{2/3}k^{-5/3}, \tag{3}$$

which is the Kolmogoroff-Onsager-von Weizäcker[1–3] limiting law. When the Reynolds is very small (and $\langle\epsilon\rangle$ small), then for large decay times

$$F(k)\sim Ck^4\exp\{-2\nu k^2t\}, \tag{4}$$

which is the Batchelor-Karman-Lin[4,5] limiting law. Since $t/7=\langle u^2\rangle/\langle\epsilon\rangle$ when (4) applies,

$$F(k)\sim Ck^4\exp\{-14\nu k^2\langle u^2\rangle/\langle\epsilon\rangle\}. \tag{5}$$

* This research was supported by the United States Air Force under a contract monitored by the Office of Scientific Research, Air Research and Development Command.

[1] A. N. Kolmogoroff, Compt. rend. acad. sci. (U.R.S.S.) **30**, 301 (1941).
[2] Lars Onsager, Phys. Rev. **68**, 286 (1945).
[3] C. F. von Weizsäcker, Z. Physik **124**, 614 (1948).
[4] G. K. Batchelor, Proc. Roy. Soc. (London) **A195**, 513 (1949).
[5] Th. von Karman, Compt. rend. **226**, 2108 (1948).

2. DERIVATION OF $F(k)$

It is well known that turbulence has some features which are similar to those of blackbody radiation and that $\langle\epsilon\rangle$ plays a role in turbulence which suggests the role of temperature in the blackbody problem. It is also known that there are two energy transport processes in turbulence, inertial transfer and viscous dissipation. The former process tends to lengthen and concentrate vortex lines and the latter process tends to destroy them.

The point of view taken in this paper is that each of the limiting laws (3) or (5) is the theoretical result if one of the transport processes is virtually absent. Since this can never be realized in practice, (3) and (5) are asymptotic statements.

The spectrum can be written as

$$F(k)=\phi_1+\phi_2 =\lim_{t\to\infty}\left\{-\int^t W(k,\langle\epsilon\rangle,t')dt'-2\nu k^2\int^t F(k,t')dt'\right\},$$

where ϕ_1 and ϕ_2 represent the contributions from each of the two energy transport processes; then

$$\begin{aligned}&\lim_{\phi_1\to 0} F\to(\langle\epsilon\rangle)^{2/3}k^{-5/3},\\ &\lim_{\phi_2\to 0} F\to Ck^4\exp\{-14\nu k^2\langle u^2\rangle/\langle\epsilon\rangle\}.\end{aligned}\tag{6}$$

The fundamental assumption in this note is that for a given change in $\langle\epsilon\rangle$ each transport process changes independently of the other process. It is now possible to calculate the change in one process as though the other were not present. Thus

$$\frac{\partial\phi_1}{\partial\langle\epsilon\rangle}+\frac{\partial\phi_2}{\partial\langle\epsilon\rangle}=\left.\frac{\partial\phi_1}{\partial\langle\epsilon\rangle}\right|_{\phi_2=0}+\left.\frac{\partial\phi_2}{\partial\langle\epsilon\rangle}\right|_{\phi_1=0},\tag{7}$$

and from (6) it therefore follows that

$$-\frac{\partial F}{\partial(1/\langle\epsilon\rangle)}=14\nu k^2\langle u^2\rangle F+\frac{2k^{5/2}}{3}F^{5/2}.\tag{8}$$

Hence,

$$F=\frac{(14\nu\langle u^2\rangle)^{2/3}Ck^4\exp\{-14\nu k^2\langle u^2\rangle/\langle\epsilon\rangle\}}{[14\nu\langle u^2\rangle+\frac{2}{3}C^{3/2}k^{13/2}(1-\exp\{-21\nu k^2\langle u^2\rangle/\langle\epsilon\rangle\})]^{2/3}},$$

where the arbitrary constant of the first order differential equation was chosen as

$$M=\tfrac{2}{3}k^{5/2}+14\nu\langle u^2\rangle C^{-3/2}k^{-4}.\tag{9}$$

3. A LIMITING CASE AND THE CONSTANT C

The most interesting limit occurs when viscosity approaches zero. Then

$$F(k)=\frac{Ck^4}{[1+(C^{3/2}k^{17/2}/\langle\epsilon\rangle)]^{2/3}}.\tag{10}$$

A similar formula,

$$F(k)\sim k^4/[1+Ak^2]^{17/6},\tag{11}$$

was produced empirically by Karman[6] from some data by Liepmann, Laufer, and Liepmann.[7]

By integrating (10) above it follows that

$$C=\Lambda(\langle u^2\rangle)^{17/2}(\langle\epsilon\rangle)^{-5},\tag{12}$$

where $\Lambda=[2\Gamma(10/17)\Gamma(4/51)/17\Gamma(2/3)]^{-17/2}$ is the fifth power of a universal number suggested by Kolmogoroff.[8] This number should be checked experimentally to ascertain the validity of the $k^{-5/3}$ limiting law.

4. CONCLUSION

The fundamental assumption (7) is probably incorrect. The right-hand sides of Eqs. (7) and (8) are the first two terms of a series. The assumption in question is merely the simplest and most economical way of disposing of the remainder terms. Nevertheless, the main result seems to agree with experience in turbulence.

It is well known that if two processes which produce fluctuations are statistically independent, then the total mean square of the fluctuations is the sum of the mean squares due to each process separately. In the present problem the energy spectrum and mean square fluctuations of velocity are related by the linear operator,

$$\langle[u(P+r)-u(P)]^2\rangle=4\int_0^\infty F(k)\left(1-\frac{\sin kr}{kr}dk\right),$$

so that the arguments in Sec. 2 apply to either of these principal functions. However, the analysis does not yield the function $\langle[u(P+r)-u(P)]^2\rangle$ in closed form.

The author is much indebted to Prof. Max Born's fine book *Natural Philosophy of Cause and Chance* (Clarendon Press, Oxford, 1949). The author would also like to acknowledge the valuable encouragement and assistance given him by R. J. Diamond, T. B. Smith, and A. A. Linthicum.

[6] Th. von Karman, Proc. Natl. Acad. Sci. **34**, 530 (1948).

[7] Liepmann, Laufer, and Liepmann, "On Some Turbulent Measurements Behind Grids," National Advisory Committee for Aeronautics report (unpublished).

[8] A. N. Kolmogoroff, Compt. rend. acad. sci. (U.R.S.S.) **31**, 538 (1941).

Minimum in the Electrical Resistance of Metals at Low Temperatures

A. B. BHATIA*
National Research Council, Ottawa, Canada
(Received March 15, 1954)

A discussion is given of the effect on the electrical properties of normal metals at low temperatures of the same interaction as that invoked by Frölich and Bardeen in the theory of superconductivity. In particular it appears possible to explain qualitatively the resistance minimum experimentally observed in slightly impure metals, though a final decision must await an improvement in the general mathematical techniques for dealing with the Fröhlich-Bardeen interaction.

RECENTLY Fröhlich[1] has made it likely that metals are superconductive if a certain factor F, which is a measure of the strength of the interaction between the electrons and the lattice vibrations, is greater than unity. If too weak for this ($F<1$), the interaction can lead to modifications in the properties of the normal state at low temperatures. The variation of electronic specific heat with temperature has been discussed qualitatively by Buckingham[2] from this point of view. In this note the effect of this interaction on the electrical properties of normal metals (impure specimens) is *qualitatively* discussed.

We first consider the electrical resistivity. The specific electrical resistance R of a metal at temperatures T sufficiently below the Debye temperature Θ_D, may be written under usual assumptions in the form:

$$R \equiv R_T + R_i = [E'(k_0)]^{-2}[aT^5+\rho], \tag{1}$$

where a is a constant characteristic of the metal, $\rho[E'(k_0)]^{-2}$ the resistance due to impurities and faults in the crystal (ρ can be generally assumed to be independent of T), and $E'(k_0)$ the derivative of the energy E of an electron with respect to the momentum wave number $k(=k_0)$ at the Fermi surface (assumed spherical). The term $[E'(k_0)]^{-2}$ in (1) arises as follows: The resistance R of a metal is inversely proportional to the relaxation time τ and to the effective number of free electrons in the metal and both these quantities are proportional to $E'(k_0)$.[3] Of course, the constants a and ρ also depend on the magnitude of k_0, but they are approximately independent of the $E-k$ relation near the surface of the Fermi distribution. The reason for writing R in the form (1) will become clear later.

Now if the electrons are treated as free apart from their interactions with the lattice vibrations, the energy E of an electron with wave vector $\mathbf{k}$ is given (at absolute zero of temperature) by[1]

$$E(\mathbf{k}) = E_0(\mathbf{k}) + E_2(\mathbf{k}) = \hbar^2k^2/2m + E_2(\mathbf{k}), \tag{2}$$

where

$$E_2(\mathbf{k}) = \frac{8F\xi\sigma_0}{3nV}\sum_{\mathbf{w}} \frac{wf(\mathbf{k}-\mathbf{w})}{|\mathbf{k}-\mathbf{w}|^2-k^2+\sigma_0 w}. \tag{3}$$

Here $f(\mathbf{k}-\mathbf{w})$ denotes the probability that the state of wave vector $\mathbf{k}-\mathbf{w}$ is occupied by an electron, and $\sigma_0(\sim 10^{-3}k_0)$ is the wave number of an electron moving with the velocity of sound. We should at once make it clear that formula (3) is based on a perturbation theory whose validity for highly degenerate systems is questionable;[4] therefore one cannot be certain whether results deduced from it are quantitatively correct. Nevertheless, it seems useful to discuss the consequences of this formula.

The summation in (3) over all phonon wave-vectors $\mathbf{w}$ can be replaced by an integral which is evaluated in (HF) for values of k such that $|(k-k_0)k_0^{-1}| \ll 1$. One can similarly evaluate (3) for any k also. One finds

$$E_2(k) = -\frac{\nu F\hbar^2}{2mk}(\sigma_0/k_0)\left[\int_0^{k_0-k} w^2dw \log\left|\frac{w+\sigma_0-2k}{w+\sigma_0+2k}\right| + \int_{k_0-k}^{w_0} w^2dw \log\left|\frac{(w+\sigma_0-2k)w}{\sigma_0 w+k_0^2-k^2}\right|\right] \tag{4a}$$

for $k<k_0$, and

$$E_2(k) = -\frac{\nu F\hbar^2}{2mk}(\sigma_0/k_0) \times \int_{k-k_0}^{w_0} w^2dw \log\left|\frac{(w+\sigma_0-2k)w}{\sigma_0 w+k_0^2-k^2}\right| \tag{4b}$$

for $k>k_0$. In Eq. (4), w_0 is the maximum value of w (in the Debye approximation) and ν the number of free electrons per atom. Expanding (4) in powers of $(k-k_0)k_0^{-1}$, one may deduce after some lengthy algebra:

$$E_2'(k_0) = -(\hbar^2/m)k_0(\tfrac{1}{2}\nu)^{\frac{1}{3}}F = -E_0'(k_0)(\tfrac{1}{2}\nu)^{\frac{1}{3}}F, \tag{5a}$$

* National Research Laboratories Post-doctorate Fellow.

[1] H. Fröhlich, Phys. Rev. **79**, 845 (1950); this paper is referred to as (HF) and its notation is employed here. See also the papers of J. Bardeen, Phys. Rev. **79**, 167 (1950); **80**, 567 (1950); **81**, 829 (1951).

[2] M. J. Buckingham, Nature **168**, 281 (1951).

[3] See, for example, N. F. Mott and H. Jones, *A Theory of Properties of Metals and Alloys* (Oxford University Press, London, 1936), pp. 262–263, Eqs. (48) and (55). Note that the factor $E'(k_0)$ in τ appears because the transition probabilities are proportional to the density of states $N(E)$ ($N(E) \propto [E'(k_0)]^{-1}$) at the Fermi surface; it, therefore, occurs independently of the nature of the perturbation causing the transitions.

[4] H. Fröhlich, Physica **19**, 755 (1953).

and

$$E_2''(k_0) = -3(k_0/\sigma_0)E_0''(k_0)(\tfrac{1}{2}\nu)^{\frac{1}{2}}F \sim 10^3 E_0''(k_0). \quad (5b)$$

Further, it may be seen from (4) that for values of k such that $|k-k_0| \gtrsim 2\sigma_0$, $E_2'(k)$ becomes negligible in comparison with $E_0'(k_0)$.

Although a theory describing the effect of electron-lattice interaction on $E(k)$ at finite temperatures is difficult and has not yet been developed, one can see that $E_2'(k_0)$ would become vanishingly small at high temperatures for the following reasons:

(1) The growth of the tail of the Fermi distribution would reduce $E_2'(k_0)$; for instance, if $f(\mathbf{k}_0-\mathbf{w}) \sim 1$ for all $\mathbf{k}_0-\mathbf{w}$ for which the moduli of the denominators in (3) are $\lesssim \sigma_0 w_0$, then $E_2'(k_0) \sim 10^{-3} E_0'(k_0)$.

(2) At nonzero temperatures the effect of radiation damping due to phonon emission is likely to be appreciable; this would further reduce $E_2'(k_0)$.

(3) At high temperatures the current is carried not only by electrons of momentum wave number k_0, but also by electrons with neighboring wave numbers, and for these $E_2'(k) \lesssim E_2'(k_0)$.

Now, as will be obvious presently, the qualitative nature of the results to be deduced are independent of the precise rate of fall of $E_2'(k_0)$ with temperature; for definiteness, therefore, we assume that $E_2'(k_0)$ falls off exponentially with temperature. Hence $E'(k_0)$ may be written in the form

$$E'(k_0,T) = E_0'(k_0)[1-(\tfrac{1}{2}\nu)^{\frac{1}{2}}Fe^{-T/T_e}], \quad (6)$$

where T_e is an unknown constant which depends on F and is *presumably* of the order of a few degrees Kelvin.

It will be seen from the foregoing that $E'(k,T)$ and hence the density of states $N(E)$ $[N(E) \propto [E'(k)]^{-1}]$ differs from the corresponding free electron value only in a small region near the top of the Fermi distribution; hence the value of k_0 and consequently of the constants a and ρ in (1) will suffer little change with temperature due to that of $E'(k,T)$. With the help of (6) and (1), one may now draw the following conclusions regarding the variation of R with T:

(a) For an ideally pure metal ($\rho=0$), no minimum in R appears as the temperature is lowered; but R goes down to zero slightly more slowly than suggested by the T^5 law.

(b) For an impure specimen ($\rho \neq 0$), as the temperature is lowered in the neighborhood of absolute zero, the resistance R rises, attaining at 0°K a value $[1-(\tfrac{1}{2}\nu)^{\frac{1}{2}}F]^{-2}$ times the residual resistance at temperatures $T \gg T_e$, so that the R, T curve shows a minimum.[5]

(c) Assuming T_e to be independent of the impurity concentration, which will be true only for small concentrations, one finds that the temperature T_m at which the minimum occurs increases with the concentration of impurity.

(d) Lastly, $\Delta R = \{R(0)-R(T_m)\}/R(0)$ also decreases as the impurity concentration is reduced. All these qualitative features have been experimentally observed in several metals, namely Cu, Ag, Au, and Mg.[6]

The above conclusions hold only for low impurity concentrations (say ~0.1 percent). For higher concentrations, the density of states ($\propto [E'(k_0)]^{-1}$) will itself depend on the concentration of the impurities, since these will then perturb the free-electron wave functions. This may be the cause of the saturation of the magnitude of the minimum with increasing concentrations.[7] It would be of interest in this connection to experiment with order-disorder alloys in which the concentration deviates only slightly from the stoichiometric ratio. Such experiments are to be tried by Dr. W. B. Pearson of this laboratory.

For reasons already mentioned, a detailed quantitative comparison of the experimental data with the above formulas would be unjustifiable. However, the present experimental data suggest a value of $T_e \sim 1$°K for Cu, Ag, and Au, and $T_e \sim 4$°K for Mg. For best agreement with the experiments, the values of F for these metals have to be chosen of the order of 0.1 or 0.2; these are lower by a factor of 2 or 3 than those estimated in (HF) from high-temperature resistivity data. From the considerations given earlier, one would also have expected T_e to be higher than the above values.

Finally we note that this interaction will also affect the magnetoresistance and thermoelectric powers of the specimens. The formulas for these effects involve $E_2''(k_0)$. From (5b) one has $E_2''(k_0) \sim 10^3 E_0''(k_0)$—small effective mass ~$10^{-3}$ times the electronic mass— so that one would expect rather large deviations from the normal behavior. Although such deviations[8] have been observed, especially in the thermoelectric power,[9] we shall not discuss these effects further since any quantitative estimates based on Eqs. (3) and (6) are likely to be unreliable. It may be mentioned here, however, that recently MacDonald and Pearson,[10] independently of the above considerations, have semi-empirically found interesting correlations between the phenomenon of the resistance

[5] One would expect a similar minimum in the W/T, T curve, where W is the thermal resistance.

[6] See, for example, G. J. van den Berg, thesis, Leiden, 1938 (unpublished); D. K. C. MacDonald and K. Mendelssohn, Proc. Roy. Soc. (London) **A202**, 523 (1950); E. W. Mendoza and J. G. Thomas, Phil. Mag. **42**, 291 (1951) and **43**, 900 (1952); A. N. Gerritsen and J. O. Linde, Physica **17**, 573, 584 (1951).

[7] D. K. C. MacDonald, Phys. Rev. **88**, 148 (1952); D. K. C. MacDonald and W. B. Pearson, Phys. Rev. **88**, 149 (1952).

[8] See, for example, A. N. Gerritsen and J. Korringa, Physica **19**, 457 (1953).

[9] D. K. C. MacDonald and W. B. Pearson, Proc. Roy. Soc. (London) **A219**, 273 (1953); Proc. Roy. Soc. (London) **A221**, 534 (1954).

[10] D. K. C. MacDonald and W. B. Pearson, Phil. Mag. (to be published). I am grateful to Dr. MacDonald for showing me the manuscript before publication.

minimum and the anomalous variation of the thermoelectric power with temperature.

It seems, therefore, that the interaction introduced by Fröhlich is at least partly responsible for the resistivity minimum and other anomalous properties of metals at low temperatures, although a final decision will of course have to await an improvement in the general mathematical technique.

It is a great pleasure to thank Professor H. Fröhlich, F.R.S., for suggesting this investigation and for many helpful discussions, and Dr. D. K. C. MacDonald for his interest in this work.

PHYSICAL REVIEW VOLUME 95, NUMBER 4 AUGUST 15, 1954

Temperature Variation of the Mean Debye Temperature of Cu_3Au, 20°C to 450°C

S. L. Quimby
Columbia University, New York, New York
(Received April 19, 1954)

The temperature variation of the mean Debye temperature of crystalline Cu_3Au at equilibrium order is computed from the values of the elastic constants at equilibrium order obtained by Siegel. The Debye temperature decreases from the value 272°K at 20°C to the value 234°K at 450°C, with a discontinuous drop from 249°K to 239°K at the critical temperature for disordering, 387°C.

THE mean Debye temperature Θ_D of a cubic crystal is given by the expression

$$\Theta_D=(h/k)v_m\{3N/4\pi V\}^{\frac{1}{3}},$$

where N is the number of atoms in volume V of the crystal and v_m is defined by the formula

$$3/v_m^3=\sum_i(1/v_{mi}^3), \quad i=1, 2, 3,$$

in which the v_{mi} are the three velocities of propagation of plane elastic waves in the crystal, averaged over all directions in the crystal.

A facile method for computing v_m with given values of the crystal elastic constants is described in a recent issue of this journal.[1] The accuracy of the result obtained with this method is determined solely by that of the given data. The method is here applied to the measurements reported by Siegel, of the elastic constants of Cu_3Au in a state of equilibrium order appropriate to the temperature of measurement.[2] The result is given in Table I. The value of $(h/k)\{3N/4\pi V\}^{\frac{1}{3}}$ employed in the calculations in 1.2583×10^{-3} cgs units.

TABLE I. The temperature variation of the mean Debye temperature of crystalline Cu_3Au at equilibrium order.

T°K	θ_D°K	T°K	θ_D°K
293.3	272.4	653.3	250.6
373.3	268.8	658.3	249.0
473.3	263.5	663.3	238.9
573.3	258.9	673.3	238.1
623.3	254.3	723.3	234.0

[1] S. L. Quimby and P. M. Sutton, Phys. Rev. **91**, 1122 (1953).
[2] S. Siegel, Phys. Rev. **57**, 537 (1940).

The density of crystalline Cu_3Au at 20°C, measured in this laboratory on one of Siegel's specimens, is 12.15 g/cm³. Densities at other temperatures are computed with Siegel's values of the linear dilatation. These differ slightly from the highly precise measurements of Nix and MacNair,[3] but the latter, of course, appertain to a specimen of slightly different composition. The critical temperature T_c of Siegel's specimens is 660.8°K. Departures of the tabular values from a smooth representative curve are less than 0.5°K.

The Debye temperature decreases linearly with temperature from 20°C to about 280°C, and thereafter at an increasing rate to the critical temperature. A discontinuous drop of about 10°C occurs at T_c, followed by a linear decrease at a rate slightly greater than the preceding. A similar decrease in the characteristic temperatures of ordered and disordered specimens is deduced by Bowen from measurements of electrical resistivity, with the aid of Gruneisen's formula.[4] But the value of Θ_D obtained in this manner is 175°K.

It is of interest to compare the value of Θ_D at 20°C of nearly perfectly ordered Cu_3Au, 272.4°K, with that of Au, 157.6°K, and Cu, 330.7°K. The latter are computed with the elastic constant measurements of Rohl[5] and Goens,[6] respectively.

The author acknowledges the assistance of Mr. Leonard Weisberg, of this laboratory, who measured the density of Cu_3Au.

[3] F. C. Nix and D. MacNair, Phys. Rev. **60**, 320 (1941).
[4] D. Bowen, Phys. Rev. **91**, 220 (1953).
[5] H. Rohl, Ann. Physik **16**, 887 (1933).
[6] E. Goens, Ann Physik **38**, 456 (1940).

A Theory of Domain Creation and Coercive Force in Polycrystalline Ferromagnetics*†

JOHN B. GOODENOUGH‡
Lincoln Laboratory, Massachusetts Institute of Technology, Cambridge, Massachusetts
(Received December 17, 1953; revised manuscript received April 30, 1954)

Granular inclusions, grain boundaries, lamellar precipitates, and the crystalline surface have been examined as possible nucleation centers for domains of reverse magnetization in ferromagnetic materials. It is concluded that the surface density of magnetic poles at the grain boundaries ω^* is the most common source of nucleation energy in polycrystalline materials.

The concept of nucleation of domains of reverse magnetization has led to a calculation of three more terms which may contribute to the coercive force in polycrystalline materials, *viz.*, a grain-boundary, a lamellar-precipitate, and a domain-wall-surface-tension contribution.

The theoretical predictions are compared with several old experiments. New insight is gained on the problem of stress sensitivity of polycrystalline ferromagnetics and *B-H* loop shape.

I. INTRODUCTION

CURRENT magnetic-domain theory and experiment has shown that if a magnetic specimen, which is not finely divided, is in a strong, external, slowly alternating magnetic field, then the induced change in magnetic flux through the sample is primarily due to the motion of domain walls. In order to understand the characteristics of any *B-H* hysteresis loop, it is necessary to know the origins of the individual domain walls and the factors which hinder their motion through the sample when driven by an external magnetic field.

The principal cause of flux change may be assumed to be the motion of 180° domain walls if the specimen does not have a special geometry or orientation of its axes of easy magnetization which would energetically favor the creation of many domains at right angles to the applied field. It will be assumed that the specimen has a cubic lattice, is polycrystalline, and is in the form of a toroid or of a long rod parallel to the applied field.

If a specimen is saturated, no domain walls exist within it. If the flux in a saturated sample is to be reversed by the motion of 180° domain walls, domains of reverse magnetization must first be created. The new domains will be bounded by 180° walls, and as any domain grows in the presence of a favorably oriented external field, its boundary walls will move.

If an external field, which has saturated a magnetic specimen, is reduced and reversed, domains of reverse magnetization may be created in several regions of the specimen before irreversible wall motion, or irreversible domain growth, begins. H_{ni} will be defined as the critical field strength for domain creation in any ith region of the specimen. It will be defined as positive if it is oriented in the direction of the magnetization within the new domain.

If all $H_{ni}>0$, the difference in induction between saturation, B_s, and the remanence, B_r, is given by the rotation of the elementary atomic moments from the external-field direction to a crystallographically preferred direction of magnetization. If some $H_{ni}<0$, however, there is a further reduction of the remanence which is proportional to the volume of material which is included in the reverse domains. In order to obtain a material of high retentivity, therefore, one requirement is that all $H_{ni}>0$.

If the induction is reversed by the irreversible motion of 180° domain walls, the coercive force will usually represent some average critical field for irreversible wall motion. H_{wi} will be defined as the critical field strength for irreversible motion of the domain walls which enclose the ith domain of reverse magnetization. If all $H_{ni}>H_{wi}$, the *B-H* loop will be square because a domain of reverse magnetization, once created, will be in an external field of sufficient magnitude to drive its boundaries across the specimen. If the $H_{wi}\gg H_{ni}$ and if the H_{ni} are randomly spread over a wide range of H about some mean value, the *B-H* loop will have rounded shoulders, shallow-sloping sides, and a large coercivity.

The domain-wall contribution to the initial permeability of a sample is proportional to the area of 180° walls which are present within the specimen at zero net magnetization. If many domains exist, the total domain-wall area will be large. It is also inversely proportional to the force which holds these walls to a given location within the sample. H_{wi} gives a measure of this force. A high-initial-permeability material will contain a large area of domain wall which has low H_{wi}.

A knowledge of H_{ni} and H_{wi} is therefore of great practical importance as well as of theoretical interest. In Secs. II and III some of the factors which contribute to H_{ni} and H_{wi} are considered theoretically. In Sec. IV the theoretical predictions are compared with experiment.

II. MAGNETIC-DOMAIN CREATION

Domains of reverse magnetization are created at lattice imperfections. An examination of those imper-

* The research reported in this document was supported jointly by the Department of the Army, the Department of the Navy, and the Department of the Air Force.

† This paper contains the work that was reported in Phys. Rev. 91, 434 (1953).

‡ Staff Member, Lincoln Laboratory, Massachusetts Institute of Technology, Cambridge, Massachusetts.

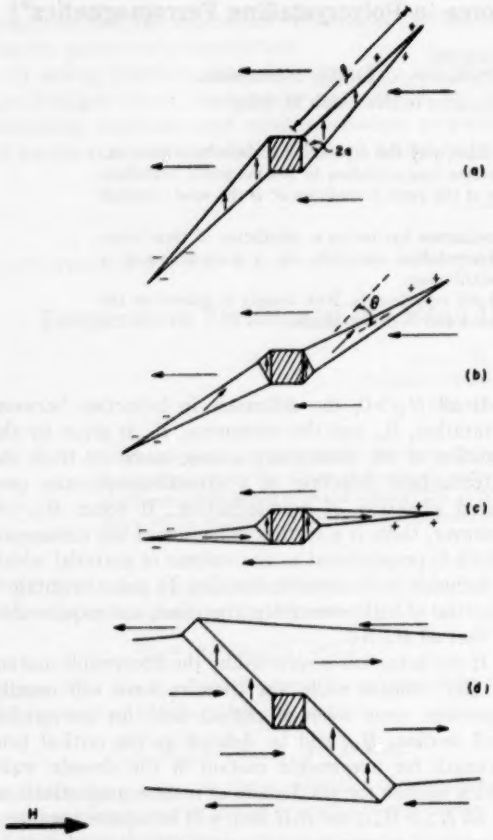

FIG. 1. The creation and growth of a domain of reverse magnetization by the rotation of a closure domain at an inclusion.

fections which might act as the nucleating centers for new domains suggests the study of granular inclusions, lamellar precipitates, grain boundaries, and the crystalline surface. The field strength at which the new domains are formed, H_n, and, where pertinent, the field strength at which the new walls are moved irreversibly away from the imperfection, H_w, will be considered for each of these cases.

A. The Granular Inclusion

(1) In many lattices there is a large density of inclusions present. These inclusions may be precipitates of another phase, impurity aggregates, or voids. Néel[1] predicted that in lattices with three axes of easy magnetization closure domains form about inclusions, as in Fig. 1(a), in order to reduce the energy associated with the magnetic poles at the inclusion surfaces. Williams[2] has observed these closure domains in colloidal-magnetite patterns on polished surfaces of metals.

Only those inclusions whose radius is larger than a critical size R_c will have closure domains about them. In Appendix I it is shown that $R_c \approx 10^{-5}$ cm in iron. In the ferrites which have a low saturation magnetization I_s, however, it is possible that $R_c \approx 10^{-6}$ cm. If an inclusion is too small to support a closure domain, it will not act as a nucleating center for a domain of reverse magnetization.

In order that an inclusion with closure domains act as a nucleating center for a domain of reverse magnetization, the closure domains must be rotated through 45° by the external field. The domain of reverse magnetization can then grow as shown in Fig. 1. In Appendix II it is shown that, for inclusions in materials with three axes of easy magnetization, $H_n > 10$ oersteds. Since this is larger than the coercivity of most soft magnetic materials, it is concluded that these inclusions are not imperfections at which 180° domain walls are created. It will be shown in Sec. III, however, that the presence of the inclusions does influence the coercive force.

(2) Williams and Goertz[3] have observed domains of reverse magnetization at large inclusions in a perminvar ring with only one axis of easy magnetization. These domains formed as shown in Fig. 2(a). In order to estimate the nucleation field strength, it is assumed that the energy of the surface poles after domain formation is much less than before. Then, since there is no magnetostrictive energy associated with the domains of reverse magnetization,

$$\frac{8\pi^2}{9} I_s^2 R^3 = \frac{\pi^2 R^2}{2\lambda}\sigma_w + \frac{16\pi^2\eta}{3\sqrt{2}}\lambda[\ln(2/\lambda)-1] I_s^2 R^3 - 2H_n I_s \cos\theta \frac{2\pi R^3}{3\sqrt{2}\lambda},$$

where R is the radius of the inclusion, θ is the angle between the applied field H and the magnetization, and $\lambda = R/\sqrt{2}l \ll 1$ is the ratio of the semiminor to semimajor axes of the domain of reverse magnetization which, for simplicity, is assumed a prolate ellipsoid. The critical field strength for domain creation is then

$$H_n = \left\{\frac{9}{16}\left(\frac{\sigma_w}{RI_s^2}\right) + 3\sqrt{2}\lambda^2\eta[\ln(2/\lambda)-1] - \lambda\right\}\frac{2\sqrt{2}\pi}{3\cos\theta} I_s \approx \left[1.7\left(\frac{\sigma_w}{RI_s^2}\right) - 0.18\right] I_s, \quad \text{for } \lambda \approx 1/30,\ \eta = 0.1. \quad (1)$$

In iron if $R > 10^{-5}$ cm, Eq. (1) gives $H_n < -10$ oersteds. It is concluded that if the radius of an inclusion in a material with one axis of easy magnetization is large ($R > 10^{-5}$ cm in metals or 10^{-6} cm in ferrites), $H_n \ll 0$. If the inclusion density is low, the fractional volume of

[1] L. Néel, Cahiers phys. **25**, 21 (1944).
[2] H. J. Williams, Phys. Rev. **71**, 646 (1947).
[3] H. J. Williams and M. Goertz, J. Appl. Phys. **23**, 316 (1952).

material which is enclosed by such domains of reverse magnetization is small.

A more significant field strength to be examined, perhaps, is the critical field H_w at which the reverse-domain walls move irreversibly away from the inclusion which generated them. The principal resistance to the growth of an inclusion-nucleated reverse domain comes from the energy associated with the inclusion-surface magnetic poles. If the inclusion is so small that the reverse domain grows away from the inclusion without the formation of a new domain within the reverse domain, then

$$2H_wI_s\cos\theta\Delta V=(8\pi^2/9)I_s^2R^3+\sigma_w\Delta A_w+\Delta E_d;$$

$$H_w\approx[0.9(\sigma_w/RI_s^2)+0.05]I_s \text{ for } \lambda\approx 1/30,\ \eta=0.1. \quad (2)$$

Even in the ferrites this is a high field strength. At inclusions of larger radius, the domain will be free to grow irreversibly if a second domain of reverse magnetization is created inside the first (see Fig. 2). The inner domain can then grow to balance the poles on the surface of the inclusion as the original domain walls move away. H_w is therefore calculated in Appendix III as the field strength at which a second domain of reverse magnetization is created inside the first. It is found that

$$H_w>I_s\{0.005+0.13R_c/R\}, \quad (3)$$

where R_c is the critical radius of an inclusion for reverse-domain formation in zero external field. Unless $R_c/R\ll 1$, Eq. (3) gives, for soft magnets, $H_w>H_c$. These domains do not, in general, contribute 180° walls which move irreversibly through a magnetic material to reverse its flux.

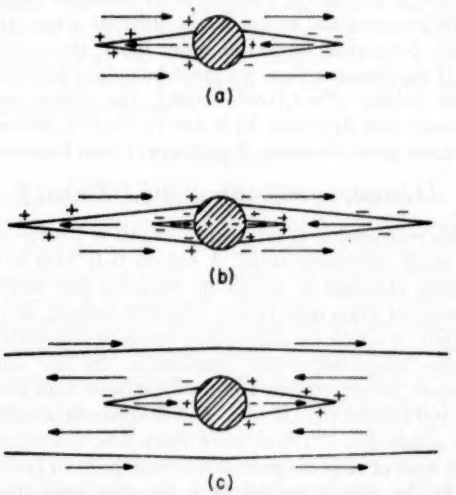

FIG. 2. Schematic representation of the growth of a domain of reverse magnetization away from an inclusion in a parallel, external field H. The crystal has but one axis of easy magnetization.

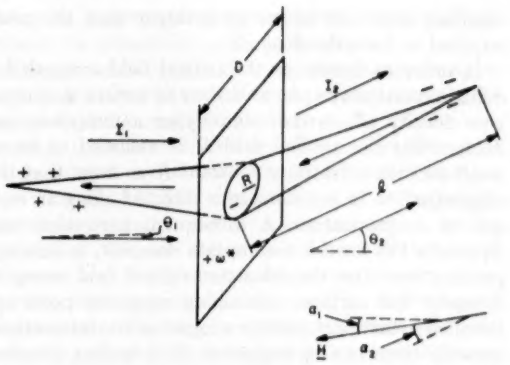

FIG. 3. Schematic nucleation of a domain of reverse magnetization at a grain boundary.

B. Lamellar Precipitates and Grain Boundaries

For ease of calculation the grain boundary will be considered planar. It is therefore considered together with the lamellar-precipitate imperfection. A crystal lattice is, in general, anisotropic with regard to ease of magnetization. If a crystal is not under tensile stress, this anisotropy is determined by the crystallographic configuration. The grain boundaries in a polycrystalline specimen separate regions of different crystallographic orientation or easy-magnetization direction. At low field strengths, the magnetization vectors of the neighboring grains are not rotated from their easy-magnetization directions into complete alignment. Consequently there is generally a discontinuity across the boundaries in the magnetization-vector component normal to the boundary. Therefore magnetic poles exist at the grain boundaries, and magnetic energy is associated with these poles. If θ_1 and θ_2 are the angles made by the spontaneous-magnetization vector I_s of the neighboring grains and the normal to their common boundary, the grain-boundary-surface pole density is $\omega^*=I_s(\cos\theta_1-\cos\theta_2)$.

Similarly there will be magnetic energy associated with the poles which exist at the planar surface of a lamellar precipitate. If I_p is the spontaneous magnetization of the precipitate and α_s, α_p are the angles the normal to the lamellar plane makes with I_s and I_p, the lamellar-surface pole density is $\omega_l^*=(I_s\cos\alpha_s-I_p\cos\alpha_p)$. The angle α_p will so adjust itself as to minimize the energy associated with ω_l^* and the anisotropy of the precipitate.

The magnetic energy associated with these surfaces of magnetic poles would be reduced if domains of reverse magnetization existed to produce a pole distribution of alternating sign. This is illustrated in Fig. 3. Work must be done, however, in the formation of the domains of reverse magnetization. The grain boundaries or lamellar precipitates will act as nucleating centers for domains of reverse magnetization only if the

resulting reduction in energy is larger than the work required to form the domains.

In order to determine the critical field strength for domain creation at a planar surface of surface magnetic-pole density ω^*, further simplifying assumptions are made. First the applied field H is assumed to be so small and the anisotropy constant K so large that the magnetization in any domain is directed along an easy axis of magnetization. A subsequent correction (see Appendix IV) for this assumption does not, in zero approximation, alter the calculated critical field strength. Secondly the surfaces containing magnetic poles are assumed so far apart that the magnetostatic interactions between them can be neglected. It is further assumed that when reverse-domain creation occurs, it occurs periodically over the planar surface with elementary area D^2. The domains of reverse magnetization are taken to be prolate ellipsoids of semimajor axis l and semiminor axis $r<D$ such that $\lambda=r/l\ll 1$. The angles θ_1 and θ_2 are assumed small so that the two halves of the domain of reverse magnetization can be considered to have a common major axis in the estimation of the demagnetization factor $N=4\pi\lambda^2[\ln(2/\lambda)-1]$, the volume $V=4\pi r^2 l/3$, and the surface area $A_w=\pi^2 rl$. The change in internal energy of the crystal due to reverse-domain creation is then given by

$$\Delta E=(\sigma_0-\sigma_n)A_s-n[\sigma_w A_w+2NI_s^2V - HI_s(\cos\alpha_1+\cos\alpha_2)V+E_p+E_{np}], \quad (4)$$

where n is the number of domains of reverse magnetization created on the area A_s of planar surface. The surface-energy densities σ_0, σ_n, σ_w refer, respectively, to the grain boundary before and after nucleation has taken place and to the 180° Bloch walls. The demagnetization energy is $2NI_s^2V$, and α_1, α_2 are the angles the external field H makes with the direction of easy magnetization in the two neighboring grains. The interaction energies of the Bloch-wall poles with the plane-surface poles and with the neighboring Bloch-wall poles are, respectively, E_p and E_{np}.

The nucleation field strength H_n is that for which the change in free energy, $\Delta F=\Delta E-T\Delta S$, between the prenucleated and post-nucleated state vanishes. If $D=br$ and $b\lambda\ll 1$, then (see Appendix IV)

$$\Delta F=\frac{A_s I_s^2 l}{b^2}\left\{(\gamma_0-\gamma_n)\lambda-\frac{a\gamma_w}{r}-\gamma_p\lambda^2+\gamma_H+\gamma_S\frac{V_t}{r^2 l}\right\}, \quad (5)$$

where a is the distance between atoms whose magnetic moments give rise to the magnetization of the specimen and V_t is the total volume of the material. The dimensionless parameters γ_n, γ_w, γ_H, and γ_S are independent of r whereas $\gamma_0\propto 1/r$. The dimensionless parameter γ_p is, for $\lambda\ll 1$, dependent upon r only through the $\ln(2/\lambda)$. The parameter γ_p varies slowly with r and is, therefore, assumed independent of r. Since $n=A_s/D^2=A_s/(br)^2$, the optimum value of n is obtained by setting $\partial(\Delta F)/\partial r=0$ for a given value of l. This gives a relationship between the parameters, *viz.*,

$$-\gamma_p\lambda^2=\tfrac{1}{2}\gamma_n\lambda-\tfrac{1}{2}a\gamma_w/r+\gamma_S V_t/(r^2 l),$$

which, when substituted into Eq. (5) under the condition $\Delta F=0$, yields the nucleation field strength

$$H_n\cong\frac{3b^2\{(3\pi^2\sigma_w/2b^2\lambda)-(\sigma_0-\sigma_n/2)-(2T\Delta S/A_s)\}}{4\pi I_s l(\cos\alpha_1+\cos\alpha_2)}. \quad (6)$$

If typical values of l_m, V, and λ are chosen, where l_m is an average distance between planar surfaces of magnetic poles, at room temperatures

$$\frac{2T|\Delta S|}{A_s}\Big/\frac{3\pi^2\sigma_w}{2b^2\lambda}\ll 1.$$

Although the entropy term will be of increasing importance as the Curie temperature is approached, at room temperatures it can be neglected compared to the other terms. Also $\sigma_n\ll\sigma_0$ and is neglected. The nucleation field strength reduces, therefore, to

$$H_n\approx\frac{3b^2\{(3\pi\sigma_w/2b^2\lambda)-\sigma_0/\pi\}}{4I_s l(\cos\alpha_1+\cos\alpha_2)}. \quad (6')$$

It has been pointed out that a condition for a high retentivity is $H_{ni}>0$. If $\lambda=1/30$, the requirement that $H_n>0$ gives the condition

$$\sigma_0/\pi<(3\pi/2b^2\lambda)\sigma_w\approx 20\sigma_w\approx 80[A(K+\lambda_i\sigma)]^{\frac{1}{2}}, \quad (7)$$

where K is the anisotropy constant and $A=2JS^2/a$ is the usual exchange parameter.[4] It can be shown[5] that, for a cylindrical wall in a b.c.c. lattice, $\sigma_w\approx 4[A(K+\lambda_i\sigma)]^{\frac{1}{2}}$, where λ_i is the isotropic magnetostrictive constant and σ is the internal stress at the wall. Numerical factors of order unity are neglected.

If the planar surface is a grain boundary with surface pole density $\omega^*=I_s(\cos\theta_1-\cos\theta_2)$, the surface energy density (see Appendix V) is $\sigma_0\approx(1/3)\pi\omega^{*2}L$, where L is a mean grain diameter. Equation (7) then becomes

$$LI_s^2(\cos\theta_1-\cos\theta_2)^2<60\sigma_w\approx 240[A(K+\lambda_i\sigma)]^{\frac{1}{2}}. \quad (7')$$

This relationship is satisfied in metals if $(\cos\theta_1-\cos\theta_2)$ is made extremely small. A square B-H loop is commonly obtained in metals by reducing this factor by means of grain orientation, magnetic anneal, or application of tensile or compressive stress to materials with large magnetostriction coefficients. In the square-looped, polycrystalline ferrites I_s^2 is more than a factor of 100 smaller than in iron. This is apparently sufficient to satisfy Eq. (7') even when there is no orientation of the axes of easy magnetization from grain to grain.

If the planar surface is a lamellar precipitate of

[4] C. Kittel, Revs. Modern Phys. **21**, 541 (1949).

[5] N. Menyuk and J. B. Goodenough, J. Appl. Phys. (to be published).

thickness d_l, then the demagnetization factor is 4π and

$$\sigma_0 = -\tfrac{1}{2}\int_0^{d_l} \mathbf{H}\cdot\mathbf{I}dz = 2\pi\omega_l^{*2}d_l.$$

Equation (7) then becomes

$$d_l\omega_l^{*2} < 10\sigma_w \approx 40[A(K+\lambda_i\sigma)]^{\frac{1}{2}}. \qquad (7'')$$

In metals this relationship is satisfied only if $d_l \approx 10^{-5}$ cm or less and in ferrites if $d_l \approx 10^{-4}$ cm or less. Materials in which extensive precipitation in lamellar sheets has occurred will have low remanence values.

C. The Crystal Surface

Every ferromagnetic lattice is bounded by its surface. If there were no internal defects to act as nucleating centers for a domain of reverse magnetization, the lattice would nevertheless not reverse its magnetization by a simultaneous rotation of all of its elementary magnetic moments unless it were so fine a particle that its diameter was the magnitude, or less, of a Bloch-wall thickness. Instead, a Bloch wall would enter from the surface of the crystal and move across the specimen. The crystal surface is another possible nucleating center for a domain of reverse magnetization. Both because the surface is irregular and because it is not, in general, parallel to a direction of easy magnetization in the adjacent grains, magnetic poles exist on the surface of the specimen even if it has a toroidal shape. These poles nucleate domains of reverse magnetization in a manner analogous to that of the grain boundary and lamellar precipitate. Since the surface pole density is large, however, H_w is generally large relative to H_c. The crystal surface is, therefore, an important source of mobile, 180° Bloch walls only if the H_n for the grain boundaries is larger than the H_w for the walls which are nucleated at the crystalline surface. In such cases the material usually exhibits a large Barkhausen discontinuity at $H=H_c$.

D. Summary

Of the lattice imperfections at which domains of reverse magnetization, and therefore 180° domain walls, might be created in a polycrystalline ferromagnetic, the grain boundary and, if present, the lamellar precipitate appear to be the most important. Small granular inclusions will not act as nucleating centers for domains of reverse magnetization. Larger inclusions may generate closure domains or, if there is but one axis of easy magnetization, domains of reverse magnetization, but these domains will be restricted to the region of the imperfection unless strong external magnetic fields are present. Similarly the domains associated with the magnetic poles on the surface of a specimen will be significant only if their H_w is smaller than the H_n and H_w for grain-boundary domains. The existence of closure or reverse domains, however, correspondingly reduces the retentivity of the specimen.

Since the nucleating field strength for reverse domains at grain boundaries is sensitive to the magnitude of the grain-boundary magnetic-pole strength $\omega^*=I_s(\cos\theta_1 - \cos\theta_2)$, the character of the B-H loop can be significantly altered by a variation of ω^* which changes $H_n<0$ to $H_n>0$. The magnitude of ω^* is frequently altered by magnetic anneal, grain orientation, or the application of tensile stress. In the next section it will be shown that the grain-boundary contribution to the coercive force is proportional to ω^{*2}/I_s. If this contribution is relatively large, a sufficient decrease in ω^* may make $H_n \geq H_s$ and therefore produce a square B-H loop.

III. THE COERCIVE FORCE

There are always several independent factors which contribute to the coercive force in any ferromagnetic material. If domain walls are present in a material, they are those factors which resist irreversible motion of these walls. In this paper four of these independent mechanisms will be discussed. They are the contributions to the total coercive force from granular inclusions, H_w(incl), grain boundaries, $H_w(\omega^*)$, lamellar precipitates, $H_w(\omega_l^*)$, and the surface tension in the expanding walls of a growing domain, $H_w(\sigma_w)$.

A. Granular Inclusions

Kersten[6] and Néel[7] have discussed the resistance to irreversible domain wall motion which is caused by inclusions that are free from associated closure domains. Williams and Shockley[8] have observed that when closure domains exist about inclusions, they retard 180° Bloch walls which move past them with a force proportional to their domain-wall surface tension. This mechanism is shown diagramatically in Fig. 4. If the inclusion resistance to irreversible motion of the 180° Bloch walls is due to the surface tension in the 90°

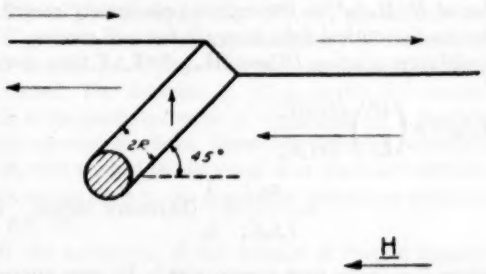

FIG. 4. The domain structure around an inclusion before the connection between the closure domain and the moving, 180° Bloch wall is broken.

[6] M. Kersten, *Grundlagen einer Theorie der Ferromagnetischen Hysterese und Koerzitivkraft* (S. Hirzel, Leipzig, 1943); Z. Physik **124**, 714 (1948).

[7] L. Néel, Cahiers phys. **25**, 21 (1944); Ann. univ. Grénoble **22**, 299 (1946); Physica **15**, 225 (1949); Bull. soc. franc. elec. [6] **9**, 308 (1949).

[8] H. J. Williams and W. Shockley, Phys. Rev. **75**, 178 (1949).

walls of the closure domains, then

$$2\mathbf{H}\cdot\mathbf{I}_s\Delta V=\sqrt{2}\pi R\sigma_w\Delta x,$$

where σ_w, the surface energy density of a 180° domain wall, is taken to be twice that for a 90° wall. If α is the angle between the applied field $\mathbf{H}$ and the spontaneous magnetization vector $\mathbf{I}_s$, if n is the average number of inclusions per cm² of 180° domain wall which have closure domains in contact with the moving wall, and if the average radius of the inclusions is $\langle R\rangle$, then

$$H_w(\text{incl})=(\pi/\sqrt{2}\cos\alpha)\cdot(\sigma_w/I_s)\langle R\rangle n.$$

If h is the mean distance between near-neighbor inclusions, $n\propto h^{-2}$. If P is the percentage of precipitate in the matrix, it is proportional to the ratio of the volumes of precipitate to total material, or to $\langle R\rangle^3/h^3$. Therefore $n\langle R\rangle=C_1P^{\frac{1}{2}}/\langle R\rangle$ and

$$H_w(\text{incl})=C_2(\sigma_w/I_s\langle R\rangle)P^{\frac{1}{2}}. \tag{8}$$

This mechanism cannot, of course, apply to those inclusions which are too small for closure domains to form about them.

B. Grain Boundaries and Lamellar Precipitates

1. If domains of reverse magnetization are created at planar surfaces of magnetic poles as indicated in Fig. 3, then the surface pole energy density which created the Bloch walls will resist their motion. If cylindrical domains of reverse magnetization are created at a planar surface with base radius r in elementary, periodic areas D^2, the energy associated with the surface magnetic poles is

$$\sigma=\sigma_0|\,(2\pi r^2/D^2)-1\,|+(\text{harmonic terms}).$$

At $H=H_w(\omega^*)$ the increase in energy associated with the surface magnetic poles must equal the decrease in energy resulting from the increased volume $\Delta V=\Delta[l_m\pi r^2(\cos\theta_1+\cos\theta_2)]$ which is aligned in the direction of H. $H_w(\omega^*)$ is the surface-pole-density contribution to the critical field strength for wall motion. The equilibrium relation $D^2\Delta\sigma=2\mathbf{H}_w(\omega^*)\cdot\mathbf{I}_s\Delta V$ then gives

$$H_w(\omega^*)=\left(\frac{D^2}{l_m}\right)\frac{d\sigma/d(r^2)}{2\pi I_sC_s}\approx\frac{\sigma_0}{I_sl_mC_s}+\frac{1}{l_m}(\text{harmonic terms}), \tag{9}$$

where $C_s=(\cos\alpha_1\cos\theta_1+\cos\alpha_2\cos\theta_2)$. In zero approximation the contribution from the harmonic terms may be neglected.

If the planar surface is a grain boundary, $\sigma_0=(1/3)\pi\omega^{*2}L$ and $l_m=L$. Therefore, for small angles α_1, α_2, θ_1, and θ_2,

$$H_w(\omega^*)\approx\tfrac{1}{6}\pi I_s\langle(\cos\theta_1-\cos\theta_2)^2\rangle. \tag{9'}$$

Since $(\theta_1-\theta_2)\leq\pi/4$ in a lattice with three axes of easy magnetization, the grain-boundary contribution to the coercive force should be $H_w(\omega^*)\leq10^{-3}I_s$.

2. If the planar surface is a lamellar precipitate, its surface energy density is $\sigma_0=2\pi\omega_l^{*2}d_l$, and the percentage of foreign material present as precipitate is $P\propto$ (precipitate volume)/(volume of crystal). If, therefore, $2\alpha L^2$ is the principal surface area of parallel-oriented precipitate in a volume L^3, then

$$P\propto d_l\alpha L^2/L^3=d_l/l_m,$$

since the average distance between lamellar areas is $l_m=L/\alpha$. The contribution to the coercive force from the magnetic poles on the lamellar precipitate is, by Eq. (9), then

$$H_w(\omega_l^*)=C_3(\langle\omega_l^{*2}\rangle/I_s)P. \tag{9''}$$

The hypothesis of creation of domains of reverse magnetization at lamellar precipitates predicts, therefore, a linear increase in the coercivity with percent precipitate present.

C. Surface Tension

If domains of reverse magnetization are created as prolate ellipsoids of large eccentricity, the surface tension in the Bloch walls will resist domain growth. The force per unit area to contract a cylindrical wall of radius r and surface energy density σ_w is σ_w/r. The surface-tension contribution to the coercivity is therefore,

$$H_w(\sigma_w)=\sigma_w/2I_s\langle r_0\cos\theta\rangle \tag{10}$$

where $\langle r_0\rangle$ is the mean equilibrium radius of the newly created domains. If typical values $\langle r_0\rangle=\langle D/b\rangle\approx L/10$ and $L\approx5\times10^{-3}$ cm are chosen for a grain-boundary-nucleated domain,

$$H_w(\sigma_w)\approx10^3[\text{cm}^{-1}](\sigma_w/I_s)\approx4\times10^3[\text{cm}^{-1}][A(K+\lambda_s\sigma)]^{\frac{1}{2}}/I_s. \tag{10'}$$

This term may be especially significant in square-looped ferrites in which (σ_w/I_s) is, by Eq. (7'), relatively large.

Further, it should be noted that $H_w(\text{incl})$ and $H_w(\sigma_w)$ are dependent directly upon the amount of internal strain present. This internal-strain dependence is in addition to that previously suggested[9,10] which is due to strain gradients in the material.

D. Temperature Dependence

Kersten[6] predicted, on the basis of his foreign-body theory of coercivity, a temperature dependence $H_c(T)\propto[K(T)]^{\frac{1}{2}}/I_s(T)$ for the coercivity of a strain-free material. The model of this paper predicts, for a strain-free material with no lamellar precipitates, a tempera-

[9] E. Kondorsky, Physik. Z. Sowjetunion 11, 597 (1937).

[10] M. Kersten, *Probleme der technischen Magnetisierungskurve*, edited by R. Becker (Julius Springer, Berlin, 1938); reprinted by J. W. Edwards, Ann Arbor.

ture dependence

$$H_c(T)=H_w(\sigma_w)+H_w(\text{incl})+H_w(\omega^*)$$
$$=a_1[AK(T)]^{\frac{1}{2}}/aI_s(T)+a_2I_s(T), \quad (11)$$

where a is the lattice parameter and a_1, a_2 are dimensionless, temperature-independent parameters given by

$$a_1=4a/\langle 2r_0\cos\theta\rangle+C_2P^{\frac{1}{2}}4a/\langle R\rangle\approx 10^{-4}+10^{-8}P^{\frac{1}{2}}\langle R\rangle,$$
$$a_2=\tfrac{1}{8}\pi\langle(\cos\theta_1-\cos\theta_2)^2\rangle$$
$$\approx 0.5\times 10^{-3} \text{ if no grain orientation.}$$

IV. CONCLUSIONS

A. Coercive Force and Starting Field

Of the four contributions to the coercive force which have been predicted in Sec. III, $H_w(\text{incl})$, $H_w(\omega_l^*)$, and $H_w(\omega^*)$ have been measured for typical cases. Measurements of H_c *vs* grain size are interpretable in terms of the fourth, $H_w(\sigma_w)$. The temperature-dependence of the coercive force in iron and nickel are available for comparison with Eq. (11).

1. In Fig. 5 are shown the measurements of Köster[11] on the change in coercivity with percent carbon in iron which is precipitated as lamellar and as granular cementite. The curved line is a graph of Eq. (8) with $C_2\sigma_w/I_s\langle R\rangle=6$, or $\langle R\rangle\approx 2\times 10^{-5}$ cm. This value of $\langle R\rangle$ is comparable with a critical radius for closure-domain formation. A $P^{\frac{1}{2}}$ law will prevail only so long as $\langle R\rangle$ does not vary appreciably with percent carbon content. For larger carbon content $\langle R\rangle$ should increase and H_c should fall below a strict $P^{\frac{1}{2}}$ plot. Such considerations indicate, therefore, that although the domains which are nucleated by inclusions will not grow away from them at low field strengths, they will offer a resistance to independent wall motion which is comparable to the coercive force of the material.

2. The straight line in Fig. 5 is $H_c=H_c'+12P$. The saturation magnetization of cementite is 1000 and of pure iron is 1700.[12] Therefore $\langle\omega_l^{*2}\rangle/I_s\approx 100$ oersteds. Since $C_2\approx 0.1$, Eq. (9′) not only predicts the straight-line relationship between H_c and P, but it also gives the correct order of magnitude for the slope of the line. This is to be contrasted with the granular-precipitate case which more nearly obeys a $P^{\frac{1}{2}}$ law.

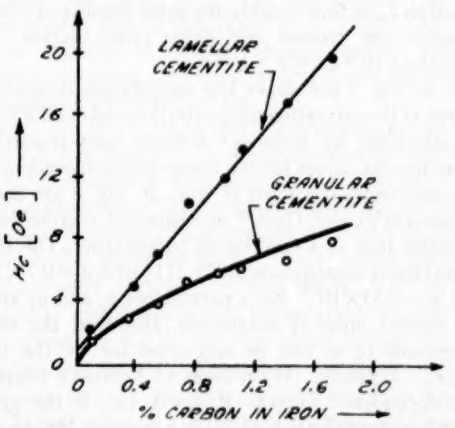

FIG. 5. The dependence of the coercive force, H_c, on the amount of carbon in iron in the form of granular and lamellar cementite (after Köster).

[11] W. Köster, Arch. Eisenhüttenw. 4, 289 (1930).

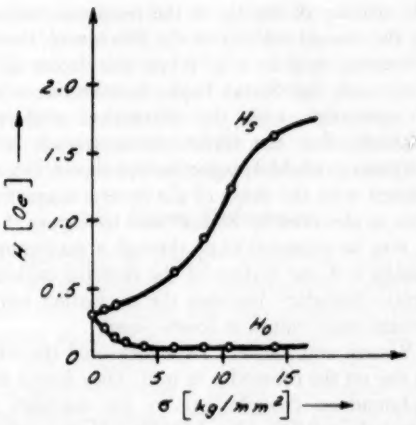

FIG. 6. The starting field, H_s, and the threshold field for domain-wall motion, H_0, *vs* applied tensile stress for a 78.5 Permalloy rod annealed 5 minutes at 800°C in vacuum (after Preisach).

3. Sixtus[13] and Preisach,[14] while studying the nucleation and propagation of domains of reverse magnetization in long wires of high-magnetostrictive-constant materials, observed the variation of H_s and H_0 with applied tensile stress σ on the wire. The starting field H_s represents the critical field strength necessary to initiate the single, large Barkhausen jump characteristic of this material. It corresponds to the nucleation field strength $H_n>H_c$. Since there is an alignment of the easy axis of magnetization by the applied tensile stress, $(\cos\theta_1-\cos\theta_2)$ decreases with increasing σ. Since $H_w(\omega^*)$ contributes to H_0, H_0 should decrease with σ according to Eq. (9′) whereas, by Eq. (7′), H_s should increase. In Fig. 6 are shown the measurements of Preisach on 78.5 Permalloy. These variations are as qualitatively predicted. The decrease in H_0 is nearly 0.3 oersted. This is the predicted order of magnitude for a partially grain oriented specimen. Sixtus has observed reductions in H_0 with applied tensile stress of as much as 6 oersteds. This corresponds to the maximum reductions predicted by Eq. (9′).

If the nucleation of the domain of reverse magnetization in these experiments is initiated at a grain boundary, as these figures strongly suggest, then the velocity of propagation of the reverse-magnetization zone as measured by a Sixtus-Tonks experiment will

[12] F. Stablein and K. Schroeter, Z. anorg. allgem. Chem. 174, 193 (1938).

[13] K. J. Sixtus, *Probleme der Technischen Magnetisierungskurve* (Verlag Julius Springer, Berlin, 1938).

[14] F. Preisach, Physik. Z. 33, 913 (1932).

be the velocity of the tip of the reverse-domain cone. If v is the normal velocity of the Bloch wall, the measured velocity will be v/λ. When this factor is taken into account, the Sixtus-Tonks measurements are in good agreement with the theoretical wall-velocity calculations and the direct measurements of wall velocity using colloidal magnetite techniques. It is also in agreement with the shape of the reverse-magnetization nucleus as observed by Sixtus[15] and by Ogawa.[16]

H_c may be expected to go through a maximum with increasing σ if the surface of the material rather than the grain boundary becomes the nucleation center at extremely small values of $(\cos\theta_1-\cos\theta_2)$.

4. Yensen and Ziegler[17] have measured the effect of grain size on the coercivity in iron. They found, for the grain-boundary contribution to the coercive force, $H_c[\text{oersteds}]=0.033\sqrt{N}\approx 3.7\times10^{-3}/L[\text{cm}]$, where N is the number of grains per square millimeter and L is the mean grain diameter. Mager[18] postulated that one ellipsoidal domain of reverse magnetization is created at each grain boundary. He used Döring's[19] formulation for reverse-domain growth. He equated the average starting field for reverse-domain elongation with the observed H_c to obtain

$$H_c[\text{oersteds}]\approx\langle H_s\rangle=\frac{3}{2}\cdot\frac{3\pi\sigma_w}{4I_sL}\approx\frac{3.1\times10^{-3}}{L[\text{cm}]}.$$

Mager is essentially calculating the contribution to the coercive force due to the surface tension of the 180° Bloch walls. Measurements[5] of flux-reversal times in magnetic cores as a function of the amplitude of a square-wave driving current indicate that the greatest distance a wall moves before the flux in a core is reversed is $\sim L$. However, the distance a wall moves before it collides with another is less than L. If more than one domain of reverse magnetization is created per average grain cross section, it is reasonable to take $\langle r_0\cos\theta\rangle \approx L/8$. Then Eq. (10) becomes

$$H_c[\text{oersteds}]=H_w(\sigma_w)\approx 4\sigma_w/I_sL=3.5\times10^{-3}/L[\text{cm}].$$

This is a good order-of-magnitude agreement. The only other terms in the calculated contributions to the coercive force which vary as $1/L$ are the higher order terms in $H_w(\omega^*)$ [see Eq. (9)], and these are expected to be at least an order of magnitude smaller. Although Yensen and Ziegler's curve represents a mean of points with a certain amount of scatter, it is interesting to note that their measurements suggest that r_0 is proportional to L, or that roughly the same number of reverse domains are created per grain cross section over variations $10^{-2}\text{ cm}\leq L\leq 1\text{ cm}$.

5. In Fig. 7 are shown the temperature dependence in iron of the saturation magnetization and of $(AK)^{\frac{1}{2}}/aI_s$ as calculated by Kersten.[6] Kersten used Bozorth's[20] experimental values for the temperature dependence of the anisotropy constants of iron. In Fig. 8 are shown Kühlewein's[21] and Gans'[22] experimental coercivities of annealed iron as a function of temperature. The theoretical curve corresponds to Eq. (11) with $a_1=0.7\times10^{-4}$ and $a_2=0.33\times10^{-3}$. Both parameters a_1 and a_2 are of the correct order of magnitude. However, the entire magnitude of a_1 can be accounted for by the term $H_w(\sigma_w)$. Equation (11) reduces to Kersten's temperature-dependence formula if $a_2=0$, i.e., if the grain-boundary contribution to H_c is neglected. He shows a

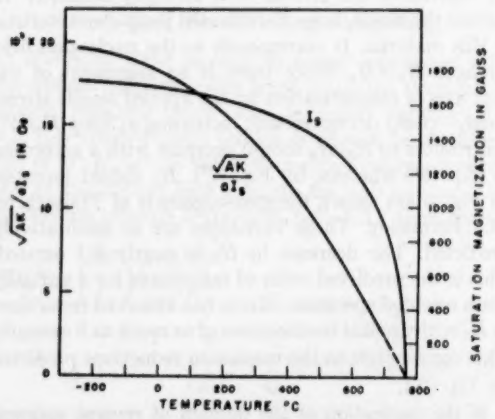

FIG. 7. Temperature dependence of the saturation magnetization I_s and the calculated temperature dependence of $(AK)^{\frac{1}{2}}/aI_s$ for iron where a is the lattice parameter, K the anisotropy constant, and $A=kT_c/a$ the exchange parameter (after Kersten).

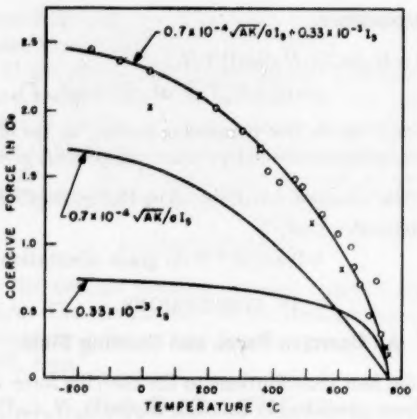

FIG. 8. Comparison of the experimental and theoretical temperature dependence of the coercivity in iron. Experimental points are ×, for "Swedish charcoal iron" after H. Kühlewein, and ○, for "soft iron annealed at 800° C" after R. Gans.

[15] K. J. Sixtus, Phys. Rev. **48**, 425 (1935).
[16] S. Ogawa, Science Repts. Research Insts. Tôhoku Univ. Ser. A, **1**, 53 (1949).
[17] T. D. Yensen and N. A. Ziegler, Trans. Am. Soc. Metals **23**, 556 (1935).
[18] A. Mager, Ann. Physik **11**, 15 (1952).
[19] W. Döring, Z. Physik **108**, 137 (1938).
[20] R. M. Bozorth, J. Appl. Phys. **8**, 575 (1937).
[21] H. Kühlewein, Wiss. Veröffentl. Siemens-Werke **11**, 126 (1932).
[22] R. Gans, Ann. Physik **48**, 514 (1915).

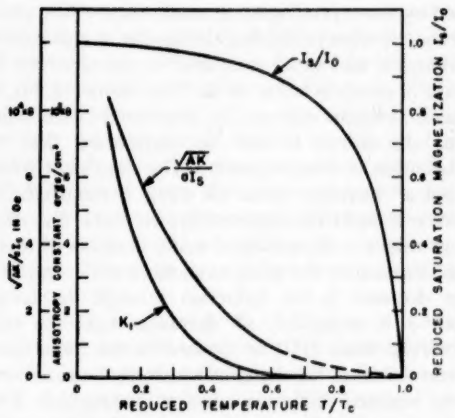

FIG. 9. Calculation of $(AK)^{\frac{1}{2}}/aI_s$ for nickel, where a is the lattice parameter and $A=kT_c/a$ is the exchange parameter. The curves for the anisotropy constant K and the reduced saturation magnetization I_s/I_0 are taken from R. Becker and W. Döring, *Ferromagnetismus* (Julius Springer, Berlin, 1939; reprinted by J. W. Edwards, Ann. Arbor, Figs. 78 and 25.

best-fit for the experimental data with $a_1=1.05\times10^{-4}$, but his curve does not follow the data nearly as well as that shown in Fig. 7. There can be no doubt that the grain-boundary contribution to the coercivity cannot be neglected in this case.

Gerlach[23] has measured the coercivity of nickel as a function of the temperature (Fig. 9). He sintered nickel-carbonyl powder in a quartz tube at 1000°C for 1 to 2 hours. The sample was a long, thin rod of density roughly 98 percent that of crystallized nickel. In Fig. 10 is shown a comparison of the experimental coercivities with the theoretical H_c *vs* T curve for $a_1=0.96\times10^{-4}$ or 1.14×10^{-4} and $a_2=0.33\times10^{-3}$. In the case of nickel the grain-boundary contribution to the coercivity is much smaller than the other terms because of the relatively low value of I_s. For this reason Gerlach assumed that the relation $H_c(T)\propto[K(T)]^{\frac{1}{2}}/I_s(T)$ was proven sufficient to explain the experimental results. It should be noted that again a_1 and a_2 are the orders of magnitude predicted by Eq. (11).

There can be no doubt that the predominant contribution to the coercivity in the nickel sample varies as $K^{\frac{1}{2}}/I_s$. This indicates that whatever contribution to the coercive force arises from inclusions which are too small to have closure domains associated with them is either small or also varies as $K^{\frac{1}{2}}/I_s$. Néel's[7] model predicts a temperature variation $[0.386+\log(2\pi I_s^2/K)^{\frac{1}{2}}]K/I_s$. Kersten's[6] model predicts a temperature dependence proportional to $K^{\frac{1}{2}}/I_s$, but this model is open to the criticism that an assumed periodic distribution of the inclusions leads to too high a coercive-force contribution. If the inclusions are randomly distributed through the lattice, the number of inclusion per unit area of wall which are intersected by a 180° Bloch wall should be roughly constant for various wall positions. Since the contributions $H_w(\sigma_w)$ and $H_w(\text{incl})$ of this paper are sufficient to account for the magnitude of the coercivity, there is no need to invoke an artificially periodic inclusion distribution. The contribution to the coercivity from inclusions which are too small to cause closure-domain formation may indeed be a minor one.

[23] W. Gerlach, Z. Physik **133**, 286 (1952).

B. Stress Hysteresis

Since the work of Ewing[24] before the turn of the century, stress hysteresis in ferromagnetic materials at constant field strengths has been observed, but no satisfactory explanation of this phenomenon has been offered. The hypothesis of nucleation at grain boundaries, however, provides a simple, qualitative understanding of the complex phenomenon. Besides rotation of the spontaneous magnetization vectors in an applied field, there are two principal mechanisms which are responsible for flux change in a magnetic material, *viz.*, domain creation and Bloch-wall movement. Each of these may be either reversible or irreversible. The hypothesis of nucleation at grain boundaries predicts, through Eqs. (7′) and (9′), that in an external field H the change of an applied stress which alters ω^* will have two important effects. First, if ω^* is decreased until $H_w(\omega^*)<H$, an existing domain will grow or

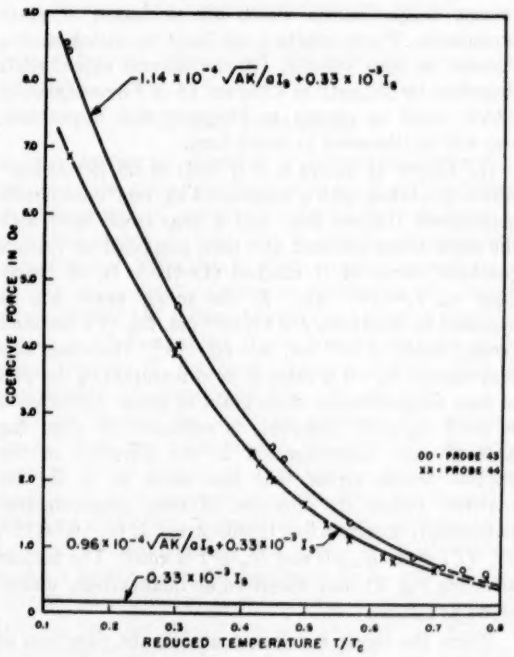

FIG. 10. Comparison of the experimental and theoretical temperature dependence of the coercivity in nickel. Experimental points after W. Gerlach.

[24] J. A. Ewing, *Magnetic Induction in Iron and Other Metals* ("The Electrician" Printing and Publishing Company, London, 1900), third edition.

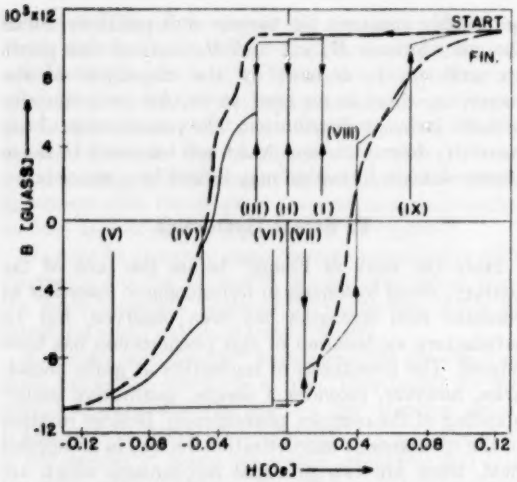

FIG. 11. Hysteresis loop of 68 Permalloy under tension of 4 kg/mm² except when stress removed and reapplied at certain field strengths (after Bozorth).

contract according to its orientation with respect to H. Second, the number of nucleated domains present at a given H will vary with the value of ω^*. If a decrease in ω^* makes $H_n > H$, the surface tensions in the Bloch walls will exceed the net force to maintain domains of reverse magnetization which are nucleated at grain boundaries. There results a net force to shrink such a domain to zero volume. Of the several experiments described by Bozorth in Chapter 13 of *Ferromagnetism* which could be chosen to illustrate this hypothesis, two will be discussed in detail here.

(1) Figure 11 shows a B-H loop of 68 Permalloy[25] which was taken with a stress $\sigma = 4$ kg/mm² continually maintained (broken line) and a loop (solid line) with the same stress released and then reapplied at various constant values of H marked (I)–(IX). In 68 Permalloy $\sigma_w/I_s^2 \approx 10^{-7}$ cm. If the mean grain size is assumed to have been $L = 5 \times 10^{-3}$ cm, Eq. (7′) becomes $(\cos\theta_1 - \cos\theta_2)^2 < 10^{-6}$ or $(\theta_1 - \theta_2) < 15°$. Therefore one may expect $H_n < 0$ if there is no orientation of the axis of easy magnetization from grain to grain. Application of $\sigma = 4$ kg/mm², however, is sufficient to align the axes of easy magnetization in the direction of the applied tensile stress. The low value of K in this material makes its direction of easy magnetization particularly sensitive to a tensile stress. If $(\theta_1 - \theta_2) \ll 15°$, Eq. (7′) gives $H_n > 0$ and $H_w(\omega^*)$ is small. The factors affecting Fig. 11 may therefore be qualitatively understood as follows.

When the stress is released at (I), the direction of easy magnetization is no longer aligned by the stress. The spontaneous magnetization vectors of the individual grains rotate to a set of axes which are determined by the crystallographic orientation of the grains. The contribution to the flux change due to this rotation is reversible and small compared to the observed flux change of nearly a factor of six. The change of flux due to such rotations will not be mentioned in the subsequent discussion. It will be understood that this contribution is always present. The significant feature is that ω^* increases when the stress is removed. This increase is sufficient, apparently, to make $H_n < H(\mathrm{I})$. There results a nucleation of many domains of reverse magnetization at the grain boundaries with a resultant large decrease in the induction through the sample. When σ is reapplied, ω^* decreases again to make $H_n > H(\mathrm{I})$. Since $H(\mathrm{I})$ is opposed to the formation of reverse domains, the domains which were created when σ was released disappear when σ is reapplied. There are a few domains which are irreversibly created, however, so that the induction through the sample is not completely regained by the reapplication of σ.

At (II) and (III) the process is the same as at (I) except that more domains of reverse magnetization are irreversibly created. The field $H(\mathrm{III})$ opposes the Bloch-wall-surface-tension forces which are acting to destroy the new domains when the stress is reapplied.

At (IV) there is, initially, a large percentage of the specimen's volume within domains antiparallel as well as parallel to $H(\mathrm{IV})$. When σ is released, the increase in ω^* is sufficient to create new domains. These are oriented parallel or antiparallel to $H(\mathrm{IV})$ depending upon the orientation of the larger domain in which they are formed. Since a larger volume of material is oriented parallel than antiparallel to $H(\mathrm{IV})$, more new domains are oriented antiparallel to $H(\mathrm{IV})$ and the induction decreases slightly. When σ is reapplied, however, the domains which were created antiparallel to $H(\mathrm{IV})$ disappear whereas those created parallel to $H(\mathrm{IV})$ remain and even grow. The marked increase in $|B|$ results.

The mechanisms at (V) and (IX) are the same as at (IV) except that the proportion of created domains which are oriented parallel to H is greatly reduced. The mechanisms at (VI) and (VII) are the same as those at (I), (II), and (III).

When σ is released and ω^* increases at (VIII), the majority of new domains are oriented parallel to $H(\mathrm{VIII})$. A sharp decrease in $|B|$ results. Since $H(\mathrm{VIII}) \approx H_c(\sigma = 4$ kg/mm²$)$, the favorably oriented domains grow while the unfavorably oriented ones disappear when σ is reapplied. Consequently the induction continues to decrease until it changes sign and increases in the opposite direction.

Completely analogous reasoning can account for the B-H loop[25] taken with no stress applied except at certain values of H at which it is applied and subsequently released.

(2) Figure 12[25] shows the effects on the initial magnetization curve for 68 Permalloy of applying the tensile stress σ and the magnetization field H in different

[25] R. M. Bozorth, *Ferromagnetism* (D. Van Nostrand Company, Inc., New York, 1951), Chap. 13.

orders. Curve (a) is the normal initial-magnetization curve. Since ω^* is large, $H_w(\omega^*)$ is large. For $H<0.1$ oersted, therefore, there is little Bloch-wall motion, and the permeability remains low. When $\sigma=4$ kg/mm^2 is applied, the term $H_w(\omega^*)$ is reduced, and the total coercivity is lowered to $H_c=0.042$ oersted. At $H=0.1$ oersted on curve (b), therefore, most of the domain-wall motion has taken place. Since the spontaneous-magnetization vectors are largely aligned by the stress and the wall motion is nearly completed, the induction has already increased to nearly its saturation value at $H=0.1$ oersted.

If a field H is applied prior to σ, a force will exist to shrink those domains which are aligned antiparallel to H which is the sum of that due to the field and that due to the surface tensions in the Bloch walls. Even at field strengths $H<H_c(\sigma=4$ kg/mm$^2)$, this sum will be sufficient to collapse many domains which are antiparallel to H if $H_w(\omega^*)$ is reduced by the application of σ. The initial permeability for curve (d) is, therefore, extremely large. Domain-wall surface tensions in excess of tension equilibrium do not exist if the material is demagnetized under a tensile load and then magnetized without removing the stress, as in curve (b).

If the stress is applied and then released after the field H has been applied, the initial magnetization curve traces out the curve (c). When the stress is released, the magnetization drops from curve (d) to curve (c) because of the nucleation of domains of reverse magnetization within the large domains oriented parallel to H. The initial permeability is high because the domains which are nucleated when σ is released occupy considerably less than half the volume whereas the original domains oriented antiparallel to H occupied, from curve (a), nearly half the total volume of the specimen.

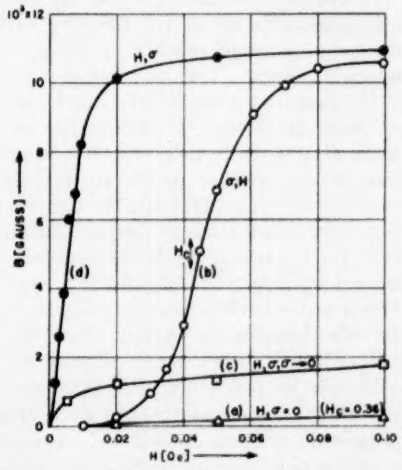

FIG. 12. Various kinds of initial magnetization curves of 68 Permalloy: (a) Normal curve with no tension. (b) $\sigma=4$ kg/mm^2 applied first, and then the external field H. (c) H applied, σ applied and removed several times. (d) H applied first, and then σ (after Bozorth).

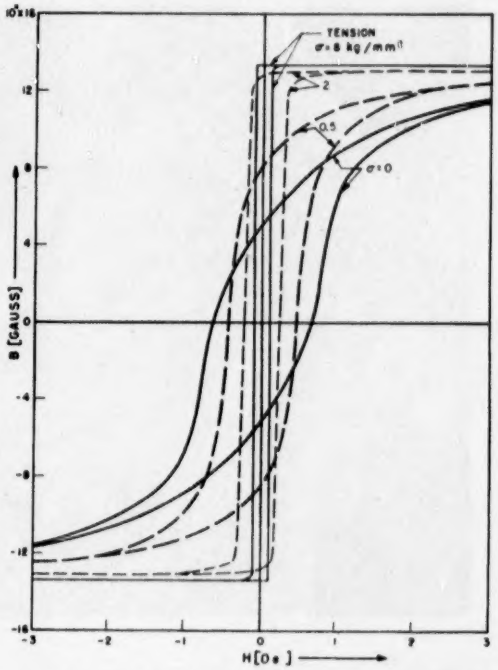

FIG. 13. Hysteresis loops of 68 Permalloy under various tensions σ. Maximum field strength 5 oersteds (after Bozorth).

C. *B-H* Loop Shape

If nucleation of domains of reverse magnetization occurs at the grain boundary with an $H_n<0$, the *B-H* loop shape will be profoundly affected by a decrease in ω^* which makes $H_n>0$. This is usually accomplished in metals by a reduction in $(\cos\theta_1-\cos\theta_2)$ through grain orientation, magnetic anneal, or application of a tensile stress. Figure 13[25] shows the effect of applying a tensile stress to 68 Permalloy. H_n is seen to increase with stress whereas H_c decreases some 0.6 oersted. This is in complete agreement with Eqs. (7′) and (9′).

In the ferrites the available methods for reducing $(\cos\theta_1-\cos\theta_2)$ are more limited. Williams[26] has recently squared the *B-H* loop of a nickel-zinc ferrite by the application of a compressive stress. Since the magnetostrictive coefficient is negative in this material, this behavior is analogous to that found in 68 Permalloy under a tensile stress. The increase in H_c with $\sigma>0.65$ kg/mm^2 is attributed $H_c=H_n>H_w$. It should also be realized that the application of σ increases the amount of internal strain present in the material. The internal-strain contribution to σ_w should increase the coercive force with an increase of σ. The surprising fact that in some metal specimens H_c decreases with σ is attributed

[26] Williams, Sherwood, Goertz, and Schnettler, Communications and Electronics No. 9, 531 (1953).

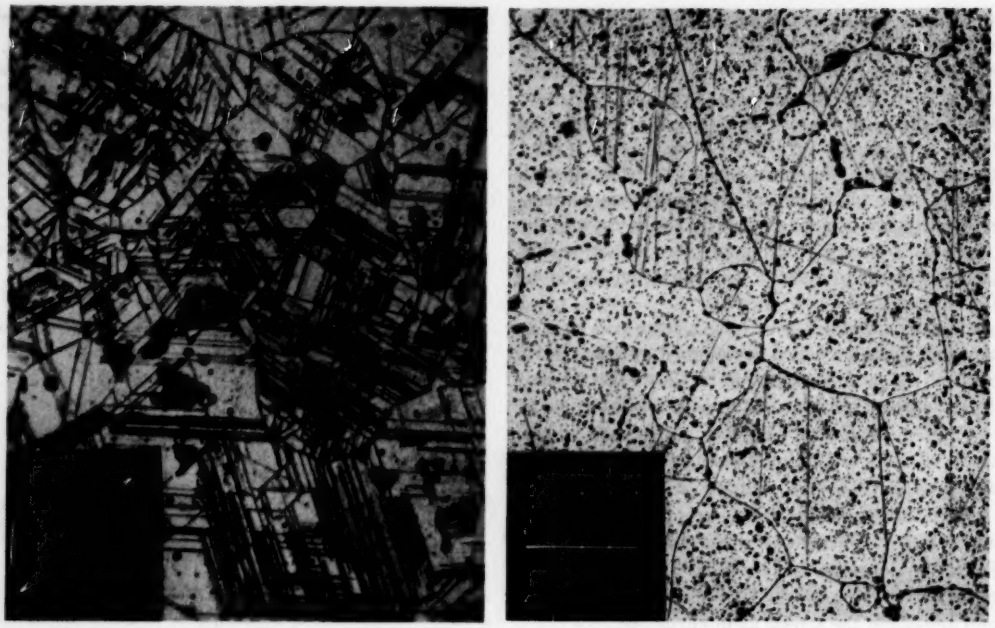

(a) (b)

FIG. 14. Microstructure and maximum-squareness-ratio B-H loop for a General Ceramics Company MF-1371-B ferrite body (a) before anneal (white light×498, $B_m=150$ gauss, $H_m=2.25$ oersteds) and (b) after anneal (white light×100, $B_m=1128$ gauss, $H_m=0.46$ oersted).

to a predominance of $H_w(\omega^*)$ in the coercivity of these materials. In the ferrites $H_w(\omega^*)\lesssim 0.1$ oersted is usually a small fraction of H_c.

An alternative approach to attain a material with a square B-H loop is to reduce I_s and to increase $\sigma_w \propto [A(K+\lambda_i\sigma)]^{\frac{1}{2}}$. Square-looped materials have correspondingly been obtained in magnesium and in magnesium-manganese ferrites. The magnesium ferrite has a low I_s. The addition of manganese is believed to introduce internal strains e which increase the effective anisotropy constant $(K+\lambda_i Ee)$, where E is Young's modulus.

D. Micrograph Studies

If nucleation of domains of reverse magnetization occurs at grain boundaries, the corresponding Bitter patterns on polished surfaces parallel to a direction of easy magnetization should show triangles with their base at a grain boundary. Such patterns have been observed by Williams in silicon iron.[4] Fowler and Fryer[27] have observed the predicted nucleation and growth of domains of reverse magnetization from the surface (rather than a grain boundary) of a single crystal of silicon iron. Martin[28] has observed the creation and growth of dagger-shaped closure domains at lattice imperfections and the crystal surface in a single crystal of 3 percent silicon iron which was rotated from an easy axis of magnetization in an external field.

In Fig. 14 is shown[29] a photograph of the microstructure in a General Ceramics and Steatite Corporation MF-1371B ferrite body before and after an anneal. The preannealed sample is heavily twinned. Precipitation has occurred at the twinning surfaces. There results a lamellar precipitate along certain crystallographic planes. (The dark spots, or blobs, correspond to voids in the lattice.) This material had a nonsquare loop. It showed the characteristics of a sample with $H_n<0$. It is proposed that nucleation takes place at the lamellar precipitate because the condition of Eq. (7″) is not fulfilled. The coercive force is relatively large through the precipitate contribution of Eq. (9″). During anneal the Widmanstätten structure disappeared. The B-H loop became extremely square. This is understandable on the basis that though $H_n<0$ for the lamellar precipitate, for the grain boundary $H_n>0$. It is to be expected that $\omega_l^*>\omega^*$.

It should also be noted that the Widmanstätten lines indicated no grain orientation in the material. As there has been no magnetic anneal and there are no apparent microscopic stresses which could align the directions of easy magnetization away from preferred

[27] C. A. Fowler and E. M. Fryer, Revs. Modern Phys. **25**, 33 (1953).
[28] D. H. Martin, Proc. Phys. Soc. (London) **B66**, 712 (1953).
[29] S. Andrew Kulin, Lincoln Laboratory, Massachusetts Institute of Technology (unpublished research).

crystallographic directions, the squareness of the *B-H* loop of the annealed sample is not attributed to a low value of $(\cos\theta_1-\cos\theta_2)$. It is rather attributed to a relatively low ratio I_s^2/σ_w.

ACKNOWLEDGMENT

The author would like to express his thanks to R. M. Bozorth of the Bell Telephone Laboratories and to his publishers, the D. Van Nostrand Company, Inc., for permission to reprint Figs. 11, 12, and 13 from Chapter 13 of *Ferromagnetism* (copyrighted 1951). He would also like to thank N. Menyuk for his lively interest in the work and for checking the arithmetic calculations.

APPENDIX I

The energy associated with a small, spherical inclusion imbedded in a material of spontaneous magnetization I_s is given by its demagnetization energy

$$-\tfrac{1}{2}\int \mathbf{H}\cdot\mathbf{I}_s dV=(8\pi^2/9)I_s^2R^3. \tag{I.1}$$

The critical radius, at absolute zero of temperature, is that for which this energy just equals the energy of the configuration with closure domains present. Since the closure domain essentially eliminates the magnetic poles at the inclusion surface,

$$(8\pi^2/9)I_s^2R_c^3=\tfrac{1}{2}\sigma_wA_w+E_d+E_{el}, \tag{I.2}$$

where σ_w, the energy per unit area of a 180° wall, is taken as twice that for a 90° wall. A_w is the area of 90° wall which bounds the closure domains. E_d is the demagnetization energy of the closure domain, and E_{el} is the elastic energy associated with the closure domain as a result of the magnetostriction. For simplicity, the closure domain may be considered a prolate ellipsoid whose ratio of semiminor to semimajor axes is $\lambda=R_c/\sqrt{2}l\ll 1$. The demagnetization energy and Bloch-wall area are then

$$E_d=(4\pi^2\eta/3\sqrt{2})\lambda[\ln(2/\lambda)-1]I_s^2R_c^3, \quad A_w=\pi^2R_c^2/2\lambda,$$

where η is a numerical factor which takes account of the permeability of the matrix.[30]

The conventional first-order magnetostriction equation is given by Becker and Döring[31] as

$$e=\delta l/l=\tfrac{3}{2}\lambda_{100}(\alpha_1^2\beta_1^2+\alpha_2^2\beta_2^2+\alpha_3^2\beta_3^2-\tfrac{1}{3})+3\lambda_{111}(\alpha_1\alpha_2\beta_1\beta_2+\alpha_1\alpha_3\beta_1\beta_3+\alpha_2\alpha_3\beta_2\beta_3),$$

where $\boldsymbol{\alpha}=(\alpha_1,\alpha_2,\alpha_3)$ is a unit vector in the direction of the magnetization, $\boldsymbol{\beta}=(\beta_1,\beta_2,\beta_3)$ is a unit vector in the direction in which the strain e is measured; λ_{100} and λ_{111} are the saturation values of the longitudinal magnetostriction in the directions [100] and [111], respectively. The elastic energy density in a cubic crystal is given by[32]

$$f_{el}=\tfrac{1}{2}c_{11}(e_{xx}^2+e_{yy}^2+e_{zz})+\tfrac{1}{2}c_{44}(e_{xy}^2+e_{yz}^2+e_{zx}^2)+c_{12}(e_{yy}e_{zz}+e_{xx}e_{zz}+e_{xx}e_{yy})$$

where the c_{ij} are the elastic moduli and the e_{ij} are strains as defined by Love.[32] To estimate the elastic energy E_{el}, it is assumed that the lattice outside the closure domain is not distorted. If the [100] direction is an axis of easy magnetization, $f_{el}=\frac{1}{2}c_{11}\lambda_{100}^2$ and

$$E_{el}=(\pi/3\sqrt{2}\lambda)R_c^3c_{11}\lambda_{100}^2.$$

If the [111] direction is an axis of easy magnetization, $e=\frac{1}{4}\lambda_{100}+\frac{3}{2}\lambda_{111}$ and $f_{el}=\frac{1}{2}(c_{11}+c_{12})e^2$ so that

$$E_{el}=(\pi/3\sqrt{2}\lambda)R_c^3(c_{11}+c_{12})(\tfrac{1}{4}\lambda_{100}+\tfrac{3}{2}\lambda_{111})^2.$$

Equation (I.2) therefore gives

$$R_c=f(\lambda)\cdot(\sigma_w/I_s^2);$$
$$f(\lambda)=9/\{32\lambda-C-24\sqrt{2}\lambda^2\eta[\ln(2/\lambda)-1]\},$$

where

$$C=(6\sqrt{2}/\pi I_s^2)C';$$

$$C'=\begin{cases}c_{11}\lambda_{100}^2 & \text{if magnetization along [100]}\\ (c_{11}+c_{12})(\frac{1}{4}\lambda_{100}+\frac{3}{2}\lambda_{111})^2 & \text{if magnetization along [111].}\end{cases}$$

The colloidal-magnetite patterns of Williams[2] show a $\lambda\approx 1/30$. In iron[4] $C\approx 5\times 10^{-3}$ and $(\sigma_w/I_s^2)\approx 10^{-6}$ cm so that $R_c\approx 10^{-5}$ cm.

APPENDIX II

The field strength, at absolute zero, which is required to rotate a closure domain through an angle θ_1 is given by

$$H\left\{\int_0^{\theta_1}\int_{-l(\theta)}^{l(\theta)}\rho_l^*(x,\theta)x\sin\left(\frac{\pi}{4}-\theta\right)dxd\theta+I_sV\sin 2\theta_1\right\}+\Delta E_{el}=\tfrac{1}{4}VK\sin^2 4\theta_1+\Delta E_d+\Delta(\sigma_wA_w),$$

where K is the anisotropy constant. $V=(4\pi/3\lambda)a^3\cos^3\theta_1$ is the volume of the domain after rotation through θ_1. The ratio of the semiminor to semimajor axes of the original closure domain, $\lambda=a/l$, is assumed to remain constant. The torque exerted by the interaction of the external field with the Bloch-wall magnetic poles is taken as the torque the field would exert on the closure-domain axis if it contained an equivalent linear pole density ρ_l^*. If the equation of the closure-domain ellipsoid is taken as

$$F(x,y,z)=\frac{x^2}{l^2}+\frac{y^2+z^2}{r^2}-1=0,$$

[30] Williams, Bozorth, and Shockley, Phys. Rev. **75**, 155 (1949).

[31] R. Becker and W. Döring, *Ferromagnetismus* (Julius Springer, Berlin, 1939; reprinted J. W. Edwards, Ann Arbor).

[32] A. E. H. Love, *A Treatise on the Mathematical Theory of Elasticity* (Cambridge University Press, Cambridge, 1927), fourth edition, p. 38.

the surface pole density is

$$\omega_d^* = \eta(1+\sin 2\theta) I_s F_a / |\nabla F|.$$

The equivalent linear pole density is

$$\rho_l^*(x,\beta) = \omega_d^* 2\pi y |\nabla F| / F_y = 2\pi(1+\sin 2\theta)\eta I_s \lambda^2 x.$$

The change in demagnetization energy is

$$\Delta E_d = (8\pi^2\eta/3) I_s^2 \lambda [\ln(2/\lambda) - 1] \times a^3 \{(1+\sin 2\theta_1)^2 \cos^2\theta_1 - 1\},$$

and the change in wall energy is

$$\Delta(\sigma_w A_w) = \frac{\pi^2 a^2}{\lambda} \sigma_w \left\{ \frac{\sigma_w(\theta_1)}{\sigma_w} \cos^2\theta_1 - 1 \right\}.$$

Although the volume of material completely within the closure domain decreases as it is rotated to form a domain of reverse magnetization, the Bloch walls are increasing in thickness. It is assumed that the change in volume is absorbed in this greater wall thickness. As the wall thickness increases, the surface wall-energy density increases from σ_w to $\sigma_w(\theta_1)$. The change in total elastic energy due to rotation through θ_1 is given approximately by

$$\Delta E_{el} = (2\pi a^3/3\lambda) C' (1 - \cos 2\theta_1).$$

This elastic energy is relieved when the closure domain is rotated to become a domain of reverse magnetization.

If the magnetic anisotropy of the crystal offers the greatest resistance to rotation of the closure domain in the external field, then the minimum field strength in which a domain of reverse magnetization can be created is that which rotates the domain $\pi/8$ radians. If $\theta_1 = \pi/8$, $\eta = 0.1$, and $\lambda = 1/30$, then

$$H_n \approx -\frac{1}{3}\frac{K}{I_s} + 0.004 I_s + \frac{5}{2}\frac{\sigma_w}{R I_s} - \frac{1}{4}\frac{C'}{I_s},$$

where R is the mean radius of the inclusion.

APPENDIX III

In order to calculate H_w for a domain of reverse magnetization at a spherical inclusion, it is assumed that the inner domain of Fig. 2(b) forms with a semiminor axis $r_1 = R_c/\sqrt{2}$. The critical radius R_c is the smallest radius a spherical inclusion can have and nucleate a domain of reverse magnetization in zero external field. Both domains are assumed to be prolate ellipsoids of revolution. The ratio of semiminor to semimajor axes λ is taken to be the same for both domains and to remain constant as the domains grow. The critical radius, at absolute zero of temperature, is that for which the demagnetization energy of Eq. (I.1) just equals the energy of the configuration with a domain of reverse magnetization present. Since the energy of the new polar configuration about the inclusion will be to the old as a quadruple term to a dipole term, it can, to a first approximation, be neglected and

$$(8\pi^2/9) I_s^2 R_c^3 = \sigma_w A_w + E_d. \qquad \text{(III.1)}$$

Since $\lambda \ll 1$ and $r_1 = R_c/\sqrt{2}$, the demagnetization energy is

$$E_d = \frac{16\pi^2\eta}{3\sqrt{2}} \left[\ln\left(\frac{2}{\lambda}\right) - 1 \right] \lambda I_s^2 R_c^3,$$

and the area of 180° Bloch wall is

$$A_w = \pi^2 R_c^2 / 2\lambda.$$

Equation (III.1) therefore gives

$$r_1 = R_c/\sqrt{2} = F(\eta,\lambda)\sigma_w / I_s^2;$$

$$F(\eta,\lambda) = \frac{9/16\lambda}{\sqrt{2} - \eta 6\lambda[\ln(2/\lambda) - 1]}.$$

If ΔV is the increase in the volume of material magnetized parallel to the external field and if the interaction energies between the Bloch-wall poles of the two domains and between them and the inclusion-surface poles are E_{np} and E_p, then H_w, at absolute zero of temperature, can be derived from the energy balance

$$2 I_s H_w \Delta V = \Delta(\sigma_w A_w) + \Delta E_p + \Delta E_d + E_{np}. \qquad \text{(III.2)}$$

The change in energy associated with the interaction of the inclusion-surface poles is negligible compared to the other terms.

Let $r_0 = R/\sqrt{2}$ be the minor axis of the first nucleated domain when there is no field present and r_2 be its value at $H = H_w$, the field strength at which the second domain of minor axis r_1 is nucleated within it. Then $r_2^3 = r_1^3 + R^3/2$ and, provided $r_1/R \ll 1$,

$$\Delta V \approx \frac{\pi}{\lambda} r_1^3 R \left\{ \sqrt{2} - \frac{4}{3}\left(\frac{r_1}{R}\right) \right\},$$

$$\Delta(\sigma_w A_w) = \frac{2\pi^2 I_s^2}{\lambda F(\eta\lambda)} r_1^3, \qquad \text{(III.3)}$$

$$\Delta E_d = 8\pi^2\eta \left[\ln\left(\frac{2}{\lambda}\right) - 1 \right] I_s^2 \lambda r_1^2 R \left\{ \sqrt{2} + \frac{4}{3}\left(\frac{r_1}{R}\right) \right\}.$$

Since $\lambda \ll 1$, it is possible to estimate E_p by assuming the Bloch-wall poles are equivalent to an axial linear pole density $\rho_l^* = 4\pi I_s \eta \lambda^2 x$. Since the inclusion-surface poles are equivalent to a plane with concentric circles circumscribing regions of uniform surface pole density $\pm I_s$,

$$\frac{1}{2}\Delta E_p = \frac{1}{2}\int_0^{l_1} \int_S \frac{\omega^*(2) dS \rho_l^* dx}{(x^2+r^2)^{\frac{1}{2}}} + \frac{1}{2}\int_0^{l_2} \int_S \frac{\omega^*(2) dS \rho_l^* dx}{(x^2+r^2)^{\frac{1}{2}}} - \frac{1}{2}\int_0^{l} \int_S \frac{\omega^*(1) dS \rho_l^* dx}{(x^2+r^2)^{\frac{1}{2}}},$$

where

$$\omega^*(2)=\begin{cases} I_s \text{ for} \begin{cases} 0\le r\le r_1 \\ r_2\le r\le R \end{cases} \\ -I_s \text{ for } r_1\le r\le r_2, \end{cases}$$

$$\omega^*(1)=\begin{cases} -I_s \text{ for } 0\le r\le r_0 \\ I_s \text{ for } r_0\le r\le R. \end{cases}$$

Integration yields

$$\Delta E_p=f_p(\lambda, r_1/R)I_s^2R^3. \qquad \text{(III.4)}$$

If the inner-domain-Bloch-wall poles are approximated by the axial linear pole density ρ_l^*, then

$$\frac{1}{2}E_{np}=\frac{1}{2}\int_{S_2}\int_0^{l_1}\frac{\rho_{l1}^*dx_1\omega_2^*dS_2}{[(x_1-x_2)^2+\lambda^2(l_2^2-x_2^2)]^{\frac{1}{2}}},$$

where $\omega_2^*dS_2=4\pi\eta I_s\lambda^2x_2dx_2$. Since $\lambda\ll1$, this gives

$$E_{np}=f_{np}(\lambda, r_1/R)I_s^2r_1^2R. \qquad \text{(III.5)}$$

If Eqs. (III.3), (III.4), and (III.5) are substituted into (III.2), there results

$$H_w=I_s\left\{Q_1(\eta,\lambda)+\frac{R_c}{R}Q_2(\eta,\lambda)+\cdots\right\}.$$

If the values $\lambda=1/30$, $\eta=0.1$ are taken, Eq. (3) results.

APPENDIX IV

To estimate the various terms in ΔF [see Eq. (5)], several simplifying assumptions are made. Obviously σ_0 is independent of r, and σ_n can be calculated as outlined by Kittel.[4] Thus $\sigma_n=f(b)\omega^{*2}D$, where $f(b)$ is a term of the order of unity which depends upon $b=D/r$.

Since $\lambda\ll1$ and $r<D$, the Bloch-wall poles are assumed equivalent to an axial pole density $\rho_l^*=4\pi I_s\lambda^2x$. To estimate E_p, it is further assumed that this axial pole density is perpendicular to the grain boundary and that the first zone of positive and negative grain-boundary-surface poles at its foot gives the major contribution to E_p. Then if r' is the radius vector from the foot of the major axis in the grain-boundary plane and $b\lambda\ll1$,

$$E_p\approx\pi\int_{r'}\int_{-l}^{l}\frac{\omega^*r'dr'\rho_l^*dx}{(x^2+r'^2)^{\frac{1}{2}}}\approx8\pi^2\left(\frac{b^2}{2}-1\right)|\omega^*|I_s\lambda r^3,$$

where

$$\omega^*=\begin{cases} -|\omega^*| & \text{if } 0\le r'\le r \\ +|\omega^*| & \text{if } r\le r'\le D. \end{cases}$$

Since each domain of reverse magnetization has four near neighbors a distance D away, if θ_1 and θ_2 are small and $b\lambda\ll1$,

$$E_{np}\approx2\int_{-l}^{l}\rho_{l1}^*dx_1\int_{-l}^{l}\frac{\rho_{l2}^*dx_2}{[D^2+(x_2-x_1)^2]^{\frac{1}{2}}}=\Phi(\ln(2/\lambda))I_s^2\lambda r^3.$$

The entropy is estimated from the assumption that the total volume of the material is composed of elementary volumes V. The total number of such elementary volumes is $N_t=V_t/V$. These may be aligned either parallel or antiparallel to their prenucleation direction. The number which align themselves antiparallel at nucleation is $N_d=V_d/V$, where V_d is the volume of material which has reversed its magnetization at nucleation. The entropy change is therefore

$$\Delta S\approx-k\ln\left(\frac{N_t!}{N_d!(N_t-N_d)!}\right)\approx-N_tk\left\{p\ln\left(\frac{1}{p}\right)+(1-p)\ln\left(\frac{1}{1-p}\right)\right\},$$

where k is the Boltzmann constant and $p=V_d/V_t\approx4\pi l/3b^2l_m$. Since $N_t=3V_t/4\pi r^2l$, the dimensionless parameters of Eq. (8) are

$$\gamma_0=b^2\sigma_0/rI_s^2,$$

$$\gamma_n=f(b)b^3\omega^{*2}/I_s^2,$$

$$\gamma_p=\Psi(\ln(2/\lambda))+8\pi^2\left(\frac{b^2}{2}-1\right)(\cos\theta_1-\cos\theta_2),$$

$$\gamma_w=\frac{\pi^2}{a}\frac{\sigma_w}{I_s^2},$$

$$\gamma_H=\frac{4\pi}{3}\frac{H}{I_s}(\cos\alpha_1+\cos\alpha_2),$$

$$\gamma_S=\frac{3b^2kT}{4\pi A_sdI_s^2}\left\{p\ln\left(\frac{1}{p}\right)+(1-p)\ln\left(\frac{1}{1-p}\right)\right\}.$$

It should be noted that the poles on the Bloch-wall surfaces will not be as large as was assumed in the calculation of the terms E_d, E_p, and E_{np}. This results from a deflection of the magnetic moments in the vicinity of the wall away from the easy magnetization direction. They are deflected against the anisotropy forces by the small transverse-field component associated with the Bloch-wall poles. A so-called μ^* correction[30] should, therefore, be made to these terms. Such a correction would, however, only alter the parameter γ_p. Since γ_p is eliminated through the condition of optimum periodicity area D^2, the μ^* correction will not affect the value of H_n.

APPENDIX V

The surface energy density σ_0 for a grain boundary of area $\pi(L'/2)^2$ can be approximated by calculating

$$\sigma_0=-\tfrac{1}{2}\int_0^L\mathbf{H}\cdot\mathbf{I}_sdz$$

along an axis normal to the boundary through its center. The magnetic field along this axis due to the surface poles of density ω^* is

$$H_z=-\int\frac{\omega^* dS}{z^2[1+(r'/2)^2]^{\frac{1}{2}}}=-2\pi\omega^*\left\{1-\frac{z}{(z^2+L'^2/4)^{\frac{1}{2}}}\right\},$$

where r' is the distance from the foot of the axis to the element of area dS. The surface energy density then becomes

$$\sigma_0=\pi\omega^{*2}LG;\quad G=\{1+(L'/2L)-[1+(L'/2L)^2]^{\frac{1}{2}}\}.$$

If $L'=L$, $G=\frac{1}{2}$. If only those grain boundaries which are nearly perpendicular to the applied field are considered, θ_1 and θ_2 are each less than 45°, and the μ^* correction to σ_0 will be small. It is therefore neglected in this approximation.

PHYSICAL REVIEW VOLUME 95, NUMBER 4 AUGUST 15, 1954

Magnetic and Thermal Properties of Chromic Methylamine Alum Below 1°K*

R. P. HUDSON AND C. K. MCLANE†
National Bureau of Standards, Washington, D. C.

(Received April 9, 1954)

The earlier measurements of de Klerk and Hudson on a spherical mass of small crystals of chromic methylamine alum have been repeated, and extended, using a one-inch sphere ground from a large single crystal. The variation of susceptibility with entropy follows closely—down to 0.1°K—the predictions of the theory of Hebb and Purcell when a suitable choice is made for the value of δ, the splitting between the two spin-doublets in the ground level of the Cr^{+++} ion. It is found that $\delta/k=0.269\pm0.003$ degree.

Measurements have been made of the ballistic susceptibility χ, remanent magnetic moment Σ, and the in-phase and out-of-phase components of the ac susceptibility, χ' and χ'', respectively (these latter being measured at both 150 cps and 210 cps). The variation of χ' with entropy S is found to agree closely with that reported for the powder specimen, except in the region of the susceptibility maximum where the behavior appears to depend upon the rate of precooling the specimen.

At approximately the same entropy as that corresponding to maximum χ', χ'' shows an extremely sharp maximum. The ballistic susceptibility depends upon the measuring field in the region of the maximum; remanence appears here and goes through a maximum as the entropy is reduced. The remanence maximum is found at a lower entropy the larger is the measuring field. Associated with this hysteresis are very marked "time-effects" in the adjustment of the magnetization to a change in measuring field, as encountered in tracing out hysteresis loops.

Measurements of the susceptibility in superimposed steady magnetic fields of 0–500 oersted show unusual behavior below the Curie point and suggest the existence of anisotropy. For application of the field along a cubic axis, a magnetization of about one-half the saturation value appears to have special significance; this value is attained in fields as small as 150 oersted, but increasing the field up to about 500 oersted produces little further change in the magnetization.

I. INTRODUCTION

THE magnetic and thermal properties of chromic methylamine alum, $Cr(CH_3NH_3)\cdot(SO_4)_2\cdot 12H_2O$, below 1°K were first described in an article by de Klerk and Hudson[1] (hereinafter referred to as A) dealing with adiabatic demagnetization experiments upon a powder specimen. The reasons for the interest in the properties of this particular salt are given in A. The present work concerns similar experiments made upon single-crystal specimens, wherein the magnetic properties might reasonably be supposed to be somewhat simple and more readily yielding to theoretical treatment. Independent measurements on this same salt have also been reported recently by Gardner and Kurti,[2] and by Steenland.[3]

II. APPARATUS

The salt specimen comprised a one-inch diameter sphere ground from a large single crystal.[4] This was mounted on a soft glass pedestal within a soft glass vacuum case as shown in Fig. 1. The crystal A rests on three raised points and is securely tied to the platform B by means of a nylon thread passing through holes in a polystyrene ring C and underneath B. The support D is a thin-walled glass tube with a rough ground joint at each end. Four flats were ground off the male part of each joint in order to diminish the area of thermal contact without impairing the rigidity or axial alignment of the assembly.

The vacuum case E is closed at the lower end by a plug F which constitutes another ground joint, and this is sealed by means of a glycerine-n-propanol mixture.[5] It is essential, of course, that this joint be tight to liquid helium II. The case E may be evacuated through

* A brief summary of this work was presented at the Third International Conference on Low Temperature Physics and Chemistry at the Rice Institute, Houston, Texas, December 17–22, 1953 (unpublished).

† On a one-year leave of absence from the University of Wisconsin. Present address: Linde Air Products Company, Tonawanda, New York.

[1] D. De Klerk and R. P. Hudson, Phys. Rev. **91**, 278 (1953), hereinafter referred to as A.

[2] W. E. Gardner and N. Kurti (private communication).

[3] M. J. Steenland, in Rice Institute, Third International Conference on Low Temperature Physics and Chemistry; Abstracts of Papers, Houston, Rice Institute, 1953.

[4] We are greatly indebted to Mr. Walter Kuper for the preparation of the crystals used in this work.

[5] R. P. Hudson and C. K. McLane, Rev. Sci. Instr. **25**, 190 (1954).

the 6-mm o.d. tube G, which is spiralled just above E to provide a radiation trap. [Using this apparatus, it was possible to reduce the heat leak to the crystal to 20–50 ergs per minute at 0.1°K. The leak increased considerably at higher temperatures.]

The whole apparatus was silvered on the outside and coated with several layers of well-thinned varnish (General Electric GE7031). A coil of No. 43 B. & S. "Formex" was wound astatically in three sections of 400, 800, and 400 turns, respectively, on the outside of E so that the center 800-turn section surrounded the crystal A. This winding formed the secondary of a mutual inductance of which A is the core and the primary was wound on to the outside of the liquid-helium Dewar. The coefficient of mutual inductance, which is proportional to the "experimental susceptibility" of the salt (the ratio of intensity of magnetization to measuring field), was measured by means of a Hartshorn-type mutual inductance bridge,[6] modelled on that used in the Kamerlingh Onnes Laboratory. Absolute values of the susceptibility were determined by calibrating against absolute temperature in the liquid helium range —always below the lambda point, since in the HeI region the points would scatter somewhat from the expected straight line owing to temperature inhomogeneities in the bath.

III. PROCEDURE

The salt was cooled by adiabatic demagnetization from fields up to 23 000 oersteds starting with temperatures of 1.1° to 1.2°K. The entropy was calculated from the starting conditions for a given demagnetization using a Brillouin function with $J=\frac{3}{2}$. A correction was applied for the influence of the crystalline electric field upon the pattern of the energy level separation in a magnetic field.[7]

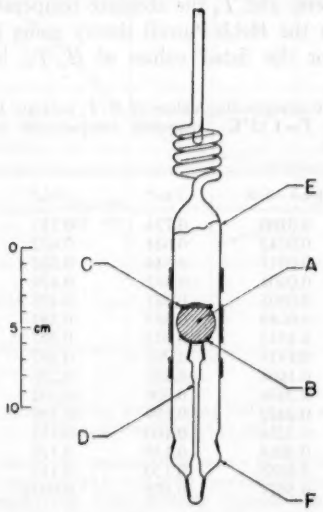

FIG. 1. Apparatus: specimen holder and vacuum case.

[6] L. Hartshorn, J. Sci. Instr. 2, 145 (1925).

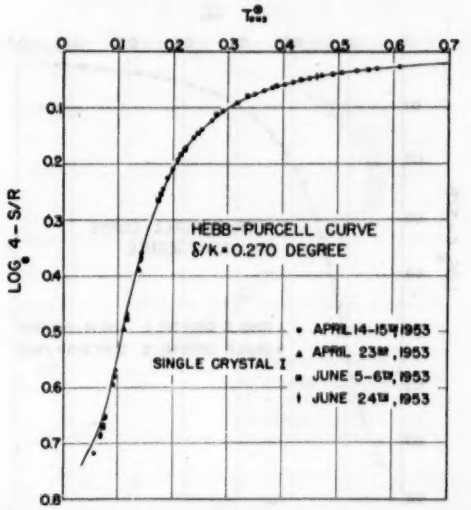

FIG. 2. "Magnetic temperature" T_{Ons}^* as a function of entropy. Measurements on Single Crystal I, April–June 1953.

The cryostat was swung out of the electromagnet and susceptibility measurements made at intervals of a few seconds, commencing within 30 seconds of the instant of demagnetization. Curves of bridge reading *versus* time were plotted and extrapolated to time zero. At the lowest entropies, where field-dependent effects are encountered, the influence of the earth's field was neutralized at the position of the crystal by a surrounding system of three mutually-perpendicular sets of Helmholtz coils. Either ac or ballistic measurements could be made as desired.

IV. RESULTS

(i) Susceptibility above 0.1°K

The "magnetic temperature" T^* is defined[8] by the Curie-law relation $T^*=CH_e/M$, where C is the Curie constant per cm^3, M is the magnetic moment per cm^3, and H_e, the external field. Above 1°K, T^* is equal to the absolute temperature T.

Assuming that the equivalence of T^* and T might persist to lower temperatures if one substituted for H_e in the foregoing expression the local field H_{loc}, i.e., the field actually acting on the ions, one may so define other "magnetic temperatures" (no longer simply experimental quantities) according as one uses the Lorentz, Onsager, or Van Vleck methods for calculating H_{loc}. Following the Leiden convention[9] we shall use the symbol T^* with a suffix to denote a magnetic temperature derived in terms of H_{loc}—thus T_{Ons}^*, T_{Lor}^*, etc.

[7] R. P. Hudson, Phys. Rev. 88, 570 (1952); R. P. Hudson and C. K. McLane, J. Research Natl. Bur. Standards 52, 33 (1954).
[8] N. Kurti and F. Simon, Phil. Mag. 26, 840 (1938).
[9] D. De Klerk, thesis, Leiden (unpublished), p. 15.

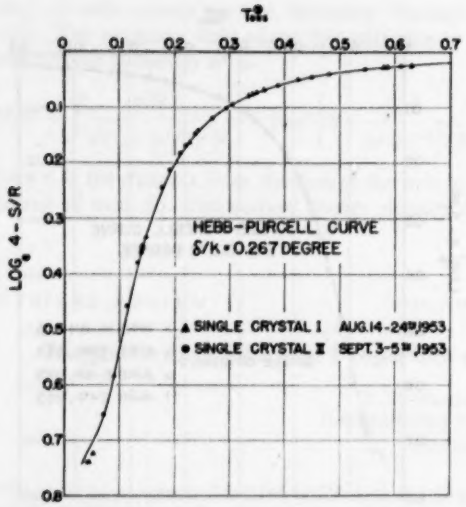

FIG. 3. "Magnetic temperature" T_{Ons}^* as a function of entropy. Measurements on Single Crystal I, August 1953, and on Single Crystal II, September 1953.

Hence $T_{Ons}^* = C[H_{loc}]_{Ons}/M$, etc.

The method of calculation is given fully in A. The density of this alum is 1.645 g cm^{-3},[10] and so 1.69 is a reasonable estimate for the density at liquid helium temperatures.

The best agreement between theory and experiment was obtained when the Onsager method of calculating H_{loc} was used. A graph of entropy *versus* T_{Ons}^* is shown in Fig. 2. The curve is calculated from the Hebb-Purcell theory[11] using a value for the level splitting δ/k of 0.270 degree; this was chosen to fit the experimental points at the highest temperatures. It may be seen that the points lie very close to this curve down to about 0.08°. In actual fact, small systematic differences are detectable between the results of different runs—for example, in the region of 0.3° the points for June 5–6 fall a little above the curve.

After this series of experiments the protective coat of varnish on the crystal (for minimizing possible damage by dehydration), which was badly cracked and peeling, was removed and then the crystal was recoated. During this process a few small grains of material were lost from points where the surface of the sphere had deteriorated (there was, however, no evidence of dehydration). The material removed was of the order of a few milligrams; the mass of the sphere was about 13 grams. (A more satisfactory coating, used in later work, was a dilute solution of Apiezon grease in benzene.)

Further experiments were then made with this crystal and the susceptibility now showed slightly larger values than those of the earlier measurements. Following these, a new series of measurements was carried out on a second specimen and the results are shown in Fig. 3. In order to fit a theoretical curve to the points it was necessary to choose $\delta/k = 0.267$ degree. It may be seen, however, that the points obtained for Crystal I only begin to deviate markedly from the curve at 0.08° whereas those for Crystal II show a small displacement towards lower temperature in the range 0.1° to 0.25°.

The difference in the two values of δ/k, although small, is none the less definite and is most probably a rate-of-precooling effect (see the following). Single Crystal I was grown from a solution of the alum prepared at NBS, while Crystal II was grown from material supplied by Johnson-Matthey (and used in powder form in A). The experimental results may be fairly summarized by $\delta/k = 0.269 \pm 0.003$ degree.

[The value of δ/k obtained for a powder specimen, as reported in A, was 0.275 degree, which is in fairly satisfactory agreement with the present results. The interpretation of results for a loosely-packed powder, however, presents considerable difficulty. The situation has been examined by de Klerk[9] who derives four different formulas, resulting from combinations of the Lorentz and Onsager viewpoints. The Onsager (magnetostatic) approach may be used throughout—dealing first with the macroscopic and then the microscopic situations—as was done in A. It can be argued, however, that a Lorentz-Onsager combination is *no less* valid in dealing with the complicated situation for a powder. Using the latter approach, T_{Ons}^* values derived from the results reported in A would give best agreement with theory for $\delta/k = 0.272$ degree.]

In Table I a list of corresponding values is given of T^* (for a sphere) and T, the absolute temperature calculated from the Hebb-Purcell theory using $\delta/k = 0.269$ degree. For the listed values of H_i/T_i, initial field

TABLE I. Corresponding values of H/T, entropy (actually calculated for $T = 1.15$°K), magnetic temperature and absolute temperature.

H/T	$\log 4 - S/R$	T_{Lor}^*	T_{Ons}^*	T
1000	0.0180	0.724	0.722	0.719
1250	0.0242	0.624	0.622	0.618
1500	0.0317	0.544	0.542	0.538
1750	0.0404	0.482	0.479	0.474
2000	0.0505	0.431	0.427	0.422
2500	0.0739	0.355	0.351	0.344
3000	0.1013	0.302	0.297	0.289
3500	0.1325	0.262	0.257	0.248
4000	0.1668	0.232	0.226	0.216
4500	0.2034	0.208	0.202	0.191
5000	0.2422	0.189	0.183	0.170
6000	0.3234	0.160	0.152	0.138
7000	0.4064	0.138	0.129	0.114
8000	0.4885	0.120	0.111	0.0938
9000	0.5677	0.105	0.0936	0.0763

Values of T are calculated from the Hebb-Purcell entropy-temperature relation with $\delta/k = 0.269$ degree. From these are derived values of T_{Ons}^* (using the Hebb-Purcell susceptibility formula) and T_{Lor}^* follows simply from the latter.

[10] We are indebted to C. T. Collett for this determination. The value of the Curie constant C used in A was based upon an incorrect estimate of the density. In consequence, the value of $4\pi C/3$ (for a powder) quoted therein, *viz.*, 0.0191, should be amended to 0.0180 but this has no significant effect on the results.

[11] M. H. Hebb and E. M. Purcell, J. Chem. Phys. 5, 338 (1937).

divided by initial (magnetization) temperature, corresponding values of the entropy have been calculated with the tacit assumption that T_i is not very different from 1.15°K. (The entropy correction to be applied to the "Brillouin value" is a function of T_i.) The Hebb-Purcell entropy-temperature relation then leads to the values of T in Column V, for each of which one may calculate a "magnetic temperature" by using the Hebb-Purcell susceptibility-temperature formula. This has been identified with $T_{\text{Ons}}{}^*$—as supported by the experimental observations—and T^* (which is identical with $T_{\text{Lor}}{}^*$ in the case of a sphere) is readily derived from the $T_{\text{Ons}}{}^*$ as described in A.

(ii) Susceptibility in the Region of the Maximum

The variation of susceptibility with entropy throughout the entire range of the experiment is shown in Fig. 4. In the region of the maximum it was found that the values of χ' could vary considerably from run to run, dependent upon the rate at which the specimen was precooled to liquid nitrogen temperature. The more rapid the precooling the smaller were the values of χ' and the extent to which reproducibility could be obtained by careful, slow precooling (several hours) is illustrated in Fig. 5.[12] The latter is an enlargement of the region around $\chi'_{\max}$ in Fig. 4.

In Fig. 5 the June measurements are sufficiently numerous to show up a fine detail of the curve at the maximum, where it is not smoothly rounded but shows what might be construed as two maxima separated slightly in entropy. These occur at entropies of 0.54_1R and 0.52_6R, respectively.

The ballistic susceptibility χ was also investigated and remanence was detected by using small measuring

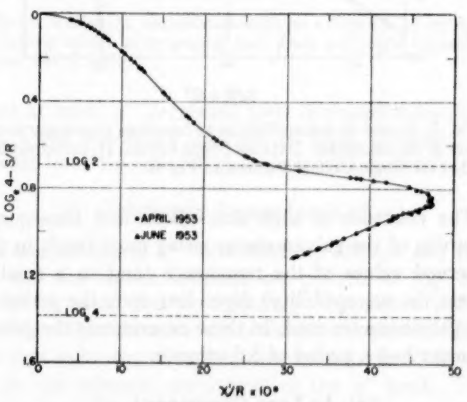

FIG. 4. Ac susceptibility, measured at 210 cps, as a function of entropy, for Single Crystal I.

[12] In this paper, the experimental points in the diagrams are plotted with open symbols and solid symbols for poor and good reliability, respectively. The reliability depends upon the degree of certainty with which one may extrapolate measurements back in time to the instant of demagnetization, and upon the stability of the magnetic field and bath temperature prior to demagnetization.

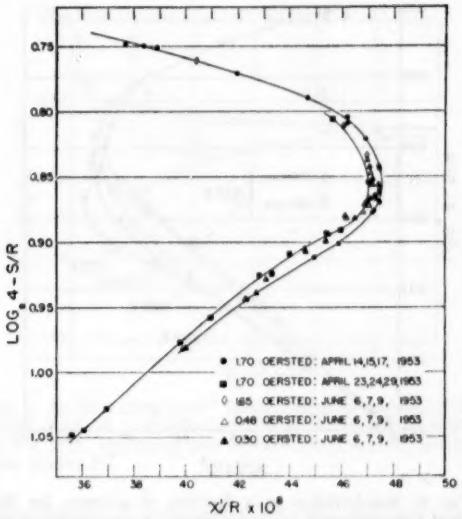

FIG. 5. Ac susceptibility as a function of entropy in the region of the maximum (enlarged from Fig. 4). Measurements at 210 cps and with various values of measuring field.

fields in the sequence: on, off, on-reversed, and off again. By using an appropriate value of bridge mutual inductance in opposition to that of the measuring coils, the remaining uncompensated part of the latter could be measured at the maximum galvanometer sensitivity, thus greatly increasing the accuracy of measurement.

For small measuring fields, χ also showed the "double-peak" feature but as the measuring field was increased the susceptibility values at the lower-entropy peak decreased progressively until the latter had effectively disappeared. This field-dependence effect may be seen in Fig. 6. The higher-entropy peak occurs at an entropy of 0.53_6R, almost coincident with the first peak of the ac (χ') curve.

It should be emphasized that the curves of χ are less well defined than those of χ' because of the relatively small number of experimental points per curve and because the ballistic method of measurement was less accurate than the ac method. From the available evidence, however, one would conclude that χ shows a field dependence only in the region of the maximum.

Susceptibility measurements on Single Crystal II, both ac and ballistic, yielded curves very similar to those of Fig. 6 with the exception that the values of χ' and χ were about five percent greater in the region of the maximum. They are shown in Fig. 7.

(iii) Frequency Dependence of χ'

Measurements of χ' were made at frequencies of 210 cps and 150 cps. Both sets of points lie on a single curve (dashed curve of Fig. 6) within the accuracy of measurement. (Note, however, that the χ' values at the maximum are about four percent higher than those obtained for the same crystal two months earlier.)

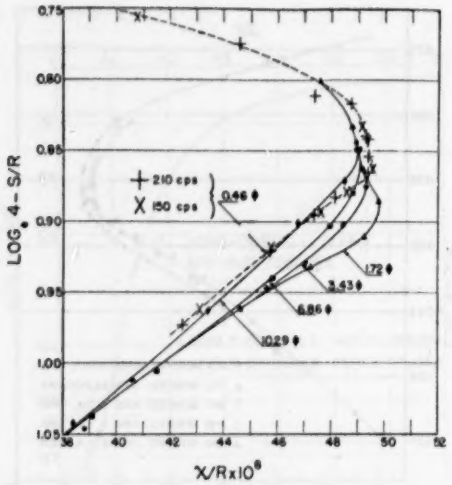

FIG. 6. Susceptibility as a function of entropy, for Single Crystal I, in the region of the maximum. Ac susceptibility measured at 150 cps and 210 cps, August 21–24, 1953 (broken line); dc susceptibility for various values of measuring field, August 14–15, 1953 (full lines)

(iv) Hysteresis and Remanence

By using the well-known cyclical procedure referred to above in the ballistic measurements, the occurrence of hysteresis was detected for all values of the entropy below $0.53R$ (corresponding to $H_i/T_i = 14.9$ kilogauss/1.11°K). This is also the position of the low-entropy peak in χ'. The variation of the remanence with entropy and with measuring field was investigated and some results are given in Fig. 8. It is seen that curves of remanence *versus* entropy for constant measuring field display a maximum which occurs at a lower entropy the larger the measuring field. These results were closely reproduced in similar measurements on Single Crystal II.

Before commencement of a series of ballistic determinations the galvanometer (period 5.6 seconds) was made slightly underdamped and the circuit calibrated. With the onset of remanence it was found that the apparent damping increased and at the lowest entropies the "time-effects" became enormous. These varied, moreover, from an "on" throw to an "off" throw; for example at "on" the mirror would swing to its maximum deflection and then creep slowly back to zero in a time of the order of 15 seconds, whereas equilibrium would be restored after an "off" throw in about 5 seconds.

The difference in the two cases is that "on" involves a reversal of the magnetic moment, from an initial state of remanence under forces within the crystal to a final state maintained by the presence of an external field, whereas "off" involves the opposite case of initial and final states with, too, a decrease but not reversal of the magnetic moment. For "on," the external field is present during the realignment of the ionic moments but not in the case of "off." The time-delay cannot, however, be simply a function of external field since no time effects could be observed for double throws, i.e., for successive complete reversals of the current. [This had the corollary that a double throw was always greater than the sum of successive "on" and "off" throws.]

For an "on-off" sequence involving *no* reversal of field, however—that is, remaining in one quadrant of a hysteresis cycle—reproducible throws were obtained but with the "on" values now greater than the "off."

Thus the time-effects were most marked for "on" throws in a hysteresis cycle, less so for "off," still less for "off" in a no-reversal on-off sequence, unnoticeable for the corresponding "on" throw, and also negligible for a simple complete-reversal sequence.

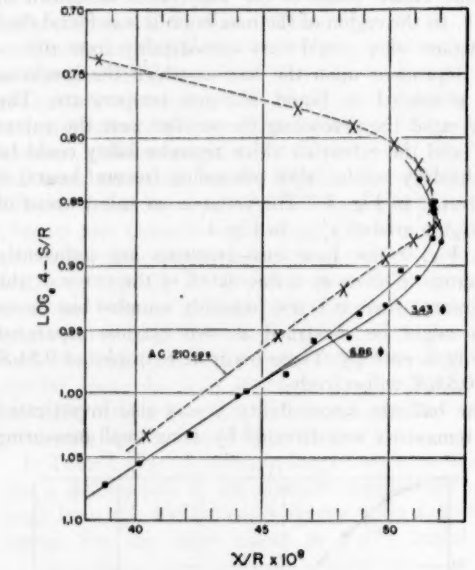

FIG. 7. Ac and dc susceptibilities as functions of entropy in the region of the maximum. Data for Single Crystal II, corresponding to that for Single Crystal I shown in Fig. 6.

The existence of such time-effects and consequent damping of the galvanometer swing must result in the observed values of the remanence (and to a smaller extent the susceptibility) depending upon the period of the galvanometer used. In these experiments the galvanometer had a period of 5.6 seconds.

(v) Ac Loss Component, χ''

As reported in A, an out-of-phase component of the ac susceptibility χ'' occurs in a relatively small range of entropy in the neighborhood of that corresponding to the χ' maximum. More precise determinations of this quantity made on Single Crystal I are summarized in Fig. 9, a plot of entropy *versus* χ''. These data were

essentially duplicated in corresponding measurements on Single Crystal II.

The values of χ''/R are small compared with those found in potassium chrome alum[13] and the curve is seen to rise to a very sharp peak at an entropy of $0.52R$. The apparent field dependence of χ''/R in Fig. 9—curves A and B being drawn through points obtained with measuring fields of 0.30 oersted and 0.45 oersted, respectively—may or may not be real. These fields are very small and not very different. It was practically impossible to measure χ'' with the field normally used at higher temperatures, *viz.*, 1.7 oersted, since the heat developed in the salt was sufficient to warm the salt through the entropy range of measurable χ'' values in such a short time that extrapolation to time zero would have been meaningless. The few such measurements that were attempted, however, and particularly in cases where the measuring current was changed during warm-up, suggested that up to this

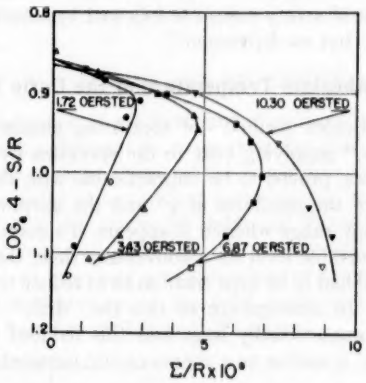

FIG. 8. Remanent magnetic moment as a function of entropy for various values of measuring field. Data for Single Crystal I, August 14–15, 1953.

point at least, χ'' decreased with increased measuring field. [The possibility that the χ'' peak is double, as appears to be the case for χ', is dealt with in Sec. V.]

(vi) Frequency Dependence of χ''

Measurements of χ'' were made at 210 cps and 150 cps and the values obtained are plotted in Fig. 10. It will be noted that no frequency dependence is detectable within the accuracy of the measurements. This is at first sight surprising but the explanation doubtless lies in the extreme narrowness of the χ'' peak. The mechanism of this low-frequency loss phenomenon has yet to be explained but, discussing it in terms of some characteristic relaxation time τ, it is evident that τ changes from a value very small compared with the period of the alternating field to a value very much greater than that period in an extremely narrow range

[13] De Klerk, Steenland, and Gorter, Physica **15**, 649 (1949).

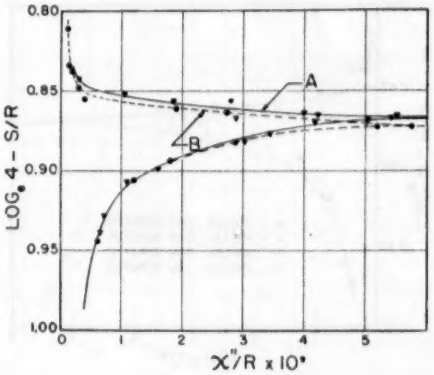

FIG. 9. Ac "loss component" (out-of-phase component of susceptibility) χ'', as a function of entropy for Single Crystal I, June 5–9, 1953. Measuring field 0.30 oersted (Curve A) and 0.45 oersted (Curve B).

of temperature. In comparison, the change from 1/210 sec to 1/150 sec is relatively insignificant and the effect must be obscured by the limited accuracy of measurement.

(vii) Magnetic Field Dependence of χ'

When a magnetic field H is applied to a paramagnetic substance, a certain moment M will be established. If now a susceptibility determination be carried out by applying a small field h perpendicular to H and measuring the corresponding moment m, then it may be readily shown that—for $h \ll H$ and with an isotropic substance—$m/h = M/H$. Thus the saturation curve (M *vs* H) may be obtained directly. [Alternatively, h may be applied parallel to H, when the differential susceptibility ($\partial M/\partial H$) is measured and the $M-H$ curve must be obtained by integration.]

The measurements were carried out using a polarizing field of up to 540 oersteds and an ac measuring field of 0.45 oersted at 210 cps. After demagnetization, the field H was increased in 8 steps to the aforementioned maximum value, an m/h determination being carried out for each value of H. The sequence was retraced several times and curves plotted for extrapolation to zero time; the corresponding entropy was, of course, determined by the initial demagnetization conditions.

The behavior above the Curie point was that for normal paramagnetic saturation but below this point (where the zero-field susceptibility reaches its maximum and thereafter decreases for further decrease in entropy) the behavior underwent a radical change. For small polarizing fields (about 20 oersteds) the value of m/h still decreased with increasing H, but for larger fields the susceptibility suddenly rose very steeply and with $H = 180$ oersted for example, became much larger over a part of the entropy range than the maximum value on the $H = 0$ curve. For the highest fields the susceptibility decreased again to relatively small values at all entropies.

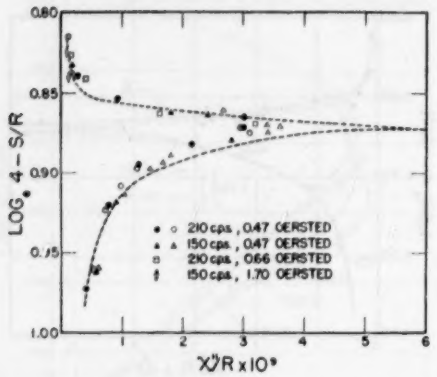

FIG. 10. χ'' as a function of entropy. Measurements on Single Crystal I at frequencies of 150 cps and 210 cps, August 21–24, 1953. The broken curve is identical with B of Fig. 9 and is given here for comparison, and to indicate the degree of reproducibility of the data.

The course of m/h *versus* entropy for various fixed values of H is shown in Fig. 11. Thus once again the methylamine salt was found to behave in a manner markedly different from that of potassium chromic alum, for which m/h was found to decrease with H for all values of the entropy.[14]

The variation of m/h with H for various fixed values of the entropy is shown in Fig. 12. The susceptibility is seen to go through a preliminary minimum and then a pronounced maximum for entropies slightly less than that of the Curie point. At still lower entropies (that is, less than about $0.48R$) the preliminary minimum is not observed, while the maximum becomes progressively more accentuated.

On the assumption that the relation $m/h=M/H$ is valid, the M *vs* H curves at constant entropy may be derived and these are given in Fig. 13. On this type of plot the curves are difficult to separate near the origin and for this reason only four curves have been plotted. Below the Curie-point entropy one sees that the (apparent) magnetic moment increases very rapidly with increasing H before leveling off at a value which is roughly one-half of the saturation moment ($M/R = 2.015\times10^{-4}$ gauss cm^3 degree erg^{-1}). The fact that the plateaux are not flat but actually show a depression (negative differential susceptibility) must be taken, presumably, as evidence that the assumption made above is not strictly valid and that the substance is no longer magnetically isotropic.[15] [The relatively small number of experimental points in Figs. 12 and 13 introduces some uncertainty in the course of the curves, particularly in the region of highest susceptibility (or magnetic moment) for the curves of lowest entropy. The two figures were constructed, however, so as to be smooth and quite consistent with each other, and in such a construction it is a great help that the most curved portion of a particular curve in one figure corresponds with a fairly linear portion of the associated curve in the other. The portions of greatest uncertainty have been drawn with broken lines.]

An anisotropy below the Curie point is not surprising, however, since the appearance of a susceptibility maximum and hysteresis effects (above) must be associated with antiferromagnetic (or perhaps ferromagnetic) ordering[16] in which the crystal structure will play a dominant role. The chromic alums present a complicated case in that there are four ions in unit cell. The spins will most probably be aligned in four groups, with one of the four spins in each unit cell along one of the four trigonal axes. Since, however, h and H were each directed along a (different) cubic axis, and a cubic axis makes very closely equal angles with all the trigonal axes, the true course of M with H might still be fairly well represented by the curves of Fig. 13 to the extent of a very steep rise followed by a temporary levelling—but no depression.[17]

(viii) Absolute Temperature of the Curie Point

The "Leiden method" of measuring absolute temperatures,[18] supplying heat to the specimen by means of ac losses, proved to be impracticable with this salt, because of the smallness of χ'' and the narrowness of the entropy range wherein it appears. To maintain χ'' at a measurable level for a convenient time, the measuring field had to be kept small so as to reduce the heating rate. In consequence of this the "drift" heating became proportionally large and this reduced the accuracy. χ' is useless as a thermometric parameter since

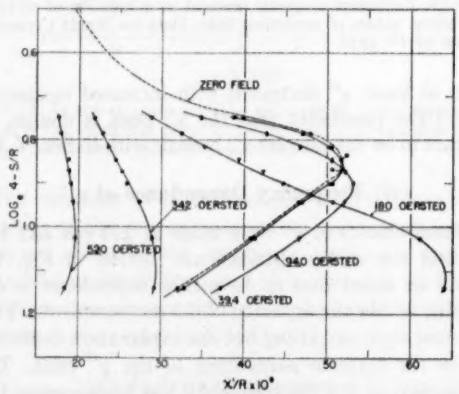

FIG. 11. Ac susceptibility as a function of entropy, in the region of the maximum, for various values of superimposed transverse steady field. Single Crystal II, measuring field 0.47 oersted at 210 cps.

[14] M. J. Steenland, thesis, Leiden (unpublished), p. 44.

[15] Steenland (see reference 3) has recently reported observing marked anisotropy in ballistic measurements of susceptibility for various directions of the polarizing field.

[16] N. Kurti, J. phys. **12**, 281 (1951).

[17] This appears to be confirmed by preliminary measurements of the differential susceptibility.

[18] Casimir, de Haas, and De Klerk, Physica **6**, 255 (1939).

in the range of useful χ'' it is an insensitive function of entropy and it is here that the course of the susceptibility during warmup deviates most widely from the "ideal" χ *vs* S curve (Fig. 4). χ'' is also a bad thermometric parameter since it changes so very rapidly with time that $d\chi''/dt$ is very difficult to estimate accurately. (χ'' heating can only be usefully employed, in any case, on the high-entropy side of its maximum, otherwise its effect will be to aggravate temperature inhomogeneities and it is on this side where it falls most rapidly to inconveniently small values.) The remanence Σ is the best thermometric parameter, but the measurements take longer to perform, magnifying problems of temperature inhomogeneity. It would appear that a combination of γ-ray heating with use of Σ to trace the change of entropy would be the most reliable method of determining absolute temperatures and such experiments are in course of preparation. Many attempts were made to measure thermodynamic temperatures but the scatter in the results was extremely bad. The temperature of the Curie point most probably lies in the range 0.015–0.020°K.

V. SUMMARY AND DISCUSSION

The behavior of methylamine chromic alum below 1°K is very different in many respects from that of potassium chromic alum and the former salt appears to be more useful as a standard thermometric substance. Above 0.1°K the theory of Hebb and Purcell fits the behavior very well although the nonreproducibility is sufficient to introduce an uncertainty of several millidegrees in the value of the level splitting δ/k. This value is found to be 0.269 ± 0.003 degree.

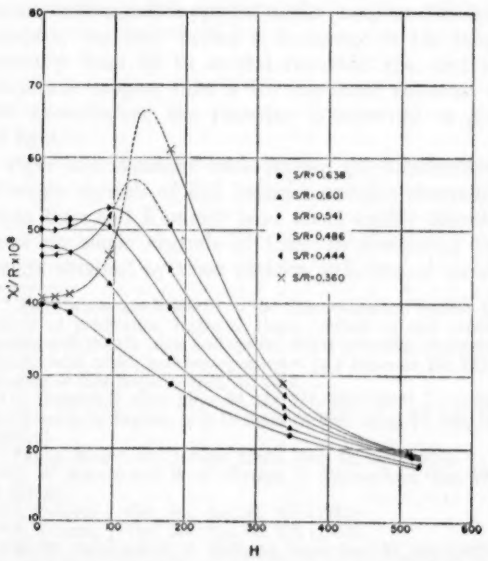

FIG. 12. Ac susceptibility in superimposed transverse field as a function of that field, along isentropes. Data correspond to that of Fig. 11.

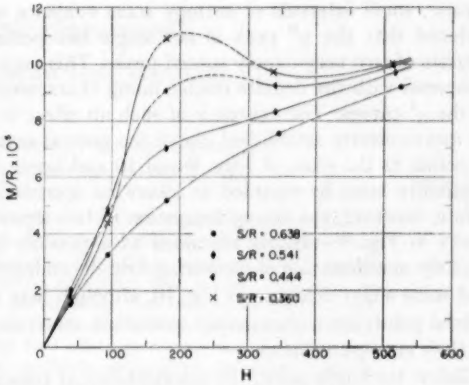

FIG. 13. Magnetic moment as a function of field, along isentropes. Values are derived from data of Fig. 12 on the assumption that $M/H=m/h$ (see text).

The nonreproducibility becomes most marked in the region of the susceptibility maximum and may be associated with the rate of precooling to liquid nitrogen temperature, since unusually small susceptibility values could be obtained for this region by precooling rapidly. No crystallographic transition takes place between 1° and 300°K which might account for this behavior—as there does in the potassium salt. There was some evidence with Crystal I that measurements on a not-previously-cooled specimen yielded higher susceptibility values than were found in subsequent runs. The initial experiments with I, however, were not very precise owing to high drift-heating rates (subsequently improved by redesign of apparatus) and only one cooling of Crystal II has been made so far. The latter gave the highest susceptibility values reported here. A further possibility, which cannot yet be excluded, is that once "low-susceptibility behavior" has been induced by a rapid precooling the crystal recovers to a "normal" state only after being kept for a number of weeks at room temperature.

The variation with entropy of both χ'' and the remanence is very different from that found with the potassium salt[13] and indicative of a long relaxation time within the spin system below the Curie point. The χ'' rises to a very sharp peak and falls again within a very small range of entropy centered on the entropy of the χ' maximum. (Within the accuracy of measurement, both χ' and χ'' appeared to be independent of frequency for the range 150–210 cps.) Remanence is detected at all entropies below a point slightly less than that of χ'_{max}, namely $0.53R$, and for a constant measuring field the remanence goes through a maximum as the entropy decreases. For a larger measuring field the remanence maximum is found at a lower entropy. The time effects observed in the ballistic measurements are so large as to greatly modify the swing of a 5.6 second galvanometer.

From a sequence of measurements made at fairly

regular, small intervals of entropy some evidence was adduced that the χ'' peak is not single but perhaps consists of two very closely spaced peaks. This may be compared with the definite double-hump characteristic of the χ' curves. The existence of such an effect is by no means clearly established above the general scatter of points in the plots of Figs. 9 and 10 and hence the possibility must be regarded as somewhat speculative. (Note, however, the strong suggestion of two separate peaks in Fig. 9—already discussed as a possible but unlikely manifestation of measuring-field-dependence—and some slight evidence in Fig. 10, although here the crucial points are unfortunately somewhat uncertain as to their entropy values.)

Below the Curie point, the susceptibility at constant entropy changes markedly with applied field—first decreasing for small fields, then increasing to a high maximum before falling again. This behavior is suggestive of a rather abrupt change from antiparallel to parallel ordering as the external field exceeds a certain critical value. The latter is seen to be a function of entropy and presumably provides a measure of the antiferromagnetic interaction (compare Garrett[19]). The method of measuring the magnetic moment in an applied field by determining the susceptibility for a small measuring field applied perpendicularly to the polarizing field most probably breaks down below the Curie point, presumably owing to the development of anisotropic behavior. For application of the two fields along different cubic axes the magnetic moment *appears* to level off in the range of 100–500 oersted at a value approximately one-half the saturation moment. [See IV, (vii) and reference 17.]

The method of measuring thermodynamic temperatures by measuring the entropy change for a known heat input and supplying the latter by means of the ac losses in the salt could not be employed satisfactorily. This was due to the fact that (a) χ'' values are small even at their maximum, (b) χ'' decreases very rapidly to vanishingly small values in an extremely narrow range of entropy, and (c) the range of existence of a measurable χ'' is just that region where χ' is a very insensitive function of entropy.

[19] C. G. B. Garrett, Proc. Roy. Soc. (London) **A206**, 242 (1951).

ACKNOWLEDGMENT

One of the authors (CKM) gratefully acknowledges the financial assistance of the John Simon Guggenheim Memorial Foundation.

Experiments on Electroluminescence*

JOHN F. WAYMOUTH, *Sylvania Electric Products, Salem, Massachusetts*

AND

FRANCIS BITTER, *Massachusetts Institute of Technology, Cambridge, Massachusetts*

(Received December 17, 1953; revised manuscript received May 12, 1954)

A summary of recent observations of the properties of ZnS:Cu:Pb and ZnS:Cu:Pb:Mn electroluminescent phosphors is reported. The experiments include studies of the optical and electrical response of these phosphors dispersed in "Lucite" to sudden changes in a constant applied field, as well as microscopic studies of the luminescence of individual particles. Both green and yellow phosphors were studied. The most important results observed primarily on green phosphors are the following: Slow changes are found to take place in a phosphor in any given constant electric field, but a steady state is finally approached. A sudden departure from this state produced by changing the applied field will in general produce very little light compared to that produced on returning promptly to the conditions under which the steady state was established. Further, the luminescence in alternating electric fields of individual grains is extremely inhomogeneous, being restricted to small "pinpoints" or "spots" very much smaller than the individual particles. The spots studied luminesced only once per cycle.

It is concluded that excitation of luminescent centers occurs primarily by ionization, with recombination and radiation occurring when subsequent electrical changes make this possible. Although excitation of luminescent centers to bound states followed by prompt radiation does occur, under the conditions of these experiments this process is of secondary importance in producing light in all the phosphors studied, and is quite negligible in the green phosphors. These and other results are discussed in connection with the several possible mechanisms by which electric fields may bring about the excitation of luminescent centers.

I. INTRODUCTION

THE experiments to be described below were undertaken in order to learn as much as possible concerning the mechanism whereby the energy of an oscillating electrical field applied to ZnS:Cu:Pb phosphor particles in an insulating matrix is converted into light. The phenomenon to be explained has been reported for other phosphors by Destriau,[1] and described in a variety of papers by various investigators.[2–5] When an alternating field is applied to the phosphor-dielectric complex, the field having a frequency in the range typically from 60 to several thousand cps, and an amplitude ranging from a few thousand volts/cm to 100 kilovolts/cm, the phosphor is observed to give off light.

Piper and Williams[6] have studied the luminescence of single crystals of ZnS between metallic electrodes, while Boer and Kummel[7] have made similar observations on single crystals of CdS. In comparing the results obtained by these authors with ours, it should be borne in mind that the presence or absence of metallic contacts may alter the relative magnitudes of currents and fields in the phosphors, and hence also the mechanism of light production.

Phosphors which electroluminesce generally can also be made to respond to ultraviolet or cathode ray excitation, but it is not established that this is a requirement for electroluminescence. ZnS containing 10^{-4} gram atoms Cu per mole and 10^{-5} gram atoms Pb per mole seems to be as effective as any other green-emitting electroluminescent phosphor mentioned in the literature.[8,9] The addition of 2×10^{-2} gram atoms Mn per mole to the green phosphor yields a yellow-emitting phosphor.[10] The observations to be described below are confined to such green and yellow phosphors. Details of the preparation of this type of electroluminescent phosphor have been reported elsewhere.[10]

It has already been demonstrated that the emission spectrum of an electroluminescent ZnS phosphor is composed of the same "bands" as are emitted during fluorescence.[11] The radiation process in both cases quite surely involves the excitation of the same kinds of luminescent centers, the primary difference between the two being the manner of supplying the energy needed for excitation. It has also been shown that the intensities of the emission bands depend on the concentration of the various activators[10] as well as on the frequency of the exciting alternating field.[11] The time-average intensity emitted in the green (5200A) band increases

* The authors are indebted to the Electrochemical Society for waiver of publication rights to those portions of this article, dealing with the electrical and optical effects of sudden changes in electric field, which had been presented in a paper at the 103rd Meeting of that Society, April 13, 1953.

[1] G. Destriau, J. chim. phys. **34**, 117, 327, 462 (1937). [A review of this work, in English, is to be found in Phil. Mag. **38**, 700, 774 (1947).]

[2] Payne, Mager, and Jerome, Illum. Eng. **45**, 688 (1950).

[3] C. W. Jerome and W. C. Gungle, J. Electrochem. Soc. **100**, 34 (1953).

[4] S. Roberts, J. Opt. Soc. Am. **42**, 850 (1952).

[5] S. Roberts, J. Opt. Soc. Am. **43**, 590 (1953).

[6] W. W. Piper and F. E. Williams, Phys. Rev. **81**, 151 (1952). [See also Brit. J. Appl. Phys., Supplement 4, Paper 7 (1954) for description of theory.]

[7] K. W. Boer and U. Kummel, Z. physik. Chem. **200**, 193 (1952).

[8] H. C. Froelich, J. Electrochem. Soc. **100**, 280 (1953).

[9] Zalm, Diemer, and Klasens, Philips Research Repts. **9**, 81 (1954).

[10] Homer, Rulon, and Butler, J. Electrochem. Soc. **100**, 566 (1953).

[11] J. F. Waymouth, J. Electrochem. Soc. **100**, 81 (1953).

linearly with frequency up to several hundred cycles per second, and then saturates, becoming independent of frequency above 1000 cycles per second. The time-average intensity emitted in the blue band increases linearly with frequency at least to 2000 cycles per second.

In order to study more in detail the processes involved during excitation and radiation, we have studied the electrical and optical changes which take place in a multiparticle sample of phosphor in a dielectric when electric fields are applied or removed at a predetermined rate. The results of these observations are summarized in the next section. We have also undertaken extensive microscopic observations on individual grains. The primary result of these observations is that electroluminescence is confined to "spots" much smaller than the particles themselves, and that the spots studied emitted light only once, rather than twice per cycle, as is characteristic of lamps.[2,3] The results of these observations are summarized in Part III.

II. BALLISTIC OBSERVATIONS

The changes, optical and electrical, which occur in a multiparticle sample of phosphor in a dielectric when the electric field is changed have been studied using a ballistic galvanometer to measure the desired quantities.

In the study of the optical effects, the light emitted by the phosphor in a thin slab when a constant dc applied field was suddenly changed in some definite manner was measured by the deflection of a ballistic galvanometer connected to a phototube. The integrated light output (ILO) which followed any given electrical change could thus be measured. In particular, we wanted to determine whether the frequency dependence of the light output from lamps is determined by the time rate of change of the applied field. This was studied by varying the time constant of the circuit which produced the electric field applied to the phosphor.

In the second kind of experiment, closely related to the above, an attempt was made to find out something about the time rate of change of electric polarization under varying conditions, particularly to separate the usual reversible polarization of a dielectric from more complex effects, possibly involving conduction currents, hysteresis, slow thermally induced changes, and so on.

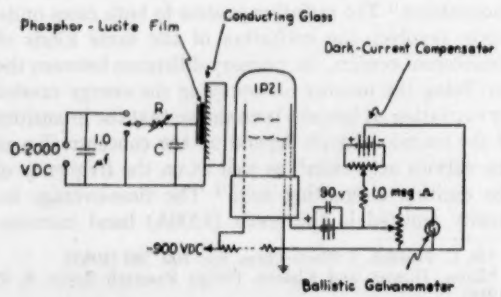

FIG. 1. Sketch illustrating apparatus used for the measurement of the integrated light output (ILO) from a phosphor-plastic sample upon application or removal of an electric field.

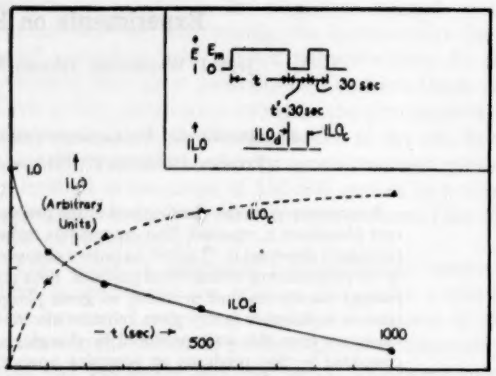

FIG. 2. Dependence of ILO_c and ILO_d on charging time t, in experiment diagramed schematically in inset. Phosphor was ZF 1081 AC, a green phosphor prepared by firing for one hour at 1580°F in a covered crucible ZnS containing several percent $ZnCl_2$, 0.002 gram atoms Pb per mole (added as $PbCO_3$), 0.001 gram atoms Cu per mole (added as CuO).

The apparatus used in the optical ballistic measurements is shown in Fig. 1. The phosphor was imbedded in a Lucite film, 0.010 in. thick, which was aluminized on one side. A phosphor-bronze spring, making contact with the aluminized side, pressed the film against a piece of conducting glass, which formed the other electrode. A thin film of castor oil served to establish good dielectric contact between the phosphor-Lucite film and the conducting glass. The resistance R could be varied in steps of a factor of three from 1000 ohms to 30 megohms. Since the capacitance C was 0.05 μf, time constants from 50 microseconds to 1.5 seconds were available.

The light pulse emitted by the electroluminescent phosphor upon the change in electric field was allowed to fall upon the cathode of the 1P21 photomultiplier. The integral of the anode-current pulse from the photomultiplier was measured by means of the ballistic galvanometer.

The first observations with the green-emitting phosphor indicated that only erratic results could be obtained unless steps were taken to produce a standard condition of the sample to be investigated. Thus, the ILO resulting from the application of a field depended markedly on the time elapsed since the previous application of a field. A long waiting period, of the order of many hours, was needed to produce equilibrium. However, if the sample was left in zero field for a long time, overnight, for instance, then a reproducible condition was established. Upon the application of a field after the establishment of equilibrium in zero field, only a very small ILO was observed, if any. Then upon removal of the applied field within a matter of seconds after its application, a relatively very large light output was observed. This suggests that some sort of excitation

of the luminescent centers takes place when the equilibrium is disturbed by the application of the field; the emission of light occurs only upon return to initial conditions. Yellow-emitting phosphors, containing several percent of manganese in addition to copper and lead, display a larger light output than the green phosphors when the field is applied to the phosphor in zero field equilibrium. This light pulse has under some circumstances been observed as great as 25 percent of the light pulse on return to equilibrium in these phosphors.

It was soon found that the equilibrium condition could be established in a few seconds by the application of red-plus-infrared light with the sample condenser shorted out, instead of by waiting for hours. It has been established that the "erasure" of previous charging history and establishment of equilibrium is brought about by the photon energy of the light, and not simply through a heating of the sample. Photon energies between one and two volts are used for this purpose (that portion of the spectrum of a Sylvania 250-watt heat lamp that is transmitted through a water filter in series with a Corning 2412 red filter). The steady state which is produced by irradiation closely approximates that which is produced by allowing sufficient time to elapse for the cell to return to equilibrium of its own accord. It is doubtful that a true equilibrium state can be achieved at all, as more and more accurate measurements seem always to reveal small departures from a reproducible condition. We shall, however, refer to the steady state produced by infrared light as an equilibrium condition.

By using this technique of establishing equilibrium by the application of infrared light, it was found that once equilibrium of a green phosphor is established in any arbitrary field, a change from this equilibrium condition produces very little or no light, but a return to this equilibrium produces considerable light. Typical results of such experiments are shown in Figs. 2 and 3.

Figure 2 shows the results of the following experiment, which is diagrammed schematically in the inset.

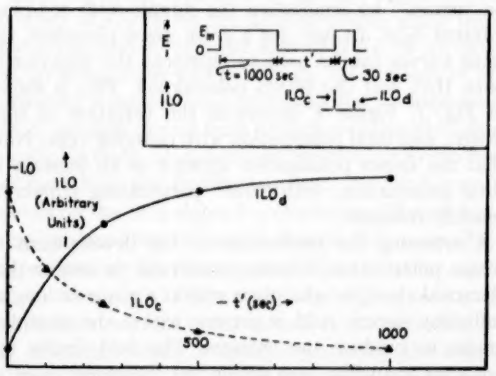

FIG. 3. Dependence of ILO_c and ILO_d of ZF 1081 AC (green) on discharging time t' in experiment diagramed schematically in inset.

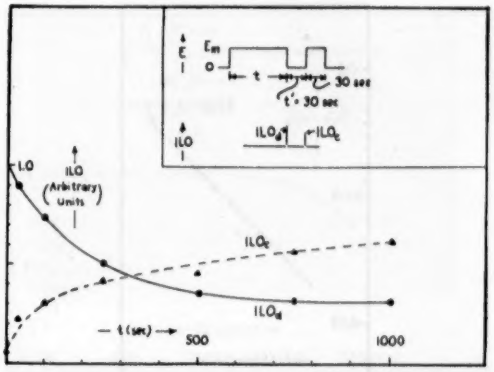

FIG. 4. Dependence of ILO_c and ILO_d on charging time t for ZF 774 AC, a yellow phosphor, prepared by firing for one hour at 1600°F in a covered crucible, ZnS containing several percent $ZnCl_2$, 0.002 gram atoms Pb per mole (added as $PbCO_3$), 0.001 gram atoms Cu per mole (added as CuO) and 0.015 gram atoms Mn per mole (added as $MnCO_3$).

With the sample in the discharged equilibrium condition, at $t=0$, a field E_m was applied to the sample for a length of time t seconds. At the conclusion of this period, the electric field was removed, and the integrated light output on discharging the sample condenser (ILO_d) was measured. Thirty seconds after the removal of the field, it was reapplied, and the integrated light output on charging the sample condenser (ILO_c) was measured. The thirty-second interval between discharging and charging was dictated by the requirement that the ballistic galvanometer return to zero after the measurement of ILO_d. The effect of the initial charging time t on ILO_c and ILO_d is shown in the figure. Note that ILO_c is zero for $t=0$, but increases toward a saturation value as t increases. ILO_d, initially high, approaches zero as t increases. One thousand seconds is insufficient time for equilibrium to be established.

Figure 3 shows the results of the inverse experiment, which is diagrammed schematically in the inset.

With the sample in the discharged equilibrium condition at $t=0$, a field E_m was applied for a period of 1000 seconds. As previously noted, this is insufficient time for the sample to reach equilibrium, but it permits the sample to reach a reproducible state. It was not realized at the time these experiments were performed that the sample could be gotten into equilibrium with any desired field in a few seconds simply by irradiating with red-plus-infrared light with the field applied. At the conclusion of this charging period, the field was removed for a time t'; at the conclusion of the time t', the field was reapplied, and ILO_c measured; after thirty seconds, the field was again removed and ILO_d measured. The dependence of ILO_c and ILO_d on the discharging time t' is shown in the figure. Note that ILO_c decreases toward zero, while ILO_d increases toward its zero field equilibrium value as t' increases.

Figure 4 shows the dependence of ILO_c and ILO_d of a yellow phosphor on charging time t. Note that the

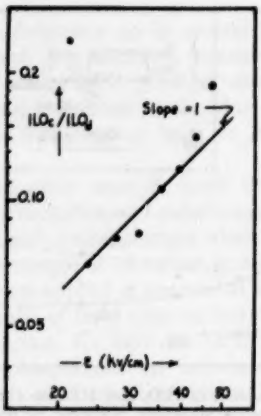

FIG. 5. Dependence of the ratio ILO_e/ILO_d on field strength E, for ZF 774 AC (yellow).

dependence is quite similar to that displayed by the green phosphor, except that ILO_e is not zero for $t=0$, and that ILO_d apparently does not approach zero as t increases. These data indicate that the same process occurring in the green phosphor takes place here, but that there is in addition a greater tendency for excitation of some luminescent centers to states which promptly radiate upon a first application of the field to a phosphor in equilibrium, in which there are supposedly no excited centers. This result suggests the existence of two processes which produce light, one involving excitation with prompt radiation, the other involving the retention of the excited center in this excited state for long times, of the order of hundreds of seconds. The existence of two processes is also suggested by Fig. 5 in which the ratio of ILO_e to ILO_d at $t=0$ is plotted for this same phosphor as a function of electric field. Note that this ratio varies approximately as E at low fields, and varies at a higher power of E at higher fields.

To study the electrical changes which take place in a multiparticle sample of phosphor when a constant dc field is applied or removed, the movable-plate condenser

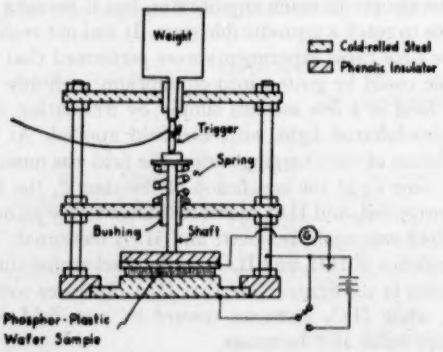

FIG. 6. Sketch illustrating construction of movable plate condenser employed for the measurement of frozen polarization.

illustrated in Fig. 6 was employed. The phosphors were impregnated in Lucite wafers 0.050 in. thick which were mounted in the condenser for measurement. The spring-loaded upper plate of the condenser, normally held in contact with the phosphor-Lucite wafer by the weight, could be rapidly elevated by pulling out the trigger.

It was found that if the sample condenser were charged for some minutes and then discharged, there still remained a "frozen" dipole moment per unit volume in the sample, which could be measured by quickly elevating the upper plate of the condenser and measuring the sizable charge which passed through the ballistic galvanometer. It was verified that this frozen polarization was a property of the phosphor and not of the binder by performing similar experiments on wafers containing no phosphor, wafers containing finely divided Cu powder, and on loose piles of phosphor. Only the latter displayed the frozen polarization.

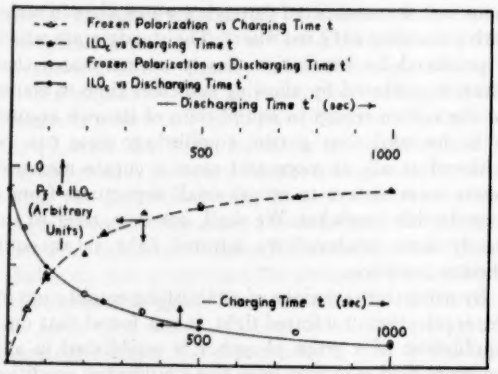

FIG. 7. Dependence of ILO_e and frozen polarization on charging time t (lower scale) and on discharging time t' (upper scale) ZF 1081 AC (green).

The behavior of frozen polarization with charging and discharging time is the same as that of ILO_e. It can be "erased" by irradiating the sample with red-plus-infrared light. In fact, for a given green phosphor, the same curves can be used to represent the behavior of both ILO_e and the frozen polarization. This is shown in Fig. 7. Figure 8 illustrates the variation of free, frozen, and total polarization with charging time. Note that the frozen polarization appears as an increase in total polarization, with "free" polarization remaining sensibly constant.

Concerning the mechanism of the development of frozen polarization, it seems reasonable to assume that electrical changes take place within a grain as long as sufficient electric field is present within the phosphor grains to produce the changes. The field finally approaches the value zero within the "working" part of the grain regardless of the magnitude of the applied field, provided the movable charge within the grains is

large enough. We specify "working" part of the grain, since there is ample evidence, to be discussed in the section immediately following, that the electroluminescent emission from grains of these phosphors is confined to a small fraction of the volume of the grain. The optical results are, therefore, explicable without assuming that the zero field condition is established in the entire grain.

The fact that the frozen polarization approaches a limiting value proportional to the field strength also indicates the validity of the above "zero-field" hypothesis. The only difference between the equilibrium condition with and without field is that in an externally applied field there is a certain frozen polarization which is absent if no constant field is present. We then conclude that luminescent centers are excited by the production of an applied field within the phosphor grains, and light is emitted when the region within the grains returns to its equilibrium condition.

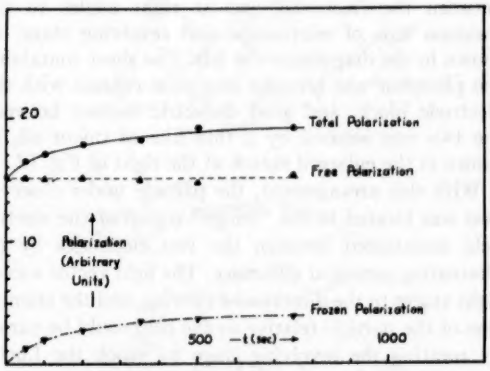

FIG. 8. Dependence of free, frozen, and total polarization on charging time t for ZF 1081 AC (green).

Having established the above points, we were in a position to return to one of the problems we had in mind in initiating these experiments, namely, to determine the effect of dE/dT on the light output in going from some initial field E_1 to some final field E_2. As we have said, in going from an equilibrium field, which in all probability is zero or small within a grain, to some final field E, the light output from a green-emitting phosphor is negligible under all conditions. On returning from the final field E to the equilibrium field, the light output depends on the time elapsed in the nonequilibrium condition, as has already been indicated, but is sensibly independent of the rate at which the return to equilibrium takes place in the entire range of time constants from 50 microseconds to 0.5 second, as shown in Fig. 9. The excitation which is brought about by the application of an electric field is also only slightly dependent on the rate of rise of the electric field, as shown in Fig. 10.

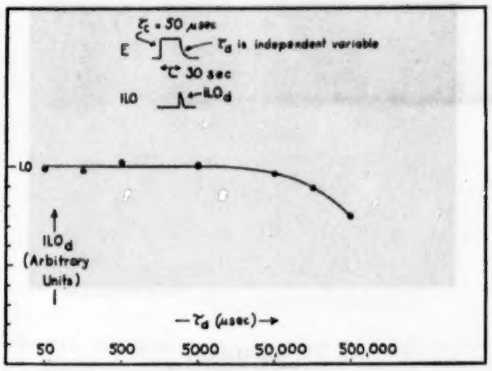

FIG. 9. Dependence of ILO$_d$ on the time constant, τ_d, of removal of the electric field, for ZF 1081 AC (green).

It is thus established that the frequency dependence of the light emission from lamps is not due to the variation of dE/dT. The light "pulse" each half-cycle is at low frequencies independent of frequency, and the linear increase of light output with frequency results from the increase in the number of equal light pulses per second. At higher frequencies, other effects, involving either the duration of the voltage "pulse," or the interval between voltage "pulses," predominate and modify the magnitude of the light pulses emitted each half-cycle.

III. THE LUMINESCENCE OF INDIVIDUAL PARTICLES

While the measurements that have been described represent averages over large numbers of particles, the observations reported in this section consist of observations of the luminescence of single particles or small polycrystalline aggregates. The most fundamental observation to be made is that the luminescence of these particles is by no means uniform, but is confined almost exclusively to small, discrete, bright "spots."

Figure 11 shows a photograph of two large polycrystalline aggregates (about 50 microns in diameter),

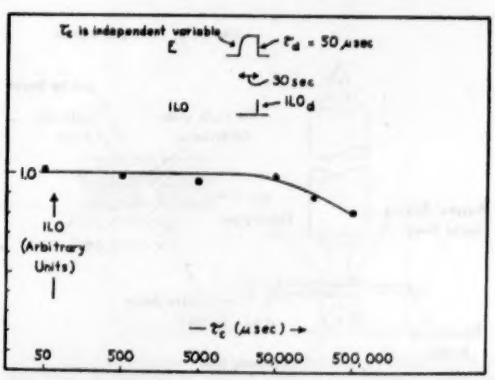

FIG. 10. Dependence of ILO$_d$ on the time constant, τ_c, of application of the electric field, for ZF 1081 AC (green).

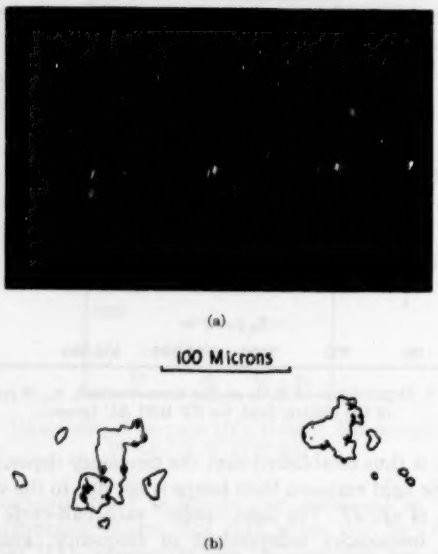

FIG. 11. (a) "Auto-micro-photograph" of two particles of electroluminescent phosphor taken by their own electroluminescence. (Photo by Herndon Associates, Inc., Ipswich, Massachusetts.) (b) Sketch showing approximate outlines of particles illustrated in (a), and approximate locations of "spots."

taken by their own electroluminescence. This photograph was obtained from a dilute dispersion of phosphor in Lucite between two sheets of 100-mesh gauze. The electric field strength was 100 kv/cm rms, and the viewing direction was approximately parallel to the field. The luminescence is far from uniform, and seems to be localized in certain bright pinpoints, which appear to be of the order of microns in size. If the particles are illuminated by 3600A ultraviolet light, no such nonuniformity is observed in their fluorescence. It is our firm belief that the striking properties of these spots, to be described in the following, make it unlikely that they are optical illusions due merely to the emergence of a volume luminescence at particular points owing to

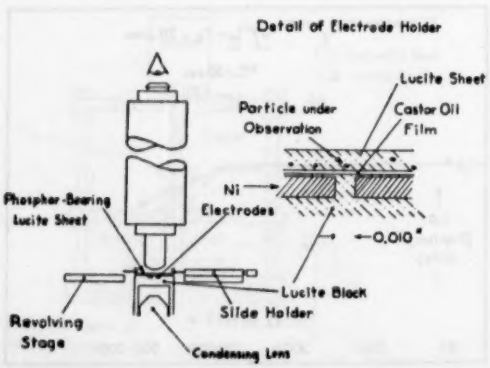

FIG. 12. Sketch of apparatus employed for microscopic observations of electroluminescing particles.

multiple internal reflection and focusing. The inhomogeneous electroluminescence shown here has also been observed by Roberts[6] in Zn(S·Se):Cu and by Zalm *et al.*[9] in ZnS:Cu.

The arrangement with which the photograph of Fig. 11 was taken suffers from the fact that the direction of viewing of the particle is parallel to the electric field. In general, if many spots are present in a particle, they are "in series" along the electric field vector. For this reason, it is usually desirable to have the direction of viewing at right angles to the direction of the electric field. In order to accomplish this, as well as to make it possible to study the influence of relative orientation of particle and electric field, we have used extensively the method of mounting shown in Fig. 12.

A thin sheet of Lucite containing a dilute dispersion of phosphor was fastened to the slide holder on the rotating stage of the microscope. A Lucite block containing two nickel electrodes was mounted on the condenser stage in such a way that the electric field between the electrodes was at right angles to the common axis of microscope and revolving stage, as shown in the diagram at the left. The sheet containing the phosphor was brought into close contact with the electrode block, and good dielectric contact between the two was assured by a thin film of castor oil, as shown in the enlarged sketch at the right of Fig. 12.

With this arrangement, the particle under observation was located in the "fringe" region of the electric field maintained between the two electrodes by an alternating potential difference. The field vector was at right angles to the direction of viewing, and the orientation of the particle relative to the field could be varied by rotating the revolving stage to which the Lucite sheet containing the phosphor was attached.

While only a small fraction of the observable spots can be classified, it has proved possible with this method of observation to identify at least two classes of spots, by their locations on the particles, and by their different dependence on the relative orientations of particle and field. Typical examples are shown in Fig. 13. The first class of spot is illustrated in Fig. 13 (a). It is to be found at the junction or interface between two apparently similar crystallites of an aggregate. It luminesces most brilliantly for the electric field approximately perpendicular to the interface. The second class of spot is illustrated in Fig. 13 (b). It is to be found at the tip of what appears to be a long needle-shaped crystallite, and luminesces most brilliantly when the field is approximately parallel to the axis of the crystallite.

In order to determine the effects of orientation of field, the voltage across the electrodes at which the spot seemed to the dark-adapted eye to extinguish was measured for each orientation. This is a quantity which is easily measured, and is related to brightness; the higher the extinction voltage, the lower the brightness

at a fixed voltage.[12] It is this extinction voltage which is plotted as a function of field angle for the two particles illustrated in Fig. 13. The difference in minimum extinction voltage for the two types which is shown in Fig. 13 is quite characteristic.

It has proved to be possible to photometer quantitatively the light emitted from the brightest of the junction spots. This was accomplished by means of the apparatus illustrated schematically in Fig. 14. The phosphor grains were mounted in the same manner as for the orientation experiments. The 45× objective formed an image of the spot, which could be considered to be a point source. Exactly in the image plane, a diaphragm stop with a diameter of about 0.5 mm masked off the image of the rest of the particle. The light from the image of the spot was then focused on the cathode of a 1P21 photomultiplier by a Huygens ocular which had been modified by the removal of one lens. By suitable calculations, based on the assumption that the spot is a point source, and on the response of the photomultiplier when the point source spot was replaced by an area source of known brightness having the same emission spectrum, namely a green electroluminescent lamp, we could calibrate the system in absolute terms.

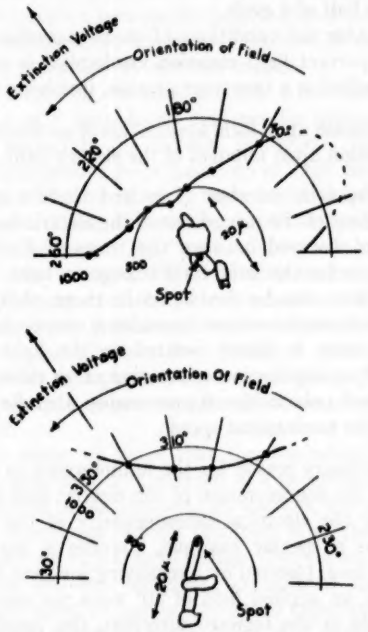

FIG. 13. (a) Sketch showing particle with "junction" type of spot, and showing variation in extinction voltage with orientation of field. Zero degree azimuth is arbitrary. (b) Sketch showing particle with "point" type of spot, and showing variation in extinction voltage with orientation of field. Zero degree azimuth is arbitrary.

[12] These observations were made prior to the development of techniques for quantitative photometry described below. Subsequent observations verify the conclusions which are reached here.

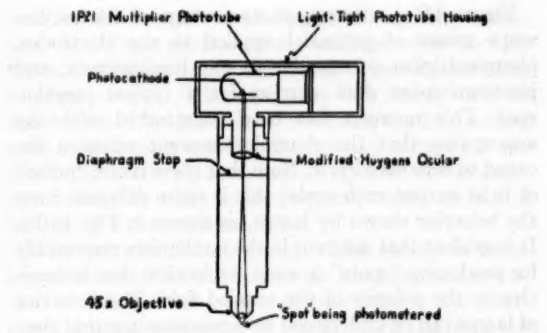

FIG. 14. Sketch illustrating adaptation of microscope for photometry of the luminous emission from "spots."

The average light output from a number of spots has been measured, using a galvanometer as an indicator. Photometry was performed almost exclusively on well-defined junction spots, as these were the brightest. The fluctuating light output has also been measured, using an oscilloscope as an indicator. Figure 15 shows a plot of the light emitted from the spot shown in the inset, as a function of the 60-cps alternating voltage across the electrodes. Note that there appears to be a threshold potential, above which the luminous emission increases linearly with voltage, over a considerable range. It is possible that departure from the linear relation is caused by light originating in other parts of the particle being scattered into the optical system.

For the purposes of comparison, a curve of light emission *versus* applied potential for a typical lamp is also reproduced in Fig. 15, with arbitrary scales. Note the considerably greater curvature, especially at low voltage. We feel this to be due to the fact that lamps are composed of large numbers of particles having a variety of luminescent thresholds and orientations.

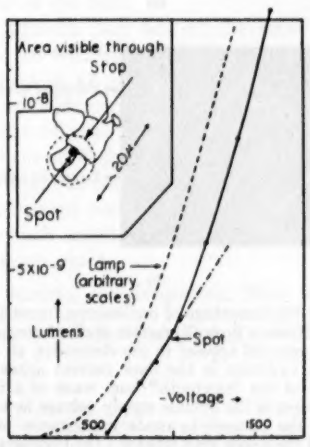

FIG. 15. Dependence of average luminous emission from spot illustrated in inset on ac voltage applied to electrodes (solid line). Variation of light output with voltage for a typical lamp is shown plotted with arbitrary scales (dashed line) for comparison.

Figure 16(a) shows a photomontage of the oscilloscope traces of potential applied to the electrodes, photomultiplier current due to spot luminescence, and photomultiplier dark current for a typical junction spot. This montage has been constructed with the assumption that the electroluminescent emission decayed to zero each cycle. Note that there is one "pulse" of light output each cycle; this is quite different from the behavior shown by lamps, as shown in Fig. 16(b). It is evident that inherent in the mechanism responsible for producing "spots" is some mechanism that is sensitive to the *polarity* of the applied field. The behavior of lamps can be understood by again recalling that they are composed of many spots, some of which are oriented to emit light during one-half of the cycle, others of which are oriented to emit light on the other half of the cycle. Hence, the light emitted by lamps pulsates at 120 cps, while the light emitted by spots pulsates at 60 cps.

It may be of interest to add that probably thousands of electroluminescing grains have been examined under the microscope leading to the qualitative observation that electroluminescence is inhomogeneous and particularly marked in small spots. Also the light output of hundreds of spots has been examined with an oscilloscope, leading to the conclusion that the appearance of essentially only one major light pulse per cycle is not an exceptional phenomenon but the characteristic standard of behavior.

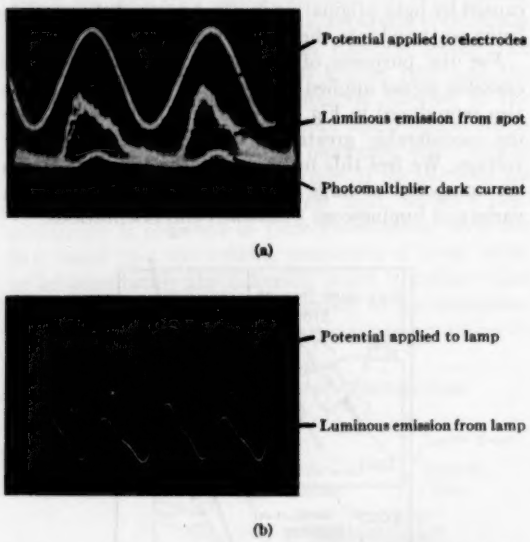

FIG. 16. (a) Photomontage of oscilloscope traces showing luminous emission from a typical junction spot, photomultiplier dark current, and potential applied to the electrodes, all as a function of time. (The variation in the dark current arises through the differentiation of the "sawtooth" hum wave of a few millivolts amplitude present in the dynode supply voltage by the *RC* circuit consisting of the cathode-to-anode capacitance of the photomultiplier and the anode load resistor.) (b) Photograph of oscilloscope traces showing luminous emission from a typical lamp, and potential applied to the lamp, as a function of time. The sensitivity used was sufficiently low that the variation in dark current with phase was negligible.

IV. DISCUSSION

We feel that the most important facts about electroluminescent phosphors to emerge in this investigation are the following.

(1) The luminous emission under alternating electric field excitation at fields of the magnitudes used is confined almost entirely to small, discrete "spots," of which at least the "junction" type appear to be "optically rectifying," in the sense that they emit light during only one half of a cycle.

(2) Under the conditions of these experiments, the most important light emission mechanism in all phosphors studied is a two-stage process, involving:

(a) excitation upon local application of an electric field.
(b) emission upon removal of the electric field.

(3) The total number of excited centers is nearly independent of the rate of rise of the electric field. This has been observed between rise times of 5×10^{-5} sec and 0.5 sec for the same total changes in field.

(4) There can be developed in these phosphors a frozen polarization whose dependence on previous electrical history is closely related to the light output obtained on application or removal of an electric field. This frozen polarization is presumably, therefore, localized at the luminescent spots.

The primary reason for the luminescence in "spots" may be the concentration of the electric field at those spots by the electrical inhomogeneity of the particle itself. As a specific example, consider a particle 20 microns long, bisected by a rectifying junction 1 micron thick, in an applied field of 10^5 volts per centimeter. For fields in the forward direction, the junction will behave as a conductor. There will be little or no electric field in it except that necessary to overcome the natural "bias" of the rectifying junction. For fields in the reverse direction, the junction will behave as an insulator; 200 volts will appear across the rectifying junction, giving a local field therein of 2×10^6 volts per centimeter. If the barrier were thinner, the local field would be correspondingly greater.

Such a barrier would have the required "optically rectifying" properties if we assume that the high fields present on the "reverse" half-cycle are responsible for excitation, either directly by a barrier penetration process, or indirectly by accelerating electrons which in turn produce excitation by collision. Among other workers in the field, the "collision" mechanism is almost unanimously believed to be responsible for the majority of the excitation. Curie[13] has endeavored to show theoretically how it might take place at the comparatively

[13] D. Curie, J. phys. radium 13, 317 (1952).

low average field strengths (2×10^4–10^5 volts/centimeter) at which the electroluminescence of powdered phosphors occurs. Burns[14] and Zalm[9] have also considered it; Piper and Williams[6] have based a detailed theory of the electroluminescence of single crystals upon it.

Barrier penetration, or direct field-ionization of luminescent centers has, on the other hand, been largely discounted. Piper and Williams[6] have proposed that electrons emitted from a negative metal electrode into the ZnS are responsible for the excitation of the "in phase" luminescence peak they observe in their single crystal experiments. However, they regard direct field-ionization of the luminescent centers in ZnS as being out of the question because the fields required, according to their calculations, are much higher than those required for ionization by electron impact.

It is interesting to note, in this connection, that McKay *et al.*,[15] have found evidence for ionization by electron impact in the increase in reverse current in "thick" germanium $p-n$ junctions at high back voltages, while McAfee *et al.*,[16] have found evidence for barrier penetration of the Zener type[17] in the increase of reverse current in "thin" germanium $p-n$ junctions at high back voltages, without ionization by electron impact. This apparent contradiction has been discussed by McKay,[15] who points out that, exactly as in gaseous discharges, the distance over which a high field is maintained is as important to the mechanism of ionization by electron impact as the existence of the high field itself.

At this stage we know that the electroluminescing junctions appear to be the result of a nonuniformity of the properties of the phosphor crystallites, but we have no exact knowledge of their thickness or of the charge distribution or luminescent center distribution within them. We hesitate, therefore, to make a choice of mechanism based on purely theoretical arguments as to which might occur at lower fields in a hypothetical crystal of uniform properties.

We may conclude at present, however, from the fact that the total number of excited centers in a given sample is independent of the rise time of the electric field over such a wide range, that if excitation by electron impact does occur, the primary electrons must be initially bound, either in "donor centers" or in luminescent centers themselves, in a region of very long relaxation time. These electrons must be liberated by the field when the field is already high enough to accelerate them to high energies. Otherwise, they will simply drift to the surface of the particle, neutralizing the field as fast as it is applied. A possible site for such a region is the rectifying barrier, postulated to explain the luminescence of spots, which in the "reverse" direction would be devoid of free charge.

Whatever the mechanism by which energy is transferred from the electric field to the luminescent centers, the most important process of excitation in the phosphors studied appears to be one in which electrons are removed from the luminescent centers. Emission occurs upon removal of the electric field when the electrons are allowed to return to the ionized centers, where they recombine with the emission of radiation. It is difficult to conceive of any excitation process other than actual ionization in which luminescent centers can be maintained in an excited state by an electric field for hundreds of seconds.

This may not be the only process of excitation. The result obtained with the yellow phosphors, in which light is emitted upon application of an electric field to a phosphor in equilibrium at zero field is compatible with the existence of another process. In this case, an electron in a luminescent center might be raised to an excited state which is bound, from which it promptly reverts to the ground state with the emission of radiation.

The mechanism of recombination of injected carriers, postulated by Lehovec *et al.*,[18] to account for the luminescence of silicon carbide crystals and described by Haynes *et al.*,[19] in germanium $p-n$ junctions, would seem not to be the dominant mechanism involved in light emission in the ZnS here studied since it would lead one to expect light emission upon application rather than removal of the field.

It is our opinion that one of the most important properties of an electroluminescent phosphor which is to be dispersed in an insulating medium and excited by alternating fields may be the high degree of electric inhomogeneity of the individual particles which we believe to be responsible for the "spots." It is this feature that might be responsible for the fact that effects normally associated with dielectric breakdown can be confined to such small regions that no macroscopic breakdown takes place.

[14] L. Burns, J. Electrochem. Soc. **100**, 572 (1953).
[15] K. G. McKay and K. B. McAfee, Phys. Rev. **91**, 1079 (1953).
[16] McAfee, Ryder, Shockley, and Sparks, Phys. Rev. **83**, 650 (1951).
[17] C. Zener, Proc. Roy. Soc. (London) **A145**, 523 (1934).
[18] Lehovec, Accardo, and Jamgochian, Phys. Rev. **83**, 603 (1951).
[19] J. R. Haynes and H. B. Briggs, Phys. Rev. **86**, 647 (1952).

Transmission of X-Rays Through Calcite in Laue Diffraction*

GUENTER SCHWARZ AND GEORGE L. ROGOSA
Department of Physics, Florida State University, Tallahassee, Florida

(Received March 18, 1954)

Precise measurements of the shape of the transmitted intensity curve in the case of Laue diffraction in high quality calcite have been made at a wavelength of 0.708 A. The range of crystal thicknesses investigated, from 0.05 cm to 0.620 cm, clearly shows the transition from extinction to anomalous transmission. Values of the crystal absorption coefficient at the diffracting position are given. For the thick crystal case, for example, the absorption coefficient at anomalous transmission for a 0.563-cm crystal was 6.61 cm^{-1} compared with a normal absorption coefficient value of 22.0 cm^{-1}. Comparison of the data with theoretical results of Hirsch, Ramachandran and Kartha, and Zachariasen shows reasonable agreement.

I. INTRODUCTION

WHEN x-rays are incident on single crystals and undergo Laue diffraction, anomalous effects result for the radiation transmitted in the direction of the incident beam. This transmitted intensity may increase, decrease, or go through a maximum and minimum as the crystal is rotated through the diffracting angle. This effect is pronounced for perfect, absorbing crystals and is dependent on the crystal thickness and the wavelength of the radiation. A simple classification of the effect can be given in terms of $\mu_0 t_0$, where μ_0 is the ordinary linear absorption coefficient of the crystal and t_0 is its thickness. For $\mu_0 t_0 \ll 1$ a pronounced dip occurs in the transmitted intensity curve at the Bragg angle. This effect usually is termed extinction. For $\mu_0 t_0 \gg 1$ a sharp peak occurs in the transmitted intensity curve at the Bragg angle. Such a case is called anomalous transmission. For intermediate values of $\mu_0 t_0$, intensity curves are obtained which show both a peak and a dip near the Bragg angle. Studies of this phenomenon have now been reported by several investigators employing different experimental techniques.[1-4]

In a previous paper[3] we have reported the results of investigations on the transmitted and reflected x-ray intensities in Laue diffraction for calcite using wavelengths from 0.631 A to 2.29 A and crystal thicknesses from 0.01 cm to 0.306 cm. In that work we were able to correlate the angular positions of the transmitted and reflected intensity curves and to measure the changes in the intensities. However, since the x-ray intensities were measured by a Geiger counter in conjunction with a counting rate meter and a graphic recorder, we reported no values of absorption coefficients. Employing the same general experimental arrangement but taking point-by-point counts instead of using the rate meter, we have now measured the transmitted intensity curves for calcite at the wavelength of Mo $K\alpha_1$, 0.708 A for crystal thicknesses up to 0.620 cm. These new point-by-point measurements allow a better comparison with the theoretical curves such as obtained by Hirsch[5] and Ramachandran and Kartha.[6] We are also able for the case of anomalous transmission to report values of the absorption coefficient for calcite, which can be compared with the theoretical calculations of Zachariasen.[7]

II. EXPERIMENTAL

As in the earlier work, x-rays were obtained from a Machlett A-2 tube, the high voltage and tube current being electronically regulated. The radiation was monochromatized by a double crystal x-ray spectrometer set to pass the peak of Mo $K\alpha_1$. This radiation then passed over the axis of another spectrometer[8] on which the investigated calcite crystal was mounted.

In order to simplify changing and aligning crystals, a new crystal holder was designed.[9] An exploded view of the holder is shown in Fig. 1. The spectrometer is provided with two slides mounted on the vertical shaft in order to translate the crystal in two perpendicular horizontal directions. The base plate of the crystal holder is secured to this slide arrangement. The table is fastened to the base plate by a strong tension spring (not shown) which passes through the opening at the center of the floating plate. Two screws having 80 threads per inch are provided to adjust the tilt of the table. Two small tension springs (not shown) connect the table to the base plate, one near each screw in order to insure positive seating of the table on each of the screws. A circular plate graduated in degrees is secured to the table by a circular retainer allowing the circular plate to be rotated with respect to the table. A vise in which the crystal specimen can be clamped is

* This work was supported by a grant from the National Science Foundation.

[1] G. Borrman, Physik. Z. **43**, 157 (1941); Z. Physik **127**, 297 (1950).

[2] H. N. Campbell, Acta Cryst. **4**, 180 (1951); J. Appl. Phys. **22**, 1139 (1951).

[3] G. L. Rogosa and G. Schwarz, Phys. Rev. **87**, 995 (1952).

[4] G. Brogen and O. Odell, Arkiv Fysik **7**, 1 (1953).

[5] P. B. Hirsch, Acta Cryst. **5**, 176 (1952).

[6] G. N. Ramachandran and G. Kartha, Proc. Indian Acad. Sci. **35**, 145 (1952).

[7] W. H. Zachariasen, Proc. Natl. Acad. Sci. (U. S.) **38**, 378 (1952).

[8] This spectrometer is on loan from the University of Chicago through the courtesy of Professor S. K. Allison.

[9] This crystal holder was designed by L. Carlton Brown, now at Ohio State University.

mounted on the graduated circle. This arrangement expedited the finding of the crystal diffracting position and the adjusting of the diffracting planes to give the narrowest rocking curve.

The angular position of the crystal could be changed in steps of 1″ by manual operation of the spectrometer. The radiation transmitted through the crystal in the direction of the incident beam entered a Geiger counter filled with Krypton to a pressure of 70 cm Hg. Intensities were measured by counting for a fixed time.

The transmitted intensity was recorded at each position as the crystal was rotated in steps of seconds of arc through the diffracting position. The crystal was then repositioned for maximum transmission and additional counts were taken. In some cases, crystals were adjusted, set for peak transmission, and the transmitted intensity measured without recording the full rocking curve.

In order to calculate absorption coefficients the primary intensity must be known. Since this intensity is too high to be measured directly, calibrated aluminum absorbers were interposed in the x-ray beam, the crystal of course being removed.

It has been found that the anomalously transmitted beam suffers a lateral displacement on one side with respect to the primary beam, this displacement depending on the crystal thickness.[10] The displacement amounted to about 12 percent of the crystal thickness. This displacement has been explained theoretically by von Laue.[11] Since the counter had a constant efficiency over most of its cross section this displacement did not affect the comparison of the anomalously transmitted intensity with the primary intensity.

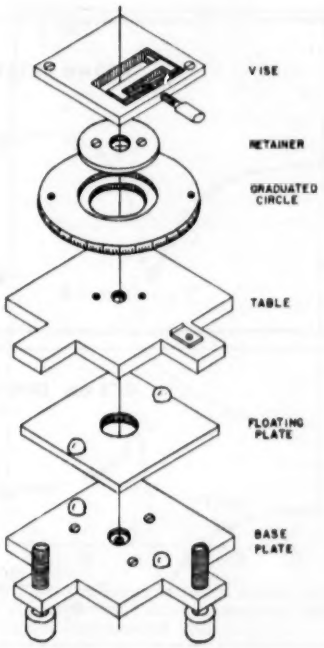

FIG. 1. Crystal holder.

III. RESULTS AND DISCUSSION

The transmitted intensity was measured for twenty calcite crystals. The calcite used was of high quality and of various geographical origin. Thicknesses from 0.05 cm to 0.620 cm were investigated. Figure 2 shows representative transmission curves. It is observed that for "thin" crystals the transmitted intensity decreases while for "thick" crystals the transmitted intensity increases. In the case of an "intermediate" crystal thickness, the transmitted intensity passes through a maximum and minimum. The short horizontal lines on each side of the curves in the figures give the intensity at a position about 10′ off the Bragg angle, this intensity representing the normal transmission through the calcite crystal. The background radiation of about 60 counts per minute has not been subtracted in these plotted intensity curves.

The absorption coefficients at the peak of each transmitted intensity curve (Fig. 2) and 10′ off the peak have been calculated. The ordinary exponential absorption law has been assumed, the thickness of

TABLE I. Measured values of calcite absorption coefficient off and at the diffracting position.

t_0 cm	0.075	0.102	0.130	0.159	0.210	0.226	0.257	0.513
μ_0 cm^{-1}	21.4	21.0	21.1	21.1	21.4	21.4	21.9	
μ cm^{-1}	18.4	16.3	14.4	12.7	12.3	11.8	10.7	9.32

TABLE II. Measured values of calcite absorption coefficient at anomalous transmission.

t_0 cm	0.307	0.351	0.390	0.397	0.412	0.482	0.515	0.563	0.573	0.600	0.620
μ cm^{-1}	14.5	10.8	11.8	8.57	12.6	10.9	11.3	6.61	9.44	11.3	9.59

[10] G. Borrman, Z. Physik **127**, 297 (1950); see also Schwarz, Brown, and Rogosa, Phys. Rev. **90**, 351 (1953).
[11] M. von Laue, Acta Cryst. **5**, 619 (1952).

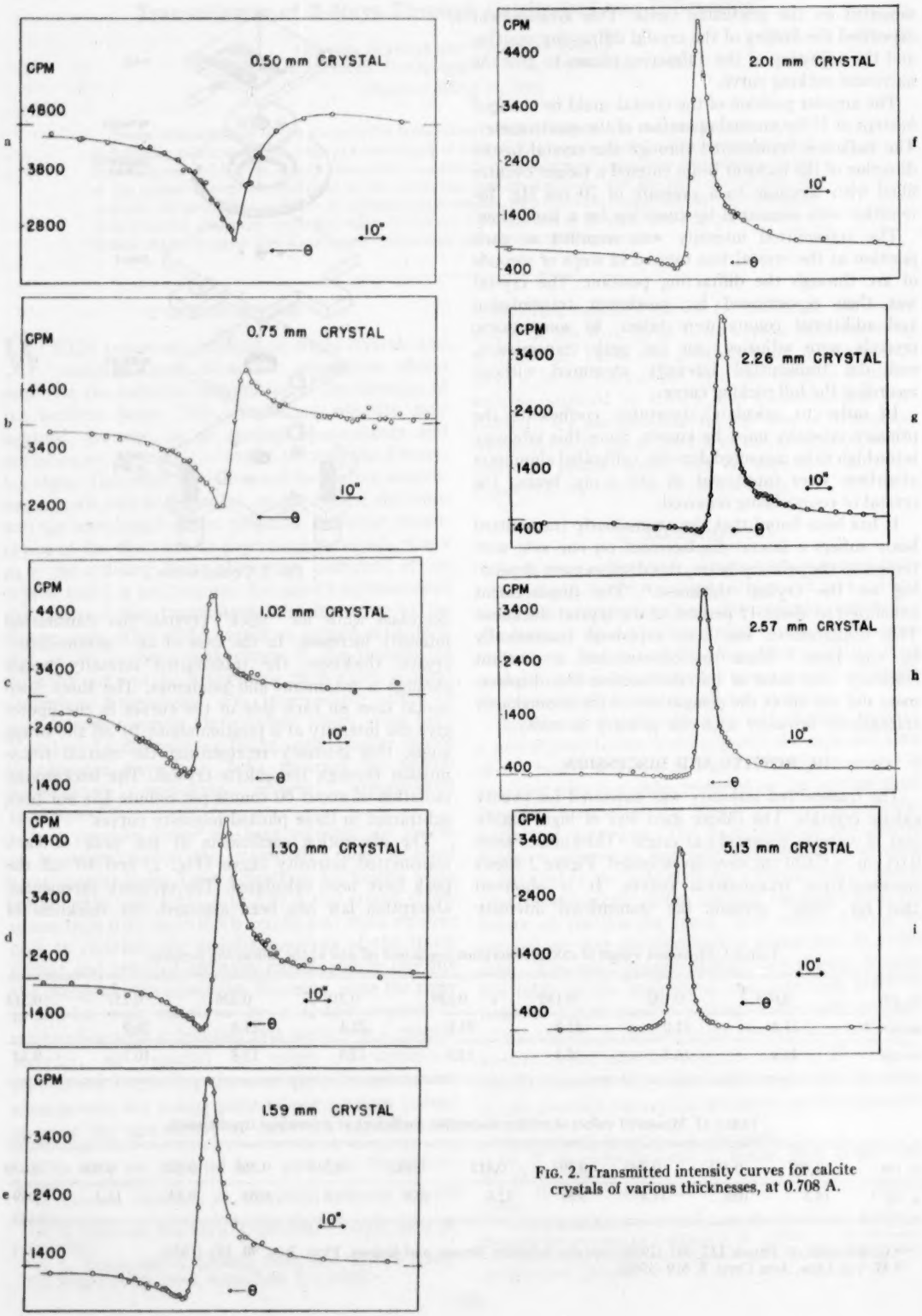

FIG. 2. Transmitted intensity curves for calcite crystals of various thicknesses, at 0.708 A.

absorber being taken as the thickness of the crystal measured in the direction of the incident radiation. This absorption coefficient μ which depends on crystal thickness is listed in Table I for various crystal thicknesses. The decrease in absorption coefficient with increasing crystal thickness is apparent. The absorption coefficients calculated from the measurement of the transmitted intensity of the other crystals are listed in Table II. In all cases the total number of counts accumulated in the intensity measurements at the diffracting position was such as to give the value of the absorption coefficient with a probable error of 2 percent or less. The normal absorption coefficient values were calculated in all cases when the transmitted intensity was high enough to permit the value to be given with a probable error of 5 percent or less. For "thick" crystals the transmitted intensity off the Bragg angle was not much above background.

The shape of the curves in Fig. 2 is in good agreement with the calculated curves of Hirsch[5] and Ramachandran and Kartha.[6] The range of crystal thicknesses investigated clearly shows the transition from extinction to anomalous transmission. Because of the unavoidable divergence of the x-ray beam from the monochromator, the experimental curves are broadened out. The width of the x-ray beam coming from the second crystal of the monochromator has been measured by translating a narrow slit with a counter across it. This has been done at several positions up to a distance of about 1000 cm from the crystal. Preliminary results indicate a divergence of about 8″ for the beam leaving the second crystal.

Zachariasen[7] has shown that for the thick crystal case the absorption coefficient at the diffracting position for anomalously transmitted radiation is given by

$$\mu=\mu_0\left[1+\frac{\log(8\epsilon\mu_0 t_0/\pi\gamma_0)+2}{2\mu_0 t_0/\gamma_0}-\epsilon\right],$$

where t_0 represents the perpendicular distance between the crystal faces and γ_0 is the cosine of the diffracting angle. Taking $\epsilon=0.941$ and $\mu_0=22.0$ cm^{-1}, we have plotted μ as a function of t_0/γ_0 in Fig. 3 for values of

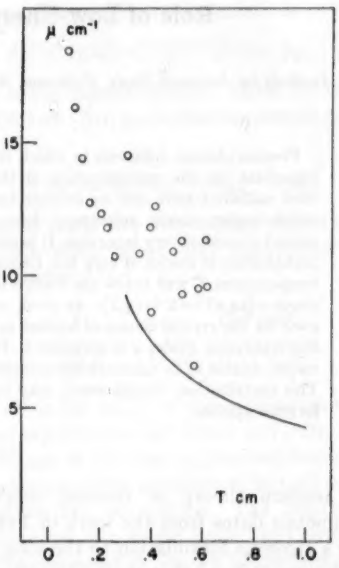

FIG. 3. Absorption coefficient of calcite crystal at 0.708 A as a function of thickness. Solid curve, theoretical calculation of Zachariasen. Circles, experimental measurements.

t_0/γ_0 from 0.3 cm to 1.0 cm. The experimentally measured values of μ are also shown in Fig. 3. Of twelve crystals belonging to the "thick" crystal case, two have been found which give an absorption coefficient approaching the theoretical value. Other values are too high and, as pointed out by Hirsch,[5] this is probably the result of imperfections which one would expect to find in thicker crystals. The measurements of the normal absorption coefficient served as a check on possible impurity content in the crystals. Because of the orientation of the internal diffracting planes in our arrangement, the straightforward path T through the crystal is 1.01 t_0.

We may conclude that our measurements for calcite are in substantial agreement with the results obtained by consideration of the dynamical theory of x-ray diffraction for perfect, absorbing crystals.

We wish to express our appreciation to Mr. Rudolph R. Verderber who assisted with the taking of data.

Role of Low-Energy Phonons in Thermal Conduction

CONYERS HERRING
Institute for Advanced Study, Princeton, New Jersey and Bell Telephone Laboratories, Murray Hill, New Jersey
(Received May 13, 1954)

Phonon-phonon collisions in which one of the phonons is of very low frequency have recently become important for the understanding of the thermoelectric powers of semiconductors at low temperatures. Such collisions have also an interest from the standpoint of thermal conduction, since previous theories, which neglect elastic anisotropy, have predicted a very large thermal conductivity for a hypothetical perfect crystal of very large size. It is shown here that elastic anisotropy has a drastic effect on the collision probabilities of modes of very low frequency. A relaxation time τ can be defined, for any mode, which at temperatures T well below the Debye temperature and for wave vectors q well within the acoustic range obeys $\tau(\lambda\mathbf{q},\lambda T)=\lambda^{-5}\tau(\mathbf{q},T)$. As $q\to 0$, $\tau^{-1}\sim A_a q^a$, where normally, for modes of the longitudinal branch, $a=2$ for the crystal classes of highest symmetry, 3 and perhaps sometimes 4 for those of lower symmetry. For transverse modes a is normally 1. These asymptotic laws, whose range of validity can be roughly estimated, enable us to calculate the contribution of the low-frequency longitudinal modes to the conductivity. This contribution, though small, may be perceptible at temperatures far above the range where Casimir's formula applies.

THE modern theory of thermal conduction in nonmetals dates from the work of Peierls,[1] who first gave a rigorous formulation to the idea, proposed much earlier by Debye,[2] that thermal resistance is due to the mutual scattering of vibrational waves, a scattering due to the anharmonicity of the interatomic forces. A number of papers have been written since, attempting to develop Peierls' picture in greater detail. As the theory is rather complicated, all these have made the plausible simplification of treating the medium as elastically isotropic. With this assumption it is easily shown that, if terms of higher than the third order are neglected in the elastic potential energy, the expression for the thermal conductivity of an infinite perfect crystal diverges.[3,4] This divergence is due to the fact that the relaxation time τ of a longitudinal mode of wave number q goes as q^{-4} when q is small,[3-5] so that $\int \tau q^2 dq$ diverges at the lower limit.

It has been felt generally that this divergence of the conductivity does not really occur for actual materials, since observations suggest that, except at very low temperatures, the conductivities measured for specimens of usual laboratory size are substantially the same as would be observed for an infinite crystal. To make the conductivity finite, or, more precisely, to avoid predicting that the measured conductivity should depend markedly on the size of the specimen, Pomeranchuk[3] invoked fourth-order terms in the elastic potential energy. This is rather unsatisfactory, as these terms must have an extremely small effect at moderately low temperatures. Herpin,[4] on the other hand, invoked imperfections in the crystal structure. This is also an unsatisfactory escape, since isolated impurities and lattice defects also give $\tau\propto q^{-4}$, while the number of dislocations and stacking faults present in a reasonably good crystal is too small to have an appreciable effect. Klemens,[6] in what is in many ways the most satisfactory treatment of thermal conduction, dismisses the divergence by a remark in a footnote to the effect that it is eliminated by Umklapp collisions. As far as I can see, this statement is not correct, at least for the type of dispersion relation normally expected.

The present study of low-energy phonons was stimulated by their influence on the thermoelectric power of semiconductors.[7-9] The most important object of this paper is therefore to get expressions for the variation of the relaxation time $\tau(\mathbf{q})$ of a phonon of wave number $\mathbf{q}$ with $\mathbf{q}$ and with temperature, for the low-energy acoustic modes which contribute to the scattering of charge carriers in semiconductors at moderately low temperatures. An important by-product, however, is the clarification of the role of these low-energy phonons in thermal conduction. Since the theory of thermoelectric power is itself a complicated subject, the application of the present results to thermoelectricity is given in a separate paper,[9] and we shall confine the present discussion to phonons and thermal conduction.

Briefly put, the thesis which we wish to develop here is that the elastic anisotropy of a crystal can cause the scattering of low energy longitudinal phonons to differ profoundly from the behavior predicted for an isotropic medium. For a great many crystals this difference entirely removes the divergence of the thermal conductivity; for many others it reduces the divergence to a logarithmic one. For these crystals the variation of conductivity with specimen size would be extremely small at temperatures above a few percent of the Debye temperature and over the practical range of

[1] R. Peierls, Ann. Physik **3**, 1055 (1929).
[2] P. Debye, *Vorträge über die kinetische Theorie der Materie und der Elektrizität* (Teubner, Leipzig, 1914).
[3] I. Pomeranchuk, J. Phys. (U.S.S.R.) **4**, 259 (1941); **6**, 237 (1942); Phys. Rev. **60**, 820 (1941).
[4] A. Herpin, Ann. Phys **7**, 91 (1952).
[5] L. Landau and G. Rumer, Physik. Z. Sowjetunion **11**, 18 (1937).
[6] P. G. Klemens, Proc. Roy. Soc. (London) **A208**, 108 (1951).
[7] H. P. R. Frederikse, Phys. Rev. **91**, 491 (1953); **92**, 248 (1953).
[8] T. H. Geballe, Phys. Rev. **92**, 857 (1953).
[9] C. Herring, Phys. Rev. **92**, 857 (1953); full paper to be published.

sizes; however, it might sometimes be measurable. Among the lower symmetry classes it is possible that crystals may exist for which the original divergence applies in full force. Such crystals should show a greater dependence of conductivity on size; however, the dependence would be conspicuous only for rather large single crystals of good quality.

I. THE RELAXATION TIME

Our main concern in this paper will be with temperatures rather smaller than the Debye temperature. In this range, as the calculations of Pomeranchuk[3] show, there are very few collisions involving four or more phonons, i.e., collisions in which the occupation numbers of four or more normal modes are altered. We may therefore restrict attention to three-phonon collisions. These are a consequence of the term U_3 in the elastic potential energy which is of the third order in the relative displacements of the atoms, or equivalently, for modes of long wavelength, of the third order in the strain amplitudes. Detailed expressions for the matrix elements of U_3 have been given by Herpin.[4] For our present purpose, since we are interested in long wavelengths and low temperatures, it will suffice to consider merely the dependence upon the phonon wave numbers when the latter are small. This dependence is determined by the fact that the strain in any normal vibration is proportional to the product of the amplitude by the wave number q, and the fact that the matrix element of the amplitude connecting states of quantum numbers N and $N-1$ is proportional to $(N/\omega)^{\frac{1}{2}}$, where ω is the frequency of the mode. Therefore for any three acoustic modes 0, 1, 2, whose wave vectors satisfy

$$\mathbf{q}_0+\mathbf{q}_1=\mathbf{q}_2, \tag{1}$$

we must have, since $\omega(\mathbf{q})\propto q$,

$$|(N_0, N_1, N_2|U_3|N_0-1, N_1-1, N_2+1)|^2 \propto q_0q_1q_2N_0N_1(N_2+1), \tag{2a}$$

$$|(N_0, N_1, N_2|U_3|N_0+1, N_1+1, N_2-1)|^2 \propto q_0q_1q_2(N_0+1)(N_1+1)N_2. \tag{2b}$$

Here and below the factor implied in each proportionality sign is independent of the N's and the magnitudes of the wave vectors, but depends on the directions of the wave vectors and the polarizations of the three modes. We may note, finally, that even if modes 1 and 2 are high-energy modes to which the acoustic approximation $\omega\propto q$ does not apply, the proportionality of the squared matrix element to q_0N_0 or $q_0(N_0+1)$ will still hold if mode 0 is in the acoustic range.

The transition probability for the process $N_{0,1}\rightarrow N_{0,1}-1$, $N_2\rightarrow N_2+1$, or for the reverse process, is appreciable only in the neighborhood of the surface S_1 in q_1-space where the energy conservation condition

$$\hbar\omega_0+\hbar\omega_1=\hbar\omega_2 \tag{3}$$

is satisfied. The transition probability associated with an element of area dS_1 of this surface is

$$dW(0,1\rightleftarrows 2)\propto|U|^2dS_1|\partial\Delta\omega/\partial q_{1n}|^{-1}, \tag{4}$$

where U is the matrix element, given for the acoustic case by (2a) or (2b), q_{1n} is the component of $\mathbf{q}_1$ normal to dS_1, and

$$\Delta\omega=\omega(\mathbf{q}_0+\mathbf{q}_1)-\omega(\mathbf{q}_0)-\omega(\mathbf{q}_1) \tag{5}$$

measures the departure from energy conservation.

With each mode $\mathbf{q}_0$ we may associate a relaxation time $\tau(\mathbf{q}_0)$ defined by[6]

$$\frac{1}{\tau(\mathbf{q}_0)}=-\lim_{N_0\rightarrow N_0^{(0)}}\frac{(dN_0/dt)_e}{N_0-N_0^{(0)}}, \tag{6}$$

where $N_0^{(0)}$ is the value of the occupation number N_0 in thermal equilibrium and where $(dN_0/dt)_e$ is the total rate of change of N_0 due to phonon-phonon collisions when N_0 departs from equilibrium but all other modes have equilibrium occupation. The relation of this "relaxation time of a single mode" to thermal conduction will be discussed in Sec. IV below; for the present we wish merely to investigate the asymptotic behavior of this quantity for modes of very low frequency. Now $(dN_0/dt)_e$ is a sum of transition probabilities

$$(dN_0/dt)_e=W(2\rightarrow 0,1)-W(0,1\rightarrow 2)+W(1,2\rightarrow 0)-W(0\rightarrow 1,2), \tag{7}$$

where the first two W's are to be obtained by integrating (4) and the last two W's by evaluating similar expressions with 0 and 2 interchanged. For the contribution of an element dS_1 to the part of (6) arising from the first two W's we have, if (2a) and (2b) are adequate on dS_1,

$$-\lim_{N_0\rightarrow N_0^{(0)}}\frac{dW(2\rightarrow 0,1)-dW(0,1\rightarrow 2)}{N_0-N_0^{(0)}} =-\frac{\partial}{\partial N_0}[dW(2\rightarrow 0,1)-dW(0,1\rightarrow 2)] \propto q_0q_1q_2(N_1^{(0)}-N_2^{(0)})dS_1|\partial\Delta\omega/\partial q_{1n}|^{-1}. \tag{8}$$

If any of the q's are too large for (2a) and (2b) to apply, as for Umklapp collisions, only the proportionality to these q's is altered in (8). Consider now the contribution of the last two W's in (7). For these transitions the modes 1 and 2 must have lower frequencies than mode 0, so the area of S_1 is of order q_0^2 as $q_0\rightarrow 0$. The expression analogous to (8) contains $N_1^{(0)}+N_2^{(0)}+1$, a quantity of the order q_0^{-1}, in place of $N_1^{(0)}-N_2^{(0)}$. As the last factor in (8) is finite as $q_0\rightarrow 0$, the total contribution to (6) from the last two W's in (7) is $O(q_0^4)$. Thus $1/\tau(\mathbf{q}_0)$ will be $O(q_0^4)$ as $q_0\rightarrow 0$ if integration of (8) on dS_1 gives $O(q_0^4)$ or smaller, while the value obtained from (8) will predominate if it is larger than $O(q_0^4)$. Thus the problem of determining

the asymptotic dependence of $\tau(\mathbf{q}_0)$ on q_0 is reduced to the problem of evaluating the integral of (8).

In the next two sections we shall determine the behavior of the integral of (8) by determining the form of the energy conservation surface S_1 and the magnitude of the normal derivative of $\Delta\omega$ on it. However, one or two scaling laws for $\tau(\mathbf{q}_0)$ can be derived without any detailed information on these topics. Consider a range of temperatures low enough so that all the phonons which take appreciable part in the scattering of phonons of type $\mathbf{q}_0$ are in the acoustic range. In this range let us compare the relaxation time of $\mathbf{q}_0$ at temperature T and that of $\lambda\mathbf{q}_0$ at temperature λT. Since all phonons are in the acoustic range, the conservation surface S_1 for $\lambda\mathbf{q}_0$ differs only by a scale factor λ from that for $\mathbf{q}_0$. Therefore the dS_1 in (4) is $\propto\lambda^2$. Since $N^{(0)}(\lambda\mathbf{q},\lambda T)$ is the same as $N^{(0)}(\mathbf{q},T)$, $|U|^2\propto\lambda^3$, and as the last factor in (4) is independent of scale, every W in (7) is $\propto\lambda^5$. Thus in the low temperature range

$$\tau(\lambda\mathbf{q},\lambda T)\propto\lambda^{-5}. \tag{9}$$

Finally, we may note that for fixed $\mathbf{q}$'s (8) and its counterpart for the last two W's in (7) contain T only through a term linear in the $N^{(0)}$'s. Therefore in the limit of high temperatures, where all modes are highly excited,

$$\tau(\mathbf{q})\propto T^{-1} \tag{10}$$

provided, of course, that higher order processes such as four-phonon collisions are still negligible compared with three-phonon collisions.

II. THE ENERGY CONSERVATION CONDITION

We are interested in the form of the surface S_1 in q_1-space on which the energy conservation Eq. (3) and the wave vector conservation Eq. (1) are simultaneously satisfied, for a given $\mathbf{q}_0$, ω_0. Moreover, our main interest is in very small values of q_0. Consider the two surfaces $\omega(\mathbf{q})=\omega_1$ and $\omega(\mathbf{q})=\omega_1+\omega_0$ in $\mathbf{q}$-space. Let the second of these be displaced rigidly by the vector $-\mathbf{q}_0$, as shown in Fig. 1. The line of intersection (if any) of this displaced surface with the first surface is then a line in q_1-space on which the two conservation conditions (1), (3) are fulfilled, and as ω_1 varies this line generates the desired surface S_1. It is clear from the examples of Fig. 1 that as $q_0\to 0$ intersections will always occur in the neighborhoods of points such as P, Q, where the frequencies of two branches coincide, but may or may not occur in places far removed from such points. We shall use the term *point of degeneracy* to designate any such point $\mathbf{q}$ where two or more modes of wave vector $\mathbf{q}$ have the same frequency. Degeneracies at certain points of $\mathbf{q}$-space or along certain lines or planes are often necessitated by crystal symmetry.[10,11] Degeneracies may also occur accidentally,[12] although this is not likely to occur for crystals of high symmetry at points of the acoustic branch close to the origin, the region of major interest to us. We have to examine the possibility of satisfying the conservation conditions as $q_0\to 0$ for fixed direction of $\mathbf{q}_0$, for the following cases:

(i) *At points R of the ω_1-surface not in the neighborhood of any point of degeneracy, when at every such point R the component of group velocity in the direction of $\mathbf{q}_0$ is less than the phase velocity of the mode 0.* This is the case for points such as R in Fig. 1(a). For such points the different branches of the ω_1-surface have a finite separation, so as $q_0\to 0$ no such point can be a point of intersection of one branch of the ω_1-surface with a different branch of the displaced ω_2-surface. But intersections of a given branch of the former with the same branch of the latter are also impossible for sufficiently small q_0, since when only a single branch is involved (1) and (3) imply

$$\mathbf{q}_0\cdot\partial\omega(\mathbf{q}_1)/\partial\mathbf{q}_1+O(q_0^2)=\omega(\mathbf{q}_0), \tag{11}$$

and this must become impossible as $q_0\to 0$ if the component of the group velocity $\partial\omega(\mathbf{q}_1)/\partial\mathbf{q}_1$ along $\mathbf{q}_0$ is less than $\omega(\mathbf{q}_0)/q_0$. The latter condition will probably nearly always be fulfilled when mode 0 is a longitudinal mode (i.e., belongs to the highest frequency branch of the acoustic spectrum).

(ii) *At points J not in the neighborhood of any point of degeneracy, when for some such points J the component of group velocity in the direction of $\mathbf{q}_0$ is greater than the phase velocity of mode 0.* Here again intersections of different branches are ruled out, but intersections involving only one branch will occur, since as $q_0\to 0$ Eq. (11) will always be satisfied somewhere. An example is shown at J in Fig. 1(b). For the present case the intersection line will approach a limiting position on the ω_1-surface as $q_0\to 0$, and so the area of those parts of the conservation surface S_1 which lie outside the neighborhoods of contact points will approach a finite limit.

It is easy to show that this case must occur for small (but not infinitesimal) values of ω_1, whenever the mode $\mathbf{q}_0$ belongs to one of the transverse branches, i.e., does not belong to the highest frequency branch. For when ω_1 is small enough to be practically uninfluenced by dispersion, the construction of Fig. 1 amounts to finding the intersection of the ω_1-surface with the surface formed from this by a linear projection of each point away from that point F of the ω_1-surface which has $\omega_1,\mathbf{q}_1\propto\omega_0,\mathbf{q}_0$. Such a linear projection is illustrated in Fig. 1(c), which, however, is drawn for a longitudinal mode and a rather large ratio q_0/q_1, instead of the case we wish to consider now. As $q_0\to 0$, such an intersection will always occur in the neighborhood of any point where the ω_1-surface is tangent to a line through F. Such a tangency will always occur unless (as in the case shown) F lies on the innermost branch of the ω_1-surface, i.e., unless the mode $\mathbf{q}_0$ is longitudinal.

(Although it is legitimate to make a construction

[10] Bouckaert, Smoluchowski, and Wigner, Phys. Rev. **50**, 58 (1936).
[11] C. Herring, Phys. Rev. **52**, 361 (1937).
[12] C. Herring, Phys. Rev. **52**, 365 (1937).

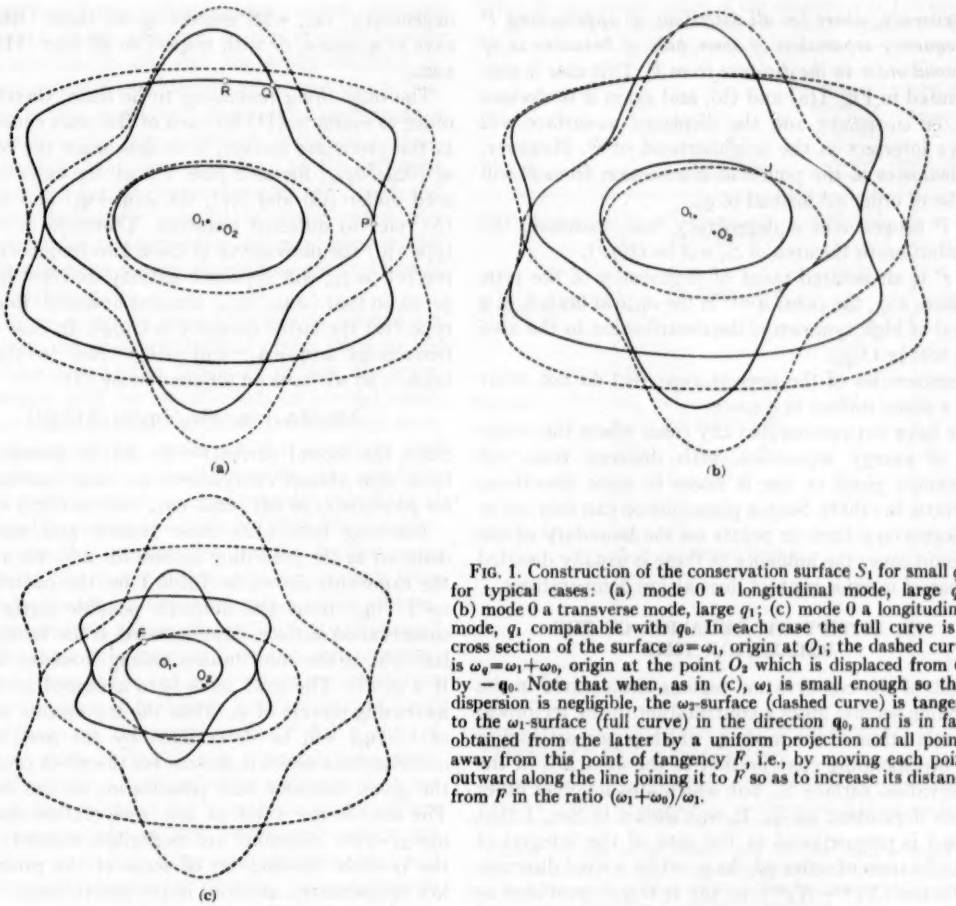

FIG. 1. Construction of the conservation surface S_1 for small q_0, for typical cases: (a) mode 0 a longitudinal mode, large q_1; (b) mode 0 a transverse mode, large q_1; (c) mode 0 a longitudinal mode, q_1 comparable with q_0. In each case the full curve is a cross section of the surface $\omega=\omega_1$, origin at O_1; the dashed curve is $\omega_2=\omega_1+\omega_0$, origin at the point O_2 which is displaced from O_1 by $-\mathbf{q}_0$. Note that when, as in (c), ω_1 is small enough so that dispersion is negligible, the ω_2-surface (dashed curve) is tangent to the ω_1-surface (full curve) in the direction $\mathbf{q}_0$, and is in fact obtained from the latter by a uniform projection of all points away from this point of tangency F, i.e., by moving each point outward along the line joining it to F so as to increase its distance from F in the ratio $(\omega_1+\omega_0)/\omega_1$.

like that described, based on the conception of a point of tangency F, it should be noted that there will normally be a tiny separation of the two frequency surfaces in the region of their near-tangency, because of dispersion in the velocity of sound. This makes it unnecessary to consider collisions with $q_1 \approx F$.)

(iii) *At points in the neighborhood of a point of degeneracy Q, or of a line or plane of degeneracy, where for all directions of approaching Q the frequency separations of the branches which come together at Q are all of the first order in the distance from the degeneracy point, line, or plane.* For this case, illustrated in Fig. 1(a) and (b), the ω_1-surface and the displaced ω_2-surface will always intersect in the neighborhood of Q, regardless of group velocity considerations. Except in the vanishingly improbable case where the intersection occurs exactly at Q, the points of intersection will occur at distances from Q which are $O(q_0)$ as $q_0 \to 0$.

If Q ranges over such a degeneracy line, therefore, this part of S_1 will be a thin cylinder about this line, and the contribution to the area of S_1 will be $O(q_0)$.

Although line degeneracies are the most important type in the present category (iii), degeneracy at all points of a boundary plane of the Brillouin zone is possible for crystals of certain space groups,[11] and will be important for the relaxation times of low-energy longitudinal modes in these cases. The crystals for which this will occur are those with a boundary plane of the Brillouin zone normal to a twofold screw axis. The part of the conservation surface S_1 neighboring such a plane has an area which obviously approaches a finite limit as $q_0 \to 0$.

As we shall see in the next section, the contributions from isolated degenerate points Q are usually unimportant when, as we are assuming under the present heading (iii), the frequency separations of the branches are of the first order in the distance from Q. The principal case where such a point may be important is that of a crystal of such low symmetry that no degeneracies occur except at $q=\omega=0$. For this contact point q_1 and q_2 are both of the same order as q_0. Whether the point is at $\mathbf{q}=0$ or not, the contribution to S_1 from such a point will be $O(q_0^2)$.

(iv) *At points P in the neighborhood of a point or line*

of degeneracy, where for all directions of approaching P the frequency separation of some pair of branches is of the second order in the distance from P. This case is also illustrated in Fig. 1(a) and (b), and again it is obvious that the ω_1-surface and the displaced ω_2-surface will always intersect in the neighborhood of P. However, the distances of the points of intersection from P will now be of order $q_0^{\frac{1}{2}}$ instead of q_0.

If P ranges over a degeneracy line, therefore, the contribution to the area of S_1 will be $O(q_0^{\frac{1}{2}})$.

If P is an isolated point of degeneracy of the type specified, e.g., the point $\mathbf{q}=0$ in the optical branch of a crystal of high symmetry, the contribution to the area of S_1 will be $O(q_0)$.

Degeneracies of the present type (iv) do not occur over a plane surface in q-space.

We have not enumerated any cases where the variation of energy separation with distance from the degeneracy point or line is linear in some directions, quadratic in others. Such a phenomenon can only occur for degeneracy lines or points on the boundary of the Brillouin zone; the influence of these is usually dwarfed by that of interior contact lines at low temperatures.

III. ASYMPTOTIC BEHAVIOR OF THE RELAXATION TIME

Each of the conservation regions enumerated in the preceding section gives a contribution to the reciprocal relaxation time of the mode $\mathbf{q}_0$ which is proportional to the corresponding contribution to the area ΔS_1 of the conservation surface S_1, but which also involves other factors dependent on $\mathbf{q}_0$. It was shown in Sec. I that $1/\tau(\mathbf{q}_0)$ is proportional to the sum of the integral of (8) and a term of order q_0^4. As $q_0 \to 0$ for a fixed direction the factor $(N_1^{(0)}-N_2^{(0)})$ in (8) is $O(q_0)$, provided ω_1 and ω_2 remain finite, as they will in all cases except that of Fig. 1(c). When this proviso is fulfilled, the integral of (8) over a given part of the S_1-surface gives

$$\text{contrib. to } 1/\tau(\mathbf{q}_0) \propto q_0^3 \Delta S_1 |\partial\Delta\omega/\partial q_{1n}|^{-1}, \quad (12)$$

provided the factor implied by the proportionality sign in expressions such as (2) for the matrix element remains finite as $q_0 \to 0$.

The assumption of finiteness of the matrix element needs to be examined group-theoretically, of course, since the commonest cause of degeneracy is the occurrence of symmetry operations in the space group of the crystal, and it is conceivable that this same symmetry property may cause the matrix element in question to vanish. The necessary examination is carried out in Appendix A and summarized in Table III there. The result is that, at least for degeneracies on interior lines and boundary planes of the Brillouin zone, symmetry never requires the matrix element to approach zero as $q_0 \to 0$, except for certain special directions and polarizations of the mode $\mathbf{q}_0$. For crystals of the cubic system no mode $\mathbf{q}_0$ is "special" in this sense with respect to all members of an equivalent set of lines of degeneracy, i.e., with respect to all three (100) type axes in $\mathbf{q}_1$-space, or with respect to all four (111) type axes.

The only thing remaining to be done, therefore, in order to evaluate (11) for each of the cases enumerated in the preceding section, is to determine the behavior of $|\partial\Delta\omega/\partial q_{1n}|$ for each case. For all the cases enumerated under (iii) and (iv), the $\omega(\mathbf{q}_0+\mathbf{q}_1)$ and $\omega(\mathbf{q}_1)$ in (5) refer to different branches. Therefore in cases of type (iii) the derivatives of these two frequencies with respect to q_{1n} will approach entirely different limits as $q_0 \to 0$, so that $|\partial\Delta\omega/\partial q_{1n}|$ remains bounded. In cases of type (iv) the latter quantity is $O(q_0^{\frac{1}{2}})$. In case (ii) the frequencies $\omega(\mathbf{q}_0+\mathbf{q}_1)$ and $\omega(\mathbf{q}_1)$ refer to the same branch, so we have on differentiating (5)

$$\partial\Delta\omega/\partial q_{1n} = \mathbf{q}_0 \cdot \partial^2\omega_1/\partial\mathbf{q}_1\partial q_{1n} + O(q_0^2). \quad (13)$$

Since the second derivative in (13) in general differs from zero almost everywhere, we may conclude that for points of type (ii) $|\partial\Delta\omega/\partial q_{1n}|$ will be $O(q_0)$ as $q_0 \to 0$.

Inserting into (12) these results and the forms deduced in the preceding section for ΔS_1, we arrive at the exponents shown in Table I for the contributions to $1/\tau(\mathbf{q}_0)$ from the different possible parts of the conservation surface. Also included in the table, on the last line, is the contribution arising from the last two W's of (7). The rows have been arranged in order of increasing powers of q_0. Thus the asymptotic behavior of $1/\tau(\mathbf{q}_0)$ will be determined by the first of these contributions which is present for the given crystal and the given direction and polarization of the mode $\mathbf{q}_0$. The entries are valid at any temperature for which higher-order collisions are negligible, subject only to the possible freezing-out of some of the processes at low temperature, as noted in the last column.

It is now a straightforward matter to compute, for any space group, which of the rows of Table I are required by crystal symmetry to be present. Such a calculation will give an upper limit to the exponent of $\mathbf{q}_0$ in the asymptotic behavior of $1/\tau(\mathbf{q}_0)$. We can of course not predict with certainty that this upper limit

TABLE I. Contributions to the asymptotic behavior of $1/\tau(\mathbf{q}_0)$ as $q_0 \to 0$.

Type of phonon collision		Illustration in Fig. 1	Behavior of $1/\tau(\mathbf{q}_0)$ for most modes	Remarks
$2\rightleftarrows 0, 1, q_1 \gg q_0$	(ii)	J in (b)	q_0	Valid for any T
	(iii) plane	Q in (a)	q_0^2	High T only
	(iv) line	P in (a)	q_0^2	Valid for any T if interior line
	(iv) point	P in (a)	$q_0^{5/2}$	High T only
	(iii) line	Q in (a)	q_0^3	Valid for any T if interior line
	(iii) point	Q in (a)	q_0^4	Valid for any T
$2\rightleftarrows 0, 1, q_1 \sim q_0$		G in (c)	q_0^4	Valid for any T
$0\rightleftarrows 1, 2$			q_0^4	Valid for any T

Except for cubic crystals, there will usually exist special combinations of direction and polarization with longer relaxation times (higher exponents) than shown in the second to fifth rows.

will be realized for any given crystal, unless we know the complete elastic spectrum of this crystal, for two reasons: one has to do with the group velocity inequalities involved in deciding whether case (ii) applies; the other is that accidental degeneracy may cause a higher row to apply than symmetry degeneracy. However, it is likely that the upper limit to the exponent will be realized for longitudinal modes (i.e., modes of the highest frequency branch) in many cases. For transverse modes, or course, the argument given under (ii) of the preceding section shows that the first line of Table I always applies.

It would of course be very laborious to construct a table giving the group-theoretical upper limit to the exponent for each of the 230 space groups. However, if we consider only the contributions to $1/\tau(\mathbf{q}_0)$ which arise from acoustic modes $\mathbf{q}_1$ inside the Brillouin zone, as distinguished from modes on the boundary and modes belonging to optical branches, the problem simplifies greatly, since one need consider only lines of degeneracy lying inside the Brillouin zone. The enumeration of these line degeneracies and the decision as to whether case (iii) or case (iv) applies can be made from a knowledge merely of the point group of the crystal. The procedure for a given point group G is as follows.[13] Determine those subgroups of G whose unit representations are contained in the polar vector representation of G once and once only.[14] Each such subgroup G^i will be the "group of the wave vector"[10] for a line of points $\mathbf{q}_i$ in $\mathbf{q}$-space, i.e., G^i will comprise those operations which take a mode of wave vector $\mathbf{q}_i$ into the same or another mode of the same wave vector. Select those representations of the various G^i which are contained in the polar vector representation of G and which are two-dimensional (higher dimensionalities will not occur) or which, though one-dimensional, are required by the time-reversal symmetry of the problem[11] to coincide in frequency with another one-dimensional representation. These will be the representations to which the various line degeneracies belong. Coincidence in frequency of two modes belonging to one-dimensional representations of a G^i will occur only for the cases listed in Table II of reference 11. For each such representation or pair of representations of a G^i, determine whether a vector operator with the transformation properties of a vector normal to $\mathbf{q}_i$ can split the degeneracy in first order. If it can, the frequency separation in the neighborhood of the line will be linear in the distance from the line, so that case (iii) will apply.[12] If it cannot, the frequency separation will be quadratic and case (iv) will apply.

Table II summarizes in the next to the last column the results obtained for the various point groups by the procedure just outlined. However, these results must be used with caution, as they may be quite misleading in a certain class of cases. For example, consider the scattering of a low-frequency longitudinal mode $\mathbf{q}_0$ by modes $\mathbf{q}_1$ in the neighborhood of the line $q_y=q_z=0$ in the Brillouin zone of a cubic crystal. If the crystal is of class O_h, the transverse modes are degenerate all along this line, and there will be a scattering contribution from a surface in $\mathbf{q}_1$-space closely surrounding this line. If the crystal is of class O, on the other hand, the procedure outlined above predicts no degeneracy along this line, hence no contribution to the scattering, if q_0 is small enough. But in the acoustic approximation, i.e., with neglect of the dispersion of the sound waves, the frequencies along this line are given by a secular equation involving the

TABLE II. Asymptotic values of the exponent a in $1/\tau(\mathbf{q}_0)\propto q_0^a$, for longitudinal acoustic modes in various crystal classes.

System	Class	G^i for lines of degeneracy	Type of frequency variation near line, for acoustic branch	Dominant value of a for most directions: With dispersion[a]	Dominant value of a for most directions: Without dispersion[b]
Cubic	O_h	C_{4v}, C_{3v}	(iv), (iii)	2	2
	O	no degen. lines		4	2
	T_d	C_{2v},[c] C_{3v}	(iv), (iii)	2	2
	T_h	C_{3v}	(iii)	3	2
	T	no degen. lines		4	2
Hexagonal	D_{6h}	C_{6v}	(iv)	2	2
	D_6	no degen. lines		4	2
	C_{6v}	C_{6v}	(iv)	2	2
	C_{6h}	C_6[c]	(iv)	2	2
	C_6	no degen. lines		4	2
Trigonal	D_{3h}	C_{3v}	(iii)	3	3
	C_{3h}	no degen. lines		4	3
	D_{3d}	C_{3v}	(iii)	3	3
	D_3	no degen. lines		4	3
	C_{3v}	C_{3v}	(iii)	3	3
	C_{3i}	C_3[c]	(iii)	3	3
	C_3	no degen. lines		4	3
Tetragonal	D_{4h}	C_{4v}	(iv)	2	2
	D_4	no degen. lines		4	2
	C_{4v}	C_{4v}	(iv)	2	2
	C_{4h}	C_4[c]	(iv)	2	2
	C_4	no degen. lines		4	2
	V_d	C_{2v}[c]	(iv)	2	2
	S_4	C_2[c]	(iv)	2	2
Orthorhombic, monoclinic, and triclinic		no degen. lines		4	3 or 4

[a] Tabulated a is $\lim_{q\to 0}[-d\ln\tau(\mathbf{q},T)/d\ln q]$.

[b] Tabulated a is $\lim_{q\to 0}\lim_{\lambda\to 0}[-d\ln\tau(\lambda\mathbf{q},\lambda T)/d\ln(\lambda q)]$.

[c] Cases where two one-dimensional representations of G^i are required by time-reversal symmetry to have the same frequency.

Except for the cubic classes and for the cases where $a=4$, there will usually be special combinations of direction and polarization of the mode q_0 with longer relaxation times (higher a than those shown). However, a will never exceed 4.

For any direction of q_0 which is not "special" in the sense mentioned above, an entry 2 in the table will be the true value of a, rather than merely an upper limit, except when the group velocity condition (ii) of Sec. II is fulfilled. Similarly an entry 3 will be the true value when (ii) does not apply and when the temperature is sufficiently low. For an entry 4 to be the true value, it suffices that these two conditions be satisfied and that there be no accidental degeneracy.

[13] For a fuller exposition of the theory underlying this procedure see references 10, 11, and 12.

[14] For tables of characters of the point groups see E. Wigner, Nachr. Akad. Wiss. Göttingen, Math-physik. Kl., p. 133 (1930).

elastic constants c_{11}, c_{12}, and c_{44} in just the same way as for class O_h, and so in this approximation there is degeneracy on this line. The truth is, therefore, that the frequencies of the two transverse modes going with a $\mathbf{q}_1$ in the x direction are always different, but that as $q_1 \to 0$ their difference becomes a smaller and smaller fraction of the frequency of either. If the temperature is low, the modes $\mathbf{q}_1$ which are most important in the scattering of $\mathbf{q}_0$ will be modes which come very close to being degenerate along the coordinate axes, and for any given ratio of $\hbar\omega_0$ to kT the scattering processes will become, as $T \to 0$, qualitatively the same as for class O_h. Thus to assess the significance of the entries in the next to the last column of Table II one should have, for comparison, values of the exponent computed with neglect of dispersion. These can easily be obtained by analyzing the consequences of crystal symmetry for the solution of the 3×3 secular equation for acoustic waves without dispersion. The results are given in the last column of Table II.

At temperatures sufficiently low for (9) to apply, the temperature variation of $1/\tau(\mathbf{q}_0)$ is given by

$$1/\tau(\mathbf{q}_0) \propto q_0{}^a T^{b-a}, \tag{14}$$

where a is the exponent given in Table II.

Finally, a word or two should be said about how small q_0 must be in order for the asymptotic behavior of Table II to be approximately realized. Consider, for example, the intersections near the points P and Q in Fig. 1(a). For the conditions shown, the linear behavior of ω_1 near Q is approximately valid out to the intersection, but the quadratic behavior near P has become more nearly a linear one before the intersection has occurred. Thus the contribution to $1/\tau(\mathbf{q}_0)$ from the neighborhood of P already departs considerably from the asymptotic behavior. The departure is less pronounced at the point diametrically opposite P. Still, it is clear that for these two types of points the contribution to $1/\tau(\mathbf{q}_0)$ from any given ω_1-surface will not have the asymptotic form until ω_0 is a small fraction of ω_1.

A sample plot of the type of Fig. 1 was made for the low energy acoustic spectrum of germanium, using the known elastic constants.[15] A study of this suggested that the contribution from a given scattering phonon frequency ω_1 to the $1/\tau(\mathbf{q}_0)$ of a longitudinal mode should be fairly well proportional to $q_0{}^2$ for $\omega_0 < 0.05\omega_1$, but not at all for $\omega_0 = 0.10\omega_1$. Now because of the way the various factors in (8) depend on $\mathbf{q}_1$ or ω_1, the phonons which contribute most to the scattering at low temperatures are those with energies $\hbar\omega_1$ rather larger than kT. For sufficiently small q_0, the median $\hbar\omega_1$ of all the contributions to $1/\tau(\mathbf{q}_0)$ can in fact be shown to be close to $3kT$ for a crystal of the type giving $1/\tau(\mathbf{q}_0) \propto q_0{}^2$ at low T. For such a crystal, therefore, we might expect the asymptotic behavior to be approximated for longitudinal modes with $\hbar\omega_0$ below something like $0.15kT$.

For a crystal giving $1/\tau(\mathbf{q}_0) \propto q_0{}^3$, with an over-all degree of elastic anisotropy similar to that found for germanium, one might expect asymptotic behavior to be approximated out to a slightly larger value of ω_0/ω_1 than that mentioned in the preceding paragraph. On the other hand, the median ω_1 would be lower. So the critical $\hbar\omega_0/kT$ for asymptotic behavior might well be about the same.

For crystals which give $1/\tau(\mathbf{q}_0) \propto q_0{}^4$ the asymptotic behavior should be realized when q_0 is small enough so that the conservation condition can only be satisfied by modes $\mathbf{q}_1$ with frequencies in the equipartition range. The limiting q_0 for this will depend on the minimum separation in sound velocity between the transverse branches. If this separation is of the order of 10 percent, for example, absence of an energy-conserving collision in Fig. 1(c) requires that the radii of the dashed curves, measured from F, be no more than, say, 7 percent greater than those of the corresponding full curves, so that $\omega_0/\omega_1 \lesssim 0.07$. If this is to hold for values of $\hbar\omega_1$ as small as $\frac{1}{2}kT$ or less, we must have, as the condition for asymptotic behavior to be realized, something like $\hbar\omega_0 < 0.03kT$.

For longitudinal modes $\mathbf{q}_0$ of an elastically isotropic continuum, only the last two lines of Table I apply; this is the result of Landau and Rumer,[5] Pomeranchuk,[8] and Herpin.[4] It is interesting to consider the behavior of $\tau(\mathbf{q}_0)$ with decreasing q_0 for longitudinal waves in a crystal which is almost elastically isotropic, but not quite. For such a crystal, at low T, $\tau(\mathbf{q}_0)$ will behave as for an isotropic body until q_0 gets small enough for intersections of types (iii) or (iv) to occur. The critical q_0 below which such intersections will occur will be one for which ω_0 is of the order of the frequency difference between the two transverse branches, for the modes most important in scattering. Thus this critical q_0 will become smaller and smaller the more nearly the crystal approximates elastic isotropy. When $q_0 \ll$ this critical value, the relaxation time will usually be determined by one of the upper rows of Table I.

IV. THERMAL CONDUCTION AT LOW TEMPERATURES

We wish now to see if the long relaxation times which the theory predicts for longitudinal acoustic phonons of long wavelength can have a significant effect on the thermal conductivity. To this end we shall use the standard formula[6] for the thermal conductivity, which is based on the assumption that the recovery of the phonons from the perturbing influence of the temperature gradient is describable by a relaxation time $\tau(\mathbf{q})$. According to this formula each mode of a unit volume of the crystal contributes an amount $v_\mu v_\nu \tau C_q$ to the thermal conductivity tensor $\kappa_{\mu\nu}$, where $\mathbf{v}(\mathbf{q})$ is the group velocity of the mode $\mathbf{q}$ and C_q is its heat capacity. We shall first undertake to show that for the calculation

[15] Bond, Mason, McSkimin, Olsen, and Teal, Phys. Rev. 78, 176 (1950).

of the contribution of the modes of very low frequency it is indeed legitimate to use this formula, with $\tau(\mathbf{q})$ interpreted as the relaxation time of a single mode, defined by (6). Then we shall derive expressions for the contribution of these low frequency modes to the conductivity. These expressions will depend on the size of the specimen, since as $q \to 0$ phonon-phonon scattering will eventually become less important in determining $\tau(\mathbf{q})$ than scattering from the boundaries of the specimen. The result will therefore be a predicted dependence of thermal conductivity on size, valid at temperatures where the great majority of the phonons are limited by phonon-phonon scattering and only the lowest frequency longitudinal modes are dominated by boundary scattering. It will thus give information on how the size effect diminishes as the temperature is raised from the range where all modes are dominated by boundary scattering[16] to the range where boundary scattering is completely negligible.

We have first, then, to justify the use of the relaxation times of single modes, i.e., of (6) combined with boundary scattering, to calculate the contribution of low frequency modes to the thermal conductivity. This procedure could fail if, and only if, the rate of randomization of the energy flux associated with a particular mode in thermal conduction were significantly different from what it would be if all the other modes were in equilibrium. These two rates of randomization may differ considerably for modes of thermal energy and above, but for the low-energy longitudinal modes they cannot differ very much under most circumstances. The reason is that in a thermal gradient the latter modes, because of their long relaxation times, are much more "off balance" than the modes with which they have most of their collisions.[17] An exception may occur at very low temperatures, when the Umklapp collisions which the phonons require in order to get rid of their heat current may become rare enough to give a relaxation time comparable with the $\tau(\mathbf{q}_0)$'s we have been discussing. Also, at lowest temperatures all modes become limited by boundary scattering, so all have the same unbalance. In this condition (6) will not correctly describe the phonon-phonon scattering rate, but this will not matter much because boundary scattering predominates.

Having accepted the use of (6), let us consider explicitly the contribution of the low-frequency longitudinal modes to the thermal conductivity κ in a given direction x, i.e., to $\sum v_x^2 \tau C_q$. For the low-energy modes of interest to us, C_q is very close to the Boltzmann constant k, so if c is an average longitudinal sound velocity we can write

$$\kappa \approx \text{constant} + (c^2 k/8\pi^3) \int \tau(q) q^2 dq \cos^2\theta d\Omega, \quad (15)$$

where θ is the angle between the group velocity of mode $\mathbf{q}$ and the direction in which κ is measured and where the integration is over longitudinal modes with q's in some neighborhood of the origin. Variations in the dimensions or crystal grain size of the specimen, and sometimes also variations in its dislocation content, can affect the value of the integral in (15). However, in the case of interest to us these factors will have much less effect on the contributions from modes with shorter τ's, and so we have lumped these together in the "constant" term. This will clearly be justified if $\tau(\mathbf{q})$ increases sufficiently rapidly with decreasing q; a simple calculation, which need not be given in detail, shows that the size-dependence of the integral in (15) outweighs that of the "constant," in the limit of large specimens or high temperatures, whenever $\tau(q) \propto q^{-a}$ with $a > 3/2$. This is fulfilled for all the cases listed in Table II.

For a crystal sufficiently free of dislocations, then, we can calculate the size-dependence of the conductivity, in the range of sizes and temperatures where this dependence is very small, by evaluating the integral in (15) with a $\tau(\mathbf{q})$ which follows one of the laws given in Table II until $c\tau(\mathbf{q})$ becomes comparable with the diameter L of the crystal, and which for smaller q departs from its behavior in an infinite crystal and approaches a constant limit $\tau_b \approx L/c$. The usual procedure in cases of this sort is to assume τ^{-1} to be compounded additively out of τ_b^{-1} and the phonon-phonon scattering probability, i.e., the value $\Lambda_a q^a$ given by Table II. This procedure is correct if the boundary scattering can be regarded as occurring uniformly throughout the volume of the specimen, a condition which might be approximated in a polycrystalline specimen with only a small acoustic mismatch from one grain to the next. For a single crystal specimen, however, the boundary scattering occurs nowhere except at the edges of the specimen, and to make an accurate calculation it is necessary to take account of the distribution of the energy flux over the cross section of the specimen.[9] This refinement amounts to using in the usual theory a τ_b which varies with $\mathbf{q}$; the effective τ_b turns out to be twice as large for large q as for small, "large" and "small" referring to whether the phonon-phonon $\tau(\mathbf{q})$ is $\ll$ or $\gg \tau_b$. However, we shall not attempt to introduce this refinement here, as it does not modify the computed conductivity contributions in any major way. In fact, for an order-of-magnitude calculation it is accurate enough simply to assume $\tau = (\Lambda_a q^a)^{-1}$ when this quantity is $< \tau_b$, and $= 0$ when it is $> \tau_b$. Equations (16) to (18), which have been computed in Appendix B using the assumption of additivity of reciprocal relaxation times, can in fact be obtained from this simpler assumption, to within a small error in each numerical coefficient. If angular brackets are used to denote averages over solid angle,

[16] H. B. G. Casimir, Physica **5**, 495 (1938); Berman, Simon, and Ziman, Proc. Roy. Soc. (London) **220**, 171 (1953).
[17] See also reference 6, p. 115.

these equations are

$$\kappa \approx \text{constant} - \frac{c^2 k}{4\pi}\left\langle \frac{\cos^2\theta}{\tau_b^{\frac{1}{2}}\Lambda_2^{\frac{1}{2}}}\right\rangle, \quad (a=2) \quad (16)$$

$$\kappa \approx \text{constant} + \frac{c^2 k}{6\pi^2}\left\langle \frac{\cos^2\theta \ln\tau_b}{\Lambda_3}\right\rangle, \quad (a=3) \quad (17)$$

$$\kappa \approx \text{constant} + \frac{2^{\frac{1}{2}} c^2 k}{8\pi}\left\langle \frac{\cos^2\theta \tau_b^{\frac{1}{2}}}{\Lambda_4^{\frac{1}{2}}}\right\rangle, \quad (a=4). \quad (18)$$

A ticklish question has to do with whether the neighborhoods of the "special directions" of $\mathbf{q}_0$, for which the entries in Tables I and II are invalid, can contribute significantly to the conductivity. If there are only isolated directions which are "special," we may assume that near any such direction the matrix element in (2) is of the first order in the angle ψ between q_0 and this direction. Then the Λ_a of (16) or (17) will be of order ψ^2, and the average over directions will in general diverge. Divergence of this calculation of course merely means that one should have used a higher value of a than that given in Table II, probably usually 4. The situation is even worse when there is a plane or cone of special directions. However, if the direction in which κ is measured is perpendicular to the group velocity of all the special modes, the $\cos^2\theta$ factor in (16) or (17) will be of order ψ^2, and the average over directions will converge. Thus we may conclude that use of (16) to (18) with the a values of Table II is often, perhaps usually, not legitimate for noncubic crystals when Table II gives $a<4$, except when the axis of measurement is perpendicular to the special directions of group velocity. The latter condition may frequently be fulfilled for a direction of measurement normal to the axis of a uniaxial crystal.

Equations (16) to (18) are of course only valid at temperatures sufficiently high so that boundary scattering is negligible for all modes except the low-frequency longitudinal ones. At temperatures low enough for all modes to be dominated by boundary scattering the theory of Casimir[16] must be used.

It remains to make some rough quantitative estimates of the values to be expected for the coefficients Λ_a occurring in Eqs. (16) to (18), and hence of the magnitudes of the size-dependent terms in the conductivity. Reasonably reliable estimates of Λ_2 can be made for semiconducting crystals for which the phonon effect on the thermoelectric power[7,8] has been measured. For example, from a comparison of theory[9] and observation for germanium one can deduce $\Lambda_2 \approx 3\times10^{-6}$ cm^2 sec^{-1} at 80°K, and proportional, of course, to T^2 at other temperatures. The uncertainty in this value arises from uncertainties in the nature of the processes by which phonons scatter the charge carriers; it is such that the value quoted might be in error by a factor two. Insertion of this into (16) gives, with the known conductivity[18]

$$\kappa \approx \kappa_\infty(1-0.017L^{-\frac{1}{2}}) \quad (19)$$

at 80°, where $\kappa_\infty = 2.7$ watts/cm deg is the conductivity of an infinite specimen, and $L=c\tau_b$ is the boundary scattering length in millimeters, roughly equal to the diameter of the specimen if the latter is a single crystal, or to a few times the grain diameter, if a polycrystal. The coefficient 0.017 in (19) varies roughly as $T^{-\frac{3}{2}}$, since in this region κ goes about as $T^{-1.5}$. However, it would not be safe to extrapolate this coefficient to say 20° by this law, since a simple calculation shows that below about 50° the values of q for which the asymptotic expression for $\tau(\mathbf{q})$ is of the order of τ_b fail to satisfy the inequality $\hbar cq \lesssim 0.15kT$ derived in the preceding section as necessary if the asymptotic expression for $\tau(\mathbf{q})$ is to be trusted. If the behavior of germanium is at all typical, we may conclude that for crystals with $a=2$, very accurate measurements would be required to establish the $L^{-\frac{1}{2}}$ dependence of the size-dependent term in the temperature range where this exponent can safely be predicted. At lower temperatures (but still far above the range where Casimir's formula applies) the size effect should be more easily detectable, but less simply interpretable.

Similar conclusions can be drawn, with a little more uncertainty, for crystals with $a=3$. Such crystals might be expected to behave as germanium would if scattering of the low-energy longitudinal phonons by modes with $\mathbf{q}_1$ near a cube edge direction were suppressed. The dominant modes for scattering would then be those with $\mathbf{q}_1$ near a cube diagonal direction. If the matrix element for scattering by such modes is roughly the same as for those with $\mathbf{q}_1$ near a cube edge direction, the ratio of the Λ_3 for the hypothetical case to Λ_2 for the actual case would be determined by the relative areas of the conservation surfaces S_1 for the two cases and the relative values of the density of states. These can be estimated from the known elastic spectrum. The result is $\Lambda_3 \approx 4\times10^{-13}$ cm^3 sec^{-1} at 80°, and of course proportional to T^2 at other temperatures. From this and (17) and the conductivity of germanium we get, for the hypothetical substance,

$$\Delta\kappa/\kappa \approx 0.021 \ln(L_1/L_2) \quad (20)$$

at 80°K, where $\Delta\kappa$ is the difference in the conductivities of two specimens with diameters (or grain sizes) L_1 and L_2, respectively. The coefficient in (20) should be roughly proportional to $T^{-\frac{1}{2}}$, but here again both this proportionality and the logarithmic dependence would probably break down below say 60°.

A rather larger effect will occur for a crystal with $a=4$, if such exists. As an estimate of the probable size of the Λ_4 of such a crystal would be difficult to make and doubtless very unreliable, we shall be content

[18] J. F. Goff, thesis, Purdue, 1953 (unpublished); T. H. Geballe (unpublished).

merely to set a rough upper limit to the size-dependent term in (18). The latter formula is applicable only when the maximum q_0 for the validity of the asymptotic formula $\tau \propto q_0^{-4}$, estimated in the preceding section as about $0.03kT/\hbar c$, is one for which $\tau(\mathbf{q}_0) < \tau_b$. If this condition is not fulfilled, the dependence of κ on τ_b will presumably be more gradual than that given in (18). With $\tau_b = L/c$ we find, therefore, that in the range where (18) is valid its size-dependent term $\Delta\kappa$ must satisfy

$$\Delta\kappa < 5\times 10^{-6}(kT/\hbar c)^3 cLk. \tag{21}$$

If $L=1$ mm, $T=300°$K, $c=5\times 10^5$ cm/sec, this is 0.17 watt/cm deg. Thus even for crystals with $a=4$ it is likely that the divergence of the conductivity contribution from low frequency longitudinal modes will have only a small to moderate effect on the conductivities of specimens with diameters or grain sizes of the order of a millimeter or less. For large single crystals, the limitation (21) becomes unimportant, and an easily measurable size effect, with $\Delta\kappa \propto L^{\frac{1}{2}}$, is conceivable.

V. CONCLUDING REMARKS

What we have calculated in the preceding section is only the high-temperature tail of the curve giving the influence of specimen size L on conductivity as a function of temperature. This curve, shown schematically in Fig. 2, approaches the Casimir limit $L\kappa^{-1}\partial\kappa/\partial L = 1$ as $T\to 0$. Near this point the ordinate falls below unity by an amount determined by the magnitude of the Umklapp and impurity scattering of modes with $\hbar\omega \sim kT$. This part of the curve can be described, at least roughly, by the equations given by Klemens.[6] At high temperatures, on the other hand, the ordinate of the curve is determined almost entirely by the behavior of longitudinal modes with $\hbar\omega \ll kT$; it is calculable from the equations of the preceding section. In the intermediate region of temperatures the detailed behavior is harder to predict, but might be very roughly estimated by interpolation between the two extremes. To show more clearly the difference between these extremes, let τ_b be the relaxation time for boundary scattering, τ_e a mean relaxation time, due to other processes, for all modes of thermal energy, and C a constant proportional to the specific heat. Then the procedure used by Klemens is roughly equivalent to writing

$$\kappa = \frac{C}{\tau_b^{-1}+\tau_e^{-1}} \sim C\tau_b\left(1-\frac{\tau_e}{\tau_b}\right) \quad \text{if} \quad \tau_e \ll \tau_b. \tag{22}$$

The formula (16) of the preceding section, on the other hand, gives, for a cubic crystal,

$$\kappa \sim C\tau_e\left(1-\frac{D}{T^{9/2}C\tau_e\tau_b^{\frac{1}{2}}}\right), \tag{23}$$

where D is a constant. From these equations it is clear,

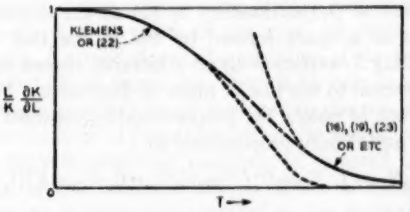

FIG. 2. Schematic temperature-dependence of the sensitivity of the effective thermal conductivity of a rod-like specimen to changes in its diameter L.

for example, that increasing the amount of impurity scattering decreases the ordinate of Fig. 2 at the left-hand end, but increases the ordinate at the right-hand end.

Although the high-temperature tail in Fig. 2 is not of very great interest for its own sake, the theory underlying it turns out[9] to be of considerable importance for the understanding of the thermoelectric powers of semiconductors at low temperatures. The interpretation of data in this field is greatly simplified if one can safely assume that the relaxation times of the longitudinal phonons which the charge carriers emit and absorb are long compared with those of the corresponding transverse phonons, and that the dependence of these times on q and T is substantially the same as the asymptotic form deduced in Sec. III. The range of validity of these asymptotic forms might conceivably be indicated by experimental studies of the size effect in thermal conduction at temperatures corresponding to the right of Fig. 2. Moreover, such studies might give rough values for the Λ coefficients occurring in (16) to (18), which enter importantly into the thermoelectric effect.

I am indebted to Dr. B. Goodman for a number of helpful comments, to Dr. T. H. Geballe for discussions of experimental data, and to the staff of the Institute for Advanced Study for their hospitality during the year 1952–1953.

APPENDIX A. SYMMETRY RESTRICTIONS ON THE MATRIX ELEMENTS OF U_3

As $\mathbf{q}_0 \to 0$ in a fixed direction the strain tensor due to the mode 0 approaches some limiting form $N_0^{\frac{1}{2}} q_0 u_{0\mu\nu}$ times a sinusoidal function of long wavelength. The strain amplitude tensor $\mathbf{u}_0$ depends only on the direction of $\mathbf{q}_0$ and on the branch of the acoustic spectrum to which mode 0 belongs. The matrix elements (2) of the anharmonic potential U_3 become asymptotically matrix elements of the change $U'(u_0)$ in elastic energy due to a homogeneous strain of the form u_0. In this Appendix we are interested in the behavior of the proportionality constant in (2) at points of the conservation surface S_1 in the neighborhood of a line or plane of degeneracy in q_1-space. As $q_0 \to 0$, a part of the conservation surface will shrink down onto the line or plane of degeneracy. Let us consider, for definiteness, the behavior of the

constant of proportionality in (2) at the sequence of points in $\mathbf{q}_1$-space formed by the intersection of the shrinking S_1-surface with an arbitrarily chosen straight line normal to the line or plane of degeneracy. For this sequence of points the proportionality constant in (2) is asymptotically proportional to

$$|[N_{10}=1, N_{20}=0|U'(\mathbf{u}_0)|N_{10}=0, N_{20}=1]|^2, \quad \text{(A1)}$$

where the modes 10, 20 are the modes in the degeneracy line or plane which are approached by 1 and 2, respectively ($\mathbf{q}_2=\mathbf{q}_1+\mathbf{q}_0$). Thus, 10 and 20 have the same wave vector $\mathbf{q}_{10}$ and the same frequency, but are not the same. The task of this Appendix will be to determine under what conditions symmetry considerations require (A1) to vanish.

Since U' is linear in the components of the symmetrical part of the strain tensor $\mathbf{u}_0$, its transformation properties under the operations of the space group of the crystal will be those of a symmetrical second rank tensor. It will thus consist of an invariant part, arising from the dilatation of $\mathbf{u}_0$, and a part transforming according to the representation D_2 of a spherical harmonic with $l=2$. Of course, D_2 is in general reducible into a sum of representations Δ_i when considered as a representation of a crystallographic point group. For certain directions and polarizations of mode 0 the part of U' going with one or more of these representations Δ_i may vanish. Now the initial and final states in (A1) may or may not be orthogonal. If $\mathbf{q}_1$ and $\mathbf{q}_2$ approach $\mathbf{q}_{10}$ from the same direction, modes 10 and 20 will be orthogonal and the initial and final states will be orthogonal. In such case the part of U' transforming according to the unit representation can make no contribution to (A1). But if $\mathbf{q}_{10}$ lies on a line of symmetry near which the frequency separation of two branches varies linearly with distance from the line in any direction, the directions of $\mathbf{q}_1$ and $\mathbf{q}_2$ from $\mathbf{q}_{10}$ will in general be different, and so it may happen that mode 10 represents the limiting mode of the lower branch as $\mathbf{q}_{10}$ is approached from one direction, while mode 20 represents the limiting mode of the upper branch as $\mathbf{q}_{10}$ is approached from a different direction. In such case modes 10 and 20 need not be orthogonal, and the part of U' belonging to the unit representation will in general give a nonvanishing contribution to (A1). Since the latter contribution is not related by any symmetry operation to that of the D_2 part of U', and since it vanishes only for special choices of the direction of $\mathbf{q}_0$ and the orientation of the line along which $\mathbf{q}_1 \rightarrow \mathbf{q}_{10}$, we may state the partial result: *When the frequency separations of two branches vary linearly with distance in any direction from a line of degeneracy, symmetry does not require the constant of proportionality in (2) to vanish, as $q_0 \rightarrow 0$, at a general point of the conservation surface near this line, except possibly when $\mathbf{q}_0$ is parallel to the line.*

For cases where the initial and final states in (A1) are orthogonal, we may put for U' its part transforming as D_2. When, as is usually the case, the modes 10 and 20 belong to the same irreducible representation Δ_{10} of the group of the wave vector of a line of symmetry on which q_{10} lies, the obvious thing to do first is to see whether, for each Δ_i in D_2, $\Delta_i \times \Delta_{10}$ contains Δ_{10}. This will always happen for at least one of the Δ_i, since for any direction of the line of symmetry there will always be at least one of the Δ_i which is the unit representation Δ_1 of the group of the wave vector. The part of U' belonging to this unit representation can never give any contribution to the off-diagonal matrix element (A1), so we may restrict consideration to the other Δ_i. If any of these $\Delta_{i\neq 1}$ has a cross product with Δ_{10} containing Δ_{10}, the contribution of the corresponding part U_i' of U' to (A1) will be in general nonvanishing unless either $U_i'=0$ or the choice of basis 10, 20 in Δ_{10} is just that which diagonalizes U_i'. If the modes 10, 20 vary with the direction from which the symmetry line is approached, the latter condition can be satisfied only for particular directions. The proviso of the last sentence is always fulfilled when Δ_{10} is a two-dimensional representation on a line of degeneracy in the interior of the Brillouin zone, since if 10 were the same from all directions, it would be taken into a multiple of itself by all operations of the group of the wave vector, so Δ_{10} would have to be one-dimensional. Therefore we can state the result: *Let Δ_{10} be a two-dimensional representation of the group of the wave vector*[19] *for a line of symmetry inside the Brillouin zone, and let Δ_i be an irreducible representation of this group, other than the unit representation, contained in D_2. Then if $\Delta_i \times \Delta_{10}$ contains Δ_{10}, symmetry does not require the constant of proportionality in (2) to vanish at a general point of the conservation surface near this line, as $q_0 \rightarrow 0$, except when the direction and polarization of the mode 0 are such as to make $U_i'\equiv 0$.*

Except for special directions and polarizations of the mode 0, to which we shall return later, we have now answered the question before us for interior lines of the Brillouin zone on which there is a group-theoretical degeneracy. However, even though we have chosen to omit a general discussion of lines of symmetry lying in the boundary of the Brillouin zone, there are two types of cases still to be covered. These are interior lines and boundary planes, respectively, on which the degeneracy is due only to time-reversal symmetry.[11] Now interior lines of this type—enumerated in Table II of reference 11—are all derivable from cases covered in the italicized statements above, by lowering of the symmetry of the crystal. Therefore if the matrix of any U_i' in the subspace spanned by 10 and 20 does not have to be a mere multiple of the unit matrix for the more symmetrical case, it does not have to be so for the present case either. It is easily shown, as before, that as the symmetry line is approached from different directions, the limiting form of mode 10 is not always the same, and so we can extend the conclusions of the

[19] Defined in Sec. III, or more fully in reference 10.

preceding paragraph to degeneracy lines of the present type.

For boundary planes of degeneracy—those perpendicular to a screw axis[11]—the situation is most conveniently appraised by considering the matrix of any U_i' in the subspace spanned by the four modes going with a given frequency and having wave vectors q_{10} and $-q_{10}$. In this subspace a real basis can be chosen, and if $\bar{G}$ is the group of space group operations taking this subspace into itself, the general form for the matrix of any U_i' in this subspace can easily be written down, this matrix vanishing if and only if $\Delta_i \times \Delta_{10}$ does not contain Δ_{10}, all representations being now real representations of $\bar{G}$. When the matrix of U' does not vanish, we wish to know whether it is diagonalized simultaneously with the matrix of the operator F which determines the form and frequencies of the modes 1, 2, at points just off the plane, in terms of the subspace spanned by 10, 20. This F is an operator of zero wave vector with the transformation properties of the component of a polar vector normal to the plane. It is easily proved that F and U' can be simultaneously diagonal if and only if they belong to the same representation of $\bar{G}$, or if one of them (U') belongs to the unit representation. This type of argument can be extended to provide an alternative proof of the results derived above for symmetry lines.

Table III summarizes the conditions which the mode 0 must satisfy in order that the constant of proportionality in (2) be required to vanish, as $q_0 \to 0$, everywhere on the part of the conservation surface neighboring a degeneracy line or plane of the type we have been discussing. A straightforward application of the criteria enunciated above shows that there is no case in which vanishing is required for all modes 0, so the results are given in the form of properties which the special modes 0 must have in order that vanishing be required. When the first of the italicized criteria above is used, the requirement is that $\mathbf{q}_0$ be parallel to the line; this is stated in the last column. When the second italicized criterion is used, the requirement is that the strain $\mathbf{u}_0$ in the mode 0 be of one or more specific forms; these are listed in the next to the last column.

It is clear from inspection that no mode 0 can be special with respect to all threefold axes in a cubic crystal, or with respect to all fourfold axes. For uniaxial crystals, on the other hand, a longitudinal mode with $\mathbf{q}_0$ parallel to the axis will always be special.

TABLE III. Conditions on the mode 0 under which symmetry requires the constant of proportionality in (2) to approach zero at a general point of the conservation surface near a boundary plane or interior line of degeneracy. The Z axis is taken along the symmetry line, or normal to the boundary plane. When there are just two twofold axes normal to the Z axis, the X and Y axes are to be taken along these.

Type of degeneracy	G^{10}	Strain tensor type for special modes (second criterion)	Direction of $\mathbf{q}_0$ for special modes (first criterion)
Boundary plane	C_s or C_1	$x^2+y^2-2z^2$, x^2-y^2, xy	
Interior line, degeneracy due to symmetry only	C_{6v}	$x^2+y^2-2z^2$, xz, yz	
	C_{4v}	$x^2+y^2-2z^2$, xz, yz	
	C_{2v}	$x^2+y^2-2z^2$	Z
Interior line, degeneracy due to time-reversal (conditions for degeneracy listed in reference 11)	C_6	$x^2+y^2-2z^2$, xz, yz	
	C_4	$x^2+y^2-2z^2$, xz, yz	
	C_2	$x^2+y^2-2z^2$	Z
	C_{2v}	$x^2+y^2-2z^2$, xz, yz	
	C_2	$x^2+y^2-2z^2$, xz, yz	

APPENDIX B. DERIVATION OF (16) TO (18)

We wish to evaluate

$$I = \int_0^{q'} \tau(q) q^2 dq, \tag{B1}$$

where

$$\tau(q) = [\tau_b^{-1} + \Lambda_a q^a]^{-1}, \tag{B2}$$

and q' is a value of q small enough for the asymptotic expression for the phonon-phonon scattering to be valid for $q < q'$, yet large enough so that increasing q' would not appreciably change the dependence of I on τ_b. If $a \leq 3$ the integral (B1) does not converge as $q' \to \infty$. However,

$$\frac{\partial I}{\partial \tau_b^{-1}} = -\tau_b^2 \int_0^{q'} \frac{q^2 dq}{(1+\tau_b \Lambda_a q^a)^2} \tag{B3}$$

converges if $a > \frac{3}{2}$. Now[20]

$$\int_0^\infty \frac{x^2 dx}{(1+x^a)^2} = \frac{(3-a)\pi}{a^2} \csc \frac{(3-a)\pi}{a}. \tag{B3}$$

Inserting this in (B3) and integrating on τ_b^{-1}, we obtain for large q',

$$I \sim \text{constant} - \frac{\tau_b}{(3-a)(\Lambda \tau_b)^{3/a}} \cdot \frac{p\pi}{a} \csc \frac{p\pi}{a}. \tag{B4}$$

Equations (16) to (18) are special cases of this.

[20] D. Bierens de Haan, *Nouvelles tables d'integrales definis* (Royal Academy of Sciences, Amsterdam, 1867), Table 17, No. 18.

Relativistic and Magnetic Spin Interactions in Helium-Like Atoms*

J. SUCHER AND H. M. FOLEY
Columbia University, New York, New York
(Received May 7, 1954)

Relativistic and magnetic spin corrections to the ionization energy of He and O^{6+} are given. The magnetic spin interaction given by Sessler and Foley has been derived by a careful evaluation of the Breit operator. The relativistic corrections obtained by reduction of the Dirac equation differ from some previous expressions. With all known corrections taken into account, there remains a discrepancy with experiment of about 30 cm^{-1} in the case of He. Within the rather large experimental and theoretical uncertainties, there appears to be no residual discrepancy in the case of O^{6+}.

INTRODUCTION

CHANDRASEKHAR, Elbert, and Herzberg[1] have recently reviewed the agreement between the theoretical and experimental values of the ionization energy of He and the isoelectronic series to He. Sessler and Foley[2] have pointed out that a magnetic spin-spin interaction which does not vanish in a ^1S state must be included, and they have attempted an evaluation of the relativistic effects in He. There are several numerical errors in Ia and Ib. It is the purpose of the present paper (1) to give a quantum theoretical derivation of the magnetic spin interaction which was deduced on classical grounds in Ia, (2) to point out and correct certain errors in the previous treatments of the relativistic term, and (3) to give corrected and extended results for the magnetic and relativistic energies for He and O^{6+}.

In Sec. I it is shown that a consistent reduction of the two-electron Dirac equation leads unambiguously to the relativistic corrections to be applied to the Schrödinger nonrelativistic eigenvalue. Because of the singular potentials between the point charges in the problem there are certain pitfalls to be avoided. In Sec. II a careful working out of the expectation value of the "Breit operator" interaction between electrons is shown to include the magnetic spin-spin term given by Sessler and Foley (Ia). In Sec. III are given what are believed to be fairly accurate values for the energy terms for He and less accurate values for O^{6+}. It will be seen that a discrepancy of about 30 cm^{-1} remains in the case of He. Within the rather large theoretical and experimental uncertainties existing in the case of O^{6+}, however, there is no apparent discrepancy.

I. THE REDUCTION OF THE TWO-ELECTRON DIRAC EQUATION[3]

In the notation of Schiff,[4] the two-electron relativistic Hamiltonian is

$$H_D=-c(\boldsymbol{\alpha}_\mathrm{I}\cdot\mathbf{p}_\mathrm{I}+\boldsymbol{\alpha}_\mathrm{II}\cdot\mathbf{p}_\mathrm{II})-mc^2(\beta_\mathrm{I}+\beta_\mathrm{II})+U.$$

In the Dirac equation, $H_D\Psi=E\Psi$, we write the 16-component Ψ in the form

$$\Psi=\begin{pmatrix}\phi\\ \omega_1\\ \omega_2\\ \chi\end{pmatrix},$$

eliminate the "small" components ϕ, ω_1, ω_2, and obtain the "reduced" equation, correct to order α^2 ($\alpha=e^2/\hbar c$):

$$H_R\chi=E\chi, \tag{1}$$

$$H_R=H_0+H_1+H_2, \tag{2}$$

with

$$H_0=\mathbf{p}_\mathrm{I}^2/2m+\mathbf{p}_\mathrm{II}^2/2m+U, \tag{3}$$

$$H_1=-\frac{1}{4m^2c^2}\left[\mathbf{p}_\mathrm{I}\cdot f\mathbf{p}_\mathrm{I}+\mathbf{p}_\mathrm{II}\cdot f\mathbf{p}_\mathrm{II}-\frac{\mathbf{p}_\mathrm{I}^2\mathbf{p}_\mathrm{II}^2}{m}\right], \qquad f=E-U, \tag{4}$$

$$H_2=\frac{eh}{4m^2c^2}[\boldsymbol{\sigma}_\mathrm{I}\cdot(\mathbf{E}_\mathrm{I}\times\mathbf{p}_\mathrm{I})+\boldsymbol{\sigma}_\mathrm{II}\cdot(\mathbf{E}_\mathrm{II}\times\mathbf{p}_\mathrm{II})], \qquad \mathbf{E}_\mathrm{I}=\boldsymbol{\nabla}_\mathrm{I}(U/e). \tag{5}$$

The nonrelativistic equation,

$$H_0\psi=E_0\psi, \tag{6}$$

is imagined to have been solved to a high accuracy and the expectation values of H_1 and H_2 are to be evaluated with the resulting ψ function.

The spin-orbit energy H_2 vanishes in the ground state of helium-like atoms.

We expand (4) with the aid of the equation

$$\mathbf{p}_\mathrm{I}\cdot f\mathbf{p}_\mathrm{I}=f\mathbf{p}_\mathrm{I}^2+\langle\mathbf{p}_\mathrm{I}f\rangle\cdot\mathbf{p}_\mathrm{I},$$

in which the angular bracket indicates that the differential operator $\mathbf{p}_\mathrm{I}$ acts only on the f function within the bracket. Thus the expectation value of H_1 becomes

$$E_1=E_1'+\epsilon, \tag{7}$$

$$E_1'=-\frac{1}{8m^3c^2}[(\mathbf{p}_\mathrm{I}^2\psi,\mathbf{p}_\mathrm{I}^2\psi)+(\mathbf{p}_\mathrm{II}^2\psi,\mathbf{p}_\mathrm{II}^2\psi)], \tag{8a}$$

$$\epsilon=-\frac{1}{4m^2c^2}[(\psi,\langle\mathbf{p}_\mathrm{I}f\rangle\cdot\mathbf{p}_\mathrm{I}\psi)+(\psi,\langle\mathbf{p}_\mathrm{II}f\rangle\cdot\mathbf{p}_\mathrm{II}\psi)], \tag{9}$$

* Supported by the National Science Foundation.

[1] Chandrasekhar, Elbert, and Herzberg, Phys. Rev. **91**, 1172 (1953).

[2] A. M. Sessler and H. M. Foley, Phys. Rev. **92**, 1321 (1953), and Phys. Rev. **92**, 1321–1322 (1953); hereafter referred to as Ia and Ib respectively.

[3] G. Breit, Phys. Rev. **34**, 553 (1929); Phys. Rev. **39**, 616 (1932).

[4] L. I. Schiff, *Quantum Mechanics* (McGraw-Hill Book Company, Inc., New York, 1949), p. 311.

in which the relations

$$[(\mathbf{p}_I^2+\mathbf{p}_{II}^2)/2m]\psi=f\psi,$$

$$(\psi,f(\mathbf{p}_I^2+\mathbf{p}_{II}^2)\psi)=\frac{1}{2m}((\mathbf{p}_I^2+\mathbf{p}_{II}^2)\psi,(\mathbf{p}_I^2+\mathbf{p}_{II}^2)\psi),$$

$$(\mathbf{p}_I^2\psi,\mathbf{p}_{II}^2\psi)=(\psi,\mathbf{p}_I^2\cdot\mathbf{p}_{II}^2\psi),$$

have been used. Now for potential functions which are everywhere bounded $\mathbf{p}_I^2\psi$ is well behaved and the usual Hermitean property of the operator $\mathbf{p}_I$ enables one to transform E_1' as

$$E_1'\rightarrow-\frac{1}{8m^3c^2}[(\psi,\mathbf{p}_I^4\psi)+(\psi,\mathbf{p}_{II}^4\psi)]. \tag{8b}$$

For the singular potentials corresponding to point particles, however, this transformation cannot be performed; in fact, the two forms of E_1' in Eq. (8) differ by finite terms which have the form of delta functions at the singular points. This can be seen clearly by evaluating the two forms of (8) for an extended nuclear charge distribution and considering the limiting values for point charges. [See Eq. (19).] In his *Handbuch* article[5] Bethe has given E_1' in the form (8b), but the evaluation of this energy term was actually carried out with the correct form (8a).

The term ϵ in E_1 may be written, after an integration by parts, as

$$\epsilon=E_1''+E_1'''=(\psi,H_1''\psi)+(\psi,H_1'''\psi), \tag{9}$$

$$H_1''=2\pi\mu_0^2Z[\delta(\mathbf{r}_1)+\delta(\mathbf{r}_2)], \tag{10}$$

$$H_1'''=-4\pi\mu_0^2\delta(\mathbf{r}_{12}). \tag{11}$$

Eriksson[6] has evaluated H_1 [Eq. (4)] by an expansion in which the singular terms $\Delta_I U$ and $\Delta_{II} U$ have been dropped. (See the last equation on p. 764 of reference 6.) It is clear that a finite energy contribution has thus been neglected.

II. BREIT INTERACTION

The magnetic and retarded electrostatic interaction between electrons, to order α^2, has been given by Breit[3] as

$$B=\frac{-e^2}{2r_{12}}[\boldsymbol{\alpha}_I\cdot\boldsymbol{\alpha}_{II}+(\boldsymbol{\alpha}_I\cdot\mathbf{n})(\boldsymbol{\alpha}_{II}\cdot\mathbf{n})]. \tag{12}$$

The expectation value of B has been shown by Breit to be

$$E_3=\frac{-e^2}{8m^2c^2}[(\chi,M\xi_I\xi_{II}\chi)+(\xi_I\chi,M\xi_{II}\chi)+(\xi_{II}\chi,M\xi_I\chi)+(\xi_I\xi_{II}\chi,M\chi)] \tag{13}$$

where χ is defined by Eq. (1) and

$$\xi_I\equiv\boldsymbol{\sigma}_I\cdot\mathbf{p}_I,\quad \xi_{II}\equiv\boldsymbol{\sigma}_{II}\cdot\mathbf{p}_{II},$$
$$M\equiv\frac{1}{r_{12}}[\boldsymbol{\sigma}_I\cdot\boldsymbol{\sigma}_{II}+(\boldsymbol{\sigma}_I\cdot\mathbf{n})(\boldsymbol{\sigma}_{II}\cdot\mathbf{n})]. \tag{13'}$$

It is desirable to express E_3 as the expectation value of an operator H_3 which is applied to the Schrödinger-Pauli function χ. It is easily seen that one may write

$$(\xi_I\chi,M\xi_{II}\chi)=(\chi,\xi_IM\xi_{II}\chi),$$
$$(\xi_{II}\chi,M\xi_I\chi)=(\chi,\xi_{II}M\xi_I\chi) \tag{14}$$

by an integration by parts. When we consider, however, the last term in Eq. (13) we have

$$(\xi_I\xi_{II}\chi,M\chi)=(\xi_{II}\chi,\xi_IM\chi)\neq(\chi,\xi_{II}\xi_IM\chi),$$

since the function $\xi_IM\chi$ varies as $1/r_{12}^2$, so that a second integration by parts leads to a nonvanishing "surface" term. The evaluation of this term is carried out in the Appendix. The result is

$$(\xi_I\xi_{II}\chi,M\chi)=(\chi,\xi_{II}\xi_IM\chi)+(16\pi/3)\hbar^2(\chi,\boldsymbol{\sigma}_I\cdot\boldsymbol{\sigma}_{II}\delta(\mathbf{r}_{12})\chi). \tag{15}$$

We combine these results and write

$$E_3=(\chi,H_3\chi)=E_3'+E_3''=(\chi,H_3'\chi)+(\chi,H_3''\chi), \tag{16}$$

$$H_3'=\frac{-e^2}{8m^2c^2}[M\xi_I\xi_{II}+\xi_IM\xi_{II}+\xi_{II}M\xi_I+\xi_I\xi_{II}M], \tag{17}$$

$$H_3''=-(8\pi/3)\mu_0^2\boldsymbol{\sigma}_I\cdot\boldsymbol{\sigma}_{II}\delta(\mathbf{r}_{12}). \tag{18}$$

H_3' was obtained and reduced by Breit;[3] the additional operator H_3'' is just the quantum theoretical form of the magnetic spin-spin interaction given by Sessler and Foley (Ia).[7]

Our results appear to differ from those of Chraplyvy,[8] who employed a Foldy-Wouthuysen transformation on this same problem.

III. THE IONIZATION ENERGIES OF He AND O^{6+}

A. He

The corrections E_1', E_1'', E_1''', and E_3'' to the nonrelativistic energy E_0 have been calculated with the Hylleraas three-parameter function;[9] the results are given in Table I, together with those from a Hartree wave function and a Hydrogenic function.

We have examined the accuracy of these results by repeating the calculations for E_1'', E_1'', and E_3'' $(=-2E_1''')$ with the Hylleraas six-parameter function,[9]

[5] H. A. Bethe, *Handbuch der Physik* (Springer, Berlin, 1933), Vol. 24, II, p. 384.
[6] H. A. S. Eriksson, Z. Physik **109**, 762 (1938).
[7] Since the completion of this paper it has come to our attention that this result was derived by V. Berestetskii and L. Landau, J. Exptl. Theoret. Phys. (U.S.S.R.) **19**, 673 (1949) by the same procedure that we have employed.
[8] Z. V. Chraplyvy, Phys. Rev. **91**, 388 (1953).
[9] E. A. Hylleraas, Z. Physik **54**, 347 (1929).

TABLE I. The relativistic and magnetic spin corrections in $\alpha^2 Ry$, with various wave functions.

	He			O^{6+}
	Present calc	Hartree	Hydrogenic	Present calc
$-E_1'$	26.71	26.23[a]	20.30[b]	9174.6
$-E_1''$	−22.60	−22.60[a]	−19.20[b]	−7492.0
$-E_1'''$	0.73	1.18	1.20	101.5
$-E_3''$	−1.46	−2.36	−2.40	−203.0
E_{ion}	−4.00			−1024.0
$\Sigma(\alpha^2 Ry)$	−0.62			557.1
$\Sigma(\text{cm}^{-1})$	−3.62			3255.7

[a] See reference 2.
[b] See reference 5.

giving, in units of $\alpha^2 \times Ry$: $E_1'' = 22.83$, $E_1''' = 0.70$, and with the ten-parameter variational function, obtained by Chandrasekhar, Elbert, and Herzberg,[10] giving: $E_1'' = 22.74$, $E_1''' = 0.69$. The close agreement between these values and those obtained with the three-parameter function leads us to believe that our results are accurate to within one or two wave numbers.

Most of the labor in the calculation of E_1' was avoided by using the equation

$$(\mathbf{p}_1^2\psi, \mathbf{p}_1^2\psi) = (\psi, \mathbf{p}_1^4\psi) - 4\pi \int \left\{ \left(\frac{\partial \psi^2}{\partial r_1} \right)_{r_1=0} + \left(\frac{\partial \psi^2}{\partial r_{12}} \right)_{r_{12}=0} \right\} d\mathbf{r}_2. \quad (19)$$

The term $(\psi, \mathbf{p}_1^4\psi)$ has been calculated previously by Eriksson.[6]

The agreement between the values obtained for E_1' and E_1'' with Hylleraas and Hartree functions is satisfactory. The difference in values of E_1''' (and E_3'') is ascribed to the absence of correlation in the Hartree function. There can be little doubt that the Hylleraas results are more reliable.

The value of E_3'' from the Hylleraas function given in Ia is in error because of an incorrect normalization of the wave function. The operator expression for E_1''' given in Ib is in error by a factor of two. Consequently the remark that the calculation of this quantity by Bethe is incorrect was not justified.

TABLE II. The theoretical and experimental values of the ionization energies of He and O^{6+}, in cm^{-1}.

Atom	$(\text{I.E.})_{\text{nonrel}}$	$+\Sigma$	$-E_3'$	Mass pol.	$(\text{I.E.})_{\text{theor}}$	$(\text{I.E.})_{\text{exp}}$
He	198 290.7[a]	−3.62	0.88[b]	−5[c]	198 283	198 313 ± 5[a]
O^{6+}	5 939 898[a]	3256	53[b]	2[c]	5 963 209	5 963 000 ± 600[a]

[a] See reference 1.
[b] See reference 6.
[c] See reference 11.

[10] Chandrasekhar, Elbert, and Herzberg (see reference 1); the normalization constant given there should be 1.359625 [G. Herzberg (private communication)].

B. O^{6+}

Inasmuch as the various relativistic, magnetic, and Lamb shift terms vary as Z^4 and Z^3, whereas the nonrelativistic eigenvalue varies only as Z^2, it is of interest to examine the case of O^{6+}. The calculations were made with the wave function obtained by Eriksson[6] by an expansion in inverse powers of Z. The results are given in Table I. The accuracy of the nonrelativistic eigenvalue, and of the quantities given for O^{6+} in the table is uncertain.

C. Ionization Potentials of He and O^{6+}

In Table I, E_{ion} denotes the relativistic correction for He^{1+} and O^{7+}. The quantity Σ gives the correction to the ionization energy from the terms evaluated above. In Table II these quantities and the additional small terms, E_3' evaluated by Eriksson[6] and the "mass polarization" term from Robinson,[11] are added to the nonrelativistic ionization energies to give $(\text{I.E.})_{\text{theor}}$.†

It is seen that a difference between this theoretical result and experiment of about 30 cm^{-1} exists in the case of He. The Lamb shift would add about 1 cm^{-1} to this quantity, as estimated by Hakansson.[12] (The Hylleraas "eighth approximation" calculation of the nonrelativistic eigenvalue, which is presumably less reliable[1] than the strictly variational result employed in Table II, would give an almost exact agreement between theory and experiment.) Presumably the discrepancy may be accounted for by the inaccuracy in the nonrelativistic energy calculated from the Hylleraas wave function. The corresponding difference in the case of O^{6+} is about -200 cm^{-1} to which the Lamb shift would add about 400 cm^{-1},[12] giving about $+200$ cm^{-1} for the remaining discrepancy. This is well within the rather large experimental uncertainty.‡

We wish to acknowledge a profitable discussion with Dr. A. M. Sessler.

APPENDIX

We have

$$(\xi_{II}\chi, \xi_I M\chi) = \int\int (\xi_{II}\chi)^\dagger (\xi_I M\chi) d\mathbf{r}_1 d\mathbf{r}_2, \quad (1)$$

the symbols being defined in Eq. (13′). We may write

$$(\xi_{II}\chi)^\dagger (\xi_I M\chi) = \chi^\dagger \xi_{II} \xi_I M\chi - \mathbf{p}_{II} \cdot (\chi^\dagger \boldsymbol{\sigma}_{II} \xi_I M\chi),$$

[11] H. A. Robinson, Phys. Rev. **51**, 14 (1937).

† *Note added in proof.*—The value of E_3' taken from Ericksson does not agree with Ericksson's formula (p. 771 of reference 6), but should be increased by a factor 2 to 1.76 cm^{-1}. This result was obtained independently by R. P. Feynman and M. Baranger (private communication).

[12] H. E. V. Hakansson, Arkiv. Fysik **1**, 555 (1950).

‡ *Note added in proof.*—Professor G. Herzberg has kindly communicated to us the result of a 10-term variational calculation of the nonrelativistic ionization energy of O^{6+}. His result increases $(IE)_{\text{nonrel}}$ by only 40 cm^{-1}. This removes the principal uncertainty in the calculation and thus confirms the general agreement of theory and experiment for O^{6+}.

whence

$$(\xi_{II}\chi,\xi_I M\chi,)=(\chi\xi_{II}\xi_I M\chi)+J,$$

$$J=-\int\int \mathbf{p}_{II}\cdot(\chi^\dagger\boldsymbol{\sigma}_{II}\xi_I M\chi)d\mathbf{r}_1 d\mathbf{r}_2. \tag{2}$$

Let S_a be a sphere of radius a about the point $\mathbf{r}_1$. Then, by Gauss' theorem, we have

$$J=\hbar^2\int I(\mathbf{r}_1)d\mathbf{r}_1,$$

$$I(\mathbf{r}_1)=\lim_{a\to 0} I_a, \tag{3}$$

$$I_a=-\int_{S_a}(\chi^\dagger\boldsymbol{\sigma}_{II}(\boldsymbol{\sigma}_1\cdot\boldsymbol{\nabla}_1 M\chi))\cdot\mathbf{n}dS_a,$$

where $\mathbf{n}$ is the outward normal on S_a. I_a may be rewritten, on carrying out the differentiation,

$$I_a=-[I_a'+I_a''],$$

$$I_a'=\int_{S_a}\chi^\dagger Q\chi d\Omega,\quad I_a''=\int_{S_a}\chi^\dagger P\chi d\Omega, \tag{4}$$

$$Q=r_{12}^2(\boldsymbol{\sigma}_{II}\cdot\mathbf{n})(\boldsymbol{\sigma}_1\cdot\langle\boldsymbol{\nabla}_1 M\rangle),$$

$$P=r_{12}^2(\boldsymbol{\sigma}_{II}\cdot\mathbf{n})\boldsymbol{\sigma}_1\cdot M\boldsymbol{\nabla}_1.$$

Since $M\sim 1/r_{12}$, $\lim_{a\to 0}P=0$, whence

$$\lim_{a\to 0} I_a''=0, \tag{5}$$

if χ is regular at $\mathbf{r}_1=\mathbf{r}_2$, as is assumed. Carrying out the differentiation of M, we get

$$\begin{aligned}\boldsymbol{\sigma}_1\cdot\boldsymbol{\nabla}_1 M&=\frac{1}{r_{12}^2}\boldsymbol{\sigma}_1\cdot\{[\boldsymbol{\sigma}_1\cdot\boldsymbol{\sigma}_{II}+(\boldsymbol{\sigma}_1\cdot\mathbf{n})(\boldsymbol{\sigma}_{II}\cdot\mathbf{n})]\mathbf{n}\\&\quad+(\boldsymbol{\sigma}_1\cdot\mathbf{n})[(\boldsymbol{\sigma}_{II}\cdot\mathbf{n})\mathbf{n}-\boldsymbol{\sigma}_{II}]\\&\quad+(\boldsymbol{\sigma}_{II}\cdot\mathbf{n})[(\boldsymbol{\sigma}_1\cdot\mathbf{n})\mathbf{n}-\boldsymbol{\sigma}_1]\}\\&=\frac{2i}{r_{12}^2}\boldsymbol{\sigma}_{II}\cdot[\boldsymbol{\sigma}_1\times\mathbf{n}]\end{aligned}$$

on repeated use of the formula,

$$(\boldsymbol{\sigma}\cdot\mathbf{A})(\boldsymbol{\sigma}\cdot\mathbf{B})=\mathbf{A}\cdot\mathbf{B}+i\boldsymbol{\sigma}\cdot(\mathbf{A}\times\mathbf{B}),$$

for arbitrary vectors $\mathbf{A}$ and $\mathbf{B}$. Hence we find

$$\begin{aligned}Q&=2i(\boldsymbol{\sigma}_{II}\cdot\mathbf{n})(\boldsymbol{\sigma}_{II}\cdot[\boldsymbol{\sigma}_1\times\mathbf{n}])\\&=-2[\boldsymbol{\sigma}_1\cdot\boldsymbol{\sigma}_{II}-(\boldsymbol{\sigma}_1\cdot\mathbf{n})(\boldsymbol{\sigma}_{II}\cdot\mathbf{n})].\end{aligned}$$

Then

$$\int_{S_a}Qd\Omega=-2\sum_{i,j}\sigma_{1i}\sigma_{IIj}\left(4\pi\delta_{ij}-\frac{4\pi}{3}\delta_{ij}\right)=-\frac{16\pi}{3}\boldsymbol{\sigma}_1\cdot\boldsymbol{\sigma}_{II},$$

and, as follows quite rigorously for continuous χ,

$$\lim_{a\to 0} I_a'=-\frac{16\pi}{3}[\chi^\dagger\boldsymbol{\sigma}_1\cdot\boldsymbol{\sigma}_{II}\chi]_{a=0}. \tag{6}$$

Combining (3), (4), (5), and (6) we get

$$\begin{aligned}J&=\frac{16\pi}{3}\hbar^2\int[\chi^\dagger\boldsymbol{\sigma}_1\cdot\boldsymbol{\sigma}_{II}\chi]_{r_1=r_2}d\mathbf{r}_1\\&=(16\pi/3)\hbar^2(\chi,\boldsymbol{\sigma}_1\cdot\boldsymbol{\sigma}_{II}\delta(\mathbf{r}_{12})\chi),\end{aligned}$$

where $\delta(\mathbf{r}_{12})$ is the Dirac delta function between the two two electrons. This yields Eq. (15) if we recall Eq. (2) which defines J.

Polarization of Mn^{55} Nuclei: Cryogenic Aspects*

J. W. T. Dabbs and L. D. Roberts
Oak Ridge National Laboratory, Oak Ridge, Tennessee

(Received May 7, 1954)

A brief discussion of certain cryogenic aspects of nuclear polarization is given. This discussion is applied to Mn^{55} in the paramagnetic salt $Mn(ND_4)_2(SO_4)_2\cdot 6D_2O$. Measurements on this salt of the temperature in the range $0.12°\leq T\leq 0.35°$K and of magnetic moment up to 90 percent of saturation as a function of magnetic field in the range $660\leq H\leq 4560$ gauss and for an entropy $S/R=0.514$ are described. These measurements are used to calculate the nuclear polarization as a function of field in this magnetic field range and at this entropy, and they form the cryogenic basis for Mn^{55} polarization experiments reported previously.

INTRODUCTION

THIS paper is concerned with cryogenic aspects of work on the polarization of Mn^{55} nuclei. Results of observations on the interaction of these polarized nuclei with polarized thermal neutrons have been described.[1]

The polarization of nuclear magnetic moments by the use of hyperfine structure coupling has been suggested independently by Rose[2] and Gorter.[3] In their procedure, it was proposed to use the hfs coupling occurring in salts of suitable paramagnetic ions to obtain a splitting of the different nuclear spin orientations comparable to kT. As this coupling may be equivalent to a magnetic field at the nucleus of the order of several hundred thousand gauss, temperatures of the order of 0.1°K may give a useful nuclear polarization f_N of order 10 percent.

Because the splitting of the nuclear levels is produced by interactions internal to the salt many of the problems of the "brute force" method proposed earlier by Gorter[4] and by Kurti and Simon[5] are minimized or eliminated. For example, the time required for the electron spin system to cool the nuclear spins, i.e., the electron spin-nuclear spin relaxation time, may become quite short since the electron spin system, which is cooled by the adiabatic demagnetization, is directly coupled by the hfs coupling to the nuclear spins.

Thus, if the "free" electron spins of the paramagnetic ions are oriented, i.e., magnetized by an applied magnetic field H, and if the temperature is then lowered to a value having kT comparable to the hfs splitting, nuclear polarization will result. Equation (1) which describes this has been given by Rose,[2] and has been further discussed by Rose, Simon, and Jauch:[6]

$$f_N=S_e(I+1)(Ahc/3kT)\cdot f_e(H,T). \quad (1)$$

Here A is the coupling constant in the hfs operator, $A\mathbf{I}\cdot\mathbf{S}_e$ and f_e is the electron magnetization expressed as the fraction of magnetic saturation, S_e is the electron spin, I is the nuclear spin, k is the Boltzmann constant, T is the absolute temperature, h is Planck's constant, and c is the velocity of light *in vacuo*. Thus, knowing A, we may calculate f_N from Eq. (1) and measurements of H, f_e, and T.

To obtain the largest available value of the nuclear polarization f_N, the electron magnetization must be brought close to saturation, $f_e\cong 1$, and the temperature T must be made small. The path of an adiabatic demagnetization is suited to these requirements. If a sufficiently large magnetic field H is isothermally applied to the paramagnetic sample at ~ 1°K to bring f_e close to unity, and H is then removed adiabatically, the temperature will fall initially almost in proportion to H, and f_e will remain very nearly constant, as shown by deHaas and Wiersma[7] and by Casimir.[8] This behavior of T will continue until the magnetic field has fallen to a value such that the magnetic field term in the Hamiltonian for the salt becomes comparable in magnitude with the internal interaction terms. For values of H less than this, the temperature will remain roughly constant while f_e will fall to zero at $H=0$. Thus, in this nuclear polarization procedure, there is an optimum final field for which the maximum value of nuclear polarization f_N will be obtained. This is the field at which f_e/T is maximum.

POLARIZATION OF Mn^{55} NUCLEI IN $Mn(ND_4)_2(SO_4)_2\cdot 6D_2O$

The hfs Constant A

The hfs coupling constant has been measured by Bleaney and Ingram.[9] For $Mn(NH_4)_2(SO_4)_2\cdot 6H_2O$ they found this coupling to be almost isotropic and to give a term in the Hamiltonian for the salt of the form

$$\mathcal{H}_{hfs}=aS_3I_3+b(S_2I_2+S_1I_1), \quad (2)$$

* Presented at the Chicago meeting of the American Physical Society [Phys. Rev. **93**, 935 (1954)].

[1] Bernstein, Roberts, Stanford, Dabbs, and Stephenson, Phys. Rev. **94**, 1243 (1954).

[2] M. E. Rose, Oak Ridge National Laboratory Report ORNL-48, 1948 (unpublished); Phys. Rev. **75**, 213 (1949).

[3] C. J. Gorter, Physica **14**, 504 (1948).

[4] C. J. Gorter, Physik. Z. **35**, 923 (1934).

[5] N. Kurti and F. Simon, Proc. Roy. Soc. (London) **149**, 152 (1935).

[6] Rose, Simon, and Jauch, Phys. Rev. **84**, 1155 (1951).

[7] W. J. de Haas and E. C. Wiersma, Physica **3**, 491 (1936).

[8] H. B. G. Casimir, *Magnetism and Very Low Temperatures* (Cambridge University Press, Cambridge, 1940).

[9] B. Bleaney and D. J. E. Ingram, Proc. Roy. Soc. (London) **205**, 336 (1951).

with $|a| = 0.00911$ and $|b| = 0.00943$, both in cm^{-1}. For a powder sample the spatial average A of the hfs coupling is $A = |a|/3 + 2|b|/3 = 0.00932\ cm^{-1}$. This measurement of a and b was made on a magnetically very dilute salt while a polarized neutron observation of the nuclear polarization must be performed on the normal and relatively concentrated salt. It seems reasonable to assume that the values of a and b are very little dependent on Mn^{++} concentration in that they have been found to have essentially the same values in a number of dilute salts with chemically very different anions.[9,10] The salt was deuterated to avoid incoherent neutron scattering by protons. It was assumed that the hfs coupling was not affected thereby.

Measurement of f_e

In 1940, Casimir[11] proposed a method for determining magnetic moments of paramagnetic materials which consists in applying to the sample a small measuring field H_0 at right angles to the magnetizing field H_e. If $H_0 \ll H_e$, and the sample is isotropic and spherical, the application of H_0 rotates both the total field and the magnetic moment through the same small angle at essentially constant magnitude. When H_0 is applied, an induction pickup coil (or secondary) coaxial with the coil producing H_0 and centered on the sample, delivers a signal proportional to the component of magnetic moment along H_0 if the usual bucking arrangement, familiar from susceptibility measurements, is used.[8,12] The apparatus is thus the usual ballistic susceptibility measurement arrangement, with the addition of the Weiss magnet which produces H_e.

Because of crystalline electric field effects, a single crystal of manganous ammonium sulfate is magnetically anisotropic; but a powder sample will, of course, have "net" magnetic properties which are independent of direction. If we adiabatically demagnetize a powder sample slowly compared to the time for thermal equilibrium among the crystallites of the powder, the total entropy of the sample will be constant, and in the final field H_e all of the crystallites will have the same temperature. When the small field H_0 is applied, the total field will be rotated and slightly increased. This change will produce temperature changes in the individual crystallites which will vary from one to another depending on their orientation. For $H_0 \ll H_e$, however, these temperature changes will be negligible compared to the sample temperature.[13] Thus, we conclude that the magnetic moment f_e of a powder sample may be measured by the above method if the demagnetization is performed slowly and $H_0 \ll H_e$. In these measurements, we used a $\frac{3}{4}$-inch sphere machined from a pressed powder cylinder of $Mn(ND_4)_2(SO_4)_2 \cdot 6D_2O$. The powder density was within 1–2 percent of the crystalline density; no corrections were made for this deviation which has a negligible effect.

It can be shown that the ballistic galvanometer deflection D, arising when H_0 is suddenly applied to the sample, is very closely given by

$$D/H_0 = (\alpha/H_e) f_e + \beta(H_e), \tag{3}$$

where α is the ballistic sensitivity constant, and β reflects the residual unbalance of the coil system and the effect of the nearby iron pole tips. The dependence of β on H_e was minimized by making the length of the secondary coil approximately equal to the pole face diameter of the Weiss magnet. This dependence was almost negligible but was taken into account.

The accuracy with which Eq. (3) applies was determined in the liquid helium temperature region. Galvanometer deflections D were taken as a function of T from 1.2° to 4.2°K at constant H_e and H_0. By holding these fields constant, the effect of the iron magnet poles on β and H_0 was held constant. f_e was calculated for the various temperatures using the Brillouin function $B_{5/2}(H_e/T)$. Values of H_e up to 4560 gauss were used. This led to an over-all range of f_e for all combinations of H and T of $0 < f_e \leq 0.5$.

In this range the linear relation between D and f_e was demonstrated to hold within 0.3 percent using the Royal Society Mond Laboratory liquid helium temperature scale (1948)[14] and to better than 0.1 percent using the corrections to this scale given by Kistemaker[15] and those recently obtained at this laboratory.[16] These measurements also showed that the coefficient of f_e [Eq. (3)] was inverse in H_e within 0.3 percent, i.e., the quantity α was constant.

After demagnetization, the magnetic moment f_e was calculated from readings of the galvanometer deflection D, using Eq. (3), with values for α and β obtained *for the particular* H_e as described above.

The cryostat used in these measurements was the same as that used for the nuclear polarization experiments[1] and was similar to one recently described by Erickson, Roberts, and Dabbs.[17] In the earliest of these experiments, building induced vibration of the pickup coil in the field H_e gave a large "noise" signal to the ballistic galvanometer which made precise observations of f_e very difficult. This situation was corrected by inserting a 7 henry air-core inductance in series with the galvanometer. The time constant introduced by this inductance was very short compared to the galvanometer period.

Figure 1 gives the observed variation of f_e with H_e at an entropy value $S/R = 0.514$, where R is the gas

[10] T. S. England and E. E. Schneider, Nature **166**, 437 (1950); D. J. E. Ingram, Proc. Phys. Soc. (London) **A66**, 412 (1953); R. S. Trenhan, Proc. Phys. Soc. (London) **A66**, 118 (1953).

[11] See reference 8, p. 20.

[12] W. J. de Haas and E. C. Wiersma, Physica **2**, 335 (1935).

[13] L. D. Roberts and J. W. T. Dabbs, paper presented at the Southeastern Section meeting, American Physical Society, April, 1954 [Phys. Rev. **95**, 307(A) (1954)].

[14] H. Van Dijk and D. Shoenberg, Nature **164**, 151 (1949).

[15] J. Kistemaker, Physica **12**, 272, 281 (1946).

[16] R. A. Erickson and L. D. Roberts, Phys. Rev. **93**, 957 (1954).

[17] Erickson, Roberts, and Dabbs, Rev. Sci. Instr. (to be published).

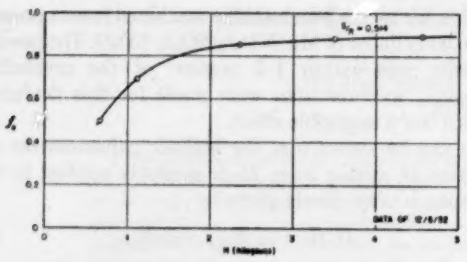

FIG. 1. The electron polarization f_e as a function of magnetic field H_e at constant entropy, $S/R=0.514$.

constant. This is the entropy value which was used in the nuclear polarization work.[1] Figure 2 shows a typical measurement of the f_e *versus* S/R relation at a final field H_e of 2350 gauss. This was obtained from a series of adiabatic demagnetizations at different entropies to the given H_e. The entropy values were calculated from the initial H_e and T ($\sim$1°K) assuming the salt to be an ideal paramagnetic material.

Temperature Measurements

Absolute temperature measurements below 1°K were made using the same apparatus and the same sample of $Mn(ND_4)_2(SO_4)_2\cdot 6D_2O$ as for determining f_e. Here f_e served as the "thermometric parameter"[18] for γ-ray heating experiments. One uses

$$T(H_e,S)=(\partial Q/\partial f_e)_H/(\partial S/\partial f_e)_H$$
$$=(\partial Q/\partial t)_H\cdot(\partial t/\partial f_e)_H/(\partial S/\partial f_e)_H, \quad (4)$$

where $\partial Q/\partial t$ is the heat input per unit time from the γ-ray source (assumed independent of temperature[19,20] and magnetic field), $(\partial f_e/\partial t)_H$ is the measured time rate of change of f_e during the γ-ray heating, and $(\partial S/\partial f_e)_H$ is the slope of the f_e-S curve, Fig. 2.

For these measurements, a pair of two-curie Co^{60} γ-ray "point" sources (furnished by the Radioisotopes Division of this laboratory) were used. They were placed 10 cm from the sample in Pb housings on opposite sides of the cryostat and on a line perpendicular to the axis of the Weiss electromagnet. The γ-ray heating could be turned "on" or "off" within one second by moving the sources within their housings. The ratio of the γ-ray intensity at the sample for the two positions was about 35.

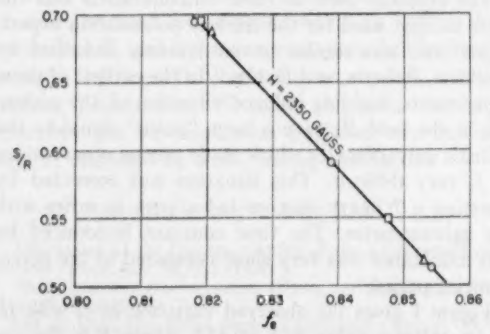

FIG. 2. The entropy S/R as a function of electron polarization f_e at constant $H=2350$ gauss for three separate experiments.

Thermometric parameters which have been used previously[18] are the reactive and resistive components of the susceptibility and the magnetic remanence. The variation of these quantities with entropy is so small that they cannot be used in the magnetic field-entropy region of interest here. However, as is shown in Fig. 2, the variation of f_e with entropy is sufficiently large compared to the measurement errors to allow a satisfactory determination of $(\partial S/\partial f_e)_H$.

dQ/dt is obtained by measuring the rate of rise of temperature due to the γ rays in a temperature region of known specific heat. If this measurement is made near 1°K where the specific heat is usually well known, the background heat leak is usually quite large compared to that at the lower temperatures and compared to the specific heat of the salt. If this calibration is made at lower temperatures where the salt specific heat is larger and the background heat leak relatively small and temperature independent, the specific heat is usually not well known. The resulting uncertainties in dQ/dt have been one of the larger sources of error in the measurement of temperature below 1°K by γ-ray heating. To reduce this error we have made a comparison of the γ-ray heating with a measured electrical heat input in the temperature region near 0.4°K where the thermal conductivity of the salt is adequate. At lower temperatures electrical heating would lead to serious temperature inhomogeneities, while γ-ray heating does not. At 0.4°K, the specific heat of the salt is sufficiently large compared to the "background" heat leak to permit precise measurements of susceptibility as a function of time for either heat source.

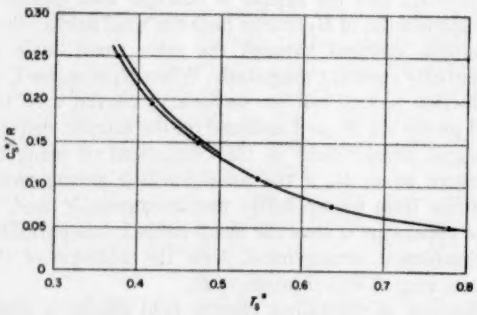

FIG. 3. The lower curve is the measured specific heat C_e^*/R as a function of the magnetic temperature T_e^*. The upper curve is calculated. See text.

Figure 3 gives a curve of the specific heat $C_e^*=dQ/dT_e^*$ of $Mn(ND_4)_2(SO_4)_2\cdot 6D_2O$ as a function of

[18] D. de Klerk, thesis, Leiden, 1948 (unpublished).
[19] R. L. Platzman, Phil. Mag. 44, 497 (1953).
[20] N. Kurti and F. Simon, Phil. Mag. 44, 501 (1953).

T_e^* (reciprocal susceptibility) as determined by electrical heating. For this measurement the salt was pressed into a slitted cylindrical Cu sleeve, $\frac{5}{16}$ in. in diameter$\times\frac{15}{16}$ in. long. A Constantan wire heater was wound on the Cu cylinder using baked Araldite to obtain thermal contact. Heater leads through the wall of the sample tube into the liquid He were made of 1-mil Pb-coated Constantan wire. Heater current and potential measurements were made using precision potentiometers and a standard resistor. The observed magnetic temperature T^* was corrected to that for a sphere T_s^* assuming the sample to be an ellipsoid with $c/a=3$. These measurements lead to a γ-ray heat input $dQ/dt=2890$ ergs/min for our $\frac{3}{4}$-in. spherical sample.

It is interesting to note in passing that the Constantan heater showed a minimum of electrical resistance at about 0.5°K.

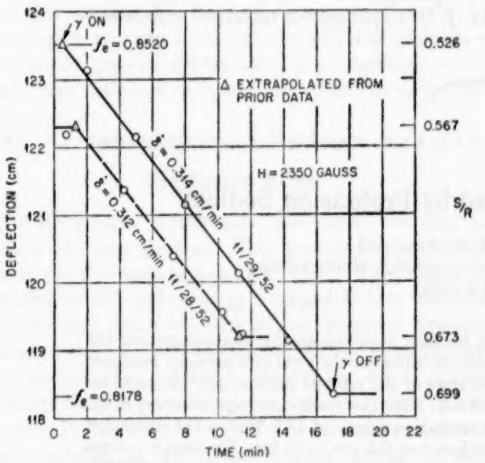

FIG. 4. Two typical warmup curves for the sample in a magnetic field of 2350 gauss showing the galvanometer deflection as a function of time.

A first term approximation to C_e^* is given by the specific heat[21] $0.0314R/T^2$ together with the T *versus* T_e^* relation given by Cooke.[22] This procedure yields a C_e^* in fair agreement with our measured values as is shown in Fig. 3. It is, however, not as acceptable in that this specific heat assumption is probably a few percent in error at the lower temperatures, and in that the T *vs* T_e^* relationship is normalized to a value based on a Stark splitting pattern recently shown to be incorrect.[9]

$(\partial f_e/\partial l)_H$ was obtained after demagnetization ($S/R<0.514$) by observing the galvanometer deflection D as a function of time, and using Eq. (3). Figure 4 gives typical results.

A substitution of the above results in Eq. (4) yields a temperature of 0.201°K at $S/R=0.514$ and $H_e=2350$ gauss.

[21] R. A. Erickson and L. D. Roberts (unpublished).
[22] A. H. Cooke, Proc. Phys. Soc. (London) **A62**, 269 (1949).

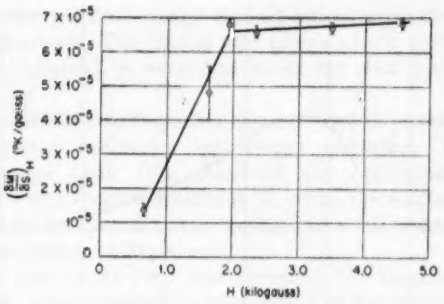

FIG. 5. $(\partial M/\partial S)_H$ as a function of magnetic field H at $S/R=0.514$.

Dependence of T on H_e

In order to obtain $T(H_e)$ at $S/R=0.514$ we use one of the Maxwell relations of magnetic thermodynamics, *viz.*, $(\partial T/\partial H)_S=-(\partial M/\partial S)_H$. Integrating this equation, we obtain the expression

$$T_2-T_1=-\int_{H_1}^{H_2}\left(\frac{\partial M}{\partial S}\right)_H dH$$
$$=-Ng\beta S_e\int_{H_1}^{H_2}\left(\frac{\partial f_e}{\partial S}\right)_H dH \quad (5)$$

for isentropic changes of temperature with applied field.[8] Here, N is Avogadro's number, g is the gyromagnetic ratio, and β is the Bohr magneton. Measurements similar to those shown in Fig. 2 were made for a number of fields in the entropy region $0.36\leq S/R\leq 0.9$. In this region as is illustrated in Fig. 2, the f_e-S function was remarkably linear for the H_e values covered. The slopes obtained from these measurements are plotted as a function of H_e for the entropy $S/R=0.514$ in Fig. 5. A numerical integration of these slopes, using Eq. (5) gives the temperature as a function of H_e when normalized to our γ-ray heating point at 0.201°K and 2350 gauss, as is shown in Fig. 6.

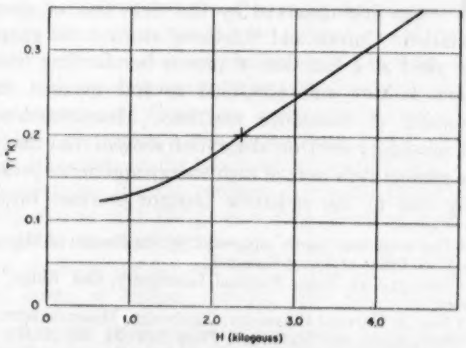

FIG. 6. Absolute temperature T as a function of magnetic field at $S/R=0.514$.

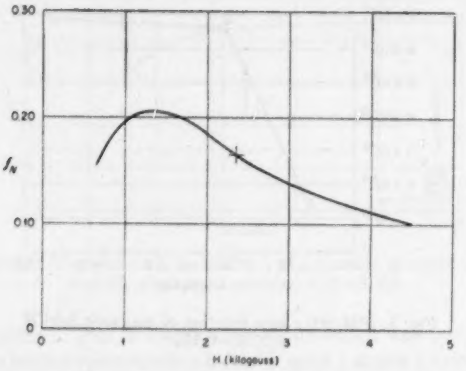

FIG. 7. The nuclear polarization f_N as a function of magnetic field H at $S/R=0.514$ as calculated from the measured f_e and T.

The measurement of the magnetic moment-entropy curve over a range of magnetic fields is especially convenient in that the same data are useful in γ-ray heating measurements and in experiments based on Eq. (5).

Calculation of f_N from Measured f_e and T

These measured values of f_e and T may now be substituted in Eq. (1) to obtain the nuclear polarization f_N as a function of H_e at $S/R=0.514$. This result is plotted in Fig. 7. It is seen that a maximum polarization $f_N=0.207$ is obtainable at a final field of 1300 gauss, and that the final fields (2260–2350 gauss) used in the nuclear polarization experiments[1] correspond to $f_N=0.165$ to 0.170 for the initial polarization of the nuclei.

ACKNOWLEDGMENTS

We wish to express our appreciation to Dr. M. E. Rose, Dr. S. Bernstein, Dr. C. P. Stanford, and Dr. T. E. Stephenson for many interesting discussions, and to Mr. J. B. Capehart for technical assistance.

PHYSICAL REVIEW VOLUME 95, NUMBER 4 AUGUST 15, 1954

Resonant States of Mg^{24} Excited by Protons on Sodium*

P. H. STELSON† AND W. M. PRESTON‡
Massachusetts Institute of Technology, Cambridge, Massachusetts

(Received April 8, 1954)

The gamma-ray yield from sodium was measured as a function of proton bombarding energy over the range 1.0 to 2.5 Mev using resolutions of 2.5 kev or better. In addition, the yield of α particles produced by the $Na^{23}(p,\alpha)Ne^{20}$ reaction and leading to the ground state of the residual nucleus was measured for proton energies of 1.0 to 2.2 Mev, with a resolution of 10 kev. Fifty-two resonances were observed in all. The resulting average level spacing is 28 kev at a mean excitation energy of 13.5 Mev in the compound nucleus Mg^{24}. The resonances vary in natural width from less than 0.3 kev to 50 kev. The energy spectra of the gamma rays from a number of resonances were investigated with a single-crystal NaI(Tl) scintillation spectrometer. The spectra consist mainly of two gamma rays, with energies of 0.45 ± 0.01 and 1.63 ± 0.02 Mev. These are interpreted as transitions from the first excited states of the residual nuclei formed by the reactions $Na^{23}(p,p')Na^{23}$ and $Na^{23}(p,\alpha')Ne^{20}$, respectively.

INTRODUCTION

THE interaction of fast protons with sodium nuclei was first observed by the detection of gamma radiation.[1] Curran and Strothers[2] studied the gamma-ray yield as a function of proton bombarding energy below 1 Mev and identified several maxima characteristic of resonance reactions. Measurements of the secondary electron absorption showed that many of the gamma rays were of high energy and hence presumably due to the radiative capture process. Burling[3] confirmed and more clearly resolved the resonances below 1 Mev and found a number of additional resonances in the region 1.0 to 1.9 Mev. However, even with the improved resolution of 10 to 25 kev, Burling concluded that the measured half-widths of the resonances were largely experimental in origin. Tangen,[4] using better resolution, found three new resonances in the low-energy region 0.25 to 0.50 Mev.

It was recognized that the (p,α) reaction is energetically possible and might give rise to gamma radiation of lower energy characteristic of the low-lying excited levels of the residual Ne^{20} nucleus. Curran aud Strothers showed that this was not a prominent mode of decay for resonances below 1-Mev proton energy. Burling did not undertake energy measurements of the gamma radiation. As one proceeds to higher proton energies,

* This work was jointly supported by the Bureau of Ships and the U. S. Office of Naval Research.

† Now at Oak Ridge National Laboratory, Oak Ridge, Tennessee.

‡ Now at Harvard University, Cambridge, Massachusetts.

[1] Herb, Kerst, and McKibben, Phys. Rev. **51**, 691 (1937).

[2] S. C. Curran and J. E. Strothers, Proc. Roy. Soc. (London) **A172**, 72 (1939).

[3] R. L. Burling, Phys. Rev. **60**, 340 (1941).

[4] R. Tangen, Kgl. Norske Videnskab. Selskabs Skrifter Nr. 1 (1946).

the Coulomb barrier effect is reduced and one expects that eventually the states will decay predominantly by particle emission rather than by radiative capture. In the present case, for proton energies of less than 5 Mev, the gamma rays associated with particle emission are restricted to two reactions: those due to the de-excitation of Ne^{20} produced by the (p,α) reaction and those due to the de-excitation of Na^{23} as the result of inelastic proton scattering.

Electrostatic generator techniques have advanced sufficiently to permit an increase in the energy homogeneity of the proton beam by a factor of 10 to 30 over that of the previous investigations. In addition, the advent of the scintillation crystal counter offers a highly efficient detector and one with which the energy spectrum of the gamma radiation can be rather simply determined. We therefore throught it worthwhile to undertake a new study of the gamma radiation from this reaction. We have also measured directly, by means of a particle detector, the relative yield as a function of proton energy of the α particles which result from the reaction when Ne^{20} is left in its ground state.

EXPERIMENTAL METHOD

The Proton Beam

The Rockefeller electrostatic generator[5] was used to produce the fast protons. This generator has an ion source of the radio-frequency type. The beam is analyzed by 90° deflection in a magnetic field which is stabilized and measured by a proton magnetic moment resonance device. The generator voltage is stabilized by a corona load which is driven by error signals produced by the proton beam at the exit slits of the analyzer. Proton beam currents of several microamperes were available in which the energy spread of the protons was approximately 0.02 percent. Experimental points taken at less than 0.01 percent difference in energy were reproducible over short intervals of time.

Energy measurements are based on the $Li(p,n)$ threshold calibration point which is taken to be 1.8822 ±0.0019 Mev as determined by Herb *et al.*[6] Over periods of several days, variations of about 0.1 percent in the voltage calibration have been observed. Hence, our absolute proton energies are subject to this uncertainty in addition to the 0.1 percent uncertainty of the calibration standard itself.

Gamma-Ray Counter and Target

The NaI crystal scintillation counter used for gamma-ray detection was constructed in the following way: a cylindrical NaI crystal 1½ in. in diameter and 1 in. long was ground smooth and solvent polished on one end. The crystal and a 5819 photomultiplier were placed in a thin-walled, airtight aluminum container with the polished crystal surface butted against the photocathode. The crystal and photocathode surface were immersed in water-free Nujol for good optical coupling.

The 661-kev Cs^{137} gamma ray was used to establish the energy calibration and energy resolution. The full-energy peak (the result of the photoelectric process or Compton scattering in which the scattered quantum is captured in the crystal) had a full width at half-maximum of 20 percent.[7]

For gamma-ray yield measurements, thin targets of sodium were prepared by evaporation of the metal in vacuum onto 10-mil tantalum disks. Target preparation was carried out in the target assembly of the generator. To reduce the carbon buildup effect and to prevent deterioration under proton bombardment the targets were rotated eccentrically and cooled by an air jet sprayed on the outside of the tantalum backing. The scintillation counter was located in the forward direction with respect to the proton beam and target; the distance from the target to the center of the NaI crystal was approximately 3 cm.

α-Particle Detector and Target

One expects in general from the target, in addition to the ground-state group of α particles, (a) alphas of lower energy from transitions in which Ne^{20} is left in an excited state; (b) elastically scattered protons from the target and the target backing, in relatively much larger numbers; and (c) inelastically scattered protons from the target or backing. Within the bombarding proton energy range of 1.0 to 2.5 Mev, it proved practical to detect separately the α-particle group associated with transitions to the ground state by using a special gas-filled proportional counter and pulse-height discrimination.

A thin nickel foil window, 0.4 air cm thick and 0.1 cm^2 area, was mounted on the side of a cylindrical counter of 1-in. diameter and 4-in. length. The particles pass through the window and traverse the counter perpendicular to its axis so that the path length in the gas is about 1 in. The counter was mounted in a small scattering chamber and placed so as to detect particles emerging from the target at 135° to the forward direction. The window was approximately 3 cm from the target. The counter center wire was 5-mil tungsten. A gas mixture of 90-percent argon−10-percent CO_2 was used; the pressure was varied from ¼ to ½ atmosphere depending on the bombarding proton energy.

In operation, the gas pressure in the counter could be adjusted so that the ground-state group of alphas, at a given bombarding energy, was barely stopped before reaching the far wall of the counter. Then any other group of alphas, coming from transitions to

[5] W. M. Preston and C. Goodman, Phys. Rev. **82**, 316 (1951).
[6] Herb, Snowdon, and Sala, Phys. Rev. **75**, 246 (1949).

[7] Considerably better resolution (half-widths as low as 10 percent) has been reported for this type of counter. The quality of the photomultiplier probably limited our resolution. We were not able to undertake the testing of a large number of tubes.

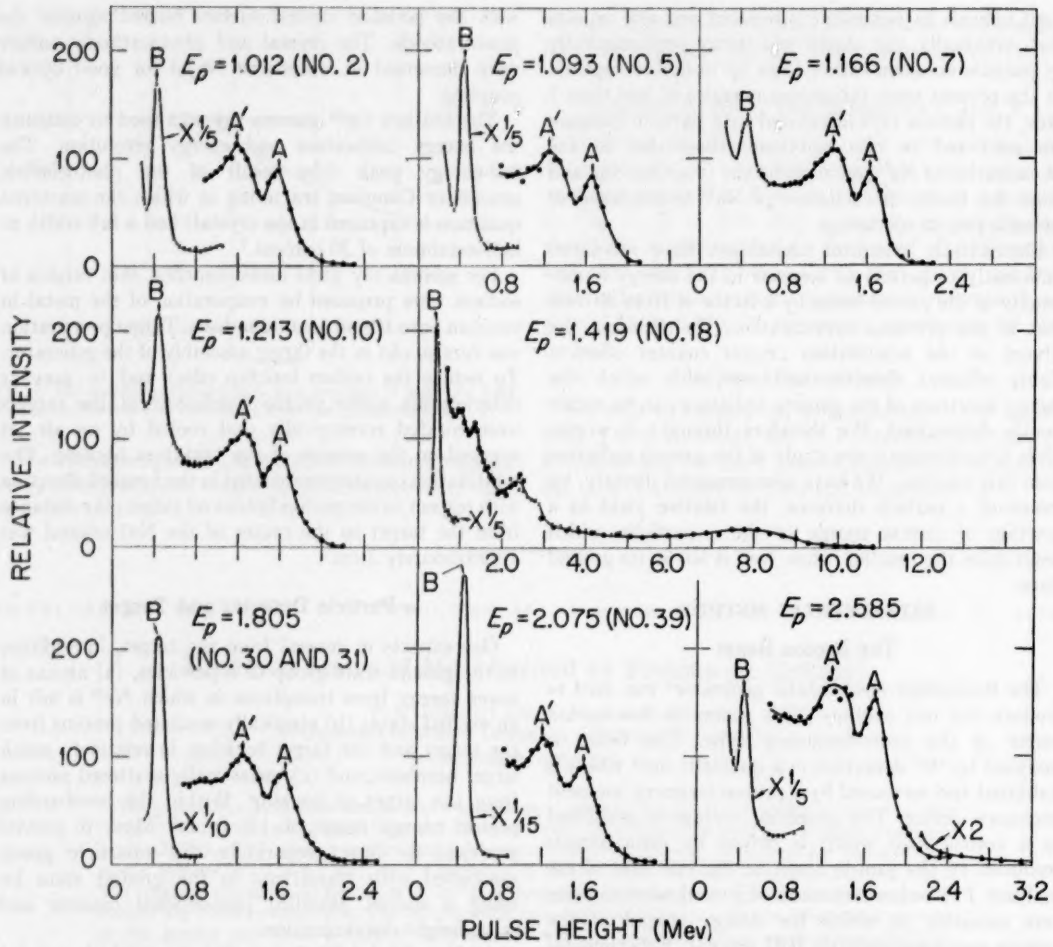

FIG. 1. Differential bias curves for a single-crystal NaI scintillation spectrometer, used to analyze the γ rays from sodium bombarded by protons, at various energies E_p. The abscissa scale is in Mev at the full-energy peak.

excited levels in Ne^{20}, would give smaller pulses. Protons of the same range, just able to cross the counter, gave substantially smaller pulses because of their smaller energy. Protons of greater range gave still smaller pulses because of their decreasing density of ionization along the effective path in the counter.

Although pulses from scattered protons were relatively small, their high intensity resulted in a serious pile-up problem. It was necessary to use thin Formvar target backings to reduce this to manageable proportions. The Formvar films are estimated to be roughly 25 micrograms/cm^2 thick. These were supported on small copper wire frames. The main drawback to the use of these thin backings is the limited beam current densities which they can take without disintegrating. We were forced to reduce the current to about 1/10 microampere which we dispersed over a target area of approximately 1 cm^2. The targets were prepared by evaporation of sodium metal, in vacuum, onto the backings. Surprisingly enough, the evaporation of a sodium layer onto the target backings did not drastically reduct the beam current capacity of the backings.

EXPERIMENTAL RESULTS

Gamma-Ray Energy Spectra

After preliminary yield curves had been run to locate resonances, the gamma-ray energy spectra at several resonances were measured. Some are shown in Fig. 1. With one exception, they exhibit a general similarity and a somewhat unexpected simplicity. Peaks A and A' may be attributed to the photoelectric and Compton electrons, respectively, from a gamma ray of 1.63±0.02-Mev energy. Peak B is interpreted as the photoelectric peak of a gamma ray of 0.45±0.01-Mev energy.

The processes which produce the two low-energy

gamma rays are revealed by the study of the energy level diagram of the relevant nuclei given in Fig. 2. The first excited state of Ne^{20} at 1.63 Mev has been observed in several different reactions.[8] The 1.63-Mev gamma ray therefore results from the (p,α) reaction in which Ne^{20} is left in the first known excited state, designated as channel α_1.

A level in Na^{23} at 0.43 ± 0.02 Mev has been observed by Endt *et al.*[9] from a study of the $Mg^{25}(d,\alpha)Na^{23}$ reaction. Recently, Donahue *et al.*[10] found this level by measuring the energy spectrum of protons inelastically scattered from sodium. It is thought, therefore, that the 0.45-Mev gamma ray is the result of the breakup of a compound state through channel p_1.

The existence of a second excited state in Ne^{20} at 2.2 Mev is questionable.[8] Even if this level exists and is excited through channel α_2, the decay by gamma emission directly to the ground state is not observed. If the decay were by cascade to the 1.63-Mev level, one would expect a low-energy gamma ray of about 0.5 or 0.6 Mev and one might take this as an alternative explanation for the peak *B*. This is certainly not the case, however, since several resonances are observed for which there is an abundance of 0.45-Mev gamma rays but no detectable 1.63-Mev radiation. Recent work by Cox *et al.*[11] on the gamma rays excited by inelastic proton scattering on Ne^{20} shows no evidence of a level at 2.2 Mev.

At the highest proton energies the decay through channels p_2 and α_3 is energetically possible, but it is probably suppressed because of the relatively low energy of the emerging particles. The gamma-ray spectra taken at the higher proton energies give no evidence for decay by these channels. However, decay by channel p_2 might escape notice if it is predominantly by cascade to the 0.45-Mev level, since this would give rise to a 1.63-Mev gamma ray which cannot be distinguished from the 1.63-Mev gamma ray from Ne^{20}.

The spectra suggest that the radiative capture process is generally much less probable than particle emission for proton energies of 1 Mev and higher. Of the resonances studied, only the one at 1.419 Mev (No. 18) shows a fairly large intensity of high-energy radiation.[12] A rough measure of the relative importance of the capture process for some of the other resonances is given by the following. From the counting rates and the variation of counter efficiency with energy it is estimated that the ratio of the number of gamma rays of 3 Mev or larger to the number of 1.63-Mev gamma rays is less than 0.04 for resonance 2, less than 0.02 for resonance 5, and less than 0.01 for resonances 7, 10, 30, and 31.

Although the capture gamma-ray intensity may be small compared to that of the low-energy gamma rays which follow particle emission, it is not expected to be zero. Teener *et al.*[13] have measured the gamma-ray energy spectra by taking pictures of the pulses from a NaI crystal counter, displayed on the face of an oscilloscope. This is a technique well suited to the detection of weak, high-energy radiation. They observed high-energy gamma rays at a number of resonances.

Gamma-Ray Yield Curves

The γ-ray yield from a thin sodium target is plotted in Fig. 3 as a function of the energy of the bombarding protons. The output of the linear amplifier, which followed the scintillation counter, was fed into two discriminator circuits in parallel. The first circuit was biased at 0.75 Mev, the second at 0.3 Mev.[14] The first circuit counting rate, corrected for background with zero proton beam, is plotted as a solid line Fig. 3; it is a measure of the number of γ rays above approximately 0.75 Mev. From the sample spectra shown in Fig. 1,[15] we can conclude that at most resonances there are only two γ rays present with appreciable intensities above 0.3 Mev, namely the 1.63- and 0.45-Mev rays. To this extent, the solid curve represents the yield of 1.63-Mev γ rays and therefore the yield of the $Na^{23}(p,\alpha)Ne^{20*}$ reaction through channel α_1. The curve has not been corrected for a background of γ rays produced by protons in the tantalum target backing. As shown by the inset in Fig. 4, this correction increases smoothly with E_p and is still small at the upper limit of the energy range investigated.

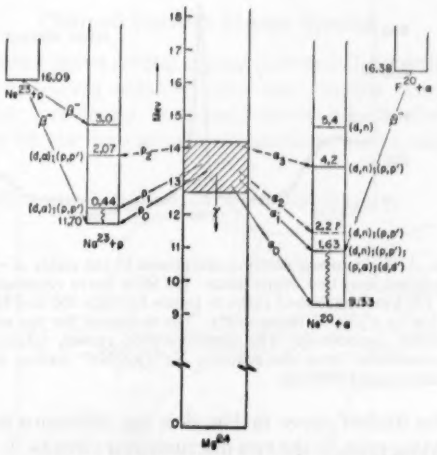

FIG. 2. Simplified energy level diagram for Mg^{24} and neighboring nuclei.

[8] See review article of F. Ajzenberg and T. Lauritsen, Revs. Modern Phys. **24**, 321 (1952).

[9] Endt, Haffner, and Van Patter, Phys. Rev. **86**, 518 (1952).

[10] Donahue, Jones, McEllistrem, and Richards, Phys. Rev. **89**, 824 (1953).

[11] Cox, Loef, and Lind, Phys. Rev. **93**, 925 (1954).

[12] The energy scale is not very accurate at the high energies since it is based on the low-energy Cs^{137} gamma ray.

[13] Teener, Seagondollar, and Krone, Phys. Rev. **93**, 1035 (1954) and private communication.

[14] More accurately stated, the first discriminator bias was set to pass all pulses larger than the most probable pulse height due to photoelectrons from a 0.75-Mev γ ray.

[15] It did not seem worth while to measure the γ-ray spectra at all resonances.

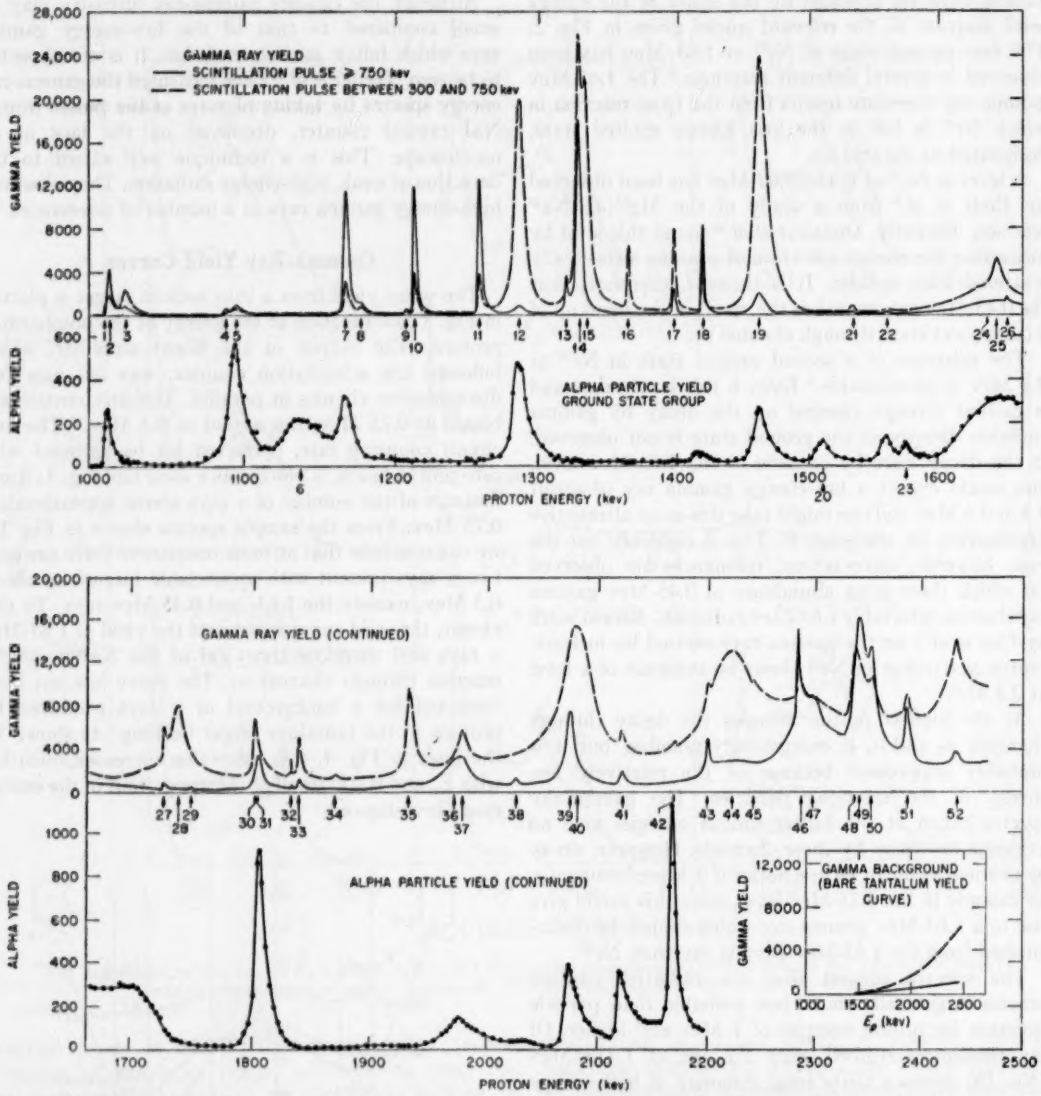

FIG. 3. Yield curves showing resonances in the yields of γ rays and α particles from sodium bombarded by protons. The γ-ray yield is analyzed into two components: the solid curve represents pulses from the scintillation counter corresponding to energies greater than 750 kev, the dashed curve to pulses between 300 and 750 kev. These are interpreted as due largely to the reactions $Na^{23}(p,\alpha')Ne^{20*}$ and $Na^{23}(p,p')Na^{23*}$, respectively. The ordinates for the solid and dashed curves are counts/40 microcoulombs and counts/20 microcoulombs, respectively. The α-particle yield curves, taken with a gas-filled proportional counter, show the relative yield (counts/2 microcoulombs) from the reaction $Na^{23}(p,\alpha)Ne^{20}$ leading to the ground state. The insert shows the yield of γ rays from the bare tantalum target backing.

The dashed curve in Fig. 3 is the difference in the counting rates in the two discriminator circuits It may be interpreted as roughly proportional to the yield of 0.45-Mev γ rays, and hence of the reaction $Na^{23}(p,p')Na^{23*}$ through channel p_1. The correction for background from the tantalum backing, shown again in the insert of Fig. 3, is considerably larger in this lower range of pulse heights.[16]

Experimental points were spaced so closely that they cannot be shown in Fig. 3. Figure 4 shows two typical

[16] A further correction arises from the fact that some pulses would be recorded in this channel, even from a pure source of 1.63-Mev γ rays, due to the low-energy tail of the pulse-height distribution. That this correction is relatively small can be seen as follows. At resonance No. 7 in Fig. 3, the yield of pulses in the nominally p_1 channel is approximately one-half the yield above 750 kev. (The figure shows the ratio as one-fourth since the ordinates for the dotted curve and solid curve are counts/20 microcoulombs and counts/40 microcoulombs, respectively.) In Fig. 1, peak B of No. 7 is still pronounced, which indicates that a large share of these pulses in the p_1 channel really come from the 0.45-Mev γ rays.

sections of the γ-ray yield curve on a much enlarged scale. Of the resonances shown in Fig. 4, Nos. 13, 14, 17, 18, 32, and 33 coincide exactly in both reactions, p_1 and α_1. Nos. 15 and 16 show no trace in the α_1 reaction. Nos. 30 and 31 are distinct; the former is due largely to the p_1 channel, the latter to the α_1.

Most of the γ-ray yield curves of Fig. 3 were taken with targets of about 2.5-kev stopping power for 1-Mev protons, and less at higher energies. The energy calibration and the condition of the target were checked several times during the run by careful measurements of the contour of the sharp resonance No. 18, which has a natural width less than 300 ev, and of the counting rate at the peak of the broad resonance No. 19. In this way, carbon buildup on the target, loss of sodium by evaporation, or increase in effective thickness could be measured.

For reasons not well understood, it was impossible to produce uniform sodium targets with effective thickness $\Gamma_t<2$ kev (measured for protons at 1 Mev) which would remain unchanged for any length of time. With targets having $\Gamma_t\sim 2$ kev, the natural width Γ of the broader resonances could be measured directly from the yield curves. We assume that $\Gamma^2=\Gamma_m^2-\Gamma_t^2$, where Γ_m is the measured width of a peak at half-maximum amplitude. This method is reasonably accurate for resonances having $\Gamma\geq\Gamma_t$.

The natural widths of a number of narrower resonances were measured by a modified "thick target" method. If an infinitely thick target is employed, the yield increases in a rounded step (see Fig. 5) in going over a resonance. If the total increase in yield is ΔY, and the bombarding-energy interval between the points $\Delta Y/4$ and $3\Delta Y/4$ is called Γ', it can be shown[17] that Γ' measures directly the combined effect of the natural width Γ and any energy spread in the bombarding beam. An infinitely thick target is not very useful for studying the width of a resonance which is preceded by many others at lower energies, since in traversing the resonance the yield will merely rise by a small increment over a large background. However, if a particular narrow resonance of natural width Γ is not too closely preceded by a neighboring resonance at lower energies, it is possible to use a target of intermediate thickness, say 5Γ, which involves only small corrections over an infinitely thick target. At the same time, the yield from resonances at lower energies will be relatively small.

Figure 5 shows a number of such "rise curves." Of all resonances studied, No. 18 appeared to be the sharpest, with a $\Gamma'=0.31$ kev. The γ-ray spectrum for this resonance, Fig. 1, indicates that the capture radiation process competes favorably with particle emission. Since "radiation" widths are expected to be of the order of 0.01 kev or less, the natural width Γ of this resonance is probably substantially less than 0.31 kev. We can infer that the measured value of $\Gamma'=0.31$ kev is due largely to spread in energy of the incident proton beam. The indicated homogeneity of about one part in 4500 is somewhat better than that estimated from the geometry of the magnetic analyzer. This inferred value for the energy spread in the beam was used to correct other narrow measured half-widths, assuming that $\Gamma^2=(\Gamma')^2-(0.31)^2$.

In Table I we have listed the positions and estimated natural half-widths of all resonances measured. The positions have all been corrected for target thickness. They have been recorded to the nearest 0.1 kev, an accuracy justified only for computing the separations of neighboring resonances.

Charged Particle Energy Spectra

Figure 6 shows several typical differential discriminator bias curves obtained with the charged particle detector previously described. From Fig. 2, the Q values for reactions going by channels α_0, α_1, p_0, and p_1

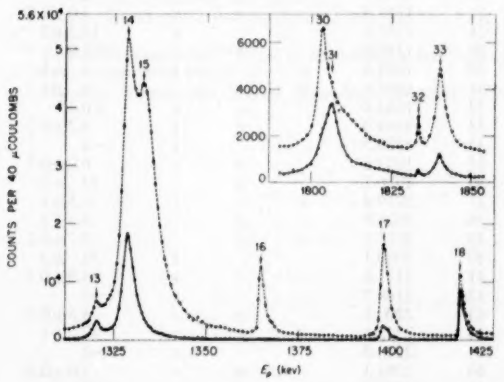

FIG. 4. Two portions of the γ-ray yield curves of Fig. 4 on an enlarged scale, showing the actual data points. The ordinates are counts/40 microcoulombs.

[17] Fowler, Lauritsen, and Lauritsen, Revs. Modern Phys. **20**, 236 (1948).

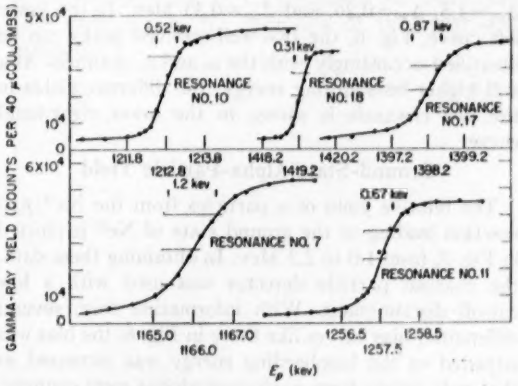

FIG. 5. Thick target γ-ray yield curves taken over five resonances, for protons of energy E_p on sodium. The indicated resonance widths are measured between the one-quarter and three-quarters rise points of thick-target yield curves.

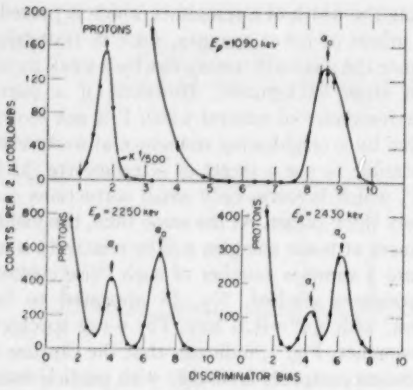

FIG. 6. Differential bias curves for a gas-filled proportional counter, used to detect scattered protons and α particles from sodium bombarded by protons, at three different energies E_p.

are, respectively, 2.37, 0.74, 0.00, and −0.44 Mev. For a bombarding proton energy of 1.090 Mev, the energies of the alphas and protons coming off at 135 degrees from the forward direction are computed to be $E_{\alpha 0}=2.65$, $E_{\alpha 1}=1.34$, $E_{p0}=0.94$, $E_{p1}=0.53$ Mev. Allowing for a loss of 0.40 cm air NTP in the nickel window and assuming a pressure in the counter of about 0.4 atmosphere, the energy loss of the various particles in the gas is estimated to be $\Delta_{\alpha 0}=2.00$, $\Delta_{\alpha 1}=0.46$, $\Delta_{p0}=0.42$, $\Delta_{p1}=1.18$ Mev. Inspection of the upper curve, Fig. 6, shows two peaks completely separated. They occur at energies with the ratio 4.7, in good agreement with that calculated for $\Delta_{\alpha 0}/\Delta_{p0}$; the high-energy peak can therefore be identified as arising from α particles from transitions to the ground state of Ne^{20}. Alphas from channel α_1 and inelastically scattered protons, if present, are obscured by the large intensity of elastic protons.

In a similar manner, at a counter pressure of 0.56 atmosphere and a bombarding energy of 2.25 Mev, the calculated energy losses in the counter are $\Delta_{\alpha 0}=2.6$, $\Delta_{\alpha 1}=1.5$, $\Delta_{p0}=0.26$, and $\Delta_{p1}=0.33$ Mev. In the lower left curve, Fig. 6, the two well-resolved peaks can be identified accordingly with the α_0 and α_1 channels. At a still higher bombarding energy, the different yields in the two channels is shown in the lower right-hand curve.

Ground-State Alpha-Particle Yield

The relative yield of α particles from the $Na^{23}(p,\alpha)$ reaction leading to the ground state of Ne^{20} is plotted in Fig. 3, from 1.0 to 2.2 Mev. In obtaining these data, the charged particle detector was used with a low cut-off discriminator. With information from several differential bias curves like those in Fig. 6, the bias was adjusted as the bombarding energy was increased so that only pulses from α_0-channel alphas were counted. When necessary, the pressure in the counter was adjusted to get improved discrimination. The target thickness was about 10 kev; resolution and statistical accuracy were considerably poorer than for the γ-ray yield curves.

In the α_0 yield curve, three new resonances appear, Nos. 6, 20, and 23, which are entirely absent from the γ-ray spectra. Conversely, a number of resonances which are strong in the α_1 or p_1 channels are absent in the α_0 channel. These results are summarized in Table I.

DISCUSSION

Burling[4] identified 15 resonances in the bombarding proton energy range of 1.0 to 1.9 Mev; with the better

TABLE I. The columns headed α_0, H and $L-H$ refer to the yield curves given in Fig. 3. H and $L-H$ are the gamma-ray yield curves given by the solid and dotted lines, respectively. See the text for discussion of the interpretation of these yield curves in terms of the reaction channels α_1 and p_1. An x indicates that a measurable yield was obtained at a particular resonance.

No.	E_r	α_0	H	$L-H$	Γ
1	1010.9			x	≤0.5
2	1012.3	x	x	x	0.8±0.1
3	1022.4		x	x	6.6±0.5
4	1087.1			x	1.1±0.5
5	1093.3	x	x	x	7.9±0.5
6	1137	x			30 ±5
7	1166.0	x	x	x	1.2±0.1
8	1176.2		x	x	<2.3
9	1206.6		x	x	0.3±0.1
10	1212.8		x	x	0.4±0.1
11	1257.5		x	x	0.6±0.1
12	1287.5	x	x	x	7.1±0.2
13	1320.6		x	x	2.1±0.5
14	1328.7		x	x	3.5±0.2
15	1333.5			x	6.7±0.2
16	1364.9			x	1.2±0.2
17	1398.2		x	x	0.8±0.1
18	1419.2	x	x	x	≤0.3±0.05
19	1460.4	x	x	x	9.8±0.2
20	1511	x			<10
21	1518.9		x	x	3.2±0.5
22	1558.2	x	x	x	6.5±0.5
23	1575	x			<10
24	1637.9	x	x	x	~50
25	1645.2			x	~8
26	1653.1		x		~2
27	1718.6		x	x	2.0±0.5
28	1737.3			x	15.2±2
29	1748.6		x		≤1.0
30	1802.3	x		x	4 ±1
31	1805.1	x	x		6 ±1
32	1832.4		x	x	<0.35
33	1839.0		x	x	3.2±0.2
34	1870.2			x	~1
35	1933.3		x	x	6.9±0.5
36	1976.1		x		23 ±3
37	1979.4	x		x	9.5±1
38	2026.8		x		3.3±1
39	2075.2	x	x		8.7±0.5
40	2080.1			x	31 ±2
41	2121.6	x	x	x	4.8±0.5
42	2169.5	x		x	~2
43	2200.1		x	x	3.5±0.5
44	2222.6		x	x	47 ±5
45	2243.0			x	~2
46	2284.3		x	x	2.0±0.5
47	2297.4		x	x	~28
48	2340.0			x	~10
49	2342.8		x		~14
50	2354.4		x	x	~4
51	2387.9		x	x	4.9±0.5
52	2435.9		x	x	6.5±0.5

resolution available to use, we have found 32 in the same interval. The average spacing for 52 resonances in the range 1.01 to 2.44 Mev is 28 kev. There is no indication of any decrease in the average level separation with increasing excitation energy.

The ground state of the even-even nucleus Ne^{20} is 0^+ (total angular momentum $I=0$, even parity); the first excited state is predicted to be 2^+.[18] Seed[19] has confirmed this assignment. The ground state of Na^{23} predicted by shell theory is $5/2^+$;[20] it is actually found to be $3/2^+$, so it is quite likely that the first excited state is $5/2^+$. With these assignments for the final states, the barrier penetrabilities can be computed for the decay of any excited state of Mg^{24} with given spin, parity, and excitation energy, by the channels α_0, α_1, p_0, and p_1. If the relative decay probability in different channels depended primarily on the penetrability factor, we might hope to make some headway in assigning spin and parity by a study of the experimental data summarized in Fig. 3 and Table I. Unfortunately, the factor in the decay probability which contains the matrix element for the transition[21] exhibits such wide variations[22] that detailed analysis seems unprofitable.

Since the α particle has zero intrinsic spin, decay to the ground state of Ne^{20} in the channel α_0 can occur only from states in Mg^{24} belonging to the series 0^+, 1^-, 2^+, 3^-, with the orbital angular momentum l of the α particle necessarily equalling the spin I of the compound state (see Table II). This applies to sixteen of the 52 resonances listed in Table I. Three of these, Nos. 6, 20, and 23, could not be detected at all in the α_1 or p_1 channels. It is likely that these latter are 0^+ states, which can decay by s-wave emission through α_0 but only by d waves ($l=2$) in the α_1 and p_1 channels. The corresponding penetrabilities differ by a factor of over 1000, in the case of resonance No. 6.

TABLE II. For states in Mg^{24} of total angular momentum and parity as indicated in the top line, the table shows the lowest permitted value of the orbital angular momentum, l, of a particle emitted in decay through four channels: p_0 and p_1, proton emission to the ground state and first excited state of Na^{23}; α_0 and α_1, α-particle emission to the ground and first excited states of Ne^{20}, respectively.

State	0^+	0^-	1^+	1^-	2^+	2^-	3^+	3^-
Channel								
p_0	2	1	0	1	0	1	2	1
p_1	2	3	2	1	0	1	0	1
α_0	0	—	—	1	2	—	—	3
α_1	2	—	2	1	0	1	2	1

Eight or nine resonances, of which Nos. 15 and 16 are the most striking examples, are not observed in either the α_0 or the α_1 channels. Decay from a 0^- state is strictly forbidden by α_0 or α_1, but must go by f wave in channel p_1; an assignment of 3^+ is more reasonable for the resonances which are strong in p_1.

Another possible explanation for levels which do not decay by α emission is found in the operation of isotopic spin selection rules. The proton has isotopic spin $T=\frac{1}{2}$. Combining with the lowest states of Na^{23}, which also have $T=\frac{1}{2}$, it can excite both singlet ($T=0$) and triplet ($T=1$) states in Mg^{24}. The positions of the ground states of the isobars F^{20}, Ne^{20}, and Na^{20} show that the low-lying states of Ne^{20} have $T=0$. Hence only the singlet states of Mg^{24} are able to decay to Ne^{20} by emission of α particles ($T=0$). The positions of the isobars Na^{24}, Mg^{24}, Al^{24} indicate that the triplet states of Mg^{24} should first occur at excitation energies of 9 or 10 Mev; in the region here investigated, 3 or 4 Mev higher, the spacing of triplet levels is probably considerably larger than that of singlet levels.

In conclusion, we wish to thank Professor Clark Goodman and Mr. Clyde McClelland for their interest and help during the early stages of the work, and Mr. I. E. Slawson and Mr. D. C. Thompson for their invaluable assistance in the operation of the electrostatic generator.

[18] G. Scharff-Goldhaber, Phys. Rev. **90**, 587 (1953).
[19] J. Seed, Phil. Mag. **44**, 921 (1953).
[20] Mayer, Moszkowski, and Nordheim, Revs. Modern Phys. **23**, 315 (1951).
[21] Expressed sometimes in terms of an "effective level spacing" D or a "reduced level width" γ.
[22] Hinchey, Stelson, and Preston, Phys. Rev. **86**, 483 (1952).

Reorientation of Aligned Nuclei

N. R. STEENBERG*
Division of Physics, National Research Council, Ottawa, Canada
(Received March 18, 1954)

Where nuclei aligned at low temperatures decay by a two-stage cascade, the degree of alignment of the intermediate state may be influenced by magnetic coupling. If the second stage is γ radiation, the angular distribution will be influenced as a consequence. This effect is treated by assuming a static interaction and twofold ionic degeneracy. In particular for high temperatures very explicit results are given for Δ', the mean degree of alignment of the intermediate state. This is dependent primarily on the mean life and magnetic moment of the intermediate state. If is found that if the properties of the intermediate state are similar to those of the initial state. (1) Reorientation effects will be present if $\tau > 10^{-9}$ sec; (2) They may either increase or decrease Δ'; (3) A strong external field cancels the effect altogether; (4) Reorientation can introduce $\cos^4\theta$ terms into the angular distribution even at the highest temperatures; (5) Where τ is very long, Δ' tends to a finite limit. The calculations are applied to an experiment.

I. INTRODUCTION

THE phenomenon of nuclear alignment at low temperatures is experimentally well established,[1-3] and the elementary theory has been given.[4,5] The experimental method has been to substitute radioactive isotopes in salts whose low-temperature properties are known. Nuclear alignment is then measured by the anisotropy of emitted γ radiation. It has not been possible so far to compare theory and experiment exactly since the magnetic moment of the radioactive nucleus is an unknown. If the theory is accepted, a value for this parameter can be deduced. This is dependent, however, on the theoretical assumptions being correct. For example, if the ground-state spin of Co^{60} is 4, as has been recently proposed,[6] the experiments referred to will need reinterpretation.

The similarity between the problem of the angular distribution from aligned nuclei and the problem of angular correlations has been pointed out.[7] It is known that magnetic coupling in the intermediate state can affect the angular correlation of successive nuclear radiations[8] and that such effects may yield information about the magnetic moment and the lifetime of the intermediate state. Where nuclei aligned at low temperatures decay, for example by a $\beta-\gamma$ cascade, disturbances, such as hfs coupling and external fields, may be expected to influence the degree of alignment of the γ-emitting state and thus the angular distribution of the γ radiation. If the lifetime of the intermediate state is long enough the probability will grow that the nucleus is reoriented by such coupling.

This effect can most conveniently be incorporated into the population functions for the substates of the intermediate nucleus, that is, into the statistical matrix of the intermediate spin system.

In the following we treat in detail a situation of experimental interest in which, in a single crystal, the ionic degeneracy before emission is twofold, having anisotropic hfs. By assuming a static interaction in the intermediate state and restricting ourselves to terms of order $(1/kT)^2$, i.e., to "high" temperatures, very explicit results are obtained. These show that reorientation can have a pronounced effect and must be considered whenever the intermediate lifetime is greater than 10^{-10} sec.

The calculations are applied to the experiment of Ambler *et al.*[3] which disagrees with the simple theory. The result is inconclusive, however, in that the effect of reorientation in this case is not sufficient to wipe out the alignment altogether.

II. GENERAL

The first stage of this problem is similar to the problem of angular correlations and our starting point is the expression given by Biedenharn and Rose,[7] whose notation is adopted, for the probability amplitude of a two-stage transition as follows: The system ion plus nucleus goes over from a gross state A having substates α, emitting radiation ρ to a gross intermediate state B, substates β, and then emitting γ radiation σ to a final state C, substates γ. The nuclear spins involved are successively J, J_1, and J_2. The probability amplitude after emission is,

$$C_{\gamma\rho\sigma}=\sum_{\alpha\beta}\frac{P_\alpha(\alpha|H_\rho|\beta)^*(\beta|H_\sigma|\gamma)^*\exp[i(\omega_\rho+\omega_\sigma+\epsilon_\gamma)t]}{(\omega_\rho+\omega_\sigma-\epsilon_{\alpha\gamma}-i\gamma_A)(\omega_\sigma-\epsilon_{\beta\gamma}-i\gamma_B)}. \quad (1)$$

The fundamental difference between the present problem and that of angular correlations should here

* National Research Laboratories Postdoctorate Fellow.
[1] Daniels, Grace, and Robinson, Nature **168**, 780 (1951).
[2] Gorter, Poppema, Steenland, and Beun, Physica **17**, 1050 (1951).
[3] Ambler, Grace, Halban, Kurti, Durand, Johnson, and Lemmer, Phil. Mag. **44**, 216 (1953).
[4] Simon, Rose, and Jauch, Phys. Rev. **84**, 1155 (1951); H. A. Tolhoek and J. A. M. Cox, Physica **19**, 101 (1953).
[5] N. R. Steenberg, Proc. Phys. Soc. (London) **A65**, 791 (1952); Proc. Phys. Soc. (London) **A66**, 399 (1953).
[6] G. L. Keister and F. H. Schmidt, Phys. Rev. **93**, 140 (1954).
[7] L. C. Biedenharn and M. E. Rose, Revs. Modern Phys. **25**, 729 (1953).
[8] Aeppli, Albers-Schönberg, Bishop, Frauenfelder, and Heer, Phys. Rev. **84**, 370 (1951).

be noted. For angular correlations $P_\alpha = e^{i\varphi_\alpha}$, that is, it can be assumed that both phases and spin orientations are distributed at random so that for an assembly of systems $\langle P_\alpha \bar{P}_{\alpha'}\rangle = \delta_{\alpha\alpha'}$. For the present problem the probability amplitude for the state α is $P_\alpha = |P_\alpha| e^{i\varphi_\alpha}$ and $\langle P_\alpha \bar{P}_{\alpha'}\rangle = |P_\alpha|^2 \delta_{\alpha\alpha'}$, that is, while we can assume that the phases are randomly distributed, the spin states α are occupied with a varying probability $|P_\alpha|^2 = w_\alpha$.

The angular distribution of the γ ray σ is given now by integrating $\langle |C_{\gamma\rho\sigma}|^2\rangle$ over all radiation energies and summing over polarization and final states in the usual way and also integrating over all directions of the first radiation, $(\int d\Omega_\rho)$, i.e.,

$$I(\theta) = \mathfrak{S}_{\rho\sigma} \int d\Omega_\rho d\omega_\rho d\omega_\sigma \sum_\gamma \langle |C_{\gamma\rho\sigma}|^2\rangle$$

$$= \mathfrak{S}_{\rho\sigma} \int d\Omega_\rho d\omega_\rho d\omega_\sigma \sum_{\alpha\beta\beta'\gamma} w_\alpha \times \frac{(\alpha|H_\rho|\beta)^*(\beta|H_\sigma|\gamma)^*(\alpha|H_\rho|\beta')(\beta'|H_\sigma|\gamma)}{(1+i\epsilon_{\beta\beta'}\tau)}, \quad (2)$$

where $\tau = 1/2\gamma_B$ is the mean life of the intermediate state B and $\epsilon_{\beta\beta'}$ is the energy difference between the substates β and β'. Because of the Hermitian property of the matrix elements we can replace $(1+i\epsilon_{\beta\beta'}\tau)$ at once by $(1+\epsilon_{\beta\beta'}{}^2\tau^2)$.

We must now consider the type of interaction which both is responsible for the initial nuclear alignment and may cause reorientation in the intermediate state. For the initial state ordinary hfs coupling with no external field cannot give rise to nuclear alignment since no direction in space is preferred. (It will be seen, however, that nuclear alignment can arise solely through the reorientation terms.) We assume our source to be a single crystal having an axis of magnetic symmetry along which an external field H is applied. The interaction Hamiltonian for the initial state is then,

$$\mathfrak{IC} = g\mu H S_z + g_n \mu_n H J_z + A S_z J_z + B(S_x J_x + S_y J_y), \quad (3)$$

where

S_z = z component of ionic spin;

g, g_n = ionic and initial nuclear g factors;

μ, μ_n = Bohr and nuclear magnetons.

The nuclear interaction $g_n\mu_n$ is of the order of 10^{-3} times the ionic interaction, and since it is found to play no significant part by itself for magnetic ions, it is discarded in what follows.

In analogy with the theory of ordinary hfs, we label the zeroth-order states of the system with quantum numbers F and μ and express them as linear combinations of ionic and nuclear states as follows:

$$\chi_{F^\mu} = \sum_{\sigma M} (\sigma M|\mu F)\psi_J{}^M \varphi_S{}^\sigma. \quad (4)$$

The perturbation problem can now be solved for the energy levels, $E_\mu{}^F$ and the transformation coefficients $(\sigma M|\mu F)$ of the system in the initial state. The $(\sigma M|\mu F)$ are real and unitary and vanish unless $\mu = \sigma + M$. If $H=0$ and $A=B$ (which would result, however, in no nuclear alignment at all) $(\sigma M|\mu F)$ becomes the regular vector addition coefficient, $(JSM\sigma|JSF\mu)$, in the notation of Condon and Shortley.[9] Note that while χ_{F^μ} is an eigenfunction of $F_z = J_z + S_z$ with eigenvalue μ, it is not (unless $H=0$, $A=B$) an eigenfunction of $\mathbf{F}^2 = \mathbf{J}^2 + \mathbf{S}^2 + 2\mathbf{J}\cdot\mathbf{S}$. F is, however, a convenient label.

For the interaction in the intermediate state we shall choose a static Hamiltonian $\mathfrak{IC}'$ of similar form and label the intermediate states with F_1 and μ_1. Equation (2) can now be rewritten replacing α by $F\mu$, β by $F_1\mu_1$, etc., $\epsilon_{\beta\beta'}$ by $\epsilon(F_1F_1'\mu_1\mu_1')$ and w_α by $w_\mu{}^F = \exp(-E_\mu{}^F/kT)$ and transforming the matrix elements as follows:

$$(\alpha|H_\rho|\beta) = \sum_{M M_1 \sigma} (\sigma M|\mu F)(\sigma M_1|\mu_1 F_1)(M|H_\rho|M_1),$$

$$(\beta|H_\sigma|\gamma) = \sum_{M_1' M_2 \sigma'} (\sigma' M_1'|\mu_1 F_1) \times (\sigma' M_2|\mu_2 F_2)(M_1'|H_\sigma|M_2).$$

We now assume for simplicity that the first radiation is emitted with one value only of total angular momentum j. It can then be shown that except for constants,

$$\mathfrak{S}_\rho \int d\Omega_\rho (M|H_\rho|M_1)^*(M'|H_\rho|M_1') = (J_1 j M_1 M - M_1|J_1 j J M) \times (J_1 j M_1' M' - M_1'|J_1 j J M') \times \delta(M - M_1, M - M_1'). \quad (5)$$

It is further assumed that the γ ray is a pure multipole of order L, then

$$\mathfrak{S}_\sigma \sum_{M_2} |(M_1|H_\sigma|M_2)|^2 = I(M_1,\theta), \quad (6)$$

$$I(M_1,\theta) = 1 + \sum_k X_k(J_1) P_k(\cos\theta) \Pi_k(M_1 J_1). \quad (7)$$

Here X_k is a factor[5] depending on the transition and the multipole order, $P_k(\cos\theta)$ is a Legendre polynomial, and k takes even values 2, 4, $\cdots$ up to $2L$ or $2J_1$, whichever is smaller. It will be found that under certain reasonable circumstances, only the term with $k=2$ will enter. $\Pi_k(M_1 J_1)$ is related to $(kJ_1 0 M_1|kJ_1 J_1 M_1)$, in particular $\Pi_2(M_1) = 3M_1{}^2 - J_1(J_1+1)$. The angular distribution (2) can now be written

$$I(\theta) = \sum_{M_1} W(M_1) I(M_1,\theta), \quad (8)$$

where by utilizing Eq. (5) and Eq. (6) and the orthogo-

[9] E. U. Condon and G. H. Shortley, *The Theory of Atomic Spectra* (Cambridge University Press, Cambridge, 1951).

nalities inherent in the transformation coefficients,

$$W_{M_1}=\sum_{F M\lambda\rho} w_{M+\rho}{}^{F} \times[(\rho M|\rho+MF)(\rho+\lambda M-\lambda|\rho+MF)H(\rho\lambda\sigma M_1) \times(J_1 jM_1+\sigma-\rho\rho+M-M_1-\sigma|J_1 jJM) \times(J_1 jM_1+\sigma-\rho-\lambda M-M_1-\sigma+\rho|J_1 jJM-\lambda)], \quad (9)$$

and

$$H(\rho\lambda\sigma M_1)=\delta_{\rho\sigma}\delta_{\lambda 0}-\tau^2 K(\rho\lambda\sigma M_1),$$

$$K(\rho\lambda\sigma M_1)=\sum_{F_1F_1'}\frac{\epsilon^2(F_1F_1'M_1+\sigma M_1+\sigma)}{[1+\epsilon^2(F_1F_1'M_1+\sigma M_1+\sigma)\tau^2]} \times[(\rho M_1+\sigma-\rho|M_1+\sigma F_1)(\sigma M_1|M_1+\sigma F_1) \times(\rho+\lambda M_1+\sigma-\rho-\lambda|M_1+\sigma F_1')(\sigma M_1|M_1+\sigma F_1')]. \quad (10)$$

This may be compared with a similar expression given by Goertzel[10] in the theory of angular correlations. It should be noted that $H(\rho\lambda\sigma M_1)$ depends on properties of the intermediate state only. $W(M_1)$ can be interpreted as the mean relative population of the nuclear state M_1 at the emission of the second radiation.

III. STATISTICAL MATRIX INTERPRETATION

It can be seen from Eqs. (9) and (10) that when $\tau=0$, $W(M_1)$ reduces to

$$W(M_1)=\sum_{M}(J_1 jM_1M-M_1|J_1 jJM)^2 W(M), \quad (11)$$

where

$$W(M)=\sum_{F\rho} w_{M+\rho}{}^{F}(\rho M|M+\rho F)^2.$$

It will be recalled that $W(M)$, the relative population of a given substate of the initial nucleus is the function to which special attention has been paid in previous treatments of this subject.[11] $W(M)$ [or more correctly, perhaps, $W(MM)$] is a diagonal element of the statistical matrix referring to the nuclear spin system alone, i.e.,

$$W(M)=(M|\mathrm{Tr}'\,\rho|M)(\mathrm{Tr}\,\rho)^{-1},$$

where Tr′ implies a sum over non-nuclear quantum numbers and ρ is the statistical operator $\rho=\exp\{-\mathcal{H}/kT\}$. From this point of view the mean value of any nuclear observable O is calculated from the formula

$$\langle O\rangle=\mathrm{Tr}[O\rho](\mathrm{Tr}\,\rho)^{-1},$$

which, if O is diagonal in M, becomes

$$\langle O\rangle=\sum_M W(M)(M|O|M).$$

However, $\langle O\rangle$ is independent of representation so that if it is more convenient (it generally is not, from the point of view of numerical computation) we can choose, for example, the representation in which the intermediate state is quantized, i.e.,

$$\langle O\rangle=\sum_{M_1} W(M_1)(M_1|O|M_1),$$

if O is diagonal in M_1, where

$$W(M_1)=(M_1|\mathrm{Tr}'\,\rho|M_1)(\mathrm{Tr}\,\rho)^{-1} =\sum_M (J_1 jM_1M-M_1|J_1 jJM)^2 W(M).$$

(Tr′ ρ does not operate on coordinates of the emitted particle.) Thus Eq. (11) represents a change of representation of the statistical matrix from one in which M is a good quantum number to one in which M_1 is a good quantum number. Equation (11) gives $W(M_1)$ where the intermediate state is not perturbed and leads to an angular distribution which is identical to that previously given. Where it is disturbed it can be seen from Eqs. (9) and (10) that while our operator, the angular distribution from an intermediate state, is diagonal in M_1 [$I(M_1,\theta)$] it is not diagonal in M. We have thus chosen the M_1 representation, and Eq. (9) represents the change of representation. The coefficient of τ^2 arises from nondiagonal elements of $[\rho]$ in the M representation. It may be observed here that the statistical matrix considered here develops in time, tending in fact as will be seen, to an equilibrium value.

From this point of view we can define the mean degree of nuclear alignment of the intermediate state at emission in analogy with a previous definition[4] as follows

$$\Delta'=\langle\Pi_2(J_1)\rangle/3J_1{}^2=\sum_{M_1} W(M_1)\Pi_2(M_1J_1)/3J_1{}^2. \quad (12)$$

It has been shown previously[5] that where τ is zero and $(A/kT)^2\ll 1$ the angular distribution depends on $\langle\Pi_2(J)\rangle$ alone, *viz.*,

$$I(\theta)=1+X_2(J)P_2(\cos\theta)\langle\Pi_2(J)\rangle.$$

In this approximation the anisotropy, $\epsilon=1-I(0)/I(\frac{1}{2}\pi)$, is given by

$$\epsilon=-\tfrac{3}{2}X_2(J)\langle\Pi_2(J)\rangle. \quad (13)$$

The same result is obtained if the J_1 representation is used in place of the J. Since $\Pi_k(M_1)=\Pi_k(-M_1)$ for k even, so far as $I(\theta)$ or Δ' are concerned, it is sufficient to consider $W^E(M_1)=\frac{1}{2}[W(M_1)+W(-M_1)]$. In what follows we shall deal exclusively with $W^E(M_1)$.

IV. TWOFOLD IONIC DEGENERACY

We now restrict our discussion to ionic systems which at low temperatures can be described by a fictitious "ionic spin," $S=\frac{1}{2}$, a situation of frequent occurrence and obtaining in the experiments already carried out on nuclear alignment. With this assumption the transformation coefficients and energy levels of the initial system become

$$E_\mu{}^{\pm}=\tfrac{1}{2}[2\lambda\mu-\tfrac{1}{2}A\pm\tfrac{1}{2}AQ(\mu)], \quad (14)$$

[10] G. Goertzel, Phys. Rev. **70**, 897 (1946).
[11] N. R. Steenberg, Phys. Rev. **93**, 678 (1954).

where

$$Q(\mu)=[(2\delta-2\lambda+2\mu)^2+4x^2(J+\tfrac{1}{2}+\mu)(J+\tfrac{1}{2}-\mu)]^{\frac{1}{2}},$$
$$\delta=g\mu H/A,\quad \lambda=g_n\mu_n H/A,\quad x=B/A,$$

and

$$(\tfrac{1}{2},\mu-\tfrac{1}{2}|\mu+)=(-\tfrac{1}{2},\mu+\tfrac{1}{2}|\mu-)=\left[\frac{2\delta-2\lambda+2\mu+Q(\mu)}{2Q(\mu)}\right]^{\frac{1}{2}},$$
$$(-\tfrac{1}{2},\mu+\tfrac{1}{2}|\mu+)=-(\tfrac{1}{2},\mu-\tfrac{1}{2}|\mu-)=\frac{2x(J+\tfrac{1}{2}-\mu)(J+\tfrac{1}{2}+\mu)}{[2Q(\mu)(2\delta-2\lambda+2\mu+Q(\mu))]^{\frac{1}{2}}}. \quad (15)$$

The + and − signs correspond to $F=J+\frac{1}{2}$ and $F=J-\frac{1}{2}$, respectively.

There now arises the difficult problem of the representation of the interaction in the intermediate state. While the choice made here of a static interaction, such as is assumed in the theory of the attenuation of correlations, is open to the objections discussed in VIII, it does have the merit of a straightforward, easily interpreted solution. The Hamiltonian for the intermediate state is then

$$\mathcal{H}'=g'\mu HS_z'+g_n'\mu_n HJ_{1z}+A'S_z'J_{1z}+B'(S_x'J_{1x}+S_y'J_{1y}),$$

where the constants have the same meaning as those given for Eq. (3) except that they refer to the intermediate state, and again we take $S'=\frac{1}{2}$.

The perturbation problem for the intermediate state is now identical to that for the initial state and the energy levels and transformation coefficients are given by expressions analogous to Eqs. (14) and (15). It then follows that the quantities $K(\rho\lambda\sigma M_1)$ Eq. (10) are given by

$$K(\tfrac{1}{2}0\tfrac{1}{2}M_1)=-K(-\tfrac{1}{2}0\tfrac{1}{2}M_1)=G(M_1);$$
$$K(\tfrac{1}{2}0-\tfrac{1}{2}M_1)=-K(-\tfrac{1}{2}0-\tfrac{1}{2}M_1)=-G(M_1-1);$$
$$K(\tfrac{1}{2}-1\tfrac{1}{2}M_1)=K(-\tfrac{1}{2}1\tfrac{1}{2}M_1)=-F(M_1);$$
$$K(\tfrac{1}{2}-1-\tfrac{1}{2}M_1)=K(-\tfrac{1}{2}1-\tfrac{1}{2}M_1)=F(M_1-1);$$
$$\tau^2G(M_1)=2x'^2\alpha^2(J_1+M_1+1)(J_1-M_1)[1+\alpha^2Q^2(M+\tfrac{1}{2})]^{-1};$$
$$\tau^2F(M_1)=\frac{x'\alpha^2[(J_1+M_1+1)(J_1-M_1)]^{\frac{1}{2}}(2\delta'-2\lambda'+2M_1+1)}{[1+\alpha^2Q^2(M+\tfrac{1}{2})]},$$

where $x'=A'/B'$ and $\alpha=\tau A'/2h$. α may be thought of as the mean angle precessed through by the nucleus under the influence of the hfs field, analogous to the Larmor precession in an external field.

It should be observed here that $W(M_1)$ can be written in the form

$$W(M_1)=\sum_M(J_1jM_1M-M_1|J_1jJM)^2W(M)-\tau^2[A(M_1)-A(M_1-1)], \quad (16)$$

$$A(M_1)=\sum_{FM\lambda\rho}w_{M+\rho}{}^F\times[(\rho M|\rho+MF)(\rho+\lambda M-\lambda|\rho+MF)K(\rho\lambda\tfrac{1}{2}M_1)\times(J_1jM_1-\rho+\tfrac{1}{2}\rho+M-M_1-\tfrac{1}{2}|J_1jJM)\times(J_1jM_1-\rho+\tfrac{1}{2}-\lambda\rho+M-M-\tfrac{1}{2}|J_1jJM-\lambda)]. \quad (17)$$

Thus, since

$$\sum_{MM_1}(J_1jM_1M-M_1|J_1jJM)^2W(M)=1,\quad \sum_{M_1}W(M_1)=1,$$

as should be expected on the interpretation of $W(M_1)$ as the probability of a nucleus to be in the state M_1.

Two important features can be seen here. The first is that for a sufficiently strong external field $K(\rho\lambda\sigma M_1)$ vanishes. Then, as is the case in angular correlations, the angular distribution is independent of interaction in the intermediate state. It is found that for typical values of the constants [$A=10^{-18}$ erg ($\simeq 5\times10^{-3}$ cm^{-1}) and $g=3$] the effect of reorientation vanishes for $H\geq10^3$ gauss. The second feature is that the effect of reorientation vanishes altogether if $x'=A'/B'$ is zero. The intermediate interaction is then diagonal in M_1 and σ so that no transitions are possible which affect $W(M_1)$.

V. EXPANSION IN POWERS OF $1/kT$

For arbitrary temperatures no further reduction of the above expression, Eq. (16), for $W(M_1)$ is possible. However, it has been found that the leading terms in an expansion in powers of $1/kT$, i.e., for relatively high temperatures, contains explicitly nearly all the features which enter the exact expression and is often sufficient to interpret experimental results. Where this is not the case the series expansion does give an indication in direction and order of magnitude of the effect of introducing factors neglected in the simple theory.

Therefore, expanding the exponentials, $w_\mu{}^F=\exp(-E_\mu{}^F/kT)$ in powers of $\gamma=-A/2kT$, it is found that the sums indicated in Eq. (17) can be performed with the aid of the Racah sum formulas.[12] This expansion requires that $g\mu H$ be of the order of A or less. When $g\mu H\gg A$, the leading term in the nuclear alignment is[11] $(A/2kT)^2$ rather than $(A^2-B^2)(2kT)^2$.[13] For such a field the effect of reorientation is of course eliminated.

The first feature to emerge is the rather surprising

[12] See, for example, L. C. Biedenharn, Oak Ridge National Laboratory Report ORNL-1098 (unpublished).

[13] In reference 11, due to an error on the author's part, it is stated that as $H\to\infty$, $a_2\to(1-x^2)/8$. This should read instead $a_2\to\frac{1}{4}$, and hence Eq. (20) of reference 10 should read

$$W_M{}^F\simeq(2I+1)^{-1}\{1+\tfrac{1}{8}(A(2kT)^2\Pi_2(M)\}.$$

result that arising from the effect of reorientation there is in $W^E(M_1)$ a term of order γ. This is in contrast to previous results where the first term was in all cases of order γ^2. To order γ,

$$W^E(M_1)=(2J_1+1)^{-1}\{1-\gamma\alpha^2x'[2(\delta x'-x\delta' S_1)\Theta(M_1) +S_1(x'-x)\chi(M_1)]+\cdots\}, \quad (18)$$

where $S_k=S_k(J_1jJ)$ is related to the Racah coefficient

$$S_k(J_1jJ)=\left[\frac{(2J_1-k)!(2J+k+1)!}{(2J_1+k+1)!(2J-k)!}\right]^{\frac{1}{2}} \times(2J_1+1)W(Jjk J_1|J_1J),$$

and

$$\Theta(M_1)=\tfrac{1}{2}[g(M_1)-g'(-M_1)-g'(M_1)+g(-M_1)];$$

$$\chi(M_1)=\tfrac{1}{2}[(g(M_1)+g'(-M_1))(2M_1+1) -(g'(M_1)+g(-M_1))(2M_1-1)];$$

$$g(M_1)=(J_1+M_1+1)(J_1-M_1)[1+\alpha^2Q^2(M_1+\tfrac{1}{2})]^{-1};$$

$$g'(M_1)=g(M_1-1).$$

It should be noted that where all variables (τ, H, x, and x') are arbitrary $\sum_{M_1}\Theta(M_1)\Pi_k(M_1J_1)$ and $\sum_{M_1}\chi(M_1)\Pi_k(M_1J_1)$ are both finite for all values of k except $k=0$ and $k>2J_1$. An important consequence of this fact is that even at the highest temperatures the effect of reorientation is to introduce $\cos^4\theta$, $\cos^6\theta$, etc., terms of order γ into the angular distribution [provided of course that they are present in $I_{M_1}(\theta)$]. In the absence of reorientation $\cos^4\theta$ terms only appear in terms of order γ^4. This $\cos^4\theta$ term may be large enough to provide a decisive test as to whether reorientation is taking place.

A further interesting point which is shown by Eq. (18) is that nuclear alignment in the intermediate state can arise through the reorientation terms alone where none would be present if the intermediate lifetime were zero. In the first place, where $H=0$ and $x=1$, isotropic hfs in the initial state, no alignment would normally be expected. However, $W^E(M_1)$ will still differ from its isotropic value $1/(2J_1+1)$ unless $x'=1$, that is unless the hfs in the intermediate state is isotropic also. Secondly, if the initial nucleus has spin $\frac{1}{2}$ no alignment under any circumstances would be expected on the simple theory. This is shown in the formula for $W^E(M_1)$ by the fact that $S_k(J_1j\frac{1}{2})=0$ for $k\geq 2$. However, for a $(\frac{1}{2}\overset{j}{\rightarrow}J_1\overset{L}{\rightarrow}J_2)$ transition where $J_1>\frac{1}{2}$, $S_1(J_1j\frac{1}{2})$ does not vanish. In particular if

$$J_1=j+\tfrac{1}{2}, \quad S_1(J_1, J_1-\tfrac{1}{2}, \tfrac{1}{2})=1/(2J_1).$$

It should also be noted that the sign of alignment to order γ will depend on the sign of magnetic moment of the initial nucleus through the coupling constant A.

While under some circumstances the term in $1/kT$ will be important, in general both this and the term in $(1/kT)^2$ will have to be considered together. To order γ^2,

$$W^E(M_1)=(2J_1+1)^{-1}\{1-\gamma\alpha^2x'[2(\delta x'-\delta' xS_1)\Theta(M_1) +S_1(x'-x)\chi(M_1)]\} -\tfrac{1}{2}\gamma^2\alpha^2(2J_1+1)^{-1}\{2S_1(xx'\delta'-x'^2\delta)\Theta(M_1) -[S_2x'^2(1-x^2)-S_1xx'(1-xx')]\chi(M_1)\} +\tfrac{1}{6}\gamma^2(1-x^2)S_2\Pi_2(M_1)(2J_1+1)^{-1}+\cdots. \quad (19)$$

The last term will be recognized as the only term responsible for nuclear alignment where the effect of reorientation is neglected.

We can now consider several reasonable situations for which the above formula simplifies considerably. If the first emission is a γ ray which does not appreciably disrupt the electronic system we can assume $x=x'$, i.e., that the intermediate state "sees" much the same field as does the initial state. Then in zero field the term in γ vanishes altogether and

$$W^E(M_1)=(2J_1+1)^{-1}[1+\tfrac{1}{2}\gamma^2\alpha^2\chi(M_1)x^2(1-x^2)(S_2-S_1) +\tfrac{1}{6}\gamma^2(1-x^2)S_2\Pi_2(M_1)+\cdots], \quad (20)$$

where

$$\chi(M_1)=g(M_1)(2M_1+1)-g'(M_1)(2M_1-1),$$

$$g(M_1)=g'(M_1+1) =\frac{(J_1+M_1+1)(J_1-M_1)}{1+\alpha^2[(2M_1+1)^2(1-x^2)+x^2(2J_1+1)^2]}.$$

Note in Eq. (20) how the alignment given by the simple theory may be either enhanced or diminished by the effect of reorientation through the factor (S_2-S_1). In particular for a $(J_1+j\overset{j}{\rightarrow}J_1\overset{L}{\rightarrow}J_2)$ transition $(S_2-S_1)=2(J_1+j+1)j/[(J_1+1)(2J_1+3)]$ which is always positive and thus causes a diminution of alignment; and for a $(J_1-j\overset{j}{\rightarrow}J_1\overset{L}{\rightarrow}J_2)$ transition $(S_2-S_1)=-2(J_1-j)j/[J_1(2J_1-1)]$ which is always negative causing enhancement, $\sum\chi(M_1)\Pi_2(M_1)$ being always negative.

It may be that, particularly where β emission initiates the cascade, the interaction in the intermediate state is better described by an isotropic hfs coupling $x'=1$. Then in zero field with $x'=1$, $Q^2(\mu)=(2J_1+1)^2$ and

$$\chi(M_1)=-2\Pi_2(M_1J_1)[1+\alpha^2(2J_1+1)^2]^{-1}.$$

Here, and indeed wherever the M_1 dependence of $W^E(M_1)$ is through $\Pi_2(M_1)$ alone, the angular distribution will contain only the $\cos^2\theta$ term, i.e., $P_2(\cos\theta)$.

$W^E(M_1)$, Eq. (19) is now

$$W^E(M_1)=(2J_1+1)^{-1}+\frac{\Pi_2(M_1J_1)}{(2J_1+1)}\left\{\frac{2\gamma\alpha^2S_1(1-x)}{1+\alpha^2(2J_1+1)^2}\right.$$
$$\left.-\frac{\gamma^2\alpha^2[S_2(1-x^2)-S_1x(1-x)]}{1+\alpha^2(2J_1+1)^2}+\tfrac{1}{6}\gamma^2(1-x^2)S_2\right\}. \quad (21)$$

For this situation we can write the mean degree of nuclear alignment for the intermediate state Δ', defined in Eq. (12), to order $(1/kT)^2$ for an arbitrary lifetime and show that for very long lifetimes Δ' approaches a finite limit. Thus

$$\Delta'=\frac{(J_1+1)(2J_1+3)(2J_1-1)}{15J_1}\left\{\frac{\alpha^2(1-x)}{1+\alpha^2(2J_1+1)^2}\right.$$
$$\left.\times[2\gamma S_1-\gamma^2S_2(1+x)+S_1\gamma^2x]+\tfrac{1}{6}\gamma^2(1-x^2)S_2\right\}, \quad (22)$$

which approaches an evident limit as $\alpha^2\to\infty$, i.e., as $\alpha^2/[1+\alpha^2(2J_1+1)^2]\to 1/(2J_1+1)^2$. When $A=10^{-18}$ erg, the requirement that $\alpha^2(2J_1+1)^2\gg 1$ implies a lifetime $\tau\geq 5\times10^{-9}/(2J_1+1)$ sec. It may be borne in mind that for very long lifetimes the effects under discussion may overlap the effects of thermal relaxation.

From Eq. (22) an idea can be obtained of the minimum lifetime necessary in order that reorientation be appreciable. If we take as our criterion that the first term in the square bracket be at least $\frac{1}{4}$ of the second and put $x=0$, $\gamma=\frac{1}{4}$, $S_1=S_2=1$, we find that α must be at least 0.08 for $J_1=1$ or at least 0.15 for $J_1=5$. This implies, for $A=10^{-18}$ erg, lifetimes of 1.6×10^{-10} and 3×10^{-10} sec, respectively.

Another plausible assumption is that α is small enough that in an expansion in powers of α terms in α^4 may be neglected in comparison to terms in α^2. This approximation must be used with care, however, since the most stringent criterion would require that $\alpha^2\ll 1/(2T_1+1)^2$, see Eq. (22), while α^2 must still be appreciable in order that reorientation have any effect at all. The two requirements are all but mutually exclusive. Nevertheless, if we discard terms in α^4, i.e., replace $\alpha^2/[1+\alpha^2Q^2(M_1+\frac{1}{2})]$ by α^2 we obtain

$$W^E(M_1)=(2J_1+1)^{-1}+\frac{\Pi_2(M_1)}{(2J_1+1)}\left\{2\gamma\alpha^2x'(x'-x)S_1\right.$$
$$-\gamma^2\alpha^2[S_2x'^2(1-x^2)-S_1xx'(1-xx')]$$
$$\left.+\tfrac{1}{6}\gamma^2(1-x^2)S_2+\cdots\right\}. \quad (23)$$

This expression is independent of the external field.

Where both the term in γ and that in γ^2 must be considered, the expression Eq. (13) for the anisotropy must be modified. When $I(\theta)=1+X_2(J_1)P_2(\cos\theta)\times\langle\Pi_2(J_1)\rangle$ and $\langle\Pi_2(J_1)\rangle=(C\gamma+D\gamma^2)$, ϵ is given by

$$\epsilon=-\tfrac{3}{2}X_2(J_1)[\langle\Pi_2(J_1)\rangle+\tfrac{1}{2}X_2(J_1)C^2\gamma^2]$$

in place of Eq. (13). When $W^E(M_1)$ is such that the angular distribution involves a $\cos^4\theta$ term, this will also affect ϵ.

VI. AN APPLICATION

To illustrate the ideas discussed above, they may be applied to the experiment of Ambler *et al.*[3] There Co^{60} was used in a Ce-Co salt and a high degree of alignment was obtained with an external field. The stable Co ions in this salt are found to be magnetically of two types,[14] X and Y in the ratio 2:1. The X-type ions have very nearly isotropic hfs at 20°K while the hfs of the Y ions is strongly anisotropic, $A=286.6\times10^{-4}$ cm^{-1}, $B<1\times10^{-4}$ cm^{-1},[15] i.e., $x\simeq 0$. When reorientation effects are neglected the theory predicts a substantial degree of alignment in zero field arising from the Y ions alone. In fact, for $1/T=46$ (deg)$^{-1}$, the anisotropy of γ radiation should be $\epsilon=0.11$,[16] whereas the experimental result in zero field at this temperature was $\epsilon=0.0\pm0.03$. At an external field of 430 oersted, however, experiment and theory were in good agreement.

Let us now assume a finite lifetime for the first intermediate state in the decay of Co^{60}, i.e., the second excited state of Ni^{60}, and see for the Y ions what effect this has on the zero-field angular distribution of the first only of the two γ rays. It has been seen that if $x'=0$ there can be no reorientation at all. Since the first stage is a β emission it is reasonable that the coupling in the intermediate state (insofar as it can be described by a static interaction) should be different from that in the initial state. For simplicity then we take $x'=1$. The mean degree of nuclear alignment of the intermediate state is now given by Eq. (22) with $x=0$. The decay scheme of Co^{60} is here taken to be $(5\xrightarrow{1}4\xrightarrow{2+}2\xrightarrow{2+}0)$, whence $S_1=6/5$, $S_2=78/55$. A, to refer to Co^{60}, must be scaled according to the gyromagnetic ratios of Co^{60} and Co^{59}; thus for a nuclear magnetic moment of 3.5 nuclear magnetons for Co^{60},[17] $A=3\times10^{-18}$ erg, larger in this case than that previously taken as typical. Taking $\alpha=0.3$ and $1/T=46$ deg^{-1} (i.e., $\gamma=-\frac{1}{2}$), it is found that the mean nuclear alignment and the anisotropy is reduced by 30 percent. If we assume that the alignment in the second intermediate state (first excited state of Ni^{60}) is disturbed by the same amount, the average reduction in the anisotropy is 38 percent, and ϵ is reduced from 0.11 to 0.068. For $\alpha=0.3$, $\alpha^2/(1+81\alpha^2)$ and thus the degree of reorientation is very nearly at its maximum value. Thus we must conclude that on this basis, while reorientation

[14] R. S. Trenam, Proc. Phys. Soc. (London) **A66**, 118 (1953).
[15] R. S. Trenam (unpublished).
[16] N. R. Steenberg, thesis, Oxford University, 1953 (unpublished).
[17] M. A. Grace and H. Halban, Physica **18**, 1227 (1952).

may be responsible for part of the disagreement, it cannot account entirely for it.

The value 0.3 for $\alpha=A'\tau/2h$ implies if A' is taken equal to A, a mean life of $\tau=2\times10^{-10}$ sec for the second excited state of Ni^{60}. Engelder,[18] by delayed coincidence studies finds for this state $\tau<10^{-9}$ sec. Aeppli *et al.*,[19] as a result of failure to restore an attenuated angular correlation, conclude that the mean life of the first excited state of Ni^{60} is of the order of 10^{-11} sec.

If the electronic g factor for the intermediate state is assumed to be the same as that for the initial state $g=7.29$,[14] a field of 500 oersted is ample to restore the anisotropy to its unperturbed value.

These arguments are not materially affected if the original experiment[17] is reinterpreted as the basis of spin 4 for the ground state of Co^{60}.[6] This would require a magnetic moment of between 3.33 and 3.63 ± 0.5 nuclear magnetons depending on the relative contributions of Fermi and Gamow-Teller selection rules.

The considerations in this paragraph are put forward primarily to illustrate the arguments in the body of the paper. Before further speculation on this experiment is justified, certain additional experimental data are necessary. In particular, the hfs constants A and B should be remeasured at helium temperature and if possible it should be discovered if there is an antiferromagnetic transition between 4° and 0.01°. Furthermore it would be highly desirable to measure the spin and magnetic moment of Co^{60} by conventional methods in order to resolve the present ambiguity. As these experiments may serve as a pattern for future developments, they should be understood as fully as possible.

VII. DISCUSSION

This analysis, even if incomplete, at least shows clearly that the effect of finite lifetime and consequent nuclear reorientation must not be neglected in the theory of nuclear alignment at low temperatures. If the properties of the intermediate state are similar to those of the initial state, these effects may appear for lifetimes of the order of 10^{-10} sec and will certainly be present for lifetimes greater than 10^{-9} sec. A number of nuclei suitable for nuclear alignment fall into this class.

If the foregoing treatment is substantially correct, then we know further that the effect of reorientation reaches a maximum for $\tau\simeq10^{-8}$ sec and that thereafter the alignment of the intermediate state is constant until the effect of thermal relaxation becomes appreciable. The application of an external magnetic field of the order of 10^2 oersted will eliminate the effect of reorientation. The effect on the anisotropy may be of the order of 40 percent, and it may either enhance or diminish the anisotropy. The effect may depend in part on the sign of the magnetic moment of the initial nucleus.

Abragam and Pound[20] have drawn attention to the importance of nonstatic interactions. A static perturbation for the intermediate state in a single crystal is most plausible when the first transition is a γ emission which does not disturb the electronic system. We would then expect the intermediate nucleus to see much the same field as the initial nucleus except for the change in nuclear spin and magnetic moment. In this case only the effect of nuclear recoil is neglected. For a nucleus of mass 60 the recoil energy from a 1-Mev γ ray is approximately 9 ev or 10^5 degrees. This may affect our assumption that the intermediate state can be described as an ionic doublet.

Where β emission initiates the cascade, the disruption of the atomic shell, autoionization and change of Z, are serious objections to a static perturbation. It would not be expected that the electronic structure would be settled into its final state as an impurity atom in the lattice of charge $Z\pm1$ in times comparable to those we are considering, 10^{-7} sec. But how far the process would advance in this time, and what forces the atomic system would exert on the nucleus during the process are the questions involved.

The case of K capture is even more obscure. Here, until the K shell is filled, a time of $\sim10^{-11}$ sec, the intermediate nucleus is in the field of the one odd K electron, of the order of 10^8 gauss. This field would be expected to produce pronounced effects even for very short-lived nuclear states. However, the results[21] for Co^{58} decaying 85 percent by K capture are very similar to those of Co^{60}. It may be that this field must be thought of as in fact oscillating so rapidly that it averages to zero.

VIII. ACKNOWLEDGMENT

The author is indebted to the National Research Council of Canada for a Postdoctorate Fellowship which made this work possible.

[18] T. C. Engelder, Phys. Rev. **90**, 259 (1953).
[19] Aeppli, Frauenfelder, Heer, and Rüetachi, Phys. Rev. **87**, 379 (1952).
[20] A. Abragam and R. V. Pound, Phys. Rev. **92**, 943 (1953).
[21] Daniels, Grace, Halban, Kurti, and Robinson, Phil. Mag. **43**, 1297 (1952).

Neutron Inelastic Scattering*

ROBERT M. KIEHN† AND CLARK GOODMAN
Department of Physics and Laboratory for Nuclear Science, Massachusetts Institute of Technology, Cambridge, Massachusetts
(Received May 3, 1954)

Neutron inelastic scattering cross sections of Fe, Al, Cr, Ni, Pb, and Bi have been measured with ~20-kev resolution for neutron energies between 0 and 2.7 Mev. A gamma-ray spectrometer measured the monoenergetic gamma rays emitted by the excited nucleus. The cross sections are in agreement with predictions based on the Hauser-Feshbach theory. The energies of the first few excited states of the stable nuclei were found to be in good agreement with values obtained by other means.

INTRODUCTION

MEASUREMENTS of inelastic scattering[1–4] have generally employed either heterogeneous neutron sources or detectors with poor energy resolution, or both. Inelastic scattering of monoenergetic neutrons can give useful information about the compound nucleus and the target nucleus. However, the experimental problem is complicated by the lack of adequate fast-neutron spectrometers, low neutron yields from monoenergetic neutron sources, and, especially at low neutron energies, low values of the inelastic cross section itself. Threshold detectors,[1] cloud chambers,[2] photographic plates,[3] and to some extent recoil counters[4] have been used to measure the yield of inelastically scattered neutrons as compared to the incident or elastically scattered neutrons. These techniques are satisfactory for high-energy neutrons (>3 Mev) but are either inapplicable or of limited usefulness in the interesting range 0–3 Mev, which corresponds to the major yield of fission neutrons.

After several discouraging attempts[5] to measure the inelastically scattered neutrons in this energy range, it was decided instead to study the gamma rays emitted by the excited residual nucleus. It is interesting to note that this method as used by Lea[6] and by Kikuchi *et al.*[7] confirmed the earlier conclusions of Danysz *et al.*[8] and Amaldi *et al.*[9] that the change of radioactivity induced in various substances resulted from inelastic scattering of the neutrons when different scatterers were interposed between the source and the detector.

More recently there have been a number of investigations[10] of inelastic scattering by the observation of the resulting gamma radiation. However, only because of the development of sensitive, high-resolution scintillation counters is it now possible to achieve detailed information[11] such as that represented by the present work.

PRESENT TECHNIQUE

The photoelectric absorption peak in a NaI crystal was used as a measure of the yield of monoenergetic, de-excitation gamma rays.

In the energy region covered $0 \leq E_n \leq 2.7$ Mev, most nuclei with $A \leq 70$ have levels which are separated by more than 100 kev. For the heavy nuclei, except those which are magic, the level spacing is of the order of 100 kev or less. This situation imposes extreme demands upon the resolution of the gamma-ray detector. After some effort, single-crystal NaI(Tl) gamma-ray spectrometers were constructed which have a resolution of about 5 percent for 1.2-Mev gamma rays. As a result the nuclei which may be investigated by this technique are those with level spacings of 100 kev or more. Furthermore, if the element in question has several isotopes, differentiation between isotopes is difficult. Cascade gamma processes could be established by coincidence techniques, but no work of this kind has yet been done for inelastic scattering of neutrons.

* This work was supported by the joint program of the U. S. Office of Naval Research and the U. S. Atomic Energy Commission.

† Gulf Oil Corporation Fellow, now at Los Alamos Scientific Laboratory.

[1] C. H. Collie and J. H. E. Griffiths, Proc. Roy. Soc. (London) **A155**, 434 (1936); D. C. Graham and G. T. Seaborg, Phys. Rev. **53**, 795 (1938); A. Soltan, Nature **142**, (1938); Nature **142**, 252 (1938); Amaldi, Bocciarelli, Cacciapuoti, and Trabocchi, Nuovo cimento **3**, 203 (1946); Gittings, Everhart, and Barschall, Phys. Rev. **75**, 1610 (1949); W. D. Allen and C. Hurst, Proc. Phys. Soc. (London) **52**, 501 (1940); S. G. Cohen, Nature **161**, 475 (1948); Martin, Diven, and Taschek, Phys. Rev. **93**, 199 (1954). A. A. Ebel and C. Goodman, Phys. Rev. **93**, 197 (1954).

[2] H. F. Dunlap and R. N. Little, Phys. Rev. **60**, 693 (1941); Little, Long, and Mandeville, Phys. Rev. **69**, 414 (1946).

[3] P. H. Stelson and C. Goodman, Phys. Rev. **82**, 69 (1951); P. H. Stelson and W. M. Preston, Phys. Rev. **86**, 132 (1952); Jennings, Weddell, and Hellens, Bull. Am. Phys. Soc. **29**, No. 4, 48 (1954).

[4] Barschall, Battat, Bright, Graves, Jorgensen, and Manley, Phys. Rev. **72**, 881 (1947).

[5] Willard, Preston, and Goodman, M.I.T. Tech. Rept. No. 45, September 27, 1950 (unpublished), p. 69; P. H. Stelson and W. M. Preston, Phys. Rev. **86**, 132 (1952).

[6] D. E. Lea, Proc. Roy. Soc. (London) **150**, 637 (1935).

[7] H. Aoki, Proc. Phys.-Math. Soc. Japan **19**, 369 (1935); Kikuchi, Aoki, and Husimi, Nature **137**, 398 (1936); Proc. Phys.-Math. Soc. Japan **18**, 115, 297 (1936).

[8] Danysz, Rotblat, Wertenstein, and Zyw, Nature **134**, 970 (1934).

[9] Amaldi, D'Agostino, Fermi, Pontecorvo, Rasetti, and Segre, Proc. Roy. Soc. (London) **149**, 522 (1937).

[10] Seaborg, Gibson, and Graham, Phys. Rev. **52**, 408 (1937); Grace, Preston, and Halban, Phys. Rev. **77**, 286 (1950); M. A. Rothman and C. E. Mandeville, Phys. Rev. **93**, 796 (1954); G. L. Griffith, Bull. Am. Phys. Soc. **29**, No. 4, 48 (1954); C. P. Swann and F. R. Metzger, Bull. Am. Phys. Soc. **29**, No. 4, 48 (1954); Eliot, Hicks, Beghian, and Halban, Phys. Rev. **94**, 144 (1954).

[11] Grace, Beghian, Preston, and Halban, Phys. Rev. **82**, 969 (1951); R. B. Day, Phys. Rev. **89**, 908 (1952).

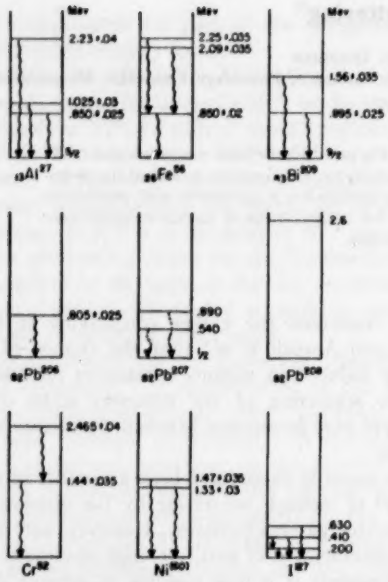

FIG. 1. Energy-level diagrams. The energies of the excited levels were determined by measuring the energy of the emitted gamma ray with a scintillation spectrometer. Utilization of the incident neutron energy and the yield of the gamma rays as two independent variables enabled the assignment of cascade processes. The gamma-ray yields, except for Pb^{207}, were studied in detail as a function of incident neutron energy. The energy assignments are in agreement with other determinations within the given experimental uncertainty. The 1.47-Mev level is probably in Ni^{58}.

The elements chosen for study were Al, Ni, Cr, Fe, Pb, and Bi. This choice illustrated the application of the technique to light, medium weight, and heavy magic nuclei, including elements with many isotopes.

After several preliminary experiments a method was evolved for examination of the inelastic neutron cross section for each of the excited levels of the target nucleus in the same detail as in total cross-section measurements. Accordingly experiments were conducted using neutron beams of $\leq$25-kev resolution for the first few Mev. Many reasonances in the yields of the individual gamma rays were observed. These are attributed to resonance formation in the compound nucleus. A summary of the experimental method has been published.[12]

RESULTS

Using neutron beams of $\leq$25-kev energy width, the gamma-ray yields for Fe, Al, Bi, Pb, Ni, and Cr were measured at 50-kev energy intervals for $0<E_n\leq 2.7$ Mev. The yield of gamma rays was calibrated in terms of the inelastic scattering cross section, σ_{in}, assuming that the observed yield is proportional to the number of inelastic events taking place in the scatterer. The measurement of the line spectrum of gamma rays insures that only inelastic events are recorded. If two or more levels are neutron excited and each emits gamma rays in transitions to the ground state, the cross section for each level excited may be determined. If the gamma rays are in cascade, the lower-level gamma ray gives the total inelastic cross section immediately, and a subtraction yields the cross section for the production of higher levels. The interpretation of the results, therefore, requires some preconception, or a preliminary determination, of the energy-level diagrams of the nuclei under consideration. The incident neutron energy and the gamma-ray energy calibration provide two independent variables by means of which the level structure may be determined for those excited states capable of being produced by neutron bombardment.

Figure 1 portrays the results obtained for six elements. The levels in Bi^{209} have recently been observed in inelastic neutron scattering.[13] The other levels indicated have been confirmed by other means.[14]

Absolute values of σ_{in} were obtained by experimentally determining the efficiency of the detector and geometry using a known source of gamma rays distributed throughout the scatterer, and calculating the neutron flux incident upon the scatterer using the Los Alamos data for the neutron yield from the $Li^7(p,n)Be^7$ reaction.[15] This method was applied for the determination of σ_{in} for iron with an estimated uncertainty of 15 percent at $E_n\simeq 1.3$ Mev; the inelastic cross section for the other elements was then deter-

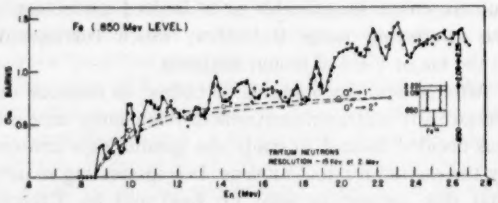

FIG. 2. The neutron inelastic scattering cross section of iron. The cross section was obtained by observing the yield of the line spectrum of gamma rays emitted from the excited state of Fe^{56}. The ordinate was calibrated by experimentally determining the counter efficiency and by computing the number of neutrons incident upon the scatterer from the measured proton current and target thickness. The absolute values for the cross sections of the other elements studied were calibrated by comparing relative gamma yields with the gamma yield from $Fe(n,n'\gamma)Fe$. The neutron energy resolution is $\sim$20 kev for all data presented in this paper. A comparison with the Hauser-Feshbach theory (see reference 17) has been made for the single level excitation for the assumed transitions $0^+\rightarrow 1^-$ and $0^+\rightarrow 2^+$ (the smooth curves). The experimental contributions of the three levels to the total inelastic cross section are given at $E_n=2.64$ Mev; note that the 850-kev level contribution falls close to the extrapolated theoretical curve.

[12] R. M. Kiehn and C. Goodman, Phys. Rev. **93**, 177 (1954).

[13] M. A. Rothman and C. E. Mandeville, Phys. Rev. **93**, 796 (1954); Eliot, Hicks, Beghian, and Halban, Phys. Rev. **94**, 144 (1954).

[14] *Nuclear Data*, Natl. Bur. Standards Circ. 499 (U. S. Government Printing Office, Washington, D. C., 1950); Hollander, Perlman, and Seaborg, Revs. Modern Phys. **25**, 469 (1953); Hausman, Allen, Arthur, Bender, and McDole, Phys. Rev. **88**, 1296 (1952).

[15] Hansen, Taschek, and Williams, Revs. Modern Phys. **21**, 635 (1949).

mined relative to iron by applying first-order correction terms for self-absorption and detector efficiency, Figs. 2 to 8.

It was assumed that the anisotropy of the resulting gamma radiation was small and that "poor" geometry would average over the angular distribution. Although the scattering samples were fairly thick (1 to 1.5 mean free paths), corrections for neutron scattering were made only for single collisions, i.e., multiple scattering was neglected. Experiments are in progress to determine the effects of multiple scattering and to calibrate the elements by the source-substitution method used for iron.

The gamma rays observed were between 800 kev and 2.5 Mev in energy; lower-energy gamma transitions were either not investigated in detail or not observed. A high background radiation of 200, 410, and 630-kev gamma rays, produced by $(n,n'\gamma)$ processes in the NaI spectrometer, made determinations of low-energy gamma yields difficult. As the gammas investigated fell in the energy interval 800 kev $<E_\gamma<$2.5 Mev, no corrections for internal conversion processes were made. The transitions observed were fast (low multipole order); hence, the internal conversion corrections would be small (<5 percent) even for the heaviest elements.

One obvious fault of the gamma-ray technique, in addition to the problems of low-energy gamma transitions, finite resolution and complex competing spectra,

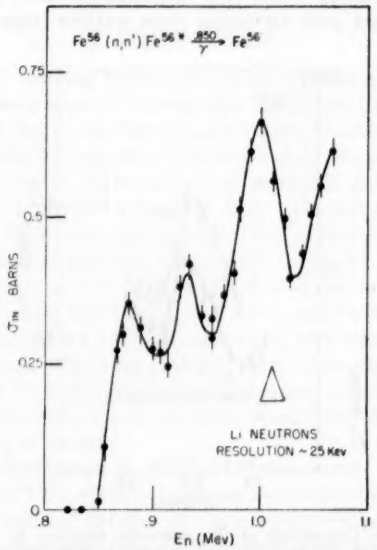

FIG. 3. Detail of the initial rise of the Fe cross section. The data represent the yield of the line spectrum of gamma rays emitted by Fe^{56}. The resonance structure in the inelastic scattering cross section, which is clearly defined in the figure, prevents the definite assignment of spin and parity to the excited state by comparison of the slope of the initial rise with the Hauser-Feshbach theory.

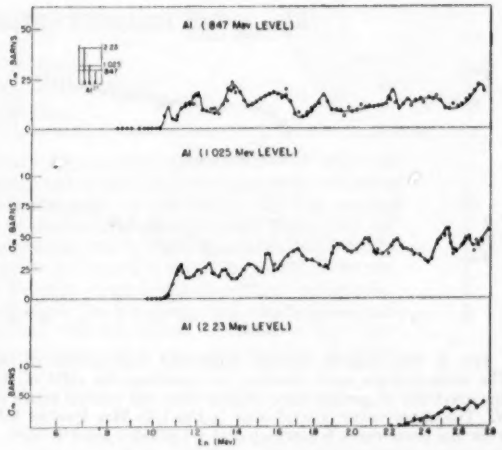

FIG. 4. The neutron inelastic scattering cross section of aluminum. The cross sections were obtained by observing the yield of the line spectrum of gamma rays emitted from the excited states of Al^{27}. The first curve is attributed to the excitation of the 0.847-Mev level in Al^{27}; the second, the 1.025-Mev level; the third, the 2.23-Mev level. The assumption has been made that no cascade processes are taking place.

is the fact that spin 0 to spin 0 transitions are not observed because this gamma transition is completely forbidden.[16]

Many resonances in the inelastic scattering cross sections of the lighter nuclei were observed. These are attributed to resonant formation of the compound nucleus. In most cases, however, the total neutron cross section has not been measured with the same degree of resolution as used in these inelastic cross section experiments. Corrections for the total cross section were based on averaged values.

For one of the major Al resonances, both the total and inelastic cross sections were measured with neutrons of the same energy. Figure 9 shows the agreement between resonance structure in both cross sections.

Several calculations based on the theory of Hauser and Feshbach[17] were made in order to compare theoretical prediction with experiment. The theoretical results, based on the assumption that the level density

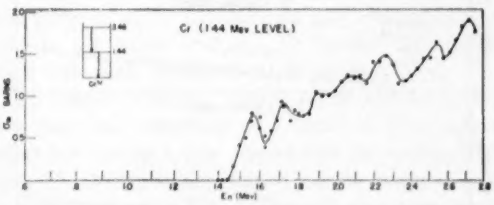

FIG. 5. The neutron inelastic scattering cross section of Cr. The cross section was obtained by observing the yield of the line spectrum of gamma rays emitted from the first excited state of Cr^{52}. The excitation of the 2.46-Mev level was not studied.

[16] J. M. Blatt and V. F. Weisskopf *Theoretical Nuclear Physics* (John Wiley and Sons, Inc., New York, 1952).
[17] W. Hauser and H. Feshbach, Phys. Rev. **87**, 366 (1952).

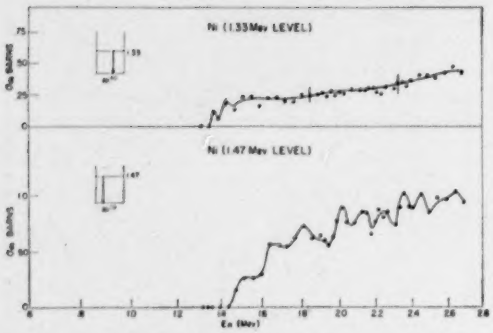

FIG. 6. The neutron inelastic scattering cross section of Ni. The cross sections were obtained by observing the yield of the line spectrum of gamma rays emitted from the excited states in Ni. The upper curve is attributed to the 1.33-Mev level in Ni^{60} while the lower curve is attributed to a 1.47-Mev level in Ni^{58}.

of the compound nucleus can be treated statistically, should be comparable to an average over the resonances in the experimental cross sections.

The results of the calculations for the excitation of the first excited states in Fe, Pb, and Bi are shown by dashed lines in the appropriate figures for the assumed

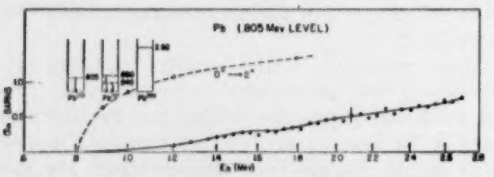

FIG. 7. The neutron inelastic scattering cross section of Pb. The cross section was obtained by observing the yield of the line spectrum of gamma rays emitted from the excited state of Pb^{206}. A theoretical curve for the assumed transition $0^+ \rightarrow 2^+$ is also shown.

spin transitions and for nuclear radii obtained from total neutron cross sections.[15] The calculations are quite sensitive to the assumed nuclear radius. The agreement between theory and experiment for Fe is probably fortuitous as the theory is expected to give shape and order of magnitude results only. The dis-

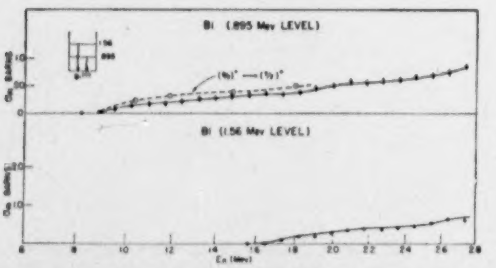

FIG. 8. The neutron inelastic scattering cross section of Bi. The cross sections were obtained by observing the yield of the line spectrum of gamma rays emitted from the first two excited states of Bi. A theoretical curve is also shown for the assumed transition of $9/2^- \rightarrow 7/2^-$ for the first excited state of Bi (incorrectly designated as + parities in the figure).

agreement between theory and experiment for Pb is probably significant. One possible explanation is that the 2+ spin assignment to the first excited state is incorrect. Another explanation would be that the statistical theory does not apply to this magic, heavy nucleus. However, fair agreement was obtained, both in shape and in magnitude, for the magic, heavy nucleus Bi^{209}.

Experiments in which the spins of the ground state and excited state of the target nucleus, and the spins of the compound levels excited are known would be very significant. Such experiments would yield information concerning a resonance theory of inelastic scattering. In the elements studied thus far, only the spins of the ground states were known.

It is to be noted that the data obtained for the individual level excitation cross sections immediately

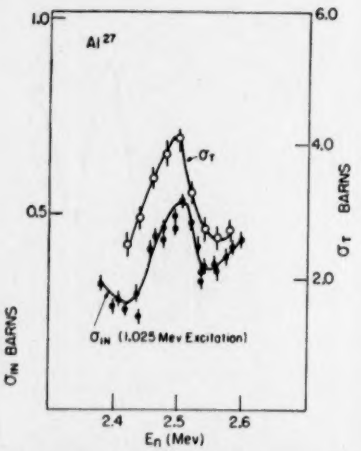

FIG. 9. Comparison of the resonance structure in the total cross section and the inelastic cross section of Al. The agreement between the resonance structure of the total neutron cross section and the inelastic neutron cross section indicates resonance formation of the compound nucleus.

give the spectral distribution, χ_{in}, of the inelastically scattered neutrons, a quantity of importance in reactor design and in neutron shielding. For each partial inelastic scattering cross section, the emergent neutron has an energy essentially equal to the incident neutron energy minus the excitation energy of the particular level excited.

We wish to acknowledge the support of the Gulf Oil Corporation fellowship program and the use of scattering samples provided by Pratt and Whitney Corporation. M. K. Salomaa helped with the electronics, T. H. Magel prepared the T-Zr targets, and C. Borkowski generously assisted by calibrating the Mn^{54} standard solution. The members of the Neutron Physics Group have given valuable assistance. Discussions with V. F. Weisskopf, R. B. Day, and H. Feshbach were particularly stimulating.

Conservation of Isobaric Spin in the Reaction $Be^9(p,\alpha)Li^6$

R. MALM AND D. R. INGLIS
Argonne National Laboratory, Lemont, Illinois

(Received May 10, 1954)

The reaction $Be^9(p,\alpha)Li^6$ involves transitions to the ground state and first excited state of Li^6 which are shown to display only a gradual dependence on proton energy and no indication of resonance at the known gamma-ray resonance at 2.565 Mev which goes by way of the second excited state of Li^6. This may be explained in terms of conservation of isobaric spin and verifies that the second excited state of Li^6 has isobaric spin $T=1$ (or odd charge parity) as does also the resonant state of the compound nucleus B^{10}. The lack of resonance in the two alpha groups does not provide a very sensitive test of the purity of isobaric spin in the resonant state, because the contribution of an impurity would be superposed on a background, but the sharpness with which the gamma resonance falls off on the low-energy side does indicate that neighboring $T=0$ states have remarkably little $T=1$ admixture. The observations were made by means of a 16-in. two-dimensional focusing magnetic spectrometer, the construction and characteristics of which are described.

I. INTRODUCTION

THE reaction $Be^9(p,\alpha)Li^6$ yields relationships between some of the very light nuclei, the structure of which one would like to understand as completely as possible. Li^6 has been known[1] for over two years to have its lowest three states well separated from one another, the ground state with $J=1^+$. The first excited state at 2.187 Mev has recently been shown[2] to have $J=3^+$, as was expected theoretically,[3] and the second excited state at 3.58 Mev has been identified with the ground state of He^6, having thus $J=0^+$ and presumably isobaric spin $T=1$, as is also compatible with theoretical expectations. The experimental verification that this state has $T=1$ appeared in the early stages of this work[4] and is found very clearly in recent work[2,5] on deuteron scattering in helium.

Our investigation of $Be^9(p,\alpha)Li^6$ was started in the summer of 1951, when only one excited state of Li^6 had been recognized[6] because the gamma-ray energy[7] had not been measured carefully enough to show up a discrepancy, and our first indication that there must be two excited states came from the failure of the excited-state alpha group to display the gamma-ray resonance. The work suffered an unusually long delay while the laboratory was moved to a new site, and the spectrometer was considerably improved. The present interest of the results is mainly in their relation to the purity of isobaric spin.

II. EXPERIMENTAL APPARATUS

For the purposes of this investigation and other research relating to the properties of light nuclei, a high-resolution, two-dimensional focusing, magnetic spectrometer was constructed for use with the ANL statitron which provides monoergic protons or deuterons up to about $3\frac{1}{2}$ Mev. This spectrometer is designed to focus protons of energy up to 15 Mev and to be capable of admitting through a solid angle of approximately 0.01 steradian the products from nuclear reactions emitted at angles from zero to 135 degrees with respect to the bombarding particles. Since only a portion of the running time of the statitron is available for charged-particle research, the mounting of the spectrometer and the necessary electrical, water, and vacuum connections are designed to enable the spectrometer to be moved easily to and from the experimental area by use of an overhead crane.

The magnet is of an inhomogeneous field type explored by Siegbahn and is essentially the same as the magnet of the 16-in. proton spectrometer at the California Institute of Technology.[8] It differs from that one in having windings with internally cooled conductor and consequent high currents, and in some of the detailed dimensions. The cross section of the magnet is shown in Fig. 1. The pole pieces are shaped, as shown in Sec. A-A of Fig. 1, to provide a magnetic field with a radial dependence proportional to $r^{-\frac{1}{2}}$ in the midplane. The magnet is semicircular with a mean radius of 16 in. The dimensions of the gap are roughly 6 in. radially by 2 in. in depth, providing the possibility of a fairly large solid angle in which the particles may emerge from a point in the target and still be focused to a point (aside from slight astigmatism) in the focal plane.

The magnet windings consist of 20 kidney-shaped coils, each coil consisting of 7 turns of $\frac{3}{8}$-in. square copper bar having a $\frac{1}{4}$-in. square hole for cooling purposes. The twenty kidney-shaped coils fit snugly around the poles as shown in Fig. 1. The coils are connected in series, and power is supplied by a 600-amp, 40-v welding

[1] F. Ajzenburg and T. Lauritsen, Revs. Modern Phys. **24**, 321 (1952).
[2] Lauritsen, Huus, and Nilsson, Phys. Rev. **92**, 1501 (1953).
[3] D. R. Inglis, Revs. Modern Phys. **25**, 390 (1953).
[4] Reference 1, p. 347.
[5] H. T. Richards and A. Galonsky (private communications).
[6] Hornyak, Lauritsen, Morrison, and Fowler, Revs. Modern Phys. **22**, 219 (1950).
[7] R. B. Day and R. L. Walker, Phys. Rev. **85**, 582 (1952).
[8] Svartholm and Siegbahn, Arkiv Mat. Astron. Fysik **A33**, Nos. 21, 24 (1946); Snyder, Rubin, Fowler, and Lauritsen, Rev. Sci. Instr. **21**, 852 (1950); W. Whaling and C. W. Li, Phys. Rev. **81**, 150 (1951). C. Mileikowsky, Arkiv Fysik **4**, 337 (1952); **7**, 33, 47 (1954).

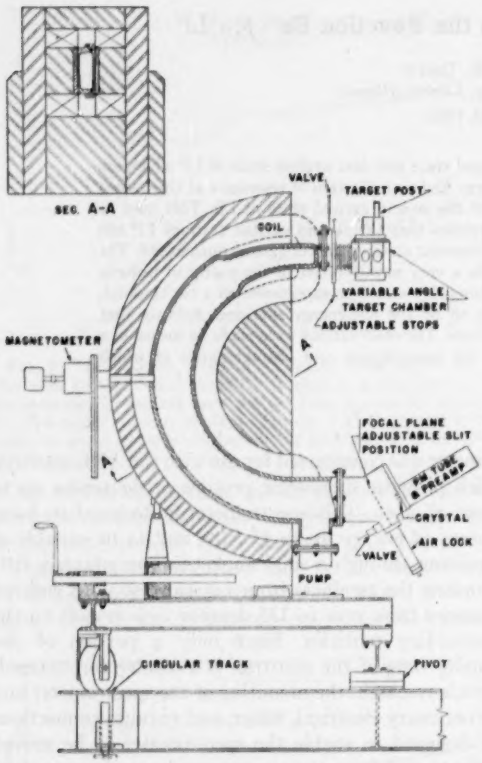

FIG. 1. The two-dimensional-focusing "proton spectrometer."

generator. The windings are cooled internally by the flow of distilled water in a closed system consisting of the windings, turbine pump, heat exchanger, and reservoir. To prevent condensation of moisture in the windings, the heat exchanger is automatically by-passed when the water temperature drops below a certain temperature.

The magnet is supported on four jacks which rest on a pivoted stand. This stand travels on a circular track and permits variations in the angular position through about 135°, permitting observation of angular distributions of the product particles of nuclear reactions.

To articulate the vacuum system and permit this observation at various angles in a horizontal plane with a horizontal incident beam, a variable-angle target chamber is used. It consists essentially of two parts with matching cylindrical surfaces. The fixed inner part contains a fixed beam entrance aperture, an adjustable post holding the target along the vertical central axis, and a wide horizontal exit slot permitting egress at all angles between about 140° from the beam direction and 0° or a little beyond. The exit slot is surrounded by an O-ring groove in the outer cylindrical surface and covered by the inner cylindrical surface of the sliding outer part of the target chamber. The continuous sliding motion about the vertical axis is limited to an angle of about 30° because of the conflict with the beam entrance in the backward direction, so the outer part of the chamber contains several exit ports spaced at about 30°, making it possible to reach any angle within the range covered by the exit slot. The exclusion of angles more nearly backward than this arises from the thickness of the magnet (16 in.) and the limited "object distance" of the magnetic lens (11 in.). The target chamber also contains a vacuum valve wide enough to span the exit slot, making it possible to change ports without exposing the target to the atmosphere.

The particles leaving the target chamber pass through a sylphon bellows and enter the deflection chamber of the spectrometer through a variable aperture and a vacuum valve. Because of an excess downward deflection in the fringing field, the target chamber is mounted a little low, with the target spot about 8 mm below the horizontal extension of the median circle. The deflection chamber fits between the poles of the magnet as shown in Fig. 1. It consists of two aluminum castings, a boxlike structure, and a cover. The joint between them is sealed by means of a round gasket in a groove. In order to minimize scattering from the inner walls of the chamber, these walls are cast with narrow ridges about $\frac{1}{16}$ in. high and $\frac{3}{4}$ in. apart.

On leaving the lower end of the deflection chamber, the particles enter the detection chamber where particles of different monoenergetic groups are focused at various points along the focal plane indicated in Fig. 1. An air lock permits placing a photographic plate in this focal plane without breaking vacuum, but in the principal use of the instrument with electronic detection a defining slit of variable width is placed in this plane at the central position. Behind this, exposed directly to the vacuum, is a thin NaI(Tl) scintillation detector, kindly supplied by Mr. Robert Swank. Behind this is a 5819 photomultiplier feeding pulses into a 10-channel kicksorter. (A proportional counter was used for the earlier part of the work.) On the bottom of the detection

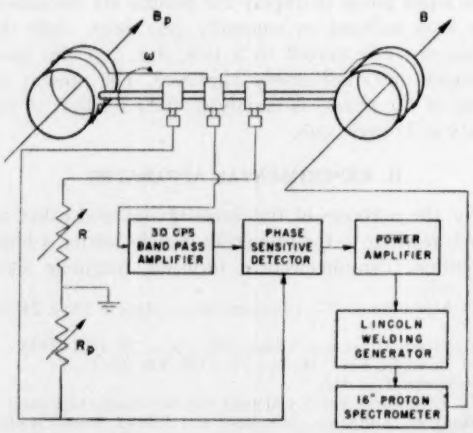

FIG. 2. Schematic diagram of the spectrometer magnet control.

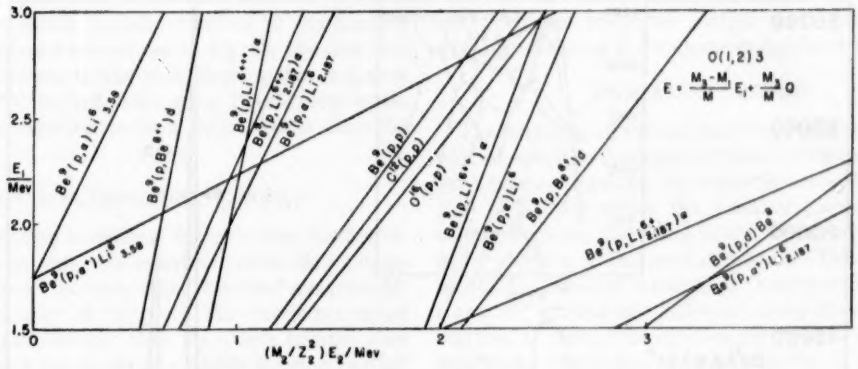

FIG. 3. Focusing field as dependent on bombarding energy for various ions.

chamber is a pumping port supporting a D.P.I. VFM260 diffusion pump.

The control and stabilization of the magnetic field is accomplished by means of the feedback system shown in Fig. 2. The sensing element is a rotating type magnetometer which generates two 30-cycle voltages, one proportional to the field of an Alnico V permanent magnet, the other proportional to the magnetic field in the central plane near the edge of the pole pieces of the spectrometer magnet. These voltages are added in phase and applied across the two 100 000-ohm resistance boxes. A signal is obtained from the network as shown in the diagram, passed through a 30-cycle band-pass amplifier and phase-sensitive detector, and the resulting dc signal is applied to the grids of three 807 cathode followers connected in parallel which drive the field windings of the exciter for the welding generator. The current supplied to the magnet tends to assume a value for which the input signal to the 30-cycle amplifier is zero. The field B thus obtained is related to the field B_p of the permanent magnet $B=B_pR/R_p$, and if B_p and R_p remain constant, B is proportional to R. Thus, adjusting R automatically produces a field in the spectrometer proportional to R.

This type of generating magnetometer has the advantage of ruggedness and the disadvantage that it measures the field only between the edges of the poles, since making its armature protrude any farther would intercept some of the valuable solid angle. The torsion type used by Lauritsen[9] can be made to present a very small area to the deflected particles when placed in the central position, but a modification of it employing quartz fibers to avoid fiber hysteresis was found to break as a result of fiber fatigue. The generating magnetometer has displayed a gradual drift on warming up of about 1 percent because of an unexpectedly large change of the permanent magnet field with temperature. This has been corrected since the measurements here reported were made by redesigning the magnetometer for use with a thermostated oil bath. At the fields employed in the work with magnet currents up to about 400 amp, fields to 10 kilo-oersteds, and deflected proton energies to 10 Mev, the focused particle momentum has been found to be proportional to the field observed at the edge to within the accuracy of observation permitted by the temperature variations. At higher fields, more serious nonlinearity from differential saturation may be anticipated.

[9] C. C. Lauritsen and T. Lauritsen, Rev. Sci. Instr. **19**, 916 (1948).

PULSE-HEIGHT DISCRIMINATION

With a given target and type of bombarding particle, the counting rate depends on the four variables bombarding energy E_1, magnet setting B, and two variables of pulse-height discrimination, say the channel width and channel level. When measuring a particle-energy spectrum with E_1 fixed and B variable, the range of pulse height must be chosen to give all or a representative sample of the pulses from particles of the desired sort. The 10-channel kicksorter helps greatly in eliminating trouble from these additional variables. It is ordinarily set so the peak in pulse size covers some of the middle channels with low counting rates in the end channels, which provides assurance that the total count is valid and indicates when an occasional change of channel level is needed.

At a given B it was found possible to distinguish by peak bias between Li^{++} ions, alphas, and protons (in ascending order of peak bias), but not to resolve these peaks completely, with the NaI crystal used in this work.

ENERGY DISTRIBUTION OF PRODUCT PARTICLES

A fairly thin (roughly 3×10^{-5} cm) beryllium target, of a type prepared by Dr. Hugh Bradner (and kindly supplied by him) by evaporation without adhesion onto a flexible steel backing from which it was peeled, cemented without backing in a light frame, was bombarded by protons of well-defined energy. The particles leaving the target are alphas, deuterons, Li^6 and Be^8 ions of various charges, as well as (elastically) scattered

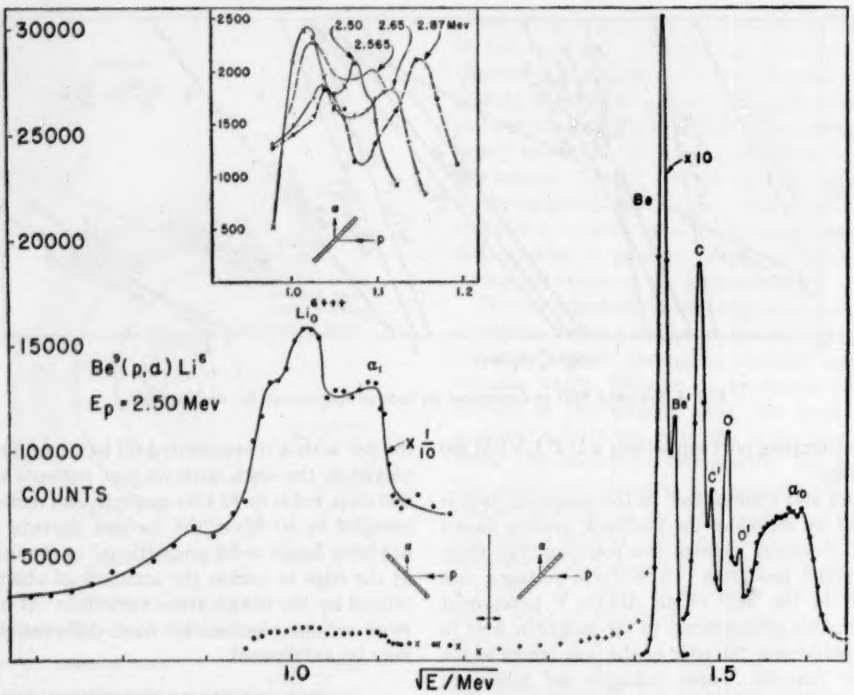

FIG. 4. The observed spectrum from a fairly thin Be target bombarded by 2.5-Mev protons.

protons. The (constant) radius of the median circle multiplied by the magnetic field B on it is proportional to the particle momentum divided by its charge, so B^2 is proportional to the energy E_2 of the product (of mass M_2 and charge Z_2e) through the quantity M_2E_2/Z_2^2. The dependence of this quantity on the incident proton energy E_1 for the various reactions, reaction energies, and product particles encountered is plotted in Fig. 3. This is based on data found in the literature[1] for reaction energies and for excitation energies of the various excited states of the final nuclei (indicated by subscripts, in Mev). Crossovers of these lines are places where particles of different energies and charges and/or masses are observed at the same magnetic field.

The appearance of the energy spectrum of the product particles observed at an incident proton energy $E_p = E_1 = 2.50$ Mev is shown in Fig. 4. The abscissa gives energy directly in Mev for alphas and protons, $(3/2)^1E_2$ for the Li^{6++} ions that happen to fall near the alpha groups. The main reaction peak corresponding to the ground state of Li^6 is seen at the right, near 1.6 Mev, and the much weaker peak corresponding to the 2.187-Mev excited state appears in the vicinity of 1 Mev. The ordinate gives number of counts per observed point but the numbers for the weak peak have been multiplied by ten in plotting the secondary curve that shows the shape of the peak. Both these peaks are quite broad as a result of target thickness, and in neither of them is the alpha peak resolved from the Li-ion peak. The sharp elastic-scattering peaks from the Be target and from C and O impurities (surface layers) are to be seen near 1.5 Mev, together with their "ghosts" which are discussed below.

Target orientation as well as target thickness, of course, influences the shape of the peaks observed, and two orientations were used in the observations of Fig. 4, as indicated by the small inserts. The "transmission" orientation indicated at the lower right and used above about 1.2 Mev tends to give sharper peaks than does the "reflection" position at the left, since even at 45° the transmission orientation more nearly approximates the ideal orientation nearer grazing incidence in which the energy loss by a proton traversing the foil to make a reaction on the back surface is the same as that of an alpha traversing it from a reaction on the front surface. The excited-state peak is broader not only because the "reflection" orientation was used but also because of the greater specific energy loss of the lower-energy emerging particles. It will be noted, too, that in Fig. 3 there is a juxtaposition of three possible energy groups in this region, and the peak at 1.0 Mev rising above the broader plateau is attributed to Li^{6+++} ions from the ground-state transition. This identification was possible as a result of the subsidiary observations depicted in the insert at the top of Fig. 4. Here the "transmission" orientation was used for better resolution, and the bombarding energy E_p was varied, displaying the property that the position of the Li-ion

ground-state group is less sensitive to bombarding energy (showing a steeper rise in Fig. 3). The observed energy dependence of the peak shape makes it appear that the Li^{6++} excited state group is relatively weak. It would be expected to be a little broader than the other two.

THE SPECTROSCOPIC "GHOSTS"

It is interesting to observe in Fig. 4 that this heavy-particle spectroscopy has something more than a name in common with the early days of optical spectroscopy in the appearance of "ghosts." The elastic scattering peaks are much sharper than the others because they do not involve the egress of a highly ionizing particle heavier than a proton from the target, and each of them displays a satellite peak of slightly higher apparent momentum, giving the composite peak a rather similar structure in all three cases. If it appeared only for C and O, one might want to attribute it to surface layers on the front and back of the target, but its appearance (marked Be′) on the side of the Be peak too makes it clear that it must be instrumental.

The ghosts appear to arise from secondary scattering from the small-radius side of the deflection chamber, for they could be eliminated by reducing the entrance aperture from its lower side. Particles entering the surface at nearly grazing incidence can by relatively intense small-angle scattering emerge with slightly reduced energy, and the outward change in direction may be just compensated by the greater inward magnetic deflection over the remainder of the path as a result of the energy loss, permitting the particle to reach the exit slit. The emerging energy may decrease with increasing angle in a fairly definite way, giving a focusing effect in the neighborhood of an optimum scattering angle. It seems plausible that a focus caused by balancing the effects of energy loss and scattering angle might fall near the focus where the particle would have arrived without scattering if the chamber had been wider.

EXCITATION CURVES

The intensities of various reaction products of interest were observed as functions of bombarding energy, with particular emphasis on the immediate neighborhood of $E_p = 2.565$ Mev where the 3.6-Mev gamma ray resulting from the transition to the second excited state of Li^6 shows a pronounced resonance. (This resonance was, in fact, used to calibrate our energy scale, because a new 90° electrostatic deflector on the diatomic beam was used to control the statitron for the first time during this work.) These data are shown in Fig. 5, on the left on a contracted scale to cover a broad energy region and on the right on an expanded scale to cover the resonance region. The points marked α_1 and indicated as dots show the behavior of the shoulder near 1.1 Mev of the low-energy peak in Fig. 4. It passes smoothly through the resonance region with no fluctuations outside of statistical expectations, and starts to rise slightly at lower energies. In following it to lower energies, as suggested by extrapolating from the trend in the insert of Fig. 4, the shoulder merges with the Li^{6+++} ground-state peak and from there on to lower energies that peak was followed as the alpha peak "passed under it," the resultant intensity being shown by the crosses marked $\alpha_1 + Li_0^{6+++}$ in Fig. 5. The curve shows only a very gradual rise and fall, with no pronounced resonance structure at all. Readings were taken at 20-kev intervals, and over some short regions at intervals as small as 8 kev in an unsuccessful attempt to resolve any fine structure there might be. As a result of this lack of structure, the data taken for the other particle groups are more sketchy, but also show no evidence for anything but a fairly gradual change of intensity with energy. The ground-state alphas, indicated by circles,

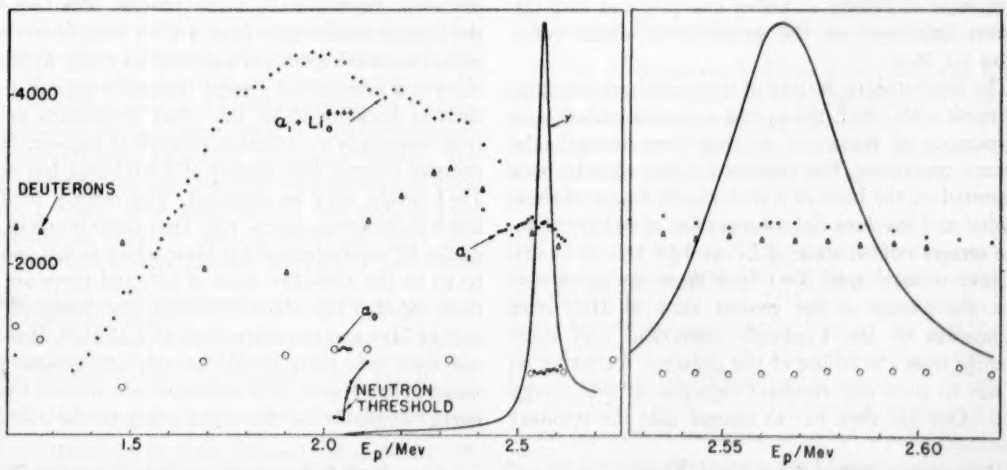

FIG. 5. Excitation curves for the various energy groups of the heavy-particle spectrum and for the 3.58-Mev gammas.

show an initial decrease between 1.2 and 1.5 Mev, indicating how the curve joins on to the low-energy curve reported earlier.[10] The curve then shows a much more gradual rise from 1.5 to 2 Mev than does the $\alpha_1+Li_0^{6+++}$ curve, indicating that the rise must arise largely from the composite nature of the latter. The maximum does indeed agree closely with the crossover of the curves labeled $Be^9(p,\alpha)Li^6_{2.187}$ and $Be^9(p,Li^{6+++})\alpha$ in Fig. 3. The ground-state alphas are seen to pass very smoothly past the gamma resonance and to show no influence of neutron competition at the $Be^9(p,n)$ threshold, the observation of which with a "long counter" is indicated at 2.06 Mev. The deuterons from $Be^9(p,d)Be_0^8$, indicated by deltas, show a fairly pronounced maximum (not entirely expected for a stripping reaction) at 2.3 Mev, and pass smoothly (as in this case is hardly surprising) through the γ-resonance region as shown in the right side of Fig. 5.

The width at half-maximum of the gamma resonance plotted in Fig. 5 is 43 ± 1 kev. From the low-energy tail extending down to the neutron threshold, it is apparent that there is some neutron background, and if a background linearly interpolated between the apparent backgrounds on the two sides of the resonance is subtracted off, the width at half-maximum is reduced to 41 ± 2 kev, in agreement with the reported value[10] 39 ± 2 kev.

CONCLUSIONS

The fact that none of the excitation curves observed seems to show any sharp or pronounced resonances, no more than a gradual rise and fall, in the region 1.3 to 2.7 Mev suggests that the level density in this region of excitation of the compound nucleus, 7.7 to 9 Mev in B^{10}, is too high in comparison with the level width for the levels to appear individually. This is consistent with what is known of the energy levels just below this region,[1] where they are dense and expected to continue to increase in density at higher energies, and with the known behavior[10] of the ground-state alpha curve below 1.1 Mev.

The most striking feature of these results is the completeness with which the α_0 and α_1 curves exclude any appearance of resonance as they pass through the gamma resonance. The explanation has already been suggested on the basis of a preliminary report of these results[4] and involves the conservation of isobaric spin. The second excited state of Li^6 at 3.58 Mev is known to have isobaric spin $T=1$ both from the agreement with the energy of the ground state of He^6, after application of the Coulomb correction, and more recently from the failure of the deuteron scattering on helium to show any resonant behavior at this energy level.[5] One has then but to assume that the resonant level at $E_p=2.565$ Mev, or at an excitation energy 8.89 Mev in the compound nucleus B^{10}, is a $T=1$ level to understand the selective transition to the $T=1$ but not to the $T=0$ levels of $Li^6+\alpha$, or rather of Li^6 since the alpha has $T=0$. (If one wishes to make the distinction between charge symmetry and charge independence of nuclear forces, the same statements may be made less restrictively by replacing $T=1$ and 0 by charge parity odd and even, except for the statement about the level of He^6.) The low states of Li^6 are a particularly favorable place for the expectation of high purity of isobaric spin, the Coulomb energy being so small and the levels widely spaced. B^{10} is also favorable in having small Coulomb energy, but the $T=1$ value seems to be confined quite completely to the 8.89 level in spite of the high density of $T=0$ levels nearby.

The failure of the α_0 and α_1 curves to show any resonance behavior at 2.565 Mev is not a very sensitive test of the purity of the isobaric spin $T=1$, without any $T=0$ admixture, of the compound state at that level, because the effect of a small $T=0$ admixture would be superposed on the background provided by essentially a continuum of $T=0$ states.

The most convincing evidence of lack of isobaric spin mixing is the rather sharp tailing off of the gamma resonance toward low energies, indicating that the $T=0$ states of B^{10} just below the resonance are quite pure, not much contaminated by $T=1$ admixture from the 8.89-Mev state. Some of them would be expected to have the same J as this state. Since the "tail" starts at the neutron threshold, a considerable part of it may be attributed, in spite of its proximity, to neutrons, but how much was unfortunately not ascertained. Thus the height of the "tail" indicates only an upper limit to the amount of $T=1$ admixture.

The $T=0$ level of Li^6 at 2.187 Mev does not give a gamma because its isobaric spin $T=0$ (as well as its $J\neq0^+$) permits it to disintegrate into an alpha and a deuteron, an essentially faster process. The fact that the gamma results only from a $T=1$ level of the compound nucleus explains in a general way why we should observe a pronounced gamma resonance against a continuous background of the other transitions arising from essentially a continuum of levels at high-excitation energies where a high density of $T=0$ levels, but not of $T=1$ levels, may be expected. The density of $T=1$ levels is, however, not so very low: there is one in Be^{10} at the B^{10} equivalent of 8.0 Mev, which is just too low to go to the 3.58-Mev state of Li^6; and there are two close together just above 8.89 Mev, one (assigned[11] 3^+) at 9.12 Mev and the other (>0) at 9.24 Mev. It is thus not clear that there should be only one gamma resonance in this region, until one takes into account the low energy available for the alpha going to the 3.58-Mev

[10] Hahn, Snyder, Willard, Blair, Klema, Kingston, and Green, Phys. Rev. **85**, 934 (1952).

[11] Adair, Barshall, Bockelman, and Sala, Phys. Rev. **75**, 1124 (1949).

state which would be expected to bring angular momentum selection rules into play. If the B^{10} state at 8.89 Mev corresponds to the Be^{10} state at the equivalent of 9.24 Mev with, say, $J=1$ or 2, it could make the transition with $l_\alpha=0$ or 1 much more easily than could a B^{10} state with $J=3^+$, requiring $l_\alpha=2$. Thus the 3^+ assignment to one of the two Be^{10} states helps to explain why the gamma resonance is not double.

In summary, the appearance of a single gamma resonance where the higher-energy alphas show only the influence of a continuum of states may indeed be explained by assuming conservation of isobaric spin.

ACKNOWLEDGMENTS

We are grateful to C. C. Lauritsen and W. Whaling of the California Institute of Technology for early design and performance information on their spectrometer, to G. M. Lobell, R. K. Swank, T. Brill, and J. P. McMahon for help with the construction and electronics of our spectrometer, to A. S. Langsdorf, Jr., R. E. Holland, F. P. Mooring, J. R. Wallace, and R. R. Weeks for their contributions to the performance of the statitron and its appurtenances, to H. Bradner of Berkeley for thin Be targets, and to L. Darlington for participation in taking the data.

PHYSICAL REVIEW VOLUME 95, NUMBER 4 AUGUST 15, 1954

Decay of the Odd-Odd Isomer Tl^{198m}†

T. O. Passell, M. C. Michel, and I. Bergström*
Radiation Laboratory and Department of Chemistry, University of California, Berkeley, California

(Received May 4, 1954)

The electron spectrum of Tl^{198m} has been investigated in a 25-cm double-focusing beta spectrometer with a resolution of approximately 0.4 percent. The electron lines have been assigned to three gamma rays with energies (in kev) 261.5, 284, and 48.4, respectively. The multipolarities assigned from conversion ratio and lifetime considerations are $M4$, $M1+E2$, and $E2$, respectively. A tentative decay scheme is proposed which is consistent with all the available data.

I. INTRODUCTION

A 1.9-HOUR isotope of thallium was first observed and assigned to Tl^{198} by Orth *et al.*[1] Recently this activity has been independently assigned by two different groups of investigators to the decay of an isomeric state. The previously unobserved ground-state decays by electron capture to Hg^{198} with a half-life of 5.3 ± 0.5 hours.

Michel and Templeton[2] of this laboratory produced these activities by the $Au^{197}(\alpha,3n)Tl^{198}$ reaction in the Crocker Laboratory 60-inch cyclotron. Mass separation was made on a time-of-flight isotope separator[3] and the 1.75-hour and 5.3-hour activities shown to be Tl^{198}. Bergström, Hill, and DePasquali[4] at the University of Illinois produced the same activities by bombarding mercury with 11.5-Mev deuterons. Among the many electron lines they observed were several approximately 1.9-hour lines assignable to two gamma rays converting in thallium with energies of 282.4 and 260.7 kev, and a third gamma ray of 48.7 kev whose assignment was not unambiguous. The authors suggested that all three gamma rays were in cascade from an isomeric state having the unusually high spin of 9 with odd parity. Because of the unusual decay scheme suggested, the ambiguity of the 48.7-kev gamma-ray's assignment, and the uncertainties in the photographically determined intensities, further work on this isomer was thought to be desirable.

II. EXPERIMENTAL WORK

Means of Production and Chemical Separation

In this investigation 0.001-inch gold foil was bombarded in the Crocker Laboratory 60-inch cyclotron with 38-Mev helium ions to produce the Tl^{198m} by the $(\alpha,3n)$ reaction. This choice of foil thickness and bombarding energy was effective in minimizing the production of Tl^{199}.

The thallium was chemically separated from the gold target by the following process: (1) the gold was dissolved in aqua regia leaving the gold and thallium in solution as Au^{+3} and Tl^{+3} ions, respectively; (2) sulfur dioxide gas was bubbled through the solution to reduce the Tl^{+3} to Tl^+ and the gold to the metal; (3) the solution was centrifuged and supernatant containing Tl^+ and traces of Au^{+3} carried through varying purification procedures including an ethyl ether extraction; (4) the solution containing thallium was then passed through a Dowex A-2 ion exchange column in $6M$

† This work was performed under the auspices of the U. S. Atomic Energy Commission.
* On leave of absence from the Nobel Institute for Physics, Stockholm, Sweden, with a grant from Svenska Atomkommitten.
[1] Orth, Marquez, Heiman, and Templeton, Phys. Rev. **75**, 1100 (1949).
[2] M. C. Michel and D. H. Templeton, Phys. Rev. **93**, 1422 (1954).
[3] M. C. Michel, Ph.D. thesis, University of California Unclassified Report UCRL-2267, 1953 (unpublished).
[4] Bergström, Hill, and DePasquali, Phys. Rev. **92**, 918 (1953).

TABLE I. Electron spectrum data of Tl^{198m}.

Line	Abundance (assuming $\Sigma 260\epsilon^- = 100$)	
48.4_{LI}	<1.5	$L_{II}/L_{III} = 1.11 \pm 0.1$
48.4_{LII}	37.3	
48.4_{LIII}	33.6	$L/M = 3.7_6 \pm 0.1$
48.4_{LM}	18.9	$L/N = 13.4 \pm 1.0$
48.4_{LN}	5.3	
$\Sigma 48.4\epsilon^-$	95.0	
260.7_K	44.3	$K/L = 1.0 \pm 0.1$
260_L	26.0	
260_{LIII}	17.8	
260_{M+N}	11.9	
$\Sigma 260\epsilon^-$	100	
282.4_K	19.1	$K/L = 9 \pm 1$
282.4_{LI}	2.1	

HCl after first oxidizing the Tl^+ to Tl^{+3} with persulfate. The Tl^{+3} and last traces of Au^{+3} stick at the top under these conditions. Successively more dilute hydrochloric acid solutions were used for washing out impurities, (5) the Tl^{+3} was finally stripped from the column by reduction with water saturated with sulfur dioxide gas, any Au^{+3} being reduced to the metal and remaining on the column. This carrier-free solution was used to make the spectrometer samples.

Sample Preparation

The sample which gave the most clearly resolved electron peaks was one in which the thallium was vaporized onto a palladium leaf from a tungsten filament. The palladium leaf had a thickness of 160 $\mu g/cm^2$. This vaporized sample had the dimensions 1 mm×6 mm.

Beta Spectrometer

The double-focusing beta spectrometer used was one previously described by O'Kelley.[5] The detector has been changed from an end window to a side window Geiger counter. The detector window consisted of three layers of a vinyl copolymer film supported by a grid of 0.001-in. tungsten wires spaced 0.008-in. apart on a copper ring. The window energy cutoff was about 4 kev.

Electron Spectrum

The experimental data are summarized in Table I. The spectrum itself is shown in Figs. 1 and 2. The K Auger lines are not included since at the time they were observed >70 percent of them were being produced by 5.3-hour electron capture of the ground state. It might be of interest, however, to note that we obtained for the ratio $KLL/KLY/KXY$ the values 1.0/0.53/0.063 (where X and Y denote M, N, etc., orbital electron shells). The L Auger lines were also observed, but no inferences can be made therefrom because of the large and uncertain window absorption correction necessary at such low energies. In Table I the gamma-ray energies are also given. Except for the 48.4-kev gamma ray, the energy values of the Illinois group[4] are more accurate and will be used in the following discussion.

It should be mentioned that there was initially present a very small percentage of 7.4-hour Tl^{199}. The only Tl^{199} electron line which coincided with any of those from Tl^{198m} was the 50.0_{LI}. This line was of insignificant abundance at the time the 48.4_{LII} and 48.4_{LIII} lines of Tl^{198m} were observed, but several hours later it was a useful calibration point for determining the energy of the 48.4-kev gamma ray.

The ratios given in Table I depend considerably upon the half-life assumed for decay corrections. The limits of error do not necessarily encompass those introduced by the unknown uncertainty in half-life. We used a half-life value of 1.75 hours which was measured by Michel and Templeton[2] on a mass-separated sample.

III. DISCUSSION

The Gamma Rays

Bergström and co-workers[4] found that the 260.7-kev gamma ray was definitely the cascade initiator, being of the $M3$ or $M4$ type with a possible admixture of electric radiation. Our K/L ratio (1.0) is in excellent agreement with that for pure $M4$ radiation.[6-8] According to the curves of Tralli and Lowen,[9] where L_{III}/L_I is plotted as a function of Z^2/E, the isomeric transition would be of $M3$ type. ($L_{III}/L_I = 0.80$ for $M3$ and 1.4 for $M4$). These curves, however, are based on approximate calculations and were performed for $Z = 35$.

Mihelich[10] has summarized the experimental values of L_{III}/L_I for $M4$ transitions in the same region of

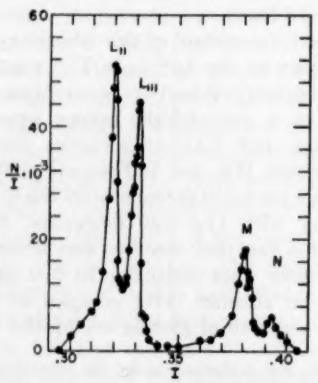

FIG. 1. Electron lines from the 48.4-kev gamma ray of Tl^{198m}.

[5] G. D. O'Kelley, Ph.D. thesis, University of California Unclassified Report UCRL-1243, 1951 (unpublished).

[6] W. L. Bendel, Ph.D. thesis, University of Illinois, 1953 (unpublished).

[7] Bergström, Nybö, Thulin, Wapstra, and Aström, Arkiv Fysik 7, No. 22 (1953).

[8] M. Goldhaber and A. W. Sunyar, Phys. Rev. 83, 906 (1951).

[9] N. Tralli and I. S. Lowen, Phys. Rev. 76, 1541 (1949).

[10] J. W. Mihelich and A. deShalit, Phys. Rev. 93, 135 (1954).

atomic number as thallium. Figure 3 shows these values with the inclusion of our value of 0.68 ± 0.07 for the 260.7-kev gamma ray of Tl^{198m}. Since all of these transitions occur in the same region of atomic number, one may plot these values *versus* energy. It is apparent that our value would fit reasonably well with the other four on a smooth curve, supporting our $M4$ assignment for the 260.7-kev gamma ray.

The experimental mean life of the 260.7-kev gamma ray may be calculated using the theoretical K conversion coefficient for $M4$ radiation from the tables of Rose *et al.*[11] (18), our $260.7_K/\sum 260$ ratio (0.44), and the half-life of the isomeric state (1.75 hours). The mean life thus calculated is 3.7×10^5 seconds. The theoretical value one obtains using the nomogram of Weisskopf's lifetime-energy-spin formula prepared by Montalbetti[12] is 5×10^5 seconds. This agreement may be fortuitous. The $M4$ assignment is therefore reasonable from the comparisons we have been able to make with existing theories and empirical correlations.

Because of the high intensity of the Tl^{199} 50.0_{LI} line, Bergström *et al.*[4] were unable to resolve the 48.4_{LIII} line. As a result they designated the 48.4_{LII} line as 48.7_{LI}. The two lines we observe can be only an $L_{II}-L_{III}$ pair, and using the 50.0_{LI} line of Tl^{199} as a standard, we arrive at an energy of 48.4 ± 0.2 kev for the gamma ray. The L_{II}/L_{III} ratio is in better agreement with $E2$ (1.6) than with $E1$ ($\sim$1.8) or $M1$ ($\sim$900) although only $M1$ can be ruled out on this basis.[13] The $E1$ assignment was eliminated by a scintillation spectrometer experiment which determined the total conversion coefficient of the gamma ray to be greater than 10. Therefore, the $E2$ assignment seems to be the only reasonable one.

The Illinois group has shown the 260.7- and 282.4-kev gamma rays to be converting in thallium. Coincidence measurements performed by Mr. Frank Stephens of this laboratory have shown the 282-kev gamma ray

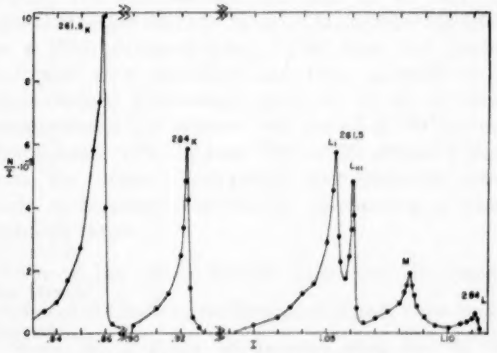

FIG. 2. Electron lines from the 261.5-kev and 284-kev gamma rays of Tl^{198m}.

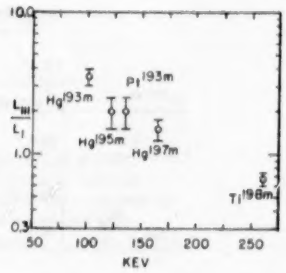

FIG. 3. Plot of experimental L_{III}/L_I ratios for some $M4$ transitions *versus* energy in kev.

to be in coincidence with K x-rays. Thus it appears that the 282.4 and 260.7-kev gamma rays are in cascade. If one assumes no electron capture from excited states of Tl^{198}, the K conversion coefficient of the 282.4-kev gamma ray can be calculated from the intensity ratio $(282_K)/(260_{K+L+M\ \ldots})$. The value (0.24) thus obtained may indicate a mixture of $E2$ (0.076) and $M1$ (0.52) radiation.[11] The high K/L ratio (9 ± 1) of this gamma ray supports an $M1$ assignment.[8]

If the 48.4-kev gamma ray is emitted in cascade with the other two and is assumed to be $E2$ radiation, the total intensity of its conversion electrons should equal the total intensity of those of the 260.7-kev gamma ray. As can be seen from Table I these intensities are equal within experimental error. This does not exclude the possibility of an approximately 50 percent electron capture branching from the 1.75-hour isomeric state, with the 48-kev transition taking place in Hg^{198}. The $L_{II}-L_{III}$ binding energy differences are too similar in mercury and thallium to allow an assignment on that basis. If, however, the electron capture were occurring, one would expect to observe gamma rays from levels in Hg^{198} in high intensity with a 1.75-hour half-life. A scintillation spectrometer experiment gave no indication of such gamma rays. We can therefore conclude that the three gamma rays are very probably emitted in cascade as suggested by the Illinois group.[4]

Spin Assignments

If one assumes that our assignments of multipolarity are correct and that the three gamma rays are in cascade, a tentative decay scheme can be constructed (see Fig. 4) in which the spin difference between the 1.75-hour Tl^{198m} and the 5.3-hour Tl^{198} can be as high as 7 with a parity change. The fact that no crossover radiation was observed supports this large spin difference. The positions of the 282.4- and the 48.4-kev transitions may be as shown in Fig. 4 or reversed. The spin alternatives in the left column in Fig. 4 are based upon the assumption of a 2− ground state for Tl^{198}.[4] The alternatives in the right column are based upon the assumption of a coupling between the spins of the 81st proton and the 117th neutron. The 260.7-kev $M4$ transition would then represent a transition of the 81st proton from an $h_{11/2}$ to a $d_{3/2}$ configuration, the

[11] Rose, Goertzel, and Perry, Oak Ridge National Laboratory Unclassified Report ORNL-1023, June 1951 (unpublished).
[12] R. Montalbetti, Can. J. Phys. **30**, 660 (1952).
[13] Gellman, Griffith, and Stanley, Phys. Rev. **85**, 944 (1952).

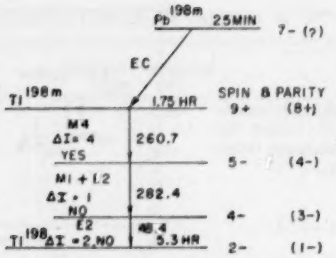

FIG. 4. Tentative decay scheme of Tl^{198m}.

117th neutron remaining in an $f_{5/2}$ configuration; the 282.4-kev $M1+E2$ transition may perhaps represent a transition of the same proton between the $d_{3/2}$ and $s_{1/2}$ configurations, the neutron again remaining in the $f_{5/2}$ configuration; the 48.4-kev $E2$ transition then represents a transition of the odd neutron from its $f_{5/2}$ to a $p_{1/2}$ configuration, the proton remaining in an $s_{1/2}$ configuration. This interpretation is, of course, extremely speculative.

Also shown in Fig. 4 is the electron capture decay from Pb^{198} which was first observed by Neumann and Perlman.[14] If the 25-minute Pb^{198} parent of Tl^{198m} is the 0+ ground state of Pb^{198}, then Tl^{198m} must have a low spin and Tl^{198} must have a high spin. The assignment of a high spin to Tl^{198} is in sharp disagreement with the interpretation of its electron capture decay given by Bergström and co-workers.[4] These workers' data indicate that the electron capture decay of Tl^{198} goes predominantly to the 2+ first excited state of Hg^{198}. Thus of the two isomeric states of Tl^{198} the 1.7-hour Tl^{198m} most probably has the higher spin. The fact that other even-even lead isotopes have high spin isomers suggests that Pb^{198} might also have one. For example, the isomeric state of Pb^{204} has been suggested to be 6+[15] or 7−.[16] Very recently Maeder and Wapstra[17] have found indication of a 9− isomeric state in Pb^{202}. Alburger[18] assigned the isomeric level in Pb^{206} as 7−. If Pb^{198} has a similar high-spin isomer, direct electron capture decay from a high-spin Pb^{198m} to a high-spin Tl^{198m} would be possible. We therefore conclude that there is indeed another case of isomerism in Pb^{198}.

It is apparent that a study of the Tl^{198} electron capture decay is needed to make more definite spin assignments for Tl^{198} and Tl^{198m}. We can only state that the spin difference between the isomers may be as high as 7 and that Tl^{198m} most probably has the higher spin.

The authors wish to acknowledge the help and cooperation of Mr. G. B. Rossi and the crew of the 60-inch cyclotron in making the bombardments necessary for this investigation. We appreciate the assistance of Mr. Frank S. Stephens in making the coincidence measurement.

[14] H. M. Neumann and I. Perlman, Phys. Rev. **78**, 191 (1950).

[15] Frauenfelder, Lawson, Jentschke, and DePasquali, Phys. Rev. **92**, 1241 (1953).

[16] M. Goldhaber and R. D. Hill, Revs. Modern Phys. **24**, 179 (1952).

[17] D. Maeder and A. H. Wapstra, Phys. Rev. **93**, 1433 (1954).

[18] D. E. Alburger and M. H. L. Pryce, Phys. Rev. **92**, 514 (1953).

Gamma Radiation from B^{10} Bombarded by Protons

ROBERT B. DAY* AND TORBEN HUUS†
Kellogg Radiation Laboratory, California Institute of Technology, Pasadena, California
(Received May 10, 1954)

A sodium iodide scintillation spectrometer has been used to study the gamma radiation produced when B^{10} is bombarded by protons. The following gamma rays have been found: a 432-kev gamma ray from the $B^{10}(p,\alpha\gamma)Be^7$ reaction, a 718-kev gamma ray from inelastic scattering in B^{10}, and a high-energy gamma ray from the reaction $B^{10}(p,\gamma)C^{11}$. Excitation curves and cross sections for these gamma rays are given.

INTRODUCTION

VERY little information is available about the gamma radiation produced from B^{10} reactions with protons. In their work on the mirror nuclei, Li^7 and Be^7, Brown *et al.*[1] investigated the gamma-ray yield from the reaction $B^{10}(p,\alpha\gamma)Be^7$ up to proton energies of 1.6 Mev. They found a single resonance near 1.5 Mev with a peak cross section of 0.14 barn. Other results are available from the pair spectrometer work of Walker[2] on $B^{10}(p,\gamma)C^{11}$. Bombarding a thick B^{10} target with 1.2-Mev protons, he found a gamma ray at 9.47 Mev, in addition to 12.1- and 16.7-Mev gamma rays from the reaction $B^{11}(p,\gamma)C^{12}$. Krone and Seagondollar have also given some data on $B^{10}(p,\gamma)$ in a recent publication.[3]

Following our earlier work on the gamma radiation from B^{11} reactions,[4] we have investigated the energies and yields of the gamma rays produced in $B^{10}+p$ reactions using a sodium iodide scintillation spectrometer.[5] The results of this work have revealed a gamma ray from inelastic scattering in B^{10} as well as the gamma rays from the two reactions mentioned previously.

EXPERIMENTAL PROCEDURE

The scintillation spectrometer and procedure used with it have been described in an earlier report.[4] Briefly, the spectrometer consisted of an NaI(Tl) crystal 1½ inches long and 1½ inches in diameter mounted on a 5819 photomultiplier. Pulses from the photomultiplier were amplified and then analyzed in a single-channel pulse-height analyzer. In all of these measurements the counter was placed at 90° to the proton beam with the front face of the crystal ¾ inch from the target. Background measurements were made at frequent intervals by bombarding a clean tantalum target.

Two types of targets were used: one consisted of a thin layer of $(B^{10})_2O_3$ evaporated *in vacuo* on a tantalum backing; the other was a thin boron layer prepared by cracking diborane on hot tantalum. In both of these the boron was enriched to about 95 percent B^{10}. The number of B^{10} nuclei per cm^2 in these targets was determined by comparing the yield of the $B^{10}(p,\alpha\gamma)Be^7$ reaction from the various targets with the yield from a target of normal B_2O_3. The thickness of this target had previously been measured from the apparent width of the 163-kev resonance of $B^{11}(p,\gamma)C^{12}$; from the target thickness the number of boron nuclei per cm^2 was then calculated by using the stopping cross section of B_2O_3.

Protons were accelerated in an electrostatic generator and analyzed in energy by either a 90° electrostatic or magnetic analyzer set to give an energy resolution of 0.1–0.2 percent. The beam striking the target was measured by means of a current integrator having an accuracy of a few percent.

RESULTS

$B^{10}(p,\alpha\gamma)Be^7$

This reaction was already known to have a resonance near 1.5 Mev; consequently the pulse-height spectrum was investigated in detail at this bombarding energy. Figure 1 shows the spectrum obtained, as well as the background produced by bombarding a clean piece of tantalum. The peak at 432 kev is from the well-known first excited state of Be^7. A number of measurements,

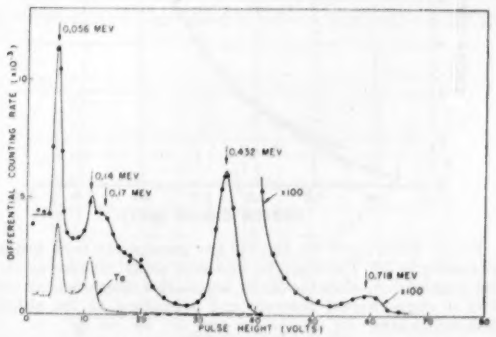

FIG. 1. Pulse-height distribution for low-energy gamma rays from B^{10} reactions. Proton energy = 1.52 Mev.

* Now at Los Alamos Scientific Laboratory, Los Alamos, New Mexico.

† Now at the Institute for Theoretical Physics, Copenhagen, Denmark.

[1] Brown, Snyder, Fowler, and Lauritsen, Phys. Rev. **82**, 159 (1951).

[2] R. L. Walker, Phys. Rev. **79**, 172 (1950).

[3] R. W. Krone and L. W. Seagondollar, Phys. Rev. **92**, 935 (1953).

[4] T. Huus and R. B. Day, Phys. Rev. **91**, 599 (1953).

[5] A preliminary report of part of this work has been given in Phys. Rev. **85**, 761 (1952).

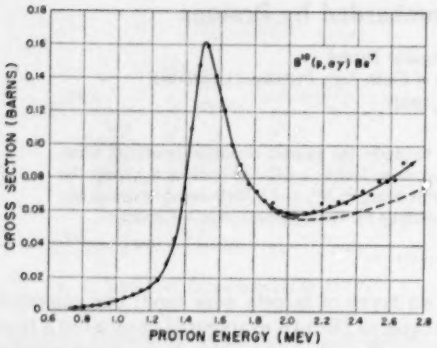

FIG. 2. Yield curve for the 432-kev gamma ray from $B^{10}(p,\alpha\gamma)Be^7$. For the dashed curve the contribution of the 718-kev gamma ray has been subtracted.

which had a standard deviation of 2 kev, were made of the energy of this peak. However, taking into account the possibility of unsuspected systematic errors, we would take the gamma-ray energy to be 432±3 kev.

Since the possibility of other levels in Be^7 near 200 and 700 kev had previously been suggested,[6] a careful examination was made for peaks in these regions of the pulse-height spectrum. A peak does indeed appear at 718 kev in Fig. 1, but its energy and yield show fairly conclusively that it arises from the decay of the first excited state of B^{10} in an inelastic scattering reaction (see below). We are less certain as to the origin of the peak at 170 kev; however, its position and magnitude are just what would be expected from Compton scattering in the backward direction of the 432-kev gamma ray. Other low-energy gamma rays were checked with the same counter and showed a similar peak of about the same magnitude. It is clear from Fig. 1 that the peaks at 56 and 140 kev are characteristic of the tantalum target backing. The first is the K x-ray of tantalum, while the second results from the Coulomb excitation of the tantalum nucleus.[7] The difference in the relative magnitudes of the peaks is due to the fact that there was more absorber between the target and detector in the background measurements. From these data we conclude that there is no evidence for any low levels in Be^7 other than the one at 432 kev.

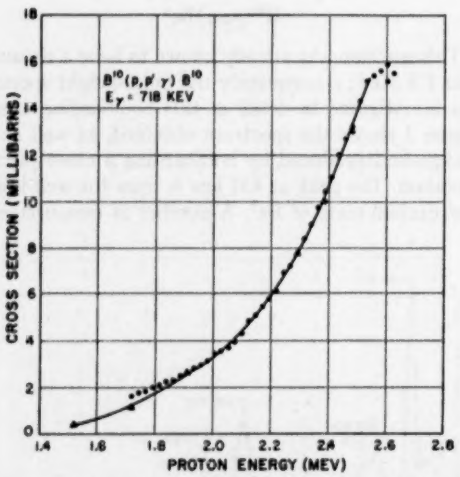

FIG. 3. Yield curve for the 718-kev gamma ray from inelastic scattering in B^{10}. The triangles represent actual measurements of the cross section, while the circles are relative measurements made with a single-channel analyzer and normalized to the absolute data at 2.3 Mev.

[6] J. C. Grosskreutz and K. B. Mather, Phys. Rev. **77**, 580 (1950).

The excitation curve for this reaction was investigated by setting a discriminator at 28 volts (Fig. 1) and counting all pulses larger than this. The counting rate obtained as a function of proton energy for a thin target is shown in Fig. 2. At the higher energies a correction is required for the contribution of the 718-kev gamma ray. The corrected curve is shown as the dashed line in Fig. 2. A number of measurements were made of the energy of the resonance peak. With corrections made for the target thickness, the value obtained was 1.52 Mev.

The gamma-ray yield at the resonance peak was obtained by integrating under the differential pulse-height curve and dividing by the counter efficiency. The cross section could then easily be calculated from the known target thickness. The value thus obtained was 0.21±0.07 barn, which is to be compared with the value 0.14±0.03 barn obtained by Brown *et al.*[1] These have been averaged to give 0.16 barn, and this result was used to normalize the curve in Fig. 2.

$B^{10}(p,p'\gamma)B^{10}$

The peak appearing at 718 kev in Fig. 1 was investigated at other bombarding energies as well. It was found that the intensity of the peak increased very rapidly with energy, while its position remained constant. The average of several determinations of the gamma-ray energy gave 718±5 kev. This agrees very well with the value 719±1.6 kev found for the energy of the first excited state of B^{10} by Craig *et al.*[8] Thus it seems very likely that this gamma ray originates in an inelastic scattering reaction.

The yield of this gamma ray was measured as a function of proton bombarding energy with the aid of a single-channel pulse-height analyzer set to straddle the photopeak. The results are shown in Fig. 3. Since the photopeak is superimposed on the high-energy tail of the 432-kev gamma ray, one obtains in this way too high a value for small yields. Therefore, the yield

[7] This gamma ray has been investigated in more detail by T. Huus and C. Zupancic, Kgl. Danske. Videnskab. Selskab Mat.-fys. Medd. **28**, No. 1 (1953); and by C. L. McClelland and C. Goodman, Phys. Rev. **91**, 760 (1953).

[8] Craig, Donahue, and Jones, Phys. Rev. **88**, 808 (1952).

was also obtained at several energies by measuring the area under the photopeak. The actual cross section could also be obtained from the area under the photopeak relative to the area under the photopeak of the 432-kev gamma ray by applying a correction for the relative photopeak efficiency for the two energies. This relative efficiency was obtained semiempirically. The yield data obtained with the single-channel analyzer were then normalized to the cross section obtained at 2.3 Mev to give the curve in Fig. 3. Near 2.6 Mev the data were unreliable, hence it is not possible to tell whether one is approaching a resonance as the data seem to indicate. At 2.2 Mev the cross section obtained here is in order of magnitude agreement with the value 3×10^{-27} cm^2/steradian obtained by Craig *et al.*[8] for the protons scattered inelastically at 134°. This agreement tends to strengthen the hypothesis that the gamma ray originates in an inelastic scattering reaction and not a (p,α) reaction.

A search was made for gamma rays from higher levels in B^{10}, but without success. A gamma ray at 1.63 Mev was a possible candidate, but it is now believed to have originated in the $Na^{23}(p,\alpha\gamma)Ne^{20}$ reaction[9] from sodium contamination of the target.

$B^{10}(p,\gamma)C^{11}$

A search for the ground-state gamma ray reported by Walker was made by displaying the photomultiplier pulses on an oscilloscope and making a long time exposure. This procedure showed the following gamma rays: at $E_p=0.86$ Mev, $E_\gamma=9.9\pm0.5$ Mev; at $E_p=1.21$ Mev, $E_\gamma=9.4\pm0.5$ Mev. The energies expected for the ground-state transitions at these two bombarding energies are 9.48 Mev and 9.80 Mev, respectively. Since no other high-energy gamma rays were present except those from proton capture in B^{11} it was concluded that the $B^{10}(p,\gamma)$ reaction takes place mainly by a transition to the ground state of C^{11}.

An attempt was made to measure the excitation curve for the $B^{10}(p,\gamma)$ reaction. Figure 4 shows the results of two runs that were made. Since the yield from the B^{11} capture reaction was of about the same intensity as that from B^{10} even though the target was enriched to 95 percent B^{10}, the problem of separating the B^{10} radiation from the two B^{11} gamma rays would normally require taking excitation curves at three bias settings in order that one might obtain the true yield curve of the $B^{10}(p,\gamma)$ radiation. Unfortunately it was not possible to do this in the time available. However, from the data obtained here and those obtained earlier in an experiment on $B^{11}(p,\gamma)C^{12}$, it was possible to get a fairly good idea of the excitation curve for the $B^{10}(p,\gamma)$ reaction. The technique used in separating out the effects of the three gamma rays present was the same as that used in reference 4.

[9] F. Ajzenberg and T. Lauritsen, Revs. Modern Phys. **24**, 321 (1952).

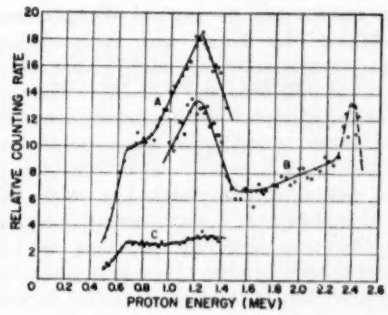

FIG. 4. Yield data for the reaction $B^{10}(p,\gamma)C^{11}$. Curves A, B, and C were taken with a discriminator set to record pulses greater than 6.0 Mev, 7.0 Mev, and 9.9 Mev, respectively. Thus the contribution to curve C is entirely from the $B^{11}(p,\gamma)C^{12}$ reaction.

To aid in doing this, integral bias curves were taken at several energies to get a good check on the yield of the B^{10} radiation there. The results (Fig. 5) show that the bump evident at 0.7 Mev in Fig. 4 is due to the $B^{11}(p,\gamma)$ reaction, while that at 1.2 Mev is from a broad resonance in $B^{10}(p,\gamma)$. Above 1.5 Mev the backgrounds were high, and consequently the data there are not so reliable. In particular, the existence of a resonance at 2.4 Mev is in doubt since this energy region was covered only once and the uncertainties in the data are quite large. The resonance indicated here is therefore only drawn with a dashed line. Further work should be done to show whether a resonance actually exists here or not.

The resonance at 1.2 Mev is probably to be identified with the one found at 1.15 Mev in $B^{10}(p,\alpha)Be^7$ by Brown *et al.*[1] When one corrects the data obtained here for the target thickness the resonance peak is at 1.21 Mev. As in the $B^{10}(p,p'\gamma)$ reaction the cross sections indicated in Fig. 5 are really 4π times the differential cross section at 90°, since all the data were taken at just one angle. At the lower energies the cross sections are estimated to have an accuracy of 50 percent; however, above 1.5 Mev the uncertainties in the data and their interpretation were such that the cross sections are good to only a factor of two or so.

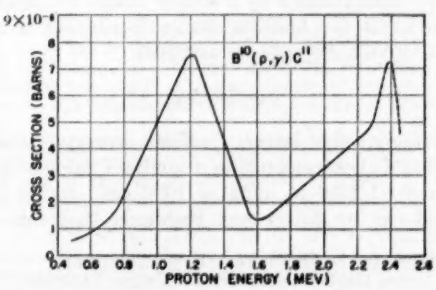

FIG. 5. Cross section of $B^{10}(p,\gamma)C^{11}$ as a function of energy.

These results are in marked disagreement with those obtained by Krone and Seagondollar,[3] who report a resonance in $B^{10}(p,\gamma)$ at 0.78 Mev and possible resonances at 0.95 Mev and 1.33 Mev. The procedure by which we obtained the excitation curve (Fig. 5) involved some uncertainties since insufficient data were taken to do it exactly. Therefore, it is possible that we would have overlooked a weak resonance at 0.78 Mev; however, it would certainly be much less intense than our observed resonance at 1.2 Mev. The latter should then have been seen easily by Krone and Seagondollar. It would appear that further work should be done to resolve the discrepancy between the two sets of data.

We would like to thank Professor T. Lauritsen for suggesting this problem and for his interest and help in this work. To Professor C. C. Lauritsen, Professor W. A. Fowler, and Professor R. F. Christy we would like to express our thanks for their continued interest and for their comments on the manuscript. We are also indebted to Dr. James N. Shoolery for producing the thin targets by the diborane method. One of us (T.H.) is grateful for a research fellowship at the California Institute of Technology.

PHYSICAL REVIEW VOLUME 95, NUMBER 4 AUGUST 15, 1954

Coulomb Radius Constant from Nuclear Masses

ALEX E. S. GREEN
The Florida State University, Tallahassee, Florida
(Received April 9, 1954)

On the assumption of a uniform charge distribution, the Coulomb energy constant obtained from a recent adjustment of the semiempirical formula to the mass data corresponds to the Coulomb radius constant 1.237 (in 10^{-13} cm). This result is in good agreement with the radius constant obtained from recent studies of μ-mesonic x-rays, and can be readily reconciled with the radii obtained from electron scattering, isotope shift measurements, and mirror nuclide mass differences. In view of the importance of the question of the Coulomb radius, an attempt is made to refine the determination of the Coulomb radius constant based upon nuclear masses by using an objective criterion for best fit. A least-squares analysis involving a new adjustment procedure yields the radius constant 1.216. An investigation of the precision of this determination leads to the assignment of a probable error of 1 percent. This new radius constant agrees with the average radius constant obtained from μ-mesonic x-rays within the small probable error assigned to each.

1. INTRODUCTION

IN a previous study Green and Engler[1] found an adjustment of constants which brought the Weizsäcker semiempirical equation into good agreement with experimental nuclear masses. It was noted that the energy constants which accomplish this were substantially larger than those appearing earlier in the literature. In view of the lack of understanding of nuclear forces, the significance of the increased nuclear energy constants is obscure. However, the increased Coulomb energy constant (a_3) has a simple interpretation if one assumes that the charge in a nucleus may be characterized by a simple charge distribution. In particular, if a uniform charge distribution and the radius formula $R=r_0A^{\frac{1}{3}}$ are accepted,

$$a_3=3e^2/5r_0. \tag{1}$$

Accordingly, the larger Coulomb energy constant (0.750 mMu) corresponds to a smaller Coulomb radius constant[2] (1.2369 in units of 10^{-13} cm). It has been pointed out by Bitter and Feshbach[3] that this new constant is in good agreement with the radius constant obtained recently from μ-mesonic x-ray studies,[4,5] electron scattering studies,[6] and isotope shift studies.[7]

Green and Engler halted their interative adjustment process when they found a convenient rounded set of energy constants ($a_1=16.720$, $a_2=18.500$, $a_3=0.750$, and $a_4=100$, all in mMU) which reduced the discrepancy between the Weizsäcker formula and the mass data to the order of magnitude of uncertainty caused by shell effects. In view of the importance of the question of the Coulomb radius, it seems worthwhile to attempt to refine the determination of the Coulomb radius constant based upon nuclear masses by the use of an objective criterion for best fit and to establish the precision of such a determination.

2. METHOD OF ADJUSTMENT

The basic assumptions made are that nuclear energies may be expressed in the form

$$E^w=-a_1A+a_2A^{\frac{2}{3}}+a_3(Z^2/A^{\frac{1}{3}})+a_4(N-Z)^2/4A, \tag{2}$$

[1] A. Green and N. Engler, Phys. Rev. **91**, 40 (1953).
[2] A. Green, Gordon Conference on Nuclear Chemistry, June, 1953 (unpublished).
[3] F. Bitter and H. Feshbach, Phys. Rev. **92**, 837 (1953).
[4] V. L. Fitch and J. Rainwater, Phys. Rev. **92**, 789 (1953).
[5] A. N. Cooper and E. M. Henley, Phys. Rev. **92**, 801 (1953).
[6] Hofstadter, Fechter, and McIntyre, Phys. Rev. **92**, 978 (1953).
[7] P. Brix and H. Kopferman, Festschr. Acad. Wiss. Göttingen **17**, 49 (1951).

and that the constant a_3 is related to the constant radius r_0 by Eq. 1. The usual procedure for evaluating the semiempirical constants[8] is to evaluate a_3 by fitting the mass differences of mirror nuclides, fix a_4 by fitting the experimental line of beta stability, and fix a_1 and a_2 by fitting the masses of beta stable nuclides. It is clear now that the first step in this procedure is in error because of the correlation effects pointed out by Cooper and Henley[5] and because of the fact that the low end of the mass scale is a poor place to adjust a constant of a statistical theory. In essence the alternative method used here is to fix a_4 to a_3 by the constraint imposed by the experimental line of beta stability, and to adjust a_1, a_2, and a_3 by fitting the masses of beta-stable nuclides.

The numerical work was greatly expedited by using the results of Green and Engler as a starting point. Accordingly, the residual between the experimental mass defects, Δ^x, for beta-stable nuclides and the best statistical expression $\Delta_m{}^b(A)$ for the mass defects of such nuclides is expressed as [9]

$$R=[\Delta^x-\Delta_m{}^r(A)]-[\Delta_m{}^0(A)-\Delta_m{}^r(A)] -[\Delta_m{}^b(A)-\Delta_m{}^0(A)], \quad (3)$$

where $\Delta_m{}^r(A)$ are the reference mass defects [Eq. (2), reference 1] and $\Delta_m{}^0(A)$ are mass defects based upon the Green-Engler constants. The difference $R^x=\Delta^x-\Delta_m{}^r(A)$ requires a study of the experimental data, whereas the residuals $R^b=\Delta_m{}^b(A)-\Delta_m{}^0(A)$ and $R^0=\Delta_m{}^0-\Delta_m{}^r(A)$ can be handled analytically.

If $D_m{}^b(A)$ and $D_m{}^0(A)$ are used to denote the functions which characterize the theoretical lines of beta stability, it is not difficult to show that, to a very good approximation,

$$D_m{}^b-D_m{}^0=(\delta\rho/\rho^b)F+(\delta a_4/a_4{}^b)G, \quad (4)$$

where

$$F=\rho^0A^{5/3}[1-(D_m{}^0/A)]/(1+\rho^0A^{\frac{1}{3}}), \quad (5)$$

$$G=A(\Delta_n-\Delta_H)/a_4{}^0(1+\rho^0A^{\frac{1}{3}}), \quad (6)$$

and $\rho^0=a_3{}^0/a_4{}^0$. To relate $\delta\rho/\rho^b$ and $\delta a_4/a_4{}^b$ to δa_3, a particular value of A (A_s) is chosen such that the difference $D_m{}^b(A_s)-D_m{}^0(A_s)$ shall equal a designated quantity γ_s. By using straightforward but tedious algebraic transformations, it is then possible to express the residual R in the form

$$R=R^x-R^0+\delta a_1A-\delta a_2A^{\frac{1}{3}}-\delta a_3S(A)-\gamma_sT(A), \quad (7)$$

where

$$S(A)=[(A_s{}^{5/3}-A_s{}^{2/3}D_s{}^0)/4D_s{}^0][D_m{}^0+G-(G_s/F_s)F], \quad (8)$$

and

$$T(A)=(a_4{}^b+\Delta_n-\Delta_H)F/F_s -S[(A_s{}^{5/3}-A_s{}^{2/3}D_s{}^0)/(a_3{}^0A_s{}^{2/3}+a_4{}^0)]. \quad (9)$$

It is convenient now to proceed by setting

$$A_s=200, \quad \text{and} \quad \gamma_s=0,$$

thus forcing $D_m{}^b$ to intersect the $D_m{}^0$ curve at $A=200$. Such an intersection at high A insures the fact that the departures $D_m{}^b-D_m{}^0$ will be very small ($\lesssim 0.05$) for all values of A. The curve $D_m{}^0$ matches closely the function determined by Fermi, and a number of studies[10,11] indicate that this smooth line of beta stability is quite satisfactory.

At this point the complex question arises as to how to handle the experimental residuals R^x which are known for about 241 beta-stable nuclides with $A>5$. It is well known that Eq. (2) neglects a number of energy effects which might be characterized as (1) shell structure, (2) pairing effects and pairing anomalies, (3) Coulomb exchange, (4) nonuniform angular distribution of charge, (5) nonuniform radial distribution of charge, (6) compressibility. Also, experiment provides only Δ values for integral N and Z values, whereas $\Delta_m(A)$ refers to hypothetical mass values usually located at nonintegral N and Z values. Accordingly the departures of the experimental data from Eq. (2) are expected to reflect these neglected energy effects to a greater extent than they reflect the real experimental errors in masses. Nevertheless, for the purpose of the present investigation, it was deemed reasonable to regard the errors due to the inadequacies of Eq. (2) on an equal footing with the real experimental error, and to assume that these errors are normally distributed.[12]

To treat the large mass of experimental data, the mass scale was divided into twenty-four intervals, each spanning 10 units in A and centered at $A=10$, 20, 30, etc. The centers of gravity of the mass residual values in each interval were then located at the centers of the interval. The twenty-four "normal places" so obtained were treated as basic experimental data with equal weight.[13]

Using these data in Eq. (7), the quantities δa_1, δa_2, and δa_3 were evaluated by least squares[14] under

[8] J. M. Blatt and V. F. Weisskopf, *Theoretical Nuclear Physics* (John Wiley and Sons, Inc., New York, 1952).

[9] Henceforth all quantities which refer to the Green-Engler set of constants will be designated by the superscript zero and quantities which relate to the "best" set of constants by the superscript b. Elsewhere the notation in reference 1 will be followed.

[10] C. D. Coryell, Ann. Rev. Nuclear Sci. **2**, 305 (1953).

[11] A. Green and D. Edwards, Phys. Rev. **91**, 46 (1953).

[12] E. R. Cohen, Revs. Modern Phys. **25**, 709 (1953). The discussion in this article of the implications of the use of least squares for non-Gaussian distributions is relevant to this present study.

[13] R. A. Birge, Revs. Modern Phys. **19**, 298 (1947).

[14] Actually, considerable difficulty was encountered in the calculations because of the cancellations of almost all of the significant figures in the evaluation of various third degree determinants. These difficulties were overcome, however, by using $A^{\frac{1}{3}}-0.2A$ as the coefficient of δa_2, and $S-6.95A$ as the coefficient of δa_3, and by changing the coefficient of A accordingly. The advantages of these devices are probably analogous to the advantages associated with the use of orthogonal polynomials in the least-squares fitting of polynomials. (See reference 13.)

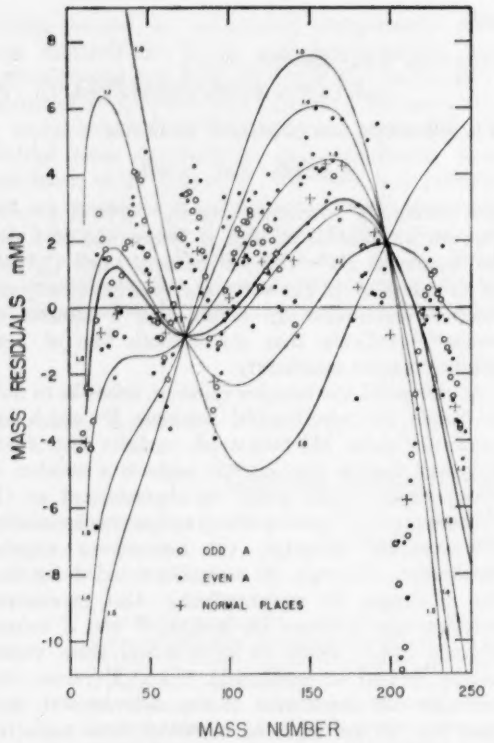

FIG. 1. The mass residuals of beta-stable nuclides in relation to the semiempirical functions obtained by least squares. The heavy curved line corresponds to the "best" fit to the normal places. The light curved lines represent the best fits attainable when the radius constant is fixed at the values indicated. All points are plotted as deviation from the reference values.

the assumption that $\gamma_s=0$. The new energy constants and the Coulomb radius obtained were

$$a_1=16.9177, \quad a_2=19.120, \quad a_4=101.777, \quad a_3=0.76278, \quad r_0=1.2162. \tag{10}$$

To determine the effect upon the radius constant of the assumption that $\gamma_s=0$, a least-squares calculation based upon Eq. (7) with nonvanishing values of γ_s was used. The Coulomb energy constant change and the corresponding fractional Coulomb radius change turned out to be

$$\delta a_3=0.00797\gamma_s, \quad \text{and} \quad (\delta r_0/r_0)=-0.0103\gamma_s. \tag{11}$$

A detailed study of the line of beta stability indicates that only small changes in $\gamma_s(\sim\pm 0.2)$ can be tolerated if one retains the functional form obtained from the Weizsäcker mass formula. Even the extreme assumption $\gamma_s=\pm 1$ leads to a shift in r_0 of only 1 percent. Since the effect of possible departures of γ_s upon a_1 and a_2 is also small, for the purposes here γ_s may be set to zero.

By using the new set of constants here obtained, the new residuals $\Delta^s-\Delta_m{}^b$ were computed for the twenty-four normal places. The standard deviation of these points was found to be

$$\sigma=1.98 \text{ mMU}. \tag{12}$$

In Fig. 1 we show the relationship of this new semiempirical curve (heavy line) to the experimental data,[15] as viewed from a reference line based upon the empirical equation,

$$\Delta_m{}^r(A)=0.01(A-100)^2-64. \tag{13}$$

Also shown are the twenty-four normal places.

For assigning an uncertainty to r_0, the usual procedure used for evaluating the standard deviation of a constant which has been fixed by least squares was employed. On the basis of the assumption that all the input data have the same absolute error (e) it was found that the error in a_3 is

$$\epsilon(a_3)=0.0295e/n^{\frac{1}{2}}, \tag{14}$$

where n is the number of observations. Assigning to e the standard deviation in mass defects for $r_0=1.216$, the standard deviation in a_3 is found to be $\sigma(a_3)=0.0119$ mMU. With $a_3=0.7628$ and $p=0.674\sigma$, the percentage probable error in r_0 is $p=(100)(0.674)(0.0119)/0.7628=1.03$.

To obtain a more intuitive picture of the sharpness of a Coulomb radius determination based upon nuclear masses the following calculations were carried out. The Coulomb radius constant r_0 was fixed at 1.0, 1.1, 1.2, 1.3, 1.4, and 1.5. The corresponding values of δa_3 in Eq. (7) were used with $\gamma_s=0$, and δa_1 and δa_2 were determined by least squares. The values of the corresponding energy constants are given in Table I. The mass defect functions, $\Delta_m{}^{r_0}(A)$ for the various values of r_0 may be placed in the form

$$\Delta_m{}^{r_0}=\Delta_m{}^b(A)-\delta' a_3 U(A), \tag{15}$$

TABLE I. Sets of semiempirical constants.

r_0	a_1	a_2	a_3	a_4	σ
1.0	19.2675	26.259	0.9277	124.70	6.50
1.1	18.0659	22.607	0.8433	112.97	3.59
1.2	17.0647	19.565	0.7731	103.21	2.01
1.3	16.2174	16.990	0.7136	94.94	2.71
1.4	15.4912	14.784	0.6626	87.86	4.24
1.5	14.8617	12.871	0.6184	81.71	5.74
1.216[a]	16.9177	19.120	0.7628	101.78	1.98
1.237[b]	16.7200	18.500	0.7500	100	2.12
1.480[c]	15.04	14.0	0.627	83	8.11

[a] Best fit.
[b] Green-Engler constants.
[c] Fermi constants with $\Delta_n=8.930$, $\Delta_H=8.123$.

[15] In addition to the mass data used in reference 1, recently determined masses by Collins, Johnson, and Nier and by Hogg and Duckworth have been included in this study. The writer wishes to express his appreciation to Professor A. O. Nier and Professor H. E. Duckworth for transmitting these data before publication.

where $\delta' a_3$ is the deviation of a_3 from the best value and

$$U(A)=S(A)+43.294A^{\frac{1}{3}}-14.2477A. \quad (16)$$

The function $U(A)$ vanishes at $A=72.6$ and $A=197.0$, and hence the $\Delta_m{}^{r_0}(A)$ curves all intersect $\Delta_m{}^{b}(A)$ at these two points. The light curves in Fig. 1 represent these functions. It is clear that $r_0=1.20$ and $r_0=1.216$ are far superior to the remaining curves. It may also be apparent that $r_0=1.216$ is somewhat superior to $r_0=1.200$ when viewed in relation to the normal places. This is an indication of the sensitivity of this method of determining the radius constant. One might use Fig. 1 to estimate variations in the nuclear radius constant. However, such a refinement in itself would appear unwarranted unless consideration were given to the other small effects which have been neglected. Such a study is underway.

As a further indication of the sensitivity of nuclear masses to the assumed radius constant, the standard deviations of the normal places from the predicted masses for the different cases are given in column 6 of Table I.

3. CONCLUSION

Since this analysis has been carried through exclusively with small residuals, it is important to point out that the fundamental physical quantity of interest here, the nuclear energy, ranges from 0 mMU to about −2000 mMU. The Coulomb energy itself ranges from 0 to about 1200 mMU. The fact that Eq. (2) with the four adjusted constants obtained here (one of which should be credited with the prediction of the line of beta stability) is capable of predicting these energies or the corresponding mass defects with a standard deviation of only 2 mMU,[16] would appear to indicate that the equation has considerable validity. It is satisfactory that the radius constant associated with this "best" fit agrees with the average radius constant[17] obtained from μ-mesonic x-ray studies to within the limits of the small errors (~1 percent) assigned to each. It is also satisfactory that this small Coulomb radius constant may be reconciled[3] with the results of electron scattering and isotope shift studies, as well as the mass differences of mirror nuclides.[5]

The writer wishes to express his sincere appreciation to B. Clanton, Anna Hendren, E. Pipkin, K. Lee, and K. Zankel for their valuable assistance; to Professor R. Sheline and Professor M. Melvin for helpful discussions; and to Professor G. Schwarz and the Research Council of The Florida State University for their kind support.

[16] This deviation may be reduced by more than a factor of two by introducing a shell correction of the type proposed in reference 11.

[17] V. L. Fitch and J. Rainwater (reference 4) quote the radius constants 1.17, 1.21, 1.22, 1.17 for $Z=22$, 29, 51, and 82. The average of these is 1.198. The accuracy of their energy measurements is about 1 percent.

PHYSICAL REVIEW VOLUME 95, NUMBER 4 AUGUST 15, 1954

Relative Photofission Yields of Several Fissionable Materials*

J. R. HUIZENGA, *Argonne National Laboratory, Lemont, Illinois*

AND

J. E. GINDLER† AND R. B. DUFFIELD, *University of Illinois, Urbana, Illinois*

(Received May 10, 1954)

Relative photofission yields of U^{238}, U^{236}, U^{235}, U^{234}, U^{233}, Th^{232}, Np^{237}, and Pu^{239} were measured at three betatron energies with a photomultiplier fission fragment detector. Results at betatron energies of 17 and 20 Mev are in agreement and give the following relative fission values: Th^{232}, 0.31; U^{238}, 1.00; U^{236}, 1.43; U^{235}, 2.40; U^{234}, 1.82; U^{233}, 2.54; Np^{237}, 2.40; Pu^{239}, 3.17. The relative (γ,f) yields are empirically correlated with the nuclear parameter Z^2/A. Some comments are made on the competition between fission and neutron emission.

INTRODUCTION

McELHINNEY and Ogle[1] measured the relative photofission yields of several fissionable materials with respect to U^{238} by a "catcher" method. They obtained the following results: U^{238}, 1.00; U^{233}, 2.49; U^{235}, 1.49; Pu^{239}, 2.51; Th^{232}, 0.257; and Th^{230}, 0.847. Owing to the importance of such measurements in the theoretical interpretation of the photofission process, we have remeasured the relative (γ,f) yields of the above materials by a different method and have extended the measurements to several other materials. The relative photofission yields were measured at three betatron energies with a photomultiplier fission fragment detector.[2]

* This work was supported by the joint program of the U. S. Atomic Energy Commission and the U. S. Office of Naval Research.

† Present address: Argonne National Laboratory, Lemont, Illinois.

[1] J. McElhinney and W. E. Ogle, Phys. Rev. 81, 342 (1951).

[2] James Gindler, University of Illinois thesis, 1954 (unpublished).

EXPERIMENTAL

Approximately 4 milligrams of the fissionable materials were mounted on 1-inch diameter platinum foils of 0.002-inch thickness. The samples were prepared by repeatedly painting and igniting many small portions of an organic-heavy element solution.[3] The samples were suspended in a vacuum in a collimated x-ray beam produced by the University of Illinois' 22-Mev betatron. Fission fragments ejected from the foils produced scintillations in a zinc sulfide screen. These scintillations were detected in a 5819 photomultiplier tube. The x-ray beam was monitored by a thick-walled ionization chamber.

Three uranium-238 samples ranging from 3.8 to 4.5 milligrams were compared for fissionability per unit mass to check the influence of sample uniformity and thickness in order to obtain a measure of the error in the experiment. The ratios of activity per atom between the different U^{238} foils were 1.05 ± 0.04, 0.97 ± 0.04, and 0.98 ± 0.04 (the error is the standard error in the fission counting). Since this is the relative activity per atom, the ratio in all cases should be one. Thus, the variation from one is a measure of the systematic error in the experiment. The weights of the samples (other than U^{235}) measured for relative fissionability varied from 3.8 to 4.2 milligrams. The experimental fission counting rate varied between the extremes of 2 and 150 counts per minute. Several background checks were made. The duration of the x-ray bursts was made approximately 100 microseconds in order to reduce the background due to pileup of secondary electrons. This background was found to be negligible by irradiating a blank platinum foil under the same conditions as the fissionable samples, The background due to alpha-particle pileup was measured by counting the samples in the absence of the betatron beam. These backgrounds were negligible except for U^{234}, U^{233}, and Pu^{239} where the values ranged up to 1 count/minute. At betatron energies of 17 and 20 Mev, the above background was less than one percent of the fission counting rate. At 12-Mev betatron energy, however, the background reached ten percent of the fission counting rate, and this uncertainty is included in the standard error of the 12-Mev results. The neutron fission background was also checked since some of the materials bombarded have high thermal neutron fission cross sections. A 2-inch thick lead brick was placed in the x-ray beam in front of the samples. With this arrangement the fission counting rate of the U^{235} and U^{238} samples both decreased by approximately a factor of 20. These results were interpreted as evidence for a negligible thermal neutron fission contribution.

RESULTS AND DISCUSSION

Four of the uranium samples irradiated had small impurities of other uranium isotopes. The isotopic content of each of the uranium samples was determined with a mass spectrometer. The isotopic concentration of the major uranium isotope in all the uranium samples was greater than ninety percent. The relative fission cross sections of the uranium samples given in Table I have been corrected for the isotopic impurities. This correction can be made rather easily since the U^{238} sample contained essentially 100 percent U^{238}. The U^{235} sample contained only the uranium isotopes 235 and 238 and thus the appropriate correction for U^{238} can be made from the previous U^{238} sample. Corrections for the other uranium samples can be made by continuing the above procedure.

Run 2 was made about 3 months after the completion of Run 1. Samples U^{238}, $U^{235}-1$, U^{234}, and U^{233} were repeated during Run 2. In addition, a Pu^{239} sample and a new sample of U^{235}, $U^{235}-2$, were irradiated and counted for relative fissionability. The results at betatron energies of 17 and 20 Mev are within the standard counting error (this is the error given in Table I), and averaging the data on each sample gives the following relative yields: Th^{232}, 0.31; U^{238}, 1.00; U^{236}, 1.43; U^{235}, 2.40; U^{234}, 1.82; U^{233}, 2.54; Np^{237}, 2.40; Pu^{239}, 3.17. The 12-Mev data are not included in the preceding averages because the fissionability ratios of some of the materials are different at this energy. The energy dependence of the fissionability of thorium relative to uranium (see Table I) has been confirmed in recent experiments employing a radiochemical

TABLE I. Fissionability of several materials relative to U^{238} at three betatron energies.

Target	12 Mev		17 Mev		20 Mev	
	Run 1	Run 2	Run 1	Run 2	Run 1	Run 2
Th^{232}	0.46 ± 0.04		0.30 ± 0.01		0.32 ± 0.01	
U^{238a}	1	1	1	1	1	1
U^{234a}	1.58 ± 0.11		1.44 ± 0.04		1.41 ± 0.05	
$U^{235}-1$	1.71 ± 0.11	1.94 ± 0.13	2.33 ± 0.07	2.31 ± 0.10	2.37 ± 0.09	2.34 ± 0.10
$U^{235}-2$		2.12 ± 0.18		2.47 ± 0.08		2.59 ± 0.09
U^{234a}	1.75 ± 0.18	2.13 ± 0.34	1.77 ± 0.08	1.86 ± 0.08	1.80 ± 0.08	1.85 ± 0.07
U^{233}	2.51 ± 0.28	2.36 ± 0.35	2.40 ± 0.11	2.62 ± 0.12	2.61 ± 0.10	2.53 ± 0.10
Np^{237}	2.53 ± 0.16		2.39 ± 0.10		2.40 ± 0.11	
Pu^{239}		3.51 ± 0.62		3.10 ± 0.10		3.23 ± 0.10

[a] These materials were supplied by the Isotopes Division of Carbide and Carbon Chemical Company, Oak Ridge, Tennessee.

[3] Huizenga, Magnusson Fields, Studier, and Duffield, Phys. Rev. 82, 561 (1951).

method for determining the relative fissionability.[4] The averages of the data obtained at 17- and 20-Mev betatron energies are plotted in Fig. 1 as a function of the Z^2/A values of the bombarded nuclei. To a first approximation, relative fissionability may be considered to be linearly dependent upon Z^2/A according to the relation,

$$\text{relative fissionability} = 1.3[(Z^2/A) - 34.7]. \quad (1)$$

The poor agreement between our results and those of McElhinney and Ogle for U^{235} and Pu^{239} cannot be satisfactorily explained at this time. The relative fissionabilities (see Fig. 1) of materials examined do not show any obvious dependence on the even-odd character of the nuclide irradiated.

In a previous experiment,[5] it was found that the fission branching ratio for U^{238}, $X_{U^{238}} = \sigma_{(\gamma,f)}/[\sigma_{(\gamma,f)} + \sigma_{(\gamma,n)}]$, had a nearly constant value of 0.2. If one assumes that the absorption cross sections of the nuclides investigated in this experiment do not differ appreciably from that of U^{238}, it is possible to calculate the fission branching ratios for other nuclides by the relation,

$$\text{relative fissionability} = X_{\text{nuclide}}/X_{U^{238}}, \quad (2)$$

where the relative fissionability is assumed to be a measure of the relative fission cross sections.

For 20-Mev bremsstrahlung, it is necessary to modify Eq. (2) for higher order contributions to the fission process such as (γ,nf) and even (γ,nnf) reactions, but to a first approximation Eq. (2) should be valid.

Substituting the fissionability of Pu^{239} from Table I into Eq. (2) gives an X value of 0.6 for Pu^{239}. This means that 60 percent of the Pu^{239} atoms are destroyed by fission and 40 percent by neutron emission. The probability for destruction by fission increases from about 6 percent for Th^{232} to 60 percent for Pu^{239}.

By equating Eqs. (1) and (2), a relationship between the fission branching ratios and the parameter Z^2/A is obtained,

$$X_{\text{nuclide}}/X_{U^{238}} = 1.3[(Z^2/A)_{\text{nuclide}} - 34.7]. \quad (3)$$

The increase in the fission branching ratio with increasing Z^2/A leads one to predict that fast neutron fission cross sections will also increase with Z^2/A since the total neutron cross sections for the heavy nuclides are about constant. Such a relationship holds for the two nuclei Np^{237} and U^{234}. The fast neutron fission cross section[6] of Np^{237} is greater than that[7] of U^{234} (compound nuclei Np^{238} and U^{235}) at 3 Mev, in agreement with the greater Z^2/A value of Np^{238}.

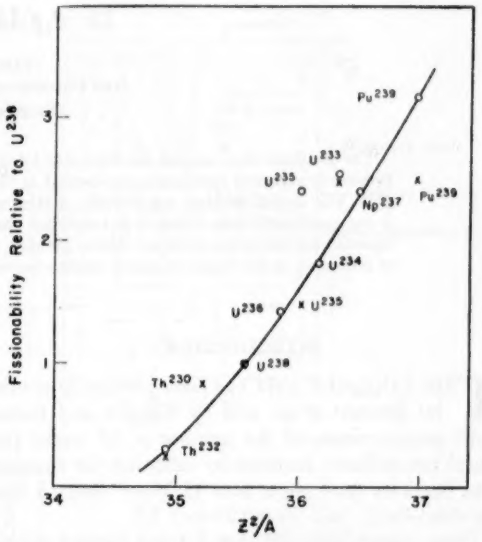

FIG. 1. The fissionability of several materials relative to U^{238} are plotted as a function of the Z^2/A values of the bombarded nuclei. The circles ○ represent an average of the data obtained from gamma rays at two betatron energies, 17 and 20 Mev. The crosses × are data of McElhinney and Ogle (see reference 1).

[4] Gindler, Huizenga, and Schmitt (unpublished).
[5] R. B. Duffield and J. R. Huizenga, Phys. Rev. **89**, 1042 (1953).
[6] E. D. Klema, Phys. Rev. **72**, 88 (1947).
[7] R. W. Lamphere, Phys. Rev. **91**, 655 (1953).

$Li^7(d,p)Li^8$ Yield Curve*

STANLEY BASHKIN
State University of Iowa, Iowa City, Iowa
(Received April 5, 1954)

The absolute cross section for the $Li^7(d,p)Li^8$ reaction has been measured from 700 kev to 3.3 Mev. Previously reported resonances are located at 800 kev and 1.04 Mev, corresponding to states in Be^9 at 17.30 Mev and 17.49 Mev, respectively. A third resonance, indicated by the earlier work to be at 1.4 Mev, is not confirmed, from which it is concluded that Be^9 does not have the 17.8-Mev level for which that reported resonance was evidence. Above 1.8 Mev, the yield is relatively flat, perhaps indicating the influence of stripping, rather than compound nucleus formation.

INTRODUCTION

THE $Li^7(d,p)Li^8$ yield has been previously studied by Bennett *et al.*[1] and by Baggett and Bame.[2] Both groups measured the number of Li^8 nuclei produced per incident deuteron by counting the energetic beta particles (end point near 13 Mev)[3] emitted from the short-lived (half-life = 0.89 sec)[4] Li^8.

These papers assumed that Li^8 was formed only in its ground state for all bombarding energies used.[5] The lifetime of this state is long enough for the Li^8 nuclei to become disoriented, and the emergent beta particles are consequently distributed isotropically in the laboratory system.

Bennett and his associates detected the betas with two Geiger counters in coincidence, the coincidence arrangement discriminating strongly against the background of neutron capture gamma rays. Baggett and Bame, using a single Geiger counter as the detector, obtained the absolute cross section for the reaction. Each of these groups found broad resonances in the Li^8 yield for bombarding energies of approximately 750 kev and 1.00 Mev, and obtained some evidence for a third resonance near 1.4 Mev. The 1.4-Mev resonance was indicated in the work of Baggett and Bame as a slight change in the slope of a steeply rising yield curve.

The present experiment has utilized a technique which allowed the determination of the beta yield in the presence of serious background effects. In addition, the range of bombarding energies has been extended beyond that of the previous work. At the highest energy used, a level[6] at 2.28 Mev in Li^8 might have been excited. However, it is assumed that neither this state nor the possible state[5] at 1 Mev affected this determination of the $Li^7(d,p)Li^8$ yield curve.

EXPERIMENTAL METHOD

The State University of Iowa Van de Graaff accelerator was used to accelerate monatomic deuterons to energies between 709 kev and 3.26 Mev. Beam energies were measured in terms of the magnet current required to deflect the beam into the target chamber. Three well-known gamma-ray resonances in the $F^{19}(p,\alpha)O^{16*}$ reaction, induced in thin CaF_2 targets by monatomic and diatomic proton beams, and the $Li(p,n)Be^7$ threshold obtained with the monatomic proton beam on thin lithium targets, served to calibrate the magnet current against energy. A reproducibility of ± 0.5 percent in beam energy is inferred from the calibration data, and the absolute energy is believed known to ± 1 percent over the range of this experiment.

Ordinary lithium was evaporated *in situ* on nickel backings 50 micro inches and 2 micro inches thick to provide targets 8 kev to 12 kev thick for 2-Mev protons. Target thicknesses were determined from the shape of the yield curve for the $Li^7(p,n)Be^7$ reaction just above the threshold, the detector being a shielded BF_3 long counter placed at zero degrees with respect to the incident beam. Frequent checks were made of the reproducibility of the beta yield at selected bombarding energies in order to guard against target deterioration. Very small beams, ranging from 0.03 to 0.1 microampere, were used to avoid target depreciation.

The target chamber, shown in Fig. 1, served as a Faraday cage. The collected charge was measured with a condenser-discharge type of current integrator circuit having a long time stability of ± 0.5 percent and an absolute calibration known to ± 1 percent. An electron repeller, shielded from the beam, was biased at 300 volts below ground to prevent secondary electrons from entering or leaving the target chamber.

A detecting system was designed to allow satisfactory measurements of the beta yield in the presence

* Work supported in part by the U. S. Atomic Energy Commission.

[1] Bennett, Bonner, Richards, and Watt, Phys. Rev. **71**, 11 (1947).

[2] L. M. Baggett and S. J. Bame, Jr., Phys. Rev. **85**, 434 (1952). We wish to thank Dr. Baggett for a private communication detailing the method used in this experiment.

[3] W. F. Hornyak and T. Lauritsen, Phys. Rev. **77**, 160 (1950).

[4] D. St. P. Bunbury, Phys. Rev. **90**, 1121 (1953).

[5] According to H. E. Gove and J. A. Harvey, Phys. Rev. **82**, 658 (1951), there is a doubtful state in Li^8 at 1 Mev. This level could have been excited for bombarding energies above 1.5 Mev. Beta or gamma-beta decays from this state would not affect the angular distribution of the betas, nor would the energy spectrum of the betas be significantly changed by direct beta emission from this level.

[6] F. Ajzenberg and T. Lauritsen, Revs. Modern Phys. **24**, 321 (1952).

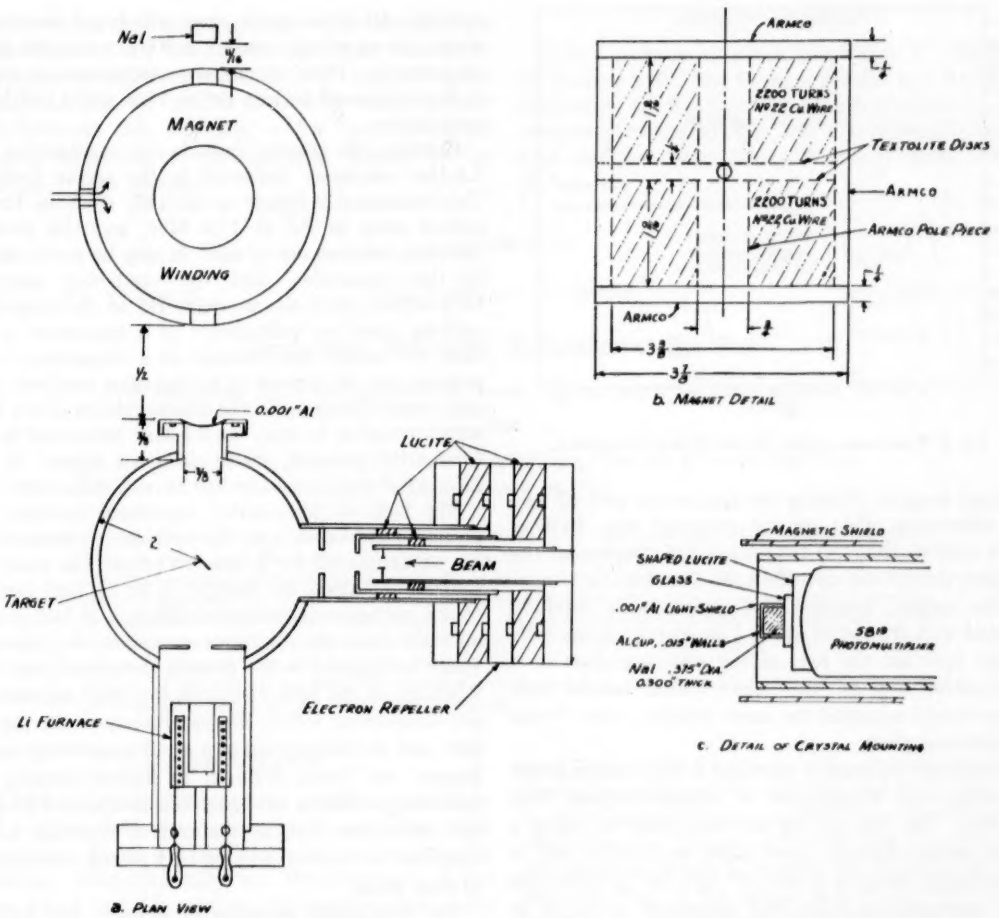

FIG. 1. Experimental arrangement for detection of betas from the $Li^7(d,p)Li^8$ reaction.

of a gamma-ray background which increased slowly with time and rapidly with bombarding energy. This background, which produced only one-tenth as many counts as did the betas at 709 kev, gave seven times the number of beta counts at 3.26 Mev. It appeared that neutron capture gamma rays contributed the major portion of the background. Large numbers of neutrons were created in the target proper via (d,n) reactions in Li^6 and Li^7. Moreover, semithick deuterium targets developed with time both in the target chamber due to the monatomic deuteron bombardment and elsewhere where the diatomic deuteron beam struck a beam stop. Despite the background, the number of betas was determined as follows, using the geometry illustrated in Fig. 1. Those betas which emerged through a small solid angle at 90° to the incident beam passed between the pole pieces of an electromagnet before entering a small NaI(Tl) crystal coupled to a 5819 photomultiplier. Sufficient current could be sent through the magnet coils to deflect all the betas away from the crystal. Thus, counts recorded with the field on were due solely to background, while "magnet off" data came from the background plus the betas. The difference between the two was attributed to the betas. This procedure had the great advantage over the use of absorbers, say, that the background could be measured without its being disturbed.

It is also worth mentioning that the frequently satisfactory method of using a blank target to determine background is inadequate in this experiment because the actual target contributes heavily to the neutron flux and, hence, to the flux of capture gamma rays.

The magnet was constructed to have a negligible external field, and tests showed that fields far higher than those actually employed in the experiment did not affect the operation of the photomultiplier. For this purpose, the radiations from Co^{60} and Cs^{137} were detected when the amplifier discriminator was so set that the counting rate changed rapidly with small

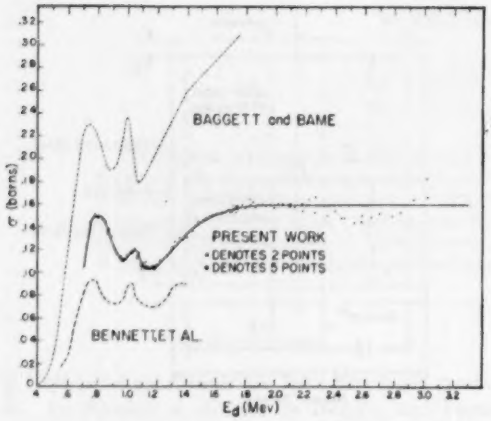

FIG. 2. Total cross section for the $Li^7(d,p)Li^8$ reaction.

changes in gain. Turning the magnet on and off had no observable effect on the counting rate. Further tests showed that the heating of the magnet by the magnet current did not affect the detector.

The magnet aperture and crystal were carefully aligned with the center of the $\frac{1}{2}$ in. high by $\frac{1}{16}$ in. wide target spot on the axis of the counting system. A mechanical stop on the target holder insured that every target occupied the same position when it was rotated into place.

Pulses due to betas of less than 2 Mev were rejected to avoid any background of neutron-induced beta activity. This bias setting was established by using a linear, single channel, pulse-height analyzer to take a pulse-height analysis of the Co^{60} and Cs^{137} gamma rays and extrapolating from their photopeak positions to 2 Mev. The crystal was too small to permit a good energy calibration, but that was unimportant since at most 2 percent of the Li^8 betas have such low energies.[3] The crystal itself had a beta stopping power of ~4 Mev.

Data at each energy were acquired in a series of runs, the magnet being alternately on and off. This procedure enabled a check on the internal consistency of the data. Sufficient data were taken so that the statistical error, defined as $(N_{off}+N_{on})^{\frac{1}{2}}/(N_{off}-N_{on})$ was ~0.01 for all points, N_{off} and N_{on} being the number of counts taken with the magnet off or on.

RESULTS AND DISCUSSION

The solid curve of Fig. 2 shows the excitation function for the $Li^7(d,p)Li^8$ reaction as obtained in this work. The dashed and dotted curves are, respectively, those of Bennett *et al.*[1] and Baggett and Bame.[2] The Bennett data have been arbitrarily plotted below the present curve since they show only relative cross sections. All three curves show two broad resonances which this experiment centers at 800 kev and 1.04 Mev, respectively. These resonances correspond to states in the compound nucleus Be^9 at 17.30 and 17.49 Mev, respectively.

However the current data do not substantiate the 1.4-Mev resonance indicated in the earlier findings. This resonance is listed[6] as the only evidence for an excited state in Be^9 at 17.8 Mev, and this level is therefore believed not to exist. It may be worth noting in this connection that the competing reaction, $Li^7(d,n)Be^8$, which also produces Be^9 as the compound nucleus, gives no indication[1,2] of a resonance at 1.4 Mev. Of course, the presence of a resonance in one process, and its absence in a competing reaction, may arise from differences in the characteristics of the final states involved. In fact, the 2.1-Mev resonance[2] in the $Li^7(d,n)Be^8$ reaction, which does not appear in the $Li^7(d,p)Li^8$ yield, might be due to such differences.

The lack of quantitative agreement between the present yield curve and the previous determinations can be accounted for in general terms. The results of Baggett and Bame are believed to be too high because of the inadequately corrected influence of background on their data. At the lower resonance, for example, where background in the present experiment was only 9 percent of the beta yield, the two cross sections are not inconsistent within the uncertainty in the present data and the assumption of a small uncertainty in the Baggett and Bame findings. At higher energies, the increasing deviation between their results and those of this experiment are in the correct direction to be explained by a steadily rising background contribution to their yield.

The coincidence counting of Bennett and his colleagues gave inherently good discrimination against background, and, indeed, the general shape of their curve is in good agreement with the present curve. It is possible that much of the differences which do exist come from dead time corrections required in that Geiger counter work.

For energies below 2.1 Mev, the relative yield is believed known to 10 percent, and the absolute cross section to 25 percent. Above 2.1 Mev, the data exhibit a very considerable scatter, making it difficult to assess the true variation of the cross section. The scatter derives from the fact that, at high energy, the background is large and the final data represent the small difference between two large numbers. At 3.26 Mev, for example, 1.2×10^6 counts were needed to obtain a net of 7.5×10^4 counts. The counting rate was kept down to ~200 counts per second, by far the highest rate used in the entire experiment, so that quite a long running time was required to accumulate the data. Over this time, relatively small percentage

fluctuations in the background had a disproportionately large effect on the net counts. The most reasonable conclusion to draw from the data is that the yield curve is substantially flat above 1.8 or 1.9 Mev. Perhaps this indicates that stripping, rather than compound nucleus formation, is the dominant feature of the reaction at high energies.

ACKNOWLEDGMENTS

It is a pleasure to thank Mr. Philip R. Malmberg for his help with some of the apparatus and the energy calibration of the Van de Graaff accelerator. This work has benefited greatly from stimulating discussions with Professor James A. Jacobs and Professor Edward B. Nelson.

PHYSICAL REVIEW VOLUME 95, NUMBER 4 AUGUST 15, 1954

Production of Cosmic Radiation at the Sun*

J. W. FIROR† AND J. A. SIMPSON, *Institute for Nuclear Studies, University of Chicago, Chicago, Illinois*

AND

S. B. TREIMAN, *Palmer Physical Laboratory, Princeton University, Princeton, New Jersey*

(Received March 31, 1954)

A calculation is made of the average production rate of 4-Bv cosmic-ray particles at the sun. The calculation is based upon the recent experimental evidence that the frequently occurring small solar flares produce temporary increases of neutron intensity in suitably located neutron pile detectors. This production rate, averaged over the 11-year solar cycle, is somewhat in excess of the absorption rate of 4-Bv particles by bodies in the solar system. If the production at the sun is to account for most of the observed cosmic radiation intensity, a trapping magnetic field is required. Limits on the size of such a trapping volume are estimated by considering the limits of cosmic-ray lifetime; the requirement of a high degree of radiation isotropy at the earth is satisfied. The existence of high-energy particles in the cosmic radiation imposes the principal difficulty for any solar origin hypothesis.

I. INTRODUCTION

THE four large increases in cosmic-ray intensity which have been observed in association with large solar flares[1] indicate that the sun occasionally produces cosmic-ray particles. More recently it has been found that the smaller, but more frequent solar flares are also associated with increases in cosmic-ray intensity at the earth.[2] That these increases represent true cosmic-ray production on or near the sun is suggested by analogy with the large flare events, where the size of the increases clearly excludes the possibility of a modulation effect on pre-existent cosmic radiation.

The results on the small flare effect may be summarized as follows:[2] A neutron detector[3] at Climax, Colorado, recorded increases of ~1 percent for flares of importance 1+ or greater during the period studied (May, 1951, to August, 1953), provided that the local solar time at Climax was 4 A.M.±2 hours. No observable effect, however, was found to accompany flares which occurred outside of this "impact zone" of local solar time. This local time dependence of the flare effect indicates that the particles which give rise to the intensity increase approach the vicinity of the earth from the direction of the sun. For both the large and small flare events increases were observed for flares near the limb of the sun as well as for those which occurred at the center of the visible solar disk. The distribution on the visible disk is shown in Fig. 1 for a group of flares which entered into the studies reported in reference 2. The indication is clear that the particles are emitted in a wide angle cone. An analysis of the cosmic-ray trajectories in the field of the earth's magnetic dipole shows that the particles from the sun which come in at Climax at 4 A.M. have a magnetic rigidity of 4 Bv.

The small flare effect appears to be a frequently occurring phenomenon; and if it represents production of cosmic rays on or near the sun, then the possibility arises that this effect has an important bearing on the question of the origin of cosmic rays. Before discussing any such implications, however, it is first necessary to obtain a numerical estimate of the production rate of (4-Bv) cosmic-ray particles at the sun. This is the main purpose of the present paper and is the subject of the following section. It should be emphasized that the calculation is based on the experimental data; we do not consider here the question of possible production mechanisms. In the remaining sections of the paper we discuss in a general way the implications of our result

* Assisted by the Office of Scientific Research, Air Research and Development Command, U. S. Air Force.

† Present address: Department of Terrestrial Magnetism, Carnegie Institution of Washington, Washington, D. C.

[1] Forbush, Stinchcomb, and Schein, Phys. Rev. **79**, 501 (1950).

[2] J. W. Firor, Phys. Rev. **94**, 1017 (1954).

[3] See Simpson, Fonger, and Treiman, Phys. Rev. **90**, 934 (1953) for a description of the experimental apparatus. Neutron pile monitors *D*-1 and *D*-3 were used for the solar flare effect studies.

for hypotheses on the origin of cosmic rays. In particular, we consider in some detail the implications for solar-origin hypotheses, although we do not ourselves wish to propose here any comprehensive theory nor suggest that the solar flare effect points uniquely to a solar-origin theory of cosmic rays.

II. PRODUCTION RATE AT THE SUN

Suppose that the particles which give rise to the solar flare effect approach the earth over a broad front, traveling essentially along the sun-earth line. (A possible small spread in direction has no effect on the following discussion.) Let $i_b d\Omega_b dN$ be the flux of these particles in element of solid angle $d\Omega_b$ and element of magnetic rigidity dN ($N=pc/Ze$, where p is the particle momentum and Ze is the charge). It is reasonable to suppose that the intensity is constant over a dimension much larger than the diameter of the earth; and it is likewise proper to assume that over this dimension the particles all travel in the same direction (before the geomagnetic field becomes significant). Outside the geomagnetic field,

$$i_b d\Omega_b dN = I(N)\delta(\Omega_b - \Omega_b^0)d\Omega_b dN, \quad (1)$$

where I is the flux (particles per unit time, area, and rigidity) and Ω_b^0 defines the direction of travel of the beam.

Let $i_e d\Omega_e dN$ be the flux of these particles at a particular location on the earth. By Liouville's theorem: $i_e = i_b = I\delta(\Omega_e - \Omega_e^0)$, where Ω_e^0 is the direction of arrival at the earth corresponding to the direction Ω_b^0 of the beam; Ω_e^0 depends on N and on the particular earth location. The flux from all permitted directions at the top of the atmosphere is, therefore,

$$\int\int I\delta(\Omega_e - \Omega_e^0)(d\Omega_e/d\Omega_b)d\Omega_b dN = \int I(d\Omega_e/d\Omega_b)_0 dN, \quad (2)$$

where $(d\Omega_e/d\Omega_b)_0$ is the ratio of the elements of solid angle as seen from the earth and in the beam for particles of given N. This factor takes into account the possibility that there may be a few directions of arrival Ω_e^0 corresponding to the given beam direction. Expression (2) may be written

$$I\langle d\Omega_e/d\Omega_b\rangle \Delta N, \quad (3)$$

where ΔN is the spread in magnetic rigidity (due to the spread in directions of arrival Ω_e^0) for the particles which arrive at the given earth location: and $\langle d\Omega_e/d\Omega_b\rangle$ is the average value of the quantity defined above. This latter quantity is difficult to estimate and represents the largest uncertainty in the present calculation. Our estimate is based on the trajectories which were obtained in the terrella experiments of Malmfors.[4] These pertain to a latitude of 58°, whereas the latitude of Climax is 48°, and further, they pertain to a different impact zone for particles from the sun. Nevertheless, because of other similarities between the two impact zones in question, we believe that our estimate of $\langle d\Omega_e/d\Omega_b\rangle$ is not in error by as much as a factor of five. Our numerical estimate will be quoted in context below.

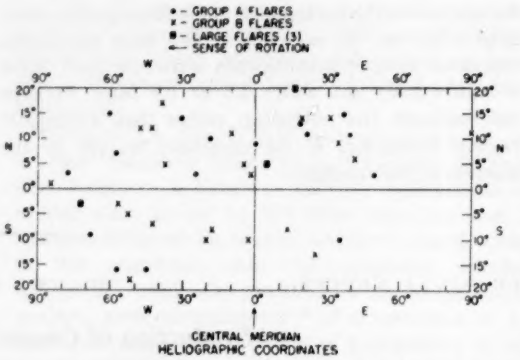

FIG. 1. The location of small and large flares is shown on the visible hemisphere of the sun. Flare Groups *A* and *B* are small flares studied in detail in reference 2. Group *A* flares occurred at times when the Climax neutron pile monitor was in the 4-Bv particle impact zone; they were associated with increases of cosmic ray intensity. Group *B* flares occurred at times when the detector was outside the impact zone, and, therefore, were not associated with increases. The three large flares were already reported.

The fractional change in the omnidirectional cosmic-ray intensity at the top of the atmosphere is given by

$$f = (I\Delta N/J)\langle d\Omega_e/d\Omega_b\rangle, \quad (4)$$

where J is the normal omnidirectional flux (at Climax). This value of f is not the same as the observed value deep in the atmosphere; it is probably not very different, however, since the average specific yield at Climax[3] (averaged over the normal spectrum) is similar to the specific yield for particles of rigidity 4 Bv.

Suppose that during a flare cosmic-ray particles are emitted in a cone of solid angle w normal to the surface of the sun. At first sight it would seem that the probability that the earth lies in this cone is $w/4\pi$. But flares actually occur in a limited range of helio-latitudes, so that this probability is better written as w/W, where W is the total solid angle within which most flares emit particles. As reported in reference 2, the cosmic-ray emission during flare events lasts for a period of about 2 hours. If we multiply this length of time by the average rate of flare events on the sun, we obtain the

[4] K. G. Malmfors, Arkiv. Mat. Astron. Fysik **32**, No. 8 (1945). This paper gives plots of the "asymptotic" longitude and latitude for trajectories which arrive from various directions in the sky at the location of Stockholm. From these curves the ratio of the elements of solid angle at the earth and in the beam were obtained for various directions of arrival; and this ratio was then averaged over all directions.

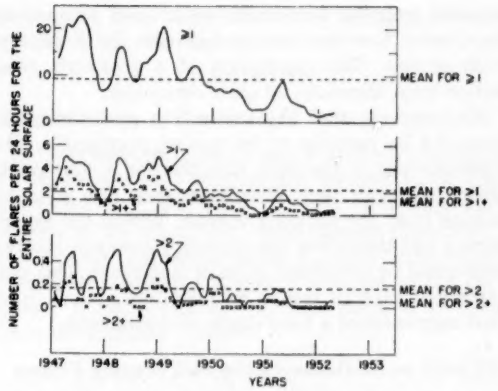

FIG. 2. The monthly averages of solar flare rates were determined from the worldwide reports of the International Astronomical Union Quarterly Bulletin on Solar Activity (published by Eidgen. Sternwarte, Zurich, Switzerland). Flares are roughly classified by their importances into groups of increasing size; namely, 1, 1+, 2, 2+, 3, and 3+ (for details see reference 2). The flare rates are corrected for the observing times of the individual observatories.

fraction of time F during which the sun is emitting particles.

The product $h=Fw/W$ is best obtained empirically from the Climax data, since it represents the fraction of all days on which a solar flare effect is registered at Climax during a transit through the impact zone. The time-averaged rate PdN (averaged over an 11-year solar cycle) at which the sun emits particles in the rigidity interval dN centered at 4 Bv is, therefore, given by

$$PdN=hWR^2\frac{fJ}{\Delta N\langle d\Omega_e/d\Omega_b\rangle}dN, \tag{5}$$

where R is the earth-sun distance (we assume that the particles travel in essentially straight lines from the sun to the earth's vicinity).[5] We have adopted the following numerical estimates: $f\approx 0.005$ (0.5 percent cosmic-ray intensity increase at Climax); $J\approx 1$ particle/cm^2-sec (omnidirectional flux at the top of the atmosphere above Climax); $W\approx 2\pi$ (this estimate of the solid angle of emission of cosmic-ray particles from the sun is suggested by the evidence quoted in the introduction and is almost certainly not off by more than a factor of two); $\Delta N\approx 0.5$ Bv (this estimate is obtained from references 2 and 4); $\langle d\Omega_e/d\Omega_b\rangle\approx 20$ (as discussed earlier, this estimate is based on the results of Malmfors and could be off by as much as a factor of five); $h\approx 0.3$. (The fraction of days on which a cosmic-ray effect was observed at Climax, during the period studied, was about 0.1. This fraction is obtained from Fig. 10 in reference 2. These data were obtained in a period of rapidly declining solar activity, the minimum of which is expected about 1954. Over an 11-year solar cycle, the average rate of occurrence of flares is about three times the average rate during the period studied, i.e., May, 1951–August, 1953, as can be seen in Fig. 2. Our estimate of P is meant to represent a time-averaged value over an 11-year solar cycle.) We obtain now the result $P\sim 2\times 10^{23}$ particles/sec-Bv, for particles of rigidity 4 Bv.

III. RELATION TO ORIGIN THEORIES

The foregoing calculation has led to an estimate of the production rate of 4-Bv particles at the sun, averaged over a period of time comparable with the sunspot cycle. Observation of solar flare effects at other geomagnetic latitudes should eventually lead to similar estimates of the production rate at other magnetic rigidities in the latitude-sensitive range.

The question now arises as to the bearing of this result on a possible solar origin of cosmic rays. For one thing, it is clear that—by whatever mechanism—the sun *does* produce particles of cosmic-ray energies. But our analysis does not reveal what fraction of the observed cosmic radiation at the earth comes from the sun. At one extreme, if the particles produced at the sun escape toward outer space along straight lines, then the time-averaged solar contribution to the cosmic-ray intensity at the earth is negligibly small. At the other extreme, if the particles are trapped in the neighborhood of the solar system by suitable magnetic fields, then a solar-origin theory becomes possible.

(a) Galactic Origin

There is one point concerned with galactic theories of the origin of cosmic rays which requires special mention here. It is sometimes asserted that the observed production rate of cosmic rays at the sun may be typical of production by other stars of our galaxy. It is easily shown, however, that this suggestion fails quantitatively. If the cosmic-ray number density n is to be maintained by stellar sources, the average stellar production rate is given by

$$n/\rho\tau, \tag{6}$$

where ρ is the number density of stellar sources and τ is the mean life of cosmic rays in our galaxy. In our vicinity of the galaxy the density of observable stars is about 1 per 1000 cubic light years, and the number density of 4-Bv particles is 10^{-11}/cm^3-Bv. The chemical composition of the cosmic radiation observed at the earth indicates that the mean life τ is no larger than about 10^6 years.[6] Thus, the average production rate of 4-Bv particles must be $\sim 10^{33}$ particles/sec-Bv. This is larger than the production rate at the sun by a factor of 10^{10}.

We have here compared the rates of production and loss of particles of a specified rigidity, 4 Bv. If, as in Fermi's theory, cosmic rays are accelerated gradually,

[5] S. B. Treiman, Phys. Rev. **94**, 1017 (1954).

[6] Morrison, Olberti, and Rossi, Phys. Rev. **94**, 440 (1954).

the appropriate comparison would be between the rate of loss of cosmic-ray particles of all energies and the production rate of particles of all energies above the threshold, or "injection" value. We have no information on solar production rates at very low energies; but it is certain that no large increase (factor of 10^{10}) occurs between 4 Bv and at least 1.5 Bv (the cutoff at the earth). On the other hand, in the galactic model of Morrison *et al.*,[6] for example, the threshold energies are extremely small (~1 Mev for protons). This is not very much larger than the energy of auroral particles. We cannot say, therefore, that the sun may not represent a typical stellar source for injection of particles into an extended acceleration mechanism; but the solar flare effect, in itself, gives no indication that this is the case.

(b) Solar Origin

If the observed solar production is to be considered as a significant process for the production of cosmic rays, we must turn to a model in which the solar-generated particles are retained in the neighborhood of the solar system by suitable magnetic fields (see, for example, the paper by Alfven[7]). The loss of cosmic-ray particles would then be ascribed either to leakage out of the trapping volume or to collisions with bodies in the solar system (only the sun need be considered in this connection). We assume that the lifetime of the cosmic-ray particles is sufficiently small so that collisions with interplanetary matter are negligible.

If the sun has no general magnetic field, then its absorption cross section is simply equal to the geometric cross section. In this case, the rate of capture of 4-Bv particles is given by

$$A=4\pi(\pi a^2)j=6\times10^{21}\text{ particles/sec-Bv},$$

where a is the solar radius, and where we have assumed that the cosmic-ray differential intensity at the sun is the same as the intensity j at the earth. If, on the other hand, the sun has a dipole field, the absorption cross section becomes dependent on the magnetic rigidity and is in general smaller than the geometric cross section. One can easily show that the absorption cross section is given approximately by

$$(\pi a^2)a(N/M)^{\frac{1}{2}},$$

where M is the dipole moment and N is the magnetic rigidity. The above equation is valid in the approximation $a(N/M)^{\frac{1}{2}}\ll1$. The solar flare effect provides evidence that the solar dipole moment has as an upper limit the value 5×10^{32} gauss-cm^3.[5] For a dipole moment of this value, the absorption cross section for 4-Bv particles would be smaller than the geometric cross section by a factor of ~100. However, any large-scale magnetic perturbations, such as might be associated with assumed ion beams from the sun or with the assumed trapping field itself, would tend to open up the allowed Stoermer cones and increase the absorption cross section. The assumption of a geometric cross section may, therefore, be quite reasonable.

We conclude that the production and absorption rates of 4-Bv particles at the sun are comparable. The difference lies in the right direction for a solar-origin theory of cosmic rays, since losses must also occur by leakage from the trapping volume. Within the experimental and theoretical uncertainties, however, the two rates could be considered to be in agreement. This near agreement may of course be fortuitous, but it is at least suggestive of a solar origin of cosmic rays.

Limits on the Dimensions of the Trapping Volume

If we assume that the cosmic radiation is retained in the vicinity of the solar system by magnetic fields, then it is possible to set rather close limits on the size of the trapping volume. If we suppose that the cosmic radiation is distributed with essentially uniform density throughout the trapping region, then we can obtain a relation between the volume V of the trapping region and the mean life τ of the cosmic radiation; evidently,

$$V=P\tau/n, \tag{7}$$

where n is the number density and average P is the production rate of 4-Bv particles.

Taking for τ the upper limit 10^6 years, we find for the linear dimension of the trapping volume ($V=L^3$) the upper limit

$$L<8\times10^{15}\text{ cm}.$$

A lower limit on the lifetime of particles in an assumed trapping volume can be obtained by noting that the rate of occurrence of solar flares follows the general changes of solar activity over successive 11-year cycles (see Fig. 2). In order to account for the approximate constancy in time of cosmic-ray intensity at the earth, it must be assumed that the lifetime of the particles in the trapping volume is large compared to 11 years. It is known from long time observations with ionization chambers that the cosmic-ray intensity over a period of many years does not vary by more than ~4 percent.[8] Since ion chambers at sea level have a low sensitivity for measuring variations in the low rigidity portion of the primary spectrum, it is possible that the long time variations in intensity of 4-Bv particles could be as large as 10–20 percent over an 11-year cycle. However, the variation in the rate of occurrence of solar flares is considerably larger than this. A rough measure of the lower limit on τ can, therefore, be obtained by setting

$$11\text{ years}/\tau\lesssim0.2,$$

from which we find $\tau\gtrsim60$ years. The corresponding

[7] H. Alfven, Phys. Rev. **77**, 375 (1950).

[8] S. E. Forbush, Duke University Cosmic Ray Conference, 1953 (unpublished). A. R. Hogg, Mem. Commonwealth Observatory **10**, July, 1949.

limit on the linear dimension of the trapping volume, from Eq. (7), is therefore

$$L \gtrsim 3\times 10^{14} \text{ cm}.$$

The Anisotropy of Cosmic-Ray Intensity at the Earth

The near isotropy of cosmic-ray intensity at the earth sets an independent limit on the volume V for any given value of τ. Let $(1+\gamma)/(1-\gamma)\approx 1+2\gamma$ represent the ratio of the cosmic-ray fluxes passing respectively out of and into a sphere of radius R_e equal to the radius of the earth's orbit; γ is then a measure of the anisotropy. If the cosmic-ray particles move at random within the volume V, then[7]

$$V = 2\pi R_e^2 c\tau\ \gamma. \tag{8}$$

For particles of low rigidity ($\sim$4 Bv), the anisotropy γ could be as large as 10^{-2}. In this case, however, the limit set by Eq. (7) is more stringent than that set by Eq. (8); i.e., our requirements on isotropy are automatically satisfied by Eq. (7).

IV. DISCUSSION

Even if a trapping field is postulated for the low-energy particles, the principal difficulties for any solar-origin hypothesis are the source of very high-energy particles and the retention of these particles in a trapping field.

On the basis of the four large flare events, it has been widely assumed that the energy spectrum of the particles associated with flares is considerably steeper than the time-averaged cosmic-ray spectrum. It is not certain, however, that this is the case. For example, the ion chambers and counter telescopes which detected the large intensity increases were distributed partly in and partly out of the impact zones for the incoming radiation. Intensity differences due to the effect of the geomagnetic field therefore make any estimate of the spectrum uncertain. Further study of the small flare effect at various latitudes should eventually provide a better estimate of the spectrum.

A related question has to do with a possible upper limit on the energy spectrum of solar-produced particles. The upper limit has been estimated to be $\sim$10 Bv; since for the four large flare events, no cosmic-ray effect was observed at the equator. On the other hand, possible evidence for higher rigidity particles coming from the sun is provided by the results of Dolbear *et al.*[9] who find a close association between cosmic-ray intensity increases and sudden ionospheric disturbances (which are often associated with solar flares) during local daytime hours. At present, however, it is not certain that these observations represent an extra-terrestrial effect.

A necessary condition for the trapping of particles in a magnetic field is that the radius of curvature for the particles of highest rigidity be small compared to the linear dimension L of the trapping region. For the largest known cosmic-ray rigidities ($\sim 10^9$ Bv), the magnetic field would have to exceed $\sim 4\times 10^{-4}$ gauss. It is not known whether or not extensive fields of this magnitude exist; and it is even less clear whether or not the assumption of a field distribution suitable to permit trapping is reasonable.

The difficulties with a solar-origin hypothesis, as we have seen, are most pronounced for the high energies. On the other hand, our results on the solar production of low-energy particles are at least suggestive of a solar origin of the cosmic radiation. It may be that the observed cosmic-ray spectrum is obtained from the combined effect of low-energy particles from the sun plus high-energy particles produced elsewhere. Present experimental evidence indicates the rigidity spectrum is fairly smooth up to at least 10^9 Bv. The smooth joining of spectra from two different origins may present a difficulty for this hypothesis.

V. SUMMARY

In this paper we have determined the average production rate of 4-Bv particles at the sun and associated with solar flares. If this production is to account for most of the observed cosmic radiation intensity a trapping magnetic field is required. Whether or not such a magnetic field exists and is capable of trapping particles of all observed rigidities is unknown at present.

In addition there are many questions which a solar-origin hypothesis, indeed any hypothesis, must answer. For example, how are the stripped heavy nuclei accelerated; can they be accelerated in the mechanism associated with the solar flare? If the source is postulated to be nearby, why are not high-energy electrons abundant in the primary cosmic radiation? These and other questions will require answers before a satisfactory theory of the origin of cosmic radiation can begin to develop.

The authors wish to thank Dr. R. P. Kane for tabulating and computing the flare rates in Fig. 2.

[9] Dolbear, Elliot, and Dawton, J. Atm. Terrest. Physics **1**, 187 (1951).

Scattering of 314-Mev Polarized Protons by Deuterium*

J. MARSHALL, L. MARSHALL, D. NAGLE, AND W. SKOLNIK
Institute for Nuclear Studies, The University of Chicago, Chicago, Illinois
(Received April 9, 1954)

The polarization of deuterium for 314-Mev protons has been examined as a function of angle. A beam of 314-Mev protons about 60 percent polarized was scattered by a liquid deuterium target. Measurements were made of the asymmetry of scattering of fast protons, namely both elastically and inelastically scattered, as a function of angle. The polarization of protons by deuterons, inferred from the asymmetry, was found to be small at small angles, to be about 0.35 from 10° to 30° laboratory angle, to be zero at 45° and negative thereafter. The polarization of quasi-free proton-proton scattering measured with the two scattered protons in coincidence, was found to be zero at 41° and 49° laboratory angle within statistical error. The polarization of quasi-free proton-neutron scattering was computed from measurements with the scattered proton and neutron in coincidence and was found to be 0.56 ± 0.12 at 29° laboratory angle. The polarization of elastic scattered protons was computed from measurements using absorbers chosen to discriminate between elastic and inelastic protons, giving 0.59 ± 0.07 at 24°, 0.29 ± 0.05 at 28°, 0.39 ± 0.18 at 32°, and -0.05 ± 0.16 at $35°\pm4°$ laboratory angle.

The polarization of protons by deuterium appears to vary with angle in approximately the same way as the proton polarization of H. One can say tentatively that the polarization of protons by neutrons at this energy has the same sign and about the same magnitude. The differential cross section of deuterium for scattering of protons is given as a function of barycentric angle of the $p-d$ system from 10 to 80 degrees.

INTRODUCTION

RECENTLY several investigations[1] have been made on polarization of protons scattered by hydrogen, showing large effects. The angular distribution of the polarization at 140 Mev indicates the dominance of the ^3P angular momentum state, and above 300 Mev there is evidence for the additional influence of the ^3F state. Evidence from scattering of protons on beryllium indicates a strong polarization of the elastically scattered protons, apparently stronger than the polarization due either to free $p-p$ scattering or to quasi-free proton-nucleon scattering at 310 Mev. Deuterium is interesting because the rather loose binding of the neutron permits the approximation of free $p-n$ scattering, and because the elastic scattering from the deuteron provides a transition from free nucleon-nucleon scattering to elastic scattering of beryllium. By examining the asymmetry of elastic scattering of polarized protons from deuterium one might hope to reach some understanding of polarization by elastic scattering from heavier nuclei.

Several different processes may occur when 300-Mev protons scatter from deuterium. The elastic scattering ($p+d\rightarrow p+d$) dominates at small scattering angles, and decreases rather slowly with angle. In addition there are events in which the proton transfers more energy to one or both nucleons. By quasi-free nucleon scattering we mean an event in which the proton and recoil nucleon emerge with approximately the angle and energy corresponding to a free proton-nucleon scattering. By asymmetry we mean that different numbers of protons are scattered at $+\theta$ and $-\theta$ measured from the beam direction.

In this work the asymmetry of the total scattered protons was measured as a function of angle. In addition, we attempted to separate and measure the elastically scattered protons at angles where it was feasible. Finally, at certain angles we have attempted to measure the quasi-free nucleon scattering, by requiring that the two nucleons mainly involved in the collision emerge coincidentally approximately 90° apart in the barycentric system of the two nucleons.

An unpolarized beam, such as the circulating proton beam of the cyclotron, is one for which the expectation value of the projection of the spin along any direction is zero. Such a beam may become polarized by a scattering, if the scattering is spin-dependent. When a previously unpolarized beam undergoes a spin-dependent scattering, there is no resulting asymmetry in numbers of scattered protons, but there is an asymmetry of scattered protons of given spin direction; that is, for a given direction the scattered protons have a net polarization. The polarization at a given angle P is defined as the difference between the fraction of the protons scattered with spin up and the fraction with spin down. In general, if a polarized beam undergoes a spin-dependent scattering, the probabilities for protons to be scattered on opposite sides of the beam will be different. For a scattering in the horizontal plane, the asymmetry A is defined as twice the difference between the numbers scattered to the right and to the left, divided by their sum. It is well known that the asymmetry resulting after the second scattering is maximal in the plane defined by the first scattering. There is no resultant asymmetry in a plane normal to the plane of first scattering, and this fact is used to test that the

* Research supported by a joint program of the U. S. Office of Naval Research and the U. S. Atomic Energy Commission.

[1] Oxley, Cartwright, and Rouvina, Phys. Rev. **93**, 806 (1954); Chamberlain, Segrè, Tripp, Wiegand, and Ypsilantis, Phys. Rev. **93**, 1430 (1954); J. M. Dixon and D. C. Salter, Proceedings of the Fourth Annual Rochester Conference, 1954 (University of Rochester Press, Rochester, to be published); Marshall, Marshall, and de Carvalho, Phys. Rev. **93**, 1431 (1954).

detecting apparatus is properly aligned. If the first and second scatterings are equivalent, the second scattering may be used to evaluate the polarization due to the first scattering of a previously unpolarized beam. The relationship is $P=(\frac{1}{2}\text{ asym.})^{\frac{1}{2}}$. Where a first scattering produces the polarization P_1, and a second scattering would produce P_2 in an unpolarized beam, the effect of the two in succession is to produce an asymmetry given by

$$A=2P_1P_2.$$

EXPERIMENTAL ARRANGEMENT

In the experiment presented here the plane of the first scattering was the plane of the circulating cyclotron beam. The first scattering was chosen so that its angle and energy loss corresponded to an elastic scattering. Recent experiments of Strauch[2] indicate, however, that many inelastic processes in which the nucleus acts collectively and is left in any one of several excited states contribute to the scattering of protons in this energy range. We shall continue to call protons scattered with very small energy loss "elastically" scattered, nevertheless.

Only protons scattered to the right at a well-defined angle and energy could reach the experimental area through the collimation system. To measure the degree of polarization of this beam we scattered it a second time in a manner like that of the first scattering except that the energy at the second scattering is inevitably somewhat smaller. After the first scattering, quasi-free nucleon scattering was excluded from the external beam by magnetic selection in the field of the cyclotron. After the second scattering it was excluded from the measuring telescope by copper so thick that only elastically scattered protons could reach the telescope.

The angles of first and second scattering were chosen equal. The degree of polarization of the beam was then estimated from the measured asymmetry after double scattering from beryllium.

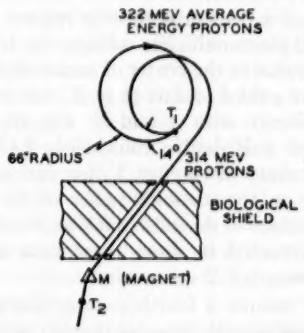

FIG. 1. Plan view of 450-Mev synchrocyclotron area, showing the experimental arrangement used to produce a 314-Mev proton beam, about 60 percent polarized in the vertical direction.

[2] K. Strauch, Proceedings of the Fourth Annual Rochester Conference, 1954 (University of Rochester Press, Rochester, to be published).

As shown schematically in Fig. 1, an internal beryllium target T_1 was placed at 66-inches radius (corresponding to 322-Mev average energy proton) in the 450-Mev Chicago synchrocyclotron. A beam of protons of energy 314 Mev, scattered at 14° from the beryllium target T_1, was analyzed in the fringing field of the cyclotron and emerged through the shield into the experimental area. It was collimated by a 1-inch vertical slit as it entered the shield and by a $\frac{3}{8}$-inch diameter collimator as it emerged.

The collimated beam was further analyzed with a magnet M in the experimental area, which deflected it about 20 degrees. The position of the deflected beam was found by vertical and horizontal exploration with a scintillation counter telescope at a position not far from the magnet. Then the beam was located at a second position by exploring with a second counter about 12 feet past the counter at the first position but connected in coincidence with it.

Next, a cathetometer was placed to look along the line of the beam defined by those two points. After this the cathetometer was used to align the second scatterer and in particular to see that the framework which held and swung the detecting counters symmetrically about the beam was coaxial with the beam.

This frame work was rigidly constructed of a 6-ft length of $3\frac{1}{2}$-in. pipe, turned smooth at two places, and mounted in V blocks on separate, adjustable tables, so that it could be accurately and conveniently placed to be coaxial with the beam. The counters were mounted on side arms fastened to the pipe, and counterweights were so placed that it was possible to rotate the counters to any position around the beam as an axis without the application of appreciable torque. The counters were rigidly clamped and the framework was stiff enough that the scattering angle to the counters θ_2 was accurately independent of rotary position of the framework.

After the magnet, the beam was defined by a 1-in. diameter round scintillation counter A. Next, a similar counter B was placed in the beam and was connected

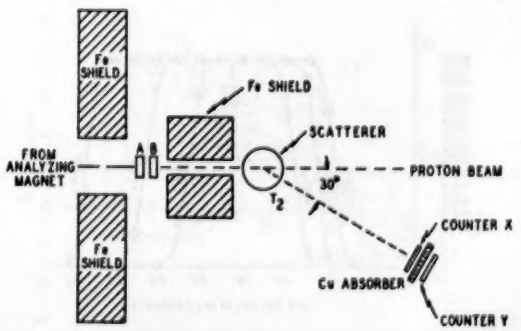

FIG. 2. Geometry for the second scattering.

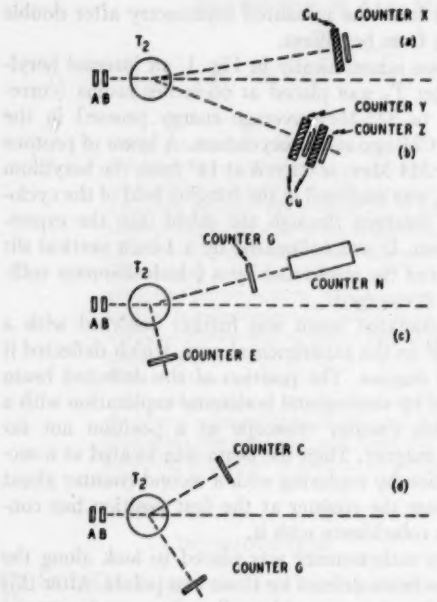

FIG. 3. Various arrangements of counter telescopes to detect scattered particles.

in coincidence with A to measure the incident proton flux, as is shown in Fig. 2. After passing through A and B the beam hit the second scatterer T_2.

The second scatterer was a liquid deuterium target. Deuterium gas was condensed in a metal Dewar using liquid hydrogen as refrigerant. By means of electrical heaters, the liquid deuterium could be switched from one container to the other, so that differences of the scattering with and without deuterium might be taken. Two cylindrical containers for the liquid deuterium were provided, one at the height of the proton beam and one above it. The container at the height of the beam was 4.23-inches inside diameter and 5 inches high. The temperature of the container was 24°K. The difference in the number of atoms of normal deuterium/cm² when liquid or gas fills the container is computed from the data of Woolley *et al.*[3] to be 4.96×10^{23} (1 ± 0.015). Of these, 98 percent are deuterium atoms and 2 percent hydrogen. The beam on entering or leaving the target had to pass through several layers of metal of total thickness 0.22 g/cm² of Al plus 0.12 g/cm² of brass.

The scintillation counters used to detect scattered particles were several in number, rather different from each other, and used in various combinations of coincidence and anticoincidence (see Fig. 3). For convenience in this discussion they are identified by letter and listed with appropriate descriptions of their characteristics in Table I.

ELECTRONICS

The counters were connected in triple, quadruple, or quintuple coincidence and anticoincidence combination. To adjust the electronics for any such combination the following procedure was followed. The counters to be used were placed in the 314-Mev proton beam. A and B were connected in double coincidence. The delay of counter A with respect to B was varied, and coincidences per second plotted as a function of angle. This was done (e.g., see Fig. 4) for a range of voltages on the photomultipliers of A and B and for various attenuations of the coincidence pulse as it entered the recording scaler. When it was evident that the system was operating on a plateau both with respect to pulse attenuation and photomultiplier voltage, the delay of A was set to the value at the center of such a delay curve as in Fig. 4. Now a third counter (e.g., X) was connected in triple coincidence with A and B. The triple coincidence rate per unit double coincidence (ABX/AB) was plotted *vs* delay of counter X, for various values of the voltage on the photomultiplier of X, and for various attenuations of the pulse ABX as it entered the scaler which recorded it; from these data a proper choice of the delay for X was made.

In a similar manner a fourth counter was added in quadruple coincidence if the measurement so required, and in the case of the $p-n$ coincidence measurement, a fifth counter was similarly added in anticoincidence. This procedure insured that the electronics were ad-

TABLE I. Characteristics of the detecting counters.

Scintillation counters	Diameter, in.	Description
A and B	1	plastic, $\frac{1}{8}$ in. thick
C and D	5½	liquid, ½ in. thick
E	4½	plastic, ¼ in. thick
G and H	6	plastic, ⅛ in. thick
N	5½	liquid, 14 in. long (for detecting neutrons)

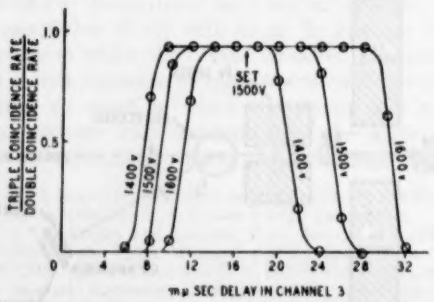

FIG. 4. Coincidence delay curves. Photomultiplier plateaus *vs* relative delay.

[3] Woolley, Scott, and Brickwedde, J. Research Natl. Bur. Standards 41, 379 (1948).

justed to give flat-topped counting rate curves when the delay in any channel was varied.

The 314-Mev beam intensity was ~1000 protons/inch² sec. The counting rate loss was less than 1 percent, even for the double coincidence rate of counters A and B. The counting rates of the telescopes ranged from a few hundred counts per minute to a few counts per minute.

ESTIMATION OF DEGREE OF POLARIZATION OF BEAM

The magnetic field at the position at 66-in. radius in the cyclotron and the energy spread of protons in the equilibrium orbit at this radius[4] define the energy of protons striking the target to be 322±10 Mev. From the parameter of the proton channel as defined by the two collimating slits and from the radial dependence of the magnetic field of the cyclotron we estimate the internal scattering angle as 14° (right). Range measurement of protons in the external beam and width of the beam after magnetic deflection define the energy of the beam as 314±11 Mev in one case and 310±11 Mev in the second case. The second scatterer was a piece of beryllium 2 in. thick. The asymmetry was measured as in Fig. 3a with counter X set at 14°, covered with various thicknesses of copper, and connected in coincidence with A and B. As the thickness of copper increased, the triple coincidence counting rate became vanishingly small, and the asymmetry increased rapidly; see Fig. 5.

We take 70-percent asymmetry as the limiting asymmetry for elastically scattered protons at 14°. $P_1=(\frac{1}{2}\times 0.7)^{\frac{1}{2}}=60$ percent is the figure we shall assume here for the polarization of beryllium at 14°. To this quick estimate many objections can be brought,

TABLE II. Asymmetry of total protons scattered by D *vs* angle. Counter geometry as shown in Fig. 3a.

Counter	Distance from scatterer, inches	Laboratory angle degrees	Total Cu absorber between counter and scatterer, inches	Asymmetry %
E	44½	8±3	2¼	15 ±13
C	30¾	11±5	2	45 ± 4
C	46½	16±3.5	2½	51 ± 7
D	46	20±3	1⅝	43.5± 6.5
D	46	26±3	1½	31 ± 6
G	31	28±4.5	1½	20.5± 4.5
E	47½	29±3	1 3/16	42 ± 8
G	28	32±6	1¼	17 ± 4
E	47⅞	35±3	1	34 ± 9
[a] G	26	42±6.5	0	6 ± 7
[a] H	27	42±6.5	7/8	
E	40	44±4	1 1/16	−22 ±12
[a] C	25¼	49±6	0	−9 ± 6
[a] D	26	49±6	½	

[a] Geometry as shown in Fig. 3b. In these cases quadruple coincidence rate was recorded, i.e., $ABGH/AB$ and $ABCD/AB$.

[4] A. H. Rosenfeld (private communication).

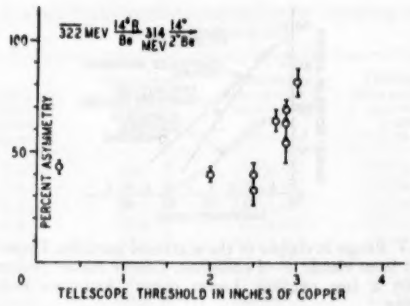

FIG. 5. Asymmetry *vs* energy threshold of the detecting counters. First scattering, 322-Mev p on Be, at 14° to the right. Second scattering, 314-Mev p on Be, at 14°.

chief of which is that the protons accepted after the second scattering through 3 inches of copper may not be scattered in a process similar to the first scattering.[2] However, the dependence of the polarization on (asymmetry)$^{\frac{1}{2}}$ makes P relatively insensitive to error in the asymmetry.

MEASUREMENT OF ALL SCATTERED PROTONS

The asymmetry of all scattered fast protons was measured as a function of angle from 8° to 48° laboratory angle. The detecting apparatus was sometimes a single counter, covered with enough copper to stop deuterons as in Fig. 3a and connected in a triple coincidence with counters A and B. Sometimes it was a telescope composed of 2 counters (see Fig. 2) connected in quadruple coincidence with counters A and B, the copper absorber for excluding deuterons being sandwiched between the two counters of the telescope. The latter arrangement was especially useful in that the quadruple coincidence reduced the large background of chance coincidences which existed at small angles in the triple coincidence arrangement. A typical measurement is discussed here briefly. Counter G was set at 31.7° laboratory angle, at a distance of 28 in. from the scattering center. It was covered with 1¼-in. copper to exclude deuterons. It was connected in coincidence with

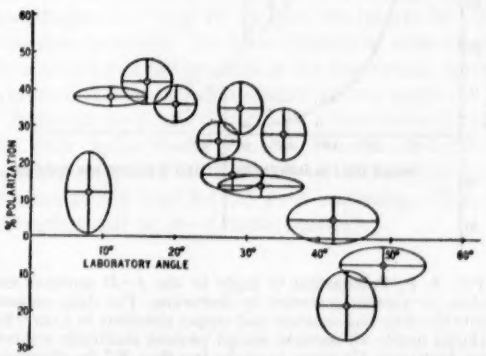

FIG. 6. Polarization *vs* angle of all protons scattered from D.

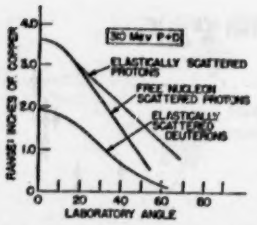

FIG. 7. Range in copper of the scattered particles. Upper curve: protons from elastic $p-d$ collisions. Center curve: protons scattered by a free nucleon. Lower curve: deuterons from $p-d$ scattering.

counters A and B; the counting rates ABG and AB were measured. With counter G to the left, and with deuterium in the scattering chamber, there were 2636 triples (T) for 80×10^6 doubles (D). Without deuterium, $T/D=250/32\times10^6$. With counter G to the right, and with deuterium, $T/D=3421/91\times10^6$; without deuterium, $T/D=225/30\times10^6$. The asymmetry, defined as $2(R-L)/(R+L)$, is calculated from these data to be 0.14 ± 0.03.

In Table II are listed the various measurements made on asymmetry of all scattered protons. The value of polarization calculated from these asymmetries are plotted in Fig. 6.

MEASUREMENT OF ELASTIC-SCATTERED PROTONS

One expects to be able to examine the reaction $p+d\rightarrow p+d$ separately from the reaction $p+d\rightarrow p+p+n$ by catching the deuteron and proton in coincidence in two counters properly placed. However, at all proton angles much different from 45° the deuteron recoils at almost the same angle as a proton scattered from a quasi-free $p-p$ collision in the deuteron; consequently such a separation must be made either by pulse height differentiation, which we were not prepared to do, or by range differentiation.

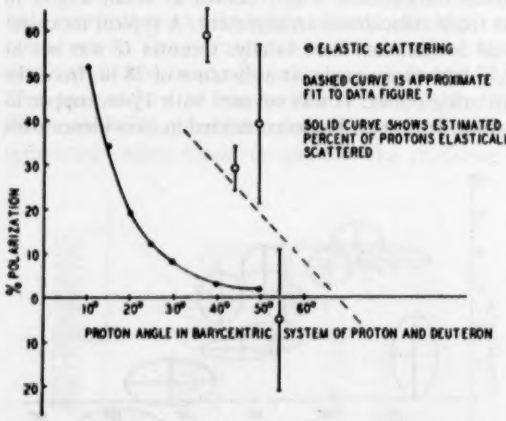
ELASTIC SCATTERING
DASHED CURVE IS APPROXIMATE FIT TO DATA FIGURE 7
SOLID CURVE SHOWS ESTIMATED PERCENT OF PROTONS ELASTICALLY SCATTERED
% POLARIZATION
PROTON ANGLE IN BARYCENTRIC SYSTEM OF PROTON AND DEUTERON

FIG. 8. P, Polarization *vs* angle in the $p-D$ center-of-mass system for protons scattered by deuterium. For these measurements the detecting counters had copper absorbers in front which excluded nearly all particles except protons elastically scattered from deuterium. However, at angles less than 30° the discrimination is incomplete.

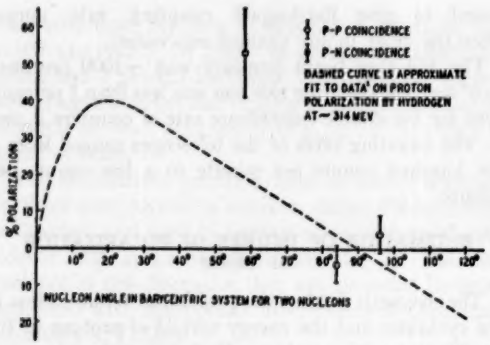
P-P COINCIDENCE
P-N COINCIDENCE
DASHED CURVE IS APPROXIMATE FIT TO DATA ON PROTON POLARIZATION BY HYDROGEN AT 314 MEV
% POLARIZATION
NUCLEON ANGLE IN BARYCENTRIC SYSTEM FOR TWO NUCLEONS

FIG. 9. Polarization of a nucleon scattered by a quasi-free nucleon-nucleon collision *vs* angle in the barycentric system of two nucleons. The $p-n$ polarization value is plotted at the angle of the scattered neutron.

It is apparent from the curves of Fig. 7 that below 20° absorbers do not distinguish between protons from elastic and inelastic scattering. At larger angles it becomes possible to attempt separation with absorbers. As used here, this is not a clean method. In any case the momentum distribution of nucleons in the deuteron smears the curve for nucleon-scattered protons into a broad energy band. In these experiments the low proton flux in the external proton beam required the use of counters of poor angular resolution. So for a given solid angle and for a given absorber thickness, some nucleon-scattered protons were able to penetrate on the small-angle side of the counter, and some elastically scattered protons were cut off on the large-angle side of the counter, owing to the steepness of the curves in Fig. 7.

In Table III are listed the measurements made on mainly elastic-scattered protons. Asymmetries have been reduced to polarizations and are plotted in Fig. 8

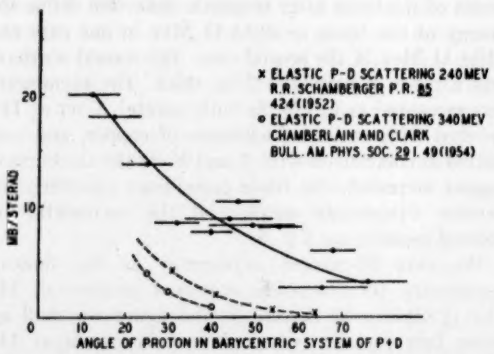
× ELASTIC P-D SCATTERING 240 MEV R.R. SCHAMBERGER P.R. 85 424 (1952)
• ELASTIC P-D SCATTERING 340 MEV CHAMBERLAIN AND CLARK BULL. AM. PHYS. SOC. 29 I. 49 (1954)
MB/STERAD
ANGLE OF PROTON IN BARYCENTRIC SYSTEM OF P+D

FIG. 10. Differential cross section for 310-Mev protons on deuterium to produce fast protons.

against the proton angle for the barycentric system of the proton and deuteron. It seems that the polarization by elastic scattering is as large as the total polarization, and perhaps slightly larger.

MEASUREMENT OF QUASI-NUCLEON-SCATTERED PROTONS

As we have said, the deuteron recoils very closely at the same angle as a proton scattered in a quasi-$p-p$ collision except in the neighborhood of 45°. Therefore we have made only one coincidence measurement of the two protons from a quasi-$p-p$ collision, this being the counter G at 42° laboratory angle, 26 in. from the scattering center, and with counter C on the other side of the beam at 48° and 25¼ in. Neither counter alone defined the solid angle. Quadruple coincidences rate $ABCG$ and double coincidences rate AB were measured simultaneously. The result was an asymmetry of -5 ± 7 percent for 42° and consequently $+5\pm7$ percent for 48°. That is, the asymmetry is essentially zero in this region. These values have been converted to polarization and plotted in Fig. 9, where also is shown the polarization by free $p-p$ collisions[1] at the same energy.

One measurement only was made of asymmetry due to quasi-free $p-n$ collision. For this, the neutron counter N was put at 29° with its front face 21 in. from the scattering center. Counter G was placed in anticoincidence in front of counter N, at the same angle and 14 in. from the scattering center. On the other side of the beam was counter E at 61°. A quintuple combination was measured: $ABEN$ in coincidence, with G in anticoincidence. The quintuple coincidence rate and the double coincidence rate were measured simultaneously, and gave an asymmetry of 68 ± 14 percent for 29°. This also has been reduced to quasi-$p-n$ polarization and is plotted in Fig. 9 at the angle of the scattered neutron where it is seen to be larger somewhat beyond

TABLE III. Asymmetries of mostly-elastic-scattered protons.

Laboratory angle, degrees	Counter	Distance from scatterer to counter, inches	Absorber between counter and scatterer, inches Cu	Telescope geometry shown in	Effective thickness of copper, inches	Asymmetry %
24±5.5°	*C*	27	0	Fig. 3b	2¼	71±8
	D	30	2¼			
28±5.5°	*G*	31	1¼	Fig. 2	2¼	35±6
	H	32	2¼			
32±6°	*G*	28	1¼	Fig. 2	2¼	47±22
	E	29	2¼			
35±4°	*D*	40	2	Fig. 3a	2	−6±19

TABLE IV. Differential cross section for scattering of protons by deuterium.

Laboratory angle of proton degrees	Barycentric angle of scattered proton degrees	Differential cross section in barycentric system mb/sterad	Differential cross section in laboratory system mb/sterad
7.9±3.7	13± 6	19.9±0.3	50.7±0.7
11.2±5	18± 8	18.0±0.7	45.2±1.9
16.1±3.5	25± 6	13.8±0.2	34.7±0.5
20.4±3	32± 5	8.5±0.5	20.7±1.3
25.6±3	40± 5	6.7±0.4	15.8±1.0
28.4±6	44±10	8.9±0.4	20.0±0.9
29.4±3	46± 5	10.4±0.9	23.3±2.0
31.7±6	50±10	8.4±0.3	18.4±0.7
35.5±3	55± 5	8.4±0.8	17.8±1.6
42 ±7	66±11	2.8±0.2	4.8±0.3
43.6±3	68± 5	6.1±0.7	11.6±1.4
49 ±6	77±10	3.4±0.1	6.1±0.3

statistical error than the free $p-p$ polarization at the same energy.

DIFFERENTIAL CROSS SECTION FOR SCATTERING OF PROTONS BY DEUTERIUM

In all these measurements of asymmetries the incident 314-Mev proton flux is measured directly with counters A and B in coincidence. So in principle an absolute cross section for scattering by deuterium of all protons fast enough to penetrate the copper barrier against deuterons (i.e., at small angles of energy above 200 Mev and decreasing to 80 Mev at 50° lab, see Fig. 7) can be calculated. For this purpose, we estimate 4.86×10^{23} atoms D/cm^2. A correction has been made for the loss of protons in the copper absorbers, using the range curve in copper for 314-Mev protons, from which the energy of the protons was determined. These corrections range from 8 to 30 percent. But this procedure underestimates the corrections somewhat for the reason that the range curve was taken with a proton beam of about 1-in. diameter whereas the asymmetry measurements were made with protons incident over the entire face of the 5¼-in. diameter counter. Even though this experiment was not designed to measure cross sections, and the corresponding values are not of high quality, nevertheless, in Table IV we give the results for what they may be worth. The total differential cross section for scattering of fast protons in the barycentric system is plotted in Fig. 10 *vs* barycentric proton angle.

Although we do not plot it here, a best curve through the data seems easily consistent with an artificial variable composed of the sum of differential cross sections at 314 Mev for (a) $p-p$ scattering, (b) $p-n$ scattering, and (c) $p-d$ elastic scattering.

Meson Production in n-p Collisions at Cosmotron Energies*

W. B. Fowler, R. P. Shutt, A. M. Thorndike, and W. L. Whittemore
Brookhaven National Laboratory, Upton, New York

(Received May 3, 1954)

154 analyzable three-prong events were observed in collisions between Cosmotron-produced neutrons, with energies up to 2.2 Bev, and protons in a hydrogen-filled diffusion cloud chamber. These events were classified as a result of the reactions $n+p \to p+p+\pi^-$, $p+p+\pi^-+\pi^0$, and $p+n+\pi^++\pi^-$ with frequencies in the ratio $(0.8\pm0.3):(1\pm0.35):(3.2\pm0.7)$, respectively. The observed ratio of the probability for double meson production to that for single meson production is more than 20 times higher than the ratio predicted from Fermi's statistical model. No triple meson production is observed, in agreement with the statistical model. The momentum distributions of the observed mesons are also in rough agreement with the theory. In the center-of-mass system, in the reaction $n+p+\pi^++\pi^-$, protons and π^+ show a tendency to be emitted backward, while neutrons and π^- tend towards forward emission. However, the data suggest that protons and π^+, and also neutrons and π^-, tend to be emitted more frequently in opposite directions than protons and π^- or neutrons and π^+. All of these results may be qualitatively in agreement with a meson production model where each nucleon is excited separately to an intermediate, possibly resonant, state which subsequently decays by emission of a meson.

THE Brookhaven Cosmotron provides a source of particles with energies up to 3 Bev and permits experiments on nuclear interactions at these energies under controlled conditions. A considerable number of experiments have been performed with synchrocyclotrons on nucleon-nucleon interactions at energies up to about 450 Mev and pion-nucleon interactions at energies up to about 250 Mev.[1] At these energies most nucleon-nucleon interactions result in elastic scattering, and inelastic scattering leads to the production of pions in at most a few percent of the cases. Similarly, the scattering of pions by nucleons has been almost entirely elastic (if this term is understood to include the possibility of charge-exchange scattering). At Cosmotron energies mesons are produced in a considerable fraction of the cases, and even "elementary" particle collisions may lead to a large number of different reactions.

This group has undertaken a preliminary cloud chamber survey of nucleon-nucleon and pion-nucleon interactions in the Bev energy range in an attempt to determine the general nature of these reactions. The results reported here have to do with neutron-proton interactions, in particular the production of pions in n-p collisions when the neutron energy is about 2 Bev.

There is, of course, a very large amount of data on nuclear interactions at these energies derived from cosmic ray experiments.[2] The interpretation of these results is difficult because the energy and even identity of the particle causing an interaction is in most cases somewhat uncertain. In addition most experiments involve interactions in emulsions or absorbers in which elements of high atomic weight predominate, so that complicated cascade processes may develop in the nucleus which is struck. It is difficult to determine any details of nucleon-nucleon or meson-nucleon interactions from such data. In some cases interactions occurring in hydrogen have been isolated,[3] but the results have not permitted a detailed comparison with theoretical predictions.

At the Cosmotron, it has been possible to achieve improvements in both of these respects. We have employed a diffusion cloud chamber filled with hydrogen gas at a pressure of about 20 atmospheres and have concentrated on interactions occurring in the cloud chamber gas. Under these conditions almost all interactions are with hydrogen.[4] The cloud chamber has been operated in the neutron beam emerging at 0° from an internal target. There is little quantitative information concerning the purity of this beam. It seems safe, however, to assume that the events studied are due to neutrons. There is, unfortunately, no reason to believe that the neutrons are monoenergetic, and little is known about their energy distribution. (This question will be discussed in Part IV.)

* Work performed under the auspices of the U. S. Atomic Energy Commission.

[1] For summaries of the results of these experiments see R. E. Marshak, *Meson Physics* (McGraw-Hill Book Company, Inc., New York, 1952), and Henley, Ruderman, and Steinberger, Ann. Rev. Nuc. Sci. **3**, 1 (1953).

[2] For summaries of these results see R. E. Marshak, *Meson Physics* (McGraw-Hill Book Company, Inc., New York, 1952), B. Rossi, *High Energy Particles* (Prentice-Hall, Inc., New York, 1952), and Camerini, Lock, and Perkins, *Progress in Cosmic Ray Physics* (Interscience Publishers, Inc., New York, 1952), p. 1.

[3] M. L. Vidale and M. Schein, Phys. Rev. **84**, 593 (1951); G. W. Rollosson, Phys. Rev. **87**, 71 (1952); W. Bosley and H. Muirhead, Phil. Mag. **43**, 783 (1952); Weaver, Long, and Schien, Phys. Rev. **87**, 531 (1952); A. B. Weaver, Phys. Rev. **90**, 86 (1953); Kusumoto, Miyake, Suga, and Watase, Phys. Rev. **90**, 998 (1953); McCusker, Porter, and Wilson, Phys. Rev. **91**, 384 (1953); S. Miyake (private communication).

[4] There is a small contamination of carbon and oxygen in the alcohol vapor (about 1 alcohol molecule in 800 hydrogen molecules) and, in this experiment, a contamination of 0.3 percent oxygen in the hydrogen, but the occasional interactions involving carbon or oxygen are easily recognized. Eleven events were observed to occur in these heavier nuclei. These were recognized either by the fact that their prong number was even, which is not possible for an n-p collision, or by the occurrence of more than two protons, or of protons which passed further backwards than is kinematically possible in n-p collisions. The prong numbers observed were 3, 4, 4, 4, 5, 5, 5, 6, 6, 6, and 8. These events had the typical appearance of collisions with heavy nuclei, showing slow "evaporation prongs" in addition to the fast prongs.

I. OBJECTIVES OF THE EXPERIMENT

While the experiment described here is exploratory in nature, it was intended to provide information on a number of specific questions as well as to give a qualitative picture of the nature of n-p interactions. The following questions are of special interest.

1. Multiplicity of Meson Production

Cosmic-ray results have not provided a clear picture as to whether a nucleon-nucleon collision frequently (or perhaps ever) leads to the emission of more than one meson.[2] The uncertainty arises from the complicated nature of the cascade process in a large nucleus, which permits the observed meson showers to be explained in terms of single meson production at each of many nucleon-nucleon collisions ("plural theory").[5] Results on n-p collisions in hydrogen gas should decide unambiguously between single and multiple production. Fermi has proposed a statistical theory of meson production which is based on the idea that pion interactions are strong, but involves no specific meson theory.[6] It is of particular interest to compare our observations with this theory.

2. Energy, Angle, and Charge of Emitted Mesons

Not only meson multiplicity but also further details of the process can be compared with theoretical predictions, for example, ratios of numbers of positive to negative to neutral mesons, and angular and energy distributions for the emitted mesons and nucleons. The charge ratios are related to ideas of the charge independence of nuclear phenomena, while the energy distributions are related to the degree of inelasticity of the collisions.

3. Angular Correlations between Emitted Particles

The presence or absence of angular correlations between emitted particles may give evidence of interactions between them, such as meson-nucleon forces, or meson-meson forces when two (or more) mesons are produced. If the forces are strong enough to produce bound intermediate states, these might also be recognized.

4. Production of "New Unstable Particles"

In addition to n-p collisions involving meson production, other events of interest might well be observed in the chamber. In particular it was hoped that V-events or other decays of members of the "new unstable particle" family would be observed. A few such V events were indeed found, which are reported elsewhere,[7] but none were produced in n-p collisions occurring in the cloud chamber gas.

5. Neutron Beam Energy

A final objective was that of obtaining some information about the neutron beam. Since measurements of the momenta of the particles emitted from n-p interactions would often determine the energy of the neutron that produced them, they should give some idea of the energies of the neutrons emitted from the Cosmotron target.

II. EXPERIMENTAL PROCEDURE

The observations were made with a diffusion cloud chamber filled with hydrogen at a pressure of about 20 atmospheres employing methyl alcohol as the condensable vapor. It was operated in a magnetic field of about 10 500 gauss. Details of the cloud chamber, its operation with the Cosmotron, projection method, and accuracy of measurements have been given elsewhere.[8]

The cloud chamber was placed in the external neutron beam emerging at 0° from a carbon target struck by the circulating proton beam of the Cosmotron at a time when the protons had energies of 2.2 Bev. A lead collimator in the Cosmotron shield defined a beam approximately 1 in.×2 in. in size. Charged particles coming from the target were deflected out of this beam by the magnetic field of the Cosmotron. The beam emerging from the collimator contained neutrons and photons from the target and charged particles from the wall of the Cosmotron vacuum tank. A 1.5-inch lead converter served to reduce the photon intensity. The beam then passed through a permanent magnet, which deflected charged particles out of the beam, and finally into the cloud chamber.

About 20 000 Cosmotron pulses were photographed. The pictures were scanned for 3-prong and 5-prong events. Any n-p interaction results in an odd number of emitted charged particles as long as all of them have unit charge and electric charge is conserved. Elastic recoil protons and other 1-prong events were not counted. They would appear as single tracks starting in the cloud chamber gas, usually with density of ionization fairly close to minimum. Such tracks are difficult to find in scanning because the limited sensitive depth and gaps in the sensitive region cause many other tracks to look similar. In principle it is possible to distinguish between them, but in practice it was not feasible to do so. Furthermore, even if 1-prong events had been counted, their interpretation would be quite ambiguous since they could be due to elastic n-p collisions or inelastic collisions resulting in production

[5] W. Heitler and L. Janossy, Proc. Phys. Soc. (London) **62**, 669 (1949). For a recent summary see H. Messel, *Progress in Cosmic Ray Physics* (Interscience Publishers, Inc., New York, 1954), Vol. 2, p. 135.

[6] E. Fermi, Progr. Theoret. Phys. (Japan) **5**, 570 (1951).

[7] Fowler, Shutt, Thorndike, and Whittemore, Phys. Rev. **90**, 1126 (1953).

[8] Fowler, Shutt, Thorndike, and Whittemore, Rev. Sci. Instr. (to be published).

TABLE I. Types of n-p reactions.

Number of pions produced	Products of reaction	Abbreviation	Number of charged prongs
0	$p+n$	pn	1
1	$p+n+\pi^0$	$pn0$	1
1	$p+p+\pi^-$	$pp-$	3
1	$n+n+\pi^+$	$nn+$	1
2	$p+n+\pi^0+\pi^0$	$pn00$	1
2	$p+n+\pi^+\pi^-$	$pn+-$	3
2	$p+p+\pi^-+\pi^0$	$pp-0$	3
2	$n+n+\pi^+\pi^0$	$nn+0$	1
3	$p+n+\pi^0+\pi^0+\pi^0$	$pn000$	1
3	$p+n+\pi^+\pi^-+\pi^0$	$pn+-0$	3
3	$p+p+\pi^-+\pi^0+\pi^0$	$pp-00$	3
3	$p+p+\pi^-+\pi^-+\pi^+$	$pp--+$	5
3	$n+n+\pi^+\pi^0+\pi^0$	$nn+00$	1
3	$n+n+\pi^+\pi^+\pi^-$	$nn++-$	3

of neutral mesons. Accordingly it was decided to concentrate on events with three or more prongs.

A total of 185 3-prong events were recorded, but no 5-prong events were seen. Two photographs of 3-prong events have already been published.[9] On each 3-prong event the following measurements were made:

1. Angles in space were measured for emitted tracks relative to the neutron direction by means of a projector which reproduced the geometry of camera and cloud chamber. The neutron direction was known within about $\pm 1°$.

2. Densities of ionization were estimated for emitted tracks by using the usual subjective methods.

3. Curvatures of tracks were measured by means of a microscope with micrometer stage.

Since the depth of the sensitive layer was only about 2 inches, the emitted tracks were often too short for accurate determination of momentum, and in some cases even the angle of the track was not well determined. In these cases, therefore, events could not be analyzed with certainty.

III. CLASSIFICATION OF n-p COLLISION EVENTS

The different reactions leading to 0, 1, 2, or 3 pions are given in Table I. It is assumed that only pions are produced, and all the following analysis is based on this assumption. One cannot prove that no heavy mesons were involved, but no decay events were seen to be associated with the n-p interactions, no track had density and momentum which identified it as a heavy meson, and few heavy unstable particles were observed to be produced in the cloud chamber walls. It is, therefore, unlikely that many heavy mesons were produced in the n-p collisions, and probably there were none. As will be seen, the interactions can be analyzed on the assumption that only pions were emitted.

Table I shows that 3-prong events can be either $(pp-)$, $(pn+-)$, $(pp-0)$, $(pn+-0)$, $(pp-00)$, or $(nn++-)$. Since no 5-prong events $(pp--+)$ were seen, it was assumed that also few, if any, of the 3-prong events involved triple meson production. The data on each 3-prong event were analyzed to determine whether it should be classified as $(pp-)$, $(pn+-)$, or $(pp-0)$.

The first step in the classification of an event was to determine which tracks were protons and which pions. Measured momenta and estimated ionization densities of negatively charged particles were consistent throughout with those of π^--mesons.[10] Positive tracks were consistent with those of π^+ mesons or protons. Where a track was too short, its sign could not be determined directly but could often be inferred from the known signs of the two other particles and conservation of charge.

In 20 percent of the cases it was possible to identify all three particles from measured momenta and estimated ionization densities. However, the laws of conservation of energy and momentum afford a number of criteria which often helped to determine an event completely. Sternheimer[11] has calculated that for 2.2-Bev nucleons incident on nucleons the maximum angle at which a nucleon can be emitted in the laboratory system with respect to the incident direction is 68° for single meson production and 58° for double meson production. Mesons can be emitted in all directions. For incident neutrons of lower energies these angles become smaller. Tracks at angles larger than the maximum nucleon angle could be identified as pions. Furthermore, a proton emitted near the maximum angle should ionize heavily, so that a minimum ionization track at an angle near the maximum had to be a pion.

Where two of the three tracks could be due to protons the classification $(pp-)$ was first investigated. If P_z is the algebraic sum of the forward components of momentum of the 3 particles, $\mathbf{P}_r$ the vector sum of their components perpendicular to the direction of flight of the incident neutron, and E_s the sum of their total energies (including rest energies), then for the reaction $(pp-)$ the two conditions for momentum and energy balance, $\mathbf{P}_r=0$ and $E_s-M=(P_z^2+M^2)^{\frac{1}{2}}$, must be satisfied, where $M=0.93$ Bev is the nucleon mass. $E_s-M(=E_0)$ is, of course, equal to the total energy of the incident neutron.

If a π^+ has been identified, the event is provisionally classified as $(pn+-)$. If both positive particles are identified as protons, but the conditions for $(pp-)$ are not satisfied, the event is provisionally classified as $(pp-0)$. In each case the classification is checked

[9] Fowler, Shutt, Thorndike, and Whittemore, Phys. Rev. **91**, 758 (1953).

[10] Only one case, not counted here, was found which has to be interpreted as due to the reaction $n+p\rightarrow p+n+\pi^0\rightarrow p+n+e^+ +e^-+\gamma$. The mode of mesonic conversion [Steinberger, Sachs, and Lindenfeld, Phys. Rev. **90**, 343 (1953); Cornelius, Sargent, Rinehart, Lederman, and Rogers, Phys. Rev. **92**, 1583 (1953)] into 2 electrons is known to occur in about 1 percent of all π^0 emissions. One estimates that only one or two such cases can be expected in this work.

[11] R. M. Sternheimer, Phys. Rev. **93**, 642 (1954).

by the calculations described below. If the event is not $(pp-)$, and positive particles are not identified in either of the above ways, then either $(pn+-)$ or $(pp-0)$ is a possibility, but a definite classification may be arrived at from the following calculations of momentum and energy balance.

We now can attempt to calculate the momentum of the neutral particle, assuming that it is a neutron or a π^0 of mass $m_4=0.93$ Bev or 0.14 Bev, respectively. Its transverse momentum component is given by $\mathbf{p}_t+\mathbf{P}_r=0$. Conservation of energy and forward momentum provide two equations which can be solved to give the momenta of incoming neutron and emitted neutron or π^0. The forward component, p_s, of the emitted particle is given by

$$p_s=-\{P_s\pm E_t[1+(m_4^2+P_r^2)Y^2/X]^{\frac{1}{2}}\}/Y, \quad (1)$$

where $E_t=E_s-M$, $X=P_s^2-E_t^2$, and $Y=2/[1+(M^2-m_4^2-P_r^2)/X]$. The sign before the second term in (1) must be chosen so that

$$E_t+(P_r^2+p_s^2+m_4^2)^{\frac{1}{2}}=[(p_s+P_s)^2+M^2]^{\frac{1}{2}}. \quad (2)$$

The latter two expressions represent the total energy of the incident neutron E_0. If a solution has been found for p_s, then a test for its validity is, of course, that $E_0-0.93\leq 2.2$ Bev, the kinetic energy of the protons circulating in the Cosmotron. However, a solution for p_s does not necessarily exist for any given combination of P_r, P_s, E_t, and m_4. It follows from (1) that for a solution to exist the value of X must lie *outside* the interval,

$$-[M-(m_4^2+P_r^2)^{\frac{1}{2}}]^2\geq X\geq -[M+(m_4^2+P_r^2)^{\frac{1}{2}}]^2. \quad (3)$$

The existence of this forbidden region often affords a quick and decisive test whether $m_4=0.93$ Bev $[(pn+-)$ classification$]$ or $m_4=0.14$ Bev $[(pp-0)$ classification$]$.

For events where all three masses and momenta are known with some certainty, the procedure described above is straightforward. Where not all momenta could be measured several assumptions can be made, consistent with the estimated ionization densities of the tracks, each assumption to be tested separately. Sometimes several different assumptions were kinematically possible, leading to different classifications of the event and different calculated values for the momenta of the neutral particles.

Uncertainties in momentum and angle measurements also have to be taken into account. Varying a measured quantity within its range of experimental uncertainty may lead to different classifications of the same event. One might restrict the analysis to well-measured events, but much information would then be ignored, and, in addition, selecting only well-measured events may lead to a bias of the results since the geometry of the events partially depends on their type. For instance, proton tracks can only pass in a forward direction, as mentioned above. Thus many of them have a good chance to remain for some distance inside the sensitive layer of the cloud chamber, which is advantageous for angle and momentum measurements. On the other hand, their momenta are most probably high, making momentum measurements more difficult. Mesons, particularly π^+, often appear to be emitted at rather large angles. Thus, because of the limited thickness of the sensitive layer in the cloud chamber, their tracks may become too short for curvature measurements and for accurate angle measurements. For these reasons only events for which no momentum measurements at all could be performed were excluded. It is felt that no bias is introduced by their omission. (A few events occurring outside the region where the direct neutron beam passed through the chamber were excluded since these could only have been secondary events produced by previously scattered neutrons of unknown direction.)

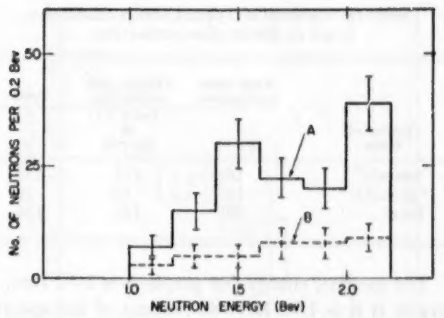

FIG. 1. Energy spectrum of the incident neutrons. Graph A was obtained making use of all events, while graph B represents a selection of 38 events which could be determined with some accuracy.

The remaining total of 154 events could be analyzed with varying degrees of certainty. In some cases, for example, the event may be classified with good certainty, while momenta of certain tracks are not measured, but given assumed values which are consistent with the classification. In the following discussion of results some are well-established, while others are uncertain and speculative because of the limitations of the basic data, as will be pointed out in the discussion.

IV. ENERGY SPECTRUM OF THE NEUTRON BEAM

The energy spectrum inferred for the neutrons producing the 3-prong events is shown in Fig. 1. Here, graph A gives the result from all events where the total energy could be estimated. Since often only upper or lower limits could be given for the measured quantities, many of the plotted energies represent only limits. Graph B gives the spectrum from 38 events where all experimental quantities could be determined, uncertainties on individual neutron energy determinations varying between ± 0.1 and ± 0.3 Bev. One sees that the apparent maximum at 1.5 Bev in graph A is probably not real, but that the general shape of this spectrum agrees with graph B. The spectrum starts at 1 Bev and rises gradually up to 2.2

TABLE II. Numbers of 3-prong events classified as single or double pion production.

Quality of event	Single pion production ($pp-$)	Double pion production ($pn+-$) or ($pp-0$)	Total
"certain"	18	115	133
"probable"	11	10	21
Total	29	125	154

Bev. The median energy for graph A is 1.72 Bev, and for graph B it is 1.76 Bev. 80 percent of the spectrum lies above 1.4 Bev.

Figure 1 probably does not represent the true spectrum of the incident neutrons since it also depends on the cross sections for producing 3-prong events. Thus the apparent absence of neutrons with energies below 1 Bev may either mean that indeed none are incident or that the cross sections for ($pp-$), ($pp-0$), and ($pn+-$) are quite small below ~1 Bev. Yang[12] has calculated that 2.2-Bev protons colliding with light nuclei should produce a neutron spectrum in the forward direction with a median value near 0.8 Bev, using the statistical theory[6] whose validity is not yet certain. Hill *et al.*[13] have observed a mean neutron energy of 1.4 Bev in a similarly produced neutron beam, indicating the presence of a number of neutrons below 1 Bev. Finally, the incident neutrons must have been produced in reactions similar to those observed in our cloud chamber. The nucleon momentum spectrum from our 154 events given in Part VI contains many nucleons emitted in a forward direction with energies much lower than those of the incident neutrons. Therefore the incident neutron beam should also contain a fairly large number of neutrons with energies far below the 2.2-Bev proton energy producing them.

The laboratory threshold energies for single and double meson production are 0.29 and 0.60 Bev, respectively. Near 0.4 Bev the (single) meson production cross section in nucleon-nucleon collisions is 0.1 to 1.0 millibarns. At energies above 1 Bev the total nucleon-nucleon cross section is ~43 mb.[13] Probably most of this cross section is responsible for meson production. One might expect that after its threshold single production rises to a maximum and then declines as double production becomes more probable, the relative multiplicities perhaps being governed by a statistical model such as considered by Fermi.[6] Thus, if many neutrons were incident below 1 Bev some ($pp-$) events should have been observed giving rise to inferred neutron energies <1 Bev in our neutron spectrum (Fig. 1). Since none were observed, the cross section for ($pp-$) below 1 Bev would have to be quite small.

[12] C. N. Yang (private communication).

[13] Hill, Coor, Hornyak, Smith, and Snow, Phys. Rev. **94**, 791 (1954).

V. PION MULTIPLICITIES AND CHARGE DISTRIBUTION

Each 3-prong event was classified as single pion production, ($pp-$), or double pion production, ($pp-0$) or ($np+-$). The numbers of single and double production events are given in Table II. The events whose multiplicities are considered to be established with fair to good certainty, called "certain" events, are tabulated in the first row. Twenty-one additional "probable" cases have been noted, which may fit either classification, but with one or the other the more probable. Each event is counted once. The "probable" group contains relatively many single production events, mostly because separation of ($pp-$) from ($pp-0$) is not always definite unless the momenta of all three tracks are well known. One sees that, for our 3-prong events, double production predominates over single production in the ratio 4:1. Since no 5-prong events were seen, triple production has been assumed to be negligible.[14] These results are compared with theoretical predictions in Part VIII.

Each 3-prong event was further classified as ($pp-$), ($pp-0$), or ($pn+-$). The numbers of events in each class are given in Table III. The classifications "certain" and "probable" are defined as before. The number of "probable" events is now larger than in Table II because of the added uncertainties in separating ($pp-0$) from ($pn+-$). One sees, as a further result, that production of a positive-negative meson pair is by far the most frequent. The ratio for ($pn+-$):($pp-0$):($pp-$) is about 3:1:1. In Part VII a reclassification of events is made which changes these ratios slightly.

To investigate the energy dependence of the multiplicity the events were divided into low- and high-energy groups. The first had incident neutron energies below the median of 1.72 Bev; the second had incident

TABLE III. Numbers of events with different charge distributions observed in n-p collisions.

Quality	($pp-$)	($pp-0$)	($pn+-$)	Total
"certain"	18	5	86	109
"probable"	11	22	12	45
Total	29	27	98	154

TABLE IV. Numbers of events with different charge distributions for low and high energy incident neutrons.

Median energy of incident neutrons	($pp-$)	($pp-0$)	($pn+-$)	Selected events ($pp-$)	($pp-0$)	($pn+-$)
1.46 Bev	16	11	40	6	3	10
2.04 Bev	13	8	46	6	1	12

[14] As far as the experimental observations are concerned, some 3-prong events could be classified as ($pn+-0$), ($pp-00$), or ($nn++-$). Such a classification, however, would force one to conclude that the reaction leading to ($pp+--$) is forbidden for some unforeseen reason. It seems more reasonable to conclude that all triple meson production is infrequent.

neutron energies above that value. The median energy for the incident neutrons in the low-energy group is 1.46 Bev; in the high-energy group it is 2.04 Bev. The numbers of $(pp-)$, $(pp-0)$, and $(pn+-)$ events in each group are given in Table IV. The selected events for which neutron energies are known best (as used for graph B in Fig. 1) are tabulated separately.

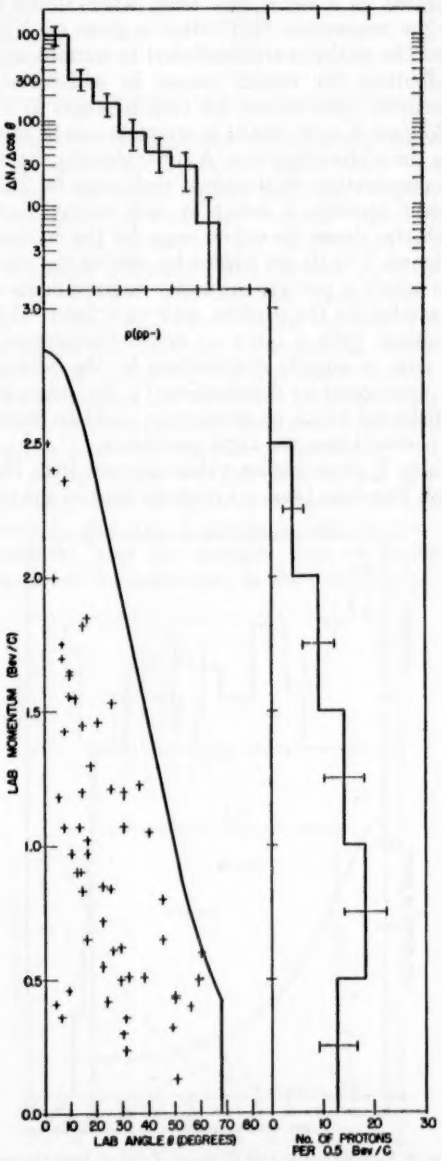

FIG. 2. Laboratory scatter diagram of the protons from the reaction $(pp-)$. At the top the differential angular distribution is plotted for the protons in the laboratory system. At the right side their momentum distribution is shown. The curve drawn in the scatter diagram represents the maximum momenta obtainable at different angles for the maximum incident neutron energy of 2.2 Bev. Note the cut-off angle at 68°.

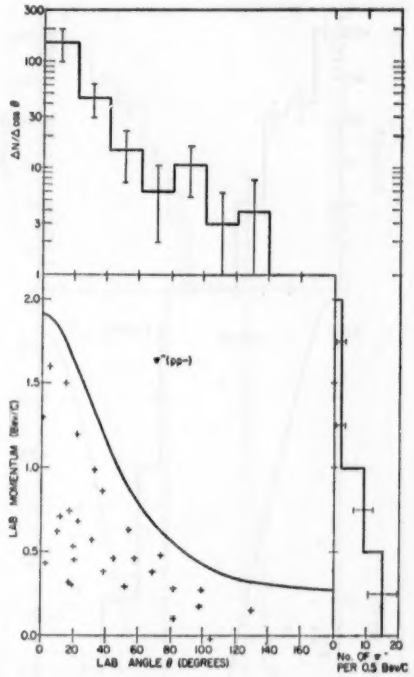

FIG. 3. Laboratory scatter diagram of the π^- from the reaction $(pp-)$. At the top the differential angular distribution is plotted for the π^- in the laboratory system. At the right side their momentum distribution is shown. The curve drawn in the scatter diagram represents the maximum momenta obtainable at different angles for the maximum incident neutron energy of 2.2 Bev. For points plotted under the abscissa the momenta could not be determined.

[One sees that for these selected events the multiplicities are apparently changed in favor of single production. The reason is that incident neutron energies can be calculated for $(pp-)$ more easily than for the other reactions because, for only 3 emitted charged particles, the momentum of one particle can be inferred if the momenta of the two others are known in addition to all of the angles.] We find that below and above 1.72 Bev the relative multiplicities agree within statistical errors for both selected and unselected events, although the slight relative increase of double production events over single production events from 3.2:1 to 4.2:1 may be real. It is surprising that the relative multiplicities have not changed more with energy. This will be discussed further in Parts VIII and IX.

Four of the $(pn+-)$ cases actually were identified as due to the reaction $n+p \rightarrow d+\pi^+ +\pi^-$. If the "Fermi energy" between bound nucleons is 20 Mev, corresponding to a momentum of 200 Mev/c, then one indeed expects some small percentage of the $(pn+-)$ cases to result in this reaction, particularly since the median momentum of the resulting nucleons in the center-of-mass system (c.m.) given in Part VIII is

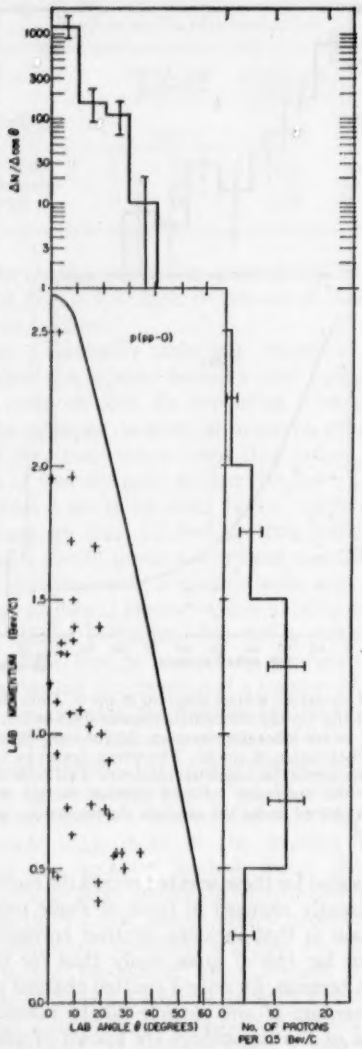

FIG. 4. Laboratory scatter diagram of the protons from the reaction $(pp-0)$. At the top the differential angular distribution is plotted for the protons in the laboratory system. At the right side their momentum distribution is shown. The curve drawn in the scatter diagram represents the maximum momenta obtainable at different angles for the maximum incident neutron energy of 2.2 Bev. Note the cut-off angle at 58°.

only about 400 Mev/c. Thus a fair amount of phase space should be available where the relative momentum of the two nucleons is $\leq$200 Mev/c, which should be favorable for deuteron formation. This has been treated theoretically by Brueckner and Kovacs.[15] The observed frequency of deuteron formation seems to be less than predicted.

[15] K. A. Brueckner and J. S. Kovacs, Phys. Rev. 94, 726 (1954).

VI. ANGULAR AND MOMENTUM DISTRIBUTIONS IN LABORATORY SYSTEM

Figures 2 to 10 give scatter diagrams which show laboratory momentum *vs* laboratory angle and angular and momentum distributions for all particles involved in the different reactions. At the top of each scatter diagram the differential angular distribution $\Delta N/\Delta \cos\theta$ is plotted on a logarithmic scale, while at the right side the momentum distribution is given on a linear scale. The statistics are insufficient to warrant angular distributions for certain ranges in momentum, or momentum distributions for certain ranges in angle. *Indications* of such details in structure can be inferred from the scatter diagrams. A curve showing the maximum momentum obtainable at each angle for 2.2-Bev incident neutrons is drawn in each scatter diagram, which also shows the cut-off angle for the nucleons.

Figures 2 to 10 are labeled by writing the reaction from which a particle originates in parenthesis after the symbol for the particle, such as $\pi^-(pn+-)$ for a π^- coming from a $(pn+-)$ event. Furthermore, we will refer to angular distributions by the subscript a and to momentum distributions by the subscript m. Particles for which no momentum could be measured are plotted below the angle coordinate.

Table V gives median values inferred from Figs. 2 to 10. The class $(pn+-)$ contains most of the events

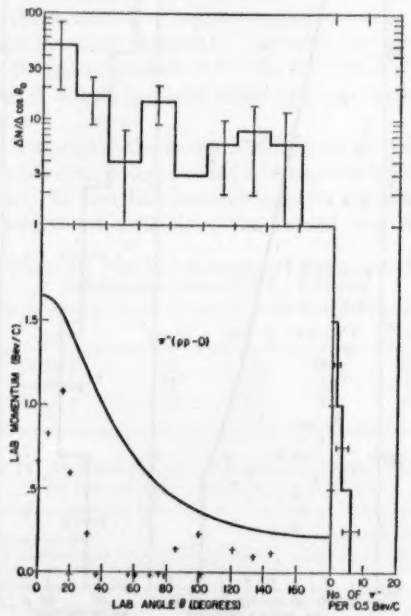

FIG. 5. Laboratory scatter diagram of the π^- from the reaction $(pp-0)$. At the top the differential angular distribution is plotted for the π^- in the laboratory system. At the right side their momentum distribution is shown. The curve drawn in the scatter diagram represents the maximum momenta obtainable at different angles for the maximum incident neutron energy of 2.2 Bev. For points plotted under the abscissa the momenta could not be determined.

TABLE V. Median values for momenta and angles observed in the laboratory system.

Particle and reaction	Median momentum (Bev/c)	Median angle
$p(pp-)$	0.95	20°
$\pi^-(pp-)$	0.46	34°
$p(pp-0)$	1.00	10°
$\pi^-(pp-0)$	0.23	61°
$\pi^0(pp-0)$	0.18	61°
$p(pn+-)$	0.82	22°
$n(pn+-)$	1.12	16°
$\pi^+(pn+-)$	0.26	43°
$\pi^-(pn+-)$	0.33	29°

and therefore its median values should be most meaningful. One sees that $p(pn+-)$ has a lower median momentum but higher median angle than $n(pn+-)$. The difference between the angular distributions $p_a(pn+-)$ and $n_a(pn+-)$ will be discussed in Part VII. A similar difference exists between $\pi_a^+(pn+-)$ and $\pi_a^-(pn+-)$. The median momentum for $p_m(pn+-)$ and $n_m(pn+-)$ taken together is 0.96, which agrees well with the corresponding values for $p_m(pp-)$ and $p_m(pp-0)$. As one might expect, the median momentum for $\pi_m^-(pp-)$ is higher than for the doubly produced mesons, since more kinetic energy is available when only one pion is produced.

The median angle for the products of $(pp-0)$ disagree with those for the other reactions. The number of events in this class is relatively small so that the disagreement may be partially due to statistical uncertainties. As mentioned in Part V the $(pp-0)$ group contains mostly rather uncertain events. The present disagreement probably indicates that some of the "probable" events in Table III have been misidentified. One might assume that $\pi^-(pn+-)$ and $\pi^-(pp-0)$ should have identical distributions, and also $\pi^+(pn+-)$ and $\pi^0(pp-0)$. Making use of this assumption we shall later reclassify some of the "probable" events. The effect on the general conclusions reached

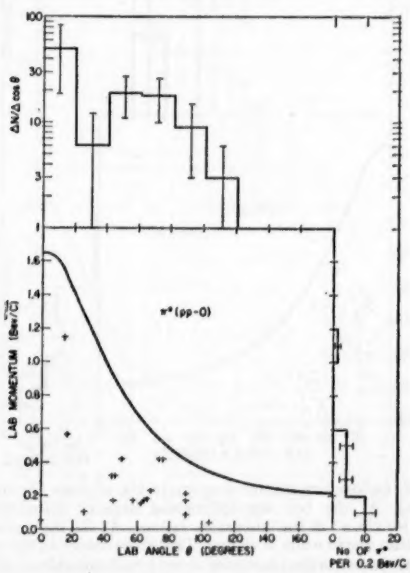

FIG. 6. Laboratory scatter diagram of the π^0 from the reaction $(pp-0)$. At the top, the differential angular distribution is plotted for the π^0 in the laboratory system. At the right side their momentum distribution is shown. The curve drawn in the scatter diagram represents the maximum momenta obtainable at different angles for the maximum incident neutron energy of 2.2 Bev.

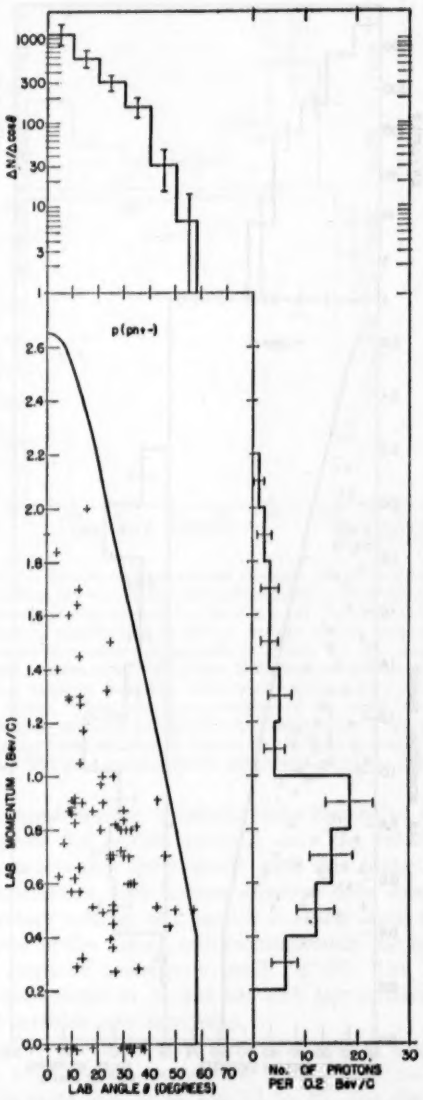

FIG. 7. Laboratory scatter diagram of the protons from the reaction $(pn+-)$. At the top the differential angular distribution is plotted for the protons in the laboratory system. At the right side their momentum distribution is shown. The curve drawn in the scatter diagram represents the maximum momenta obtainable at different angles for the maximum incident neutron energy of 2.2 Bev. Note the cut-off angle at 58°. For points plotted under the abscissa the momenta could not be determined.

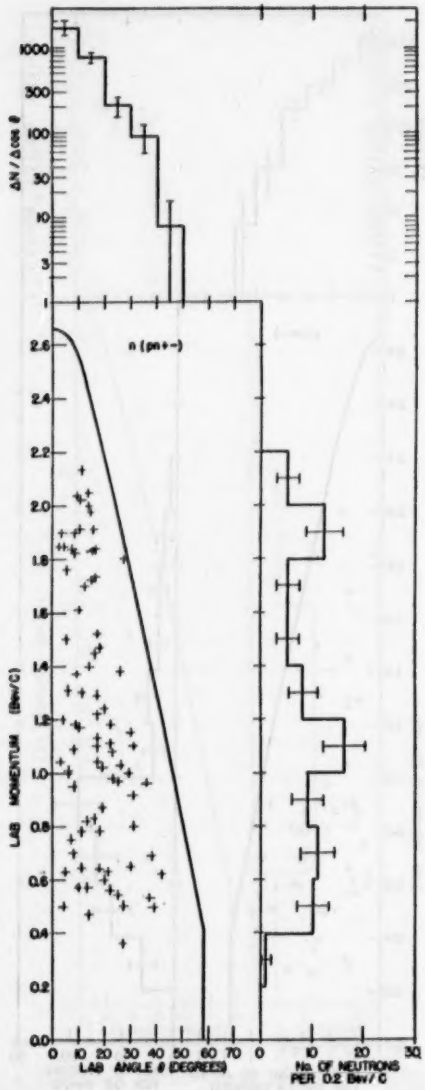

FIG. 8. Laboratory scatter diagram of the neutrons from the reaction $(pn+-)$. At the top the differential angular distribution is plotted for the neutrons in the laboratory system. At the right side their momentum distribution is shown. The curve drawn in the scatter diagram represents the maximum momenta obtainable at different angles for the maximum incident neutron energy of 2.2 Bev. Note the cut-off angle at 58°.

will be negligible, since the net changes are within the statistical errors.

Since these interactions should be similar to those by which the neutron beam is produced in the Cosmotron target, it is of interest to compare these momentum distributions with those inferred for the neutron beam. For 64 nucleons from all 3-prong events with angles of emission $<10°$, the median momentum is 1.35 Bev/c. For 21 nucleons with angles of emission $<5°$ the median momentum is the same, corresponding to a kinetic energy of 0.70 Bev. Since these values do not differ for the two angular intervals considered one might assume that nucleons emitted at very small angles ($<1°$) have similar momenta. A measure of the amount by which the energy of the incident neutrons is degraded into energy of the nucleons emitted forwards from the 3-prong events would be obtained by dividing this inferred value of 0.70 Bev by the median energy of 1.72 Bev of the incident neutrons. One obtains a ratio r of 0.41. The 2.2-Bev circulating proton beam in the Cosmotron is degraded into forward-going neutrons of median energy of 1.72 Bev,[16] or $r=0.78$, which is almost twice as large as the corresponding ratio for events in the cloud chamber. Neutrons in the beam may, however, have been produced by elastic events with $r=1.0$, while these were not counted in the cloud chamber. Yang has estimated that these might comprise 20 percent of the neutrons in the beam.[12] If these elastically produced 2.2-Bev neutrons are removed from the beam spectrum, its energy is lowered and one obtains $r=0.70$ (in place of 0.78) for comparison with the ratio of 0.41 found for 3-prong events.

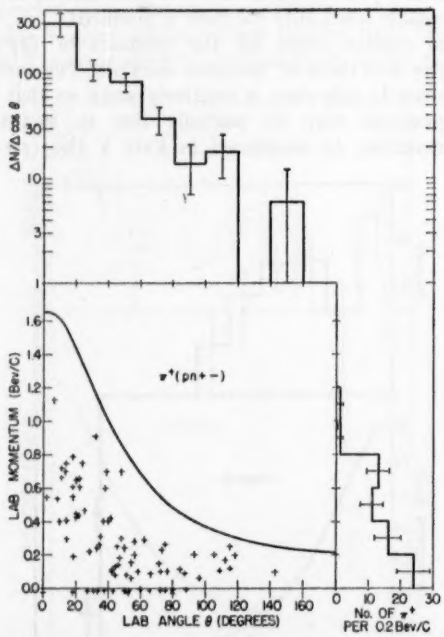

FIG. 9. Laboratory scatter diagram of the π^+ from the reaction $(pn+-)$. At the top the differential angular distribution is plotted for the π^+ in the laboratory system. At the right side their momentum distribution is shown. The curve drawn in the scatter diagram represents the maximum momenta obtainable at different angles for the maximum incident neutron energy of 2.2 Bev. For points plotted under the abscissa the momenta could not be determined.

[16] By analogy with the momenta in Table V one might expect that the protons from the interactions in the Cosmotron target would have slightly *higher* momenta than the neutrons.

This argument indicates that the neutron beam spectrum obtained in this way is biassed in favor of high energies and that there should indeed be neutrons of lower energies (less than 1 Bev) in the incident beam, as was mentioned in Part IV.

One therefore infers that the lack of neutrons with energies less than 1 Bev in Fig. 1 is due to the small cross section for producing 3-prong events at such energies. Thus even the single-meson production cross section for $(pp-)$ events must be small for neutrons of less than 1 Bev. Since above 1 Bev the reactions $(pn+-)$ and $(pp-0)$ appear to be more probable than $(pp-)$ there is evidence in these qualitative arguments that the reaction $(pp-)$ is not very likely at any energy. The evidence is only qualitative, however, and rather indirect, so that this conclusion cannot be considered very definite until confirmed by more direct experiments.

VII. ANGULAR AND MOMENTUM DISTRIBUTIONS IN THE CENTER-OF-MASS SYSTEM

From the velocity and angle of emission of a particle in the laboratory system, one can calculate the corresponding quantities in the center-of-mass system (c.m.s.) if the velocity of the incident neutron is known.

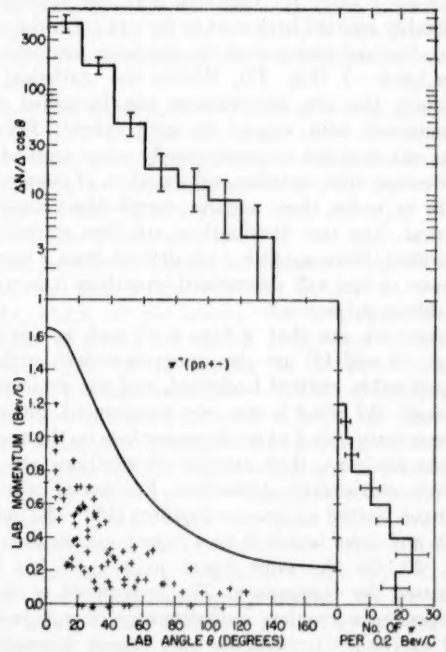

FIG. 10. Laboratory scatter diagram of the π^- from the reaction $(pn+-)$. At the top the differential angular distribution is plotted for the π^- in the laboratory system. At the right side their momentum distribution is shown. The curve drawn in the scatter diagram represents the maximum momenta obtainable at different angles for the maximum incident neutron energy of 2.2 Bev. For points plotted under the abscissa the momenta could not be determined.

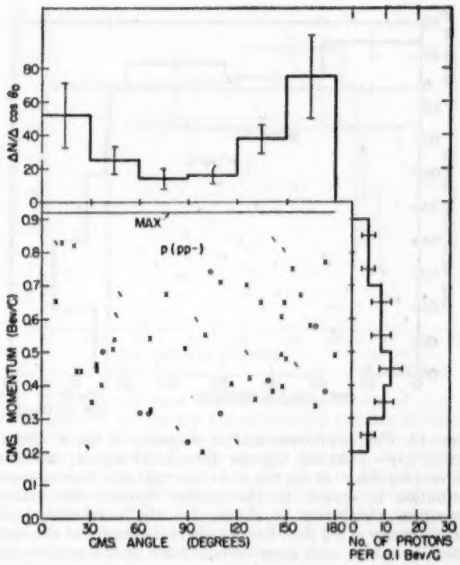

FIG. 11. Center-of-mass scatter diagram of the protons from the reaction $(pp-)$. At the top the differential angular distribution is plotted for the protons in the c.m.s. At the right side their momentum distribution is shown. In the scatter diagram the maximum momentum obtainable is shown for the maximum incident neutron energy of 2.2 Bev. Events where the energy of the incident neutron is known with some certainty are shown as open circles. Where the interpretation of the event is certain but incident energy is less definite vertical crosses (+) are shown. Where the interpretation is less certain oblique crosses (×) are plotted. The least certain events are shown as oblique lines (\).

This transformation is usually quite insensitive to the energy of the incident neutron, since the velocity of the c.m.s. varies quite slowly with this energy. The transformation does become sensitive only when the laboratory velocity of a particle is nearly equal to the velocity of the c.m.s., and simultaneously the laboratory angle of emission is small ($<10°$). The transformation could be carried out with fair certainty for most particles here considered.

Figures 11 to 19 give the c.m.s. scatter diagrams with angular and momentum distributions attached in the same way as in Figs. 2 to 10. The diagrams show the quality of the events in the following manner. Where the energy of the incident neutron could be calculated with some certainty, open circles are shown. (These events had also been used to obtain graph B in Fig. 1.) Where the energy is not known with as good a degree of certainty but the interpretation of the event is certain, vertical crosses (+) are shown. Where the interpretation is less certain oblique crosses (×) are plotted. Finally, the least certain events are shown as oblique lines (\). Particles whose momenta are not known are again indicated below the angle coordinate. Estimates for the angles for these latter particles could be obtained because from the estimated ionization densities of these particles lower velocity

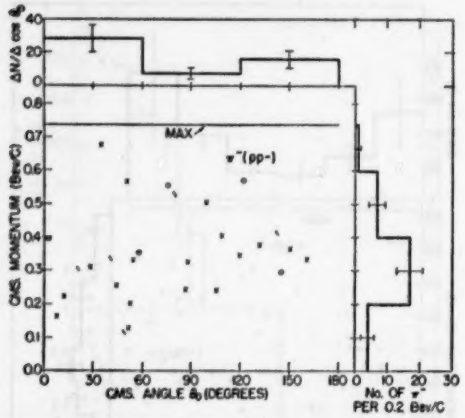

FIG. 12. Center-of-mass scatter diagram of the π^- from the reaction $(pp-)$. At the top the differential angular distribution is plotted for the π^- in the c.m.s. At the right side their momentum distribution is shown. In the scatter diagram the maximum momentum obtainable is shown for the maximum incident neutron energy of 2.2 Bev. Events where the energy of the incident neutron is known with some certainty are shown as open circles. Where the interpretation of the event is certain but incident energy is less definite vertical crosses (+) are shown. Where the interpretation is less certain oblique crosses (×) are plotted. The least certain events are shown as oblique lines (╲).

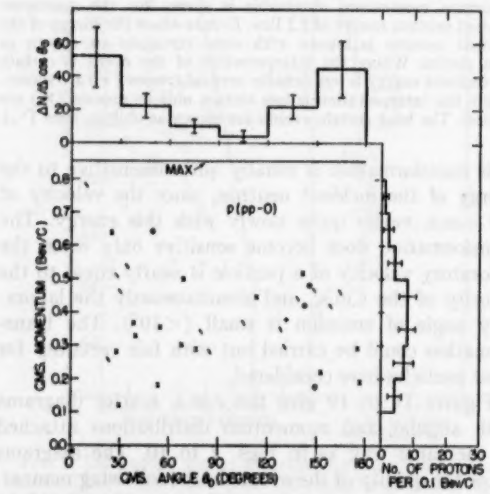

FIG. 13. Center-of-mass scatter diagram of the protons from the reaction $(pp-0)$. At the top the differential angular distribution is plotted for the protons in the c.m.s. At the right side their momentum distribution is shown. In the scatter diagram the maximum momentum obtainable is shown for the maximum incident neutron energy of 2.2 Bev. Events where the energy of the incident neutron is known with some certainty are shown as open circles. Where the interpretation of the event is certain but incident energy is less definite vertical crosses (+) are shown. Where the interpretation is less certain oblique crosses (×) are plotted. The least certain events are shown as oblique lines (╲).

limits could be inferred. Table VI gives the angular distributions numerically.

We shall first discuss the $(pn+-)$ angular distributions which have the best statistics. The distribution

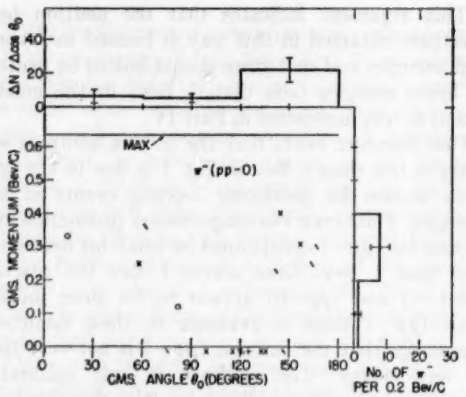

FIG. 14. Center-of-mass scatter diagram of the π^- from the reaction $(pp-0)$. At the top the differential angular distribution is plotted for the π^- in the c.m.s. At the right side their momentum distribution is shown. In the scatter diagram the maximum momentum obtainable is shown for the maximum incident neutron energy of 2.2 Bev. For points plotted under the abscissa the momenta could not be determined. Events where the energy of the incident neutron is known with some certainty are shown as open circles. Where the interpretation of the event is certain but incident energy is less definite vertical crosses (+) are shown. Where the interpretation is less certain oblique crosses (×) are plotted. The least certain events are shown as oblique lines (╲).

$p_a(pn+-)$ (Fig. 16) indicates that the protons are preferably emitted backward in the c.m.s. On the other hand, forward emission of the neutrons predominates in $n_a(pn+-)$ (Fig. 17). Within the statistical uncertainty the two distributions can be called antisymmetrical with respect to each other.[17] Since it turns out that the nucleons usually carry most of the momentum after emission, conservation of momentum tends to make their angular distributions antisymmetrical. The two distributions are thus statistically dependent. Since $n_a(pn+-)$ is derived from a number of more or less well determined quantities it is not as reliable as $p_a(pn+-)$.

Next, we see that $\pi_a^+(pn+-)$ and $\pi_a^-(pn+-)$ (Figs. 18 and 19) are also antisymmetrical, with the π^+ preferably emitted backward, and the π^- forward, although the effect is not very pronounced. Since the mesons carry only $\frac{1}{2}$ as much momentum on the average as the nucleons, their angular distributions are only slightly statistically dependent. For better statistics we have plotted $\pi_a^-(pn+-)$ against $(180°-\theta_0)$ instead of θ_0 and have added it to $\pi_a^+(pn+-)$, as shown in Fig. 20. On the same figure $p_a(pn+-)$ has been replotted for comparison. The hypothesis of charge independence requires antisymmetry of $\pi_a^+(pn+-)$ and $\pi_a^-(pn+-)$. (Actually only charge symmetry is required for this conclusion.) Antisymmetry of $p_a(pn+-)$ and $n_a(pn+-)$ would also be required on the basis of charge independence, but this feature

[17] By "antisymmetrical" we mean that the value of the first distribution at angle θ_0 is equal to that of the second at $(180° - \theta_0)$.

TABLE VI. Number of particles (ΔN) in each of 3 angular intervals in the center-of-mass system.

	0–60°	60–120°	120–180°
$p(pp-)$	17	16	24
$\pi^-(pp-)$	14	7	8
$p(pp-0)$	16	7	15
$\pi^-(pp-0)$	3	5	12
$\pi^0(pp-0)$	1	4	13
$p(pn+-)$	15	25	39
$n(pn+-)$	33	27	21
$\pi^+(pn+-)$	22	34	35
$\pi^-(pn+-)$	33	39	18
$\pi^-(pp-)$, reclassified	10	7	7
$\pi^-(pp-0)$, reclassified	11	7	10
$\pi^+(pn+-)$, reclassified	23	31	34
$\pi^-(pn+-)$, reclassified	29	37	21

would be expected for purely kinematic reasons, as mentioned above.

While the forward and backward asymmetries for $\pi_a^-(pn+-)$ and $\pi_a^+(pn+-)$, respectively, are not very pronounced, the differential cross section for emitting pions sideways (near 90°) definitely appears to be relatively low.

The distribution $\pi_a^-(pp-)$ appears to be peaked in the forward direction, although the statistical uncertainty is large and the classification of some of the events is uncertain. In that case $p_a(pp-)$ would have to be somewhat peaked backwards to balance the forward momenta of the π^-. This is also indicated. Again both distributions have few particles emitted sideways.

The distribution $p_a(pp-0)$ appears to be symmetrical (with itself) as expected, since here two identical nucleons are emitted which have to conserve most of the momentum, as previously mentioned. $\pi_a^-(pp-0)$ and $\pi_a^0(pp-0)$ are quite different from the other meson distributions inasmuch as both are very strongly peaked backward. Charge independence requires antisymmetry with $\pi_a^+(nn+0)$ and $\pi_a^0(nn+0)$, respectively, which are not known. But one might like to consider a model for double production of mesons where $\pi^-(pp-0)$ is similar to $\pi^-(pn+-)$, and $\pi^0(pp-0)$ is similar to $\pi^+(pn+-)$. Most of the $(pp-0)$ events are difficult to classify (Table III) and the above assumption provides an alternative basis for classifying the $(pp-0)$ events which may be preferable. We shall therefore try to reclassify a number of the "probable" events which are least certain so that consistent distributions are obtained. Table III shows that 11 of the $(pp-)$ events, 22 of the $(pp-0)$, and 12 of $(pn+-)$ are listed as "probable." We are essentially trying to lose backward π^- and to gain forward π^- for the distribution $\pi_a^-(pp-0)$. There are nine $(pp-0)$ events with backward π^-, which could also be $(pn+-)$, and two such events, which could also be $(pp-)$. Next, there are four $(pn+-)$ and four $(pp-)$ events with forward π^-, which could be $(pp-0)$. Transferring all of these events would change the forward-to-sideward-to-backward ratio of $\pi_a^-(pp-0)$

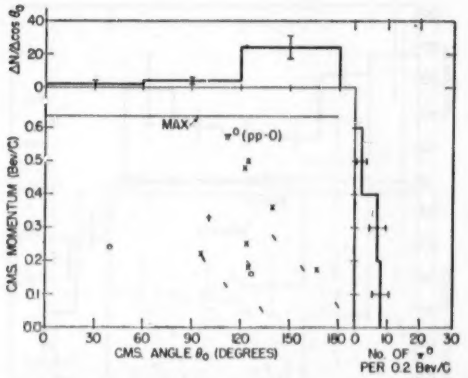

FIG. 15. Center-of-mass scatter diagram of the π^0 from the reaction $(pp-0)$. At the top the differential angular distribution is plotted for the π^0 in the c.m.s. At the right side their momentum distribution is shown. In the scatter diagram the maximum momentum obtainable is shown for the maximum incident neutron energy of 2.2 Bev. Events where the energy of the incident neutron is known with some certainty are shown as open circles. Where the interpretation of the event is certain but incident energy is less definite vertical crosses (+) are shown. Where the interpretation is less certain oblique crosses (×) are plotted. The least certain events are shown as oblique lines (╲).

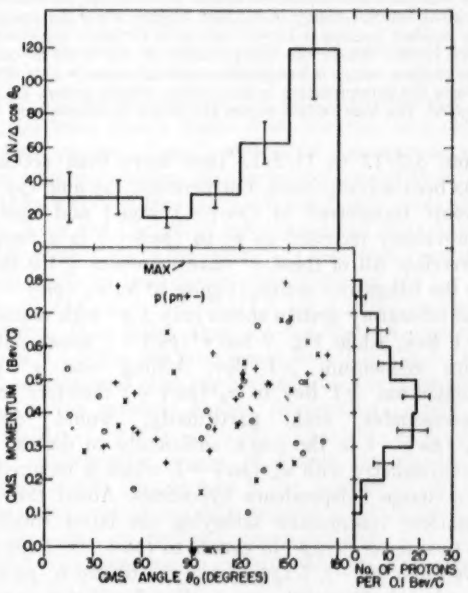

FIG. 16. Center-of-mass scatter diagram of the protons from the reaction $(pn+-)$. At the top the differential angular distribution is plotted for the protons in the c.m.s. At the right side their momentum distribution is shown. In the scatter diagram the maximum momentum obtainable is shown for the maximum incident neutron energy of 2.2 Bev. For points plotted under the abscissa the momenta could not be determined. Events where the energy of the incident neutron is known with some certainty are shown as open circles. Where the interpretation of the event is certain but incident energy is less definite vertical crosses (+) are shown. Where the interpretation is less certain oblique crosses (×) are plotted. The least certain events are shown as oblique lines (╲).

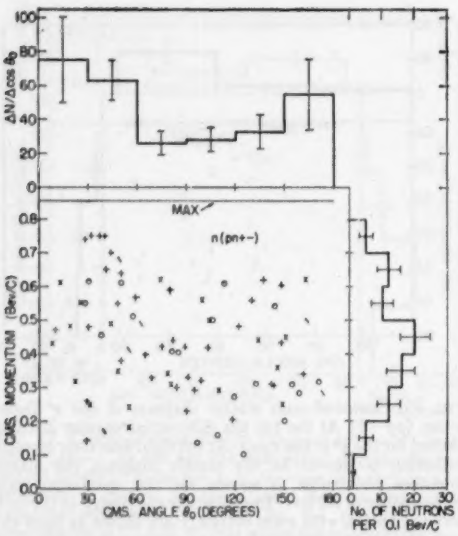

FIG. 17. Center-of-mass scatter diagram of the neutrons from the reaction $(pn+-)$. At the top the differential angular distribution is plotted for the neutrons in the c.m.s. At the right side their momentum distribution is shown. In the scatter diagram the maximum momentum obtainable is shown for the maximum incident neutron energy of 2.2 Bev. Events where the energy of the incident neutron is known with some certainty are shown as open circles. Where the interpretation of the event is certain but incident energy is less definite vertical crosses (+) are shown. Where the interpretation is less certain oblique crosses (×) are plotted. The least certain events are shown as oblique lines (\).

from 3/5/12 to 11/5/1. Thus more than necessary has been accomplished. Furthermore, the nine $(pp-0)$ events transferred to $(pn+-)$ would add nine π^+ (previously recorded as p) to $(pn+-)$ in a forward direction. All of these π^+ have momenta ≥ 1.0 Bev/c in the laboratory system. Figure 10 for $\pi_a^-(pn+-)$ in the laboratory system shows only 3 π^- with momenta >1 Bev, while Fig. 9 for $\pi^+(pn+-)$ shows only 1 with momentum ≥ 1 Bev. Adding nine π^+ with momentum ≥ 1 Bev to $\pi_a^+(pn+-)$ therefore seems unreasonable and, particularly, would distort $\pi_a^+(pn+-)$ in the c.m.s. sufficiently to destroy the antisymmetry with $\pi_a^-(pn+-)$, which is required by the charge independence hypothesis. About the only sufficient compromise satisfying the latter condition is to transfer 3 $(pp-0)$ events to $(pn+-)$, 2 $(pp-0)$ events to $(pp-)$, 7 $(pp-)$ to $(pp-0)$ and 6 $(pn+-)$ to $(pp-0)$. Five of the events then classified as $(pp-0)$ are quite uncertain, however, and it seems wisest to discard them now as "unanalyzable." The resulting "reclassified" meson distributions are given in the last 4 rows of Table VI.

One sees that a reasonable distribution for $\pi_a^-(pp-0)$ has been obtained with negligible effect on the other meson distributions. The effect on the nucleon distributions has also been negligible.

$\pi_a^0(pp-0)$ has not been redetermined since the result is uncertain because of the indefiniteness of the $(pp-0)$ events and the difficulty of determining the angles of neutral particles.

Having omitted 5 of the least definite from our original 154 events we are now left with 24 $(pp-)$, 30 $(pp-0)$, and 95 $(pn+-)$, in the reclassified events. These agree with the original numbers given in Table III within statistics, but may be a better estimate of the true frequencies of interactions leading to $(pp-)$, $(pp-0)$, and $(pn+-)$. This reclassification uses assumptions suggested by charge independence in addition to conservation of energy and momentum for determining the more doubtful events, but some uncertainties still remain.

VIII. COMPARISON WITH THEORY

Theoretical treatments of meson production at high energies have been given by several authors. Heitler and Janossy[5] predict no multiplicities >1 in nucleon-nucleon collisions, Heisenberg and Lewis *et al.*[18] predict multiplicities >1 at energies rather higher than those considered in this experiment. Fermi[6] assumes that the interactions taking part in meson production are so strong that complete thermal equilibrium is obtained before mesons are emitted. Thus it is assumed that energy is distributed statistically between the emitted particles. The interaction volume is given a radius equal to the meson Compton wavelength, but is

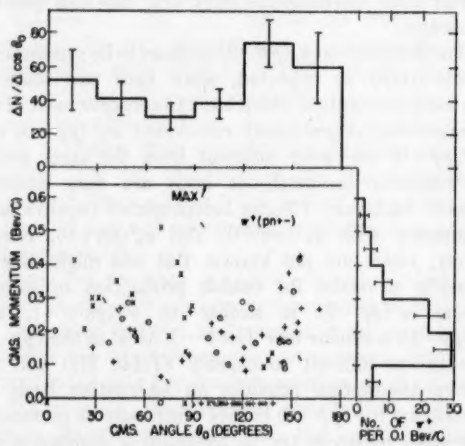

FIG. 18. Center-of-mass scatter diagram of the π^+ from the reaction $(pn+-)$. At the top the differential angular distribution is plotted for the π^+ in the c.m.s. At the right side their momentum distribution is shown. In the scatter diagram the maximum momentum obtainable is shown for the maximum incident neutron energy of 2.2 Bev. For points plotted under the abscissa the momenta could not be determined. Events where the energy of the incident neutron is known with some certainty are shown as open circles. Where the interpretation of the event is certain but incident energy is less definite vertical crosses (+) are shown. Where the interpretation is less certain oblique crosses (×) are plotted. The least certain events are shown as oblique lines (\).

[18] W. Heisenberg, Z. Physik **113**, 61 (1939); Nature **164**, 65 (1949); Z. Physik **126**, 569 (1949); Lewis, Oppenheimer, and Wouthuysen, Phys. Rev. **73**, 127 (1948).

contracted by the Lorenz transformation. The numbers of available states in phase space that conserve momentum and energy can then be calculated, resulting in relative multiplicities and momentum distributions for the emitted particles. Assuming charge independence Fermi[19] has also calculated the weights for the different charge distributions within each multiplicity state. [This gives, for example, the probabilities of $(pp-)$, $(pn0)$, and $(nn+)$, for single production.] Throughout the theory the probabilities are taken to be proportional to the squares of the individual matrix elements, so that no interference effects are considered. As pointed out to us by Dalitz,[20] if, for instance, the reactions $(pn+-)$ and $(pp-0)$ were to proceed only through certain isotopic spin states and not through all possible ones, different relative occurrences of $(pn+-)$ and $(pn-0)$ would be possible.[21]

Furthermore, angular momentum states are neglected, although Fermi[6] shows that they would have a small effect on the relative multiplicities. The experimental angular distributions discussed in the previous section might be analyzed in terms of emission in s and p states, but since higher angular momenta can also be involved, it does not seem appropriate.

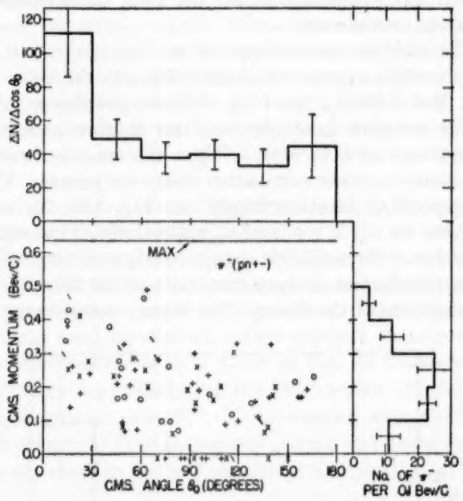

FIG. 19. Center-of-mass scatter diagram of the π^- from the reaction $(pn+-)$. At the top the differential angular distribution is plotted for the π^- in the c.m.s. At the right side their momentum distribution is shown. In the scatter diagram the maximum momentum obtainable is shown for the maximum incident neutron energy of 2.2 Bev. For points plotted under the abscissa the momenta could not be determined. Events where the energy of the incident neutron is known with some certainty are shown as open circles. Where the interpretation of the event is certain but incident neutron energy is less definite vertical crosses (+) are shown. Where the interpretation is less certain oblique crosses (×) are plotted. The least certain events are shown as oblique lines (\).

[19] E. Fermi, Phys. Rev. **92**, 452 (1953); **93**, 1434 (1954).

[20] R. H. Dalitz (private communication).

[21] For general charge-independence restrictions see, for example K. M. Watson, Phys. Rev. **85**, 852 (1952); and Van Hove, Marshak, and Pais, Phys. Rev. **88**, 1211 (1952).

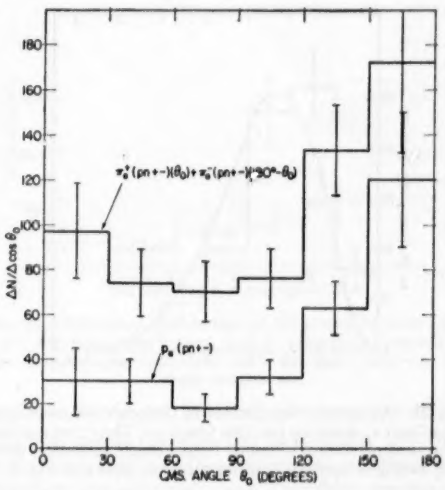

FIG. 20. Differential angular distribution in the center-of-mass system of the π mesons and protons from the reaction $(pn+-)$. For better statistics the π^- distribution has been plotted against 180° minus the c.m.s. angle θ_0 and added to the π^+ distribution.

Detailed predictions could be made only if specific information on angular momentum, spin, and isotopic spin states were available from some meson theory applicable here. In the absence of such a detailed theory any deviations from the general predictions of the statistical theory might point the way to a more detailed picture. Fermi's analytical expressions are valid either for classical or for relativistic energies of the particles involved. Neither case is completely applicable here. Yang and Christian[22] have calculated what would be the predictions of the theory at Cosmotron energies. Their result for the relative probabilities of $(pn+-)$: $(pp-0)$: $(pp-)$ is $\sim 3.3:1:12.2$ for 2.2-Bev incident neutrons. One infers that at our median neutron energy of 1.7 Bev this ratio would be $\sim 3.3:1:20.5$. Our best experimental ratio as obtained from the considerations in the previous section (reclassified events) is $95:30:24=(3.2\pm0.7):(1\pm0.35):(0.8\pm0.3)$, where the given uncertainties consist of double the statistical standard errors (square root of the number of events) to take account of the uncertainties in identification. One sees that, in the reactions studied here, the ratio of double to single meson production is about 20 times

[22] C. N. Yang and R. Christian, Brookhaven Internal Report. Their procedure consists of numerical evaluation of the expression

$$P_n(p)dp = p^2dp \int \delta(\mathbf{p}+\mathbf{p}_1+\cdots+\mathbf{p}_{n+1}) \times \delta(E+E_1+\cdots+E_{n+1}-W)\mathbf{dp}_1\mathbf{dp}_2\cdots\mathbf{dp}_{n+1},$$

where $P_n(p)$ is proportional to the number of mesons emitted with c.m.s. momentum p if n mesons are produced. $\mathbf{p},\mathbf{p}_1\cdots\mathbf{p}_{n+1}$, $E,E_1\cdots E_{n+1}$ are the momentum vectors and energies, respectively, of the $(n+2)$ outgoing particles, and W is the total energy in the c.m.s. The two δ functions under the integral represent surfaces in phase space introduced by the conditions of momentum and energy conservation.

The relative probability for emission of n mesons is given by $f_n=(\Omega^n/n!\hbar^{3n})\int P_n(p)dp$, where Ω is the volume of a sphere of radius $\hbar/\mu c$, contracted relativistically by a factor $2/W$.

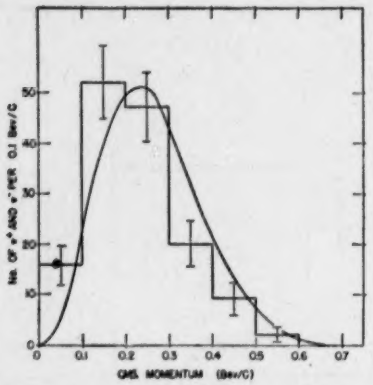

FIG. 21. Momentum distribution in the center-of-mass system of the π^+ and π^- from the reaction $(pn+-)$. The curve represents a theoretical prediction obtained from Fermi's statistical theory, having averaged over our neutron spectrum shown in Fig. 1.

as great as is predicted by the theory. On the other hand, the relative charge distribution for double production alone, as given by the ratio $(pn+-)$: $(pp-0)$, agrees very well with the predicted value. This good agreement is certainly much better than the agreement for the relative multiplicities, but it may be partially fortuitous.

Fermi's treatment[19] of charge independence gives for the relative cross sections for $(pp-)$:$(pn0)$:$(nn+)$ the ratio 1:1.5:1, and for $(pn+-)$:$(pp-0)$:$(nn+0)$:$(pn00)$ the ratio 3.3:1:1:1. From our experimental ratio of 4:1 for $(pn+-)$:$(pp-)$ we then would have for the ratio of the cross section for all double meson production, σ_2, to that for all single meson production σ_1 the value $\sigma_2/\sigma_1=2.2$, while the statistical model predicts $\sigma_2/\sigma_1=1/11$.

The energy dependence of the meson multiplicity seems to be less than expected. According to the statistical theory the ratio σ_2/σ_1 should increase by a factor of about 3 in passing from an incident energy of 1.4 Bev to 2.0 Bev. The experimental results shown in Table IV, however, indicate little change in the σ_2/σ_1 ratio. This conclusion is not certain, however, because the number of cases in each energy group is small and the determinations of incident neutron energy are indirect.

A further prediction of the theory is that only 0.6 percent of all collisions should result in triple production of mesons, or that only one five-prong event $(pp--+)$ should be observed in 300 three-prong events. This prediction follows from the small amount of phase space available for emission of 3 mesons. The fact that we have observed no five-prong events attributable to an n-p collision as against 182 three-prong events certainly agrees with this prediction. This fact makes it difficult to account for the frequent double meson production by effects which would also increase triple meson production, as, for example, by changing the size of the region in which the equilibrium of the statistical theory is reached, or by using the attraction between final state nucleons[15] to enhance multiple meson production.

Since explicit predictions of the statistical theory concerning angular distributions are not available, no comparison can be made. It seems unlikely, however, that these would involve asymmetry about 90° in the c.m.s. as seems to be shown in the experimental distributions.

Yang and Christian[22] have also calculated momentum distributions for the emitted mesons. These have been averaged over our neutron energy spectrum (graph B, Fig. 1) and reproduced in Fig. 21, together with the experimental distributions $\pi_m^+(pn+-)$ and $\pi_m^-(pn+-)$ added together. (As mentioned before, these two distributions are fairly independent kinematically because most of the momentum is carried by the nucleons.) One sees that fair agreement is obtained, although some experimental shift toward lower momenta may be indicated. Yuan and Lindenbaum have observed similar c.m.s. spectra for pions from the Cosmotron target.[23] They have interpreted the spectra and positive excess as evidence that multiple pion production predominates at 2.2 Bev, in agreement with our conclusions.

The median momentum of $\pi_m^+(pn+-)$ is 0.21 Bev/c, which agrees within statistics with the value of 0.22 Bev/c for $\pi_m^-(pn+-)$. For the protons as well as the neutrons from $(pn+-)$ one obtains a median momentum of 0.43 Bev/c. Thus the nucleons carry considerably more momentum than the mesons. The corresponding kinetic energies are 112, 120, 95, and 95 Mev for π^+, π^-, p, and n, respectively. Thus equipartition of the available energy is indicated for double meson production, in agreement with one of the original assumptions of the theory. The mean meson energy is

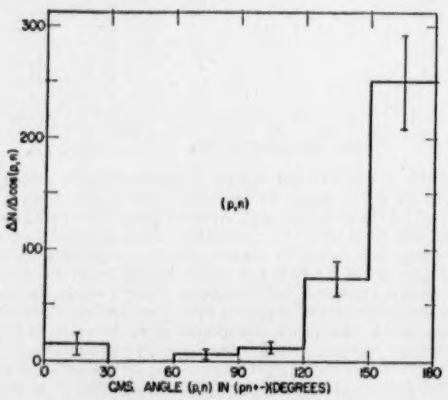

FIG. 22. Differential distribution of the angles between proton and neutron directions in the center-of-mass system, from the reaction $(pn+-)$.

[22] L. C. L. Yuan and S. J. Lindebaum, Phys. Rev. **93**, 1431 (1954).

expected to be higher than the mean nucleon energy, since the meson energy is somewhat relativistic. (Adding all of these energies to twice the rest energy of the meson one obtains 700 Mev, in sufficient agreement with the energy of 720 Mev available in a collision of a neutron of median energy of 1.72 Bev with a proton. Since the energies of neutral particles have been calculated from energy and momentum balance, this serves to check the consistency of the calculations. The two energy values were obtained as the result of very different averaging procedures so that some discrepancy is quite expected.)

The distribution $\pi_m^-(pp-)$ is statistically too poor to compare with any theoretical predictions. The median momentum of the π^- from $(pp-)$ is 0.33 Bev/c.

IX. DISTRIBUTIONS OF THE ANGLES BETWEEN INDIVIDUAL PARTICLES

We have seen that the only serious disagreement between the statistical theory and experiment is the large experimental preference for double meson production. In addition the apparent asymmetry of the c.m.s. angular distributions seems inconsistent with the ideas of the purely statistical theory. Perhaps these observations indicate that the interactions are really determined by certain specific forces between the particles or by certain specific intermediate states, rather than by statistical considerations. In order to investigate these possibilities and to gain more insight into the processes at hand we have calculated angles between individual particles (p,n), (π^+,π^-), (p,π^+), (p,π^-), (n,π^-), and (n,π^+) emitted in the reaction $(pn+-)$. The results are given in Figs. 22 to 25, and in Table VII.

The distribution (p,n) shown in Fig. 22 can be explained merely by kinematics. Since the nucleons carry most of the momentum they are also mostly responsible for conserving momentum. Thus usually a neutron must be emitted rather opposite to a proton. The distribution (π^+,π^-) given in Fig. 23 shows some preference for emission of the two mesons at relative angles greater than 90°. If the mesons were emitted independently (and isotropically) from an infinite mass, the distribution (π^+,π^-) should be independent of the relative angle. Since, however, the mesons carry an average of about one-half the momentum carried by the nucleons they are also somewhat responsible for momentum conservation, and therefore emission at relative angles $>90°$ should be somewhat prevalent for kinematic reasons. This qualitative agreement with a purely statistical picture, however, suggests no particularly strong interaction between the mesons produced in the n-p collisions. If this interaction were very attractive the mesons should have a greater tendency to be emitted at relative (π^+,π^-) angles $<90°$, and if the interaction were very repulsive they should more often be emitted in opposite directions. Whether this means that mesons are not strongly coupled to mesons or that the presence of the two nucleons interferes sufficiently to prevent any obvious effects due to meson-meson interaction remains to be seen.

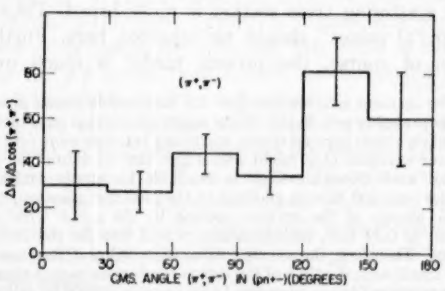

FIG. 23. Differential distribution of the angles between π^+ and π^- directions in the center-of-mass system, from the reaction $(pn+-)$.

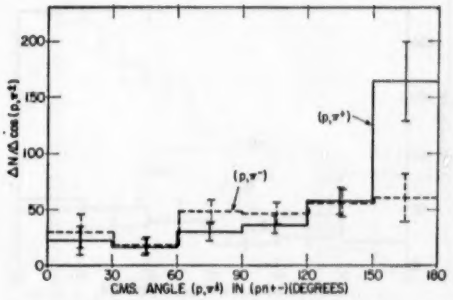

FIG. 24. Differential distribution of the angles between proton and π^+ directions, and proton and π^- directions, respectively, in the center-of-mass system, from the reaction $(pn+-)$.

That such an interference effect may indeed exist is indicated by Fig. 24, showing the distributions of the angles for (p,π^+) and (p,π^-). One sees that these two distributions differ from each other inasmuch as there appears to exist some preference for the π^+ to be emitted opposite the p, while no such preference beyond what might be expected purely statistically exists for the π^- relative to the p. The distribution (p,π^+) is all the more surprising because, as shown previously, both the p and the π^+ tend to be emitted backward in the c.m.s. Yet, by considering individual events in the present manner, we obtain the additional tendency for p and π^+ to be emitted in opposite directions. Charge independence requires that the distribution of the angles for (n,π^-), compared with that for (n,π^+), show the same preference for large angles as that for (p,π^+) when compared with (p,π^-). This is not evident from Fig. 25. However, one must remember that the momenta and angles for the neutrons were all derived from those for the charged particles. Therefore, the neutron angles are usually not very well known, except for the selected events where the momenta and angles of the charged particles are fairly well determined. Table VII gives the distributions con-

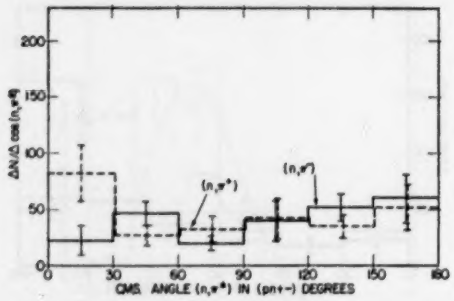

FIG. 25. Differential distribution of the angles between neutron and π^+ directions, and neutron and π^- directions, respectively, in the center-of-mass system, from the reaction $(pn+-)$.

sidered here for these selected events only. One sees that here the distributions for (n,π^-), (n,π^+) agree within statistics with the distributions (p,π^+), (p,π^-), respectively.

The present experiment is not good enough to ascertain that the effect discussed in the previous paragraph is not just due to some experimental systematic error or statistical fluctuation. Therefore deductions based on it are highly speculative until the experimental facts have been determined with greater certainty. If taken at face value, however, it would appear to indicate a strong pion-nucleon interaction or intermediate state in which pion and nucleon were combined. Observations on pion-nucleon scattering have given evidence for strong interaction in a state with angular momentum of $\frac{3}{2}$ and isotopic spin of $\frac{3}{2}$.[1] Such a state can be considered as an excited nucleon or compound state of the pion-nucleon system with an energy about 160 Mev (corresponding to the maximum cross section observed for π^+ with energies near 200-Mev laboratory energy scattered by protons) above the sum of nucleon and pion rest energies. One might imagine that pion production proceeds through such an intermediate state and that for double meson production two such excited nucleons are produced which separate by a distance of perhaps up to one nucleon diameter before each decays to nucleon and pion, thus often decaying almost freely. Peaslee has considered the consequences of such intermediate states for pion multiplicities, assuming charge independence.[24]

We can account for the angular correlations observed for the reaction $(pn+-)$ if the original proton then assumes the intermediate state of a doubly charged positive particle ("isobar" with charge component $+\frac{3}{2}$) which subsequently decays into a proton and a π^+, while the original neutron in its intermediate state becomes a singly charged negative particle (charge component $-\frac{3}{2}$) which decays into a neutron and a π^-. Both p and π^+ should then show a tendency to be emitted into the same hemisphere, while n and π^- should both be emitted into the opposite hemisphere. This agrees with the experiment (Figs. 16–19). Furthermore, if the excitation energies are high enough the observed average angles between n and π^-, and p and π^+, respectively, can be large, while the average angles between n and π^+, and p and π^-, respectively, may be smaller, the latter angles being determined only by statistical correlation between the decay planes of (n,π^-) and (p,π^+). This also agrees with some of the observations (Fig. 24, Table VII). As a matter of fact, considering that the observed large probability for double meson production may result from the possible resonance of the excited states one may say that this model fits all of the qualitative experimental features quite strikingly.

Peaslee deduces from this experiment that $\sigma_1 \approx \sigma_2$ at our energies. He also shows that in this model the cross section for the reaction $(pp-)$ is only $\frac{1}{4}$ of the single meson production cross section σ_1. This might help to explain the lack of $(pp-)$ events caused by low-energy neutrons noted in Part IV.[25]

An attempt was made to detect excitation energies for the nucleons in the intermediate states by calculating "Q values" for the combinations (n,π^-), (n,π^+), (p,π^+), and (p,π^-), in a manner identical to that used for calculating "Q values" for heavy unstable particles. The results are given in Figs. 26 and 27 and, for the selected events, in Table VIII. One might expect that the calculated "Q values" for (p,π^+) and (n,π^-) would be grouped around 160 Mev if the present model is valid, while the values for (p,π^-) and (n,π^+) should show no such grouping. No obvious differences are observed in the Q distributions, within the experimental uncertainties, but perhaps one should not expect any very definite indications. The observed maximum in the π^+-p scattering cross section is quite broad. Thus no sharp "Q values" should be expected here. Furthermore, of course, the present model is much over-

TABLE VII. Relative distributions of c.m. angles (n,π^-) and (n,π^+), and (p,π^+) and (p,π^-), respectively, obtained from selected $(pn+-)$ cases only. Actual numbers of cases observed are given.

	0°–60°	60°–120°	120°–180°
$(n,\pi^-)/(n,\pi^+)$	3/7	6/6	8/4
$(p,\pi^+)/(p,\pi^-)$	2/5	5/8	11/5

[24] D. C. Peaslee, Phys. Rev. 95, 717 (1954).

[25] For incident neutron energies <1 Bev double meson production is probably not likely, while single production may not be very likely either because elastic scattering becomes more probable at lower energies. One might also argue that σ_1 cannot be substantial until enough energy is available to supply excitation energies near 160 Mev in addition to the pion rest mass and some kinetic energy of the excited nucleon in the c.m.s. This may amount to 0.34 Bev, corresponding to 0.75 Bev for the incident nucleon. Therefore, the average value of σ_1 below 1 Bev may be fairly small, and, if only $\frac{1}{4}$ of the meson production events resulted in the reaction $(pp-)$, very few $(pp-)$ events should be expected below 1 Bev unless most incident neutrons have low energies. The fact that no $(pp-)$ cases were observed below 1 Bev, therefore, would not constitute a particular discrepancy any longer.

simplified, since states with isotopic spins other than $\frac{3}{2}$ are probably also possible and since the excited nucleons probably cannot travel far enough during their lifetime to enable them to decay as completely free particles. In addition, uncertainties in measured momenta and angles might lead to errors in the calculated "Q values." For these reasons any existing specific excitation energies would be much obscured.

X. COMPARISON WITH A PRELIMINARY p-p SCATTERING RESULT

For further comparison of the discussed models for meson production it may be of interest to state a preliminary result on p-p interactions obtained under similar conditions. Here a beam of 1.5-Bev protons was allowed to enter the hydrogen-filled cloud chamber.

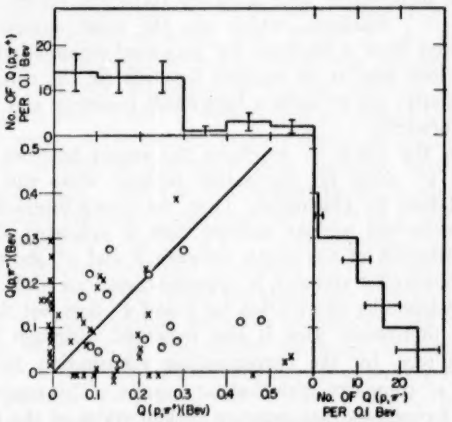

FIG. 26. Scatter diagram of "Q values" obtained for protons and π^+, and protons and π^-, respectively, from the reaction $(pn+-)$. At the top of the scatter diagram the distribution of "Q values" for protons and π^+ is given, while at the right side the distribution of "Q values" for protons and π^- is plotted. Open circles represent the energetically most certain events while oblique crosses (✖) are indicated for the less certain events. Where "Q values" could be determined only for either proton and π^+ or proton and π^- alone, these are indicated under the abscissa or to the left of the ordinate, respectively.

The result to be considered is that out of 160 interactions in the gas only two resulted in 4 outgoing prongs to be interpreted as due to the reaction $p+p\rightarrow p+p+\pi^++\pi^-$, $(pp+-)$. Unless the reaction $(pp+-)$ is specifically excluded, this seems to indicate that for p-p interactions double meson production is much less likely than for n-p collisions.

Fermi's statistical model[6,13,22] predicts that for 1.5-Bev protons incident on protons the reaction $(pp+-)$ should occur in 1 to 2 percent of all interactions. This would agree with the stated result. However, for n-p collisions we had found that double meson production is more than 20 times larger than predicted by the Fermi model.

From Fermi's weights for the different neutron-proton reactions within each state of meson multiplicity

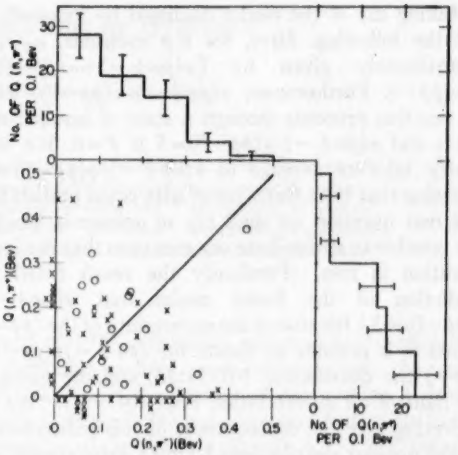

FIG. 27. Scatter diagram of "Q values" obtained for neutrons and π^- and neutrons and π^+, respectively, from the reaction $(pn+-)$. At the top of the scatter diagram the distribution of "Q values" for neutrons and π^- is given, while at the right side the distribution of "Q values" for neutrons and π^+ is plotted. Open circles represent the energetically most certain events while oblique crosses (✖) are indicated for the less certain events. Where "Q values" could be determined only for either neutron and π^- or neutron and π^+ alone, these are indicated under the abscissa or to the left of the ordinate, respectively.

one expects for the ratio of the cross section for double meson production to that for single meson production the relation $\sigma_2/\sigma_1=[\sigma(pn+-)+\sigma(pp-0)]/2.3\sigma(pp-)$. From our experiment we obtain $\sigma_2/\sigma_1=2.2$ for incident neutrons with median energy of $\sim$1.7 Bev, while the Fermi model predicts $\sigma_2/\sigma_1=0.09$. This discrepancy has been discussed in Part VIII. If the cross sections for p-p collisions are assumed to be the same as those for n-p collisions, as is indicated experimentally,[13] we would expect that for 1.5-Bev protons σ_2/σ_1 might be $\approx$1.8, having made allowance for the theoretical energy dependence of the relative multiplicities.

Out of the 160 p-p interactions as many as 70 may be elastic, leaving 90 interactions resulting in meson production. From the assumed ratio $\sigma_2/\sigma_1=1.8$ it follows that 58 events should have resulted in double meson production. Since furthermore, from Fermi's treatment of charge independence, $\sigma(pp+-)/\sigma_2=0.3$ we should have observed 17 $(pp+-)$ events, instead of 2, in the p-p experiment, if Fermi's treatment of charge independence is to apply consistently to n-p and p-p collisions.

TABLE VIII. Distributions of "Q values" for the combinations (n,π^-), (n,π^+), (p,π^+), and (p,π^-) for $(pn+-)$, for selected events alone.

Q value (Bev)	0–0.1	0.1–0.2	0.2–0.3	0.3–0.4	0.4–0.5
(n,π^-)	6	7	2	1	1
(n,π^+)	7	4	4	2	0
(p,π^+)	3	5	5	1	2
(p,π^-)	7	5	4	0	0

Making use of the model discussed by Peaslee[34] we find the following. Here, for n-p collisions, σ_2/σ_1 is approximately given by $[\sigma(pn+-)+\sigma(pp-0)]/4.8\sigma(pp-)$. Furthermore, $\sigma(pn+-)/\sigma(pp-0)=41$ if the reaction proceeds through a state of isotopic spin $T=1$, and $\sigma(pn+-)/\sigma(pp-0)=5$ if $T=0$. We shall merely take an average of $\sigma(np+-)/\sigma(pp-0)=11$ assuming that both states occur with equal probability. The first question we shall try to answer is whether it is possible to redistribute our events so that the latter condition is met. (Previously the result fitted the prediction of the Fermi model that $\sigma(np+-)/\sigma(pp-0)\approx 3$.) Because of the uncertainty of the $(pp-0)$ events it is possible to obtain for $(pn+-):(pp-0):(pp-)$ the distribution 107:14:33, and, by going to the limit of all uncertainties, even 104:9:41. (We are neglecting here the consequences of this redistribution on the angular distributions.) Thus a ratio $\sigma(pn+-)/\sigma(pp-0)\approx 10$ is experimentally not impossible in agreement with the theoretical ratio for the present model. From the given numbers for the n-p experiment we now obtain $\sigma_2/\sigma_1\approx 0.7$ at 1.7 Bev, or $\sigma_2/\sigma_1\approx 0.55$ at 1.5 Bev, allowing for a theoretical energy dependence of σ_2/σ_1. Using this for a prediction for the p-p experiment we obtain the result that 32 out of the 90 inelastic p-p events should have resulted in double meson production.

Finally, for the model under consideration one should have $\sigma(pp+-)/\sigma_2=0.2$. Therefore, for this model about six $(pp+-)$ events should have been observed in the p-p experiment, if consistency with the n-p experiment is postulated. The disagreement with the 2 events actually found is not bad, and this might perhaps be taken as further evidence in support of the discussed model.

XI. SUMMARY OF CONCLUSIONS

The following conclusions have been drawn from an analysis of 154 three-prong events due to n-p interactions with incident neutron energy in the range 1.0 to 2.2 Bev (median energy 1.7 Bev):

The ratio of double meson production to single meson production is about 20 times as great as predicted by Fermi's statistical theory. For example, the experimental ratio of $(pn+-)$ to $(pp-)$ is $(3.2\pm 0.7)/(0.8\pm 0.3)$, while the ratio from the statistical theory is 3.3/20.5. On the other hand no $(pp--+)$ events were found, so that triple meson production is probably negligible, as predicted by the statistical theory. These facts suggest that some "resonance" interaction may lead to double production of mesons. Indirect evidence suggests that the cross section for $(pp-)$ is quite low at energies below 1 Bev as well.

The experimental ratio of $(pn+-)$ to $(pp-0)$ is $(3.2\pm 0.7)/(1\pm 0.35)$, however, which agrees well with the statistical theory prediction of 3.3/1 based on an application of the hypothesis of charge independence. Similarly the momentum distributions found for π^- and π^+ from $(pn+-)$ events agree with the theory fairly well.

The angular distributions of the emitted particles show rather definite asymmetries (in the c.m.s.) which seem inconsistent with a purely statistical theory. In $(pn+-)$ reactions, which are the most numerous, protons show a tendency for backward emission while neutrons tend to be emitted forwards (in the c.m.s.). Similarly, the π^+ have a backwards tendency and the π^- forwards.

In the $(pn+-)$ reactions the angles between π^+ and π^- show no correlation beyond what can be explained by kinematics. Thus, no strong interaction between the mesons emitted here is indicated. The distribution of the angles between p and π^+ shows a preference for emission in opposite directions while the corresponding distribution for p and π^- does not show this preference. This is also indicated, although less definitely, by the corresponding distribution for n and π^- compared with that for n and π^+. This suggests the hypothesis that separate excited states of the two nucleons may be produced, with subsequent transition to the nucleon ground states by meson emission. This picture might be consistent with the observed strong preference for double meson production, as well as the angular distributions of the emitted particles. No specific excitation energy is found.

We are indebted to the Cosmotron staff for providing us with very reliable operation of the machine, and to the other members of the cloud chamber group for their effective help in operating the cloud chamber equipment. M. R. Burns and F. S. Keene have aided us considerably by scanning most of the photographs.

Scattering of 187-Mev Negative Pions by Hydrogen*

MAURICE GLICKSMAN
Institute for Nuclear Studies, University of Chicago, Chicago, Illinois
(Received May 10, 1954)

The differential cross sections for scattering of 187-Mev negative pions in hydrogen have been observed at six angles. The scattering is well represented by the angular distributions in the barycentric system: $\pi^-+p\rightarrow\pi^-+p$: $d\sigma/d\omega=0.81\pm0.13+(0.35\pm0.20)\cos\chi+(3.08\pm0.38)\cos^2\chi\times10^{-27}$ cm²/sterad, $\pi^-+p\rightarrow\pi^0+n$: $d\sigma/d\omega=1.46\pm0.24-(0.16\pm0.30)\cos\chi+(5.63\pm0.88)\cos^2\chi\times10^{-27}$ cm²/sterad. A transmission measurement of the total cross section gave $63.5\pm1.6\times10^{-27}$ cm². An analysis of these data in terms of phase shifts is discussed.

THE scattering of negative pions of energy 187 Mev in liquid hydrogen has been investigated using the methods previously applied at 217 Mev.[1] The equipment and experimental technique were the same as those described in A. The pions passed through two scintillation counters, Nos. 1 and 2, and from there into the liquid hydrogen Dewar. For observation of the ordinary scattering, $\pi^-+p\rightarrow\pi^-+p$, two large counters, Nos. 3 and 4, were placed at various angles with respect to the incident beam to detect the scattered pions. Aluminum absorbers were required between counters Nos. 3 and 4 at the forward angles to remove the recoil protons. These amounted to 9.45 g/cm² at 25.7° and 2.59 g/cm² at 51.4°. The double coincidences D of counters Nos. 1 and 2 recorded the pions entering the liquid hydrogen, while the quadruple coincidences Q of all four counters gave the number of scattered pions detected. In the charge exchange scattering, $\pi^-+p\rightarrow\pi^0+n$, the neutral pion decays promptly into two photons. To observe one of these photons, three counters, Nos. 5, 3, and 4, formed a telescope to detect electrons produced by the photon in a lead sheet placed between counters Nos. 5 and 3. Counter No. 5 was counted in anticoincidence with the quadruple coincidences Q' of the other four counters so as not to detect charged particles produced in the scattering process. The details of the arrangement and description of equipment may be found in Secs. I and II of A.

The energy of the pions was calculated from their observed range in copper. The mean pion energy in the center of the hydrogen was 187 Mev, and the beam had a spread in energy estimated from the range curve as ±6 Mev. The beam contained 97±1 percent pions.

The procedure followed in reducing the data was the same as in A. The values of the ratio Q'/D observed with and without hydrogen in the scattering cell are given in Table I. The errors quoted there are the standard deviations. The differential cross section for production of gamma rays is then given by

$$\frac{d\sigma}{d\omega}=\frac{Q'/D}{\epsilon_\gamma(0.97)(0.993)\Delta\omega N}=\frac{2.89\times10^3}{\epsilon_\gamma\Delta\omega}Q'/D,$$

in units of 10^{-27} cm²/sterad, where ϵ_γ is the efficiency for detecting gamma rays emitted into the solid angle $\Delta\omega$, 0.97 is the fraction of the number D which consists of pions, 0.993 is a correction factor due to the attenuation of the beam in the cell, N is 3.59×10^{23}, the number of hydrogen atoms per square centimeter, and $\Delta\omega$ is the solid angle subtended by counter No. 4 in steradians. The gamma-ray efficiency ϵ_γ was calculated, making corrections[2] for the scattering and absorption of the electrons produced in the 7.30-g/cm² lead converter. The lateral distribution of the pion beam was measured, and this distribution was used to calculate the mean distance traveled by the pions in the hydrogen and therefore the value of N. Corrections were made to the solid angle for the finite extent of the counters and the target. The values used, along with the calculated differential cross sections in the laboratory and barycentric systems, are presented in Table II. The last column, the barycentric system differential cross section, has the contribution of the reaction $\pi^-+p\rightarrow n+\gamma$ (estimated from the process[3] $\gamma+p\rightarrow\pi^++n$ and the ratio[4] of positive to negative pion photoproduction in deuterium as 0.05×10^{-27} cm²/sterad) subtracted. The errors quoted include estimates of the uncertainty in the pion content and the number of hydrogen atoms N.

The values of the ratio Q/D observed with and without hydrogen in the target are given in Table III. From these, the differential cross section for ordinary

TABLE I. Observed values of the fraction Q'/D of pions interacting to give a gamma ray, in units of 10^{-6}.

Laboratory angle (deg)	With hydrogen	Without hydrogen	Net
25.7	410.4±14.3	124.8±8.5	285.6±16.6
51.4	207.9± 9.2	50.9±4.8	157.0±10.4
77.1	135.4± 8.2	36.0±6.0	99.4±10.1
102.8	141.0± 8.4	31.6±5.1	109.4± 9.8
128.6	149.0± 7.0	43.0±6.6	106.0± 9.6
154.3	208.7± 9.5	93.6±8.6	115.1±12.8

* Research supported by a joint program of the U. S. Office of Naval Research and the U. S. Atomic Energy Commission.
[1] M. Glicksman, Phys. Rev. 94, 1335 (1954), quoted here as A.
[2] Anderson, Fermi, Martin, and Nagle, Phys. Rev. 91, 155 (1953).
[3] J. Steinberger and A. S. Bishop, Phys. Rev. 86, 171 (1952).
[4] White, Jacobson, and Schulz, Phys. Rev. 88, 836 (1952).

TABLE II. Differential cross sections for $\pi^-+p\to\gamma$.

Laboratory angle θ (deg)	Angle in the barycentric system χ (deg)	Solid angle $\Delta\omega$ (sterad)	Gamma-ray detection efficiency ϵ_γ	Differential cross section in laboratory (10^{-27} cm^2/sterad)	Differential cross section in barycentric system for γ from π^0 (10^{-27} cm^2/sterad)
25.7	32.3	0.107	0.585	13.19±0.82	8.63±0.54
51.4	62.8	0.107	0.561	7.56±0.53	5.79±0.41
77.1	90.7	0.106	0.540	5.02±0.52	4.72±0.49
102.8	115.6	0.106	0.521	5.73±0.52	6.65±0.61
128.6	138.4	0.107	0.506	5.66±0.52	7.78±0.73
154.3	159.6	0.107	0.507	6.13±0.69	9.43±1.07

scattering was calculated:

$$\frac{d\sigma}{d\omega}=\frac{2.89\times10^3}{\epsilon_\pi\Delta\omega}\left[(Q/D)_\pi-\frac{\epsilon_\gamma'\Delta\omega}{2.89\times10^3}(d\sigma/d\omega)_\gamma\right].$$

The symbols ϵ_π and ϵ_γ' represent the efficiencies of the counters for detecting scattered pions and gamma rays produced in the hydrogen, respectively, and $(d\sigma/d\omega)_\gamma$ is the measured gamma-ray cross section given in the second last column of Table II. These factors and the resulting differential cross sections are collected in Table IV.

The differential cross sections in the laboratory system can be integrated to give the total cross sections for ordinary and charge-exchange scattering. Such an integration gives $22.5\pm1.3\times10^{-27}$ cm^2 for $\pi^-+p\to\pi^-+p$, $82.3\pm2.9\times10^{-27}$ cm^2 for $\pi^-+p\to\gamma$, and $64.0\pm2.0\times10^{-27}$ cm^2 for the total cross section, including the contribution estimated above for $\pi^-+p\to n+\gamma$. During the course of the measurements of the differential cross sections, the total cross section was observed directly. Counters Nos. 3 and 4 were placed at 0° and the values of Q/D were recorded with and without hydrogen in the target. The total cross section was then calculated from these observations, and corrected for the scattered pions and protons detected by counters Nos. 3 and 4 using the angular distribution inferred from the measured differential cross sections. This transmission measurement yielded a total cross section of $63.5\pm1.6\times10^{-27}$ cm^2, in excellent agreement with the value obtained by integration. Both of these measurements are consistent with an interpolation of the recent results[5] of Ashkin, Blaser, Feiner, Gorman, and Stern, which would give about $65\pm2.5\times10^{-27}$ cm^2 at this energy.

TABLE III. Observed values of the fraction Q/D of elastically scattered pions, in units of 10^{-6}.

Laboratory angle (deg)	With hydrogen	Without hydrogen	Net
25.9	882.0±14.2	674.5±13.9	207.5±19.9
51.4	210.3± 6.5	137.7± 5.9	72.6± 8.8
77.1	133.0± 4.7	94.4± 4.3	38.6± 6.4
102.8	121.3± 4.9	72.5± 4.3	48.8± 6.5
128.6	141.2± 5.3	82.5± 4.5	58.7± 7.0
154.3	249.6± 7.1	174.7± 6.2	74.9± 9.4

The differential cross sections for the ordinary and charge exchange scattering can be fitted by angular distributions of the type $a+b\cos\chi+c\cos^2\chi$ which assume that the scattering can be described in terms of s- and p-wave scattering alone. The π^0 angular distribution was calculated[2] from the gamma-ray distribution as in A. Least squares values for the coefficients are given in Table V. Both fits are good. There is thus no evidence, at this level of experimental error, that higher angular momentum states, for example d waves, also need to be included in analyzing either of the reactions at this energy.

On the assumption that only s and p waves are important in the interaction at this energy, the scattering can be described in terms of six phase shifts[2] of angular momentum $\frac{1}{2}$ and $\frac{3}{2}$, isotopic spin $\frac{1}{2}$ and $\frac{3}{2}$. However, as has been pointed out,[1] there are a large number of sets of these phase shifts which fit the negative data alone at one energy. De Hoffman, Metropolis, Alei, and Bethe[6] have used the negative data at energies in the range 120 to 217 Mev to calculate these sets, and reduced considerably the multiplicity of solutions by introducing the requirement that the phase shifts should predict a positive pion total cross section which agrees with experiment. The largest number of acceptable solutions occurs with the 194-Mev data.[7] With the additional condition that the solutions vary smoothly with energy, they find that the data used in this way allow only three different sets of phase shifts.

For a number of reasons,[6] de Hoffman *et al.* conclude that the set of solutions in which[8] α_{33} passes through 90° at about 195 Mev is probably the correct one. This solution is the one in which the three phase shifts α_{31}, α_{13}, and α_{11} are small throughout this energy region, and corresponds to the phase shift set reported

[5] Ashkin, Blaser, Feiner, Gorman, and Stern, Phys. Rev. **93**, 1129 (1954).
[6] De Hoffman, Metropolis, Alei, and Bethe, Phys. Rev. (to be published).
[7] Fermi, Glicksman, Martin, and Nagle, Phys. Rev. **92**, 161 (1953).
[8] The notation of reference 2 is used.

TABLE IV. Differential cross sections for $\pi^-+p\rightarrow\pi^-+p$.

Laboratory angle θ (deg)	Angle in the barycentric system χ (deg)	Solid angle $\Delta\omega$ (sterad)	Pion detection efficiency ϵ_π	Gamma-ray detection efficiency ϵ_γ'	Differential cross section in laboratory (10^{-27} cm^2/sterad)	Differential cross section in barycentric system (10^{-27} cm^2/sterad)
25.7	33.3	0.113	0.858	0.025	5.80±0.60	3.60±0.37
51.4	64.7	0.112	0.938	0.025	1.80±0.24	1.34±0.18
77.1	93.0	0.111	0.968	0.024	0.94±0.18	0.89±0.17
102.8	118.0	0.111	0.968	0.024	1.20±0.18	1.45±0.22
128.6	140.3	0.105	0.968	0.024	1.48±0.19	2.21±0.28
154.3	160.7	0.113	0.968	0.024	1.90±0.26	3.25±0.45

in A which was calculated on the assumption that these three phase shifts were actually all zero. The data reported here were analyzed under these assumptions.

The phase shifts α_{33}, α_3, and α_1 were calculated employing the same procedure as in A. Possible sets of phase shifts were found from a geometrical analysis suggested by Ashkin and Vosko.[9] This analysis uses five of the available seven independent data (the six coefficients of the negative pion angular distributions, and the total cross section for the scattering of positive pions in hydrogen taken[10] as $190\pm10\times10^{-27}$ cm^2), but under the simplifying assumptions made ($\alpha_{31}=\alpha_{13}=\alpha_{11}=0$), only three relations for the three phase shifts are used. As a result there are phase-shift "solutions" which are very poor fits to all the data. These were dropped and the remaining sets were improved in their fit by numerically varying the phase shifts to decrease the least-squares sum

$$M=\sum_{i=1}^{7}(\Delta_i/e_i)^2.$$

In M, Δ_i is the difference between the calculated and experimental value for each of the coefficients and for the total positive pion cross section, and e_i is the experimental error assigned to these quantities.

Minimizing the least squares sum gave the phase shift set: $\alpha_{33}=83$ deg, $\alpha_3=0$ deg, and $\alpha_1=8$ deg, with a value for M at the minimum of about 4.5, which indicates a good fit to the data. However the phase-shift values are quite sensitive to the data.[11] Indeed, if each of the phase shifts is varied (holding the other two constant) to note the effect upon M, the fit becomes poor only for values beyond the limits: α_3 to $+10$ and -15 deg, α_1 to $+12$ and -2 deg, and α_{33} to 98 and 70 deg. It appears that the experimental data would need to be greatly improved to allow one to calculate more definite values of the phase shifts in this very sensitive energy region.

TABLE V. Coefficients of $d\sigma/d\omega=a+b\cos\chi+c\cos^2\chi$ in units of 10^{-27} cm^2/sterad, for the various processes.

Process	a	b	c
$\pi^-\rightarrow\pi^-$	0.81±0.13	0.35±0.20	3.08±0.38
$\pi^-\rightarrow\gamma$	4.91±0.35	−0.23±0.42	5.28±0.83
$\pi^-\rightarrow\pi^0$	1.46±0.24	−0.16±0.30	5.63±0.88

The author would like to thank Mr. Joseph Fainberg for his valuable assistance during the course of the experiment.

[9] J. Ashkin and S. H. Vosko, Phys. Rev. **91**, 1248 (1953).

[10] Ashkin, Blaser, Feiner, Gorman, and Stern (private communication).

[11] This has been noted in previous analyses of the data in this energy region. See reference 6, and R. L. Martin, Phys. Rev. (to be published).

Some Physical Consequences of Vacuum Polarization*

LESLIE L. FOLDY,† *Institute for Theoretical Physics, Copenhagen, Denmark and Case Institute of Technology, Cleveland, Ohio*

AND

ERIK ERIKSEN, *Theoretical Study Group at the C.E.R.N.,‡ Institute for Theoretical Physics, University of Copenhagen, Copenhagen, Denmark and University of Oslo, Blindern, Norway*

(Received May 3, 1954)

The phenomenon of vacuum polarization can be studied apart from other higher-order electrodynamic effects through its modification of the electrostatic interaction of heavy charged particles. In particular the principal deviations of the $2p-1s$ level separations from the Bohr formula in light mu-mesonic atoms ($Z\leq 6$) are expected to arise from vacuum polarization effects rather than relativistic effects (ordinary hydrogenic fine structure) or finite nuclear size. The vacuum polarization contribution to the electrostatic interaction of two protons requires slight changes in the usual analysis of proton-proton scattering data to obtain information about nuclear forces. The effect of vacuum polarization on the electrostatic energies of nuclei is also briefly discussed.

ONE of the most interesting of the phenomena predicted by contemporary quantum electrodynamics is the polarization of the vacuum arising from the existence of the electron-positron field.[1-4] It is in a very real sense a new physical phenomenon which may be largely distinguished from other higher order electrodynamic effects (radiation reaction) and deserves study in its own right. An important consequence of the polarization of the vacuum is a modification of the electrostatic interaction between two electrically charged particles at spatial separations of the order of or smaller than an electron Compton wavelength. Thus to first order in the fine structure constant, $\alpha=e^2/\hbar c=1/137.0$, the potential energy of two particles at rest with charges e_1 and e_2 and situated a distance r apart is predicted to be:[3-5]

$$V(r)=\frac{e_1e_2}{r}\left[1+\frac{2\alpha}{3\pi}\int_1^\infty e^{-2\kappa r}\left(1+\frac{1}{2\xi^2}\right)\frac{(\xi^2-1)^{\frac{1}{2}}}{\xi^2}d\xi\right], \quad (1)$$

where $\kappa=mc/\hbar$ is the reciprocal Compton wavelength of the electron. At separations between the particles of order 10^{-13} cm, the correction to the ordinary Coulomb law is of the order of one-half percent, and increases logarithmically at smaller separations.

This deviation from Coulomb's law leads, among other effects, to a shift of the energy levels in atoms,[4] and, in particular, it contributes about -27 mc/sec of the 1051 mc/sec difference between the $2p_{1/2}$ and $2s_{1/2}$ levels (the Lamb shift) in ordinary hydrogen. This well-known vacuum polarization contribution seems essential in order to obtain agreement[6] between theory[7] and experiment[8] for this Lamb shift, and hence the experiment may be considered as providing direct evidence for the reality of vacuum polarization phenomena.

While in the ordinary (electronic) hydrogen atom the effect of vacuum polarization in shifting atomic levels is much smaller than other electrodynamic phenomena (radiation reaction), this will no longer be the case when one deals with problems involving the electrical interaction of particles much heavier than electrons, since the effects of radiation reaction are inversely proportional to the square of the mass of the particles involved. In fact, for such heavy particles the polarization of the vacuum leads to the principal deviations from predictions based on Coulomb's law alone for the electrical behavior of heavy, slowly moving, point-charged particles. From this follows the experimental possibility of exploring vacuum polarization phenomena apart from other electrodynamic effects; it also implies that consideration must be given to the effects of vacuum polarization in analyzing experimental results which involve the electrical interaction of heavy particles. We follow with a consideration of some special situations where the effects of vacuum polarization play a significant and perhaps experimentally observable role.

LEVEL SHIFTS IN LIGHT MU-MESONIC ATOMS

Just as in the case of ordinary electronic atoms, vacuum polarization leads to a displacement of the atomic energy levels of atoms composed of a mu meson and a nucleus. Such atoms have recently become accessible to experimental study.[9] For mu-mesonic

* Publication aided by a grant from the National Science Foundation.

† Fulbright and John Simon Guggenheim Memorial Fellow.

‡ European Council for Nuclear Research.

[1] P. A. M. Dirac, *Proceedings of the Seventh Solvay Congress* (Gauthier-Villars, Paris, 1934), p. 203.

[2] W. Heisenberg, Z. Physik **90**, 209 (1934).

[3] R. Serber, Phys. Rev. **48**, 49 (1935).

[4] E. A. Uehling, Phys. Rev. **48**, 55 (1935).

[5] J. Schwinger, Phys. Rev. **75**, 651 (1949).

[6] E. E. Salpeter, Phys. Rev. **89**, 92 (1953).

[7] N. M. Kroll and W. E. Lamb, Phys. Rev. **75**, 388 (1949); J. B. French and V. F. Weisskopf, Phys. Rev. **75**, 1240 (1949); R. P. Feynman, Phys. Rev. **74**, 1430 (1948).

[8] W. E. Lamb and R. C. Retherford, Phys. Rev. **79**, 549 (1950); **81**, 222 (1951); **86**, 1014 (1952); Triebwasser, Dayhoff, and Lamb, Phys. Rev. **89**, 98 (1953).

[9] V. L. Fitch and J. Rainwater, Phys. Rev. **92**, 789 (1953).

TABLE I. Fractional displacement arising from vacuum polarization, relativity, and finite nuclear size of the $2p_{3/2}$, $2p_{1/2}$, and $2s_{1/2}$ level separations from the $1s_{1/2}$ level from the value predicted by the elementary Bohr theory for light mu-mesonic atoms.

Atom:	H^1	He^4	Li^7	Be^9	B^{11}	C^{13}	N^{14}	O^{16}
$\frac{\Delta E_{2p_{3/2}}-\Delta E_{1s_{1/2}}}{E_2-E_1}\times 10^3$								
Vac. pol.	1.00	2.22	3.17	3.88	4.49	5.01	5.48	5.88
Relativity	0.02	0.07	0.15	0.27	0.42	0.60	0.82	1.07
Nuc. size	**	−0.26	−0.88	−1.87	−3.34	−5.11	−7.72	−11.06
Total	1.02	2.03	2.44	2.28	1.57	0.50	−1.42	−4.11
$\frac{\Delta E_{2p_{1/2}}-\Delta E_{1s_{1/2}}}{E_2-E_1}\times 10^3$								
Vac. pol.	1.00	2.22	3.17	3.88	4.49	5.01	5.48	5.88
Relativity	0.01	0.05	0.11	0.20	0.31	0.44	0.60	0.78
Nuc. size	**	−0.26	−0.88	−1.87	−3.34	−5.11	−7.72	−11.06
Total	1.01	2.01	2.40	2.21	1.46	0.34	−1.64	−4.40
$\frac{\Delta E_{2s_{1/2}}-\Delta E_{1s_{1/2}}}{E_2-E_1}\times 10^3$								
Vac. pol.	0.89	2.02	2.92	3.61	4.20	4.71	5.13	5.54
Relativity	0.01	0.05	0.11	0.20	0.31	0.44	0.60	0.78
Nuc. size	**	−0.23	−0.77	−1.63	−2.92	−4.47	−6.76	−9.67
Total	0.90	1.84	2.26	2.18	1.59	0.68	−1.03	−3.35
E_2-E_1 (kev)	1.898	8.216	18.71	33.37	52.26	75.32	102.66	134.22

atoms the shifts due to vacuum polarization are relatively much larger than for electronic atoms, and in the case of atoms with nuclei having atomic numbers $Z\leq 6$, are larger than the level displacements associated with any other cause, including relativistic shifts (relativistic fine structure), radiation reaction, and the effect of the finite size of the nucleus. The study of such atoms thus provides an ideal case for investigation of vacuum polarization phenomena apart from other higher-order electrodynamic effects and makes possible the establishment of the reality of vacuum polarization phenomena in a situation in which no *real* electrons play a role.

The computation of the shifts of energy levels in hydrogenic atoms is easily carried out by the use of the potential given in Eq. (1) treating the vacuum polarization correction by first-order perturbation theory. We have calculated the displacements of the $1s_{1/2}$, $2s_{1/2}$, $2p_{1/2}$, and $2p_{3/2}$ levels in mu-mesonic atoms for nuclear atomic numbers ranging from $Z=1$ to $Z=8$. These results are summarized in Table I where there is presented a tabulation of the fractional deviations of the $2s_{1/2}-2p_{1/2}$, $2p_{1/2}-1s_{1/2}$, and $2p_{3/2}-1s_{1/2}$ level separations from the value predicted by the elementary Bohr theory for the separation of $n=2$ and $n=1$ levels: $E_2-E_1=3Z^2\mu e^4/8\hbar^2$, where μ is the reduced mass of the meson-nucleus system. For comparison the relative shifts arising from relativistic effects and from the finite size of the nucleus have also been tabulated together with the total relative shifts arising from these three effects jointly. Further small shifts might be expected to arise from the following effects:

(a) polarization of the nucleus by the mu meson.[10,11] This effect is difficult to estimate accurately since it is sensitive to the nuclear model. Rough estimates indicate it to lead to shifts which are a relatively small fraction of those associated with the finite size of the nucleus.

(b) Shifts associated with radiation reaction. Other higher-order electrodynamic effects ("ordinary Lamb shift") will be of the order of a few percent of those associated with vacuum polarization.

(c) Shifts associated with extranuclear electrons. The presence of electrons in Bohr orbits about the mu-mesonic atom leads to *relative* shifts of the $2p$ and $1s$ levels which are very small compared to any of the shifts tabulated.

Thus the tabulated total shifts will not be significantly affected by these residual effects; the largest uncertainties in the figures for the total shift probably arise from the uncertainties in nuclear radii and nuclear polarizability. The computations have been performed for a mu-meson mass of 207.0 electron masses[12] and for nuclear radii computed from the formula $R=r_0A^{1/3}$ with $r_0=1.3\times 10^{-13}$ cm. Since the shifts associated with finite nuclear size are proportional to the square of the nuclear radius, a ten percent change in the latter will lead to a twenty percent change in the figures quoted for the former.

The present experimental uncertainty in the mu-meson mass (± 0.4 electron mass) will not appreciably affect the figures for the fractional level shifts quoted in Table I, though it will lead to a 0.2 percent uncertainty in the energy separation of the $2p$ and $1s$ levels as computed from the Bohr formula. This uncertainty is of some importance therefore in attempting to verify the existence of the vacuum polarization effect

[10] L. Cooper and E. Henley, Phys. Rev. **92**, 801 (1953).
[11] W. Lakin and W. Kohn, Phys. Rev. **94**, 787 (1954).
[12] Smith, Birnbaum, and Barkas, Phys. Rev. **91**, 765 (1953).

experimentally. It means that measurements of the $2p-1s$ level separations in a single atom will hardly suffice to verify unambiguously this effect and that measurements in two or more light atoms of the transition energy to an accuracy of the order of 0.1 percent will be necessary. The fact that $(\Delta E_{2p}-\Delta E_{1s})/(E_2-E_1)$ first increases and then decreases as a function of Z would appear to be the experimental feature which would provide the most direct verification of the vacuum polarization effect. The energy splitting of the $2p_{1/2}$ and $2s_{1/2}$ levels, if resolvable, would also serve this purpose. While measurements of the x-rays from these light mu-mesonic atoms to the required accuracy does not seem possible at present, it is hoped that experimental techniques may soon be refined to the point where these predictions can be subjected to test.

For heavy mu-mesonic atoms on which experiments have already been performed,[9] the effect of vacuum polarization on level displacements is only a small fraction of the shifts associated with finite nuclear size. For these atoms the level shifts have been employed to determine nuclear radii, and the recognition of the effect of vacuum polarization leads to a correction for the radii so derived of about one percent, as has been pointed out previously.[13] There will also be a small effect of vacuum polarization on the Coulomb scattering of mu mesons, but very much refinement of scattering measurements would be required to make these effects accessible to detection.

PROTON-PROTON SCATTERING

The contribution of vacuum polarization to the electrostatic interaction of two protons requires a small modification of the theoretical analysis of proton-proton scattering data to obtain information about nuclear forces. The long range of the vacuum polarization potential relative to the range of nuclear forces means that in the analysis of proton-proton scattering by means of the f function of Breit, Condon, and Present[14] or the K function employed by Blatt and Jackson[15] there will be a slight curvature in the plot of either of these functions against energy, particularly at the lower energies. This curvature cannot be seen in the presently available data because of the magnitude of the experimental errors. However, the vacuum polarization potential also leads to a slight displacement and change in slope of the plot of either of these functions against energy in the energy region 0.2–4 Mev where the best experimental data exists.

Preliminary calculations of this last effect have been performed. The results may be expressed as follows (we employ the notation of Blatt and Jackson[15]): the contribution to the K function arising from vacuum polarization at several energies are:

Energy (Mev)	ΔK
0.670	0.031
1.200	0.023
1.830	0.020
3.04	0.019
3.53	0.018

A fit of these values by a least-squares straight line yields:

$$\Delta K=0.043-(0.007\times10^{-24})k^2,$$

with k the wave vector magnitude measured in cm^{-1}. If we now take the constants of the K plot as derived by Blatt and Jackson,

$$-R/a=3.755\pm0.024, \quad r_e=(2.65\pm0.07)\times10^{-13}\text{ cm},$$

and correct them to apply to the idealized case where vacuum polarization is absent, one obtains

$$-R/a=3.726\pm0.024, \quad r_e=(2.66\pm0.07)\times10^{-13}\text{ cm}.$$

Thus we see that the effect of vacuum polarization on the zero energy scattering length a is of the order of the present experimental error. If one further traces the consequences of these changes through Schwinger's analysis[16] of the equality of the nuclear ^1S interaction between two protons and between a proton and a neutron, one finds that for the Yukawa potential the discrepancy between the zero-energy scattering lengths for these two interactions is increased from about 7 percent to about 9 percent. (This is perhaps favorable in expanding this narrow margin in order to allow room for the possibility that the magnetic moments of nucleons are not associated with point dipoles but with a spatial distribution of magnetization.)

It is planned to refine the foregoing calculations and also to extend them to energies below 0.6 Mev in the hope that more accurate proton-proton scattering experiments may eventually allow one to recognize directly the effects of vacuum polarization through the curvature of the K- or f-function plots at these lower energies.

COULOMB ENERGIES OF NUCLEI

Since the average separation of protons in a nucleus is much smaller than the electron Compton wavelength, the electrostatic energy of the nucleus is modified to a small extent by vacuum polarization. One may readily estimate that this energy is about 0.5 percent greater than one would calculate with neglect of vacuum polarization. This means that nuclear radii as derived from the mass differences of mirror nuclei should be increased by this same percentage over their previously derived values. Similarly, the coefficient of the Coulomb energy term in the Weizsäcker semi-empirical mass formula should also be slightly increased.

[13] See note added in proof, reference 10; also H. C. Corben, Phys. Rev. **94**, 787 (1954).

[14] Breit, Condon, and Present, Phys. Rev. **50**, 825 (1936); Yovits, Smith, Hull, Bengston, and Breit, Phys. Rev. **85**, 540 (1952).

[15] J. D. Jackson and J. M. Blatt, Revs. Modern Phys. **22**, 77 (1950).

[16] J. Schwinger, Phys. Rev. **78**, 135 (1950).

Unfortunately, so many uncertainties enter into the calculation of nuclear radii from electrostatic energies as to preclude an unambiguous detection of these vacuum polarization effects.

The effects described earlier seem to be those which are least unfavorable for an unambiguous verification of the existence of vacuum polarization phenomena where they are clearly separated from other higher-order electrodynamic effects. It should be kept in mind, however, that such effects are to be expected to be present in all cases where electrostatic interactions at small distances are involved. Further examples of such cases would be: Coulomb penetration factors in nuclear reactions, alpha-particle scattering, alpha-decay theory, fission theory, the astrophysical reaction: $p+p \rightarrow d+e^{+}+\nu$, etc. In all of these cases, however, other uncertainties enter of such magnitude as to make vacuum polarization effects unimportant at the present time.

The present paper represents a preliminary report on these investigations. Details of the calculations and further numerical results will be published elsewhere.

It is a pleasure for the authors to acknowledge the gracious hospitality offered them by the Institute for Theoretical Physics and its director, Professor Niels Bohr. One of the authors (L.L.F.) is also indebted to the United States Educational Foundation in Denmark for their helpful administration of his Fulbright Research Fellowship and to the John Simon Guggenheim Memorial Foundation for their supplementary support. The other (E.E.) is grateful for having been given the opportunity of working with the C.E.R.N. Theoretical Study Group.

PHYSICAL REVIEW VOLUME 95, NUMBER 4 AUGUST 15, 1954

Gravitational Field Equations

ROBERT L. KIRKWOOD
1015 *Second Street, Santa Monica, California*
(Received January 19, 1954)

Arguments are given to show that the laws that determine the motion of the ether should not refer to the motion of anything that is not in the immediate vicinity of the point whose motion is being considered. From this assumption and from Newton's laws of gravitation, the equations of motion of the ether are derived.

I. INTRODUCTION

IN classical mechanics it was assumed that the acceleration of any massive body relative to a primary inertial system was proportional to the force that acted on it. The motion of the primary inertial system was presumed to be known from observation, and it was frequently assumed to be fixed relative to the fixed stars, an assumption which agreed well with Newton's very successful theory of planetary motion. However, this assumption has sometimes been questioned on the intuitive grounds that it is difficult to see how there can be an intimate connection between the motions of two systems that are as widely separated as the solar system and the fixed stars when there is no tangible, physical means of contact between them. It is partially for this reason that many attempts were made during the last century to introduce a fluid medium, called the ether, which could provide the desired connection and which at the same time could provide a medium for the propagation of electromagnetic disturbances.

In a previous paper,[1] it was shown that Einstein's principle of equivalence makes it possible to interpret the gravitational field in terms of an ether flow in a three-dimensional Euclidean space and that all of the verified results of the general theory of relativity can be deduced using this interpretation. It was assumed that coordinates that are fixed in the ether form both a primary inertial system of mechanics and a system in which the velocity of light is the same in all directions, and on the basis of this assumption the equations of motion of a mass point and of a light ray moving through the ether were derived for an arbitrary ether velocity. The velocity of the ether in the spherically symmetric gravitational field was determined from Newton's inverse square law of gravitational attraction, but no attempt was made to derive the laws that determine the motion of the ether in general. It is the object of this paper to discuss one fundamental aspect of this problem and to use the conclusions of this discussion and Newton's laws of gravitation to determine the equations of motion of the ether. As in the previous article, it will be sufficient to assume that a single universal time variable has been introduced. If, as is postulated in the special theory of relativity, there are several completely equivalent ways of introducing such a variable, then any one of them may be used. When the time variable has been defined, the velocity of the ether is uniquely determined everywhere by the fact that the one-way velocity of light relative to the ether is the same in all directions.

[1] R. L. Kirkwood, Phys. Rev. **92**, 1557 (1953).

II. THE POSTULATE OF LOCAL DETERMINACY

In attempting to formulate the general laws of motion of the ether, it is natural to ask if it is not necessary to compare its motion with that of some more fundamental frame of reference, such as the fixed stars or the center of mass of the universe. In fact, some assumption of this type was made in many of the classical ether theories. However, if such a comparison is made, then it is apparent that much of the intuitive advantage that was gained when the ether was originally introduced is lost, since it would then be assumed that the motion of an element of the ether is directly related to that of a system that is as remote as the stars in a way that is independent of the motion of the surrounding elements of the ether, even though these surrounding elements provide the only direct physical connection that exists between the first element and the remote physical system. Thus it would still be assumed that the motions of two widely separated physical systems are intimately related in a way that is independent of any direct physical connection that exists between them. This assumption would involve the same intuitive difficulties that appeared in classical mechanics before the ether was introduced, and if it is made in connection with the motion of the ether, then it might equally well have been made in classical mechanics, and the ether itself would be superflous. Of course, it might also be assumed that the desired connection between the ether and the stars is supplied by a second ether, but this assumption seems so complex that it is not easy to accept unless it is directly motivated by experiment. Since it has already been shown that the laws of mechanics and at least some of the laws describing the propagation of light can be understood without reference to more than one ether, it seems plausible to assume that even the most general laws of nature can be understood in the same way and that it is not necessary to postulate the existence of two or more interacting ethers. Therefore, if an ether theory is to be adopted at all, it seems very natural to assume that *the laws governing the motion of the ether at any point do not refer to the state of motion of anything that is not in the immediate vicinity of that point.*

Although this assumption seems reasonable on the basis of the argument given above, there is another argument which appears to make it even more certain. If all of space is filled with a fluid medium, it is at least strongly suggested that electromagnetic disturbances may be nothing more than ripples propagated through this medium. In fact, Maxwell, who was one of the leading supporters of the classical ether theories, felt that the primary reason for believing in an ether was that it could supply a medium for the storage and transmission of electromagnetic energy. If electromagnetic waves are interpreted in this way, then it follows that the laws of propagation of light are just one aspect of the equations of motion of the ether. Similarly, it is known that part, if not all, of the momentum of charged particles is due to the electromagnetic fields associated with them, and hence if the laws determining the motion of the ether are very closely related to the laws of electromagnetism, then they will also be closely related to the laws of mechanics. If such an intimate connection exists between the laws that determine the motion of the ether and the laws of mechanics and of the propagation of light, and if the laws that describe the motion of the ether involved a direct reference to the state of motion of some remote physical system such as the fixed stars, then it would be quite surprising if the laws of mechanics and of the propagation of light did not also involve such a reference. However, it has been shown previously that the laws of mechanics and of geometrical optics can be formulated without referring to any state of motion that is more preferred than that of the ether itself, and this fact, taken with the argument that has been given above, suggests quite strongly that the motion of the ether at any point does not depend directly on the motion of anything that is not in the immediate vicinity of that point.

This assumption will now be put in a more precise and slightly more general form. It will be postulated that *the motion or the magnitude of any physical quantity that is located within a given volume in space is not directly influenced by the motion or the magnitude of any other quantity that is located outside of this volume, regardless of how small the volume may be.* The inclusion here of the magnitudes of physical quantities as well as their motions is a natural generalization for two reasons. First, most of the known laws of physics are already expressed in the form of differential equations which relate the magnitudes of physical quantities at one point to those at another which is separated from the first by a differentially small distance, and this is sufficient to insure that these magnitudes can be included in the postulate stated above. Second, the intuitive difficulty that arose in connection with the motions of physical quantities also arises when their magnitudes are considered, since it is difficult to see how a change in the magnitude of some remote physical quantity could have a direct effect on a nearby physical event unless this effect is transmitted by some continuous process through the intervening space, and this suggests that magnitudes as well as motions should be included in the postulate made above. It is particularly to be noticed that this postulate does not imply that physical conditions that exist at distant points will not have an *indirect* effect on phenomena occurring nearby, but only that this effect must be transmitted by a continuous process across the space in between. The essential distinction is that if a change in the physical conditions existing outside of a given volume does not affect the magnitudes or motions of physical quantities that are located on the surface bounding the volume, then it does not affect physical phenomena occurring within the volume. Quantities that are entirely determined at a given point without reference to conditions

existing outside of the immediate vicinity of that point and laws that relate only such quantities will be said to be *determined locally*, and hence the postulate that has just been made is that *the most general laws of nature are determined locally.*

It is now apparent that this postulate is one of the greatest differences between most of the classical ether theories and the present one. In many of the classical theories it was assumed that the motion of the ether was described by Euler's equations of classical hydrodynamics. These equations related the force on an element of the ether to its acceleration relative to a primary inertial system, and this system was assumed to be fixed relative to either the fixed stars or the center of mass of the universe. In either case, the equations of motion were not determined locally, and the resulting fluid medium did not completely replace the primary inertial system of classical mechanics in the way that is postulated here.

III. THE FORMAL DESCRIPTION OF LOCALLY DETERMINED QUANTITIES

It is now desirable to develop formal representations of locally determined quantities so that it will be possible to decide on inspection whether or not a given equation is determined locally. The first step in this process is to determine on physical grounds whether or not the scalars or three-dimensional vectors or tensors that appear in the equation are determined locally. They will be only if the definitions of the physical quantities that they represent do not involve a reference to the magnitude or motion of anything that is not in the immediate vicinity of the point at which the quantities are being defined. For example, the velocity of a particle relative to the ether is determined locally, but its velocity relative to the fixed stars is not. Next, it is apparent that if any locally determined scalars, vectors, or tensors are combined into a vector equation by any of the usual sums or products of vector algebra, the resulting equation is determined locally. This follows from the fact that the definitions of these laws of combination do not refer to any particular frame of reference, and hence these laws do not depend on any particular state of motion. If neither the quantities being combined now the laws of combination depend on the motion of anything that is outside of the immediate vicinity of the point being considered, then the quantity resulting from the combination will be independent of any such state of motion, and an equality between two such quantities will be determined locally.

However, the situation is not quite so simple when derivatives of locally determined quantities are considered. In general, spatial derivatives of the type that are defined in vector analysis are determined locally if the quantities that are differentiated are determined locally. The reason for this is that the spatial derivatives involve a comparison of the two values of the quantity at two different points of space at the same instant of time. Since this comparison is made instantaneously, it is independent of the way in which the points under consideration are moving, and hence neither the values nor the process by which they are compared involves a reference to the state of motion of anything that is a finite distance away, and the resulting derivative must be determined locally. However, this argument obviously does not apply to time derivatives. For example, the time derivative of a vector field depends on the motion of the point at which the derivative is to be evaluated and on the rate of rotation of the frame of reference relative to which the field is described. Hence, if this derivative is to be determined locally, the motion of this point and rotation of this frame of reference must be determined by the motion of some physical quantity that is located in the immediate vicinity of the point at which the derivative is being evaluated. Unless specified to the contrary, *the locally determined time derivative of any physical quantity will be assumed to be the time derivative of that quantity as it is determined in a system of coordinates whose origin is fixed in the ether at the point where the derivative is to be evaluated and which is rotating with an angular velocity equal to the vorticity of the ether at that point.* It is apparent that any locally determined time derivative that is defined in terms of the state of motion of some physical substance other than the ether can be expressed in terms of this time derivative and the motion of the substance relative to the ether, which is a locally determined quantity. Since the time derivatives that have just been defined reduce to ordinary time derivatives in the system of Cartesian coordinates that is fixed in the ether at the particular point under consideration, it follows that these derivatives will obey all of the normal rules for the differentiation of sums and products in this system of coordinates, and therefore, since these rules are vector relations between locally determined quantities, they will also hold in any other system of coordinates. If the velocity of the ether relative to an arbitrary system of Cartesian coordinates is denoted by $\mathbf{v}$, then the vorticity of the ether relative to these coordinates is

$$\boldsymbol{\omega}=\tfrac{1}{2}\nabla\times\mathbf{v}.$$

Then, if the particular time derivative defined above is denoted by d'/dt, the locally determined time derivatives of a scalar α and a vector $\mathbf{a}$ relative to these arbitrary coordinates can be written

$$d'\alpha/dt=d\alpha/dt,$$
$$d'\mathbf{a}/dt=d\mathbf{a}/dt-\boldsymbol{\omega}\times\mathbf{a}.$$

Here d/dt implies total time differentiation at a point that is fixed in the ether. Using these relations and the rules given above for expanding the locally determined time derivative of a product, it is not difficult to obtain expressions for the local time derivative of an arbitrary tensor. This can be done by expanding the local time derivative of the scalar formed by taking the dot product

of the tensor with two arbitrary vectors. The procedure is straightforward and will not be given here.

The foregoing discussion gives a reasonably complete procedure for formulating locally determined equations that involve quantities which are themselves determined locally. However, many of the most important physical laws involve the velocities of various physical quantities relative to the arbitrary system of coordinates in which the laws are described, and these velocities are not determined locally unless the motion of the coordinates is determined by that of some nearby physical quantity, which will not generally be the case. The velocity of anything other than the ether can be measured relative to the ether, and it will then be determined locally and can enter into physical laws in the manner that is described above, but the way in which the motion of the ether itself can enter into physical laws requires some further consideration. It is apparent that the only motion of the ether that is determined locally is the *relative* motion of neighboring points that are fixed in the ether. If the position vector of one such point measured from the origin of an arbitrary system of Cartesian coordinates is $\mathbf{r}$, and $\mathbf{r}+\delta_1\mathbf{r}$ and $\mathbf{r}+\delta_2\mathbf{r}$ are the position vectors of two neighboring points that are also fixed in the ether, then the relative positions of these points can be described entirely in terms of products of the form $\delta_1\mathbf{r}\cdot\delta_2\mathbf{r}$. For example, the distance between the first two points can be determined from the product $\delta_1\mathbf{r}\cdot\delta_1\mathbf{r}$, and the angle between the directions of the second two points from the first can be determined from their distances from the first and from the product $\delta_1\mathbf{r}\cdot\delta_2\mathbf{r}$. Therefore, the only motion of the ether that can enter into physical laws is motion that can be described in terms of the rate of change of products of this type. If $\mathbf{v}$ is the velocity of the ether relative to the coordinates, then

$$\frac{d}{dt}(\delta_1\mathbf{r}\cdot\delta_2\mathbf{r})=\frac{d\delta_1\mathbf{r}}{dt}\cdot\delta_2\mathbf{r}+\delta_1\mathbf{r}\cdot\frac{d\delta_2\mathbf{r}}{dt}=(\delta_1\mathbf{r}\cdot\nabla\mathbf{v})\cdot\delta_2\mathbf{r}$$
$$+\delta_1\mathbf{r}\cdot(\delta_2\mathbf{r}\cdot\nabla\mathbf{v})=2\delta_1\mathbf{r}\cdot\boldsymbol{\phi}\cdot\delta_2\mathbf{r},$$

where $\boldsymbol{\phi}$ is the classical rate of strain tensor, whose components are

$$\phi_{ij}=\frac{1}{2}\left(\frac{\partial v_i}{\partial x_j}+\frac{\partial v_j}{\partial x_i}\right),\quad (i,j=1,2,3).$$

If this time derivative is evaluated for values of $\delta_1\mathbf{r}$ and $\delta_2\mathbf{r}$ that lie in three independent directions, then $\boldsymbol{\phi}$ will be completely determined, and therefore, since these derivatives and $\delta_1\mathbf{r}$ and $\delta_2\mathbf{r}$ are all determined locally, so also is $\boldsymbol{\phi}$. The first derivative of the ether velocity with respect to the arbitrary Cartesian coordinates can be written

$$\frac{\partial v_i}{\partial x_j}=\frac{1}{2}\left(\frac{\partial v_i}{\partial x_j}+\frac{\partial v_j}{\partial x_i}\right)+\frac{1}{2}\left(\frac{\partial v_i}{\partial x_j}-\frac{\partial v_j}{\partial x_i}\right),\quad (i,j=1,2,3).$$

The first term on the right is composed of the components of $\boldsymbol{\phi}$, which is determined locally, and the second term is composed of the components of the vorticity of the ether relative to these coordinates, which is not generally determined locally. Since the sum of these terms is the most general first spatial derivative of $\mathbf{v}$, it follows that $\boldsymbol{\phi}$ is the only first spatial derivative of $\mathbf{v}$ that is determined locally in an arbitrary system of Cartesian coordinates. The second spatial derivatives of $\mathbf{v}$ can be written

$$\frac{\partial^2 v_i}{\partial x_j\partial x_k}=\frac{\partial\phi_{ik}}{\partial x_j}+\frac{\partial\phi_{ij}}{\partial x_k}-\frac{\partial\phi_{jk}}{\partial x_i},\quad (i,j,k=1,2,3).$$

Since the terms on the right side are all determined locally, it follows that the second spatial derivatives of $\mathbf{v}$ form a locally determined tensor in any system of Cartesian coordinates, and by further differentiation it is apparent that the same is true of all the higher derivatives. Thus all second and higher vector derivatives of $\mathbf{v}$ with respect to an arbitrary set of Cartesian coordinates can occur in physical laws. For example, since $\nabla\times\nabla\times\mathbf{v}$ is a vector depending only on the second spatial derivatives of $\mathbf{v}$, it is determined locally in any system of coordinates, even though $\nabla\times\mathbf{v}$ is not.

Therefore, it has been shown that any vector equation that can be formed from locally determined scalars, vectors, or tensors, or from their spatial derivatives, or from the locally determined time derivatives that are described above, will be determined locally. Furthermore, the locally determined spatial derivatives of the ether velocity are the classical rate of strain tensor and all of the second and higher vector derivatives of $\mathbf{v}$.

IV. THE GRAVITATIONAL FIELD EQUATIONS

The conclusions that have been reached above can now be used to derive the equations of motion of the ether from Newton's laws of gravitation. According to these laws, if a body of mass m is moving under the influence of a gravitational force $\mathbf{F}_{gr}$ and a force $\mathbf{F}$ from other sources, then its motion can be determined from the equation

$$d(m\mathbf{v}_0)/dt=\mathbf{F}+\mathbf{F}_{gr},\qquad (1)$$

where $\mathbf{v}_0$ is the velocity of the particle relative to Newton's absolute space, which for practical purposes can be assumed to be fixed relative to the fixed stars, and m is assumed to be a constant. The gravitational force $\mathbf{F}_{gr}$ is proportional to m and can be derived from a potential function V:

$$\mathbf{F}_{gr}=-m\nabla V.\qquad (2)$$

The function V is a solution of Poisson's equation,

$$\nabla^2 V=4\pi K\mu,\qquad (3)$$

where K is the gravitational constant and μ is the density of the mass that is producing the field. This situation will now be compared with the one that exists

when a body of mass m moves through an arbitrary ether velocity field. The first step in this comparison is to determine the system of coordinates in the ether theory that corresponds to the one that is fixed in absolute space in Newton's theory. In Newton's theory, these coordinates are ones in which a free body at rest will remain at rest if it is far enough from any attracting mass. In the ether theory, coordinates in which a free body at rest will remain at rest are ones that are fixed in the ether, and hence it must be assumed in the ether theory that it is possible to introduce a system of coordinates in which the ether is at rest at all points that are sufficiently far from any body that is producing a gravitational field. These coordinates will then take the place of the coordinates that are fixed relative to the fixed stars in classical mechanics. It has been shown previously[1] that the motion of a body through the ether is described relative to an arbitrary system of Cartesian coordinates by the equation

$$\mathbf{F}=\frac{d_m}{dt}[m(\mathbf{v}_0-\mathbf{v})]+m(\nabla\mathbf{v})\cdot(\mathbf{v}_0-\mathbf{v}),$$

where d_m/dt implies differentiation at the point at which m is located, $\mathbf{v}_0$ and $\mathbf{v}$ are the respective velocities of the particle and the ether relative to the coordinates, and $\mathbf{F}$ is the nongravitational force acting on the particle. Now let the coordinates be chosen so that the ether velocity vanishes at all points that are sufficiently far from any gravitating mass. Then, if this equation is written in the form

$$\frac{d(m\mathbf{v}_0)}{dt}=\mathbf{F}+\frac{d_m(m\mathbf{v})}{dt}-m(\nabla\mathbf{v})\cdot(\mathbf{v}_0-\mathbf{v}),$$

and compared with the Newtonian equation of motion [Eq. (1)], it is seen that the apparent gravitational force that is produced by the ether flow is

$$\mathbf{F}_{gr}=d_m(m\mathbf{v})/dt-m(\nabla\mathbf{v})\cdot(\mathbf{v}_0-\mathbf{v}).$$

This can be rewritten in the form

$$\mathbf{F}_{gr}=m\partial\mathbf{v}/\partial t+m\nabla(\mathbf{v}^2/2)-m\mathbf{v}_0\times\nabla\times\mathbf{v}+\mathbf{v}dm/dt. \quad (4)$$

Therefore, if the ether theory is to be equivalent to Newton's theory, this expression must reduce to the one given in Eq. (2) when it is assumed that m is a constant. Since the Newtonian gravitational force does not depend on the velocity of the moving body, this is possible only if the term $-m\mathbf{v}_0\times\nabla\times\mathbf{v}$ in Eq. (4) vanishes for all $\mathbf{v}_0$, which will happen only if

$$\nabla\times\mathbf{v}=0.$$

Therefore, the ether flow must be irrotational relative to this particular system of coordinates. If this is the case, and if m is a constant, then Eq. (4) becomes

$$\mathbf{F}_{gr}=-m[-\partial\mathbf{v}/\partial t-\nabla(\mathbf{v}^2/2)],$$

which will be equivalent to Eq. (2) only if

$$\nabla V=-\partial\mathbf{v}/\partial t-\nabla(\mathbf{v}^2/2).$$

Since $\mathbf{v}$ is irrotational, a velocity potential exists, and hence it is always possible to choose V so that this condition will be satisfied. If this expression for ∇V is now substituted into Eq. (3), the resulting equation can be put in the form

$$-\left(\frac{d\nabla\cdot\mathbf{v}}{dt}+\boldsymbol{\phi}:\boldsymbol{\phi}\right)-\tfrac{1}{2}(\nabla\times\mathbf{v})^2+\mathbf{v}\cdot\nabla\times\nabla\times\mathbf{v}=4\pi K\mu,$$

where d/dt means time differentiation at a point fixed in the ether, and

$$\boldsymbol{\phi}:\boldsymbol{\phi}=\sum_{i,j=1}^{3}\phi_{ij}\phi_{ji}.$$

Since $\nabla\times\mathbf{v}=0$, the last two terms on the left side of this equation vanish, and therefore the equations that must be satisfied by the ether velocity $\mathbf{v}$ relative to these particular coordinates are

$$\nabla\times\mathbf{v}=0,$$
$$d(\nabla\cdot\mathbf{v})/dt+\boldsymbol{\phi}:\boldsymbol{\phi}=-4\pi K\mu.$$

Since $\nabla\cdot\mathbf{v}$ is the diagonal sum of the rate of strain tensor, and $\boldsymbol{\phi}:\boldsymbol{\phi}$ is an invariant product formed from the rate of strain tensor, it is apparent that the second of these two equations is determined locally and does not actually involve a reference to the motion of the particular coordinates that have been used in deriving it. However, the first equation, $\nabla\times\mathbf{v}=0$, is not determined locally and hence must be replaced by a locally determined equation which will require that $\nabla\times\mathbf{v}=0$ everywhere in the particular system of coordinates in which the ether velocity vanishes at a great distance in any direction from the system of masses that is producing the field. It is known that if the normal component of a vector field vanishes at all points on a closed surface and if its divergence and curl vanish everywhere inside of the surface, then the vector vanishes everywhere inside the surface. If the closed surface is taken to be sufficiently large and to enclose all of the masses under consideration, then it can be chosen so that $\mathbf{v}$ will vanish everywhere in the vicinity of the surface, and hence $\nabla\times\mathbf{v}$ will vanish on the surface. Then, since $\nabla\cdot\nabla\times\mathbf{v}$ vanishes identically, it is only necessary to require that $\nabla\times\nabla\times\mathbf{v}$ vanish everywhere within the surface to insure that $\nabla\times\mathbf{v}$ will also vanish everywhere in this region. Furthermore, the equation $\nabla\times\nabla\times\mathbf{v}=0$ is determined locally, and hence it does not disagree with the postulate that all physical laws must be determined locally. Therefore, it follows that the equations,

$$\nabla\times\nabla\times\mathbf{v}=0$$

and

$$d(\nabla\cdot\mathbf{v})/dt+\boldsymbol{\phi}:\boldsymbol{\phi}=-4\pi K\mu, \quad (5)$$

are both necessary and sufficient conditions that the ether theory of gravitation that is described here will reduce rigorously to the Newtonian theory if the masses of all moving bodies are assumed to be constant and if it is assumed to be possible to introduce coordinates relative to which the ether velocity vanishes at all points that are sufficiently far from the system of masses that is producing the field. Since these equations are determined locally, they hold in any system of Cartesian coordinates, even though one particular system has been used to derive them. Since the equations are not linear, the velocity field that is produced by the superposition of two mass distributions is not the sum of the fields that would be produced by the two distributions separately. However, the effective gravitational potential is still determined by a linear equation, and hence the apparent gravitational force field that is produced by the superposition of two mass distributions is the sum of the two force fields that would be produced by these distributions separately. Therefore, the Newtonian theory of perturbations is a rigorous consequence of these field equations if the masses of moving bodies are assumed to be constant. Furthermore, it has been shown previously that if the mass of a moving body is assumed to vary according to the law

$$m=\frac{m_0}{[1-(\mathbf{v}_0-\mathbf{v})^2/c^2]^{\frac{1}{2}}},$$

and if the other laws of physics that have been described previously are assumed to hold, then the spherically symmetric field that is derived from these field equations is sufficient to give all of the verifiable results of Einstein's gravitational theory. Hence, this description of gravitational fields in terms of an ether flow is as complete and as accurate as any description of gravitation that is known today. In addition, the ether theory has the advantage that it does not refer directly to the motion of any remote system such as the fixed stars or the center of mass of the universe, and hence it avoids the intuitive difficulties that arise in classical physics.

V. CONCLUSIONS

In the preceding discussion, arguments have been given to show that if an ether is to replace the primary inertial system of classical physics, then the laws governing its motion at any point should not refer directly to the motion of anything that is not in the immediate vicinity of that point. It is then shown that the equations

$$\nabla\times\nabla\times\mathbf{v}=0,$$
$$d(\nabla\cdot\mathbf{v})/dt+\boldsymbol{\phi}:\boldsymbol{\phi}=-4\pi K\mu$$

have this property and are also necessary and sufficient conditions that the ether theory described here will reduce rigorously to Newton's theory of gravitation when the masses of moving bodies are assumed to be constant and the system of coordinates that is fixed in Newton's absolute space is taken to be one relative to which the velocity of the ether vanishes at all points that are far enough from all gravitating masses. Furthermore, if the masses of moving bodies are not assumed to be constant, and if the velocity field that is determined from these equations is used with the other laws of physics that have been derived previously, it gives rise to all of the verifiable results of Einstein's theory of gravitation. Finally, the ether theory gives the following answer to the problem of relative motion:

(1) The only motion that enters into physical laws is motion relative to the ether.

(2) The laws governing the motion of the ether itself involve only the relative motion of points that are fixed in the ether at differentially small distances from each other.

(3) Hence, the most general laws of nature do not refer to any remote system such as the fixed stars or the center of mass of the universe, and these systems appear in physical science only because the ether satisfies the boundary condition that $\mathbf{v}=0$ relative to them at great distances from all gravitating masses.

The resulting gravitational theory is as complete and as accurate as any that is known today.

Conservation Theorems in Modified Electrodynamics*

J. W. DETTMAN† AND A. SCHILD
Carnegie Institute of Technology, Pittsburgh, Pennsylvania
(Received May 13, 1954)

A system of interacting particles with variable rest masses is considered, whose motion is governed by a variational principle of general form, in which there are self-action terms instead of the usual specifically inertial terms. For suitable restrictions of the action principle it is shown that, when the particles are at distances large compared to the classical electron radius, the new theory reduces to classical electrodynamics and the variable rest masses become constants of the motion. The conservation laws of energy momentum and of angular momentum are derived from the Lorentz invariance of the general action principle.

1. INTRODUCTION

IN a recent paper[1] one of us proposed an action at a distance theory of interacting particles with variable rest masses. Here we wish to consider theories of this type based on action integrals of the general form,

$$J_*^{**}=\tfrac{1}{2}\sum_{ab}\int_{u_a*}^{u_a**}\int_{u_b*}^{u_b**}\Lambda_{ab}du_a du_b, \tag{1}$$

$$\Lambda_{ab}=\Lambda(\xi_{ab}{}^\mu,\dot{x}_a{}^\mu,\dot{x}_b{}^\mu). \tag{2}$$

The notation is as follows: Latin subscripts label the different particles of the system, Greek suffixes label space-time components and are subject to the summation convention, $x_a{}^\mu$ are the space-time coordinates of particle a,

$$\xi_{ab}{}^\mu=x_a{}^\mu-x_b{}^\mu, \tag{3}$$

$$\dot{x}_a{}^\mu=dx_a{}^\mu/du_a, \tag{4}$$

and u_a is a physically significant parameter along the world line of particle a. In terms of this parameter the variable rest mass m_a is defined by[2]

$$m_a{}^2=\dot{x}_a{}^\mu\dot{x}_{a\mu}. \tag{5}$$

In Eq. (1), $u_a{}^*$ refers to a set of points obtained by choosing a point on each of the world lines of the system, and $u_a{}^{**}$ refers to any other such set, the only restriction being that $u_a{}^{**}\geqslant u_a{}^*$.

In Eq. (1), the double summation includes self-action terms for which $a=b$. Here, and throughout, such a term is to be interpreted as

$$\tfrac{1}{2}\int_{u_a*}^{u_a**}\int_{u_a*}^{u_a**}\Lambda(\xi_{aa'}{}^\mu,\dot{x}_a{}^\mu,\dot{x}_{a'}{}^\mu)du_a du_a', \tag{6}$$

where u_a and u_a' are the parameters of two independent points $x_a{}^\mu$ and $x_{a'}{}^\mu$ on the same world line a, and

$$\xi_{aa'}{}^\mu=x_a{}^\mu-x_{a'}{}^\mu,\quad \dot{x}_{a'}{}^\mu=dx_{a'}{}^\mu/du_a'. \tag{7}$$

Because of the double summation in Eq. (1) and the double integration in the self-action terms (6), we can assume, without loss of generality, that the interaction function Λ_{ab} is symmetric in the two particles:

$$\Lambda(\xi_{ab}{}^\mu,\dot{x}_a{}^\mu,\dot{x}_b{}^\mu)=\Lambda(-\xi_{cb}{}^\mu,\dot{x}_b{}^\mu,\dot{x}_a{}^\mu),$$
$$\Lambda_{ab}=\Lambda_{ba}. \tag{8}$$

We also assume that Λ is Lorentz invariant, so that the theory will be relativistic.

2. VARIATION AND EQUATIONS OF MOTION

Consider a variation of the world lines of the particles and of their parametrizations:

$$x_a{}^\mu(u_a)\rightarrow x_a{}^\mu(u_a)+\delta x_a{}^\mu(u_a). \tag{9}$$

Equation (5) shows that such a variation implies not only a variation of the classical variables of motion, but also a variation of the rest masses of the particles.

The variation of the action integral is given by

$$\delta J_*^{**}=\sum_{ab}\left[\int_{u_b*}^{u_b**}\frac{\partial\Lambda_{ab}}{\partial\dot{x}_a{}^\mu}du_b\delta x_a{}^\mu\right]_{u_a*}^{u_a**}$$
$$+\sum_{ab}\int_{u_a*}^{u_a**}\int_{u_b*}^{u_b**}\Lambda_{ab\mu}\delta x_a{}^\mu du_a du_b, \tag{10}$$

where

$$\Lambda_{ab\mu}=\frac{\partial\Lambda_{ab}}{\partial\xi_{ab}{}^\mu}-\frac{d}{du_a}\frac{\partial\Lambda_{ab}}{\partial\dot{x}_a{}^\mu}. \tag{11}$$

The equations of motion are determined by the action principle

$$\delta J=0. \tag{12}$$

Here J is the total action, obtained from J_*^{**} by putting all

$$u_a{}^*=-\infty,\quad u_a{}^{**}=+\infty. \tag{13}$$

Equation (12) is to hold for arbitrary variations $\delta x_a{}^\mu$ which vanish identically outside arbitrary but finite intervals $(\bar{u}_a,\bar{\bar{u}}_a)$ on their respective world lines. From Eq. (10) we find that the *equations of motion* of particle a are

$$\sum_b\int_{-\infty}^{\infty}\Lambda_{ab\mu}du_b\equiv\sum_b\int_{-\infty}^{\infty}\left(\frac{\partial\Lambda_{ab}}{\partial\xi_{ab}{}^\mu}-\frac{d}{du_a}\frac{\partial\Lambda_{ab}}{\partial\dot{x}_a{}^\mu}\right)du_b=0. \tag{14}$$

* This research was supported by the United States Air Force, through the Office of Scientific Research of the Air Research and Development Command.

† Now at Bell Telephone Laboratories, Whippany, New Jersey.

[1] A. Schild, Phys. Rev. **92**, 1009 (1953).

[2] The metric of space time is $ds^2=\eta_{\mu\nu}dx^\mu dx^\nu=-(dx^1)^2-(dx^2)^2-(dx^3)^2+(dx^4)^2$.

3. CONSERVATION OF LINEAR MOMENTUM AND ENERGY

From the Lorentz invariance of the action integral it follows that

$$\delta J_*^{**}=0 \tag{15}$$

is satisfied identically for variations $\delta x_a{}^\mu$ which are induced by infinitesimal Lorentz transformations. This gives rise to ten identities. In this section and the next it will be shown that, by virtue of the equations of motion, these identities can be put into the form of conservation theorems. Because of the difference between the action J_*^{**} in Eq. (15) and the total action J in Eq. (12), this last fact is not obvious *a priori*, as it is in classical mechanics or in a field theory.

To obtain the conservation laws of linear momentum and energy, we consider the variations induced by an infinitesimal space-time translation,

$$\delta x_a{}^\mu=\epsilon^\mu, \tag{16}$$

where ϵ^μ is a set of four constants. By Eqs. (10) and (15), this gives the identities

$$\sum_{ab}\left[\int_{u_b*}^{u_b**}\frac{\partial\Lambda_{ab}}{\partial\dot{x}_a{}^\mu}du_b\right]_{u_a*}^{u_a**}+\sum_{ab}\int_{u_a*}^{u_a**}\int_{u_b*}^{u_b**}\times\Lambda_{ab\mu}du_a du_b\equiv 0. \tag{17}$$

If the equations of motion (14) are used, this becomes

$$\sum_{ab}\left[\int_{u_b*}^{u_b**}\frac{\partial\Lambda_{ab}}{\partial\dot{x}_a{}^\mu}du_b\right]_{u_a*}^{u_a**}-\sum_{ab}\int_{u_a*}^{u_a**}\left(\int_{-\infty}^{u_b*}+\int_{u_b**}^{\infty}\right)\times\Lambda_{ab\mu}du_a du_b=0. \tag{18}$$

On substituting from (11) and integrating by parts, this simplifies to

$$\sum_a\left[\sum_b\int_{-\infty}^{\infty}\frac{\partial\Lambda_{ab}}{\partial\dot{x}_a{}^\mu}du_b\right]_{u_a*}^{u_a**}-\sum_{ab}\int_{u_a*}^{u_a**}\left(\int_{-\infty}^{u_b*}+\int_{u_b**}^{\infty}\right)\frac{\partial\Lambda_{ab}}{\partial\xi_{ab}{}^\mu}du_a du_b=0. \tag{19}$$

By (8) and (3), the integrand $\partial\Lambda_{ab}/\partial\xi_{ab}{}^\mu$ is skew-symmetric in a and b. It follows that the integral operator in the second term of Eq. (19) can be skew-symmetrized, since there is a double summation over a and b. By doing this and using the operator identity

$$\int_{u_a*}^{u_a**}\left(\int_{-\infty}^{u_b*}+\int_{u_b**}^{\infty}\right)-\left(\int_{-\infty}^{u_a*}+\int_{u_a**}^{\infty}\right)\int_{u_b*}^{u_b**}=\left(\int_{u_a*}^{\infty}\int_{-\infty}^{u_b*}-\int_{-\infty}^{u_a*}\int_{u_b*}^{\infty}\right)-\left(\int_{u_a**}^{\infty}\int_{-\infty}^{u_b**}-\int_{-\infty}^{u_a**}\int_{u_b**}^{\infty}\right), \tag{20}$$

Eq. (19) becomes

$$\left[\sum_{ab}\int_{-\infty}^{\infty}\frac{\partial\Lambda_{ab}}{\partial\dot{x}_a{}^\mu}du_b+\tfrac{1}{2}\sum_{ab}\left(\int_{u_a}^{\infty}\int_{-\infty}^{u_b}-\int_{-\infty}^{u_a}\int_{u_b}^{\infty}\right)\times\frac{\partial\Lambda_{ab}}{\partial\xi_{ab}{}^\mu}du_a du_b\right]_*^{**}=0. \tag{21}$$

Since the $u_a{}^{**}$ and the $u_a{}^*$ are two independent sets of points, we obtain the laws of *conservation of linear momentum and energy:*

$$\sum_{ab}\int_{-\infty}^{\infty}\frac{\partial\Lambda_{ab}}{\partial\dot{x}_a{}^\mu}du_b+\tfrac{1}{2}\sum_{ab}\left(\int_{u_a}^{\infty}\int_{-\infty}^{u_b}-\int_{-\infty}^{u_a}\int_{u_b}^{\infty}\right)\times\frac{\partial\Lambda_{ab}}{\partial\xi_{ab}{}^\mu}du_a du_b=\text{constant}, \tag{22}$$

i.e., the left side is independent of the choice of the points $u_1, u_2, u_3, \cdots$, on each of the world lines of the system.

4. CONSERVATION OF ANGULAR MOMENTUM

We consider the variations $\delta x_a{}^\mu$ induced by an infinitesimal space-time rotation

$$\delta x_a{}^\mu=\epsilon^\mu{}_\nu x_a{}^\nu, \tag{23}$$

where $\epsilon_{\mu\nu}=\eta_{\mu\rho}\epsilon^\rho{}_\nu$ is a set of six skew-symmetric constants:

$$\epsilon_{\mu\nu}=-\epsilon_{\nu\mu}. \tag{24}$$

First we establish a simple identity which will be required later. From the Lorentz invariance of the interaction function Λ we obtain

$$\Lambda(\xi_{ab}{}^\mu+\epsilon^\mu{}_\nu\xi_{ab}{}^\nu,\dot{x}_a{}^\mu+\epsilon^\mu{}_\nu\dot{x}_a{}^\nu,\dot{x}_b{}^\mu+\epsilon^\mu{}_\nu\dot{x}_b{}^\nu)\equiv\Lambda(\xi_{ab}{}^\mu,\dot{x}_a{}^\mu,\dot{x}_b{}^\mu),$$

correct to the first order in $\epsilon^\mu{}_\nu$. Expanding in powers of $\epsilon_{\mu\nu}$ and retaining first powers only, we find

$$\epsilon_{\mu\nu}\left(\frac{\partial\Lambda_{ab}}{\partial\xi_{ab\mu}}\xi_{ab}{}^\nu+\frac{\partial\Lambda_{ab}}{\partial\dot{x}_{a\mu}}\dot{x}_a{}^\nu+\frac{\partial\Lambda_{ab}}{\partial\dot{x}_{b\mu}}\dot{x}_b{}^\nu\right)\equiv 0.$$

This must hold for arbitrary skew symmetric $\epsilon_{\mu\nu}$ and therefore the bracketed expression must be symmetric in μ and ν. Writing this down and rearranging terms, we find that

$$\frac{\partial\Lambda_{ab}}{\partial\xi_{ab\mu}}x_a{}^\nu-\frac{\partial\Lambda_{ab}}{\partial\xi_{ab\nu}}x_a{}^\mu+\frac{\partial\Lambda_{ab}}{\partial\dot{x}_{a\mu}}\dot{x}_a{}^\nu-\frac{\partial\Lambda_{ab}}{\partial\dot{x}_{a\nu}}\dot{x}_a{}^\mu\equiv-\left(\frac{\partial\Lambda_{ab}}{\partial\xi_{ba\mu}}x_b{}^\nu-\frac{\partial\Lambda_{ab}}{\partial\xi_{ba\nu}}x_b{}^\mu+\frac{\partial\Lambda_{ab}}{\partial\dot{x}_{b\mu}}\dot{x}_b{}^\nu-\frac{\partial\Lambda_{ab}}{\partial\dot{x}_{b\nu}}\dot{x}_b{}^\mu\right), \tag{25}$$

i.e., the left side is skew symmetric in the particle variables a and b.

Substituting (23) in Eqs. (10) and (15), we obtain

$$\sum_{ab}\left[\int_{u_b^*}^{u_b^{**}}\left(\frac{\partial\Lambda_{ab}}{\partial\dot{x}_{a\mu}}x_a{}^{\nu}-\frac{\partial\Lambda_{ab}}{\partial\dot{x}_{a\nu}}x_a{}^{\mu}\right)du_b\right]_{u_a^*}^{u_a^{**}}$$

$$+\sum_{ab}\int_{u_a^*}^{u_a^{**}}\int_{u_b^*}^{u_b^{**}}(\Lambda_{ab}{}^{\mu}x_a{}^{\nu}-\Lambda_{ab}{}^{\nu}x_a{}^{\mu})du_a du_b\equiv 0. \quad (26)$$

If the equations of motion (14) and integration by parts are used, this becomes

$$\sum_{a}\left[\sum_{b}\int_{-\infty}^{\infty}\left(\frac{\partial\Lambda_{ab}}{\partial\dot{x}_{a\mu}}x_a{}^{\nu}-\frac{\partial\Lambda_{ab}}{\partial\dot{x}_{a\nu}}x_a{}^{\mu}\right)du_b\right]_{u_a^*}^{u_a^{**}}$$

$$-\sum_{ab}\int_{u_a^*}^{u_a^{**}}\left(\int_{-\infty}^{u_b^*}+\int_{u_b^{**}}^{\infty}\right)\left(\frac{\partial\Lambda_{ab}}{\partial\xi_{ab\mu}}x_a{}^{\nu}-\frac{\partial\Lambda_{ab}}{\partial\xi_{ab\nu}}x_a{}^{\mu}\right.$$

$$\left.+\frac{\partial\Lambda_{ab}}{\partial\dot{x}_{a\mu}}\dot{x}_a{}^{\nu}-\frac{\partial\Lambda_{ab}}{\partial\dot{x}_{a\nu}}\dot{x}_a{}^{\mu}\right)du_a du_b=0. \quad (27)$$

Since, by Eq. (25), the last integrand is skew symmetric in a and b, we can now proceed exactly as we did from Eq. (19) to Eq. (22). We obtain the law of *conservation of angular momentum:*

$$\sum_{ab}\int_{-\infty}^{\infty}\left(\frac{\partial\Lambda_{ab}}{\partial\dot{x}_{a\mu}}x_a{}^{\nu}-\frac{\partial\Lambda_{ab}}{\partial\dot{x}_{a\nu}}x_a{}^{\mu}\right)du_b$$

$$+\tfrac{1}{2}\sum_{ab}\left(\int_{u_a}^{\infty}\int_{-\infty}^{u_b}-\int_{-\infty}^{u_a}\int_{u_b}^{\infty}\right)\left(\frac{\partial\Lambda_{ab}}{\partial\xi_{ab\mu}}x_a{}^{\nu}-\frac{\partial\Lambda_{ab}}{\partial\xi_{ab\nu}}x_a{}^{\mu}\right.$$

$$\left.+\frac{\partial\Lambda_{ab}}{\partial\dot{x}_{a\mu}}\dot{x}_a{}^{\nu}-\frac{\partial\Lambda_{ab}}{\partial\dot{x}_{a\nu}}\dot{x}_a{}^{\mu}\right)du_a du_b=\text{constant}, \quad (28)$$

i.e., the left side is independent of the choice of the points $u_1, u_2, u_3, \cdots$, on each of the world lines of the system.

5. CLASSICAL ELECTROMAGNETIC THEORY

Under suitable conditions on the interaction function Λ, and for charged particles with moderate accelerations which interact at distances large compared to 10^{-13} cm, our theory reduces to classical electrodynamics and, in particular, the rest mass of each particle is a constant of the motion. We shall discuss this for the restricted class of interaction functions of the form

$$\Lambda_{ab}=e_a e_b\dot{x}_a{}^{\mu}\dot{x}_{b\mu}f(\xi_{ab}{}^2,\dot{x}_a{}^{\mu},\dot{x}_b{}^{\mu}), \quad (29)$$

$$\xi_{ab}{}^2=\xi_{ab}{}^{\mu}\xi_{ab\mu}, \quad |\xi_{ab}|=|(\xi_{ab}{}^{\mu}\xi_{ab\mu})^{\frac{1}{2}}|. \quad (30)$$

Here e_a is the charge of a fundamental particle a. The units are chosen so that $e_a=\pm 1$ for all charged particles, and the velocity of light $c=1$. All dimensions are expressible in terms of cm, and the rest mass of an electron is

$$m_0=3.6\times 10^{12}\ \text{cm}^{-1}. \quad (31)$$

We shall use the empirical fact that there exists no charged particle in nature with a rest mass smaller than that of the electron, so that

$$1/\dot{x}_a\equiv 1/m_a\leqslant 1/m_0=2.8\times 10^{-13}\ \text{cm}, \quad (32)$$

$$\dot{x}_a=|(\dot{x}_a{}^{\mu}\dot{x}_{a\mu})^{\frac{1}{2}}|. \quad (33)$$

We require that the structure function f have the following properties:

1. It is Lorentz-invariant and symmetric in the two particles [see Eq. (8)]:

$$f(\xi_{ab}{}^2,\dot{x}_a{}^{\mu},\dot{x}_b{}^{\mu})=f(\xi_{ab}{}^2,\dot{x}_b{}^{\mu},\dot{x}_a{}^{\mu}). \quad (34)$$

2. With respect to its first variable ξ^2, f must approximate a δ function. It must be normalized such that

$$\int_{-\infty}^{\infty}f(\xi^2,\dot{x}_a{}^{\mu},\dot{x}_b{}^{\mu})d\xi^2=1 \quad (35)$$

for all $\dot{x}_a{}^{\mu}$, $\dot{x}_b{}^{\mu}$. We assume that f (and its integral with respect to ξ^2) is negligibly small outside an interval of order $1/\dot{x}_a$ or $1/\dot{x}_b$ about $\xi=0$:

$$f(\xi^2,\dot{x}_a{}^{\mu},\dot{x}_b{}^{\mu})\sim 0 \quad \text{for} \quad |\xi|>k\max\left(\frac{1}{\dot{x}_a},\frac{1}{\dot{x}_b}\right), \quad (36)$$

where k is of the order of magnitude 1. From the normalization condition (35) it follows that f must be large somewhere in the range $|\xi|\leqslant k\max(1/\dot{x}_a, 1/\dot{x}_b)$. By Eq. (32), this is an interval of the order of magnitude of 10^{-13} cm or less.

3. When $a=b$, f must satisfy the condition

$$\int_{-\infty}^{\infty}f(\xi^2,\dot{x}_a{}^{\mu},\dot{x}_a{}^{\mu})d\xi=\dot{x}_a, \quad (37)$$

for all $\dot{x}_a{}^{\mu}$.

Some examples of structure functions which satisfy these three conditions are:

$$f_{ab}=\delta(\xi_{ab}{}^2-\lambda_{ab}{}^2), \quad (38)$$

$$f_{ab}=\frac{1}{2\lambda_{ab}{}^2}\exp(-|\xi_{ab}|/|\lambda_{ab}|) \quad \text{for} \quad \xi_{ab}{}^2\geqslant 0$$

$$=0 \quad \text{for} \quad \xi_{ab}{}^2<0, \quad (39)$$

where, in each case, λ_{ab} can be any one of the following expressions:

$$\lambda_{ab}{}^2=1/(\dot{x}_a{}^{\mu}\dot{x}_{b\mu}), \quad (40)$$

$$\lambda_{ab}{}^2=e_a e_b/(\dot{x}_a{}^{\mu}\dot{x}_{b\mu}), \quad (41)$$

$$\lambda_{ab}{}^2=2/(\dot{x}_a{}^2+\dot{x}_b{}^2), \quad (42)$$

$$\lambda_{ab}{}^2=2e_a e_b/(\dot{x}_a{}^2+\dot{x}_b{}^2), \quad (43)$$

$$\lambda_{ab}{}^2=4/[(\dot{x}_a{}^{\mu}+\dot{x}_b{}^{\mu})(\dot{x}_{a\mu}+\dot{x}_{b\mu})], \quad (44)$$

etc. Any two time-like vectors in Minkowski space satisfy the reversed Schwarz's inequality,

$$(A_\mu B^\mu)^2 \geqslant A_\mu A^\mu B_\nu B^\nu. \tag{45}$$

From this and Eq. (32) it follows that any of the λ_{ab} given above are small,

$$|\lambda_{ab}| \leqslant 2.8\times 10^{-13}\text{ cm}, \tag{46}$$

so that Eq. (36) is satisfied. The remaining conditions on the structure functions can be verified directly.

We now examine a system of charged fundamental particles which move under the following restrictions:

a. Relative to some suitable inertial frame, the distances between all pairs of distinct particles are at all times large compared to 10^{-13} cm.

b. The velocities of the particles may be relativistic, but they are not too close to the velocity of light.

c. For each particle a, the change in the momentum $\dot{x}_a{}^\mu$ during any proper time interval of magnitude 10^{-13} cm or 10^{-22} sec is negligible. We call this the condition of "moderate accelerations," but it includes a condition of moderate rates of change of the rest masses $m_a=\dot{x}_a$.

A typical interaction term in J_*^{**} for two distinct particles a and b is, by Eqs. (29), (30),

$$\tfrac{1}{2}e_a e_b\int_{u_a{}^*}^{u_a{}^{**}}\int_{u_b{}^*}^{u_b{}^{**}} f_{ab}\dot{x}_a{}^\mu\dot{x}_{b\mu}du_a du_b. \tag{47}$$

The restrictions a, b, c, and condition2 on the structure function, insure that this interaction term can be approximated by

$$\tfrac{1}{2}e_a e_b\int_{u_a{}^*}^{u_a{}^{**}}\int_{u_b{}^*}^{u_b{}^{**}}\delta(\xi_{ab}{}^2)\dot{x}_a{}^\mu\dot{x}_{b\mu}du_a du_b. \tag{48}$$

A typical self-action term in J_*^{**} is

$$\tfrac{1}{2}\int_{u_a{}^*}^{u_a{}^{**}}\int_{u_a{}^*}^{u_a{}^{**}} f(\xi_{aa'}{}^2,\dot{x}_a{}^\mu,\dot{x}_{a'}{}^\mu)\dot{x}_a{}^\mu\dot{x}_{a'\mu}du_a du_a'. \tag{49}$$

Condition 2, Eq. (36), and the restriction c of moderate accelerations imply that we have approximately

$$\dot{x}_{a'}{}^\mu=\dot{x}_a{}^\mu,\quad du_a'=d\xi_{aa'}/\dot{x}_a, \tag{50}$$

in the small interval about $u_a'=u_a$, outside of which $f_{aa'}$ is negligibly small. If we introduce these approximations in (49), condition 3 enables us to perform the integration with respect to u_a', and the self-action term reduces to

$$\tfrac{1}{2}\int_{u_a{}^*}^{u_a{}^{**}}\dot{x}_a{}^\mu\dot{x}_{a\mu}du_a. \tag{51}$$

Thus, for structure functions with the properties 1, 2, 3, and for systems satisfying the restrictions a, b, c, the action principle (12) simplifies to

$$\delta\left[\tfrac{1}{2}\sum_a\int_{-\infty}^{\infty}\dot{x}_a{}^\mu\dot{x}_{a\mu}du_a +\tfrac{1}{2}\sum_{\substack{ab\\a\neq b}}e_a e_b\int_{-\infty}^{\infty}\int_{-\infty}^{\infty}\delta(\xi_{ab}{}^2)\dot{x}_a{}^\mu\dot{x}_{b\mu}du_a du_b\right]=0. \tag{52}$$

The *equations of motion* of particle a are easily seen to be

$$\ddot{x}_{a\mu}=e_a\dot{x}_a{}^\nu F_{a\nu\mu}, \tag{53}$$

where

$$F_{a\nu\mu}=\partial A_{a\nu}/\partial x_a{}^\mu-\partial A_{a\mu}/\partial x_a{}^\nu, \tag{54}$$

$$A_{a\mu}=\sum_{\substack{b\\b\neq a}}e_b\int_{-\infty}^{\infty}\delta(\xi_{ab}{}^2)\dot{x}_{b\mu}du_b. \tag{55}$$

Then, if Eq. (53) is multiplied by $\dot{x}_a{}^\mu$, it follows from the skew symmetry of $F_{a\nu\mu}$ that

$$\frac{d}{du_a}(\dot{x}_a{}^\mu\dot{x}_{a\mu})=\frac{d}{du_a}(m_a{}^2)=0. \tag{56}$$

Thus the rest mass m_a of each particle is a constant of the motion. The $A_{a\mu}$ are half-retarded plus half-advanced Maxwellian electromagnetic potentials; Eq. (53) is easily seen to be equivalent to the Lorentz equations of motion for a point charge.

Thus, for a wide range of phenomena, and for a large class of structure functions, our theory reduces to classical electrodynamics.[3]

Under the same assumptions, the law (22) of *conservation of linear momentum and energy* reduces to

$$\sum_a(\dot{x}_a{}^\mu(u_a)+e_a A_a{}^\mu(u_a)) +\sum_{\substack{ab\\a\neq b}}{}'e_a e_b\left(\int_{u_a}^{\infty}\int_{-\infty}^{u_b}-\int_{-\infty}^{u_a}\int_{u_b}^{\infty}\right)\delta'(\xi_{ab}{}^2) \times\xi_{ab}{}^\mu\dot{x}_a{}^\nu\dot{x}_{b\nu}du_a du_b=\text{constant}. \tag{57}$$

This conservation law has been obtained by Fokker[4] and by Wheeler and Feynman,[3] who also showed that it is equivalent to the usual field-theoretic formulation. The law (28) of *conservation of angular momentum* reduces to

$$\sum_a\{x_a{}^\mu(\dot{x}_a{}^\nu+e_a A_a{}^\nu)-x_a{}^\nu(\dot{x}_a{}^\mu+e_a A_a{}^\mu)\}_{u_a} +\sum_{\substack{ab\\a\neq b}}e_a e_b\left(\int_{u_a}^{\infty}\int_{-\infty}^{u_b}-\int_{-\infty}^{u_a}\int_{u_b}^{\infty}\right) \times\{\delta'(\xi_{ab}{}^2)(x_a{}^\nu x_b{}^\mu-x_a{}^\mu x_b{}^\nu)\dot{x}_a{}^\rho\dot{x}_{b\rho} -\tfrac{1}{2}\delta(\xi_{ab}{}^2)(\dot{x}_a{}^\nu\dot{x}_b{}^\mu-\dot{x}_a{}^\mu\dot{x}_b{}^\nu)\}du_a du_b=\text{constant}. \tag{58}$$

[3] See J. A. Wheeler and R. P. Feynman, Revs. Modern Phys. **17**, 157 (1945); **21**, 425 (1949).
[4] A. D. Fokker, Z. Physik **58**, 386 (1929).

Suppression of Pair Coupling in Nuclear Forces

ABRAHAM KLEIN*
Harvard University, Cambridge, Massachusetts
(Received April 9, 1954)

It is demonstrated that for the nuclear force problem the effective coupling constant for the emission of a pair of mesons is the same as the renormalized coupling constant, $g_s^2/4\pi$, which occurs in the matrix element for meson-nucleon scattering in the low energy limit. The proof involves an adaptation of the techniques developed by Deser, Thirring, and Goldberger for the scattering problem. The relatively small value of the coupling constant thus obtained, $g_s^2/4\pi \sim 1$, can be interpreted as the consequence of a net pair suppression, although not in the narrow sense associated with the nucleon propagation function alone. Radiative corrections to multiple pair vertices are considered briefly.

I. INTRODUCTION

THE author has shown recently[1] that the application of perturbation theory to the computation, in the adiabatic limit, of the leading pair-term potentials of pseudoscalar meson theory was wholly unjustified for values of the coupling constant, $g^2/4\pi$, of the order of ten. Such large values of the coupling constant are, in fact, required to account for P-wave effects in the theory, for example in meson-nucleon scattering.[2] On the other hand, there is now fairly conclusive evidence[3] that the coupling constant effective for meson-nucleon scattering at low energies (S-wave) is an order of magnitude smaller. Earlier theoretical arguments[4,5] of a less rigorous character had suggested that this should be the case. In addition, several authors[6–8] have obtained results which indicate that the coupling effective for the pair contribution to nuclear forces is similarly reduced compared to the perturbation theory value when radiative corrections are taken into account.

Although individually subject to varying criticisms, these arguments for suppression of pair effects in nuclear forces are collectively quite convincing. It is the purpose of this note to strengthen the chain of evidence. The recent work of Deser, Thirring and Goldberger[3] provides the tools required to achieve this end. We shall show that the coupling constant for the leading pair contributions to the adiabatic nuclear potential is precisely the renormalized coupling constant defined by D.-T.-G., $g_s^2/4\pi$, whose value as determined by comparison with the meson-nucleon scattering data at low energies is roughly unity.

II. CONSTRUCTION OF POTENTIAL

Our notation follows that of K1, K2. For the potential we employ an expression of the form of K2, Eq. (2),

$$V(\mathbf{r},\mathbf{r}') = -iT^{-1}\int dt_1 dt_2 dt_1' dt_2' d\mathbf{R}'$$

$$\times \exp[iM(t_1+t_2-t_1'-t_2')]I(x_1,x_2;x_1',x_2'), \quad (1)$$

where the interaction kernel I is a sum

$$I=\sum_{n=1}^{\infty} I_{2n}. \quad (2)$$

If we neglect radiative corrections, then I_{2n} is the sum of all Feynman diagrams[9] for the exchange of n mesons, which it is convenient to express in the redundant form,

$$I_{2n}(x_1,x_1';x_n,x_n') = \sum P(\alpha)P(\alpha_i)(n!)^{-1}(-ig^2)^n$$

$$\times \int (dx_2)\cdots(dx_{n-1})(dx_2')\cdots(dx_{n-1}')$$

$$\times \langle \gamma_5\tau(\alpha_1)G(x_1-x_2)\gamma_5\tau(\alpha_2)\cdots G(x_{n-1}-x_n)\gamma_5\tau(\alpha_n)\rangle^{(1)}$$

$$\times \langle \gamma_5\tau(\alpha_{i,1})G(x_1'-x_2')\cdots G(x_{n-1}'-x_n')\gamma_5\tau(\alpha_{i,n})\rangle^{(2)}$$

$$\times \Delta(x(\alpha_1)-x(\alpha_1)')\cdots\Delta(x(\alpha_n)-x(\alpha_n)'). \quad (3)$$

In Eq. (3), the sum is to be taken independently over all possible permutations of the isotopic indices for the first and second nucleon. The notation $x(\alpha_i)$ means that vertex at which $\tau(\alpha_i)^{(1)}$ is effective, etc.

It is convenient at this point to introduce the fiction[3,10,11] of an external meson field $\phi(\xi)$. In the presence of this field, the Green's function $G[\phi]$, still

* Society of Fellows.
[1] A. Klein, Phys. Rev. **91**, 740 (1953); Phys. Rev. **92**, 1017 (1953), referred to as K1 and K2, respectively.
[2] Bethe, Dyson, Mitra, Ross, Salpeter, Schweber, Sundaresen, and Visscher, Phys. Rev. **90**, 372 (1953).
[3] Deser, Thirring, and Goldberger, Phys. Rev. **94**, 711 (1954), referred to as D.-T.-G.
[4] G. Wentzel, Phys. Rev. **86**, 802 (1952).
[5] S. D. Drell and E. M. Henley, Phys. Rev. **88**, 1053 (1952).
[6] G. Wentzel, Helv. Phys. Acta **15**, 11 (1942).
[7] M. A. Ruderman, Phys. Rev. **90**, 183 (1953).
[8] Brueckner, Gell-Mann, and Goldberger, Phys. Rev. **90**, 476 (1953). For a critique of this paper see reference 3 and N. M. Kroll and M. A. Ruderman, Phys. Rev. **93**, 233 (1954).
[9] Since we shall be interested in the leading pair terms, this means all reducible as well as irreducible diagrams.
[10] J. Schwinger, Proc. Natl. Acad. Sci. U. S. **37**, 452 (1951). We shall make use temporarily of the matrix notation introduced in this paper.
[11] R. P. Feynman, Phys. Rev. **80**, 440 (1950).

that of a bare particle, satisfies the matrix equations,

$$\left[\gamma p+M-\int(d\xi)\gamma_\delta(\xi)\tau\cdot\phi(\xi)\right]G=1, \quad (4)$$

$$(\delta/\delta\phi_i(\xi))G=G\tau_i\gamma_\delta(\xi)G. \quad (5)$$

Equation (3) can then be rewritten symbolically:

$$I_{2n}=\mathrm{Lim}(\phi\to 0)(n!)^{-1}(-ig^2)^n$$
$$\times\int(d\xi_1)\cdots(d\xi_n)(d\eta_1)\cdots(d\eta_n)$$
$$\times\langle G^{-1}[(\delta^n/\delta\phi_{\alpha(1)}(\xi_1)\cdots\delta\phi_{\alpha(n)}(\xi_n))G]G^{-1}\rangle^{(1)}$$
$$\times\langle G^{-1}[(\delta^n/\delta\phi_{\alpha(1)}(\eta_1)\cdots\delta\phi_{\alpha(n)}(\eta_n))G]G^{-1}\rangle^{(2)}$$
$$\times\Delta(\xi_1-\eta_1)\cdots\Delta(\xi_n-\eta_n). \quad (6)$$

All possible radiative corrections to the propagation of the nucleons can now be included by replacing G by G', the Green's function for the physical nucleon, correspondingly G^{-1} by $(G')^{-1}$. On the other hand, we shall make no provision for modification of the meson propagation functions, except to suppose that the renormalization constant Z_3 has been included as a factor, once for each Δ function. Perturbation calculations[7] indicate that finite corrections to nuclear forces arising from this source are small. We shall assume for the purpose of this discussion that corrections arising from the virtual scattering of mesons by mesons can also be neglected.

We go over next to momentum space by defining

$$V(\mathbf{p},\mathbf{p}')=(2\pi)^{-3}\int d\mathbf{r}d\mathbf{r}'$$
$$\times\exp[-i(\mathbf{p}\cdot\mathbf{r}-\mathbf{p}'\cdot\mathbf{r}')]V(\mathbf{r},\mathbf{r}'). \quad (7)$$

The term of order n in the series for $V(\mathbf{p},\mathbf{p}')$ takes the form,

$$V_{2n}(\mathbf{p},\mathbf{p}')=-i(-ig^2)^n(n!)^{-1}2\pi(2\pi)^{-4n}\int(dk_1)\cdots(dk_n)$$
$$\times[(k_1^2+\mu^2)\cdots(k_n^2+\mu^2)]^{-1}\delta(\Sigma k_0)\delta(\mathbf{p}'-\mathbf{p}+\Sigma\mathbf{k})$$
$$\times\Sigma\langle p|\gamma_\delta\tau(\alpha_1)G(p_1)\cdots G(p_{n-1})\gamma_\delta\tau(\alpha_n)|p\rangle^{(1)}$$
$$\times\langle -p|\gamma_\delta\tau(\alpha_{i,1})G(p_1')\cdots$$
$$\times G(p_{n-1}')\gamma_\delta\tau(\alpha_{i,n})|-p'\rangle^{(2)}, \quad (8)$$

where $p_1\cdots p_{n-1}$, $p_1'\cdots p_{n-1}'$ are related to p, p' and the k_i by the usual four-momentum conservation at each vertex; this relationship will depend on the permutation (Feynman diagram) considered.

Our practical interest in Eq. (8) and in the modification of it to include radiative corrections is confined to the evaluation of the limit in which we neglect energy and momentum transfer to the nucleons by the interaction. Strictly speaking this requires that we set $p_1=p_2=\cdots=p_{n-1}=p$, $p_1'=p_2'=\cdots=p_{n-1}'=-p$, $p=p'$, $p=(\mathbf{p},M)$, and $\gamma p+M=0$. However, this cannot be done indiscriminately. Thus for $n=1$, $\langle p|\gamma_\delta|p\rangle=0$, and the usual procedure to obtain the second-order potential is to evaluate $\langle p|\gamma_\delta|p'\rangle$ to the first nonvanishing order in $(p-p')/M$. The leading term of the fourth-order forces, on the other hand, provides no difficulty,

$$\langle p|\gamma_\delta\tau_i G(p_1)\gamma_\delta\tau_j|p'\rangle\cong-\tau_i\tau_j/2M, \quad (9)$$

from which we obtain the leading pair term in fourth order. It is physically clear, however, that the matter cannot be settled so simply for any order higher than the fourth. In sixth order, for example, the corresponding matrix element is proportional to the amplitude in Born approximation for the production at threshold of a meson in a meson-nucleon collision, in the limit of *vanishing* meson mass. We thus encounter the well-known infrared divergence. Similar remarks hold, *a fortiori*, for higher order terms. It was shown in K1, K2 that the leading contributions to the potential arose from matrix elements in which propagation of the nucleons was alternately in negative and positive energy states. Examination of a typical matrix element shows that it is the latter states which must be treated with care, the former giving rise simply to pair vertices. The correct evaluation of the adiabatic limit requires an additional time ordering process, which is best carried out in coordinate space.[1] We shall see below how to combine techniques so as to extract the required information about radiative corrections to the pair interaction. We merely note here that if the difficulties recorded above did not occur, we could obtain information about radiative corrections to nucleon propagation by examining the expression,

$$\mathrm{Lim}(\phi\to 0)\langle p|'G'(p)^{-1}[(\partial^n/\partial\phi(\alpha_1)\cdots$$
$$\times\partial\phi(\alpha_n))G'(p)]G'(p)^{-1}|p\rangle'$$
$$\times\langle -p|G'(-p)^{-1}[(\partial^n/\partial\phi(\alpha)\cdots$$
$$\times\partial\phi(\alpha_n))G'(-p)]G'(-p)^{-1}|-p\rangle', \quad (10)$$

which replaces the sum over the product of the last two factors of Eq. (8). As explained in D.-T.-G., it suffices in the adiabatic limit to consider a uniform external meson field.

III. EXTRACTION OF RADIATIVE CORRECTIONS

If we define

$$\Omega_{ij}(p)=\mathrm{Lim}(\phi\to 0)G'(p)^{-1}$$
$$\times[(\partial^2/\partial\phi_i\partial\phi_j)G'(p)]G'(p)^{-1}, \quad (11)$$

then the contribution of the fourth-order pair potential is determined by the quantity

$$g^2Z_3\langle p|'\Omega_{ij}(p)|p\rangle'^{(1)}g^2Z_3\langle -p|'\Omega_{ij}(-p)|-p\rangle'^{(2)}$$
$$=(\delta_{ij}g_s^2/M)^2=3g_s^4/M^2. \quad (12)$$

The evaluation recorded in Eq. (12) is the main result of D.-T.-G., Sec. III, where g_s^2 is the renormalized coupling constant introduced by these authors. It

follows directly that the fourth-order pair potential is the same as given by perturbation theory if we replace g^2 by g_s^2. We should like to establish that the mere substitution of g_s^2 for g^2 gives a true account of the pair coupling wherever it occurs. The remainder of this section will purport to demonstrate that this is at least the case for the leading *all-pair* potentials of any order.

An essential conclusion of K1, K2 was that the leading pair term of order $4n$ is the sum of contributions from all diagrams which yield closed meson line perimeters after the pair vertices have been established. Following the reasoning of those papers, with the help of Eq. (9), we obtain for the relevant contribution of the nucleon matrix elements of Eq. (8),

$$\Sigma\langle p||p'\rangle^{(1)}\langle -p||-p'\rangle^{(2)}\rightarrow\Sigma(\text{closed perimeters})M^{-2n}$$
$$\times\langle p|\delta(\alpha_i,\alpha_2)G(p_2)\cdots G(p_{2n-2})\delta(\alpha_{n-1},\alpha_n)|p'\rangle^{(1)}$$
$$\times\langle -p|\delta(\alpha_{i,1};\alpha_{i,2})G(p_2')\cdots$$
$$\times G(p_{2n-2}')\delta(\alpha_{i,n-1};\alpha_{i,n})|-p'\rangle^{(2)}. \quad (13)$$

The number of terms in Eq. (13) is easily counted. It is

$$\tfrac{1}{2}n!(n-1)!\times 2n!, \quad (14)$$

the product of the number of topologically distinct perimeters[1] by the redundancy factor $2n!$ At this stage, we can still return to coordinate space and complete the calculation according to K2. Our theorem now states that all radiative corrections that contribute significantly in the adiabatic limit will be included if we replace δ_{ij} by $\Omega_{ij}(p)$, modifying $\langle p|$, $|p'\rangle$ and the nucleon Green's functions only to the extent of including the required renormalization constants. For if this is a permissible procedure, then it follows directly from Eq. (12) that the perturbation result is maintained if we replace g^2 by g_s^2. As a first step toward justification of the theorem, we note that no finite corrections to the nucleon Green's functions need be considered, since the leading contributions to the potential arise from propagation in positive energy states, the finite corrections to which vanish in the adiabatic limit according to *any* of the renormalization methods.

To provide the justification in full, we must examine in some detail the structure of the radiative corrections in higher order. The essential points will be illustrated by the nucleon matrix element involved in the "eight-order" potential,

$$\mathrm{Lim}(\phi\rightarrow 90)\langle p|'G'(p)^{-1}[(\partial^4/\partial\phi_i\partial\phi_j\partial\phi_k\partial\phi_l)G'(p)]$$
$$\times G'(p)^{-1}|p'\rangle=\mathrm{Lim}(\phi\rightarrow 90)\Sigma P_\alpha\langle p|'\Gamma_{\alpha(1)}'(p,p)$$
$$\times G'(p)\Gamma_{\alpha(2)}'G'\Gamma_{\alpha(3)}'G'\Gamma_{\alpha(4)}'|p\rangle'$$
$$+\sum_{\alpha(1)<\alpha(2)}P_\alpha\langle p|'[\partial\Gamma_{\alpha(2)}'/\partial\phi_{\alpha(1)}]G'\Gamma_{\alpha(3)}'G'\Gamma_{\alpha(4)}'|p\rangle'$$
$$+\cdots+\sum_{\alpha(1)<\alpha(2),\,\alpha(3)<\alpha(4)}P_\alpha\langle p|'(\partial\Gamma_{\alpha(2)}'/\partial\phi_{\alpha(1)})$$
$$\times G'(\partial\Gamma_{\alpha(4)}'/\partial\phi_{\alpha(3)})|p\rangle'+\cdots$$
$$+\langle p|'\partial^3\Gamma_i'(p,p)/\partial\phi_i\partial\phi_j\partial\phi_k|p\rangle', \quad (15)$$

where $\alpha(1)\cdots\alpha(4)$ is a permutation of i, j, k, l

$$\Gamma'(p,p)=-\partial G'(p)^{-1}/\partial\phi_i, \quad (16)$$

and the restrictions on the summations follow from the chosen order of differentiation and can be removed by symmetrization. The various possibilities are illustrated diagrammatically in Fig. 1. One can easily see that the sum of the contributions corresponding to Figs. 1 (a), (b), (c), and (e) can be combined into a term of the form

$$\Sigma P_\alpha\langle p|'\Omega_{\alpha(1)\alpha(2)}(p)G'(p)\Omega_{\alpha(3)\alpha(4)}(p)|p\rangle'. \quad (17)$$

This is the term which alone contributes in leading order, according to our theorem. As it stands it is infrared divergent, but the technique for avoiding this difficulty has been indicated above. It is important to remark that according to Eq. (12), Eq. (17) depends on nucleon mass as M^{-2}.

Actually, we have included contributions other than from closed meson line perimeters in writing (17). It was argued in K1 that in the strict perturbation limit these others could be omitted because they canceled against "nonadiabatic" corrections to lower order forces. The basis of this argument can no longer be maintained when radiative corrections are included, even if one were to allow it previously. In any case, the coupling strength for these terms is g_s^2.

The remainder of the demonstration now consists in showing that the matrix elements corresponding to Figs. 1 (d), (f), (g), (h) do not contribute to the leading pair term, but rather constitute radiative corrections to a vertex for the emission of four mesons. Of course, expressions for these graphs can be obtained, using the functions of D.-T.-G., that are formally exact, but that can hardly be evaluated in the present state of the theory. It suffices for our present purposes to note

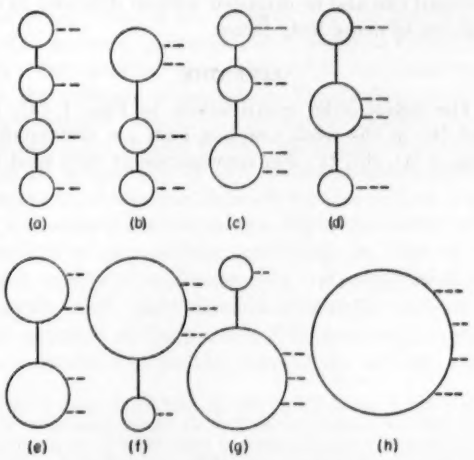

FIG. 1. Diagrams representing radiative corrections to the emission of four mesons.

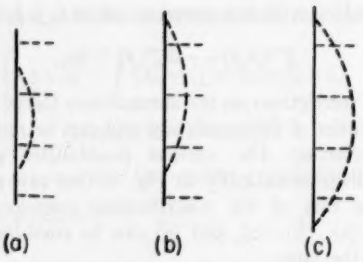

FIG. 2. Diagrams for the leading terms, in the weak coupling limit, of the processes represented in Figs. 1(d), (f), and (h), respectively.

that the matrix elements are proportional to M^{-3} and therefore correspond to potentials of higher order in μ/M. Thus, corresponding to Fig. 1(d), we have typically to evaluate

$$\begin{aligned}&\mathrm{Lim}(\phi\to 0)\langle p|'\Gamma_i'(p,p)G'(p)(\partial\Gamma_k'/\partial\phi_j)G'\Gamma_l'|p\rangle'\\&\sim\langle p|\gamma_5\tau_i G(p)(\delta_{jk}/M)G(p)\gamma_5\tau_l|p\rangle\\&\sim M^{-3},\end{aligned}\tag{18}$$

where we have used D.-T.-G., Sec. III and Eq. (5.4), discarding all terms that are irrelevant to the main aim of the demonstration. One can argue similarly for the other diagrams. In the appendix, we shall calculate these terms to lowest order in perturbation theory. The results will also demonstrate the main point which involves the mere enumeration of negative energy intermediate states.

The argument just given is in fact valid for the potential of order $4n$. Thus in twelfth order, in addition to the term of the character considered above, radiative corrections to a vertex for the emission of six mesons will enter. These will be of higher order in μ/M than anything previously considered. The results we have obtained can also be extended without difficulty to the problem of many body forces.

APPENDIX

The lowest order contributions to Figs. 1 (d), (f), and (h) in the weak coupling limit are illustrated in Figs. 2 (a), (b), (c). For convenience we shall omit the isotopic dependence, since we are interested only in the dependence on M. Thus the correction to the emission of two mesons [the central part of Fig. 1(a)] can be evaluated in the adiabatic limit from the expression

$$\begin{aligned}L_2=&-ig^2(2\pi)^{-4}\int d^4k\langle p|\gamma_5[\gamma(p-k)+M]^{-1}\\&\times\gamma_5[\gamma(p-k)+M]^{-1}\gamma_5[\gamma(p-k)+M]^{-1}\\&\times\gamma_5/p\rangle[k^2+\mu^2]^{-1}\\=&-ig^2(2\pi)^{-4}\int d^4k\langle p|-\gamma k|p\rangle\\&\times[k^2-2pk]^{-2}[k^2+\mu^2]^{-1}\\\cong&g^2(16\pi^2M)^{-1}\end{aligned}\tag{A.1}$$

to lowest order in μ/M, as follows from the most elementary application of Feynman's methods. The corresponding result for Fig. 1(a) is proportional to M^{-3} as advertised.

We obtain similarly, for the correction to the emission of three mesons,

$$\begin{aligned}L_3=&-ig^2(2\pi)^{-4}\int d^4k\langle p|\gamma_5G(p-k)\gamma_5G(p-k)\gamma_5\\&\times G(p-k)\gamma_5G(p-k)\gamma_5/p\rangle[k^2+\mu^2]^{-1}\\\cong&g^2\log(M/\mu)(64\pi^2M^2)^{-1}\langle p|\gamma_5|p\rangle.\end{aligned}\tag{A.2}$$

Equation (A.2) vanishes, strictly speaking, and a more careful evaluation of the spin dependence is required, as is usually carried out. With this in mind, we have found in Eq. (A.2) an instance where the gradient coupling is effectively modified by radiative corrections. This would be true, for example, for the leading contribution to the potential arising from the exchange of three mesons. The matrix element of Fig. 2(b) is again proportional to M^{-3}.

Finally, for Fig. 2(c) we find

$$L_4\cong g^2(128\pi^2M^3)^{-1}[\log(M/\mu)-\tfrac{1}{2}].\tag{A.3}$$

All the terms computed in this section can therefore be considered corrections of order g^2 to the coupling proportional to $g^4\phi^4/M^3$ in the nonrelativistic limit.

Structure of the Nucleon. II. Pion-Nucleon Scattering*

R. G. SACHS
University of Wisconsin, Madison, Wisconsin
(Received May 10, 1954)

The scattering of pions by nucleons is treated on the basis of the assumption that the nucleon has a rather complex structure consisting of a core surrounded by varying numbers of pions in certain bound states. The scattering phase shift is found to be composed additively of two parts, an orthogonality phase shift determined by the condition that the incoming wave be orthogonal to the bound field and a phase shift due to the interaction between the incoming wave and the bound field plus core. The former phase is shown to be negative at low energy and to decrease rapidly with increasing energy. The other term is found to have a typical resonance behavior. Each of the parameters appearing in the formulas for the phase shifts is given a rather direct physical interpretation. When the parameters are chosen in such a way as to give a good over-all fit to the data up to 400 Mev the following picture of the nucleon emerges: The bound field consists of P waves concentrated at a small distance ($\frac{1}{4}$ the pion Compton wavelength) from the core and S waves extending to about twice that distance. The states of excitation (resonances) of the bound field consist of the usual P resonance with $J=\frac{3}{2}$, $I=\frac{3}{2}$, and a much broader S-wave resonance with $I=\frac{1}{2}$. Indications are that all other states of excitation lie higher (above 300 Mev) and are smeared out into a continuum through the emission of virtual pion pairs.

1. INTRODUCTION

IT seems likely, on the basis of existing evidence, that the nucleon is a complex, structured system. Support for this notion may be found in the existence of a variety of heavy mesons and hyperons which seem to be produced rather readily by interactions between nucleons, or between nucleons and pions. The proper field of a nucleon should involve these particles and, in turn, the particles should add to the complexity of the proper field. Other support for the assumption of structure is offered by the apparent existence of a resonance in the scattering of pions by nucleons. The notion of resonance is usually closely associated with the concept of structure, and there seems to be no reason to forego this satisfying relationship at the present time.

If the nucleon is a rather complex system, it is appropriate to discuss its structure by means of a specific model. The model used here is analogous to the nuclear model of the atom; the nucleon contains a core surrounded by a cloud of pions. It is strikingly different from the Rutherford model of the atom in that the number of pions is not a good quantum number. Pions are constantly being created and absorbed. This characteristic of the pion cloud is imposed to take account of the fact that real pions can be created and absorbed by nucleons. Only pions are included in the model, although it is expected that heavier mesons also play a role in the structure. The greater mass of these mesons suggest that they have a more limited range and therefore contribute to the inner structure, or to the structure of the core. The present discussion will be limited to consideration of rather low-energy pions whose behavior should be rather insensitive to the core structure. The heavy mesons still play an important role in that they contribute to the interaction between the core and the surrounding pions. All such interactions are lumped together to form the "interaction with the core" in the present model.

It is assumed that the characteristic vectors describing the states of the core and the meson field are normalizable. In this respect the present approach seems to differ markedly from the fundamental approach based on covariant forms of Yukawa's original theory. In those theories, divergences occur and they are presumably to be removed by some renormalization procedure. Much of the structure of the proper field of the nucleon is thereby removed. On the other hand, the model proposed here gives a literal meaning to the nucleon proper field and the results are finite by virtue of the assumed normalizability of the state vectors.

The proposed model has already been used[1] as the basis for a discussion of some of the characteristics of the ground state of the nucleon. The attempt in that work was to try to establish the conditions imposed on the state vector (or wave function) of the ground state by the observed properties of the nucleons, such as their magnetic moments. The results obtained in this way are quite general (within the scope of the model) and are independent of any detailed assumptions concerning the interaction between the core and the pions. It is of some interest to apply a similar procedure to the problem of pion-nucleon scattering. In view of the great variety of scattering data, this program should provide much more detailed information concerning the structure of the nucleon. The scattering problem actually concerns excited states of the nucleon, states

* This work has been supported in part by the U. S. Atomic Energy Commission and in part by the University of Wisconsin Research Committee with funds provided by the Wisconsin Alumni Research Foundation.

[1] R. G. Sachs, Phys. Rev. 87, 110 (1952). In Sec. 3 of this paper it is erroneously stated that all the coefficients are real in the expansion of the state vector in terms of states of a fixed number of pions. Actually, the coefficients are alternately real and imaginary as a function of the number of pions. No results of that work are affected by this change.

in the continuum. The probable existence of a resonance is of particular interest since it suggests the existence of a (rather unstable) state of the proper field of the nucleon.

In his early interpretation of the preliminary data on pion-nucleon scattering in terms of a resonance, Brueckner[2] very reasonably based the analysis on well-known properties of *nuclear* resonances. Formulas of the kind suggested by Feshbach, Peaslee, and Weisskopf[3] and by Wigner and Eisenbud[4] for the nuclear problem were applied to the pion scattering without appreciable change from their original form. These theories involve the concept of a fundamental distance (interaction radius) beyond which the scattered particle does not interact with the scattering center. This writer has not found it possible to justify such a concept in the pion-nucleon problem. The difficulty has to do with the small size of the interaction radius which appears to be characteristic of this problem. The distance is of the order of the Compton wavelength μ^{-1} of the pion. Hence, even for very slow pions, the relativistic Klein-Gordon equation must be used to describe the motion of the pion in the neighborhood of the region of interaction. The Klein-Gordon equation has the property that any local disturbance of even a free wave function is propagated over distances of the order of μ^{-1}. Hence no sharp distinction between the "inside" and "outside" region is possible; the influence of the region of interaction extends beyond the surface for distances as large as the interaction region itself. Consequently the complete set of "inside functions" characteristic of the Wigner-Eisenbud theory does not seem to exist here. Since the most satisfactory interpretation of nuclear resonances leans heavily on the existence of such a set of inside functions, it seems that the direct application of nuclear resonance formulas to the pion problem is not justified. In fact, there is a great need for clarification of the concept of resonance in this problem. The analysis presented below serves to define resonances in terms of the physical structure of the nucleon, and it provides a detailed substitute for the Wigner-Eisenbud type of analysis. The notion of inside and outside regions is not involved. The characteristic length replacing the interaction radius is determined by the size of the pion orbits in the nucleon. A typical resonance formula for each phase shift is obtained, but the interpretation of the constants is quite different from the interpretation of the corresponding quantities in nuclear problems.

Our approach to the problem has much in common with other attempts to analyze pion-nucleon scattering by means of nonrelativistic meson theory, such as those of Tomonaga,[5] Chew,[6] and Takeda.[7] However, our philosophy differs markedly from theirs in that no specific form for the fundamental interaction is assumed. Those properties of the interaction which are used here are rather general, and they probably have little influence on the qualitative form of the final results. It is hoped that the resulting general theory will give some insight into the reasons for the qualitative successes of the more specific theories. At the same time, the flexibility of the present point of view makes it possible to obtain a fairly detailed quantitative interpretation of the data in terms of properties of the nucleon which also influence other phenomena such as the photoproduction of pions and the nucleon-nucleon interaction. Hence the method may provide a means for correlating the results of a variety of experiments.

[2] K. S. Brueckner, Phys. Rev. **86**, 106 (1952).
[3] Feshbach, Peaslee, and Weisskopf, Phys. Rev. **71**, 145 (1947).
[4] T. Teichmann and E. P. Wigner, Phys. Rev. **87**, 123 (1952) presents the most up-to-date view of the Wigner-Eisenbud theory.
[5] Maki, Sato, and Tomonaga, Progr. Theoret. Phys. (Japan) **9**, 607 (1953).
[6] G. Chew, Phys. Rev. **89**, 591 (1953).
[7] G. Takeda, Phys. Rev. **95**, 1078 (1954).

2. QUALITATIVE DESCRIPTION OF THE THEORY

The state vector describing the ground state of the nucleon is, according to our assumptions, a function of the core spin and the number of pions occupying certain orbital functions centered on the core. For the sake of simplicity the recoil of the core is neglected. The space distribution of the pions dies off exponentially with distance from the core since the system is stable with respect to the emission of pions. Therefore it seems reasonable to assume that the orbits occupied by the individual pions may be described by one particle functions having a limited extent. Thus we introduce a discrete set of orthonormal functions $\varphi_{blm}(\mathbf{r})$, $b=1, 2, 3\cdots$, describing single pions of angular momentum l and magnetic quantum number m. It is a fundamental assumption of the theory that *the pion structure of the ground state of the nucleon can be completely described in terms of the number of pions occupying the states* φ_{blm}.

In meson theory it is usual to expand the fields in terms of free waves and thence to describe the field operators in terms of the number of pions occupying the free wave states. Clearly, it would be advantageous to expand the fields in terms of the bound functions φ_{blm}, rather than the free waves. However the φ_{blm} do not form a complete set since they are all limited in that they can be normalized. Therefore we supplement the set by introducing a set of functions φ_{plm} which are orthogonal to the φ_{blm} but otherwise behave like free waves. They then form a continuous set of functions, and the continuous parameter p may be taken to be the magnitude of the momentum of the pion at infinite distance from the core. The set of functions φ_{plm} may be obtained explicitly in terms of the bound functions φ_{blm} if it is assumed that the propagation of a free pion is determined in the usual way by the Klein-Gordon equation. This is done in Sec. 4. Because of the condition that they be orthogonal to the φ_{blm}, the functions φ_{plm} are shifted in phase with respect to free waves in the asymptotic region. The resultant phase shift, η_l, which will be called the "orthogonality phase shift," is given explicitly in terms of the functions φ_{blm} in Sec. 4. It is

shown there that η_l is negative at low energies, and that it decreases rather smoothly from 0 to pass through the value $-\pi/2$ as the energy of the state φ_{plm} is increased. For an energy range that is not too great, the energy dependence of the orthogonality phase shift may therefore be expressed by the equation [compare Eqs. (52) and (54)]

$$\tan\eta_l \approx -\pi p p_0 \frac{f_l'^2(p)}{p_l - p_0}, \tag{1}$$

where $p_0=(p^2+1)^{\frac{1}{2}}$ and $f_l'(p)$ is a function closely related to the Fourier transform of the radial part of the most extended bound state function. Energies, momenta, and propagation vectors are given here in units of the Compton wavelength of the pion, so p_0 is the total energy (kinetic plus rest energy) of the pion when it is at a large distance from the core. The quantity p_l defines the energy at which $\eta_l=-\pi/2$. It is also closely related to the bound state function, in fact p_l^{-1} gives the order of magnitude of the radius of the bound field of the nucleon. This connection is brought out by the condition [see Eq. (55)]

$$\mathrm{P}\int_0^\infty \frac{f_l'^2(k)k^2dk}{k_0-p_0} \approx p_l - p_0, \tag{2}$$

where $k_0=(k^2+1)^{\frac{1}{2}}$ and P denotes the principal part of the integral. If p_0 is replaced by p_l in Eq. (2) it becomes evident that p_l is closely related to the average value of k associated with the function $f_l'(k)$.

The properties of the orthogonality phase shifts can be understood on qualitative grounds. The condition of orthogonality amounts to a repulsion at low energy, it forces the incident wave out of the region occupied by the bound functions. Hence the phase shift is negative at low energy. Furthermore, when the pion has long wavelength it can see only the outer regions of the nucleon, therefore only the most extended of the bound functions is important. It is also clear that a large phase shift is to be expected when the pion wavelength is of the order of the radius of the bound field, since that is the controlling length in the problem.

The existence of a phase shift η_l implies that the mere existence of a bound field will lead to scattering, the "orthogonality scattering." It seems reasonable to use the orthogonality functions φ_{plm}, which already contain part of the scattering, as a basis for discussion of the scattering due to the interactions. This is accomplished by expanding the field operators in terms of the complete set of functions φ_{blm} and φ_{plm}. Then the total phase shift α_l is the sum of the appropriate η_l and a phase shift δ_l produced by the interactions between the bound and orthogonal fields.

The determination of δ_l requires some specification of the interaction, but only the interaction between the orthogonality states and the bound states is needed. Therefore the procedure is to introduce a simple coupling between the states φ_{plm} and the nucleon. The coupling used here is linear in the creation and annihilation operators of the orthogonality states. The dependence on the bound states need not be specified in detail for our purpose. This approach to the problem differs markedly from the usual procedure based on a well defined simple coupling between *free* waves and the core. Both the bound field and the scattering are determined from the more usual specification of the coupling. The resulting interaction between the bound field and the orthogonality waves can then be given in terms of that coupling, but the connection is complicated. The main difference between the usual procedure and our procedure rests in the choice of a place to use a simplicity argument. We choose to use the argument in such a way as to make the analysis of scattering as simple as possible. For this purpose the calculation has been organized around the notion of a bound field. The coupling of unbound waves with the bound field must then be specified, but the interaction responsible for the existence of the bound field does not play a direct role in the treatment. As a consequence of the reorganization, the notion of weak or strong coupling is quite different from the usual case. When our (reorganized) coupling vanishes, the scattering is given by the orthogonality phase shift, which may be quite large. On the other hand, there is no scattering when the conventional interaction vanishes. Hence, the absence of an interaction of the usual type corresponds to a reorganized coupling large enough to cause a cancellation of the orthogonality scattering.

The energy dependence of δ_l under the assumption of linear coupling from the reorganized point of view is obtained in Sec. 5. The quantity $\tan\delta_l$ has a typical resonance form:

$$\tan\delta_{lJI}=\pi p p_0\left(\frac{p}{p_0}\right)^{2l}\sum_{\eta(J,I)}\frac{g_{l\eta}'^2}{E_\eta'-p_0}, \tag{3}$$

where J and I denote the total angular momentum and isotopic spin of the system, respectively, E_η' is the energy of a state characteristic of the bound pion field, and $g_{l\eta}'(p)$ is the coupling with that state. Only those states $\eta(J,I)$ having the total angular momentum J and isotopic spin I are included in the sum. The ground state is not to be included. Although a detailed justification for the form of Eq. (3) is presented only for the case of linear coupling, it is likely that a similar result would be obtained for any other reasonable form of the coupling.

It will be found in Sec. 5 that the quantities $g_{l\eta}'^2$ are subject to a sum rule of the form

$$\sum_\eta g_{l\eta}'^2 = g_l^2, \tag{4}$$

where the sum includes all states compatible with a given l of the incident pion and g_l is the coupling for waves of orbital angular momentum l. It is expected that the coupling will involve the size of the core, hence

g_l will be constant at low momenta but will decrease rapidly at momenta corresponding to the core radius.

3. ANALYSIS OF THE DATA

We propose here to analyze the data on pion-nucleon scattering in terms of a total phase shift α_{IJl} which is made up additively of the orthogonality and interaction phase shifts given by Eqs. (1) and (3):

$$\alpha_{IJl}=\eta_l+\delta_{IJl}. \tag{5}$$

The application of Eqs. (1) and (3) will be made in the center-of-mass system although recoil has been neglected in the development of those equations. Attention will be limited to pions of low and intermediate energies, i.e., below 400 Mev (lab), in the hope that an analysis in terms of S and P waves will be adequate. The conventional notation for the corresponding phase shifts will be used:

α_1 and α_3 = S-wave phase shifts for $I=\frac{1}{2}$ and $\frac{3}{2}$,
α_{13} and α_{33} = P-wave phase shifts for $J=\frac{3}{2}$ and $I=\frac{1}{2}$, $I=\frac{3}{2}$,
α_{11} and α_{31} = P-wave phase shifts for $J=\frac{1}{2}$ and $I=\frac{1}{2}$, $I=\frac{3}{2}$.

Corresponding to these are the interaction phase shifts δ_1, δ_3, δ_{13}, δ_{33}, δ_{11}, and δ_{31}. It is to be noted that η_l does not depend on J or I, hence the two relevant phase shifts will be denoted by η_S and η_P.

For small values of k, the Fourier transform of the bound pion function will be independent of the detailed shape of the function. Since the factor $f_l'^2(p)$ appearing in Eq. (1) is closely related to this transform, it is expected that for pions of wavelength large compared to the size of the bound field $f_l'(p)$ will be proportional to p^l. This relationship should obtain up to some value, K, of p, and then, beyond the cutoff K, $f_l'(p)$ should drop rapidly to zero. The value of K^{-1} will be of the order of the size of the bound field. Thus we write

$$f_l'(p)\approx B_l\left(\frac{p}{p_0}\right)^l, \quad p<K,$$
$$\approx 0, \qquad\qquad p>K,$$

where B_l is a constant. In this approximation, Eq. (2) may be used to determine the cutoff:

$$B_l^2\,\mathrm{P}\int_0^K \frac{k^{2(l+1)}dk}{k_0^{2l}(k_0-p_0)}\approx p_l-p_0. \tag{6}$$

In particular, at energy $p_0=p_l$:

$$\mathrm{P}\int_0^K \frac{k^{2(l+1)}dk}{k_0^{2l}(k_0-p_l)}=0. \tag{7}$$

Thus K is given as a function of p_l. It turns out that $K\approx(p_l^2-1)^{\frac{1}{2}}$ and p_l will be found to be large enough for the long wavelength approximation to be used over the range of pion energies to be considered here. Hence, Eq. (1) may be replaced by

$$\tan\eta_l\approx-\pi p p_0\left(\frac{p}{p_0}\right)^{2l}\frac{B_l^2}{p_l-p_0} \tag{8}$$

for present purposes.

The observed pion nucleon scattering is to be analyzed in terms of an orthogonality phase shift given by Eq. (8). The two parameters B_l and p_l will be chosen to fit the data. However, those parameters are not independent, but are related by the condition Eq. (6). From an experimental value of p_l, K is determined by Eq. (7) and thence B_l^2 is determined by applying Eq. (6) at some definite energy, let us say $p_0=1$ corresponding to zero kinetic energy. The value of B_l so determined may then be compared with the experimental value to test the consistency of our assumptions.

Application of the conventional nonrelativistic meson theory in weak coupling approximation leads to the conclusion that the dominant bound pion function is a P function. This P function cannot be normalized if a point coupling between pion and core is used as the basis of calculation, but the normalization integral can be made to converge by introducing a finite source function into the interaction. From our point of view, this source function may be taken as a description of the extent of the core. It is expected to have a rather small radius, possibly of the order of the nucleon Compton wavelength. The source size determines the approximate cutoff K, which may therefore be expected to be of the same magnitude as M, the nucleon mass. Then the characteristic energy p_l appearing in Eq. (8) should be of the order $p_P\approx M$ for the P wave. Hence for the P scattering we shall be considering energies that are small compared to p_P so Eq. (8) may be replaced by

$$\tan\eta_P=-\pi p p_0(p/p_0)^2C_P, \tag{9}$$

where C_P is the constant

$$C_P=B_P^2/(p_P-1). \tag{10}$$

On the other hand, the S waves in the proper field can only be generated in pairs because of the odd parity of the pion. Hence the bound S functions are due to higher-order processes and some smearing out of the influence of the source is to be expected. In this case the cutoff K, and thence p_S will be small enough that the energy denominator in Eq. (8) cannot be ignored. We write then

$$\tan\eta_S=-\pi p p_0 B_S^2/(p_S-p_0). \tag{11}$$

Present indications are that the resonances in low-energy pion nucleon scattering are thoroughly isolated so that a one-level approximation to Eq. (3) should be reliable. This is obtained by assuming that there is just one value of E_ν' within the energy region of interest and that all other values are quite high compared with this.

Then Eq. (3) may be replaced by

$$\tan\delta_{lJI}\approx\pi pp_0\left(\frac{p}{p_0}\right)^{2l}\left\{\frac{g_r'^2}{E_r'-p_0}+Q_{lJI}\right\}, \quad (12)$$

where Q_{lJI} is the energy-independent contribution of the higher levels. We may write

$$Q_{lJI}=W_{lJI}^{-1}\sum_{\eta(J,I)\neq r}g_\eta'^2, \quad (13)$$

where W_{lJI} is the harmonic mean (weighted by the $g_\eta'^2$) of the energies of the high levels. In general g_r' may be an energy dependent function because it represents the coupling with a core of finite size. However, for the energy range of interest, it should be a good approximation to treat g_r' as a constant since the size of the core is probably smaller than the pion wavelength. Then the general form of δ_{lJI} involves three constant parameters, E_r', $g_r'^2$, and Q_{lJI}.

A considerable reduction in the number of parameters can be accomplished by consideration of the data on pion-nucleon scattering. First of all, we know that the only clear-cut P-wave resonance at low energy occurs in the phase shift α_{33}. Hence all three parameters must be used to describe δ_{33}:

$$\tan\delta_{33}=\pi pp_0\left(\frac{p}{p_0}\right)^2\left\{\frac{g_{33}'^2}{E_{33}'-p_0}+Q_{33}\right\}; \quad (14)$$

but the other P waves involve only a residue term:

$$\tan\delta_{ij}=\pi pp_0\left(\frac{p}{p_0}\right)^2 Q_{ij}, \quad ij=31, 13, 11.$$

A further simplification can be made on the basis of the total pion-nucleon cross section for high energies, well above the resonance.[8] In the neighborhood of 1 Bev the cross section is so large as to suggest that the nucleon is opaque. From our point of view, this would imply that the level density is high, hence many overlapping levels may be involved in Q_{lJI}. This view is given some support by the fact that multiple production of pions becomes quite probable in pion-nucleon collisions at these energies.[9] If this description is correct, it is not unreasonable to assume that

$$Q_{31}\approx Q_{13}\approx Q_{11}. \quad (15)$$

Q_{33} is not included in this relationship because the peeling off of a single strong resonance from the higher resonances may cause the region of overlapping resonances to shift upward.

On the basis of Eq. (15), we now write

$$\tan\delta_{ij}=\pi pp_0(p/p_0)^2Q_P \quad (16)$$

for $ij=31, 13, 11$.

The behavior of the S-wave phase shifts have been something of a mystery. In most analyses of the data it has been concluded that α_3 is negative and increasing in magnitude rather rapidly with energy. This can be understood within our description as the behavior of the orthogonality phase shift given by Eq. (11). Hence we assume that the interaction, or resonance part of α_{33} involves only very high resonances. Then from Eq. (12)

$$\tan\delta_3=\pi pp_0Q_3. \quad (17)$$

The energy dependence of α_1 is even more peculiar, it seems to be roughly constant at a value of approximately 10° over a wide range of energy. We can attain such a behavior by assuming the existence of a very broad resonance in the neighborhood of p_S. Then there is competition between the resonance and orthogonality scattering (η_1 and δ_S have opposite signs) with the result that the sum of the phase shifts is quite flat. Hence we set

$$\tan\delta_1=\pi pp_0\left\{\frac{g_1'^2}{E_1'-p_0}+Q_1\right\}. \quad (18)$$

We have now provided a basis for analysis of the pion-nucleon scattering in terms of the constants C_P, B_S^2, p_S (orthogonality scattering), $g_{33}'^2$, E_{33}', Q_{33}, Q_P, $g_1'^2$, E_1', and Q_1 and Q_3 (resonance scattering). The parameters are subject to the conditions imposed by Eq. (6) and by two others due to the sum rule Eq. (4). The latter conditions may be obtained by noting that Eq. (13) leads to

$$\sum_J Q_{lJI}=W_l^{-1}\sum_{\eta(I)\neq r}g_\eta'^2,$$

where W_l is the harmonic mean of the W_{lJI}. Hence we obtain by use of the sum rule

$$3Q_P+Q_{33}=W_P^{-1}(g_P^2-g_{33}'^2), \quad (19)$$

and

$$Q_3+Q_1=W_S^{-1}(g_S^2-g_1'^2). \quad (20)$$

Before considering the problem of fitting the data on scattering we note that a condition may be imposed on the S-wave parameters by combining the Panofsky experiment[10] with the cross section for photoproduction of pions from protons near threshold. Bernardini[11] gives the condition

$$|\alpha_1-\alpha_3|=(0.17\pm0.06)\ p \text{ radians}$$

[8] The following statements are based on data reported by Yuan, Piccioni, Thorndike, and Walker, Proceedings of the Fourth Annual Rochester High-Energy Conference (University of Rochester Press, Rochester, 1954.) See also, Walker, Crussard and Koshiba, Bull. Am. Phys. Soc. **29**, No. 4, 36 (1954).

[9] It will be found in Sec. 5 that the theory strongly suggests that the discrete states at higher energies will be washed out into a continuum. This results from the mixing of the unbound state continuum with the discrete states of the bound field. As it happens, the only contributing virtual states involve pairs of pions, so the smearing of the discrete states should set in at an energy above 280 Mev.

[10] Panofsky, Aamodt, and Hadley, Phys. Rev. **81**, 565 (1951); Brueckner, Serber, and Watson, Phys. Rev. **84**, 258 (1951).

[11] Reported by G. Bernardini, Proceedings of the Fourth Annual Rochester High-Energy Conference (University of Rochester Press, Rochester, 1954).

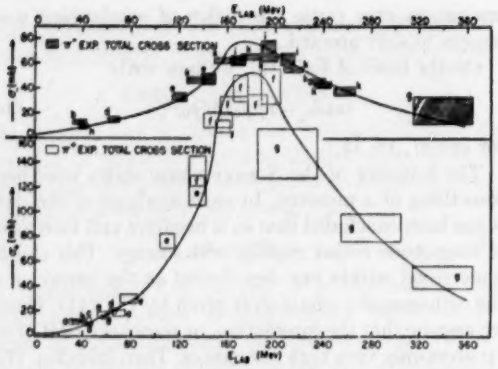

FIG. 1. Comparison of calculated total cross section of protons for pions with experiment. The lower curve refers to positive pions, the upper curve to negative pions. The curves are calculated on the basis of constants given by Eq. (23). The boxes are experimental values (see reference 14).

on the basis of the most recent data. The sign of $\alpha_1-\alpha_3$ will be taken to be positive[12] here, and since $\alpha_1-\alpha_3=\delta_1-\delta_3$, we find the condition

$$\delta_1-\delta_3=(0.17\pm0.06)p.$$

The low-energy limits of Eqs. (17) and (18) then provide the following empirical conditions on the parameters:

$$\pi\left(\frac{g_1'^2}{E_1'-1}+Q_1-Q_3\right)=0.17\pm0.06. \qquad (21)$$

The analysis of the scattering has been carried out in such a way as to maintain this condition.

The determination of the parameters has been accomplished by a method of trial and error based on the general qualitative features of the phase shifts that may be obtained from various published and unpublished direct analyses of the data. The effort has been limited to an attempt to obtain an overall fit to the data since our principal concern here is to see whether the experimental values of the parameters are in reasonable accord with the physical model on which the analysis is based.[13]

It turns out that α_{31}, α_{13}, and α_{11} are quite small so that a good approximation is obtained by setting

$$C_P=Q_P, \qquad (22)$$

the difference between them being of the order of a few percent. Then with the constants

$$B_S^2=0.25,\quad p_S=2.20,\quad Q_3=0.18,\quad Q_1=0,$$
$$g_1'^2=0.16,\quad E_1'=1.7,\quad C_P=Q_P=0.09, \qquad (23)$$
$$g_{33}'^2=0.035,\quad E_{33}'=1.79,\quad Q_{33}=0.074,$$

we have obtained the total scattering cross section curves shown in Fig. 1 along with the data.[14] To obtain the angular distributions, the quantities a, b, and c in the equation

$$d\sigma/d\Omega=a+b\cos\theta+c\cos^2\theta$$

have been calculated[15] as a function of the energy for π^+ scattering by protons (a_+, b_+, c_+), π^- elastic scatter-

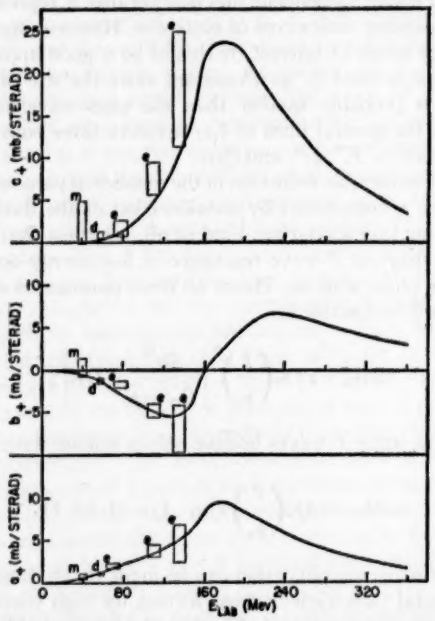

FIG. 2. The coefficients in the expression $a+b\cos\theta+c\cos^2\theta$ for the differential cross section for scattering of positive pions by protons. The curves are calculated from the constants given by Eq. (23). The boxes are experimental values (see reference 14).

[12] Bodansky, Sachs, and Steinberger, Phys. Rev. **90**, 997 (1953); J. P. Perry and C. E. Angell, Phys. Rev. **91**, 1289 (1953).

[13] Our analysis differs in one important way from that given by H. A. Bethe, Proceedings of the Fourth Annual Rochester High-Energy Conference (University of Rochester, Press, Rochester, 1954. He suggests that the phase shift α_3 is positive below 20 Mev and becomes negative above, in contrast to the behavior indicated in Fig. 5. We could provide for such a behavior by decreasing $B_S^2/(p_S-1)Q_3$. This would entail a readjustment of the other constants, but the consequent modification of the qualitative description of the nucleon has not been explored.

[14] Each experimental point shown in Figs. 1, 2, 3, and 4 is labeled to indicate its source. The references are:
[a] S. L. Leonard and D. H. Stork, Phys. Rev. **93**, 568 (1954).
[b] C. E. Angell and J. R. Perry, Phys. Rev. **92**, 835 (1953).
[c] Orear, Lord, and Weaver, Phys. Rev. **93**, 575 (1954).
[d] Bodansky, Sachs, and Steinberger, Phys. Rev. **93**, 1367 (1954).
[e] Anderson, Fermi, Martin, and Nagle, Phys. Rev. **91**, 155 (1953).
[f] Ashkin, Blaser, Feiner, Gorman, and Stern, Bull. Am. Phys. Soc. **29**, No. 4, 36 (1954).
[g] Reported by L. C. Yuan, Proceedings of the Fourth Annual Rochester High-Energy Conference (University of Rochester Press, Rochester, 1954).
[h] A. Roberts and J. Tinlot, Proceedings of the Fourth Annual Rochester High-Energy Conference (University of Rochester Press, Rochester, 1954). Barnes, Angell, Perry, Miller, Ring, and Nelson, Phys. Rev. **92**, 1327 (1953).
[i] Fermi, Glicksman, Martin, and Nagle, Phys. Rev. **92**, 161 (1953).
[j] Ashkin, Blaser, Feiner, Gorman, and Stern, Phys. Rev. **93**, 1129 (1954).
[k] J. R. Perry and C. E. Angell, Phys. Rev. **91**, 1289 (1953).

[15] Expressions for the coefficients a, b, and c in terms of the phase shifts α_{IJI} are given by Anderson, Fermi, Martin, and Nagle, Phys. Rev. **91**, 155 (1953).

ing by protons (a_-, b_-, c_-), and π^- charge exchange scattering by protons (a_0, b_0, c_0). The results are shown along with experimental values in Figs. 2, 3, and 4. The values of the three nonvanishing phases α_1, α_3, α_{33} used for the determination of the curves are shown in Fig. 5. They have been calculated by means of Eqs. (5), (9), (11), (14), (16), (17), (18), and (23). The influence of the Coulomb interaction has been ignored throughout the analysis.

The fit to the data seems adequate for present purposes. A more severe test of the theory would be provided by angular distribution measurements at high energy since almost all of the fitting has been done on the low-energy side of the resonance. The only available data appear to be those obtained at Brookhaven[16] for a pion energy of about 260 Mev. These are compared with the theory in Fig. 6. All points except the one at

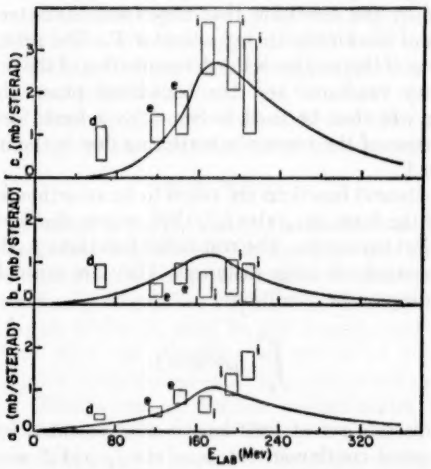

FIG. 3. The coefficients in the expression $a+b\cos\theta+c\cos^2\theta$ for the differential cross section for the nonexchange scattering of negative pions by protons. The curves are calculated from the constants given by Eq. (23). The boxes are experimental values (see reference 14).

180° are in remarkably good agreement with the theory and the experimental uncertainties in the data are so large that little weight can be given to that point. Although the number of parameters is large, the fitting of such a variety of data seems encouraging. The numerical values of the parameters are also very reasonable. Application of Eq. (7) to the S state leads to an S-wave cutoff at $K(S)=2.3$ corresponding to an energy $K_0(S)=2.5$. This may be introduced into Eq. (6) to determine B_S^2. For $p_0=1$ (the extreme case) we find $B_S^2=0.2$, in good enough agreement with the experimental value 0.25 given in Eq. (23). Although B_P^2 and P_P are not determined separately, it is possible

[16] Fowler, Lea, Shephard, Shutt, Thorndike, and Whittemore, Phys. Rev. 92, 832 (1953). It is now believed (private communication) that the energy is nearer 230 Mev than 260 Mev, but this would make but little difference in Fig. 6.

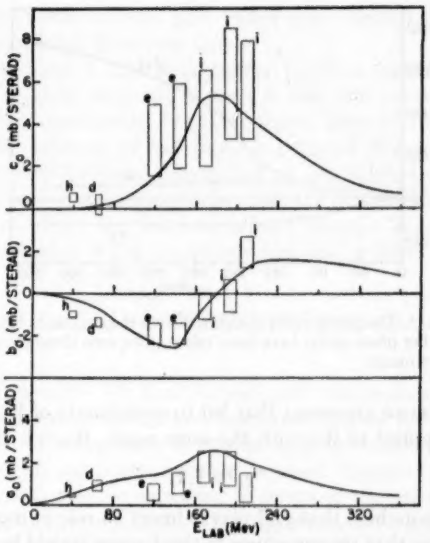

FIG. 4. The coefficients in the expression $a+b\cos\theta+c\cos^2\theta$ for the differential cross section for the exchange scattering of negative pions by protons. The curves are calculated from the constants given by Eq. (23). The boxes are experimental values (see reference 14).

to estimate the P-wave cutoff, $K(P)$ by means of Eq. (6) with $p_0=1$. It then reads

$$\mathrm{P}\int_0^{K(P)} \frac{k^4dk}{k_0^2(k_0-1)}=\frac{1}{C_P},$$

as can be seen by applying Eq. (10). Inserting the numerical value of C_P, we find $K(P)\approx 4$. This is larger than $K(S)$ as anticipated. It indicates that the source function for the P waves is smaller than that for an S wave but still somewhat larger than the nucleon Compton wavelength. The value of p_P may now be estimated from Eq. (7). The result is $p_P\approx 3.6$.

Further implications concerning the constants may be developed from the sum rules Eqs. (19) and (20). From the latter we find that

$$W_S^{-1}(g_S^2-0.16)=0.18.$$

Since W_S refers to the higher levels it is reasonable to assume that it is greater than the energy required to produce two pions,[9]

$$W_S>3.$$

But it is a harmonic mean of the higher levels so its value will probably lie close to the low end of the spectrum. Hence W_S is not likely to be much greater than the above lower limit, let us say, $W_S\approx 4$. Then

$$g_S^2\approx 0.9. \qquad (24)$$

From the corresponding sum rule for P waves, Eq. (19), we find

$$W_P^{-1}(g_P^2-0.035)=0.34.$$

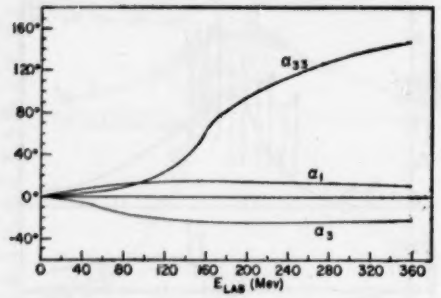

FIG. 5. The phase shifts calculated from the constants Eq. (23). All other phase shifts have been taken to be zero throughout this energy range.

The same argument that led to an estimate of W_S can be applied to W_P with the same result, $W_P \approx 4$. Hence

$$g_P^2 \approx 1.3. \tag{25}$$

We note here that $g_{33}'^2$ plays almost no role in the sum rule so that the resonance in the P wave should be considered to be a rather narrow resonance. Its "reduced width" $g_{33}'^2/g_P^2$ is about 0.03. The S resonance, on the other hand, is much broader, the reduced width being $g_1'^2/g_S^2 \approx 0.2$.

There emerges from this discussion the following over-all physical picture of the nucleon. The size of the core, or source function, as judged by the behavior of P waves, is about $\frac{1}{4}$ the Compton wavelength of the pion. The S waves are produced in a higher order so their source is spread to about twice that size. In fact the pion mass itself, rather than a source function, is probably the determining factor for the size of the bound S function. The magnitude of the coupling is about the same for S and P waves.

The excited states of the nucleon include many broad and overlapping levels at energies above 500 Mev. The famous P-wave resonance is due to a rather narrow level which is peeled off from the bottom of the group of high levels. A quite broad S level of isotopic spin $\frac{1}{2}$ also seems to occur at a lower energy. A test for the existence of this S level may be found in the photoproduction of pions from nucleons. This question is being examined at the present time.

4. FORMAL THEORY—ORTHOGONALITY SCATTERING[17]

As suggested in Sec. 2 the procedure to be followed makes use of a discrete set of bound single pion functions and the orthogonal set of unbound functions. The field operators are expanded in terms of the complete set formed by combining these two, and all operators are described in terms of the creation and annihilation operators of the bound and continuum states. The Hamiltonian of the system may then be separated into the sum of three terms. The first is the bound field Hamiltonian H_B, which involves only the bound states, the second is the kinetic energy T_u of the unbound field, and the third is the interaction V between the unbound and bound fields.

The operator H_B has a discrete set of characteristic values associated with states of the unbound field. These states form the basis for resonances in the scattering, their interaction with the unbound field being brought about by the coupling V. This coupling also causes the resonances to be somewhat shifted from their original positions and it introduces mixtures of continuum states which tend to broaden the higher resonances into an overlapping continuum.

The orthogonality or unbound functions are determined by the condition that they form characteristic states of the kinetic energy operator T_u. The principal concern of this section is the determination of the orthogonality functions and the associated phase shifts. These will then be used in Sec. 5 as a basis for the discussion of the resonance scattering due to the interaction V.

The bound functions are taken to be an orthonormal set of the form $\varphi_{blm}(\mathbf{r}) = f_{bl}(r) Y_l^m$, where the Y_l^m are spherical harmonics. The real radial functions f_{bl} decay exponentially at large distances. They are normalized according to the condition

$$\int_0^\infty f_{bl}^2 r^2 dr = 1.$$

The discrete set of functions is supplemented by an orthogonal continuous set $\varphi_{plm}(\mathbf{r}) = f_{pl}(r) Y_l^m$ so that the two sets together form a complete set for the pion field. The index p is taken to be the magnitude of the asymptotic momentum of a pion in this state. We may

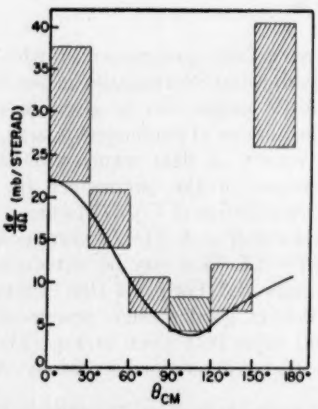

FIG. 6. Angular distribution for scattering of 260-Mev pions by protons. The curve is calculated from the constants given by Eq. (23). The boxes indicate experimental values (see reference 16).

[17] This treatment follows quite closely that of Maki, Sato, and Tomonaga (see reference 5). They consider the special case that only one bound field function need be considered and give the influence on the scattering the name "potential scattering" rather than orthogonality scattering. This kind of scattering was first noted by Wentzel, in his early treatment of strong coupling theories, see G. Wentzel, Helv. Phys. Acta **16**, 551 (1943).

now expand the field operators in terms of the functions φ_{blm} and φ_{plm} and the coefficients in the expansion will be the creation and annihilation operator for the bound states, $a^*(b,l,m,t)$, $a(b,l,m,t)$ and for the unbound states $a^*(p,l,m,t)$ and $a(p,l,m,t)$. The label t is the charge component of the isotopic spin, $t=1$, 0, or -1 implies that the operator refers to positive, neutral, or negative pions, respectively.

The Hamiltonian of the pion field in interaction with the core may now be expressed in terms of the operators a^* and a. It is convenient to write the Hamiltonian as the sum of three terms:

$$H=H_B+T_u+V, \tag{26}$$

where H_B is the Hamiltonian of the bound field; it depends only on the $a^*(b,l,m,t)$ and $a(b,l,m,t)$ but contains both the kinetic energy of these pions and their interaction with the core. T_u is the kinetic energy of the unbound field, it depends only on the $a^*(p,l,m,t)$ and $a(p,l,m,t)$, and in a manner which will be obtained in the following. V depends on the operators of both the bound and unbound fields; it will be called "the interaction" between the unbound and bound fields.

We consider first the solutions of the equation,

$$H_B\chi_\lambda=E_\lambda\chi_\lambda. \tag{27}$$

The spectrum of the E_λ will be discrete because the set of bound functions (which are the only ones involved here) is discrete. However, the number of characteristic values E_λ will be infinite. The state χ_0 corresponding to the lowest of the E_λ must be the ground state of the nucleon since the functions φ_b provide a complete description of the ground state, according to our assumptions. Other states χ_λ describe excited states of the bound field of the nucleon. They are expected to be nonstationary states because of the effect of the interaction V which has not been included in Eq. (27).

We may now consider the solutions of the equation

$$(H_B+T_u)\psi=E\psi. \tag{28}$$

Since H_B involves only bound field operators and T_u only those of the unbound field, the equation may be separated by the substitution

$$\psi=\chi_\lambda\Psi,$$

where Ψ is a function only of the occupation numbers of the unbound states. Because T_u is just a kinetic energy, it involves no interactions with the pions, hence it suffices to solve the problem for the case in which just one unbound state of energy $p_0=(p^2+1)^{\frac{1}{2}}$, and quantum numbers l, m, t, is occupied. Then we must determine the solution of

$$T_u\Psi_{plmt}=p_0\Psi_{plmt}, \tag{29}$$

and we have

$$\psi=\chi_\lambda\Psi_{plmt}, \tag{30}$$

with

$$E=E_\lambda+p_0. \tag{31}$$

The solution of Eq. (29) yields a convenient set of orthogonality functions $f_{pl}(r)$.

The form of the kinetic energy T_u of the bound field can be given explicitly because it does not involve the interactions directly. For this purpose, some description of the behavior of free pions is required. We assume that they propagate according to the Klein-Gordon equation or, more specifically, that the free pion field is described by the Pauli-Weisskopf theory. Then the Hamiltonian of the completely free field is given by

$$T=\sum_{l,m,t}\int k^2dkk_0a^*(k,l,m,t)a(k,l,m,t), \tag{32}$$

with $k_0=(k^2+1)^{\frac{1}{2}}$, if $a^*(k,l,m,t)$ and $a(k,l,m,t)$ are the creation and annihilation operators of *free* spherical waves of momentum k, orbital angular momentum l magnetic quantum number m, and charge t. The $a(k,l,m,t)$ may be expanded in terms of the operators $a(b,l,m,t)$ and $a(p,l,m,t)$. When the expansion is inserted into Eq. (32) it is found that T contains a part that depends only on the $a(p,l,m,t)$. This is the operator T_u. The required expansion is

$$a(k,l,m,t)=\sum_b f_{bl}(k)a(b,l,m,t)+\int p^2dpf_{pl}(k)a(p,l,m,t), \tag{33}$$

where

$$f_{bl}(k)=(2/\pi)^{\frac{1}{2}}\int r^2dr\,j_l(kr)f_{bl}(r), \tag{34}$$

and

$$f_{pl}(k)=(2/\pi)^{\frac{1}{2}}\int r^2dr\,j_l(kr)f_{pl}(r) \tag{35}$$

are the radial functions of bound and unbound waves in a (spherical) momentum representation. The functions $j_l(kr)$ are the usual regular spherical Bessel functions. The transformation inverse to Eq. (33) is

$$a(b,l,m,t)=\int k^2dkf_{bl}(k)a(k,l,m,t), \tag{36}$$

$$a(p,l,m,t)=\int k^2dkf_{pl}(k)a(k,l,m,t). \tag{37}$$

The operator T_u may now be obtained by replacing the $a(k,l,m,t)$ in Eq. (32) by the part of Eq. (33) referring only to unbound waves. Thus

$$T_u=\sum_{l,m,t}\int k^2dkk_0[a^*(k,l,m,t)-\sum_b f_{bl}(k)a^*(b,l,m,t)]\times[a(k,l,m,t)-\sum_{b'}f_{b'l}(k)a(b',l,m,t)].$$

Substitution of Eq. (36) then yields the result

$$T_u=\sum_{l,m,t}\Big\{\int k^2dkk_0a^*(k,l,m,t)a(k,l,m,t)$$
$$-\sum_b\int k^2dk\int k'^2dk'(k_0+k_0')f_{bl}(k)f_{bl}(k')$$
$$\times a^*(k,l,m,t)a(k',l,m,t)$$
$$+\sum_{b,b'}\omega_{bb'}{}^l\int k^2dk\int k'^2dk'f_{bl}(k)f_{b'l}(k')$$
$$\times a^*(k,l,m,t)a(k',l,m,t)\Big\}, \quad (38)$$

where

$$\omega_{bb'}{}^l=\int k^2dkk_0f_{bl}(k)f_{b'l}(k). \quad (39)$$

This operator is now applied to the state Ψ_{plmt} in which the orthogonality function $f_{pl}Y_l^m$ of energy p_0 and quantum numbers l, m, t is occupied once. The wave function appears as the coefficient of an expansion of Ψ_{plmt} in terms of singly occupied free pion states. To obtain $f_{pl}(k)$, the function in momentum representation, we expand in terms of the characteristic states $\Phi[N(k,l,m,t)=1]$ of a single free pion in an orbit of given k, l, m, t:

$$\Psi_{plmt}=\int k^2dkf_{pl}(k)\Phi[N(k,l,m,t)=1].$$

In applying T_u as given by Eq. (38), the operators $a(k,l,m,t)$ annihilate the pion in Φ and the $a^*(k,l,m,t)$ recreate it. Hence

$$T_u\Psi_{plmt}=\sum_{l,m,t}\int k^2dk\Big\{k_0f_{pl}(k)$$
$$-\sum_b\int k'^2dk'(k_0+k_0')f_{bl}(k)f_{bl}(k')f_{pl}(k')$$
$$+\sum_{bb'}\omega_{b'b}{}^l\int k'^2dk'f_{bl}(k)f_{b'l}(k')f_{pl}(k')\Big\}$$
$$\times\Phi[N(k,l,m,t)=1].$$

The equation for $f_p{}^l(k)$ is now obtained from Eq. (29) by making use of the linear independence of the state vectors Φ:

$$(k_0-p_0)f_{pl}(k)=\sum_{b,b'}f_{bl}(k)\int k'^2dk'$$
$$\times[(k_0+k_0')\delta_{b'b}-\omega_{b'b}{}^l]f_{b'l}(k')f_{pl}(k').$$

It is easily established (by multiplying by $f_{b''l}(k)$ and integrating) that the f_{pl} satisfying this equation *are* orthogonal to the bound state functions f_{bl}. Therefore the integrals involving coefficients k_0 and $\omega_{b'b}{}^l$ vanish and the integral equation takes the form

$$(k_0-p_0)f_{pl}(k)=\sum_b f_{bl}(k)\int k'^2dk'k_0'f_{bl}(k')f_{pl}(k'). \quad (40)$$

This particularly simple integral equation is susceptible to explicit solution. If we let $\Lambda_{bl}(p)$ be the integral

$$\Lambda_{bl}=\int k^2dkk_0f_{bl}(k)f_{pl}(k), \quad (41)$$

a formal solution of the equation is[18]

$$f_{pl}(k)=\frac{1}{k^2}\delta(k-p)+\frac{1}{k_0-p_0}\sum_b\Lambda_{bl}(p)f_{bl}(k). \quad (42)$$

According to Eq. (41), $\Lambda_{bl}(p)$ then satisfies the equation

$$\Lambda_{bl}=p_0f_{bl}(p)+p_0\sum_{b'}R_{bb'}{}^l(p)\Lambda_{b'l}(p)$$
$$+\sum_{b'}\int k^2dkf_{bl}(k)f_{b'l}(k)\Lambda_{b'l}(p), \quad (43)$$

where $R_{bb'}{}^l$ is the symmetric matrix

$$R_{bb'}{}^l(p)=\mathrm{P}\int k^2dk\frac{f_{bl}(k)f_{b'l}(k)}{k_0-p_0}. \quad (44)$$

The symbol P indicates that the principal part of the integral is to be taken. The last term on the right-hand side of Eq. (43) is just $\Lambda_{bl}(p)$ by virtue of the orthonormality of the f_{bl}. Hence $\Lambda_{bl}(p)$ is determined by the algebraic equations,

$$\sum_{b'}R_{bb'}{}^l(p)\Lambda_{b'l}(p)=-f_{bl}(p). \quad (45)$$

The solution of Eq. (45) at a given value of p may be introduced into Eq. (42) to give an explicit form for the orthogonality functions at energy p_0.

A formal solution of Eq. (45) is obtained by introducing the orthogonal transformation $U_{\beta b}{}^l(p)$ which brings $R_{bb'}{}^l(p)$ to diagonal form for a given value of p. If the characteristic values of $R_{bb'}{}^l(p)$ are $\rho_{\beta l}$, Eq. (45) becomes

$$\Lambda_{\beta l}'(p)=-f_{\beta l}'(p)/\rho_{\beta l}(p), \quad (46)$$

where

$$\Lambda_{\beta l}'=\sum_b U_{\beta b}{}^l\Lambda_{bl}, \quad (47)$$

and

$$f_{\beta l}'=\sum_b U_{\beta b}{}^lf_{bl}. \quad (48)$$

These results are useful for the determination of the orthogonality phase shift.

To determine the phase shift, the function (42) may

[18] Since we are dealing with waves of given l, there is no ambiguity concerning incoming and outgoing waves. Hence we choose the real solution of the equation and the quantity $(k_0-p_0)^{-1}$ is to be interpreted as the principal part in an integral operator. The delta function is the free wave transformed to the k representation.

be transformed to a space representation by the transformation inverse to Eq. (35):

$$f_{pl}(r)=(2/\pi)^{\frac{1}{2}}\int k^2dk\,j_l(kr)f_{pl}(k). \tag{49}$$

From the asymptotic form of $j_l(kr)$:

$$j_l(kr)\underset{r\to\infty}{\longrightarrow}\frac{1}{kr}\sin\left(kr-\frac{l\pi}{2}\right),$$

we then find by the usual procedure[19] that

$$f_{pl}(r)\underset{r\to\infty}{\longrightarrow}(2/\pi)^{\frac{1}{2}}\frac{1}{\cos\eta_l}\frac{1}{pr}\sin\left(pr-\frac{l\pi}{2}+\eta_l\right), \tag{50}$$

where the orthogonality phase shift η_l is given by

$$\tan\eta_l=\pi p p_0\textstyle\sum_b\Lambda_{bl}(p)f_{bl}(p). \tag{51}$$

An equivalent equation is

$$\tan\eta_l=\pi p p_0\textstyle\sum_\beta\Lambda_{\beta l}'(p)f_{\beta l}'(p),$$

since the transformation U from the unprimed to the primed quantities is orthogonal. Then Eq. (46) yields the final result

$$\tan\eta_l=-\pi p p_0\textstyle\sum_\beta\dfrac{[f_{\beta l}'(p)]^2}{\rho_{\beta l}(p)}. \tag{52}$$

Because of the simple structure of $R_{bb'}{}^l$, given by Eq. (44), it can now be established that every $\rho_{\beta l}$ is positive for $p=0$ and negative as $p\to\infty$. For an arbitrary set of constants A_b, we can write

$$\textstyle\sum_{b,b'}A_bR_{bb'}{}^l(p)A_{b'}=\mathrm{P}\int k^2dk\dfrac{F^2(k)}{k_0-p_0} \tag{53}$$

according to Eq. (44), where

$$F(k)=\textstyle\sum_b A_bf_{bl}(k).$$

But the integrand in Eq. (53) is everywhere positive for $p=0$ and negative for $p\to\infty$, so the left-hand side has the same property. If the A_b are chosen to be the $U_{\beta b}{}^l(p)$, the left hand side of Eq. (53) is just $\rho_{\beta l}(p)$.

It follows that $\rho_{\beta l}$ is positive at low energy, passes through zero with increasing energy, and becomes negative for very large energy. Hence η_l, given by Eq. (52), is negative at low energy and passes through $-(\pi/2)$ as the energy is increased. Beyond that point anything may happen because of the conflict between the various $\rho_{\beta l}$ appearing in Eq. (52), but at very large energy η_l will finally lie in the first or third quadrant. The energy at which the first crossover occurs [i.e., the lowest energy at which $\eta_l=-(\pi/2)$] is determined by the most rapidly varying of the $\rho_{\beta l}$. An examination of the form of $R_{bb'}{}^l$ indicates that this $\rho_{\beta l}$ will be closely associated with the most rapidly varying (as a function of momentum) bound field function $f_{bl}(k)$. The corresponding function $f_{bl}(r)$ in configuration space will be the most slowly varying, or the most extended of the bound field functions. Hence the behavior of the orthogonality phase shift at low energy is governed by the most extended bound function (or functions), that is by the outer parts of the nucleon.

The approximate Eq. (1) is obtained by limiting attention to the neighborhood of the first crossover point. The function $f_l'(p)$ is proportional to that one of the $f_{\beta l}'(p)$ controlling the crossover; hence it is related to the most extended bound state function. The approximation should be valid over a not too wide energy range in the neighborhood of the crossover unless another bound function of quite different character interferes with $f_l'(p)$. That would imply that the outer structure of the nucleon is quite complicated.

In the neighborhood of the crossover we may write

$$\rho_{\beta l}(p)\approx\gamma(p_l-p_0), \tag{54}$$

where p_l is the value of the energy p_0 at which crossover occurs and γ is a constant. Now according to Eq. (53) ff. we may write

$$\rho_{\beta l}=\mathrm{P}\int k^2dk\frac{F_{\beta l}{}^2(p,k)}{k_0-p_0},$$

where

$$F_{\beta l}(p,k)=\textstyle\sum_b U_{\beta b}{}^l(p)f_{bl}(k),$$

and, in particular

$$F_{\beta l}(k,k)=f_{\beta l}'(k).$$

In the approximation used here, namely, that approximation on which Eq. (8) is based, we may replace $F_{\beta l}(p,k)$ by $f_{\beta l}'(k)$ for all relevant values of p, since $U_{\beta b}{}^l$ is nearly independent of energy. This fact, when combined with the estimate (54), yields the result

$$\mathrm{P}\int k^2dk\frac{f_{\beta l}'{}^2(k)}{k_0-p_0}\approx\gamma(p_l-p_0). \tag{55}$$

The relationship Eq. (2) is obtained by noting that

$$f_{\beta l}'{}^2=\gamma f_l'{}^2.$$

5. FORMAL THEORY—THE INTERACTION

A complete determination of the scattering requires a knowledge of the interaction term V appearing in the Hamiltonian Eq. (26). The interaction involves both the operators $a(p,l,m,t)$ and $a(b,l,m,t)$. The former bring the incident orthogonality wave into the interaction and the latter show the influence of the bound field on the interaction. The dependence on the bound field will undoubtedly be rather complicated but we may just as well make the simplest possible assumptions about the effect on the unbound wave. Therefore we assume that

[19] C. Møller, Kgl. Danske Videnskab. Selskab, Mat.-fys. Medd. 22, No. 19 (1945); 23, No. 1 (1946); W. Heisenberg, Z. Naturforsch. 1, 607 (1946).

that V is linear in the creation and annihilation operators $a^*(p,l,m,t)$ and $a(p,l,m,t)$. If the usual assumption of charge independence of the interaction is introduced we may then write V in the form[20]

$$V=\sum_{l,m,t}\int p^2dp(p/p_0)^l g_l(p)[\Omega_{lmt}a^*(p,l,-m,-t) +\Omega_{lmt}^*a(p,l,-m,-t)], \quad (56)$$

where Ω_{lmt} is an operator depending on the $a(b,l,m,t)$, $a^*(b,l,m,t)$, and the spin of the core of the nucleon. It has the transformation properties of the spherical harmonic Y_l^m under rotations in ordinary space and, in charge space, it has the transformation properties of an isotopic spin one function with charge component t. The dependence of g_l on momentum is included to take account of the finite size of the region within which the pion undergoes interaction.

The coupling operator Ω_{lmt} is subject to another very important restriction due to the fact that the ground state χ_0 of the nucleon is supposed to involve just the bound field. This means that χ_0 is a characteristic function of the total Hamiltonian (as well as H_B alone) and that no orthogonality states are produced when H operates on χ_0. Hence the Ω_{lmt} must be projection operators with the property

$$\Omega_{lmt}\chi_0=0. \quad (57)$$

The calculation of the scattering is now based on the product functions Eq. (30) which describe a state of the bound field combined with a single pion in a certain orthogonality state.[21] The coupling between the functions introduced by V causes an additional phase shift δ_l over and above the phase shift η_l. The phase shift may be obtained by a straightforward application of the Møller[19] scattering formalism:[22]

$$\tan\delta_{lJI}=-\pi pp_0\left\langle\psi_{lJI}{}^0(p), \times V\frac{1}{p_0-H_0-V[1/(p_0-H_0)]V}V\psi_{lJI}{}^0(p)\right\rangle, \quad (58)$$

where $\psi_{lJI}{}^0(p)$ is a state of total angular momentum J and isotopic spin I formed by taking the proper linear combination of the products Eq. (30) in which χ_λ has been replaced by the ground state functions[23] χ_0. The zero-order Hamiltonian H_0 is

$$H_0=H_B+T_u. \quad (59)$$

Now because of the condition Eq. (57),

$$V\psi_{lJI}{}^0=\sum_{m,t}\int p'^2dp'(p'/p_0')^l g_l(p')\Omega_{lmt}{}^* \times a(p',l,-m,-t)\psi_{lJI}{}^0. \quad (60)$$

Furthermore, the function $\psi_{lJI}{}^0$ may be written in the form

$$\psi_{lJI}{}^0(p)=\sum_{m,t}\chi_{0,M-m,C-t}\Psi_{p,l,m,t} \times\langle M,M-m|J,M\rangle\langle t,C-t|I,C\rangle, \quad (61)$$

where M and C are the z component and charge component of the angular momentum and total isotopic spin, respectively, and the brackets denote the usual Clebsch-Gordan-Wigner coefficients. Application of the annihilation operator in Eq. (60) eliminates the once-occupied unbound state in Eq. (61):

$$V\psi_{lJI}{}^0(p)=(p/p_0)^l g_l(p)\sum_{m,t}\Omega_{lmt}{}^*\chi_{0,M+m,C+t} \times\langle m,M+m|J,M\rangle\langle t,C+t|I,C\rangle. \quad (62)$$

Because the χ_0 describe a state of total angular momentum $\frac{1}{2}$ and total isotopic spin $\frac{1}{2}$, the product $\Omega^*{}_{lmt}\chi_{0,M+m,C+t}$ may be expanded in terms of functions characterized by total angular momenta having the values $l\pm\frac{1}{2}$ and total isotopic spin values $\frac{1}{2}$ or $\frac{3}{2}$. The orthogonality properties of the Clebsch-Gordan-Wigner coefficients guarantee that just those terms having the incident J, I, M, and C will remain in Eq. (62), as is required by the conservation laws. Since the expression on the right depends only on the bound field, it can be expanded in terms of the bound field functions χ_λ having values of $\lambda=\lambda(J,I)$ corresponding to the given values of J and I:

$$V\psi_{lJI}{}^0(p)=(p/p_0)^l g_l(p)\sum_{\lambda(JI)}\Omega_{l\lambda}{}^*\chi_\lambda, \quad (63)$$

where the $\Omega_{l\lambda}{}^*$ are the constants (independent of M and C)

$$\Omega_{l\lambda}{}^*=\sum_{m,t}\langle\chi_{\lambda,M,C},\Omega_{lmt}{}^*\chi_{0,M+m,C+t}\rangle \times\langle m,M+m|J,M\rangle\langle t,C+t|I,C\rangle. \quad (64)$$

The introduction of Eq. (63) into Eq. (58) leads immediately to the result

$$\tan\delta_{lJI}=-\pi pp_0\left(\frac{p}{p_0}\right)^{2l}g_l^2(p)\sum_{\lambda,\lambda'}\Omega_{l\lambda}\Omega_{l\lambda'}{}^* \times\left\langle\chi_\lambda,\frac{1}{p_0-E_\lambda-V[1/(p_0-H_0)]V}\chi_{\lambda'}\right\rangle, \quad (65)$$

[20] The factors $(p/p_0)^l$ are inserted to take account of the effect of the centrifugal barrier on the coupling. Such factors usually appear in the conventional theories, as for example in the case of $\sigma\cdot\text{grad}\varphi$ coupling. They guarantee that the phase shifts will have the usual p^{2l+1} dependence on energy at zero energy characteristic of a short range interaction.

[21] The functions Eq. (42) with the asymptotic form Eq. (50) must be multiplied by $\cos\eta_l$ in order that they be properly normalized for this calculation.

[22] B. A. Lippann and J. Schwinger, Phys. Rev. **79**, 469 (1950); G. Chew and M. L. Goldberger, Phys. Rev. **87**, 778 (1952); K. A. Brueckner and K. M. Watson, Phys. Rev. **90**, 699 (1953). A very useful summary of these methods is given by Watson and Brueckner in Los Alamos report AECU-2765 (unpublished).

[23] There are four states χ_0 corresponding to two states each of spin and isotopic spin polarization. The corresponding quantum numbers are made explicit only when necessary, as in Eq. (61).

the values of λ and λ' being limited to those associated with angular momentum J and isotopic spin I. Use has been made here both of the relationship

$$H_0\chi_\lambda = E_\lambda\chi_\lambda$$

which follows from Eq. (27), and the fact that no unbound pions occur in χ_λ.

Consider the transformation that brings the operator

$$H' = E_\lambda + V\frac{1}{p_0 - H_0}V$$

into diagonal form. This transformation mixes the different bound pion states χ_λ with one another. It also mixes them with states containing even numbers of unbound pions because V depends on the creation operators linearly. For those characteristic states of H' with characteristic values (energies) E_η' that are small compared to twice the pion mass, the contributions from the unbound pions are expected to be small, and the spectrum of the E_η' will be closely related to that of the E_λ. In other words, the low-lying E_η' will be discrete although they differ from the corresponding E_λ in numerical value. For higher values of E_η' the virtual pairs of pions will play an important role and the spectrum will involve a mixing of the discrete E_λ with the continuous spectrum of the free pairs. Hence the spectrum will rapidly approach a continuum for levels above the energy required to produce two pions in addition to the incident pion.

That the E_η' are the actual resonances in the scattering can be seen by transforming Eq. (65) to the new representation. If the matrix q_l is defined in such a way that its matrix elements between bound pion states of the same J, I, M, and C are

$$q_{\Omega'\lambda} = \Omega_\Omega\Omega_{\Omega'}^*, \tag{66}$$

and all other matrix elements vanish, we have,

$$\tan\delta_{lJI} = -\pi p p_0\left(\frac{p}{p_0}\right)^{2l} g_l^2(p)\,\mathrm{Tr}\left[q_l\frac{1}{p_0 - H'}\right],$$

where the trace includes only the subspace having given J, I, M, and C. When H' is brought to diagonal form this becomes

$$\tan\delta_{lJI} = -\pi p p_0\left(\frac{p}{p_0}\right)^{2l} g_l^2(p)\sum_{\eta(J,I)}\frac{q_{l\eta\eta}'}{p_0 - E_\eta'}, \tag{67}$$

where q_l' is the transformed matrix q_l. Because of its simple form, Eq. (66), it can easily be established that the matrix q_l is non-negative. Hence the quantities $q_{l\eta\eta}'$ are positive and we can write

$$g_{l\eta}'^2(p) = g_l^2(p)q_{l\eta\eta}'. \tag{68}$$

The expression Eq. (3) for $\tan\delta_{lJI}$ then follows immediately from Eq. (67).

In order to obtain the sum rule, Eq. (4), we note that

$$\sum_{\eta(J,I)} g_{l\eta}'^2(p) = g_l^2(p)\,\mathrm{Tr}q_l' = g_l^2(p)\,\mathrm{Tr}q_l,$$

and, from the definition Eq. (66) of q_l

$$\sum_{\eta(J,I)} g_{l\eta}'^2(p) = g_l^2(p)\sum_{\lambda(JI)}|\Omega_\Omega|^2.$$

If the expression Eq. (64) is now substituted for Ω_Ω^* and the resulting expression is summed over $J = l \pm \frac{1}{2}$ and $I = \frac{1}{2}, \frac{3}{2}$, we find

$$\sum_\eta g_{l\eta}'^2(p) = g_l^2(p)\sum_{m,t} \times\langle\chi_{0,M-m,C-t},\,\Omega_{lmt}\Omega_{lmt}^*\chi_{0,M-m,C-t}\rangle,$$

by making use of the completeness of the states χ_λ (for bound fields) and of the orthonormality of the Clebsch-Gordan-Wigner coefficients. The sum is independent of M and C because Ω_Ω^*, given by Eq. (64), is independent of them. Since the normalization of the operator Ω_{lmt} has not been specified, it may be chosen in such a way that

$$\sum_{m,t}\langle\chi_{0,M-m,C-t},\,\Omega_{lmt}\Omega_{lmt}^*\chi_{0,M-m,C-t}\rangle = 1,$$

and the form Eq. (4) for the sum rule follows immediately.

6. CONCLUSION

The rather phenomenological theory that has been described here seems to offer a method for extracting from the observations on pion-nucleon scattering some information concerning the structure of the nucleon and the interactions between pions and nucleons. The method is based on the assumption that the nucleon is a complex system so it is natural that a number of parameters appear in the theory. Within the rather broad range of the uncertainties in presently available experimental data, the method looks promising; the parameters can be chosen in such a way as to fit the data and, at the same time, in such a way as to satisfy all the qualitative restrictions placed on them by the model.

The theory has the obvious weakness that the positions of the resonances, and their widths, appear as parameters to be fixed by comparison with the data. Theoretically, these parameters are determined by the interaction term in H_B, the bound field Hamiltonian, so it may be possible, on the basis of precise data, to determine that interaction as well as the coupling to the unbound field.

Further insight into the model is now to be obtained by considering the problems of photopion production and the forces between nucleons. The theory would seem to provide a rather direct correlation between these phenomena and the pion-nucleon scattering.

This work has been assisted by many people. W.

Holladay and R. Capps devoted much of their time to an attempt to formulate a theory based on the notion of free waves outside a nucleon of finite radius. As mentioned in the Introduction, this program did not succeed. Professor Gyo Takeda has been a constant adviser and critic of the work, and he has brought the details of Tomonaga's work to the author's attention. Professor K. M. Watson has made many useful suggestions, some of them quite essential to the completion of the program.

PHYSICAL REVIEW VOLUME 95, NUMBER 4 AUGUST 15, 1954

Application of the Intermediate Coupling Theory to the Scattering of Pseudoscalar Mesons by a Nucleon*

GYO TAKEDA†
Department of Physics, University of Wisconsin, Madison, Wisconsin
(Received March 29, 1954; revised manuscript received May 21, 1954)

Tomonaga's intermediate coupling theory is applied to the scattering of pseudoscalar mesons by a nucleon. The scattering cross section depends on the cut-off momentum of the meson field and the coupling strength between the nucleon and the meson field. For reasonable values of the coupling strength, we calculated numerically the wave function of the meson field around a nucleon. By making use of these results the scattering phase shifts are calculated for various values of the cut-off momentum. Agreement with recent experimental results is not very good, although most of the qualitative features of the experiments are reproduced. A modification of the source function of the meson field can be expected to give a better fit with the experimental results.

I. INTRODUCTION

RECENTLY Tomonaga, Maki, and Sato[1] applied the intermediate coupling theory to the problem of meson scattering by a free nucleon. Their calculation is based on the charged longitudinal vector theory for reasons of simplicity. In order to examine the results obtained in a somewhat more realistic theory, we shall apply the same method to the symmetrical pseudoscalar meson theory with pseudovector coupling.

According to the idea of Tomonaga, mesons are classified into bound mesons and unbound mesons. The former are supposed to be in a definite bound state around a core nucleon and the latter in states orthogonal to the bound state. As the function of the bound state we assume that characteristic of the classical field around a nucleon, which is also the same as the wave function of the meson field produced by a nucleon either in the limit of weak coupling or in the limit of strong coupling. This function depends on the cut-off momentum of the meson field or, in other words, on the form of the source function of a nucleon which is treated nonrelativistically.

A real nucleon is a complex system of the core nucleon and the bound mesons around it; its wave function depends on the value of the coupling strength between the core nucleon and the bound field. In case the coupling strength is weak, the probability of those states which have more than one bound meson can be neglected. On the other hand, a large coupling strength would imply that many mesons occupy the bound state around the core nucleon. When the coupling strength is neither weak nor strong, a knowledge of the bound field is obtained by solving the wave equation for the system composed of the core nucleon and the bound field. (Hereafter we shall call the system by the bound system.) In the present case, it is assumed that the probability amplitude of those states containing more than four bound mesons can be neglected. This assumption is justified in Sec. III by a numerical treatment of the wave function obtained for various values of the coupling strength.

The above equation for the bound system has solutions corresponding to excited states of the bound field in addition to the ground state solution. These excited states are unstable for a transition to a state of lower energy by an emission of mesons if we take into account the interaction between the unbound field and the bound system composed of the bound mesons and the core nucleon. Therefore it will not correspond to a real particle.

When we treat the pion-scattering by a nucleon, the unbound mesons have to be taken into account. The scattering process is expressed as a transition from the ground state of the bound system with an incoming unbound meson to a similar state through emissions and absorptions of unbound mesons by the bound system. In this case an excited state of the bound system is occupied during the collision time and when the incident energy of the incoming meson is near to an excitation energy of one of these excited states, we can expect a resonance scattering although its width is

* Supported by the U. S. Atomic Energy Commission
† On leave from Kobe University, Kobe, Japan.
[1] Tomonaga, Maki, and Sato, Progr. Theoret. Phys. (Japan) 9, 607 (1953).

much larger than the width characteristic of a nuclear reaction.

Another kind of scattering is to be expected due to the fact that the wave function of the unbound meson is distorted by the orthogonality condition of the unbound state on the bound state. We shall call this potential scattering[2] according to Tomonaga's paper.

The resulting phase shift due to the total effect of these two different kinds of scattering is given in Sec. IV. They are calculated numerically for various values of the coupling strength and the cut-off momentum. In the weak-coupling limit these two scattering amplitudes cancel completely with each other, as they should, and as the coupling strength increases the excited states of the bound system start to have a true physical meaning so the phase shift could show a real resonance (90° phase shift) at a certain incident energy.

Especially for an excited state of the bound system having total angular momenta 3/2 in both ordinary and isotopic space is the binding energy fairly large, and for one of the values of the coupling constant chosen here we find a real resonance for the scattering via this excited state.

II. GENERAL FORMULATION

We consider the system composed of a single nucleon plus the symmetric pseudoscalar meson field interacting through the pseudovector coupling. The system is treated nonrelativistically and the nucleon's recoil is neglected. Then the total Hamiltonian of the system is

$$\begin{aligned} H=&\int\{\pi^*\pi+\nabla\psi^*\cdot\nabla\psi+\mu^2\psi^*\psi \\ &+\tfrac{1}{2}[\pi_0^2+\nabla\psi_0\cdot\nabla\psi_0+\mu^2\psi_0^2]\}dV \\ &-(g/\mu)\int\{\tau_+(\boldsymbol{\sigma}\cdot\nabla)\psi+\tau_-(\boldsymbol{\sigma}\cdot\nabla)\psi^* \\ &+\tau_0(\boldsymbol{\sigma}\cdot\nabla)\psi_0\}U(x)dV. \end{aligned} \tag{1}$$

Here $\psi_0(x)$, $\pi_0(x)$ are the (real) field variables of the neutral field and $\psi(x)$, $\pi(x)$ those of the charged field. $\boldsymbol{\sigma}$ is the Dirac matrix and τ_+, τ_-, τ_0 those matrices in charge space defined by

$$\tau_\pm=(\tau_x\pm i\tau_y)/\sqrt{2},\quad \tau_0=\tau_z; \tag{2}$$

g is the coupling constant measuring the meson-nucleon interaction and μ is the rest mass of a meson. We use the natural units $\hbar=c=1$. The extended source function $U(x)$ is assumed to be spherically symmetric and to satisfy the normalization condition

$$\int U(x)dV=1. \tag{3}$$

Since only the p-wave part of the meson field can interact with a nucleon, the bound field around a nucleon is composed of p waves. Also in the problem of a meson scattering by a nucleon only the p-wave component of the incident meson will be scattered. So we shall consider only the p-wave part of the meson field.

Expanding the field quantities into spherical waves and leaving only the p-wave part of them, we have

$$\begin{aligned} \psi(x)\sim&\sum_{m=\pm1,0}\int\frac{1}{(2k_0)^{\frac{1}{2}}}\{a_m{}^1(k)+(-1)^m a_{-m}{}^{-1*}(k)\} \\ &\times\varphi_{k,1,m}(x)dk, \\ \pi(x)\sim&\sum_{m=\pm1,0}\int i(k_0/2)^{\frac{1}{2}}\{(-1)^m a_m{}^{1*}(k)-a_{-m}{}^{-1}(k)\} \\ &\times\varphi_{k,1,-m}(x)dk, \end{aligned} \tag{4}$$

and similar equations for ψ^*, π^*, ψ_0, and π_0.

$a_m{}^\rho(k)$ and $a_m{}^{\rho*}(k)$ ($\rho=\pm1$, 0; $m=\pm1$, 0) are the creation and annihilation operators for a meson of angular momentum 1 (P wave), z component of angular momentum m, wave number k, and charge $e\rho$. These satisfy the ordinary commutation relations with each other. $\varphi_{k,1,m}$ and k_0 are defined by

$$\varphi_{k,1,m}(x)=(k/r)^{\frac{1}{2}}J_{\frac{3}{2}}(kr)Y_{1,m}(\theta,\varphi), \tag{5}$$

and

$$k_0=(k^2+\mu^2)^{\frac{1}{2}}. \tag{6}$$

$Y_{1,m}$ is the normalized spherical harmonic of the p-wave function.[3]

According to Tomonaga's idea, we divide the p-wave part of the field quantities into a bound field and an unbound field in the following way:

$$\begin{aligned} a_m{}^\rho(k)&=a_m{}^{\rho,0}\psi_0(k)+\sum_{u=1}^{\infty}a_m{}^{\rho,u}\psi_u(k), \\ a_m{}^{\rho*}(k)&=a_m{}^{\rho,0*}\psi_0(k)+\sum_{u=1}^{\infty}a_m{}^{\rho,u*}\psi_u(k), \end{aligned} \tag{7}$$

where $\psi_0(k)$ and $\psi_u(k)$ ($u=1, 2, \cdots$) compose an orthonormal set of functions in k space. $a_m{}^{\rho,u*}$ and $a_m{}^{\rho,u}$ are the creation and annihilation operator of the meson in the p orbit "u" with the z component of the angular momentum m and charge $e\rho$.

$\psi_0(k)$ is called the bound state function (0-orbit) and it is assumed that a real nucleon is a complex system of the core nucleon and bound mesons in "0 orbits" with different m and ρ. Here $\psi_0(k)$ is taken to have the form

$$\psi_0(k)=(1/3N)^{1/2}(k^2U(k)/2\pi k_0^{3/2}), \tag{8}$$

where $U(k)$ is the Fourier transform of the source function $U(x)$ and N is the normalization constant of ψ_0.

This $\psi_0(k)$ is just the orbit associated both with the classical field and with either the weak or strong coupling limit of the quantized theory in the absence of recoil. When the coupling strength is neither weak nor

[2] This kind of scattering is particularly emphasized by R. G. Sachs, Phys. Rev. 95, 1065 (1954).

[3] E. Condon and G. Shortley, *The Theory of Atomic Spectra* (Cambridge University Press, Cambridge, 1935), p. 76.

strong, the real field around a nucleon has a different shape. But because of its simplicity which leads to some interesting features mentioned later and because of the possibility that we can take into account the deviation of ψ_0 from Eq. (8) by considering the unbound states ψ_u ($u=1, 2, \cdots$) we use ψ_0 defined by Eq. (8).

By using the expansions (4) and (7), the p-wave part of the total Hamiltonian becomes

$$H=H_0+H_u+V, \tag{9}$$

where

$$H_0=\omega_0\{\sum_{\rho,m} a_m^{\rho,0*}a_m^{\rho,0} - f\sum_{\rho,m}\tau_\rho\sigma_m(a_m^{\rho,0}+(-1)^m a_{-m}^{\rho,0*})\}, \tag{10}$$

$$H_u=\sum_{\rho,m}\sum_{u,u'}\omega_{u,u'}a_m^{\rho,u*}a_m^{\rho,u'}, \tag{11}$$

$$V=\sum_{\rho,m}\sum_{u}\{\omega_{0,u}(a_m^{\rho,0*}-f\tau_\rho\sigma_m)a_m^{\rho,u} +\omega_{0,u}^*(a_m^{\rho,0}-f(-1)^m\tau_{-\rho}\sigma_{-m})a_m^{\rho,u*}\}. \tag{12}$$

ω_0 ($=\omega_{0,0}$), $\omega_{0,u}$, and $\omega_{u,u'}$ are defined by

$$\omega_{u,u'}=\int k_0\psi_u^*(k)\psi_{u'}(k)dk \ (u \text{ or } u'=0, 1, 2, \cdots), \tag{13}$$

and f is a dimensionless coupling constant defined by

$$f=(gN^{1/2}/\mu). \tag{14}$$

H_0 is the Hamiltonian of the bound system and the lowest eigenstate of H_0 corresponds to an actual nucleon. H_u is the Hamiltonian of the unbound field and V is the interaction between the bound system and the unbound field.

Although a different choice of a set of unbound functions does not change the scattering amplitude or any physical quantity as far as they are orthogonal to $\psi_0(k)$ and to each other, we shall choose $\psi_u(k)$ in such a way that $\omega_{u,u'}$ (u or $u'=1, 2, \cdots$) are diagonal in u and u'.

$$\omega_{uu'}=\omega_u\delta_{u,u'} \ (u \text{ or } u'=1, 2, \cdots). \tag{15}$$

Then a state in which we find unbound mesons in u_1, u_2, $\cdots$, u_n orbits is an eigenstate of H_u and the energy of the state is simply a sum of $\omega_{u_1}, \omega_{u_2}, \cdots, \omega_{u_n}$. As is already shown by Tomonaga *et al.*,[4] from the orthogonality of ψ_u and the Eq. (15) ψ_u must satisfy the following equation:

$$(k_0-\omega_u)\psi_u(k)=\psi_0(k)\int k_0\psi_0^*(k)\psi_u(k)dk. \tag{16}$$

III. THE BOUND FIELD OF MESONS AROUND A NUCLEON

As mentioned in Sec. II, the lowest eigenstate of H_0 corresponds to the state of an actual nucleon. Other eigenstates of H_0 corresponding to excited states of the bound system are produced artificially by restricting our attention to H_0 rather than to H and if we include the interaction V with the unbound field, these states are unstable for an emission of unbound mesons.[5] But in the problem of pion scattering by a nucleon, these states will be present during the collision time due to the forced oscillation of the bound field by an incoming meson and make an important role for the scattering problem. So here we consider the eigenvalue of H_0 and solve it numerically for the lowest eigenstate as well as for some excited states.

H_0 allows constants of motion to be specified: the total angular momentum J of the system, its z component J_z and similar quantities T and T_3 in charge space. Here we shall express a nth excited state of H_0 for given J, J_z, T and T_3 in the following way:

$$\Psi(T_3,J_z;T,J,n)=\sum_{S,L,N,\lambda_i}C(T,J,n;S,L,N,\Lambda_i) \cdot\Psi(T_3,J_z;T,J;S,L,N,\Lambda_i), \tag{17}$$

where $\psi(T_3,J_z;T,J;S,L,N,\Lambda_i)$ is a state of the bound system with the total number of bound mesons N, the angular momentum L, and isotopic spin S, of these N mesons, Actually N, L, and S do not specify the state of the bound mesons completely for given values of J, J_z, T, and T_3, so we must introduce some other quantities Λ_1, Λ_2, $\cdots$ which commute with those and with each other in order to remove the degeneracy. We can expect the appearance of the Λ-type degeneracy only for states with $N\geqq 3$ and these quantities are related to the symmetric permutation group.[6]

As H_0 does not commute with N, L, S, and Λ_i the wave equation for the bound system,

$$H_0\Psi(T_3,J_z;T,J,n)=\epsilon_{T,J,n}\Psi(T_3,J_z;T,J,n), \tag{18}$$

becomes an equation for the coefficients $C(T,J,n;S,L,N,\Lambda_i)$:

$$\begin{aligned}(\epsilon_{T,J,n}-N\omega_0)&C(T,J,n;S,L,N,\Lambda_i)\\ &=-f\omega_0\sum_{S',L',\Lambda_i'}\{C(T,J,n;S',L',N+1,\Lambda_i')\\ &\times K(S',L',N+1,\Lambda_i';S,L,N,\Lambda_i)\\ &+C(T,J,n;S',L',N-1,\Lambda_i')\\ &\times K(S',L',N-1,\Lambda_i';S,L,N,\Lambda_i)\},\end{aligned} \tag{19}$$

where $K(S',L',N',\Lambda_i';S,L,N,\Lambda_i)$ is the matrix element of $\Sigma_{\rho,m}\tau_\rho\sigma_m(a_m^{\rho,0}+(-1)^m a_{-m}^{\rho,0*})$ from a state $\psi(T_3,J_z;T,J;S',L',N',\Lambda_i')$ to a state $\psi(T_3,J_z;T,J;S,L,N,\Lambda_i)$.

[4] See reference 2, Eq. (41).

[5] We shall neglect the possibility of the presence of some stable excited states, for which there appears to be no direct experimental evidence.

[6] Here we used

$$\Lambda=(\Sigma_{\rho,m}a_m^{\rho,0*}a_{-m}^{-\rho,0*})(\Sigma_{\rho',m'}a_{m'}^{\rho',0}a_{-m'}^{-\rho',0}).$$

For states with $N\geqq 5$ or $N=4$, $S=L=2$, Λ does not completely remove the degeneracy and other Λ_i would be required. For $N=4$, $S=L=2$ we used an operator $\Lambda'=\Sigma_{\rho,m}(a^*\times a^*)_m^\rho(a\times a)_m^\rho$ instead of Λ.

TABLE I. Calculated values of $\epsilon_{T,J,n}$, $\Delta\epsilon_{T,J,n}$ and $C(T,J,n;S,L,N,\Lambda)$ for $T=J=1/2$.

$C(1/2,1/2,n;S,L,N,\Lambda)$ / N,S,L,Λ	$f=0.2$		$f=0.4$		$f=0.6$	
	$n=0$	$n=1$	$n=0$	$n=1$	$n=0$	$n=1$
0.0.0.0	−0.8750	−0.4528	−0.7101	−0.5350	−0.5856	−0.5363
1.1.1.0	0.4636	−0.6854	0.6142	−0.1901	0.6350	0.0878
2.0.0.18	−0.0630	0.2711	−0.1567	0.4161	−0.2277	0.4121
2.1.1.0	−0.1205	0.4558	−0.2749	0.4558	−0.3695	0.2959
3.0.0.0	0.0134	−0.0861	0.0559	−0.1904	0.1023	−0.2001
3.1.1.22	0.0224	−0.1340	0.0968	−0.4124	0.1815	−0.5127
3.1.1.0	0.0160	−0.1007	0.0645	−0.2012	0.1135	−0.1947
4.0.0.44	−0.0021	0.0199	−0.0154	0.0923	−0.0366	0.1432
4.0.0.0	−0.0015	0.0130	−0.0102	0.0450	−0.0229	0.0544
4.1.1.26	−0.0042	0.0399	−0.0309	0.1753	−0.0728	0.2619
4.1.1.0	−0.0032	0.0249	−0.0198	0.0931	0.0456	0.1201
$\epsilon_{1/2,1/2,n}/\omega_0$	−0.3179	0.9081	−1.0379	0.4263	−1.9518	−0.2948
$\Delta\epsilon_{1/2,1/2,n}/\omega_0$	0	1.2260	0	1.4642	0	1.6570

For $T=J=1/2$; $T=J=3/2$; $T=1/2$, $J=3/2$ and $T=3/2$, $J=1/2$, values of K are calculated[7] by using group theory, and as an illustration we listed values of K for $T=J=1/2$ in Fig. 1.

The lowest eigenstate ($n=0$) of Eq. (17) for $T=J=1/2$ corresponds to a state of a proton or a neutron and the eigenvalue $\epsilon_{1/2,1/2,0}$ of it will give the self-energy of a nucleon, which together with the mass of the core nucleon ought to give the observed mass of a nucleon. States with a different value of T, J or n represent excited states of the bound system and the energy difference $\Delta\epsilon_{T,J,n}$ between the energy $\epsilon_{T,J,n}$ of these states and $\epsilon_{1/2,1/2,0}$ gives their excitation energy.

Equation (19) is solved numerically[8] for the ground state ($n=0$, $T=J=1/2$) and for the first excited state ($n=1$) with $T=J=1/2$; $T=J=3/2$; $T=1/2$, $J=3/2$ or $T=3/2$, $J=1/2$ under the normalization condition

$$\sum_{S,L,N,\Lambda_i} |C(T,J,n;S,L,N,\Lambda_i)|^2=1. \tag{20}$$

Here it is assumed that the coefficients C with $N\geqq 5$ are small and can be neglected, which was justified by the numerical results obtained for various values of f chosen here.

Calculated coefficients $C(T,J,n;S,L,N,\Lambda_i)$ and eigenvalues $\epsilon_{T,J,n}$ are given in Tables I, II, and III for different values of $f=0.2$, $f=0.4$ and $f=0.6$. For a value of f chosen here and for a reasonable source function, the excitation energies are larger than the rest mass of a meson.

IV. SCATTERING OF A PION BY A NUCLEON

Scattering of a meson by a free nucleon can be treated by solving

$$(H_0+H_u+V)\Psi=E\Psi. \tag{21}$$

In the absence of the interaction term V, a solution of Eq. (21) is a state where the bound system is in the ground state or in one of the excited states and the unbound field is composed of several "u" mesons in orbits u_1, u_2, $\cdots u_n$. In particular, a system composed of an incident pion in the asymptotic region and a free nucleon at rest is supposed to be the ground state of the "bound system" plus a single "u" meson.

The "u" functions already include the scattering caused by the orthogonality condition to ψ_0 as is seen in Eq. (16). Besides this, there is another kind of scattering due to the interaction V through an absorption or an emission of "u" mesons with a simultaneous transition of the bound system from one state to another.

We call these two different types of scattering "potential" scattering and "resonance" scattering, respectively, according to the previous paper.[1]

If we construct an effective potential for the scattering of an unbound meson by the bound system according to the method of Watson and Brueckner,[9] the wave equation for the pion scattering becomes

$$(H_0+H_u+U)\Psi=E\Psi, \tag{22}$$

where U is the part of the following operator which is

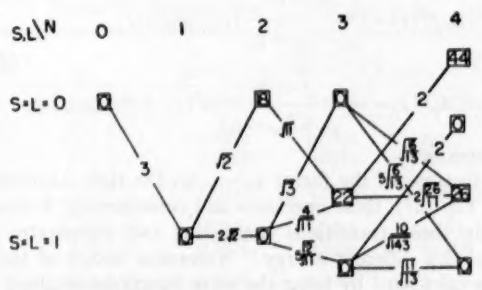

FIG. 1. Values of $K(S',L',N',\Lambda';S,L,N,\Lambda)$ for $T=J=1/2$. Each square in this figure represents a state with definite S, L, N, Λ and the value of Λ is written inside the square. A number attached to each line denotes the value of $K(S',L',N',\Lambda';S,L,N,\Lambda)$ for the corresponding transition and only nonvanishing $K(S',L',N',\Lambda';S,L,N,\Lambda)$ are written in this figure.

[7] K has the following selection rules: $\Delta N=\pm 1$; $\Delta L=\pm 1,0$; $\Delta S=\pm 1,0$. (For a state $L=0$ or $S=0$, $\Delta L=0$ or $\Delta S=0$ is prohibited, respectively.) Also the values of K do not depend on T_3 and J_3.

[8] Numerical works were done by Dr. J. L. Gammel at Los Alamos Scientific Laboratory.

[9] K. A. Brueckner and K. M. Watson, Phys. Rev. **90**, 699 (1953).

TABLE II. Calculated values of $\epsilon_{T,J,n}$, $\Delta\epsilon_{T,J,n}$ and $C(T,J,n;S,L,N,\Lambda)$ for $T=1/2$, $J=3/2$ (or $T=3/2$, $J=1/2$) and $n=1$.

$C(1/2,3/2,n;S,L,N,\Lambda)$ N	S	L	Λ	$f=0.2$ $n=1$	$f=0.4$ $n=1$	$f=0.6$ $n=1$
1	1	1	0	−0.8843	−0.6970	−0.5702
2	1	1	0	−0.2482	−0.3656	−0.3966
2	0	2	0	0.3683	0.4985	0.5170
3	1	1	22	−0.0489	−0.1246	−0.1732
3	1	1	0	0.0461	0.1071	0.1410
3	1	2	0	0.1237	0.3002	0.4000
4	1	1	26	−0.0116	−0.0477	−0.0794
4	1	1	0	0.0135	0.0541	0.0886
4	0	2	26	0.0147	0.0601	0.1005
4	0	2	0	0.0104	0.0426	0.0701
4	1	2	0	−0.0167	−0.0653	−0.1064
$\epsilon_{1/2,3/2,n}/\omega_0$				0.7356	0.06374	−0.8065
$\Delta\epsilon_{1/2,3/2,n}/\omega_0$				1.0535	1.1016	1.1453

($C(3/2,1/2,n;S,L,N,\Lambda)$ is obtained from $C(1/2,3/2,n;S,L,N,\Lambda)$ by interchanging values of S with those of L.)

diagonal in the occupation numbers of "u" mesons:

$$V\frac{1}{E-H_0-H_u}V. \tag{23}$$

In Eq. (22) we neglected those parts of wave function Ψ which have more than two "u" mesons.

If we introduce the following quantities:[10]

$$\begin{aligned} A_m{}^{\rho *}&=a_m{}^{\rho,0*}-f\tau\sigma_{\rho m},\\ A_m{}^{\rho}&=a_m{}^{\rho,0}-f\tau_{-\rho}\sigma_{-m}, \end{aligned} \tag{24}$$

H_0 and V can be written as follows:

$$H_0=\omega_0\sum_{\rho,m}A_m{}^{\rho *}A_m{}^{\rho}-9\omega_0 f^2, \tag{25}$$

$$V=\sum_{u=1,2,\cdots}\sum_{\rho,m}(\omega_{0,u}A_m{}^{\rho *}a_m{}^{\rho,u}+\omega_{0,u}{}^{*}A_m{}^{\rho}a_m{}^{\rho,u*}). \tag{26}$$

From the commutation relations between H_0 and $A_m{}^{\rho *}$ or $A_m{}^{\rho}$, the transition matrix of $A_m{}^{\rho *}$ or $A_m{}^{\rho}$ from an eigenstate ν of H_0 to another ν' is expressed by

$$\begin{aligned} (\nu'|A_m{}^{\rho *}|\nu)&=f\frac{\epsilon_{\nu'}-\epsilon_{\nu}}{\omega_0-(\epsilon_{\nu'}-\epsilon_{\nu})}(\nu'|\tau_{\rho}\sigma_m|\nu),\\ (\nu'|A_m{}^{\rho}|\nu)&=-f\frac{\epsilon_{\nu'}-\epsilon_{\nu}}{\omega_0+(\epsilon_{\nu'}-\epsilon_{\nu})}(\nu'|(-1)^m\tau_{-\rho}\sigma_{-m}|\nu), \end{aligned} \tag{27}$$

respectively.

Because of the factor $\epsilon_{\nu'}-\epsilon_{\nu}$ on the right-hand side of Eq. (27), these operators and consequently V cause only those transitions connecting two eigenstates of H_0 with different energy.[11] Numerical values of these are calculated by using the wave functions obtained in Sec. III.

Equation (22) is transformed to an equation for an amplitude $C(\nu;u,\rho,m)$ of Ψ^*, where the bound system is in a state ν and an unbound meson is in an u orbit having charge $e\rho$ and projection of angular momentum m:

$$\begin{aligned} &(E-\epsilon_{\nu}-\omega_u)C(\nu;u,\rho,m)\\ &\quad=\sum_{\nu'}\sum_{u',\rho',m'}(\nu;u,\rho,m|U|\nu';u',\rho',m')\\ &\qquad\times C(\nu';u',\rho',m'), \end{aligned} \tag{28}$$

where

$$\begin{aligned} &(\nu;u,\rho,m|U|\nu';u',\rho',m')\\ &\quad=\omega_{0,u}{}^{*}\omega_{0,u'}(\nu;\rho,m|W|\nu';\rho',m'), \end{aligned} \tag{29}$$

and

$$\begin{aligned} (\nu;\rho,m|W|\nu',\rho',m')=\sum_{\nu''}\Bigg\{&\frac{(\nu|A_{m'}{}^{\rho'*}|\nu'')(\nu''|A_m{}^{\rho *}|\nu')}{E-\epsilon_{\nu''}}\\ &+\frac{(\nu|A_m{}^{\rho *}|\nu'')(\nu''|A_{m'}{}^{\rho'*}|\nu')}{E-\epsilon_{\nu''}-\omega_u-\omega_{u'}}\Bigg\}. \end{aligned} \tag{30}$$

The first term in the bracket is due to a process of absorption of a "u" meson followed by emission of a u meson and the second one due to a process in which emission precedes absorption. Hereafter we shall replace ω_u and $\omega_{u'}$ in the denominator of the second term by some average value which, for simplicity, is taken to be equal to the incident energy p_0 of the pion.[12] The total energy is equal to a sum of p_0 and $\epsilon_{1/2,1/2,0}$ (or simple ϵ_0).

If we neglect the inelastic part of the effective potential i.e., the part connecting eigenstates ν and ν' of H_0 with different energy, Eq. (28) becomes an equation for the elastic scattering amplitude $C(\nu=0;u,\rho,m)$. We shall transform the representation of the unbound field from the u representation to the ordinary momentum representation[13] and furthermore introduce the constant of motion: the total angular momentum J and total isotopic spin T of the whole system as well as their projection J_3 and T_3.

TABLE III. Calculated values of $\epsilon_{T,J,n}$, $\Delta\epsilon_{T,J,n}$ and $C(T,J,n;S,L,N,\Lambda)$ for $T=J=3/2$ and $n=1$.

$C(3/2,3/2,n;S,L,N,\Lambda(\Lambda'))$ N	S	L	$\Lambda(\Lambda')$	$f=0.2$ $n=1$	$f=0.4$ $n=1$	$f=0.6$ $n=1$
1	1	1	0	−0.8530	−0.7058	−0.6117
2	1	1	−0	0.1198	0.1915	0.2326
2	2	2	0	0.4853	0.5976	0.6099
3	1	1	22	−0.0715	−0.1582	−0.2157
3	1	1	0	−0.0207	−0.0501	−0.0729
3	1	2	0	−0.0436	−0.0773	−0.0867
3	2	1	0	−0.0436	−0.0773	−0.0867
3	2	2	0	−0.1098	−0.2372	−0.3170
4	1	1	26	0.0084	0.0312	0.0533
4	1	1	0	0.0129	0.0420	0.0654
4	1	2	0	0.0059	0.0180	0.0262
4	2	1	0	0.0059	0.0180	0.0262
4	2	2	(0)	0.0106	0.0370	0.0604
4	2	2	(4)	0.0231	0.0774	0.1231
4	2	2	(6)	0.0099	0.0399	0.0717
$\epsilon_{3/2,3/2,1}/\omega_0$				0.5779	−0.2740	−1.2750
$\Delta\epsilon_{3/2,3/2,1}/\omega_0$				0.8958	0.7639	0.6768

[10] See Eq. (27) in reference 2.

[11] This is due to our special choice of ψ_0 Eq. (8).

[12] If our nonrelativistic treatment has any sense, the main contribution will come from low-energy u mesons in real or virtual states comparable with the incident energy, and so this substitution is consistent with our treatment.

[13] See reference 2, p. 618.

Then the elastic scattering amplitude $C(T_3,J_z;T,J,k)$ for the state with definite value of J, T, J_z, T_3 and having a meson with a momentum k is given by the following equation:

$$(p_0-k_0)C(T_3,J_z;T,J,k)=[-1+(k_0-\omega_0)W_{T,J}]\psi_0(k)\times\int_0^\infty k_0'\psi_0^*(k')C(T_3,J_z;T,J,k')dk', \quad (31)$$

$$C(T_3,J_z;T,J,k)=\delta(p-k)-[(k_0-p_0)^{-1}+i\pi\delta(k_0-p_0)]\times\frac{F_{T,J}(k_0)\psi_0(k)\psi_0^*(p)}{F_{T,J}(p_0)\int[(k_0'-p_0)^{-1}+i\pi\delta(k_0'-p_0)]|\psi_0(k')|^2dk'-W_{T,J}}, \quad (32)$$

where $W_{T,J}$[14] is defined as a diagonal element of W [Eq. (30)] for a state having the prescribed values of T, J and $\nu(=\nu'=0)$.

The solution of Eq. (31) under the boundary condition that only the incident incoming wave and the scattered outgoing wave are present in the asymptotic region is

and the phase shift of p-wave scattering for a pure T and J state is given by

$$\tan\delta_{T,J}=-\frac{\pi p_0}{p}\times\frac{F_{T,J}(p_0)|\psi_0(p)|^2}{F_{T,J}(p_0)\int(k_0'-p_0)^{-1}|\psi_0(k')|^2dk'-W_{T,J}}, \quad (33)$$

where

$$F_{T,J}(k_0)=1-(k_0-\omega_0)W_{T,J}. \quad (34)$$

If we write explicitly the energy dependence of $W_{T,J}$, we have, from Eq. (30),

$$W_{T,J}=\sum_\nu\frac{\mathfrak{A}(\nu;T,J)}{p_0-\Delta\epsilon_\nu}+\sum_\nu\frac{\mathfrak{B}(\nu;T,J)}{-p_0-\Delta\epsilon_\nu}. \quad (35)$$

$\mathfrak{A}(\nu;T,J)$ is the square of a matrix element of A^* from the ground state of the bound system to the excited state ν, while $\mathfrak{B}(\nu;T,J)$ is that of A for the same transition.

In the weak coupling limit $g\to0$ (i.e., $f\to0$), the ground state and the nth excited states of the bound system are given by states in which we find no bound meson and n bound mesons, respectively.[15] Also A^* and A become identical with a^{0*} and a^0, respectively, and can cause only those transitions in which one meson is emitted or absorbed. Therefore, the effect of A^* on the ground state of the bound system is to produce only the first excited state, and when A operates on the ground state the result vanishes. From the above consideration we find, in the limit $g\to0$,

$$\mathfrak{A}(\nu=1;T,J)\to1,\quad \mathfrak{A}(\nu\neq1;T,J)\to0,\quad \mathfrak{B}(\nu;T,J)\to0\quad(g\to0), \quad (36)$$

and so $F_{T,J}$ and $\delta_{T,J}$ vanish. This vanishing phase shift comes from the cancellation of two different scattering amplitudes, one due to the "potential" scattering and the other due to the "resonance" scattering, as it should be.

For a low-energy scattering only that part of W due to $\mathfrak{A}(\nu=T,J,n=1;T,J)$ gives the energy-dependent part of W and the other parts are almost independent of the incident energy p_0. So we replace $\Delta\epsilon_\nu$ in the latter parts by some average value $\langle\Delta\epsilon_{T,J}\rangle$,[16] and apply the closure rules to W. The necessary values of $\mathfrak{A}$ and $\mathfrak{B}$ are calculated by using the wave functions obtained in Sec. III and listed in Table IV.

The phase shifts $\delta_{3/2,3/2}$, $\delta_{1/2,3/2}$,[17] and $\delta_{1/2,1/2}$ are calculated for $f=0.4$ and $f=0.6$ by assuming various values of cut-off momenta K_c. ($K_c=3\mu$, 4μ, or 5μ; the corresponding value of ω_0 is 2.45μ, 3.07μ, or 3.71μ, respectively.) For low incident energy of a meson the phase shift for the $T=J=3/2$ state turned out to be positive, indicating the presence of an attractive force; while phase shifts for other states became negative, indicating the presence of a repulsive force. By using the calculated phase shifts, the total cross section of

TABLE IV. Values of $\mathfrak{A}(\nu;T,J)$ and $\mathfrak{B}(\nu;T,J)$.

f	T, J	$\mathfrak{A}(\nu=1;T,J)$	$\sum_\nu\mathfrak{A}(\nu=1;T,J)$ $-\mathfrak{A}(\nu=1;T,J)$	$\sum_\nu\mathfrak{B}(\nu=1;T,J)$
0.2	1/2, 1/2	1.1955	0.4858	0.0225
	1/2, 3/2 (3/2, 1/2)	0.9982	0.0034	0.0334
	3/2, 3/2	0.9132	0.0173	0.0407
0.4	1/2, 1/2	1.0339	1.509	0.0900
	1/2, 3/2 (3/2, 1/2)	0.9239	0.0572	0.1481
	3/2, 3/2	0.7634	0.2406	0.2000
0.6	1/2, 1/2	0.6170	2.8021	0.2025
	1/2, 3/2 (3/2, 1/2)	0.4864	0.1958	0.3500
	3/2, 3/2	0.7671	0.8184	0.4952

[14] $W_{T,J}$ does not depend on T_3 and J_z because of the spherically symmetric property of W in both charge and ordinary space. So Eq. (31) has the same form for different values of T_3 and J_z.

[15] Of course, there are degeneracies for larger n, even if we specify the angular momentum, isotopic spin, and their projections.

[16] We assume $\langle\Delta\epsilon_{3/2,3/2}\rangle=2\omega_0$, $\langle\Delta\epsilon_{1/2,1/2}\rangle=3\omega_0$, and $\langle\Delta\epsilon_{1/2,3/2}\rangle=\langle\Delta\epsilon_{3/2,1/2}\rangle=3\omega_0$.

[17] $\delta_{1/2,3/2}=\delta_{3/2,1/2}$ is a direct result from the symmetric property of the interaction term in Eq. (1) for an interchange of the ordinary space with the isotopic space.

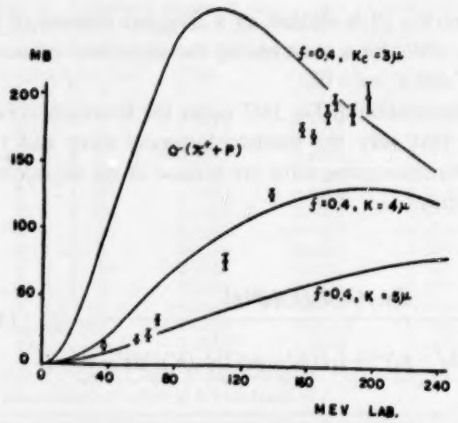

FIG. 2. Theoretical and experimental total cross section *vs* the incident energy of a pion for $\pi^+ + p$ scattering. ○: Ashkin, Blaser, Feiner, Gorman, and Stern, reports at The Fourth Annual Rochester High-Energy Conference in January, 1954 (University of Rochester, Rochester, to be published); ●: Anderson, Fermi, Martin, and Nagle, Phys. Rev. **91**, 155 (1953); Δ: Bodansky, Sachs, and Steinberger, Phys. Rev. **91**, 467 (1953); □: J. P. Perry and C. E. Angell, Phys. Rev. **91**, 1289 (1953).

$\pi^+ - p$ scattering and $\pi^- - p$ scattering (including the charge exchange scattering) are calculated, and the results are shown in Figs. 2 and 3 for $f=0.4$. The agreement with the experimental results is rather poor although most of the qualitative feature of the cross sections are obtained. The results for $f=0.6$ give worse agreement than those for $f=0.4$. As we neglected the S-wave scattering, our results cannot be applied to the scattering near zero energy.

The excited energies $\Delta\epsilon_{T,J,n}$ are proportional to ω_0 for a given value of the coupling constant f, and so, for a larger cut-off momentum K_c, $\Delta\epsilon_{T,J,n}$ become larger. The shift of the maximum in the phase shifts to higher energy with increasing cut-off momentum is explained by this increase of $\Delta\epsilon_{T,J,n}$. A real resonance is obtained when the denominator of the right-hand side of Eq. (33) becomes zero for a certain incident energy p_0, which is different from $\Delta\epsilon_{T,J,n}$. For example we find the scattering resonance for $T=J=3/2$ at a little higher energy p_0 than $\Delta\epsilon_{3/2,3/2,n}$.

For small incident energies ($\lesssim 200$ Mev) the predominant phase-shift is $\delta_{3/2,3/2,n}$. A linearly increasing character of $\delta_{1/2,1/2}$, $\delta_{1/2,3/2}$, and $\delta_{3/2,1/2}$ with increasing incident energy between 100 and 200 Mev was found, which is due to a factor $\psi_0^2(p)$ in Eq. (74); hence it is a characteristic of the bound wave function chosen here. For a more slowly increasing function $\psi_0^2(p)$, these phase shifts can remain smaller than calculated for the energy interval involved here; also a steeper decrease of the total scattering cross section from the maximum predicted by experiment will be obtained. The broader maximum found for the scattering cross section compared to the experimental results indicates that the attractive force is not strong enough. This may be due partly to the fact that in our approximation the attractive force is not fully taken into account, because the actual wave function of the bound system contains

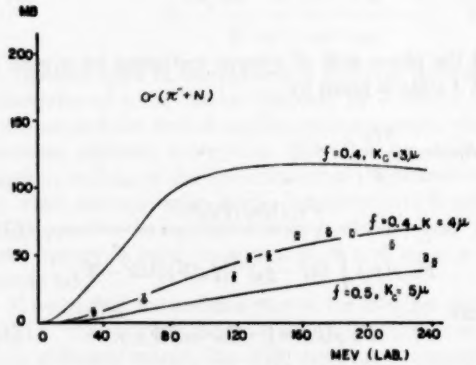

FIG. 3. Theoretical and experimental total cross section *vs* the incident energy of a pion for $\pi^- + p$ scattering including charge exchange scattering. ○: Ashkin, Blaser, Feiner, Gorman, and Stern, reports at the Fourth Annual Rochester High-Energy Conference in January, 1954 (University of Rochester, Rochester, to be published); ●: Anderson, Fermi, Martin, and Nagle, Phys. Rev. **91**, 155 (1953); Δ: Bodansky, Sachs, and Steinberger, Phys. Rev. **91**, 467 (1953); ■: J. Ring and D. N. Nelson, Phys. Rev. **91**, 1289 (1953).

mesons in unbound orbits and the excited energy will be smaller than our calculated values.

We wish to express our very sincere appreciation to Dr. J. L. Gammel for his excellent computational work on Eq. (19), and Dr. Y. Miyamoto, Dr. D. Ito, Dr. B. A. Jacobsohn, and Dr. T. D. Lee for private discussions about the content of Sec. III. We are also indebted to Professor S. Tomonaga for informing us of his paper before publication and to Professor R. G. Sachs and Professor K. M. Watson for their kind interest and valuable discussions.

Letters to the Editor

PUBLICATION of brief reports of important discoveries in physics may be secured by addressing them to this department. The closing date for this department is five weeks prior to the date of issue. No proof will be sent to the authors. The Board of Editors does not hold itself responsible for the opinions expressed by the correspondents. Communications should not exceed 600 words in length and should be submitted in duplicate.

Ionization Energies of Groups III and V Elements in Germanium

T. H. GEBALLE AND F. J. MORIN
Bell Telephone Laboratories, Murray Hill, New Jersey
(Received June 28, 1954)

THE interesting differences in the ionization energies of Group III acceptors and Group V donors in silicon recently found from Hall effect measurements[1] led us to look for similar effects in germanium. Differences very similar to those found in silicon, though less pronounced, are found in germanium.

The ionization energies were determined by analyzing curves of carrier concentration *vs* reciprocal temperature. The carrier concentration (n or p) was computed from the Hall coefficient R_H by means of the relation

$$n(\text{or } p)=\mu_H/\mu R_H e,$$

where μ_H/μ is the ratio of Hall mobility to conductivity mobility and e the electronic charge. At all temperatures conditions were chosen such that the Hall voltage was linear with the applied electric and magnetic fields. Samples having a very low total impurity content were used to minimize interactions other than those between the added atoms and the germanium lattice. Anomalous effects which have been reported[2] were not found. In most cases, two samples from different crystals were measured for each added impurity. The experimental error in determining the slope of the carrier concentration is one percent. The major source of error in determining an absolute value for ionization energy probably is the uncertainty in the temperature dependence of μ_H/μ below 20°K. This ratio has been determined[3] above 50°K for samples having the range of impurity concentration considered in this letter. It was assumed that $\mu_H/\mu=1.00$ for electrons and remained constant with temperature. Above 50°K, μ_H/μ for holes was taken from reference 2. Below 50° it was assumed to become constant at 1.10.

Typical carrier concentration results are shown in Fig. 1. These results were fitted with computed curves[4] which are shown in Fig. 1. In fitting the curves for all samples, a mass parameter m^*/m (effective mass/electronic rest mass) in the range 0.25 to 0.30 was used. This uncertainty in m^*/m is probably due to the uncertainty in μ_H/μ over the temperature range 10° to 25°K. The other parameters computed for all samples are shown in Table I. The ionization energies of Group III acceptors show a tendency to increase with atomic weight as in silicon. The ionization energies of the Group V donors also vary as in silicon, the value for Sb being the lowest and that for As the highest. These results are independent of m^*/m. A qualitative idea of the dependence of the ionization energy upon the temperature dependence of μ_H/μ may be obtained from the results of the B and As samples. It is expected that the temperature dependence of μ_H/μ will be unaffected by neutral impurity scattering and strongly affected by ionized impurity scattering. In the case of the samples containing B, neutral impurity concentration was changed by a factor of six while keeping the ionized impurity concentration within a factor of two. This did not change the ionization energy. In the

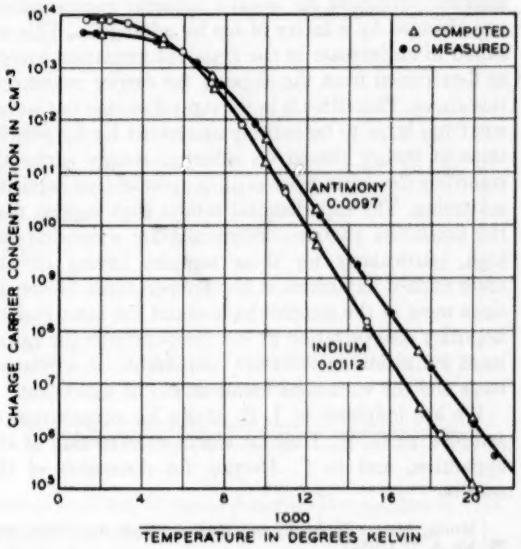

FIG. 1. Charge carrier concentration as a function of reciprocal absolute temperature in germanium samples containing indium (No. 1006) and antimony (No. 1010).

TABLE I. Composition of samples and parameters obtained in analyzing carrier concentration data.

Sample No.	Added element	Concentration of majority impurity	Concentration of minority impurity	ionization energy in ev
1003	B	5.1×10^{13}	2.9×10^{13}	0.0104
1004	B	3.2×10^{14}	1.4×10^{13}	0.0104
1001	Al	1.0×10^{14}	2.6×10^{13}	0.0102
1002	Al	3.2×10^{14}	4.2×10^{13}	0.0102
1005	Ga	8.7×10^{13}	2.1×10^{13}	0.0108
1006	In	9.5×10^{13}	1.2×10^{13}	0.0112
1011	P	1.02×10^{14}	1.1×10^{13}	0.0120
1007	As+Ga	1.2×10^{14}(As)	2.8×10^{13}(Ga)	0.0133
1008	As	9.6×10^{13}	2.9×10^{13}	0.0127
1010	Sb	6.2×10^{13}	1.4×10^{13}	0.0097

samples containing As, ionized impurity concentration was changed by a factor of ten by adding Ga. This resulted in an increase in the apparent ionization energy as determined from the slope of the carrier concentration curve. This effect is in the right direction but somewhat too large to be entirely accounted for by predictions of theory (based on spherical energy surfaces)[5] regarding the dependence of μ_H/μ upon ionized impurity scattering. The experimental results thus suggest that the ionization energies determined are somewhat too high, particularly for those samples having 10^{13} or more ionized impurities at low temperatures. However, since most of the samples have about the same ionized impurity concentration at low temperatures the calculated ionization energies are comparable on a relative basis and the variations found should be significant.

We are indebted to J. P. Maita for preparation of samples, to G. W. Hull for aid in construction of the apparatus, and to C. Herring for discussion of the results.

[1] Morin, Maita, Shulman, and Hannay, Bull. Am. Phys. Soc. **29**, No. 5, 22 (1954).
[2] C. S. Hung and J. R. Gliessman, Phys. Rev. **79**, 726 (1950); H. Fritzsche, Phys. Rev. **94**, 1415 (1954).
[3] F. J. Morin, Phys. Rev. **93**, 62 (1954).
[4] For the method used, see Sec. 16.4, W. Shockley, *Electrons and Holes in Semi-conductors* (D. Van Nostrand and Company Inc., New York, 1950).
[5] H. Jones, Phys. Rev. **81**, 149 (1951).

Low-Temperature Luminescence of Cadmium Sulfide

L. R. Furlong
Solid State Division, Naval Research Laboratory, Washington, D. C.
(Received June 1, 1954)

THIS is to report the existence of six emission bands in the wavelength range 5100–5400A at 4°K for single crystal hexagonal cadmium sulfide grown by M. E. Bishop.[1]

These bands were obtained by exciting the cadmium sulfide with 3650A radiation produced by a high-pressure Cenco mercury arc filtered with a 7–37 Corning filter. The luminescence was photographed with a Hilger medium glass spectrograph. The microphotometer trace of the spectrogram is shown in Fig. 1.

Table I. Observed and calculated values of ν.

Observed λ(A)	Observed ν(cm^{-1})	(v', v'')	Calculated ν(cm^{-1})
5133	19482	(1,0)	19488
5182	19298	(0,0)	19288
5212	19186	(1,1)	19192
5267	18986	(0,1)	18992
5290	18904	(1,2)	18896
5350	18692	(0,2)	18696

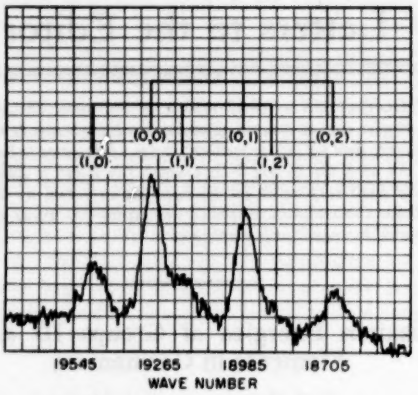

Fig. 1. Microphotometer trace of the emission of cadmium sulfide at 4°K from 5100 to 5400A.

The spacing and relative intensities of these six bands together with the absence of photoconductivity[2] at this temperature suggested that the concept of localized complexes, or centers, might be applicable in this case. The center might consist, for example, of a group of ions surrounding a sulfur vacancy or surrounding a foreign ion which has replaced the sulfur. It was found that a molecular-type wave number equation for these bands,

$$\nu=\nu_e+\omega'(v'+\tfrac{1}{2})-\omega''(v''+\tfrac{1}{2}),$$

gave a reasonable fit where ν_e is the electronic jump; ω' and ω'' are the vibrational wave numbers for the first excited and ground states, respectively; and v' and v'' are the corresponding vibrational quantum numbers. By using the observed values of ν shown in the table below and quantum numbers selected according to the relative positions and intensities of the bands, the appropriate wave-number equation was calculated to be

$$\nu=19336+199(v'+\tfrac{1}{2})-296(v''+\tfrac{1}{2});$$

and from this the calculated values of ν corresponding to the observed values were obtained as shown in Table I, where the transition associated with 19298 cm^{-1} has been assigned the quantum numbers (0,0). It should be pointed out, however, that although a molecular-type calculation has been made, the intensity distribution, as shown in Fig. 1, differs from typical molecular spectra intensity distributions. These centers are characterized by an electronic jump of 19336 cm^{-1} (5172A), a vibrational wave number of 199 cm^{-1}(50μ) in the first excited state and a vibrational wave number of 296 cm^{-1}(34μ) in the ground state. It is noteworthy that Plyler found a weak absorption band in the vicinity of 34μ at room temperature as reported by Klick.

[1] M. E. Bishop and S. H. Liebson, J. Appl. Phys. **24**, 660 (1953).
[2] C. C. Klick, Phys. Rev. **89**, 274 (1953).
[3] C. C. Klick, J. Opt. Soc. Am. **41**, 816 (1951).

Energy Levels and Photoconductivity in Electron-Bombarded Germanium*

H. Y. Fan, W. Kaiser, E. E. Klontz,
K. Lark-Horovitz, and R. R. Pepper
Purdue University, Lafayette, Indiana

(Received June 28, 1954)

IRRADIATION by high-energy particles may introduce energy levels in the forbidden gap of a semiconductor by producing defects in the crystal lattice, thus causing radical changes in the carrier concentration.[1] Hall effect measurements have revealed several energy levels introduced in germanium by irradiation with high-energy electrons. The solid curves of Fig. 1 show the Hall coefficient curves for a sample irradiated with 4.5 Mev electrons at 100°K. Curve 1 was taken before the irradiation on the *n*-type sample. Curve 2 was taken after the sample had been warmed up to 0°C following the irradiation; the sample was then *p* type. Curve 3 was measured after the sample had been warmed further to room temperature, thereby converted back to *n* type. The steep rise of the curves indicate that there were electronic states with an energy level in the forbidden gap, the electron population of which increased with decreasing temperature at the expense of conduction electrons. The dashed curve, obtained on another sample, shows a case where the Hall coefficient does not keep increasing with decreasing temperature, but becomes almost constant at low temperatures. Such behavior indicates that after the localized states have been filled, if this is possible, the number of conduction electrons becomes constant.

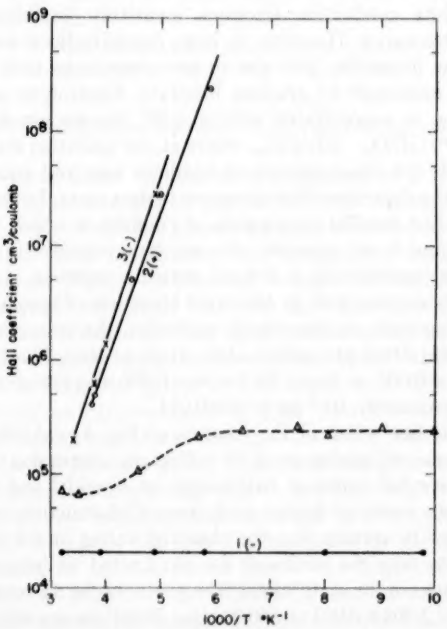

FIG. 1. Hall coefficient curves for Ge irradiated with 4.5-Mev electrons at 100°C.

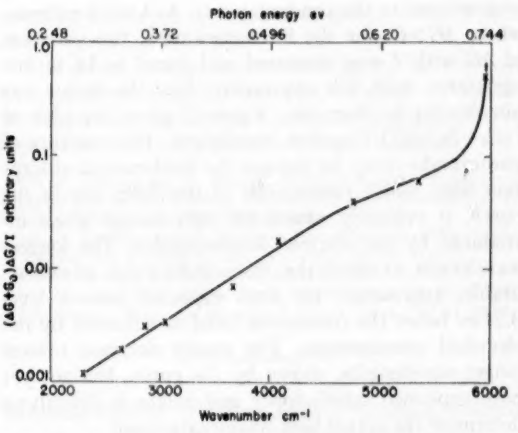

FIG. 2. Photoconductive response beyond the fundamental absorption edge plotted against wave number.

From the solid curves of Fig. 1 an energy level 0.21 ev above the valence band and a level 0.22 ev below the conduction band are deduced. Results obtained on other samples give also a level 0.11 ev above the valence band. It is interesting to note that a curve similar to curve 3 has been previously reported for neutron irradiated germanium, which corresponds to a level 0.12 ev below the conduction band.[1]

Large photoconductivity has been observed in electron-irradiated samples, which extends to wavelengths far beyond the fundamental absorption limit of germanium where the photoconductivity in unbombarded samples drops off sharply. The response becomes slower and stronger with decreasing temperature; e.g., at 83°K the extra conductivity in irradiated samples dropped to half-value in 0.5 sec after the exciting light of $\lambda = 2.7$ microns is cut off, and the resistivity of a sample was decreased from 33 ohm cm to about 4 ohm cm by exposure to the general illumination in the laboratory. We shall confine the discussion to wavelengths of exciting light beyond the absorption limit.

An *n*-type sample was studied, which after irradiation had a Hall curve similar to curve 3, Fig. 1, corresponding to the presence of levels 0.24 ev below the conduction band. The resistivity also increased steeply with decreasing temperature, and was over 10^5 ohm cm at 125°k. Photoconductivity was measured after the sample had been kept at room temperature for several days, when the resistivity at 83°K was only 350 ohm cm. This fact indicates that there had been healing of the irradiation effect and the Hall curve must have been then of the shape shown by the dotted curve in Fig. 1. We expect for steady state photoconductivity $I \propto (n_0+\Delta n)\Delta n$, where I is the intensity of radiation and n is the density of conduction electrons which is

proportional to the conductance G. At $\lambda = 2.5$ microns, where $\Delta G > G_0$ for the intensities used, the variation of ΔG with I was measured and found to be in fair agreement with this expression. Also the decay was bimolecular in character. Figure 2 gives the plot of $[(G_0+\Delta G)\Delta G]/I$ against wavelength. The existence of photoconductivity far beyond the fundamental absorption edge, which corresponds to the sharp rise in the curve, is evidently associated with energy levels introduced by the electron bombardment. The longest wavelength, at which the photoconductivity was measurable, approached the limit expected from a level 0.24 ev below the conduction band as indicated by the electrical measurement. The steady decrease toward longer wavelengths, shown by the curve, has not yet been explained satisfactorily and makes it difficult to determine the actual long-wavelength limit.

We wish to thank Dr. J. W. MacKay for his help in the electron bombardment.

* Work supported by a Signal Corps Contract.

[1] K. Lark-Horovitz, *Proceedings of Reading Conference* (Butterworths Scientific Publications Ltd., London, 1951).

Paramagnetic Resonance Absorption in Graphite

G. R. Hennig, B. Smaller, and E. L. Yasaitis
Chemistry Division, Argonne National Laboratory, Lemont, Illinois

(Received July 2, 1954)

PURE graphite manifests paramagnetic resonance at a g value of 2.00 ± 0.02.[1] This resonance has been investigated at oscillator frequencies of 360 Mc/sec, 15 Mc/sec, and 4 Mc/sec with the detection equipment already described.[2] The latter two frequencies were convenient for line width measurements requiring pronounced field homogeneity. Line intensities were calibrated approximately by comparison with signals from weighed amounts of the free radical, diphenyl picryl hydrazyl. It was found that the concentration of spin centers is about 10^{-4} per carbon atom at room temperature and is proportional to $\exp(-E/kT)$ between 77° and 300°K where the activation energy E is 0.04 ev for natural graphite and 0.05 ev for polycrystalline artificial graphite. It is unlikely that this resonance can be attributed to chemical impurities in the graphite because spectroscopic analysis has shown most impurity concentrations in these graphites to be orders of magnitude smaller than the spin center concentration. In artificial graphites but not in natural graphite, the resonance can be destroyed by vacuum annealing at 1500°K, and restored by annealing above 1700°K. These changes are not accompanied by any change exceeding 10^{-5} electrons per atom in the room temperature population of the conduction band as measured by Hall coefficients.

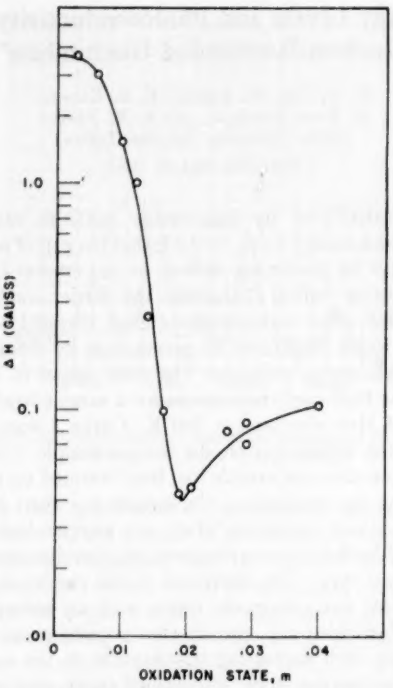

FIG. 1. Concentration dependence of the resonance line width of graphite bisulfate.

Introduction of small amounts of such impurities which are known to lower or raise the Fermi level of the graphite conduction electrons invariably annihilates the resonance. However, in large concentrations some of the impurities give rise to new resonances such as that evidenced by graphite bisulfate. Electrolytic oxidation in concentrated sulfuric acid[3] changes graphite to $C^{m+}(HSO_4^- \cdot 2H_2SO_4)_m$, where m, the oxidation state, equals the concentration of bisulfate ions and equals also the depletion of electrons per carbon atom. In these so-called lamellar compounds of graphite of which the bisulfate is an example, the reactant occupies interplanar positions in a definite periodic sequence along the hexagonal axis in the layer structure of graphite. During such an electrolytic oxidation, the spin-center concentration per carbon atom drops at least 50×10^{-5} at $m=0.003$, is about 10^{-4} at $m=0.006$ and remains at approximately 10^{-4} up to $m=0.041$.

The line width of the resonance (Fig. 1) exhibits a pronounced minimum of 45 milligauss (dispersion derivative full width at half-height) at $m\approx0.02$ and increases slowly at higher oxidations. Unfortunately one cannot be certain that the observed values of the line widths near the minimum are not limited by inhomogeneities of the earth's field. The g value of the narrowest line is 2.004 ± 0.003 at 360 Mc/sec. Bisulfate concentration also has a pronounced effect upon the temperature dependence of the line width (Fig. 2). At $m=0.02$, a

negative temperature dependence is observed at low temperatures with a marked transition at 210°K; both effects gradually disappear at higher oxidation states. Above 210°K the line width remains independent of temperature.

The integrated signal strength which is presumably proportional to the ratio of the spin-center concentration to the absolute temperature rises slowly with temperature below 210°K, increases rather abruptly near 210°K, more or less inversely as the line width (Fig. 2), and also remains constant between 210°K and 300°K.

The resonances are not characteristic for all lamellar compounds, since they were not found in saturated graphite bromide lamellar compounds whose oxidation state as estimated by Hall measurements was 0.018, nor in a series of bromide residue compounds. They

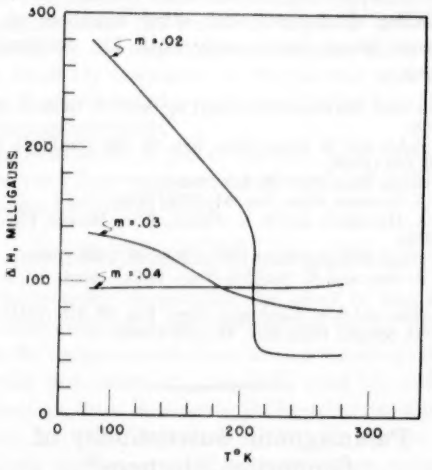

FIG. 2. Temperature dependence of the resonance line width.

were also absent in a lamellar compound of graphite with UCl_4 of oxidation state 0.007. The resonance is thus apparently not caused by positive holes in the valence band of graphite (the compounds discussed here are *P*-type conductors) because otherwise all compounds with equal oxidation state should manifest the same resonance. The spin centers are probably positive holes trapped at the acceptor states, i.e., bisulfate radicals. In graphite compounds with bromine or uranium halides, trapping either does not occur or results in molecule formation, i.e., $2Br \rightarrow Br_2$. Narrowing of the line in the bisulfate compounds with increasing concentration is probably due to exchange narrowing, possibly by coupling with the holes in the valance band,[4] and/or by a progressive increase in the dielectric constant of the compound due to the large polarizability of H_2SO_4. This increased dielectric constant would increase the overlap between wave functions of holes on adjacent traps and might split the energy levels of the traps into a band of states thus also accounting for the nearly metallic temperature dependence of the resonance intensity.

The abrupt change in line width at 210°K may well be associated with the onset of rotation[5] of sulfate molecules and/or ions and consequent disappearance of dipole broadening from proton nuclear moments.

[1] G. R. Hennig and B. Smaller, Argonne National Laboratory Progress Report ANL-5101, August 1953 (unpublished); J. G. Castle, Jr., Phys. Rev. **92**, 1063 (1953).
[2] E. L. Yasaitis and B. Smaller, Phys. Rev. **92**, 1068 (1953); B. Smaller and E. Yasaitis, Rev. Sci. Instr. **24**, 991 (1953).
[3] G. R. Hennig, J. Chem. Phys. **19**, 922 (1951).
[4] C. Zener and R. R. Heikes, Revs. Modern Phys. **25**, 191 (1953).
[5] Gutowsky, Pake, and Bersohn, J. Chem. Phys. **22**, 643 (1954).

Measurement of the Spin Paramagnetism of Conduction Electrons*

R. T. SCHUMACHER, T. R. CARVER, AND C. P. SLICHTER
Department of Physics, University of Illinois, Urbana, Illinois
(Received June 28, 1954)

THE static magnetic susceptibility χ_0 of a metal is usually slightly paramagnetic. The principal contributions to χ_0 in many cases are a paramagnetic part due to polarization of conduction electrons spins, and a diamagnetic contribution due to orbital motion of the conduction electrons and due to ion cores. The diamagnetism is of the same order of magnitude as the paramagnetic contribution. The high degree of degeneracy of the electron gas makes χ_0 small and makes its measurement difficult and sensitive to impurity effects. Unless one can measure one or the other of the two contributions separately, one must depend on a theoretical relationship to determine the contributions of each part. Different theories give different answers for the relative size. Stimulated by the recent major theoretical advances of Bohm and Pines[1] in treating electrons in metals, we have performed a measurement of that part of χ_0 arising from the spin polarization *alone* by studying the conduction-electron spin resonance. We report initial results for lithium in this Letter.

The spin resonance arises from transitions of the electron spins among the Zeeman levels produced by a static field H. In practice the resonance is plotted at fixed frequency as H is varied through the resonance condition. Our experiment involves essentially the measurement of the total area under the curve of absorption *vs* magnetic field H. This area is simply related to the static spin susceptibility χ_p in many cases. Limitations of space do not permit a discussion of the exact relationship here, but, for example, a resonance line obeying the Bloch equations[2] satisfies the relation

$$\chi_p = \frac{2\gamma}{\pi\omega}\int_0^\infty \chi'' dH, \qquad (1)$$

where ω is the frequency of the linearly polarized

FIG. 1. Oscilloscope pictures of resonance absorption in lithium *vs* magnetic field. *Left*: Electron spin resonance. Zero field at the center of the sweep. The four peaks arise from a small phase shift between the horizontal and vertical axes. Sweep amplitude about 40 gauss. *Right*: Li^7 nuclear resonance at about 10 000 gauss. Sweep amplitude approximately 3 gauss.

alternating field inducing transitions, γ is the gyromagnetic ratio of an electron, and χ'' is the imaginary or "loss" part of the complex magnetic susceptibility. This same equation is satisfied by a line of any shape which is sufficiently narrow, and by a broad line of the type discussed by Garstens.[3]

The measurement of χ_p, which involves an absolute intensity measurement, appears difficult at first glance. Such experiments have been done by Hutchison and Pastor.[4] The essential and new feature of our experiment is the elimination of most of the usual difficulties by comparing the absorption of the electron resonance in lithium with that of the nuclear resonance in Li^7 in the same sample and at the same frequency (17 Mc/sec). (See Fig. 1.) In order to observe the resonances of the electrons or nuclei we merely change H from 6 gauss to 10 000 gauss, leaving all circuits unchanged. We can measure the ratio of the areas under the absorption curve. With the use of Eq. (1) we can relate this ratio to the ratio of the electron and nuclear static susceptibilities. Knowledge of the nuclear susceptibility, the ratio of the absorption areas, and the gyromagnetic ratio of electron and nucleus is all that is needed to determine the electron susceptibility, since circuit parameters and the amount of sample cancel out in the ratio. The nuclear susceptibility can, of course, be calculated to a high degree of precision from the Langevin formula.

The value of spin susceptibility we obtain for lithium is $2.0\pm0.3\times10^{-6}$ cgs volume units. The theoretical spin value of Pines[5] is 1.87×10^{-6}, while the free-electron (Pauli) value is 1.17×10^{-6}. The experimental value of Rao and Sarithri[6] measured by conventional means is 1.35×10^{-6}, and includes, of course, a diamagnetic part associated with orbital electron motion and ion cores. Starr and Kaufmann[7] find 1.95×10^{-6}, also by conventional means. Pines' theoretical value clearly agrees much more closely with experiment than does the free-electron value.

A fuller account of this research will be published at a later date, together with a discussion of the inherent limitations in accuracy. It is worth while pointing out here, however, that the reaction of the lithium to form nonmetallic compounds is not likely to effect accuracy to first order, since the nuclear resonance in the metals is displaced several gauss from that in a nonmetal[8] (Knight shift), with the result that we measure only the ratio of electron absorption to that of metal nuclei. There is, of course, no electron resonance in the nonmetal. In support of these statements, we have not found a sample dependence in our work.

We suggest that there are other systems in which a simultaneous nuclear and electron resonance can be found (e.g., the metal ammonia solutions and free radicals) where the comparison will make possible an improved determination of electron susceptibilities and may be used to determine the concentration of electron absorbing centers.

We are continuing the work on lithium and sodium. We hope that improvement of the signal-to-noise ratio will give adequate precision for reliable values of the diamagnetism.

We wish to express our appreciation to Dr. Pines for numerous interesting conversations. We have had many stimulating discussions with other members of our resonance group, particularly with Dr. Richard E. Norberg.

* This work was supported in part by the U. S. Office of Naval Research.

[1] D. Bohm and D. Pines, Phys. Rev. **92**, 609 (1953); D. Pines *ibid.* **92**, 626 (1953).
[2] F. Bloch, Phys. Rev. **70**, 460 (1946).
[3] M. A. Garstens, Phys. Rev. **93**, 1228 (1954).
[4] C. A. Hutchison and R. C. Pastor, Revs. Modern Phys. **25**, 285 (1953).
[5] D. Pines, following letter [Phys. Rev. **95**, 1090 (1954)].
[6] S. R. Rao and K. Sarithri, Proc. Indian Acad. Sci. **6**, 207 (1942).
[7] C. Starr and A. R. Kaufmann, Phys. Rev. **59**, 476 (1941).
[8] W. D. Knight, Phys. Rev. **76**, 1259 (1949).

Paramagnetic Susceptibility of Conduction Electrons*

DAVID PINES
Department of Physics, University of Illinois, Urbana, Illinois
(Received June 28, 1954)

WE here report the results of a calculation of the effect of electron-electron interactions on the paramagnetic susceptibility of conduction electrons in metals using the collective description of electron interactions.[1] We have computed the paramagnetic susceptibility χ_p at 0°K, using the method of Sampson and Seitz,[2] which requires a knowledge of the way in which the energy of the electronic system changes as the population of electrons of spin up and spin down varies. Our calculation for χ_p differs from that of SS in that we use the expressions for the correlation energy developed in IV, rather than the earlier Wigner expression.

As shown in IV, the average energy per electron may be written as

$$E=E_0+E_P+E_{\text{exch}}+E_{\text{corr}}{}^{l.r.}+E_{\text{corr}}{}^{s.r.}, \qquad (1)$$

where E_0 is the binding energy due to the periodic field of the lattice, E_F the average Fermi energy, E_{exch} the exchange energy per electron, $E_{corr}^{l.r.}$ represents the effect of the long-range Coulomb correlations on the electronic energy and is given in IV, and $E_{corr}^{s.r.}$ represents the reduction in energy due to short-range Coulomb correlations between electrons of antiparallel spin. An approximate expression for $E_{corr}^{s.r.}$ is

$$E_{corr}^{s.r.} = -0.0764\{0.333-0.819\ln\beta+(\beta^2/12)\}\ \text{ry}, \quad (2)$$

where $\beta=(k_c/k_0)$ is the inverse electron screening length measured in units of the maximum electron wave vector. The effect of electron correlations on χ_p may be readily computed provided we assume that the effective screening length for electron-electron interactions, k_c^{-1}, is not altered by a shift in the spin populations. Physically, this assumption appears quite reasonable, since the screening length is determined primarily by the long-range correlations, which are in turn relatively insensitive to the electron spin alignment. A more detailed investigation verifies the validity of this approximation.

Our results may be put in the form, $\chi_p=-(2n\gamma^2/\alpha)$, where γ is a Bohr magneton, n the density of conduction electrons, and α is given by

$$\alpha=(20/9)E_F+(8/9)E_{exch}+\alpha_{l.r.}+\alpha_{s.r.}, \quad (3)$$

the latter terms representing the effect of long-range and short-range electronic correlations on χ_p. Table I gives the various contributions to α for the alkali metals, together with values of χ_p obtained using (3), and, for comparison, those obtained in the free-electron approximation and those calculated by SS. We see that the Coulomb correlations tend to compensate exchange, but that the resultant susceptibility is always rather higher than the free-electron value. We estimate the accuracy of our theoretical values for χ_p as about 20 percent. A direct measurement of χ_p for lithium has been carried out recently by Schumacher, Carver, and Slichter.[3] We see that our theoretical calculation of 1.87×10^{-6} cgs volume units is in substantially better agreement with their experimental result of $2.0\pm0.3\times10^{-6}$ cgs volume units than the free-electron value or that of SS.

TABLE I. χ_p for the alkali metals. Units: Rows (c)–(g), ry; Rows (h), (i), and (j), cgs volume units$\times10^6$.

Metal	Li	Na	K	Rb	Cs
(a) (m^*/m)[a]	1.45	0.98	0.93	0.89	0.83
(b) β	0.73	0.68	0.73	0.73	0.73
(c) $(20/9)E_F$	0.326	0.319	0.221	0.207	0.191
(d) $(8/9)E_{exch}$	−0.253	−0.206	−0.167	−0.157	−0.146
(e) $\alpha_{l.r.}$	0.023	0.015	0.014	0.014	0.013
(f) $\alpha_{s.r.}$	0.108	0.111	0.109	0.109	0.108
(g) α	0.204	0.239	0.177	0.173	0.166
(h) χ_p	1.87	0.85	0.61	0.53	0.44
(i) χ_p^{free}	1.17	0.64	0.48	0.44	0.38
(j) χ_p(SS)	2.92	1.21			

[a] These values of the effective mass are due to Harvey Brooks (private communication).

Details of the foregoing calculation will be described in a forthcoming paper on the effects of electronic correlations on metallic phenomena. The writer would like to thank Dr. R. E. Norberg and Dr. C. P. Slichter for stimulating his interest in the magnetic properties of the alkali metals, and Mrs. M. C. Huse for her invaluable assistance in carrying out numerical calculations.

* This work has been supported in part by the Office of Ordnance Research, U. S. Army.

[1] D. Bohm and D. Pines, Phys. Rev. **92**, 609 (1953); D. Pines, Phys. Rev. **92**, 626 (1953), hereafter referred to as IV.

[2] J. B. Sampson and F. Seitz, Phys. Rev. **58**, 633 (1940), hereafter referred to as SS.

[3] Schumacher, Carver, and Slichter, preceding letter [Phys. Rev. **95**, 000 (1954)].

[4] See A. H. Wilson, *The Theory of Metals* (Cambridge University Press, London, 1953), p. 175.

[5] S. R. Rao and K. Sarithri, Proc. Indian Acad. Sci. **6**, 207 (1942).

Self-Powered Semiconductor Amplifier*

C. G. B. GARRETT AND W. H. BRATTAIN
Bell Telephone Laboratories, Murray Hill, New Jersey
(Received June 22, 1954)

DURING the course of experiments on the electrical properties of germanium-electrolyte systems, it became apparent that the surface of a sample of n-type germanium passing anodic current acts as a multiplying collector for holes.[1] Using this principle, it becomes possible to construct a germanium-electrolyte amplifying device which incorporates its own power supply. In this device, a slice of n-type germanium, having an indium-alloyed emitter on one surface, has its other surface exposed to a suitable electrolyte. Another electrode, having a half-cell potential higher (more noble) than that of germanium, is also placed in the electrolyte. Connections are made to the indium, to a goldbonded contact to the germanium, and to the other electrode (Fig. 1).

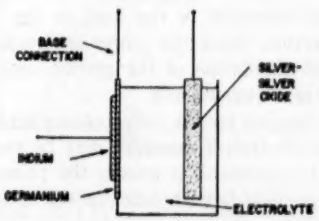

FIG. 1. The self-powered semiconductor amplifier.

A model of this device has been constructed, using $N/10$ potassium hydroxide for the electrolyte, and silver-silver oxide for the other electrode. The area of the emitter contact, and of the surface exposed to the electrolyte, was 0.073 cm². Typical characteristics are shown in Fig. 2. If a resistance R is connected between the silver-silver oxide and the germanium, current flows in the sense which leaves the germanium anodically biassed, as is shown by the dotted load line in Fig. 2. In this condition the impedance of the germanium surface is high, but creation of extra minority carriers near the surface causes additional current to flow. Measurements of the intrinsic current gain of the surface have given values between 1.4 and 2.0. Because the collector impedance is high in comparison with the emitter impedance under zero emitter bias, power gain

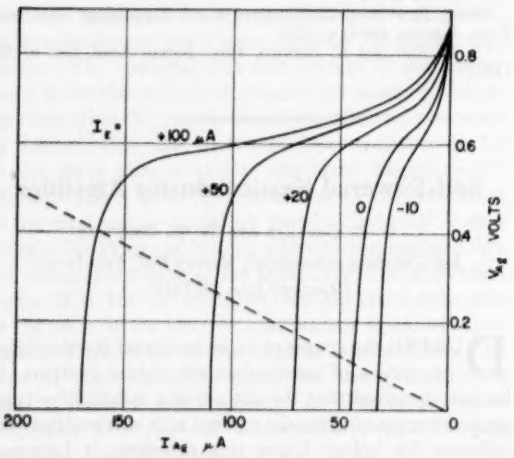

FIG. 2. Graphs showing the relation between the current flowing through the collector cell and the voltage between the silver and the germanium for various values of emitter current.

is obtained. The cut-off frequency of the device is comparable with that of a transistor of similar dimensions, since the operation does not depend on ionic mobilities. No external power supply is required, since the collector is itself part of an electrolytic cell. The power gain may be increased by applying a forward bias to the emitter, which may be done by including a common resistance in the lead to the germanium base connection. Since the power is obtained by electrochemical dissolution of the germanium, the life of the device is of course finite.

The mechanism for the collector-like behavior of the germanium-electrolyte interface may be understood as follows. At a germanium anode, the primary electrochemical reaction is with holes in the semiconductor:

$$X^- + p \rightleftarrows X,$$

as is shown by the observed dependence of electrode potential on the concentration of holes immediately inside the space-charge region of the germanium.[1] The current saturates when the flow by diffusion of holes to the surface is as great as is allowed by thermal generation in the body of the semiconductor and elsewhere. An alternative description is this: the presence of negatively charged ions near the germanium surface causes the surface region to be p type in character. Current is flowing from the n-type body across the p-type surface into the solution, and is therefore in such a sense as to bias the supposed p-n junction in the reverse direction. These descriptions are of course entirely equivalent.

A more detailed discussion of the electrical properties of germanium-electrolyte systems will be given in a forthcoming article.

[1] W. H. Brattain and C. G. B. Garrett, Phys. Rev. **94**, 750 (1954).

Photovoltaic Effect in InAs

ROBERT M. TALLEY AND DOROTHY P. ENRIGHT
United States Naval Ordnance Laboratory, White Oak, Maryland

(Received June 30, 1954)

THE intermetallic compounds of the $A_{III}B_V$ series have properties similar to the column IV semiconductors.[1] InAs has been shown to have a forbidden energy gap of about[2] 0.3 ev optically and large charge carrier mobility (14 000 cm²/volt sec for electrons and 100 cm²/volt sec for holes at room temperature).[3] We have found a photovoltaic effect in p-n junctions of InAs. The spectral dependence of the photoresponse is compared with the optical transmission in this Letter.

InAs has been prepared by reaction of the elements in an evacuated Vycor tube. The As was vacuum distilled and was determined by spectroscopic analysis to be free of all metallic impurities except for a trace of Sb. The In metal was obtained from the Indium Corporation of America and had a trace of Cu with no other impurities detectable spectroscopically. The InAs ingots were polycrystalline although single crystals several millimeters on edge were present. Both n- and p-type samples were obtained and certain ingots contained both p- and n-type regions. The hole mobility derived from Hall effect and conductivity measurements at room temperature was 10^2 cm²/volt sec while the electron mobility was 10^4 cm²/volt sec.

By means of thermoelectric measurements, it was possible to find p-n junctions in parts of the ingots. Samples about 5×2×1 mm³ were cut so that the junction was in the middle of the sample. Leads were

attached to the samples by silver paste and the samples were glued to the inner tube of a Dewar-type cell holder. Light was brought in through a NaCl or sapphire window and the cells were refrigerated by liquid N_2. Chopped light was used and the voltage from the cell was applied to a transformer to step up the impedance and then amplified and read on a General Radio wave analyzer. A photovoltaic effect was observed at all junctions, with a weaker response at the electrodes.

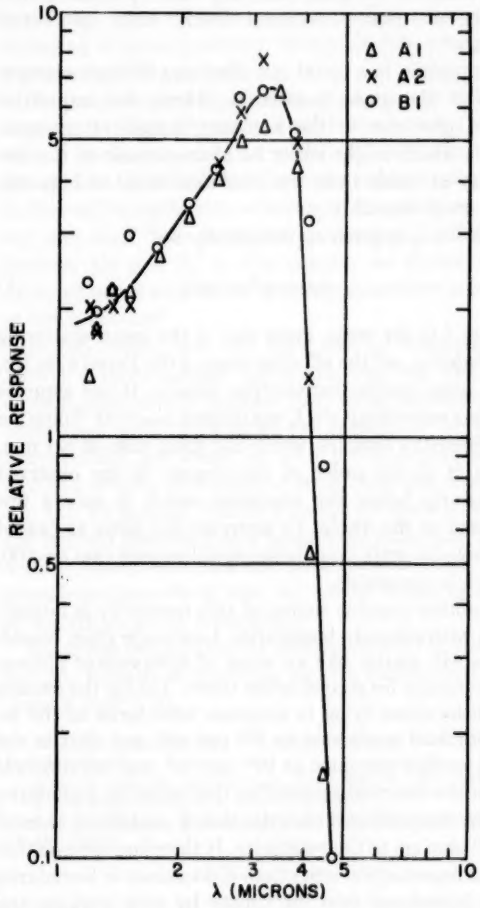

FIG. 1. Relative response, normalized at 3.5 μ, *versus* wavelength of the incident radiation for InAs photovoltaic cells measured at liquid nitrogen temperatures.

The spectrum of the photosensitivity observed with a calibrated Leiss monochromator using NaCl optics is given in Fig. 1. Three cells are plotted on the same graph and are normalized to give the same response at 3.5 μ. The signal-to-noise ratios of cells $A1$, $A2$ and, $B1$ are, respectively: 2.8, 3.1, and 6.5 for 1 μwatt/cm^2 of 3.5-μ radiation chopped at 90 cps and amplified with a 5-cps band-pass amplifier. The noise in this case was amplifier noise because the resistance of cells was of the order of 100 ohms. This photovoltaic effect was observable at room temperature, but was much stronger ($\sim$1000×) at liquid N_2 temperature. The actual temperature was somewhat higher because of inefficient heat transfer through the glass walls of the inner tube.

The time constant of these cells was determined by a light-pulse technique. The image of a ribbon filament lamp was swept past a condensing lens in front of the detector by a rotating mirror. From the geometry of the arrangement and by direct measurement with a photomultiplier, it was determined that a time constant as short as 1 μsec could be measured. The InAs cells gave a time constant of 7 μsec, where the time constant was taken to be the time required for the signal to reach $\frac{2}{3}$ of the peak value. The time constant for decay was essentially the same. The rms response to chopped radiation was independent of the chopping frequency from 400 to 1600 cps, as was expected from the short time constant.

The transmission at room temperature of two n-type samples is shown in Fig. 2 for comparison with the photovoltaic effect. These spectra are not corrected for reflection loss. Curve B represents the normal transmission obtained from undoped samples (about 10^{17} electrons/cm^3). Curve A was obtained from a predominantly n-type sample taken from one ingot which was apparently more nearly intrinsic than sample B, although Hall effect measurements did not yield a consistent value for the number of carriers, possibly because of p-n junctions in the sample. A p-type sample (3×10^{17} holes/cm^3) taken from a Cd doped ingot gave an edge about 0.2 μ longer than Curve B, and the absorption coefficients were about 24 times larger in the p-type sample. An n-type sample taken from a Se-doped ingot (about 5×10^{18} electrons/cm^3) gave an edge about 1.1 μ shorter than Curve B. It appears that InAs shows a degeneracy effect similar to InSb, in that the transmission edge is shifted to shorter wavelengths for samples containing a large number of carriers in the conduction band.[3,4]

The photovoltaic edge is the same for all three cells, although $A1$ and $A2$ were cut from the same ingot as

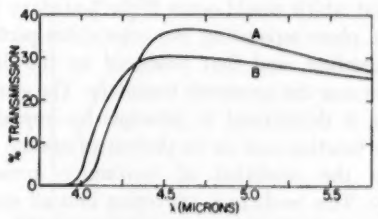

FIG. 2. Transmission of two n-type InAs samples, not corrected for reflection loss. (A) 1.12 mm thick, nearly intrinsic. (B) 1.57 mm thick, 10^{17} electrons/cm^3.

A, and $B1$ was cut from an ingot showing transmission similar to B. The temperature dependence of the transmission edge was measured to be about -4×10^{-4} ev/°C. Correcting the transmission data to liquid N_2 temperatures, the photovoltaic edge is about $0.7\,\mu$ longer than the transmission edge as taken from Curve B.

[1] H. Welker, Z. Naturforsch. **8a**, 248 (1953).
[2] Briggs, Cummings, Hrostowski, and Tanenbaum, Phys. Rev. **93**, 912 (1954).
[3] Folberth, Grimm, and Weiss, Z. Naturforsch., **8a**, 826 (1953).
[4] Observed by M. Tanenbaum and H. B. Briggs, Phys. Rev. **91**, 1561 (1953).
[5] Interpreted by Beer, Willardson, and Middleton, Phys. Rev. **93**, 912 (1953), and by Elias Burstein, Phys. Rev. **93**, 632 (1954).

Interaction of Electrons with Grain Boundaries*

M. H. Cohen and C. S. Barrett
Institute for the Study of Metals, The University of Chicago, Chicago, Illinois

(Received June 22, 1954)

A STUDY has been made by Blewitt, Coltman, and Redman[1] of the effect of cold work and subsequent recrystallization on the residual electrical resistivity of annealed single crystals of high-purity copper. Typical measured values of resistivity (in ohm cm) times 10^8 were: annealed single crystal, $\rho_{4.2°K}=0.080$; strained, $\rho_{4.2°}=1.14$; recrystallized, $\rho_{4.2°}=0.830$; and $\rho_{1.6°}=0.847$. It has been suggested[1] that the minima observed near 4.2°K in these recrystallized, high-purity samples arise from scattering or trapping of electrons at grain boundaries. Koehler[2] has proposed a model of the scattering which supports this suggestion. We also have been studying the interaction of electrons and grain boundaries and have reached conclusions somewhat different from those of the above authors.

On statistical grounds, one need only consider high-angle grain boundaries for an estimate of grain-boundary resistivity, ρ_{GB}. Electron scattering by a grain boundary is elastic and in an ideally pure metal consists of two parts: that which would occur if the boundary were a geometric plane separating two crystallites perfect up to the interface, and that produced by the disorder and strain near the geometric boundary. The geometric scattering is determined in principle by imposing on the wave function and on its derivative normal to the boundary the condition of continuity across the boundary. This leads to a scattering into all states of the same energy; the angular dependence of the scattering may easily be studied qualitatively. Such considerations yield an estimate of the value of α, the probability of scattering at a grain boundary, of $\sim$0.1 to 0.5. When the energy surface lies well within the first Brillouin zone, the change with energy of α over a range of energy equal to kT should be small. Hence the contribution of geometric scattering to ρ_{GB} in copper should be temperature independent, contrary to the conclusion reached by Koehler.[2] One should expect temperature dependence in ρ_{GB} in a pure metal only if the disorder and strain in the grain boundary makes possible bound levels, or narrow resonant levels, near the Fermi energy.[3]

Impurities in a metal can affect ρ_{GB} through segregation at the grain boundaries. There, the impurities could give rise to the necessary bound or resonant levels which might either be characteristic of the impurity or result from the combined effect of impurity and grain boundary.

Now ρ_{GB} is given approximately by

$$\rho_{GB}=m^*v\alpha/ne^2l, \tag{1}$$

where l is the mean grain size, α the mean scattering probability, m^* the effective mass, v the Fermi velocity, and n the conduction electron density. If one assumes perfect reflectivity, $\alpha=1$, one obtains $\rho_{GB}\sim10^{-10}$ ohm cm for Blewitt's samples, which had grain sizes of $\sim$1 mm. This is of the order of the change of the observed resistivity below the minimum which is only a few percent of the whole. To interpret the latter as caused entirely by grain boundaries would require that $\alpha\sim100$, which is impossible.

Another possible source of this resistivity is interaction with subgrain boundaries. Low-angle grain boundaries will scatter like an array of independent dislocations except for second-order terms. Taking the density of dislocations lying in subgrain boundaries in the recrystallized specimens as 10^8 per cm^2 and that in the cold-worked specimen as 10^{12} per cm^2, one can conclude from the observed resistivities that subgrain boundaries in the recrystallized material should contribute at most 10^{-11} ohm cm to the resistivity. It therefore appears that some imperfection other than dislocations or boundaries was introduced into the copper by cold working and subsequent annealing.

The scattering of electrons by grain boundaries has the consequence that an electric current of density j will exert a pressure p on a grain boundary normal to the current:

$$p=(m^*v\alpha/e)j. \tag{2}$$

We have attempted to observe the effect of such a pressure, but have met with negative results. In one experiment, cold-drawn aluminum wire of 99.9968 percent purity, in which several circumferential notches had been machined, was recrystallized by heating to 605°C with a direct current density of 1.1×10^4 amp/

cm². A grain boundary was subsequently found stretched over the entire cross section of the wire at the base of one of the notches. This boundary, if free to move during the recrystallization process, would have bulged until p was equilibrated by the surface tension of the boundary. We estimated from Eq. (2), taking $\alpha \sim 0.1$, that $p \sim 10^3$. No bulging was detected. The sensitivity of the experiment to bulging of the boundary, however, when converted into pressure by assuming a grain-boundary energy of 500 dynes/cm, was also $\sim 10^3$ dynes/cm².

One may show directly from a momentum balance argument, which does not invoke the concept of α, that $p = nel\rho_{GB}$, a relation which is consistent with Eq. (1) and Eq. (2). Thus if the entire residual resistance in Blewitt's experiments were due to boundary scattering, and since there should be no significant difference between Cu and Al in this respect, we should have expected in our experiment an easily observable pressure of 10^6 dynes/cm².

In conclusion, both the high residual resistance of Blewitt's recrystallized specimens and our negative experimental results indicate that some imperfections other than grain boundaries are present in Blewitt's recrystallized specimens. In view of the known sensitivity of resistance minima to impurities, and recalling Eq. (1), we suggest that an attempt be made to study the residual resistance as a function of grain size. Such a study, however, could not distinguish between pure grain-boundary effects and the effects of segregration of impurities at the boundaries.

We appreciate greatly the cooperation of Dr. Blewitt and Dr. Koehler in providing us with information concerning their work.

* Work supported in part by contract with the U. S. Office of Naval Research.

[1] Blewitt, Coltman, and Redman, Phys. Rev. **93**, 891 (1954).
[2] J. S. Koehler, Phys. Rev. **94**, 1071 (1954).
[3] See, for example, J. Korringa and A. N. Gerritsen, Physica **19**, 457 (1953).

Low-Temperature Thermal Conductivity of a Canadian Natural Graphite*

ALAN W. SMITH
Atomic Energy Research Department, North American Aviation, Downey, California

(Received July 1, 1954)

THE low-temperature thermal conductivity of artificial graphite and samples of small crystallite natural graphite have a temperature dependence[1-3] as great as $T^{2.8}$. This is anomalous with regard to the T^2 dependence of the specific heat.[4] Two interpretations of this anomaly have appeared. One interpretation attributes it to intergranular, nongraphitic carbon.[3] The other assumes it to be intrinsic to graphite but to be dependent on the ratio of crystallite width to thickness.[5] In order to distinguish between these interpretations the thermal conductivity of nearly single crystal graphite should be measured. A temperature dependence of T^2 would be predicted by the first theory[3] and a higher exponent by the second.[5]

Since large crystals of graphite are not available, an apparatus was constructed to measure small flakes of natural graphite. The apparatus consists of a small carbon resistor heater, a heat meter (consisting of a sample of artificial graphite previously measured on another apparatus), and a flake (1/4 in.×1/20 in. ×1/100 in.) of Canadian natural graphite[6] connected in series. The graphites were copper plated at the ends and soldered with Cerrolow −117°F solder. Chromel-constantan thermocouples (0.001 inch diameter) were cemented onto the graphites to measure the temperature gradients. The whole is covered with a radiation shield and placed inside an evacuated vessel with temperature control between 4° and 300°K. The graphite samples used have deformation lines on the surface indicating crystallites of the order of 10^{-2} cm. The electrical resistivity of these samples has a positive temperature coefficient similar to that of single-crystal graphite rather than artificial graphite.

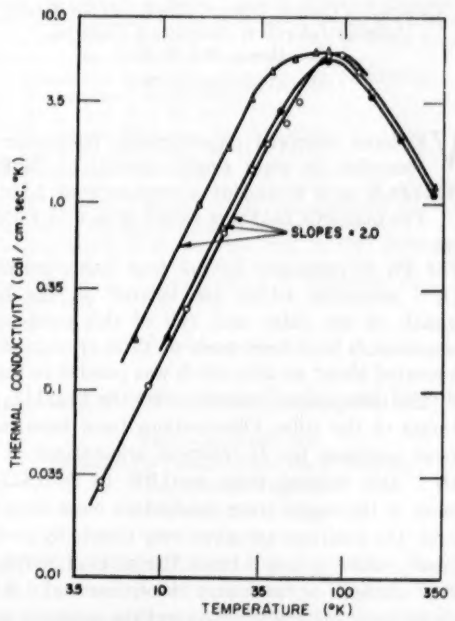

FIG. 1. Thermal conductivity of Canadian natural graphite.

The thermal conductivity of three samples is shown in Fig. 1. Due to the small size and irregular nature of the flakes, the absolute magnitudes are only approximate. The relative values are good to 5–10 percent. The maxima of the conductivity occur at around 80°K. Previously measured samples have maxima above room temperature. From this fact or from the actual conductivities at low temperatures, it is found that the mean free path, when boundary limited, is about 100 times that of any previous sample and slightly less than the crystallite size mentioned previously. The important fact, however, is that all three samples show a T^3 dependence at low temperatures. This leads to the conclusion that the intrinsic conductivity does have a T^3 dependence and substantiates the two-medium explanation of the higher exponent previously measured.

* This report is based on studies conducted for the U. S. Atomic Energy Commission.

[1] R. Berman, Proc. Phys. Soc. (London) **A65**, 1029 (1952).
[2] W. W. Tyler and A. C. Wilson, Jr., Phys. Rev. **89**, 870 (1953).
[3] A. W. Smith, Phys. Rev. **93**, 952 (1954).
[4] W. DeSorbo and W. W. Tyler, Phys. Rev. **21**, 1660 (1953).
[5] P. G. Klemens, Australian J. Phys. **6**, 405 (1953).
[6] Obtained from J. C. Bowman of the National Carbon Company.

Paramagnetic Resonance Absorption in Sodium Plutonyl Acetate*

CLYDE A. HUTCHISON, JR., AND W. BURTON LEWIS
Institute for Nuclear Studies and Department of Chemistry, University of Chicago, Chicago, Illinois and Los Alamos Scientific Laboratory, University of California, Los Alamos, New Mexico

(Received June 16, 1954)

WE have observed paramagnetic resonance absorption in pure single crystals of $NaPuO_2 \times (C_2H_3O_2)_3$ at 4°K and at a frequency of 2.3×10^{10} sec^{-1}. The magnetic field was varied from 0 to 1.4×10^4 gauss.

The Pu is contained in the four linear triatomic PuO_2^{++} molecules which are located on the body diagonals of the cubic unit cell of this compound.[1] Measurements have been made on three crystals. Each was rotated about an axis which was parallel to the γf field. The three axes of rotation were the 112, 111, and 100 axes of the cube. Observations have been made of peak positions for 21 different orientations of the PuO_2^{++} axis ranging from $\theta=0.108$ to $\theta=0.425$. A number of the angles were checked on more than one crystal. The positions are given very closely by $g=5.92\times|\cos\theta|$, where g is h/β times the ratio of frequency to field strength at maximum absorption and θ is the angle between the PuO_2^{++} axis and the magnetic field. This corresponds to $g_{\parallel}\cong5.9$, $g_{\perp}\cong0.0$.

This behavior is that to be expected for an electronic structure of PuO_2^{++} in which the two electrons not in closed shells are f electrons.[2] In the strong axial electric field of PuO_2^{++}, the two electrostatically interacting f electrons will be in states with $M=\pm3$ and $M=\pm2$. The spin, 1, will interact with the state $M=5$ so that $L_z+2S_z=\pm3$ for the lowest doublet and hence the magnetic splitting will be $6\beta H$ when H is parallel to the molecular axis and zero when it is perpendicular. Under these assumptions or taking the trigonal character of the field into account there would be no observable resonance absorptions because of the vanishing of the matrix elements of magnetic moment between the split states. Slight departures from the ideal symmetry apparently permit the observation of the transition.

The powder susceptibility would be given to first order at low temperatures by

$$\chi=\frac{N\beta^2}{kT}\left(\frac{g_{\parallel}^2\pm2g_{\perp}^2}{12}\right)=\frac{1.09}{T},$$

corresponding to $3\chi kT/N\beta^2=2.95$. This is to be compared with the measured value 2.83[3] for PuO_2^{++} and 3.17[4] for the presumably isoelectronic NpO_2^{+}.

The resonance data offer convincing evidence that the two unpaired electrons in the plutonyl compound are f electrons.

A 2 percent solution of $NaPuO_2(C_2H_4O_2)_3$ in the isomorphous diamagnetic $NaUO_2(C_2H_3O_2)_3$ has been investigated and the nuclear hyperfine structure has been observed. In one orientation a doublet (the nuclear spin of Pu is $\frac{1}{2}$)[5] with a spacing of 430 gauss was found. The hyperfine structure data have not yet been interpreted.

We thank the Institute for the Study of Metals of the University of Chicago for supplying the liquid helium used in these experiments. We thank Mr. John Anderson for assistance in part of the experimental work. Mr. Edward Bartal constructed some of the apparatus employed in the measurements.

* This work was supported in part by the U. S. Office of Naval Research.

[1] I. Fankuchen, Z. Krist. **91**, 473 (1936); W. H. Zachariasen, *The Transuranium Elements: Research Papers* (McGraw-Hill Book Company, Inc., New York, 1949), Paper No. 20.7, National Nuclear Energy Series, Plutonium Project Record, Vol. 14B, Div. IV.

[2] The theory of resonance in such ions is discussed in detail by J. Eisenstein and M. H. L. Pryce in a forthcoming paper. We wish to thank them for communicating their results to us in advance of publication. Various models of the situation resulting from crystalline field and spin-orbit perturbations of heavy metal ion electronic states have been discussed by R. J. Elliott, Phys. Rev. **89**, 659 (1953) and by D. M. Gruen and C. A. Hutchison, Jr., reference 4.

[3] J. K. Dawson, J. Chem. Soc. **1952**, 2705.

[4] D. M. Gruen and C. A. Hutchison, Jr., J. Chem. Phys. **22**, 386 (1954).

[5] Van den Berg, Klinkenberg, and Regnaut, Physica **20**, 37 (1954).

Isotope Shift in X-Ray Spectra of Heavy Elements*

G. IGO AND M. S. WERTHEIM
Yale University, New Haven, Connecticut
(Received June 7, 1954)

A RECENT attempt[1] to detect the isotope shift in x-ray spectra gave negative results. On the other hand, comparison[2] of ratios of spin hyperfine structure (spin hfs) with isotope shift available in measurements on atomic spectra with a calculation[3] on spin hfs of x-ray terms has indicated the likelihood of an isotope shift of general order of magnitude comparable with experimental resolution. For these reasons as well as the additional interest supplied by related investigations[4–6] on nuclear radii, it appeared desirable to calculate by means of the volume effect theory[7] the effects expected for the lines measured by Rogosa and Schwarz.[1] Table I

TABLE I. $(\Delta\delta E)_{n=\infty}/\Delta A$ in electron volts.

Z	U 92	Pb 82	Mo 41
$1s_{1/2}$	1.2	0.50	0.012
$2s_{1/2}$	0.24	0.088	0.0016
$2p_{1/2}$	0.028	0.00068	0.00003

lists values for the "top-slice" modification of the Coulomb potential, which corresponds to the whole nuclear charge being on the nuclear surface and to a value $n=\infty$ in $\delta V=-(\gamma/na)[-(r/a)^n+n+1]+(\gamma/r)$, which represents[7] the relative values of the potential in the nucleus. In Table I, ΔA is the difference between isotope mass numbers. The isotope shift for a uniform volume density ($n=2$) and for $n=1.5$ is obtainable from the values in Table I by means of the

TABLE II. $(\Delta\delta E)_n/(\Delta\delta E)_\infty$.

	U	Pb	Mo
$n=2$	0.67	0.65	0.61
$n=1.5$	0.63	0.61	0.57

factor given in Table II. The validity of the first-order theory has been examined by means of

$$\delta E=(\psi_0,\ (\delta V)\psi)/(\psi_0,\ \psi),$$

where ψ_0 and ψ are, respectively, the Coulomb and the exact wave functions. Here ψ is obtained by the phase-amplitude method.[8] Table III gives the values of the correction factor to the first-order treatment.

Corrections for screening on the electron making the jump were made in the Fermi-Thomas field approximation. The correction factors are 0.90 for $2s_{1/2}$ of U and 0.99 for $1s_{1/2}$ of Mo.

When a $1s_{1/2}$ electron is removed, the levels of remaining electrons suffer small differential shifts from isotope to isotope due to the change in screening field.[9]

TABLE III. Values of correction factor for wave function distortion.

Z	Mo 42	Pb 82	U 92
	0.93	0.75	0.67

The $1s_{1/2}$ isotope shift is decreased by 1 percent due to the presence of the other electrons. A decrease in the isotope shift of the $2s_{1/2}$ and $2p_{1/2}$ levels is also approximately 1 percent due to contributions from the remaining electrons.

Combining all factors for the top-slice model ($n=\infty$) yields the values of the isotope shift listed in Table IV.

TABLE IV. Corrected values for the isotope shift (ev).

	Element	$\Delta\delta E/\Delta A$
$2s_{1/2}$	U	0.14
$2p_{1/2}$	U	0.017
$1s_{1/2}$	Mo	0.011

Employing $\Delta A=3$ and 8 for U and Mo, respectively, one finds expected displacements of 0.051 ev for U $2p_{1/2}$ and 0.088 ev for Mo $2s_{1/2}$, while experiment would not have detected splittings smaller than 0.4 ev ($\cong 8\times 0.051$ ev) and 0.2 ev ($\cong 2\times 0.088$ ev). The $2s_{1/2}$ level in U is seen to have a large expected shift.

A fuller account will be published later. We wish to thank Professor Breit for stimulating discussions and for suggesting the problem.

* This research was supported by the United States Air Force, through the Office of Scientific Research of the Air Research and Development Command, and in its earlier stages was assisted in part by the joint program of the U. S. Office of Naval Research and the U. S. Atomic Energy Commission.

[1] G. Rogosa and G. Schwarz, Phys. Rev. **92**, 1434 (1953).
[2] G. Breit (private communication).
[3] G. Breit, Phys. Rev. **35**, 1447 (1930).
[4] C. H. Townes, Phys. Rev. **94**, 773 (1954).
[5] J. Rainwater, Phys. Rev. **94**, 773 (1954).
[6] R. Hofstadter, Phys. Rev. **94**, 773 (1954).
[7] J. E. Rosenthal and G. Breit, Phys. Rev. **41**, 459 (1932); G. Breit, Phys. Rev. **42**, 348 (1932). The parameter n is defined on page 469 of the first of these references.
[8] G. Breit and G. E. Brown, Phys. Rev. **76**, 1307 (1949).
[9] G. Breit, Phys. Rev. **42**, 348 (1932), pages 352, 353, and end of abstract; M. F. Crawford and A. L. Schawlow, Phys. Rev. **76**, 1310 (1949).

Annihilation of Positrons in Liquid Helium*

FRANK L. HEREFORD
Department of Physics, University of Virginia, Charlottesville, Virginia
(Received June 21, 1954)

MEASUREMENTS have recently been made[1] of the rates of three-photon annihilations of positrons stopping in liquid nitrogen and liquid Freon. The rates observed were of the same order as that for posi-

trons stopping in metals. These data were interpreted as indicating the absence of appreciable triplet positronium in the liquids due to (1) no positronium being formed, or (2) its rapid conversion from the triplet to the singlet state.

By means of a different technique (that used previously by Deutsch[2]) we have obtained similar results concerning the presence of triplet positronium in liquid helium. Approximately 1 mC of Na^{22} was sealed in a 0.001-in. aluminum envelope and lowered into a glass Dewar containing a mass of liquid helium (at about 4°K) sufficient to stop all positrons. The NaI(Tl) scintillation pulse-height spectrum of the annihilation quanta was observed and compared with that obtained

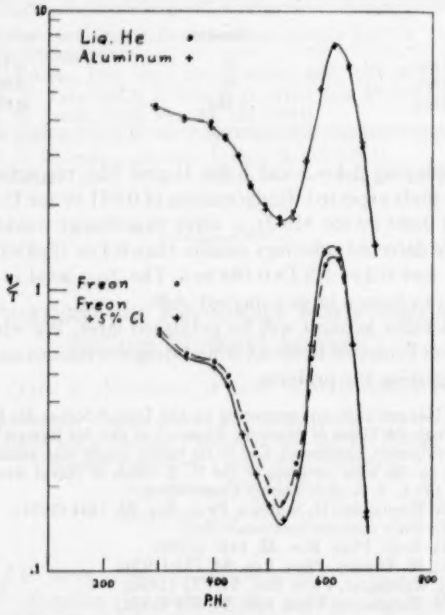

FIG. 1. Differential pulse-height spectra of annihilation radiation for positrons stopping in the indicated substances. The upper and lower pairs of curves have been separated to facilitate comparison.

upon surrounding the source (in the same container at room temperature) with a thickness of aluminum equivalent in g/cm² to the liquid helium. The two spectra (Fig. 1) were identical to within the statistical accuracy of the measurements, indicating no appreciable increase of triplet annihilations in liquid helium as compared with aluminum.

The sensitivity of the spectrum to the presence of triplet positronium was determined by repeating the Deutsch experiment[2] with the same source in the same container. Spectra were observed with the glass Dewar filled alternately with an atmosphere of Freon and an atmosphere of Freon+5-percent chlorine. As compared to the spectrum with Freon, that with the admixture of chlorine showed an increase in the 0.51-Mev 2-photon peak and a decrease in counting rate for 3-photon events at lower pulse heights. This difference was due to enhancement of the triplet to singlet conversion probability upon introduction of the chlorine. The effect was not so marked as in Deutsch's data, since the quantity of gas surrounding the source was not sufficient to stop all positrons. As a consequence, an appreciable fraction was annihilated in the glass wall.

* Sponsored by Office of Ordnance Research, U. S. Army.

[1] S. DeBenedetti and R. T. Siegel, Phys. Rev. **94**, 955 (1954). Similar results were obtained for the annihilation of positrons in liquid argon by T. A. Pond, thesis, Princeton, 1952 (unpublished).

[2] M. Deutsch, Phys. Rev. **82**, 455 (1951); M. Deutsch and E. Dulit, Phys. Rev. **84**, 601 (1951).

Low-Temperature Bleaching and Restoration of Color Centers

A. HALPERIN* AND G. F. J. GARLICK
Department of Physics, University of Birmingham, Birmingham, England

(Received June 28, 1954)

IN a recent Letter, Hesketh and Schneider[1] have suggested that a large-scale restoration of F centers occurs in KCl on warming in the dark after bleaching at 113°K by irradiation in the F band. Their main evidence is an absorption peak at 175°K in the F-band absorption *vs* temperature curve, with a similar effect for the V band. These peaks could be produced repeatedly by recooling to 113°K, optical bleaching in the F band, and rewarming.

While investigating optical absorption bands caused by trapped electrons in CdS and other crystals and their thermal bleaching characteristics, we obtained similar effects to those of Hesketh and Schneider.

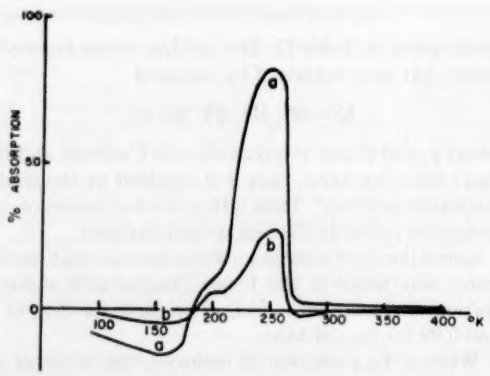

FIG. 1. Absorption peaks due to vapor condensation on crystal surfaces. (a) CdS, (b) KCl.

Almost identical curves of absorption *vs* temperature are obtained for CdS and for KCl as shown in Fig. 1. The absorption is not spectrally sensitive and occurs also for other transparent solids such as glass plates. The intensity and form of the curves shown in Fig. 1 are dependent on the rate of heating, the vacuum in the crystal cryostat, and on previous treatment. Detailed investigation shows that the peaks in Fig. 1 are due to interference effects from condensed surface films on the crystals, the latter acting as efficient vapor traps as they lag behind their surroundings during warming. Using dry air in the cryostat at atmospheric pressure reduces the effect, presumably by reduction of the mean free path of vapor molecules. Deliberate introduction of known vapors produces peaks at temperatures specific to each vapor and related to its boiling point.

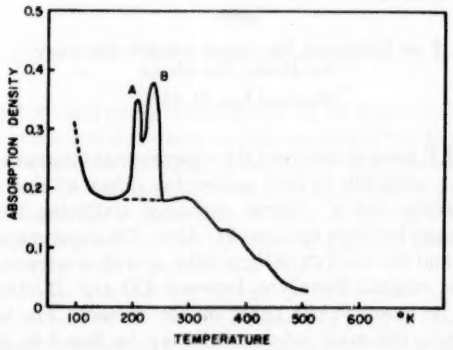

FIG. 2. Thermal bleaching curve for the F band of KCl colored by x-rays at 100°K.

Figure 2 shows the thermal bleaching curve for KCl colored by x-ray irradiation at low temperatures. Apart from the "interference" peaks, A and B, the form of the curve is as expected from previous knowledge of the thermal stability of F centers in KCl, true bleaching occurring above room temperature in the region of 400°K.

* On study leave from the Hebrew University, Jerusalem, Israel.

[1] R. V. Hesketh and E. E. Schneider, Phys. Rev. **94**, 494 (1954)

Polarization in n-p Scattering at 100–200 Mev*

A. ROBERTS, J. TINLOT, AND E. M. HAFNER
University of Rochester, Rochester, New York

(Received June 24, 1954)

THIS note reports some recent results obtained from the study of azimuthal asymmetries in the charge-exchange scattering of partially polarized neutrons by hydrogen and carbon. The experimental method and some preliminary data have already been briefly reported.[1,2] Additional runs have been made, including measurements at first-scattering angles $\theta_1 = 15°$ and 30°, and at a variety of neutron threshold energies.

Considerable work was done to obtain an accurate knowledge of the center line of the neutron beam, since the asymmetries that we observed were generally small while their sensitivity to angular error of the center line was of the order of 25 percent per degree for CH_2 second scatterers. In our procedure, an optical line-of-sight passed through the centers of targets located at three points in the cyclotron, defining first-scattering angles of $+\theta_1$, 0, and $-\theta_1$, respectively. The axis of two collimators in the second-scattering proton telescope was set to this optical line. The telescope could then be rotated to the left and right of the center line, and angles set within one minute of arc. The angular acceptance of the proton telescope was 2° at half-maximum. Inequality of left-right angular settings with respect to the actual neutron beam could be deduced from the second-scattering left-right asymmetry for neutrons produced at zero first angle; it could also be deduced from the *mean* left-right asymmetry produced by equal and opposite first angles.

In this way we have found apparent angular errors as large as nine minutes, without being able to locate their source. In such cases, however, the two methods of deducing the angular error were in good agreement and provided a consistent correction to the data.

The energy spectra of the neutron beams were found to be similar to those previously measured.[3] Lower limits to the acceptable neutron energy were set by means of copper absorbers in the proton telescope, and these limits were kept constant as the angles were changed, assuming free n-p collision kinematics.

Figures 1 and 2 present asymmetries observed in this way for a primary proton energy of 230 Mev, first angles of 15° and 30°, first targets of Be and C, a neutron threshold of 100 Mev, second scatterers of C and H, and second angles up to 55°. Asymmetries are given as 2ϵ, defined in the usual way,[1] and all angles are in the laboratory system. The asymmetries found at $\theta_1 = 30°$ are consistently larger than those found at $\theta_1 = 15°$. Results were also obtained at neutron thresholds of 125, 150, and 175 Mev, but no significant energy dependence was found.

From the results shown, an estimate can be made of the polarization, P, for the exchange scattering of neutrons by C and H, and of protons by Be and C. Assuming charge symmetry and ignoring the energy change between the two events, we obtain $P(p\text{-C-}n, 30°) = P(n\text{-C-}p, 30°) = +0.19 \pm 0.02$. Then $P(p\text{-Be-}n, 30°) = +0.13 \pm 0.03$; $P(n\text{-H-}p, 30°) = +0.15 \pm 0.05$; and

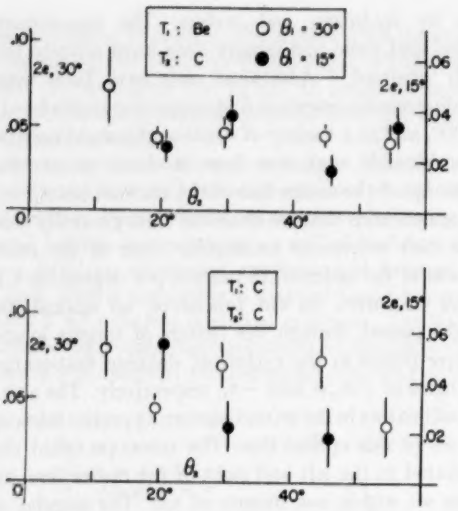

FIG. 1. Upper part: asymmetries observed with first target beryllium, second target carbon. Lower part: both targets carbon.

$P(n\text{-H-}p, 55°) = -0.55 \pm 0.15$. Errors given are purely statistical standard deviations.

As previously reported, it appears that polarization in n-p exchange scattering is small up to 45°, and that its angular dependence is strikingly different from that observed in exchange scattering from carbon. The n-p data are inconsistent with a Serber potential,[4] which predicts a polarization $P(\theta)$ that is antisymmetric about 45°.

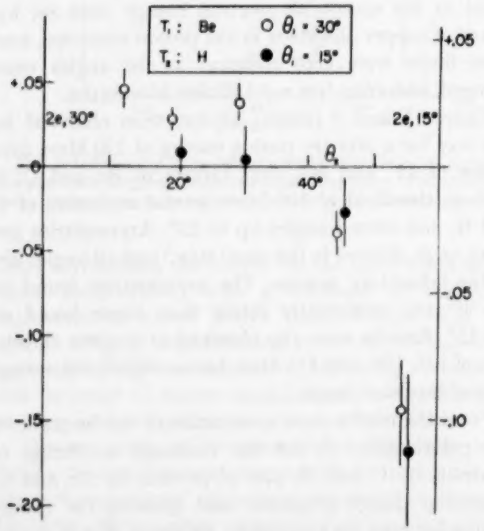

FIG. 2. Asymmetries observed with first target beryllium, second target hydrogen (from CH_2–C subtraction).

The assistance of W. Chesnut, I. Goldberg, R. Harding, S. Spital, and W. Spry in carrying out this work is gratefully acknowledged.

* Research supported by the U. S. Atomic Energy Commission.

[1] *Proceedings of the Fourth Annual Rochester High-Energy Conference* (University of Rochester Press, Rochester, 1954).
[2] Roberts, Tinlot, and Hafner, Phys. Rev. **95**, 1098 (1954).
[3] Nelson, Gr.ernsey, and Mott, Phys. Rev. **88**, 1 (1952).
[4] D. R. Swanson, Phys. Rev. **89**, 749 (1953).

Meson-Proton Scattering Phase Shift Analysis

H. A. BETHE, *Cornell University, Ithaca, New York*

AND

F. DE HOFFMANN, *Los Alamos Scientific Laboratory, Los Alamos, New Mexico*

(Received June 21, 1954)

WE have re-analyzed the experimental information available to date concerning direct π^+ and π^- scattering and π^- charge exchange scattering from hydrogen between zero and 217 Mev. The experimental data and the analysis of these data, as well as references to the original literature, between 120 and 217 Mev, may be found in our paper on the subject.[1] For low energies, the same information may be found in our forthcoming book.[2] References to the experimental work are also given in the paper by Orear.[3]

In references 1 and 2 it is shown that at low energy, arguments of continuity can be given to select the Fermi type phase shifts, as opposed to those usually denoted as Steinberger-type phase shifts.[4] Furthermore, analysis in the high-energy region[1] leads one to prefer the Fermi type solution over the Yang type. Hence, all phase shifts presented below are of the Fermi type.

Figure 1 shows the variation of the principal phase shift δ_{33} (i.e., $T=3/2$, $j=3/2$). The dotted curve indicates an η^3 dependence, where η is the meson momentum in the center-of-mass system in units of μc. Up to 80 Mev, $\delta_{33}=13.4\eta^3$ degrees, but after that it rises faster towards the resonance at about 195 Mev.

Figure 2 shows the two S-state phase shifts for $T=3/2$ and $T=1/2$, that is, δ_3 and δ_1. The numerals next to the points indicate the energy in Mev. Note that δ_3 follows a rather good straight line of the form $\delta_3=9.6-17.1\eta$ degrees from high energies down to around 60 Mev, but does *not* head for zero. On the contrary, the points at 40 and 26 Mev seem to indicate a break in slope. Previous analysis by the Rochester group[5] had placed δ_3 at 40 Mev much closer to the axis, with a simultaneous upward shift in δ_1 at 40 Mev. We do not believe that the present data bear out this conclusion. However, we must admit that our values lead to a

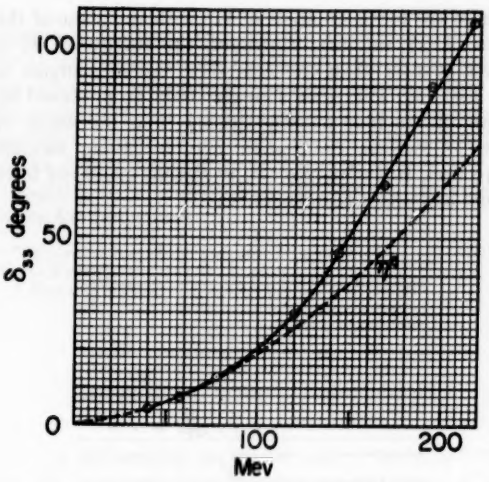

FIG. 1. The $T=3/2$, $j=3/2$ phase shift as a function of energy.

direct π^- scattering cross section at 40 Mev which is much too low compared to that measured by Barnes *et al.*[6] On the other hand, it does fit in with the values of $\sigma(\pi^-\to\pi^-)$ measured at 65 and 26 Mev, both of which are considerably lower than Barnes' value. It will be noticed that with our set of values deduced at 40 Mev, δ_{33} fit very well on the curve of Fig. 1.

δ_1 shows a somewhat erratic behavior (see curve). Our analysis[1] of the 217-Mev point does place δ_1 close to or slightly below zero, but this point might be in error.

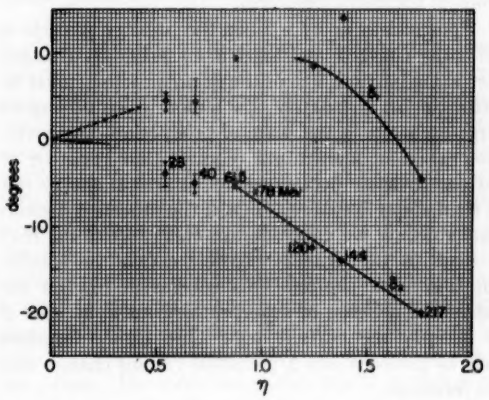

FIG. 2. S state phase shifts as a function of η, the momentum in the center-of-mass system in units of μc.

At zero energy the Panofsky experiment,[7] coupled with the recent determinations of positive photoproduction near threshold at Illinois,[8] enables one to solve for the quantity $(\delta_1-\delta_3)/\eta$. Our analysis of the photoproduction data near threshold and beyond shows that the fraction of the differential cross section for positive photoproduction at 90° which is due to S scattering has the following values: At 175 Mev: 0.88; at 185 Mev: 0.83; at 200 Mev: 0.72; and at 235 Mev: 0.54. Making use of the fraction at 175 Mev and allowing for other corrections, we find $(\delta_1-\delta_3)/\eta=10.7\pm2.5$ degrees. While one knows only the difference in slope, and not the absolute slopes at zero, we have indicated a possible choice which might not be too inconsistent with the phase shift data at 26 and 40 Mev. However, the dotted lines as shown lead to a value at 5 Mev of 4.5 millibarns for the direct π^- scattering between 90 and 180°, as compared with 8 millibarns deduced from very preliminary data of Lederman (private communication).

We wish to emphasize that we do not believe that there need be any discrepancy between the Panofsky value at zero and the very low-energy phase shifts. We believe that the δ_3 curve does show a break in slope near $\eta=0.8$, which might well be a gradual one.

[1] de Hoffmann, Metropolis, Alei, and Bethe, Phys. Rev. (to be published).
[2] H. A. Bethe and F. de Hoffmann, *Mesons and Fields* (Row, Peterson and Company, Evanston, to be published), Vol. II.
[3] J. Orear, Phys. Rev. (to be published).
[4] Bodansky, Sachs, and Steinberger, Phys. Rev. **93**, 1367 (1954).
[5] H. P. Noyes and A. E. Woodruff, Phys. Rev. **94**, 1401 (1954).
[6] Barnes, Angell, Perry, Miller, Ring, and Nelson, Phys. Rev. **92**, 1327 (1953).
[7] Panofsky, Aamodt, and Hadley, Phys. Rev. **81**, 565 (1951).
[8] G. Bernardini and E. L. Goldwasser, Phys. Rev. **94**, 729 (1954).

Possible Example of the Annihilation of a Heavy Particle*

H. S. BRIDGE, H. COURANT, H. DESTAEBLER, JR.,† AND B. ROSSI

Laboratory for Nuclear Science, Massachusetts Institute of Technology, Cambridge, Massachusetts

(Received June 21, 1954)

THE picture in Fig. 1 and the sketch in Fig. 2 show an unusual cosmic-ray event photographed with the M.I.T. multiplate cloud chamber at Echo Lake, Colorado. The chamber contained eleven brass plates, each 0.50 inch thick (11.1 g cm^{-2}) and was triggered by a penetrating-shower detector placed above it. Two additional views, taken at different angles, are available.

Three electron showers, *b*, *c*, *d*, appear to be associated with the stopping of a charged particle, *a*, in one of the plates. Within the experimental errors, the axes of the three showers and the direction of the last visible segment of track (*a*) intersect at one point in the plate.

From the number of small showers with no apparent origin occurring in our cloud chamber, we found an upper limit of 10^{-3} for the probability that either (*c*) or (*d*) may be a case of chance association. It is practically impossible to explain shower (*b*) in a similar way for a survey of about 10 000 pictures has not revealed a single shower of the size of (*b*), with no apparent origin and going upward.

To estimate the shower energy, E_0, we have made use of the equation: $E=hNt$, where h is a constant, N is the total number of electron tracks appearing in the separate sections of the chamber through which the shower develops, and t is the thickness of the plates, measured in the direction of the shower axis. Nt is an approximate value for the track length of the observable shower electrons which, according to shower theory, is proportional to the energy, E, of the initiating particle. Notice that there is an effective lower limit for the energy of the observable electrons because, as the energy decreases, electrons are more strongly scattered and have less probability of emerging from the plates. The proportionality constant, h, depends on the cut-off energy. We have determined h experimentally from a study of double-cored showers that arise from the decay of π^0 mesons, making use of the equation, $\sin(\theta/2)=m_{\pi^0}c^2/2(E_1E_2)^{\frac{1}{2}}$, which relates the energies E_1, E_2 of the two decay photons to the angle θ between their lines of flight.

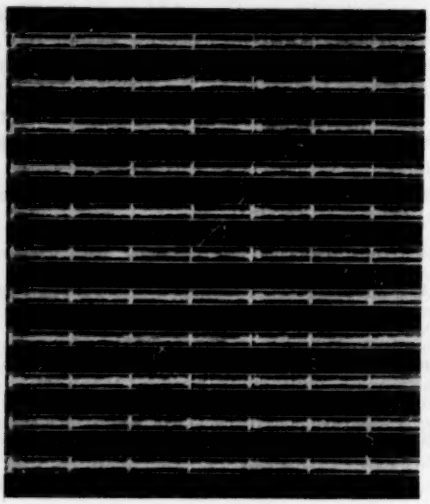

FIG. 1. Cloud-chamber photograph of the cosmic-ray event.

With this method we found $E_b=1170$ Mev and $E_c=300$ Mev for the energies of showers (b) and (c). It was not possible to make a significant estimate of the energy of shower (d), which contains only 4 visible electron tracks. The most serious uncertainty in our energy estimates arises from statistical fluctuations. Although a rigorous treatment of the fluctuation problem as applied to our method of analysis is still lacking, we feel confident that the quoted energy values could not be in error by as much as a factor of two.

Showers (c) and (d) appear to be produced by photons, while (b) could be produced by either an electron or a photon. The momenta of the particles responsible for the three showers do not add to zero. Indeed, the axis of (b) forms an angle of 11° with the plane of the axes of (c) and (d); moreover, the energy of (b) is much greater than the combined visible energies of (c) and (d). The three showers could be produced by three of the four photons arising from the decay of two π^0 mesons, the fourth photon having escaped detection. However, the two π^0 mesons could not have equal and opposite momenta.

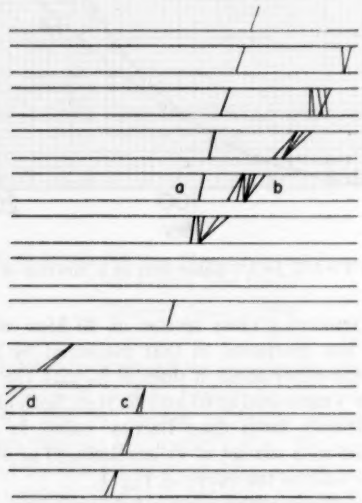

FIG. 2. Sketch of the cosmic-ray event.

In what follows we consider three possible interpretations of the event described.

1. Spontaneous decay.—Since the primary particle is electrically charged, and there is no secondary charged penetrating particle, one of the decay products must be an electron or, alternately, a π meson which undergoes charge exchange in the plate of production. Moreover, conservation of momentum requires that there be at least one invisible decay product of a total energy not less than about 500 Mev. Thus, if the process is a spontaneous decay, we conclude, on energy grounds, that the mass of the primary particle cannot be smaller than that of a proton. This conclusion implies the existence of a boson of superprotonic mass, at least if one accepts the current view that heavy fermions (such as nucleons and Λ particles) cannot change into light fermions.

2. Nuclear absorption.—In order to interpret the event as the nuclear absorption of a negative particle, one must assume (a) the existence of a boson with mass considerably greater than 1000 electron masses (although not necessarily greater than the proton mass) and (b) the possibility that, when such a particle is captured by a nucleus, practically all of its rest energy may appear in the form of photons.

3. Annihilation process.—In view of the difficulties of interpreting the event as a decay or an absorption

process, one should consider the possibility that the event represents the annihilation process of two heavy fermions. For example, the incident particle might be an antiproton (or an antihyperon) that undergoes annihilation with an ordinary proton. A large fraction of the energy liberated in such a process may well be changed into π^0 mesons and thus ultimately appear in the form of γ rays.

* Supported in part by the joint program of the U. S. Office of Naval Research and the U. S. Atomic Energy Commission.
† National Science Foundation Predoctoral Fellow.

Anomalous Event Observed in Photographic Emulsion*

J. H. Noon, M. F. Kaplon, and J. Crussard
University of Rochester, Rochester, New York

(Received June 21, 1954)

In a stack of 400μ G-5 stripped emulsions flown at high altitude an anomalous interaction of a fast heavy nucleus has been observed (Fig. 1). A fast Be

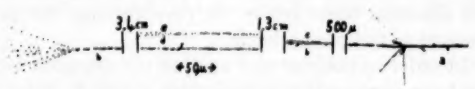

Fig. 1. A fast Be nucleus (a) interacts in emulsion, making a star. Two of the prongs are relativistic triply (b) and doubly (c) charged particles emitted in the forward direction. The triply charged particle makes a star of 6 minimum tracks, and the doubly charged particle appears to decay into 2 minimum tracks d and e.

nucleus (a) interacts producing a $6+1_{\mathrm{Be}}$ star. Two of the prongs are relativistic particles of charge 3 and 2, each making an angle less than 2×10^{-3} radian with the primary. The triply charged particle (b) interacts after 5.09 cm, giving a $0+6_{\mathrm{Li}}$ star. The doubly charged particle (c) travels for 1.37 cm, at which point it splits into two fast singly-charged particles (d and e); there is no observational evidence of nuclear interaction and the event $c\rightarrow d+e$ is coplanar within the accuracy of measurement. Since it is reasonable to assume in interactions of fast heavy nuclei that the fast heavy fragments observed originate from the incident nucleus, the charge of the fragments should not exceed that of the parent. The violation of this aspect of charge conservation provides the anomaly.

The charge of the primary was determined by gap-count comparison with slow protons and by comparison of the δ-ray count with that of fast α particles. The former gave $I_a/I_{\min}=16.2\pm0.2$ and the latter $n_\delta(a)/n_\delta(\alpha)=4.06\pm0.7$; thus $Z_a=4\pm0.1$, establishing particle a as Be. For particle b, $n_\delta(b)/n_\delta(\alpha)=1.9\pm0.3$, giving $Z_b+2.76\pm0.2$. Since b interacts giving 6 minimum ionizing tracks it cannot be a slow α particle; thus b is established as Li. For c we find $n_\delta(c)/n_\delta(\alpha)\approx1$ and $I_c/I_0\approx4$, giving $Z_c=2$.

Though the track length per emulsion averaged 6.5 mm, the only meaningful measurements were relative scattering measurements. The relative scattering was measurable between b–c for 2 emulsions and between b–d, b–e, and d–e for $2\frac{1}{2}$ emulsions using 500- and 1000-μ cells with noise elimination. The relative scattering angles per 100μ ($\bar{\alpha}_{xy}$) are given in Table I.

$$\bar{\alpha}_{xy}=k[(Z_x/A_xP'_x\beta_x)^2+(Z_y/A_yP'_y\beta_y)^2]^{\frac{1}{2}},$$

where $A_x=M_x/M_{\text{nucleon}}$ and $P_x'=P_x/A_x$. In Table II we give in radians the horizontal (H) and vertical (V) components of the angles between the tracks (θ_{xy}).

Though it is in principle possible from our data to determine the individual $\bar{\alpha}_x$, the values are not too meaningful unless these are of comparable magnitude. The most precisely determined value is $\bar{\alpha}_d$, leading to $P_dc=2.76\pm0.7$ Bev. Since $I_d/I_0=0.92\pm0.04$, d must be a proton.[1] In addition, the similarity of $\bar{\alpha}_{b-d}$ and

Table I. Relative scattering angles in degrees per 100μ between the tracks a, b, c, d, and e.

	b–c	b–d	b–e	d–e
$100\bar{\alpha}$	0.326 ± 0.09	1.052 ± 0.28	0.43 ± 0.12	0.98 ± 0.26

$\bar{\alpha}_{d-e}$ imply that $(Z/M)_e\leqslant\frac{1}{2}$ if P_b' and P_e' are not appreciably less than P_d; this is verified by the similarity of $\bar{\alpha}_{b-e}$ and $\bar{\alpha}_{b-e}$. Since $I_e/I_0=0.87\pm0.04$, we conclude that e is either a deuteron or triton. With the further assumption of comparable momenta per nucleon for b, c, and e, we obtain $2.8\leqslant P'c(\text{Bev})\leqslant7.5$. These values are consistent both with the angular distribution of the Li star and the angle θ_{bc}.

We may characterize the possible reactions for this event as follows:[2]

$$\mathrm{Be}^9+\text{“}p\text{”}(\text{“}n\text{”})\rightarrow\mathrm{Li}^{6(7)}+\mathrm{He}^{4(3)}+(\pi^-);$$
$$\mathrm{He}^{4(3)}+\text{“}n\text{”}\rightarrow\mathrm{H}^1+\mathrm{H}^{3(2)}+n; \quad (1)$$
$$\mathrm{Be}^9+\text{“}p\text{”}(\text{“}n\text{”})\rightarrow\mathrm{Li}^{6(7)}+\mathrm{He}^{*4(3)}+(\pi^-);$$
$$\mathrm{He}^{*4(3)}\xrightarrow{\text{decay}}\mathrm{H}^1+\mathrm{H}^{3(2)}; \quad (2)$$
$$\mathrm{Be}^9+\text{“}p\text{”}(\text{“}n\text{”})\rightarrow\mathrm{Li}^6+\mathrm{He}^3+n+(\pi^-);$$
$$\mathrm{He}^3+\text{“}n\text{”}\rightarrow\mathrm{H}^1+\mathrm{H}^2+n; \quad (3)$$
$$\mathrm{Be}^9+\text{“}p\text{”}(\text{“}n\text{”})\rightarrow\mathrm{Li}^6+\mathrm{He}^{*3}+n+(\pi^-);$$
$$\mathrm{He}^{*3}\xrightarrow{\text{decay}}\mathrm{H}^1+\mathrm{H}^2. \quad (4)$$

Here “p”(“n”) means a proton or neutron of the target nucleus and He* an excited state. Reactions (1) and (2) are pickups while (3) and (4) are charge exchange. Though it is impossible to rule out completely a nuclear interaction as the cause of the He breakup, the observed coplanarity tends to favor the occurrence of a decay in flight with a time τ in the rest system satisfying $0.6\times10^{-11}\leqslant\tau(\text{sec})\leqslant1.6\times10^{-11}$. Assuming that a two-

TABLE II. Horizontal and vertical components in milliradians for the angles between the tracks *ab*, *cd*, and *ce*.

	θ_{ab}	θ_{cd}	θ_{ce}
H	2.4±0.2	5.5±0.2	1.5±0.2
V	0.6±0.6	5.6±0.8	1.8±0.8

body decay in flight has occurred we find $15 \leqslant Q(\mathrm{He}^{*3}) \leqslant 250$ Mev and $3 \leqslant Q(\mathrm{He}^{*4}) \leqslant 65$ Mev, where the limits take into account estimated errors in momenta and angles consistent with the ionization and scattering measurements.

If we consider the decay in flight of an excited state of He, we can rule out ordinary nuclear excitation on a lifetime basis, since one should expect lifetimes less than 10^{-16} sec. On the other hand, the observed time of flight and Q value for He^{*3} suggest the excited state to be of the type involving a bound hyperon; either (*i*) $\mathrm{He}^{*3}=\Lambda^{+}+p+n$ or (*ii*) $\mathrm{He}^{*3}=2p+\Lambda^{0}$. Type (*i*) should have Q value of ~240 Mev while (*ii*) should have ~170 Mev. We believe the formation of the latter in reaction (4) with the production of a π^{-} the most likely interpretation. Another, though less likely a possibility, would be the mesonic decay mode of either He^{*3} or He^{*4} [of either type (*i*) or (*ii*)] in which a π^{0} meson is emitted. However, the formation of He^{*3} seems more likely than He^{*4} since the latter involves a pick-up reaction.[3] This case provides some evidence for the formation of an excited nucleus by addition of positive charge to a breakup fragment.

We wish to thank Professor J. B. French for helpful discussion and Miss P. Hull for her assistance in scanning.

* This research was supported by the United States Air Force, through the Office of Scientific Research of the Air Research and Development Command.

[1] This is corroborated by the Li star; if d was a π of $Pc=2.76$ Bev, the momentum of b should increase by $M_{\mathrm{nucleon}}/M_{\pi}$ and the Li star should show a narrow cone of at least 3 tracks; this is not the case. (We imply here equal velocities for all particles.)

[2] The minimum ionizing track emitted from the first star could be the π^{-} indicated below.

[3] Professor J. B. French has estimated the pick-up process and finds it is improbable at our energy due to the large momentum transfer involved. The charge-exchange process without meson production is almost certainly equally improbable.

Polarization of High-Energy Deuterons*

OWEN CHAMBERLAIN, EMILIO SEGRÈ, ROBERT TRIPP, CLYDE WIEGAND, AND THOMAS YPSILANTIS

Radiation Laboratory, Department of Physics, University of California, Berkeley, California

(Received June 21, 1954)

IN analogy to experiments on proton polarization,[1-4] we obtained a polarized deuteron beam by the same scattering method. The trajectories of 167-Mev deuterons as produced by the cyclotron are essentially the same as those of 312-Mev protons if the magnetic field of the steering magnet is properly adjusted and the deuteron beam enters the cave through the same channel as the proton beam.

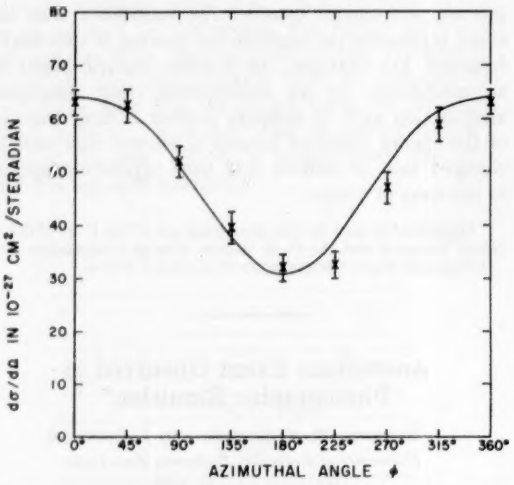

FIG. 1. Differential cross section *versus* azimuthal angle Φ for polarized deuterons scattered elastically by carbon.

In order to polarize and analyze the deuteron beam we have used carbon as scatterers A and B. After the second scatterer we have measured the intensity of the scattered beam as a function of ϕ. We have endeavored to limit ourselves to elastically scattered deuterons by the use of absorbers, as in the proton work.

It has been shown by Lakin and Wolfenstein[5] that the most general intensity distribution produced by polarized deuterons is:

$$I(\theta,\phi)=I_0(\theta)+A(\theta)\langle T_{20}\rangle + [B(\theta)\langle T_{21}\rangle+C(\theta)|\langle T_{11}\rangle|\,]\sin\theta\cos\phi + D(\theta)\langle T_{22}\rangle\sin^2\theta\cos 2\phi. \quad (1)$$

The incident deuterons travel in the z direction and have been polarized by scattering in the x, y plane. I, A, B, C, D are polynomials in $\cos\theta$ and the T_{ik}'s are expectation values, for the beam before it undergoes the second scattering, of quantities such as

$$T_{21}=-\tfrac{1}{2}\sqrt{3}[(S_x+iS_y)S_z+S_z(S_x+iS_y)],$$
$$T_{11}=-\tfrac{1}{2}\sqrt{3}(S_x+iS_y),$$
$$T_{22}=-\tfrac{1}{2}\sqrt{3}(S_x+iS_y)^2,$$

where **S** is the spin operator for the deuteron.

Experimentally we have found $I(20°,\phi)$ as in Fig. 1. An analysis of this scattering gives

$$I(20°,\phi)=p+q\cos\phi+r\cos 2\phi, \quad (2)$$

with $p=50.3\pm2.2$, $q=15.3\pm1.9$, and $r=-1.8\pm3.6$ in units of 10^{-27} cm²/steradian. The errors are based on counting statistics only, and are valid for the ratios

$p:q:r$ but not necessarily for the absolute values of these parameters. Measurements at smaller values of θ give similar results with smaller values of q/p.

This equation agrees well with Eq. (1) and shows that the coefficient of $\cos 2\phi$ is very small or zero, at least in the cases investigated up to now.

A possible explanation which is consistent with the usual spin-orbit model has been pointed out by Dr. M. Ruderman. If it is assumed that the deuteron polarization originates in an $\mathbf{L}\cdot\mathbf{S}$ coupling which acts in the scattering process in addition to a central force, and if the magnitude of the spin-orbit potential is small compared to the central part, it then follows that the $\cos 2\phi$ term is negligible because $\langle T_{22}\rangle$ is very small.

It must be noted that the description of the polarization of a deuteron beam is substantially more complicated than the similar description for particles of spin $\frac{1}{2}$, and that our analysis gives only a small part of the relevant information.

* This work was done under the auspices of the U. S. Atomic Energy Commission.

[1] Oxley, Cartwright, and Rouvina, Phys. Rev. **93**, 806 (1954).
[2] Chamberlain, Segrè, Tripp, Wiegand, and Ypsilantis, Phys. Rev. **93**, 1430 (1954). Figure 1 of the reference paper is applicable to the present work and the same notations are used throughout.
[3] Marshall, Marshall, and de Carvalho, Phys. Rev. **93**, 1431 (1954).
[4] J. M. Dickson and D. C. Salter, Nature **173**, 946 (1954).
[5] W. Lakin and L. Wolfenstein (unpublished). We thank the authors for having shown us the manuscript.

Mechanism of Proton Polarization in High-Energy Collisions*

OWEN CHAMBERLAIN, EMILIO SEGRÈ, ROBERT TRIPP, CLYDE WIEGAND, AND THOMAS YPSILANTIS
Radiation Laboratory, Department of Physics, University of California, Berkeley, California

(Received June 18, 1954)

RECENT experimental evidence has accumulated showing that high-energy collisions of protons with various nuclei induce a considerable polarization in proton beams[1–3] and mechanisms have been proposed to account for this effect.[4–9] We have tried to investigate this phenomenon experimentally and we present here a brief summary of our results.

For the sake of discussion we shall distinguish three types of collisions: (a) elastic collisions in which the struck nucleus is left unexcited; (b) inelastic collisions in which the struck nucleus is left in an excited state; (c) the limiting case (quasi-elastic) in which the impinging proton can be considered to collide with a specific nucleon of the target and recoils almost as in a free nucleon-nucleon collision.

The theory proposed in references 4 through 7 applies specifically to elastic collisions and should be applicable especially to diffraction scattering. This we have tested by measuring the differential cross section for left and right scattering for a polarized 300-Mev proton beam obtained as described in reference 2. The scatterers studied are carbon, aluminum, calcium, and iron, as well as several others less completely.

One of the important requirements of the experiment is that the scattering be elastic. This is at least partially achieved by using a detecting telescope with enough absorber to exclude all protons that have suffered an appreciable energy loss in the target. In Fig. 1, we

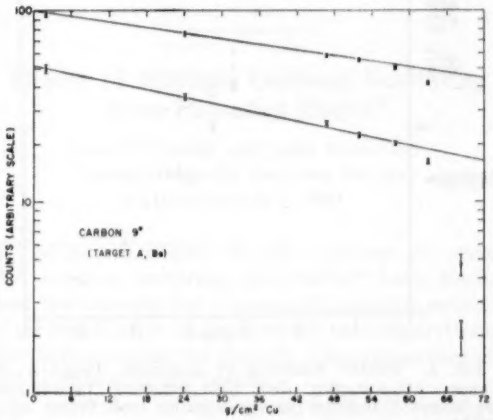

FIG. 1. Counting rate as a function of the absorber thickness in the counter telescope. Target B: carbon; beam polarization 0.64, $\theta=9°$. Dots: left scattering; crosses: right scattering. Proton energy 300 Mev.

show absorption curves for the scattered protons taken at an angle $\theta=9°$ for left and for right scattering from carbon. The curves show the effect of nuclear absorption and also the end of the range of the protons. From curves of this type one can derive values of the asymmetry e as a function of the energy of the scattered protons. The asymmetry shows an increase at high energy which indicates a high degree of polarization of the protons scattered elastically, as predicted.[4–7] However, our resolution in energy (limited by range straggling) is insufficient to distinguish the fluctuations in cross section corresponding to the levels of the residual nucleus. Fortunately, for small θ, diffraction scattering accounts for most of the scattering cross section and it is possible, by using a thick absorber in the telescope, to obtain scattering curves that show the characteristic diffraction pattern.[10] This is shown in Fig. 2, in which left and right scattering are plotted separately. The corresponding values of e are plotted in Fig. 3 and show fluctuations which we think are due to the operation of the $\mathbf{L}\cdot\mathbf{S}$ coupling as expected.[4–7] The minimum is not as pronounced as predicted by the simplified theories,[4–7] but there are probably two causes for this: Experimentally the lack of energy and angular resolution does not permit measuring elastic scattering only; theoretically the simplified models

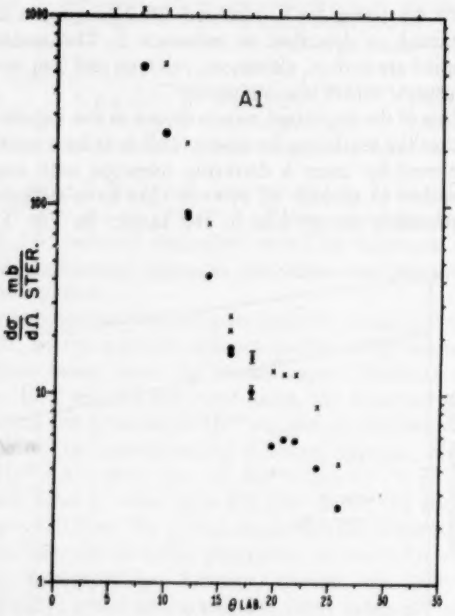

FIG. 2. "Elastic" scattering by aluminum. Target A: Be. Crosses: left scattering; dots: right scattering. Typical errors are indicated. Incident beam polarization 0.64. Proton energy 300 Mev.

used are too crude (as pointed out by some of the authors) and the true minima may be less prominent than calculated on the simplified assumptions.

Even scattering that is definitely inelastic shows a considerable degree of polarization. In the case of quasi-elastic scattering this corresponds, qualitatively at least, to the results of n-p scattering[11] and p-p scattering,[2] as is to be expected.

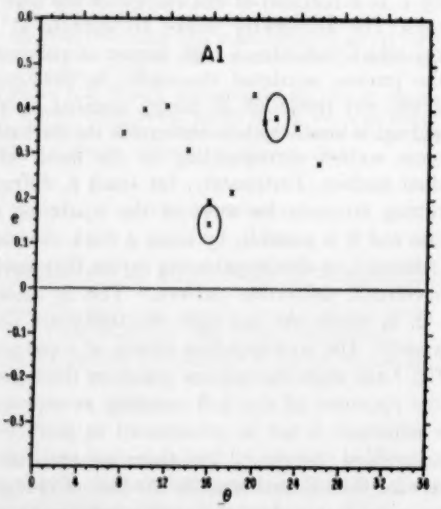

FIG. 3. Plot of the asymmetry corresponding to Fig. 2. Typical errors indicated.

For the intermediate region a study should be made to try to discern the influence on the polarization of the excitation state of the residual nucleus. This, however, is beyond our present experimental possibilities.

A detailed account of these experiments will be published later.[12]

The notation is the same as that used in reference 2.

* This work was done under the auspices of the U. S. Atomic Energy Commission.

[1] Oxley, Cartwright, and Rouvina, Phys. Rev. **93**, 806 (1954).
[2] Chamberlain, Segrè, Tripp, Wiegand, and Ypsilantis, Phys. Rev. **93**, 1430 (1954).
[3] Marshall, Marshall, and de Carvalho, Phys. Rev. **93**, 1431 (1954).
[4] E. Fermi, Nuovo cimento **11**, 407 (1954).
[5] W. Heckrotte, and J. V. Lepore, Phys. Rev. **94**, 500 (1954).
[6] B. J. Malenka, Bull. Am. Phys. Soc. **29**, No. 4, 32 (1954).
[7] Snow, Sternheimer, and Yang, Phys. Rev. **94**, 1073 (1954).
[8] S. Tamor, Phys. Rev. **94**, 1087 (1954).
[9] G. Takeda and K. M. Watson, Phys. Rev. **94**, 1087 (1954).
[10] Richardson, Ball, Leith, and Moyer, Phys. Rev. **86**, 29 (1952).
[11] Chamberlain, Donaldson, Segrè, Tripp, Wiegand, and Ypsilantis, Phys. Rev. **95**, 850 (1954).
[12] Similar results at 130 Mev are reported by J. M. Dickson and D. C. Salter, Nature **173**, 946 (1954).

Nuclear Elastic Scattering of Photons*

EVANS HAYWARD AND E. G. FULLER
National Bureau of Standards, Washington, D. C.
(Received June 18, 1954)

IN a recent note[1] an experiment was described in which the differential cross section at 120° for the nuclear elastic scattering of photons in the energy range 10–25 Mev was measured for Au, Pb, and U targets. These experiments have been extended to include the target elements Cu, Mn, Sn, Au, Bi, and Pb and the energy range 4 to 28 Mev. For all these elements but gold, in addition to the maximum associated with the "giant resonance," a pronounced peak has been found near the (γ,n) threshold. The measured points for lead are shown in Fig. 1, and Table I contains the data for the other elements.

The data given above have all been corrected for the electronic absorption of the primary and scattered photon beams in the target. No corrections have been made for nuclear self-absorption. These corrections are important for those energies where the nuclear absorption cross section is of the same order or greater than the total electronic absorption cross section, i.e., below the (γ,n) threshold where the scattering is presumably due to sharp, well-defined levels. For dipole transitions the maximum absorption cross section in these levels could be as high as $6\pi\lambda^2 \simeq 10^{-22}$ cm^2. Although this self absorption is partially compensated for by small-angle Compton scattering, preliminary estimates indicate that below the (γ,n) threshold a correction for self-absorption could raise the mean scattering cross

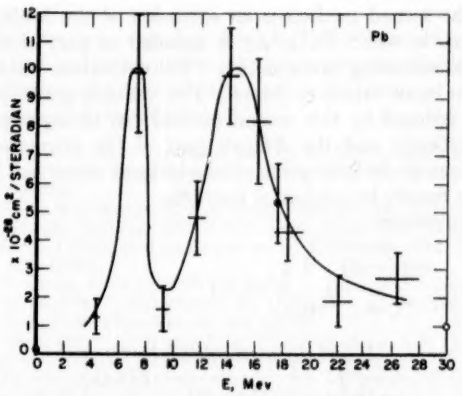

FIG. 1. Differential cross section at 120° for the elastic scattering of photons by lead. The energy spread indicated for the points is the width of the differential discriminator channel and the standard deviations on the intensities are based only on the number of counts registered. The open circles at the low- and high-energy end of the graph show, respectively, the magnitudes of the Thompson scattering cross section by the whole nucleus and by the Z free protons. The point at 17.6 Mev is taken from the data of M. B. Stearns [Phys. Rev. 87, 706 (1952)].

section given here by as much as a factor of four. Self-absorption corrections are necessary for the primary beam only, since the Doppler shift should prevent nuclear resonance absorption of the scattered photons. Experiments are now being planned to study the self-absorption effects in detail.

In spite of the crudeness of the experiment, there are significant differences in the elastic scattering cross section as a function of photon energy for the various nuclei studied. The differences depend on the level structures and oscillator strength distributions for the individual nuclei.

Bethe and Ashkin[2] have predicted the qualitative features of the scattering cross section reported here. For heavy nuclei the scattering cross section just below the (γ,n) threshold is expected to approach the value obtained by extrapolating the (γ,n) cross section into this energy region. For all of the nuclei studied except Au the general features of Fig. 42 of reference 2 are well reproduced when the present scattering data are combined with the available data on $\sigma(\gamma,n)$. The fact that in the case of Au the neutron yield curve does not join smoothly with the elastic scattering curve is probably an indication that the inelastic scattering cross section in Au is considerably larger than the elastic scattering cross section for energies just below the (γ,n) threshold. A large inelastic scattering cross section peaking near the (γ,n) threshold has been observed for gold.[3]

TABLE I. Elastic scattering cross section in cm^2/sterad.

Energy (Mev)	Cu $\times 10^{-29}$	Mn $\times 10^{-29}$	Sn $\times 10^{-28}$	Au $\times 10^{-28}$	Pb $\times 10^{-28}$	Bi $\times 10^{-28}$
4.2– 4.7	2.1 ±1.1	5.7±5.7	0.57±0.32	2.3±1.3	1.3±0.6	3.8±2.2
6.5– 7.3		9.1±2.5		1.6±0.7		13.2±2.9
7.0– 7.8	9.4 ±1.2		7.4 ±0.6		9.9±2.1	
8.9– 9.9	2.8 ±1.2	30 ±5	1.4 ±0.4	1.1±0.4	1.6±0.8	0.57±0.33
11.1–12.2	0.79±0.55	<0.42	0.17±0.17	2.6±0.7	4.8±1.3	0.25±0.07
13.5–14.7	0.95±0.54	1.3±0.7	1.1 ±0.4	6.0±1.0	9.8±1.7	7.6 ±1.6
15.2–17.0	4.4 ±1.2	2.5±0.9	1.9 ±0.4	5.8±1.0	8.2±2.2	6.7 ±1.5
17.3–19.5	8.9 ±1.3	3.5±1.0	1.9 ±0.4	3.2±0.6	4.4±1.1	4.3 ±1.2
21.0–23.0	5.6 ±1.1	5.0±1.4	1.1 ±0.3	1.1±0.4	1.9±0.9	3.9 ±1.7
24.9–28.2	4.3 ±1.0		1.2 ±0.3		2.7±0.9	

* This research was supported by the U. S. Air Force, through the Office of Scientific Research of the Air Research and Development Command.

[1] E. G. Fuller and Evans Hayward, Phys. Rev. 94, 732 (1954).

[2] *Experimental Nuclear Physics*, E. Segrè, Editor (John Wiley and Sons, Inc., New York, 1953), Vol. 1, p. 347.

[3] V. Telegdi (private communication).

Theory of Multiple Coulomb Scattering from Extended Nuclei*

LEON N. COOPER AND JAMES RAINWATER
Columbia University, New York, New York
(Received July 2, 1954)

UNCERTAINTIES in the analysis of recent μ-meson scattering experiments[1,2] have emphasized the necessity for a reasonably accurate estimate of the modification in the Coulomb multiple scattering distribution required to properly take into account the finite extension of the nucleus.

In particular, cosmic-ray experiments[2] performed recently have been interpreted as indicating the existence of an anomalous (i.e., nonelectromagnetic) μ-nuclear interaction which cannot be explained in terms of known μ-meson interaction processes. In most of these experiments the multiple scattering distribution of relativistic μ mesons from 2- or 5-cm lead plates is measured; then the experimental results are compared with the predictions of the Olbert[3] and Molière[4] multiple scattering theories. Although by no means the only difficulty arising in the interpretation of such experiments, one of the most striking is the absence of a reliable estimate of the expected electromagnetic multiple scattering distribution at large angles.

In the Molière multiple scattering theory the nucleus is treated as a point charge. The single scattering cross section is taken to be the Rutherford cross section modified at small angles due to electron shielding. In the Olbert theory an attempt is made to estimate the effect of the nuclear extension by multiplying the single scattering law for projected angles by a step function which cuts off all single scattering beyond a certain projected angle. This gives a very great underestimate of the multiple scattering at angles beyond the cutoff angle where the Olbert distribution has a Gaussian dropoff and soon falls greatly below any reasonable single scattering curve. It is easily seen that the correct multiple scattering curve should always fall above the single scattering curve at large angles (for a reasonable choice of the single scattering law).

We have, therefore, attempted to develop procedures for solving the multiple scattering problem starting

with single scattering cross sections of the form

$$f(\varphi)d\varphi=\tfrac{1}{2}QF_N(\varphi/\varphi_0)d\varphi/(\varphi^2+\varphi_m^2)^{\frac{1}{2}}.$$

φ is the projected angle and φ_m is the screening angle; $F_N(\varphi/\varphi_0)$ is the nuclear form factor,[5] where $F_N(0)=1$ and $F_N(\varphi/\varphi_0)$ decreases approximately as φ^{-4} for large values of φ; $\varphi_0=\hbar/pR$ and R is the nuclear radius.[6]

Two completely independent methods for solving this kind of problem have been developed and applied to the case of the multiple scattering of relativistic μ mesons from 2 cm of lead. The two methods give results that are in agreement with one another.

The first method might be characterized as a "brute force" numerical folding together of several partial

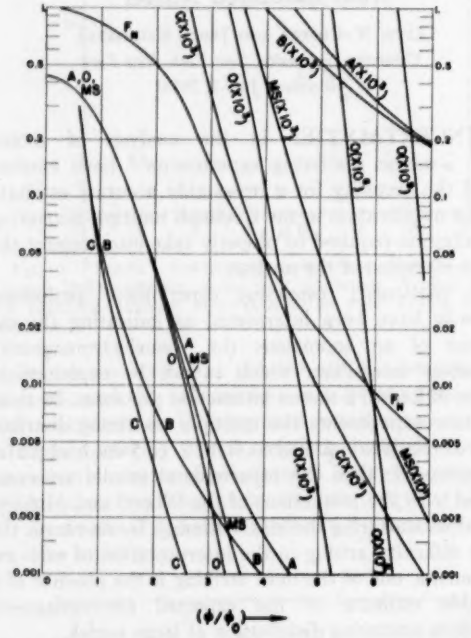

FIG. 1. Curves appropriate to $cp=1$ Bev and 2-cm Pb. Multiply (φ/φ_0) by 1.74 for Bev degrees. Curve A = Molière; B = point nucleus single scattering; F_N = assumed nuclear form factor, C = single scattering law including F_N; MS = resulting multiple scattering law; O = Olbert distribution with single scattering cutoff at $(\varphi/\varphi_0)=1.1$.

distributions which together add up to the selected distribution of single scatterings. Such a method at first seemed hopelessly tedious, but several approximations were used which greatly speeded up the calculations without introducing excessive errors. The final calculation required about two days of slide rule and desk calculator time to obtain results which are estimated to be good to 1–2 percent at small angles and 5–10 percent at large angles (aside from errors in the assumed form factor). This method has the advantage of giving a good insight into the way the final result develops in terms of the physical processes.

The second method is an extension of the Molière theory in which $F_N(\varphi/\varphi_0)$ is included as part of the single scattering cross section. (The derivation will be given in an article to follow.) The multiple scattering law deduced by this second method can be expressed analytically and the difficult part of the calculation reduces to the evaluation of one integral which can be done readily by numerical methods.

We obtain:

$$M(x)=\frac{\exp(-x^2)}{\sqrt{\pi}}+\frac{1}{4G}\left\{f'(x,\infty)-\frac{1}{\sqrt{\pi}}\int_0^\infty\frac{d\xi[1-F_N(\xi/x_0)]}{(\xi^2+x_m^2)^{\frac{1}{2}}}T(x,\xi)\right\},\quad(1)$$

$$M(x)=\frac{\exp(-x^2)}{\sqrt{\pi}}\left[1+\frac{(2x^2-1)}{4G}q\right]+\frac{1}{4G}\frac{1}{\sqrt{\pi}}\int_\epsilon^\infty\frac{d\xi F_N(\xi/x_0)}{(\xi^2+x_m^2)^{\frac{1}{2}}}T(x,\xi),\quad(2)$$

where

$$T(x,\xi)=\{\exp[-(x+\xi)^2]+\exp[-(x-\xi)^2]-2\exp(-x^2)\},$$

$$q=\ln(\kappa/1.26)^2,\quad 0.1\leq\kappa\leq 0.5,$$

and where x and x_0 are proportional to φ and φ_0.

Formula (1) is the same as Molière's formula except for the last term which gives the correction due to the nuclear extension. It is seen that if $F_N(\xi/x_0)=1$ (point nucleus) the correction term is zero. For large values of x, formula (1) is inconvenient because the correction term is large compared to the net value of $M(x)$. In this case, however, (2) is convenient; especially so where x is large enough so that the first term in (2) can be neglected due to the smallness of $\exp(-x^2)$. The two formulas can be used to evaluate $M(x)$ for all values of x. It is also to be noticed that a single calculation will serve for all momenta in the relativistic region as the integral depends upon $\beta\approx 1$. The integrals were evaluated numerically by use of Weddle's[7] rule and grid spacings and values of κ of $\frac{1}{2}$ and $\frac{1}{4}$. Comparison of the results for the two grid spacings indicates that errors resulting from the numerical integrations are quite small.

We carried through calculations for the case (Fig. 1) of 2 cm Pb and $cp=1$ Bev and used $F_N(\varphi/\varphi_0)=1.00$, 0.82, 0.50, 0.15, and $12(\varphi/\varphi_0)^{-4}$ for $(\varphi/\varphi_0)=0$, 1, 2, 3, and ≥ 4. This particular choice of F_N is intended to slightly underestimate the nuclear size effects, but otherwise to represent our best guess as to the "correct" form factor on the basis of recent experiments. We chose $R=1.1A^{\frac{1}{3}}\times 10^{-13}$ cm and applied F_N to the law for projected scattering. This should give nearly the

same result as choosing $R=1.0A^{\frac{1}{3}}\times10^{-13}$ cm with F_N applied to the law for total angle scattering. Inelastic scattering was not included here, but will be discussed in the article to follow.

* This work was supported in part by the joint program of the U. S. Office of Naval Research and the U. S. Atomic Energy Commission.

[1] W. L. Whittemore and R. P. Shutt, Phys. Rev. **88**, 1312 (1952).
[2] George, Redding, and Trent, Proc. Phys. Soc. (London) **A66**, 533 (1953); B. Leontic and A. W. Wolfendale, Phil. Mag. **44**, 1101 (1953).
[3] S. Olbert, Phys. Rev. **87**, 319 (1952).
[4] G. Molière, Z. Naturforsch. **2a**, 133 (1947); **3a**, 78 (1948).
[5] L. I. Schiff, Phys. Rev. **92**, 988 (1953).
[6] See S. Olbert, (reference 3) for definitions of φ_m, x, G, Q, and other symbols used in the modified Molière theory.
[7] H. Margenau and G. M. Murphy, *The Mathematics of Chemistry and Physics* (D. Van Nostrand Publishing Company, Inc., New York, 1947), p. 461.

Polarization of Nucleons Elastically Scattered from Nuclei*

WARREN HECKROTTE AND JOSEPH V. LEPORE
Radiation Laboratory, Department of Physics, University of California, Berkeley, California

(Received July 2, 1954)

THE polarization of high-energy nucleons elastically scattered from spin-zero nuclei must be a consequence of an effective spin-orbit potential in the nucleon-nucleus interaction. This suggests a simple generalization of the conventional optical model of the nucleus by the addition of a spin-orbit potential.[1] Calculations of the polarization to be expected from this model as applied to beryllium and carbon have been made in several instances.[1] The results are in qualitative agreement with the experimental measurements in that they show that a small spin-orbit potential, of the order of 1 Mev, can lead to the large polarizations observed. However, the calculations indicate that in the region of the diffraction minima, the polarization shows a double reversal of sign within an angular region of a few degrees. This double reversal, or dip, is not experimentally observed in Be or C.[2] It has been suggested that this dip as it appears in the calculations is a reflection of the use of a square-well central potential.[3] Our calculations for the polarization of 290-Mev neutrons elastically scattered from carbon indicate that if the real central potential is taken to be zero or sufficiently small compared to the imaginary potential, the dip is not eliminated by rounding off the edges of the square well.[4] However, if for a given potential-well shape the real central potential is increased sufficiently, relative to the imaginary central potential, the dip in the polarization becomes of less significance, so that experimentally it would not be observed. Both the shape of the well and the magnitudes of the potentials should of course be fixed by a comparison with the experimental scattering measurements. It is felt, though, that the measurements at 300 Mev are not sufficiently extensive or accurate to fix all the parameters involved.

In addition to the above considerations there is another still unconsidered point that has a bearing on the interpretations of the calculations. A formal analysis of the justification of the optical model of high-energy nucleon-nucleus scattering has been made, which leads to the conclusion that in general the predictions of this model are valid only for small scattering angles. The exact line between small- and large-angle scattering is, of course, not precise. For the light elements, Be and C, however, the predicted first diffraction minima and the associated polarization phenomena occur at an angle $\simeq20°$. One notes that not only is the dip in the polarization not observed, but also that the first diffraction minimum is not observed. Now if the absence of these phenomena in Be and C can be ascribed to the lack of validity of the model for large scattering angles, one would expect that for the heavier nuclei, where the diffraction and polarization occur at smaller angles, these phenomena would manifest themselves according to the predictions of the calculations. Such indeed is the case. Chamberlain, Segrè, Tripp, Wiegand, and Ypsilantis[5] have found that a dip in the polarization occurs for the elements Al, Ca, and Fe, in the region around the diffraction minima. The calculated polarization of 290-Mev neutrons elastically scattered from Al, assuming a parabolic-shaped central nuclear potential,[6] is shown in Fig. 1, along with the experimentally observed polarization for 290-Mev protons elastically scattered from aluminum. The second dip that is predicted by the model would not be expected to be experimentally observed because of the probable lack of validity of the model for such large angles of scattering.[7] The effect of including the Coulomb potential in the calculations to describe the scattering of protons will be to decrease the maximum polarization and to widen the region of the dip in the polarization.

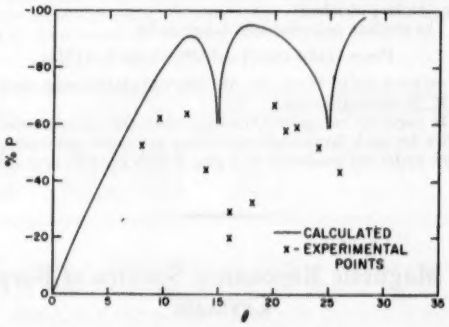

FIG. 1. The calculated polarization of 290-Mev neutrons elastically scattered from aluminum. The crosses, ×, are the experimentally measured polarizations for protons elastically scattered from aluminum as given by reference 5.

We wish to thank O. Chamberlain, E. Segrè, R. Tripp, C. Wiegand, and T. Ypsilantis for discussions relating to their experiments.

A full account of the above material will soon be submitted to *The Physical Review* for publication.

* This work was performed under the auspices of the U. S. Atomic Energy Commission.

[1] E. Fermi, Nuova cimento **11**, 407 (1954); W. Heckrotte and J. V. Lepore, Phys. Rev. **94**, 500 (1954); B. J. Malenka, Phys. Rev. **95**, 521 (1954); Snow, Sternheimer, and Yang, Phys. Rev. **94**, 1073 (1954).

[2] De Carvalho, Marshall, and Marshall, Phys. Rev. (to be published); Chamberlain, Segrè, Tripp, Wiegand, and Ypsilantis, Phys. Rev. **93**, 1430 (1954).

[3] Suggested by E. Fermi and C. N. Yang. See also calculations of R. M. Sternheimer, Phys. Rev. **95**, 587 (1954).

[4] Parabolic and Gaussian well shapes were assumed for the central potential. The spin-orbit potential was taken to be proportional to the derivative of the central potential.

[5] Chamberlain, Segrè, Tripp, Wiegand, and Ypsilantis, Phys. Rev. (to be published).

[6] The nuclear potential was taken to be

$$V=-\{(18+i30)(1-r^2/R^2)+1.2\boldsymbol{\sigma}\cdot\mathbf{L}/\hbar\}\text{Mev},$$

for $r\leq R=4.8\times10^{-13}$ cm for Al. The calculation was done with W. K. B. approximation.

[7] It must be recognized, though, that the experimental difficulties for such large-angle scattering are quite pronounced and might make the resolution of a dip, if such existed, very difficult.

Magnetic Resonance Spectra of Beryl Crystals*

L. Carlton Brown and Dudley Williams
Department of Physics, The Ohio State University, Columbus, Ohio

(Received July 1, 1954)

THE magnetic resonance absorption patterns of Be^9 and Al^{27} have been observed in single crystals of beryl, $Be_3Al_2Si_6O_{18}$. The Be^9 pattern consists of a strong central line with two weaker satellites as expected for a nucleus with $I=\frac{3}{2}$ and with a nonzero nuclear quadrupole coupling factor. The Al^{27} pattern consists of a strong central line with two pairs of satellites as expected for a nucleus with $I=5/2$ and with a nonzero quadrupole coupling factor.

The beryl crystal is hexagonal. From the structure deduced from x-ray studies,[1] it would appear that the Al^{27} nucleus is in an electric field of cylindrical symmetry with the unique electric direction parallel to the C axis or symmetry axis of the crystal. One of the principal directions of the gradient of the electric field at the site of the Be^9 nucleus is parallel to the C axis. It is probable that the largest electric gradient component is perpendicular to the C axis.

Two beryl crystals were employed in the present study. The first was a rather small crystal of optical quality. The second crystal was milky in appearance but was sufficiently large to provide a good oscillator coil filling factor. The spectrograph employed was of the superregenerative type; a constant magnetic field of 7800 gauss was provided by a large permanent magnet. The oscillator frequency was varied slowly by a clockdrive, and magnetic modulation of 40 cps was employed.

With the C axis of the crystal parallel to the magnetic field, the Al^{27} pattern was studied. The intense central line was relatively narrow; the inner satellites were broader and the weak outer satellites were extremely broad. The line frequencies predicted by theory[2] for the orientation in question are given by

$$\nu_{m\to m-1}=\mu H/Ih+(3e^2qQ/4Oh)(2m-1).$$

The observed frequencies lead to an effective value of 3.6401 ± 0.0003 nm for Al^{27} and a coupling constant $e^2qQ/h=3.070\pm0.015$ Mc/sec. The effective value of μ for Al^{27} in $AlCl_3$ solution is 3.6408 nm.

The Be^9 pattern with the C axis of the crystal parallel to the magnetic field has its central frequency $\nu_0=4.6674\pm0.0005$ Mc/sec, with a satellite separation of 116.3 ± 1 kc/sec.

The present study is being extended to include a detailed investigation of the Al^{27} and Be^9 patterns for various orientations of the crystal in the magnetic field.

The writers wish to express their appreciation to Professor Duncan McConnell and Professor Charles H. Shaw for supplying the crystals used in this study and for their advice on preparation of the crystals.

* This work was supported in part by a contract between the Office of Scientific Research of the Air Research and Development Command, Baltimore, Maryland, and The Ohio State University Research Foundation.

[1] R. W. G. Wyckoff, *Structure of Crystals* (Chemical Catalogue Company, New York, 1931).

[2] R. V. Pound, Phys. Rev. **79**, 685 (1950).

Nuclear Absorption of Negative K Particles*

Herbert DeStaebler, Jr.†
Laboratory for Nuclear Science, Massachusetts Institute of Technology, Cambridge, Massachusetts

(Received July 1, 1954)

IN a preliminary scanning of 20 000 pictures obtained with the M.I.T. multiplate cloud chamber we have observed three events that we can interpret as the nuclear absorption of negative K particles. The chamber, operated at Echo Lake, Colorado, contained eleven 0.50-inch brass plates and was triggered by a detector of high-energy nuclear interactions located directly above the chamber.

In event 86407 (see Fig. 1) an L meson (π or μ meson) and a slow V^0 particle seem to come from the point of stopping of a K particle. The probability that this is a chance association between a V^0 particle and an S particle is about 10^{-5}. The L meson stops in the chamber. The limits of its range are (29.7 and 43.7) ±2.1 g cm^{-2} brass. The V^0 particle is coplanar with the point of intersection of the K-particle and L-meson

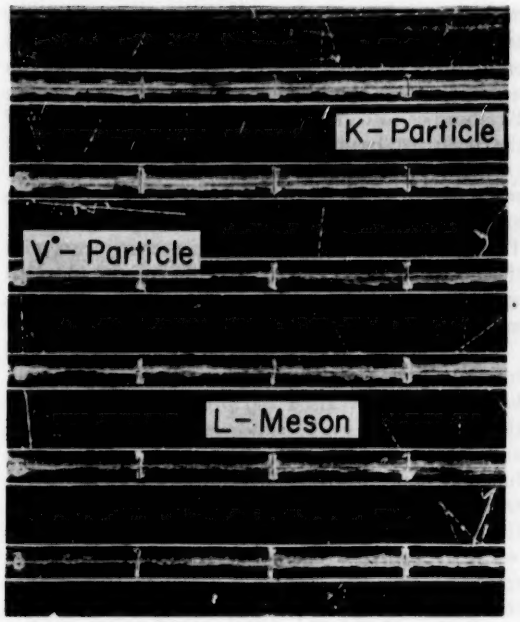

FIG. 1. Event 86407. A V^0 particle and an L meson seem to come from the point of stopping of a K particle.

tracks within the experimental error which is about 4°. The angle between the line of flight of the V^0 particle and the first section of track of the L meson is $(180°-38°)\pm2°$.

In events 91882 and 93243 a slow V^0 particle seems to come from a stopped K particle. In both events the V^0 particle travels upward and the plane of the V^0 particle intersects the line of flight of the K particle within the plate. In these two events there is no associated charged L meson as in event 86407. The probability that either of these events is a chance association between a V^0 particle and a stopped meson or proton is about $5\cdot10^{-3}$. These two events are similar to a cloud chamber event obtained by the Manchester group reported at the Duke Conference.[1]

We have calculated the limits for the Q values of the V^0 decays assuming the decay scheme $V^0\rightarrow p+\pi+Q$.[2] These values are listed in Table I. The data indicate that the V^0 particles are probably Λ^0 particles (for which Q is 37 Mev). Also listed in Table I are the kinetic energies of the V^0 particles, assumed to be Λ^0 particles, and the kinetic energy of the L meson in event 86407, assumed to be a π meson.

Although we cannot measure the mass of the primary particle in our three events accurately, our estimate of the mass, from range and ionization, suggests that the primary is a K particle.

One can interpret these events as the nuclear absorption of negative K particles according to the processes:[3]

$$K^-+n\rightarrow\Lambda^0+\pi^-, \tag{1a}$$

$$K^-+p\rightarrow\Lambda^0+\pi^0. \tag{1b}$$

This is the reciprical of the production process:

$$\pi^-+p\rightarrow\Lambda^0+\theta^0, \tag{2}$$

which has been tentatively identified at Brookhaven National Laboratory.[4] If the mass of the K particle in process (1a) is $965m_e$, the predicted kinetic energies of the Λ^0 particle and the π meson are 28 Mev and 148 Mev, respectively. If the K-particle mass is $1300m_e$ the kinetic energies of the Λ^0 particle and the π meson are 68 Mev and 280 Mev, respectively. One might expect that the motion of the nucleons in the nucleus would cause a distribution of these kinetic energies. In event 86407 the apparently low kinetic energy of the π meson and the noncolinearity of the line of flight of the Λ^0 particle and the line of flight of the π meson cannot be explained simply by the motion of the nucleon in the nucleus unless the mass of the K particle is between about 815 and $865m_e$. However, an inelastic nuclear scattering of the π meson within the nucleus could easily account for the observations. The fact that no charged π mesons were seen in events 91882 and 93243 could also be explained by a nuclear interaction of the π meson. If a neutral π meson had been ejected in either of these two events in a direction opposite to the direction of the V^0 particle, it is likely that the decay photons would not have produced any electrons in the illuminated volume of the cloud chamber.

TABLE I. Q-value and kinetic energy limits for the three events. The errors listed in the table are derived from an estimate of the uncertainties in the spatial reconstruction. The error in the kinetic energy of the π meson includes the effect of range straggling.

Event number	Limits for the Q value assuming $V_0\rightarrow p+\pi+Q$ (Mev)	Kinetic energy of Λ^0 particle (Mev)	Limits for kinetic energy of π meson (Mev)
86407	$34\pm\ 3-43\pm1$	$31\pm\ 3$	$(81-106)\pm3.5$
91882	$32\pm\ 4-60\pm8$	$30\pm\ 8$	...
93242	$33\pm14-41\pm5$	59 ± 15	...

It is a pleasure to thank Professor B. Rossi and Dr. H. S. Bridge for their help and Mr. R. A. Hewitt for his assistance in the operation of the cloud chamber.

* This research was supported in part by the joint program of the U. S. Office of Naval Research and the U. S. Atomic Energy Commission.

† National Science Foundation Predoctoral Fellow.

[1] K. H. Barker, Proceedings of the Duke University Cosmic-Ray Conference, December, 1953 (unpublished), pp. II-20.

[2] We calculate the limiting values of Q by using transverse momentum balance and deriving momentum limits for the proton and π meson from measured range limits and estimated ionization limits.

[3] M. Goldhaber, Phys. Rev. **92**, 1279 (1953).

[4] Fowler, Shutt, Thorndike, and Whittemore, Phys. Rev. **93**, 861 (1954). An event also supporting process (2) was reported by R. W. Thompson at the 1954 Washington Meeting of the American Physical Society [Phys. Rev. **95**, 661 (1954)].

The Reaction $p+p\rightarrow\pi^{+}+d$ with Polarized Protons*†

F. S. Crawford, Jr., and M. L. Stevenson
Radiation Laboratory, University of California, Berkeley, California
(Received June 21, 1954)

MARSHAK and Messiah[1] have pointed out that if mesons are present in both S and P states in the reaction $p+p\rightarrow\pi^{+}+d$, then it is possible to obtain, through interference, a large azimuthal asymmetry in the angular distribution, provided that a polarized proton beam (or target) is used. If a substantial amount of such an asymmetry is indeed observed, then the relative amounts and phases of S and P waves can be estimated. De Carvalho *et al.*[2] looked for an asymmetry in meson production in the course of examining possible asymmetric background in the scattering from hydrogen of 439-Mev polarized protons. They obtained a null result of asym$=-0.07\pm0.085$.

Following the Rochester technique,[3] Chamberlain and co-workers[4] have obtained an external beam of 315-Mev protons from the Berkeley cyclotron having a polarization[5] estimated to be $|P|=|2\langle S_y\rangle|=0.73$. With this beam, we have made measurements of the left-right asymmetry of meson production in the plane perpendicular to the proton polarization, using coincidence detection of the meson and deuteron, and a liquid hydrogen target. Measurements were made at incident proton energies of 317 and 310 Mev. The results of the raw data are $(R-L)/(R+L)=0.16\pm0.03$ and 0.23 ± 0.04 at 317 and 310 Mev, respectively. R and L refer to the direction of the produced meson, as seen by the incident proton. (The polarized proton beam is produced by a "left" scatter.[4])

In the notation of Marshak and Messiah, $(R-L)/(R+L)=PQ(A\sin\theta)/(A+\cos^2\theta)$. Here, $A+\cos^2\theta$ is the angular dependence of the differential cross section in the c.m. system for unpolarized protons, and Q is the interesting quantity, involving the relative amplitudes and phases of the transitions involved. It is apparent that the angular factor becomes unity, independent of A, at $\theta=90°$. However, measurements were made at 69° because of meson energy loss in the target. We used $A=0.40$ and 0.49[6] at 317 and 310 Mev, respectively, to average the angular factor. With $|P|=0.73$ this gives $|Q|=0.37\pm0.06$ and 0.42 ± 0.07 at 317 and 310 Mev, respectively, Analysis[7] of the excitation function shows that Q is expected to vary by less than ten percent between 310 and 317 Mev, so that we may conveniently combine these data to obtain an average $|Q|=0.39\pm0.05$ at an average proton energy of 314 Mev. $(\text{K.E.}_{\pi})_{\text{c.m.}}=11.3$ Mev.

We satisfied ourselves as to the following points: uniformity of counter sensitivity, insensitivity of counters to stray fields, target and counter alignment, exclusion of $p+p\rightarrow\pi^{+}+p+n$, and reproducibility during many interchanges of counter positions. As an over-all check, the experiment was repeated using the ordinary "scattered" beam, which has been shown[4] to be unpolarized. The beam energy was degraded with a Be absorber to correspond to the measured energy of the polarized beam. At 317 and 310 Mev, $(R-L)/(R+L)=-0.02\pm0.06$ and 0.04 ± 0.04 were obtained, respectively. These results have convinced us that no hidden asymmetries were present in the equipment. The average of the left and right measurements with the polarized beam agreed with the results obtained with the unpolarized beam, and with our previous measurements.[6]

Rosenfeld[7] has compiled data on pion production from nucleons and compared it with the phenomenological theory of Watson and Brueckner.[8] In his notation, $Q=\sqrt{2}\eta_c\eta(\eta^2+\eta_c^2)^{-1}\sin(\psi-\tau_1)$, where $\eta=p_\pi/m_\pi c$, and η_c is obtained by fitting the 90° (c.m.) excitation function data to $4\pi d\sigma_{10}(90°)/d\Omega=\alpha_{10}(\eta+\eta^3\eta_c^{-2})$. The terms in η and η^3 come from S and P mesons, respectively. $S_0/S_2+\sqrt{\frac{1}{2}}=|S_0/S_2+\sqrt{\frac{1}{2}}|\exp(i\psi)$, and $S_1/S_2=|S_1/S_2|\exp(i\tau_1)$, where S_0 and S_2 are the complex transition amplitudes giving P-state meson production from $^1S_0$ and $^1D_2$ protons, respectively, and S_1 is the amplitude for S-state meson production from $^3P_1$ protons. Our data[6] yields $\eta_c=0.62\pm0.16$. With the measured Q, at $\eta=0.41$, this gives $|\sin(\psi-\tau_1)|=0.61\pm0.10$.

The authors wish to thank Dr. Hugh Bradner, Mr. Robert E. Donaldson, Dr. Myron L. Good, Mr. H. Brook Knowles, Mr. R. Tripp, and Mr. T. Ypsilantis for assistance during the measurements.

* This work has been performed under the auspices of the U. S. Atomic Energy Commission.

† This work was reported as a post-deadline paper at the Minneapolis meeting of the American Physical Society, June 28–30, 1954 [Bull. Am. Phys. Soc. **29**, No. 5 (1954)].

[1] R. E. Marshak and A. M. L. Messiah, Nuovo cimento **11**, 337 (1954).
[2] De Carvalho, Heiberg, Marshall, and Marshall, Phys. Rev. **94**, 1796 (1954).
[3] Oxley, Cartwright, Rouvina, Baskir, Klein, King, and Skillman, Phys. Rev. **91**, 419 (1953).
[4] Chamberlain, Segrè, Tripp, Wiegand, and Ypsilantis, Phys. Rev. **93**, 1430 (1954).
[5] Chamberlain, Segrè, Tripp, Wiegand, and Ypsilantis, Phys. Rev. (to be published).
[6] F. S. Crawford, Jr., and M. L. Stevenson, University of California Radiation Laboratory Reports UCRL 2187, UCRL 2188 (unpublished) and work to be published.
[7] A. H. Rosenfeld, Phys. Rev. (to be published).
[8] K. M. Watson and K. A. Brueckner, Phys. Rev. **83**, 1 (1951).

Regularity in Magnetic Moments of Odd Nuclei*

Morris F. Scharff†
Department of Physics, University of Chicago, Chicago, Illinois
(Received June 28, 1954)

WANGSNESS[1] and de-Shalit[2] have observed a regularity between the magnetic moment of an

odd-even nucleus (Z, N) and that of the nucleus $(Z+2, N)$ or $(Z, N+2)$. De-Shalit formulated this regularity in the rule: An addition of either two protons or two neutrons to an odd nucleus, provided it leaves its spin I unchanged, pushes its magnetic moment toward the Schmidt line.

TABLE I. Comparison of intrinsic gyromagnetic ratios in odd-even nuclei (Z,N) and $(Z+2, N+2)$.[a]

Nucleus$_1$	G_1	State$_1$	Nucleus$_2$	G_2	State$_2$	G_1–G_2
H^3	2.98	$s_{1/2}+$	Li^7	2.26	$p_{3/2}+$	+0.72
Li^7	2.26	$p_{3/2}+$	B^{11}	1.69	$p_{3/2}+$	+0.57
Be^9	1.18	$p_{3/2}+$	C^{13}	2.11	$p_{1/2}-$	−0.93
B^{11}	1.69	$p_{3/2}+$	N^{15}	2.85	$p_{1/2}-$	−1.16
C^{13}	2.11	$p_{1/2}-$	O^{17}	1.89	$d_{5/2}+$	+0.22
N^{15}	2.85	$p_{1/2}-$	F^{19}	2.63	$s_{1/2}+$	+0.22
F^{19}	2.63	$s_{1/2}+$	Na^{23}	1.70	$D_{3/2}+$	+0.93
Na^{23}	1.70	$D_{3/2}+$	Al^{27}	1.64	$d_{5/2}+$	+0.06
Mg^{25}	0.85	$d_{5/2}+$	Si^{29}	0.55	$s_{1/2}+$	+0.30
Al^{27}	1.64	$d_{5/2}+$	P^{31}	1.13	$s_{1/2}+$	+0.51
Si^{29}	0.55	$s_{1/2}+$	S^{33}	1.07	$d_{3/2}-$	−0.52
P^{31}	1.13	$s_{1/2}+$	Cl^{35}	1.63	$d_{3/2}-$	−0.50
Cl^{35}	1.63	$d_{3/2}-$	K^{39}	2.35	$d_{3/2}-$	−0.72
Cl^{37}	1.86	$d_{3/2}-$	K^{41}	2.64	$d_{3/2}-$	−0.78
K^{41}	2.64	$d_{3/2}-$	Sc^{45}	1.76	$f_{7/2}+$	+0.88
Ca^{43}	1.32	$f_{7/2}+$	Ti^{47}	1.10	$F_{5/2}+$	+0.22
Ti^{49}	1.10	$f_{7/2}+$	Cr^{53}	0.47	$p_{3/2}+$	+0.63
V^{51}	2.15	$f_{7/2}+$	Mn^{55}	1.85	$F_{5/2}+$	+0.30
Cr^{53}	0.47	$p_{3/2}+$	Fe^{57}	∼0	$p_{3/2}+$	+0.47
Mn^{55}	1.85	$F_{5/2}+$	Co^{59}	1.65	$f_{7/2}+$	+0.20
Co^{59}	1.65	$f_{7/2}+$	Cu^{63}	1.23	$p_{3/2}+$	+0.42
Cu^{65}	1.38	$p_{3/2}+$	Ga^{69}	1.02	$p_{3/2}+$	+0.36
Ga^{71}	1.56	$p_{3/2}+$	As^{75}	0.44	$p_{3/2}+$	+1.12
Ge^{73}	0.88	$g_{9/2}+$	Se^{77}	1.60	$p_{1/2}-$	−0.72
As^{75}	0.44	$p_{3/2}+$	Br^{79}	1.11	$p_{3/2}+$	−0.67x
Br^{81}	1.27	$p_{3/2}+$	Rb^{85}	2.11	$f_{5/2}-$	−0.84
Kr^{83}	0.97	$g_{9/2}+$	Sr^{87}	1.09	$g_{9/2}+$	−0.12x
Rb^{85}	2.11	$f_{5/2}-$	Y^{89}	2.41	$p_{1/2}-$	−0.30
Sr^{87}	1.09	$g_{9/2}+$	Zr^{91}	1.1	$d_{5/2}+$	−0.01x
Y^{89}	2.42	$p_{1/2}-$	Nb^{93}	2.17	$g_{9/2}+$	+0.25
Zr^{91}	1.1	$d_{5/2}+$	Mo^{95}	0.91	$d_{5/2}+$	+0.19
Tc^{99}	1.68	$g_{9/2}+$	Rh^{103}	2.26	$p_{1/2}-$	−0.58
Rh^{103}	2.26	$p_{1/2}-$	Ag^{107}	2.34	$p_{1/2}-$	−0.08
Ag^{109}	2.39	$p_{1/2}-$	In^{113}	1.49	$g_{9/2}+$	+0.90
Cd^{111}	0.60	$s_{1/2}+$	Sn^{115}	0.92	$s_{1/2}+$	−0.32x
Cd^{113}	0.62	$s_{1/2}+$	Sn^{117}	1.00	$s_{1/2}+$	−0.38x
Sn^{119}	1.05	$s_{1/2}+$	Te^{123}	0.73	$s_{1/2}+$	+0.32
Sb^{123}	1.72	$g_{7/2}-$	I^{127}	0.81	$d_{5/2}+$	+0.91
Te^{125}	0.88	$s_{1/2}+$	Xe^{129}	0.77	$s_{1/2}+$	+0.11
I^{127}	0.81	$d_{5/2}+$	Cs^{131}	1.48	$d_{5/2}+$	−0.67x
I^{129}	1.64	$g_{7/2}-$	Cs^{133}	1.69	$g_{7/2}-$	−0.05
Xe^{131}	1.14	$d_{3/2}-$	Ba^{135}	1.39	$d_{3/2}-$	−0.25
Nd^{143}	1.0	$f_{7/2}+$	Sm^{147}	0.32	$f_{7/2}+$	+0.68
Nd^{145}	0.62	$f_{7/2}+$	Sm^{149}	0.26	$f_{7/2}+$	+0.36
Ta^{181}	2.56	$g_{7/2}-$	Re^{185}	1.14	$d_{5/2}+$	+1.42
Re^{187}	1.18	$d_{5/2}+$	Ir^{191}	2.72	$d_{3/2}-$	−1.54
Ir^{193}	2.72	$d_{3/2}-$	Au^{197}	2.77	$d_{3/2}-$	−0.05
Pt^{195}	1.82	$p_{1/2}-$	Hg^{199}	1.51	$p_{1/2}-$	+0.31x
Tl^{205}	1.63	$s_{1/2}+$	Bi^{209}	1.06	$h_{9/2}-$	+0.57x

[a] Nuclei giving different signs in the last two columns are marked with x after the figure in the last column.

Another such regularity has been observed by the author between the magnetic moment of an odd-even nucleus (Z, N) and that of the nucleus $(Z+2, N+2)$. It may be formulated as follows: The addition of an alpha particle to an odd nucleus pushes its magnetic moment toward the Schmidt line if the spin of the heavier nucleus is given by $I=l-\frac{1}{2}$ and away from the Schmidt line if the spin of the heavier nucleus is given by $I=l+\frac{1}{2}$. The value of l is that assigned the last odd nucleon by the jj-coupling shell model.[3]

An unambiguous definition of distance from the Schmidt lines in the case of nuclei with different spins I is obtained by solving the Landé formula for g_s, taking g_l equal unity for odd proton nuclei and zero for odd neutron nuclei, and μ and I equal their experimentally measured values. We define $G=|g_s/2|$, i.e., the absolute value of the "quenched" intrinsic moment[4] of the odd particle. Then both proton Schmidt lines are located at $G=2.79$ and both neutron Schmidt lines at $G=1.91$. All values of G were obtained in the above manner except those for Na^{23}, Ti^{47}, and Mn^{55} whose experimentally observed magnetic moments were multiplied by $j/(j-1)$ to compensate for the coupling of nucleons of total angular momentum j to the spin $I=j-1$.

In Table I we have listed all pairs of odd nuclei whose magnetic moments are experimentally known, the odd-particle state assigned by the shell model, and the value of G. The + or − following the state designation indicates whether the state has $I=l\pm\frac{1}{2}$ (except for the three nuclei mentioned above, where the + indicates the state was formed by nucleons with $j=l+\frac{1}{2}$). We shall take an increase in the value of G to mean motion toward the Schmidt line, although a few light nuclei have G greater than the free nucleon values.

The regularity may be observed by comparing the signs in the last two columns. These match in 41 of 49 cases, a circumstance which would happen by chance less than one time in five million. A comparison of the signs in the last column with those for the lighter nucleus shows they match in 27 of the cases, about the proportion to be expected by chance. The correspondence of the last two columns appears to hold regardless of the sign of the lighter nucleus. It is an interesting feature that the rule depends on the state of the heavier nucleus only.

The exceptions have been marked with an "x" after the figure in the last column. There are no exceptions for nuclei below $A=75$; the first 24 pairs obey the rule. Two of the exceptional pairs are $As^{75}-Br^{79}$ and $I^{127}-Cs^{131}$. As^{75} and I^{127} are the only two nuclei which fall within an odd-proton "forbidden zone" bounded by the two Dirac lines at $G=1$. The other six exceptions occur near the magic numbers 50 and 82, associated with the marked phenomena of closed nuclear shells.

The author wishes to thank Professor Maria Goeppert-Mayer for her advice and guidance throughout his research.

* This work was performed under a U. S. Atomic Energy Commission Pre-Doctoral Fellowship.

† Now at the University of California Radiation Laboratory, Livermore, California.

[1] R. Wangsness, Phys. Rev. **78**, 620 (1950).
[2] A. de-Shalit, Phys. Rev. **80**, 103 (1950).
[3] M. G. Mayer, Phys. Rev. **78**, 16, 22 (1950).
[4] F. Bloch, Phys. Rev. **83**, 839 (1951).

Moments of Na^{23}†

MORRIS F. SCHARFF*
Department of Physics, University of Chicago, Chicago, Illinois
(Received June 28, 1954)

SAGALYN[1] recently measured the nuclear electric quadrupole moment of Na^{23}. He shows that a $(d_{5/2})^3$ configuration of the odd protons with a resultant spin $I=3/2$ in the jj-coupling scheme[2] gives $Q=0$, in disagreement with the experimental value $Q=+0.1 \pm 0.06\times10^{-24}$ cm^2. It is the purpose of this note to point out that a configuration including the four $d_{5/2}$ neutrons of Na^{22}, that is, $[(d_{5/2})^3_P(d_{5/2})^4_N]_{I=3/2}$, can give agreement with experimental values of both the magnetic dipole and electric quadrupole moment.

The calculations were performed using the configuration $[(d_{5/2})^3_P(d_{5/2})^2_N]_{I=3/2}$ which gives the same magnetic moment as the above configuration and the quadrupole moment with the reversed sign. To obtain a wave function ψ with $M_I=3/2$, we wrote down all 33 combinations of individual particle wave-functions $u(d_{5/2}, m_j)$ of three protons and two neutrons obeying the Pauli principle, whose m_j values sum to 3/2. These "base vectors" were normalized and antisymmetrized with respect to space-spin and isotopic spin parts.

A linear combination of the base vectors with arbitrary coefficients is an eigenfunction of $M_I=3/2$. To make it an eigenfunction of $I=3/2$ also, we apply the operator $I^+\psi(I=3/2, M_I=3/2)=0$. The result of this operation is 28 linear equations involving the 33 coefficients. We used matrix methods to solve these equations and obtain the five linearly independent solutions φ_i, which give the general solution

$$\psi=\sum_{i=1}^{5} a_i\varphi_i \Big/ \sum_{i=1}^{5} a_i^2, \tag{1}$$

where the a_i are arbitrary constants.

We may reduce the arbitrariness of the solution by requiring that ψ also be an eigenfunction of the isotopic spin operators with eigenvalues $T=1/2$ and $T_z=-1/2$, for the isotopic spin is expected to be a good quantum number is low-Z nuclei. This requirement leads to two conditions on the coefficients a_i, which, for our φ_i, were these:

$$\begin{aligned} 2a_2+a_3+3a_4+3a_5&=0,\\ 5a_1/2-6a_2-4a_3+a_4+6a_5&=0. \end{aligned} \tag{2}$$

These two conditions plus the condition of normalization applied in Eq. (1) reduce to two the degrees of freedom with which we may choose the coefficients a_i in the solution. If we take $a_1=2$, $a_2=a_3=0$, $a_4=1$, and $a_5=-1$, we find $\mu=1.98$ nm and $Q=0$, in agreement with calculations by Flowers[3] for a state of seniority $v=3$. If we choose $a_1=3.2$, $a_2=-1.5$, $a_3=3$, $a_4=1$, and $a_5=-1$, we calculate $\mu=2.221$ nm and $Q=+0.095\times10^{-24}$ cm^2, in good agreement with the measured magnetic moment $\mu=2.217$ nm and Sagalyn's value for Q.

The value of Q is sensitive, and the value of μ insensitive to the choice of coefficients within a certain range. Thus, Q may be made to vary between $+0.04$ and $+0.105$ while μ takes values between 2.19 and 2.25 nm. If we interchange neutrons and protons, this calculation, with the second set of coefficients, predicts for the nucleus Ne^{21}, $Q=-0.195\times10^{-24}$ cm^2 and $\mu=-0.49$ nm.

The author wishes to thank Maria Goeppert Mayer for her aid and encouragement in the course of his research.

† This work was performed under a U. S. Atomic Energy Commission Predoctoral Fellowship.

* Now at the University of California Radiation Laboratory, Livermore, California.

[1] P. L. Sagalyn, Phys. Rev. **94**, 885 (1954).
[2] M. G. Mayer, Phys. Rev. **78**, 16, 22 (1950).
[3] B. H. Flowers, Phil. Mag. **43**, 1330 (1952).

CONTENTS—Continued

Letters to the Editor

Ionization Energies of Groups III and V Elements in Germanium . . . . . T. H. Geballe and F. J. Morin 1085

Low-Temperature Luminescence of Cadmium Sulfide . . . . . L. R. Furlong 1086

Energy Levels and Photoconductivity in Electron-Bombarded Germanium . . . . . H. Y. Fan, W. Kaiser, R. E. Kinzer, K. Lark-Horovitz, and R. R. Pepper 1087

Paramagnetic Resonance Absorption in Graphite . . . . . G. E. Hanig, B. Smaller, and E. L. Yasaitis 1088

Measurement of the Spin Paramagnetism of Conduction Electrons . . . . . R. T. Schumacher, T. R. Carver, and C. P. Slichter 1089

Paramagnetic Susceptibility of Conduction Electrons . . . . . David Pines 1090

Self-Powered Semiconductor Amplifier . . . . . C. G. B. Garrett and W. H. Brattain 1091

Photovoltaic Effect in InAs . . . . . Robert M. Talley and Dorothy P. Enright 1092

Interaction of Electrons with Grain Boundaries . . . . . M. H. Cohen and C. S. Barrett 1094

Low-Temperature Thermal Conductivity of a Canadian Natural Graphite . Alan W. Smith 1095

Paramagnetic Resonance Absorption in Sodium Pictonyl Acetate . . . . . Clyde A. Hutchison, Jr., and W. Burton Lewis 1096

Isotope Shift in X-Ray Spectra of Heavy Elements . . . . . G. Igo and M. S. Wertheim 1097

Annihilation of Positrons in Liquid Helium . . . . . Frank L. Hereford 1097

Low-Temperature Bleaching and Restoration of Color Centers . . . . . A. Halperin and G. F. J. Garlick 1098

Polarization in $n-p$ Scattering at 160-280 Mev . A. Roberts, J. Tinlot, and E. M. Hafner 1099

Meson-Proton Scattering Phase Shift Analysis . . . . . H. A. Bethe and F. de Hoffmann 1100

Possible Example of the Annihilation of a Heavy Particle . . . . . H. S. Bridge, H. Courant, H. DeStaebler, Jr., and B. Rossi 1101

Anomalous Event Observed in Photographic Emulsion . . . . . J. H. Noon, M. F. Kaplon, and J. Crussard 1103

Polarization of High-Energy Deuterons . . . . . Owen Chamberlain, Emilio Segrè, Robert Tripp, Clyde Wiegand, and Thomas Ypsilantis 1104

Mechanism of Proton Polarization in High-Energy Collisions . . . . . Owen Chamberlain, Emilio Segrè, Robert Tripp, Clyde Wiegand, and Thomas Ypsilantis 1105

Nuclear Elastic Scattering of Protons . . . . . Evans Hayward and E. G. Fuller 1105

Theory of Multiple Coulomb Scattering from Extended Nuclei . . . . . Leon N. Cooper and James Rainwater 1107

Polarization of Nucleons Elastically Scattered from Nuclei . . . . . Warren Heckrotte and Joseph V. Lepore 1109

Magnetic Resonance Spectra of Beryl Crystals . . L. Carlton Brown and Dudley Williams 1110

Nuclear Absorption of Negative K Particles . . . . . Herbert DeStaebler, Jr. 1110

Reaction $p+p \rightarrow \pi^+ + d$ with Polarized Protons . . F. S. Crawford, Jr., and M. L. Stevenson 1112

Regularity in Magnetic Moments of Odd Nuclei . . . . . Morris F. Scharff 1112

Moments of He^3 . . . . . Morris F. Scharff 1114